JOHANNES GUTENBERG UNIVERSITÄT MAINZ

Chromium(III) Luminophores:

Photochemical Property Enhancement and Tuning

Dissertation zur Erlangung des Grades eines

Doctor rerum naturalium (Dr. rer. nat.)

des Fachbereichs 09

Chemie, Pharmazie, Geographie und Geowissenschaften

der Johannes Gutenberg-Universität Mainz

im Promotionsfach Chemie

vorgelegt von

Florian Reichenauer

geboren in Wiesbaden.

Mainz, 2024

Florian Reichenauer
Chromium(III) Luminophores: Photochemical Property Enhancement and Tuning
Dissertation
Date of submission: 14th of November 2024
First reviewer: [redacted]
Second reviewer: [redacted]

Johannes Gutenberg University Mainz
Faculty 09
Department of Chemistry
Duesbergweg 10-14
55128 Mainz

This thesis was typeset with Microsoft Word. The formatting follows the *Clean Thesis* style developed by Ricardo Langner. The design of the *Clean Thesis* style is inspired by user guide documents from Apple Inc.

Download the *Clean Thesis* style at http://cleanthesis.der-ric.de/.

This thesis was written in the period from November 2019 to November 2024 at the Department of Chemistry of the Johannes Gutenberg University Mainz under the supervision of [redacted].

"I, Florian Reichenauer, hereby declare that I have written this dissertation independently and have not used any sources or aids (including AI-based applications or tools) other than those specified. All verbatim or analogous citations and quotations are labeled and referenced. I confirm that I have not used any aids whose use has been explicitly excluded by the examiner.

By submitting this work, I accept responsibility for the overall product . I have checked the accuracy of the statements and content to the best of my knowledge and belief.

I am aware that a violation of the above points has consequences under examination law and may in particular result in the doctoral work being assessed as "failed". Enrolment can be revoked for up to two years if students cheat twice or more in examinations (Section 69 (4) and (5) HochSchG)."

Mainz, 14th of November 2024

Dean: [redacted]

First reviewer: [redacted]

Second reviewer: [redacted]

Date of the oral exam:

Abstract

For the targeted optimization of emissive transition metal complexes, it is essential to systematically and reliably predict photophysical properties. Quantum chemical characterization of previously analyzed compounds aids in understanding structure-property relationships, while comparison with experimental data validates the predictive power of theoretical models for analogous systems. This acquired knowledge can then be applied to design new photoactive complexes with enhanced properties before experimental methods are accessible.

This work applies this fundamental approach to highly luminescent chromium complexes—referred to as molecular rubies—focusing on the synthesis, analysis, and optimization of photophysical properties. Since the discovery of the $[Cr(ddpd)_2]^{3+}$ complex in 2015, molecular rubies have become a pioneering class in 3d-metal photochemistry, recognized for their outstanding near-infrared luminescence efficiency, high photostability, and chemical versatility. Building on the design principles of $[Cr(ddpd)_2]^{3+}$, numerous derivatives demonstrate significant potential for applications in optical sensing, photocatalysis, and circularly polarized emission.

However, a systematic approach to the targeted modification of optical properties, such as shifting emission into the visible range, has been lacking for spin-flip systems like molecular rubies. Through quantum chemically supported structural design, this work achieves an increase in emission energy, leading to the synthesis of the first molecular chromium(III) complex with visible-light luminescence, high quantum yield of 20%, and millisecond-scale excited-state lifetime. The red phosphorescence of $[Cr(bpmp)_2]^{3+}$ can be reversibly switched on and off by *p*H regulation, enabling sensory applications like ratiometric optical *p*H measurements in combination with a *p*H-insensitive dye. The elevated energy of the photoactive state expands the applicability of molecular rubies in photocatalysis, as it allows the activation of a broader substrate scope. With the efficient sensitization of anthracenes for triplet-triplet annihilation photon upconversion and cycloadditions via a previously underexplored doublet-triplet energy transfer, this work demonstrates that molecular rubies are a viable alternative to precious metal complexes in selected photochemical systems.

The improved redox behavior of $[Cr(bpmp)_2]^{3+}$, with a favorable ligand-centered reduction, results in a high oxidation potential in the excited state, rendering it

particularly attractive for photoredox catalysis. The metal-centered nature of spin-flip states generally enables largely independent optimization of electrochemical and optical properties, as proven in this work through the controlled adjustment of the ground-state redox potential via peripheral substituents in the analogous complexes $[Cr(ddpd^{X})_2]^{3+}$ (X = CF_3, OMe, NMe_2).

In contrast to charge-transfer states, which follow well-established design rules such as substitution effects, metal-centered spin-flip states have, to date, been tunable only through qualitative criteria. Predicting spin-flip energies depends critically on interelectronic interactions and metal-ligand bond covalency, as described by the nephelauxetic effect. Based on the isostructural complex series $[Cr(ddpd)_2]^{3+}$, $[Cr(bpmp)_2]^{3+}$, $[Cr(bpop)_2]^{3+}$ and $[Cr(bptp)_2]^{3+}$ with variations in the ligand backbone, this work provides unprecedented insights into the energies and dynamics of spin-flip states and reveals the influence of structural and electronic factors on their emission. It highlights how spin-orbit coupling of heavier atoms, Jahn-Teller distortions of excited states, and thermally activated multiphonon relaxation can promote non-radiative decay in molecular rubies and thus give valuable design criteria for future systems.

In addition to enhancing photophysical properties, this work focuses on developing new synthetic methods, particularly for heteroleptic molecular rubies. The complexes $[CrL^{X}L^{Y}]^{3+}$ (L^{X}, L^{Y} = ddpd, bpmp, bptp), combined with their computational analysis, provide insights into spin-flip energy correlations based on an additive nephelauxetic effect of ligands, which allows for a precise prediction and fine-tuning of emission in analogous systems through strategic ligand pairing.

Finally, the study investigates the potential of additives such as Lewis acids for flexible modification of the optical properties in the complexes $[Cr(ddad)_2]^{3+}$ and $[Cr(bptp)(ddad)]^{3+}$, which feature free donor sites, and introduces a design strategy for red-shifting spin-allowed absorption in molecular rubies.

In summary, this work builds a deeper understanding of spin-flip system photophysics through spectroscopic, electrochemical, and theoretical investigations of new and established chromium(III) complexes. By optimizing optical and electrochemical properties and assessing potential applications, it substantiates the viability of this class of compounds as a competitive and complementary alternative to noble metal complexes in photochemistry.

Kurzzusammenfassung

Für die gezielte Optimierung emissiver Übergangsmetallkomplexe ist es von zentraler Bedeutung, photophysikalische Eigenschaften systematisch und zuverlässig vorhersagen zu können. Die quantenchemische Beschreibung bereits charakterisierter Verbindungen erleichtert das Verständnis von Struktur-Eigenschafts-Beziehungen, während der Vergleich mit experimentellen Daten die Vorhersagekraft des theoretischen Modells für analoge Systeme validiert. Das gewonnene Wissen kann dann für das Design neuer photoaktiver Komplexe mit verbesserten Eigenschaften genutzt werden, noch bevor ein experimenteller Zugang besteht.

Diese Arbeit wendet diesen Ansatz auf stark lumineszierende Chrom-Komplexe – sogenannte Molekulare Rubine – an, mit besonderem Fokus auf Synthese, Analyse und Optimierung photophysikalischer Eigenschaften. Seit der Entdeckung des Komplexes $[Cr(ddpd)_2]^{3+}$ im Jahr 2015 haben sich Molekulare Rubine als Pionierklasse in der Photochemie der 3d-Metalle etabliert, bekannt für ihre herausragende Lumineszenzeffizienz im NIR-Bereich, hohe Photostabilität und chemische Vielseitigkeit. Aufbauend auf dem Designprinzip von $[Cr(ddpd)_2]^{3+}$ bieten viele dieser Verbindungen großes Potenzial für Anwendungen in optischer Sensorik, Photokatalyse und zirkular polarisierter Emission.

Ein systematischer Ansatz zur gezielten Modifikation optischer Eigenschaften, wie der Verschiebung der Emission in den sichtbaren Bereich, fehlte bisher für Spin-Flip-Systeme wie die Molekularen Rubine. Durch quantenchemisch gestütztes Strukturdesign wurde in dieser Arbeit die Emissionsenergie erhöht und der erste molekulare Chrom(III)-Komplex mit Lumineszenz im sichtbaren Spektralbereich, bei gleichzeitig hoher Quantenausbeute von 20% und Lebensdauer im Millisekundenbereich, synthetisiert. Die rote Phosphoreszenz von $[Cr(bpmp)_2]^{3+}$ lässt sich durch *p*H-Regulierung reversibel an- und ausschalten und ermöglicht sensorische Anwendungen wie ratiometrische optische *p*H-Messungen in Kombination mit einem *p*H-unempfindlichen Farbstoff. Die erhöhte Energie des photoaktiven Zustands erweitert die Einsatzmöglichkeiten molekularer Rubine in der Photokatalyse, da sie die Aktivierung eines breiteren Substratspektrums erlaubt. Mit der effizienten Sensibilisierung von Anthracenen für Triplett-Triplett-Annihilation-Photonenhochkonversion und Cycloadditionen über einen bislang wenig erforschten Dublett-Triplett-Energietransfer zeigt diese Arbeit, dass Molekulare Rubine eine Alternative zu Edelmetallkomplexen in ausgewählten photochemischen Systemen darstellen.

Das verbesserte Redoxverhalten von $[Cr(bpmp)_2]^{3+}$, mit bevorzugt ligandenzentrierter Reduktion, führt zu einem hohen Oxidationspotential im angeregten Zustand und macht diese Verbindung besonders attraktiv für Anwendungen in der Photoredoxkatalyse. Die metallzentrierte Natur der Spin-Flip-Zustände ermöglicht generell eine weitgehend unabhängige Optimierung der elektrochemischen und optischen Eigenschaften, was in dieser Arbeit durch die kontrollierte Verschiebung des Grundzustandsredoxpotentials mithilfe von Peripheriesubstituenten mit den analogen Komplexen $[Cr(ddpd^X)_2]^{3+}$ (X = CF_3, OMe, NMe_2) bewiesen wird.

Im Gegensatz zu ladungsseparierten Charge-Transfer-Zuständen, die etablierten Designregeln wie Substitutionseffekten folgen, können metallzentrierte Spin-Flip-Zustände bisher nur nach qualitativen Kriterien getunt werden. Für die Vorhersage von Spin-Flip-Energien sind interelektronische Wechselwirkungen und die Metall-Ligand-Bindungskovalenz, beschrieben durch den nephelauxetischen Effekt, entscheidend. Anhand der isostrukturellen Komplexserie $[Cr(ddpd)_2]^{3+}$, $[Cr(bpmp)_2]^{3+}$, $[Cr(bpop)_2]^{3+}$ und $[Cr(bptp)_2]^{3+}$ mit unterschiedlichem Liganden-Rückgrat liefert diese Arbeit neue Einblicke in die Energien und Dynamiken von Spin-Flip-Zuständen und zeigt den Einfluss struktureller und elektronischer Faktoren auf deren Emission. Es wird verdeutlicht, wie die Spin-Bahn-Kopplung schwerer Atome, Jahn-Teller-Verzerrungen angeregter Zustände und thermisch aktivierte Multiphonon-Relaxation den strahlungslosen Zerfall in Molekularen Rubinen fördern können und somit wertvolle Designkriterien für zukünftige Systeme liefern.

Neben der Verbesserung photophysikalischer Eigenschaften konzentriert sich diese Arbeit auf die Entwicklung neuer Synthesemethoden, insbesondere für heteroleptische Molekulare Rubine. Die Komplexe $[CrL^XL^Y]^{3+}$ (L^X, L^Y = ddpd, bpmp, bptp) bieten zusammen mit ihrer computergestützten Beschreibung Einblicke in Spin-Flip-Energie-Korrelationen auf Basis eines additiven nephelauxetischen Effekts der Liganden, was künftig eine präzisere Vorhersage und Feinabstimmung der Emission analoger Systeme durch gezielte Ligandenpaarungen erlaubt.

Abschließend wird untersucht inwiefern Additive wie Lewis-Säuren die optischen Eigenschaften der Komplexe $[Cr(ddad)_2]^{3+}$ und $[Cr(bptp)(ddad)]^{3+}$ mit freien Donorstellen flexibel modifizieren können und eine Designstrategie zur Rotverschiebung der spin-erlaubten Absorption in Molekularen Rubinen vorgestellt.

Zusammenfassend baut diese Arbeit durch spektroskopische, elektrochemische und theoretische Untersuchung neuer und bekannter Chrom(III)-Komplexe ein tieferes Verständnis der Photophysik von Spin-Flip Systemen auf. Durch die Optimierung optischer und elektrochemischer Eigenschaften sowie der Prüfung auf Anwendungen untermauert sie das Potenzial dieser Substanzklasse als konkurrenzfähige und ergänzende Alternative zu Edelmetallkomplexen in der Photochemie.

Contents

List of Abbreviations

acac$^-$	acetylacetonate
bISC	back-intersystem crossing
bpi$^-$	1,3-bis(pyridin-2-ylimino)isoindolin-2-ide
bpmp	2,6-bis(2-pyridylmethyl)pyridine
bpop	2,6-bis(pyridin-2-yloxy)pyridine
bptp	2,6-bis(pyridin-2-ylthio)pyridine
bpy	2,2‘-bipyridine
btz	3,3‘-dimethyl-1,1‘-bis(*p*-tolyl)-4,4‘-bis(1,2,3-triazol-5-ylidene)
C^P$^-$	deprotonated benzyldiphenylphosphane
C^N$^-$	deprotonated 1-(4-(tert-butyl)phenyl)-*N*,*N*-dimethylmethanamine
CASSCF	complete active space self-consistent field
CD	circular dichroism
CPL	circularly polarized luminescence
CT	charge-transfer
cw	continous wave
DAP	Diels-Alder product
ddad	*N*,*N*’-dimethyl-*N*,*N*’-di(pyridin-2-yl)pyrazine-2,6-diamine
ddpd	*N*,*N*’-dimethyl-*N*,*N*’-di(pyridin-2-yl)pyridine-2,6-diamine
DFT	density functional theory
dgpy	2,6-diguanidylpyridine
DMB	2,3-dimethyl-1,3-butadiene
dmcbpy	dimethyl-2,2‘-bipyridine-4,4‘-dicarboxylate
DPA	9,10-diphenylanthracene

dpc$^-$	deprotonated 3,6-di-*tert*-butyl-1,8-di(pyridine-2-yl)-carbazole
dqp	2,6-di(quinolin-8-yl)pyridine
DSSC	dye-sensitized solar cell
DTET	doublet-triplet energy transfer
en	ethylenediamine
EnT	energy transfer
ES	excited state
ESA	excited state absorption
ESI	electrospray ionization
F	fluorescence
FWHM	full width at half maximum
GS	ground state
HPLC	high-performance liquid chromatography
H_2tpda	2,6-bis(2-pyridylamino)pyridine
IC	internal conversion
ILCT	intraligand-charge-transfer
ISC	intersystem crossing
IR	infrared
^{i}Pr	*iso*-propyl
KHMDS	potassium bis(trimethylsilyl)amide
LC	ligand-centered
LED	light emitting diode
LF	ligand field
LL'CT	ligand-to-ligand charge-transfer
LMCT	ligand-to-metal charge transfer
$L^{NC,bi}$	2,5-bis(3,5-di-*tert*-butyl-2-isocyanophenyl)thiophene
LT	lifetime

MC	metal-centered
Me	methyl
MECP	minimum energy crossing point
Mes	mesityl
MLCT	metal-to-ligand charge-transfer
MS	mass spectrometry
NIR	near-infrared
NR	non-radiative
OLED	organic light emitting diode
P	phosphorescence
pbmi	(pyridine-2,6-diyl)bis(1-methyl-imidazol-2-ylidene)
PC	photocatalyst
PDT	photodynamic therapy
Ph	phenyl
Ph_2phen	4,7-diphenyl-1,10-phenanthroline
PhB(MeIm)$_3^-$	phenyl[tris(3-methylimidazol-1-ylidene)]borate
phen	1,10-phenanthroline
PL	photoluminescence
pphen	deprotonated 2-(3-(*tert*-butyl)phenyl)-1,10-phenanthroline
ppy$^-$	deprotonated 2-phenylpyridine
PS	photosensitizer
Q	quencher
QY	quantum yield
r	radiative
SCE	standard calomel electrode
SDG	Sustainable Development Goal
SF	spin-flip

SOC	spin-orbit coupling
SQUID	superconducting quantum interference device
sTTA	sensitized triplet-triplet-annihilation
SV	Stern-Volmer
TA	transient absorption
TADF	thermally activated delayed fluorescence
***t*An**	*trans*-anethole
^{t}Bu	*tert*-butyl
TDET	triplet-doublet energy transfer
TMC	transition metal complex
tpe	1,1,1-tris(pyrid-2-yl)ethane
tpy	2,2‘:6‘,2“-terpyridine
TS	Tanabe-Sugano
TTA	triplet-triplet-annihilation
TTA-UC	triplet-triplet-annihilation upconversion
TTET	triplet-triplet energy transfer
UC	upconversion
UHP	ultra high power
UV	ultraviolet
VC	vibrational cooling
VIS	visible
VR	vibrational relaxation

1 Introduction

1.1 A Paradigm Change

In a world where climate change, resource scarcity, and environmental degradation are ever-present challenges, the need for sustainable scientific solutions has never been more urgent.[1,2] Today, around 80% of global energy consumption still relies on fossil fuels, such as oil, gas, and coal.[3–5] These finite resources contribute extensively to greenhouse gas emissions and environmental harm, from pollution to ecosystem disruption.[6,7] In response, the United Nations Sustainable Development Goals (SDGs) call for a shift toward renewable energy and sustainable resource management by 2030.[8] Addressing these pressing global challenges requires a paradigm change that demands transformative advances in materials science and energy technology. Among promising solutions, harnessing sunlight, a nearly limitless and renewable source of energy, presents a compelling approach, enabling the generation of electricity and driving chemical reactions with minimal environmental impact.[9–12]

Photochemistry, the study of light-induced chemical processes, stands at the forefront of this transition.[13] Solar-driven chemical reactions offer a pathway to reduce dependence on fossil fuels while enabling unique transformations that conventional methods cannot achieve.[14–16] Transition metal complexes (TMCs), which consist of a transition metal core coordinated by ligands, have emerged as essential tools in light-based applications, offering a diverse range of photophysical properties and chemical versatility.[17–22] These characteristics arise from the interactions between the metal center and its ligands, allowing for precise tuning of properties for specific energy-conversion applications.

Traditionally, research on photoactive TMCs has concentrated on complexes of precious and rare-earth metals, such as ruthenium, iridium, and europium, valued for their favorable excited-state properties (Fig. 1.1). Pioneer systems like $[Ru(bpy)_3]^{2+}$ (bpy = 2,2‘-bipyridine) and *fac*-$Ir(ppy)_3$ (ppy = 2-phenylpyridine) and their analogues have become foundational in applications ranging from basic photophysical studies[23–25] and photocatalysis[26–30] to organic light-emitting diodes (OLEDs)[31–33], dye-sensitized solar cells (DSSCs)[34–36], and even medical techniques[37–40] such as photodynamic therapy (PDT). However, the widespread industrial adoption of these precious metals is limited by high costs, scarcity, and the significant environmental impact associated

with their extraction.[41,42] As of 2023, ruthenium's market price reached $15,100 per kilogram, while iridium, one of the rarest elements, commanded $148,000 per kilogram (by comparison, chromium: $12.1).[43] Beyond these economic limitations, mining these metals is highly resource-intensive and environmentally damaging, making their large-scale use for sustainable applications impractical.[44,45]

In response to these limitations, research has turned toward TMCs based on earth-abundant metals like chromium, iron, and copper (Fig. 1.1). These metals are not only more affordable and accessible but also offer unique reactivities and mechanisms that have become a focus of scientific inquiry in photochemistry. While the shift to earth-abundant TMCs poses challenges—particularly in achieving the necessary photostability and long excited-state lifetimes—significant progress is being made through innovations in ligand design and photophysical optimization.[46–56] Chromium(III) complexes, in particular, have demonstrated considerable photostability and luminescence, positioning them as promising alternatives to precious metal-based complexes.[57–60]

This work focuses on pseudooctahedral chromium(III) compounds, specifically examining a class of representatives that show great promise in advancing the transition to earth-abundant metals. The following sections provide a general overview of relevant photophysical processes and place these systems within the broader context of photoactive TMCs, before highlighting their specific properties and potential for future applications.

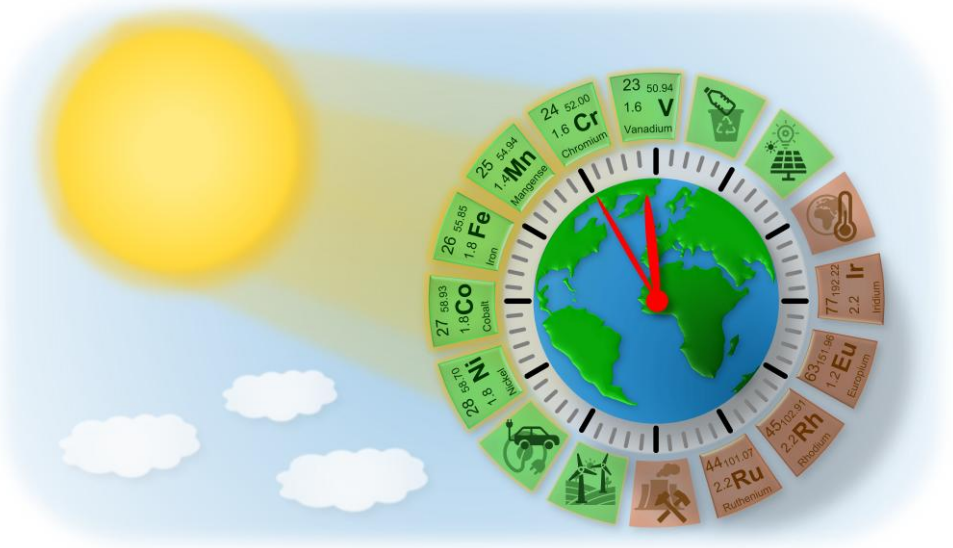

Fig. 1.1 Schematic representation of Earth as a time-critical clock, highlighting photochemically relevant precious and rare-earth metals in the shadow and earth-abundant metals in sunlight, with examples illustrating greater and lesser sustainability.

1.2 Dynamics of Excited States

Photoactive states are fundamental to the optical and photocatalytic applications of TMCs, opening reaction pathways that are inaccessible by thermal activation. Following excitation, the dynamic processes on the excited state energy surface of a molecule, leading to a (de)population of the photoactive states, play a decisive role in the applicability of a TMC. The decay mechanisms of the excited states (ESs) back to the ground state (GS) can generally be categorized into non-radiative (NR) decay pathways and photoluminescence (PL), with the latter further subdivided into fluorescence (F) and phosphorescence (P). As will be discussed, the kinetics of competing NR processes and PL are determined by the energy landscape and the structures of the GS and ESs, and can, in principle, be controlled by chemical design. Depending on the shift of electron density relative to the GS, the electronic structure of the ES can be classified into charge-transfer (CT) transitions and more localized metal-centered (MC) or inter- and intra-ligand charge-transfer (ILCT) transitions.

The following section provides an overview of typical ES decay mechanisms in TMCs relevant to this work, with a focus on pseudooctahedral chromium(III) TMCs as well-explored examples. The intrinsic challenges to be addressed, including the specific requirements on the ligand for achieving PL in $3d^n$ systems ($n \neq 0, 10$), are outlined, along with strategies to mitigate NR decay and promote PL. Finally, a benchmark system will be presented, illustrating how a detailed understanding of the photophysics of a TMC can be used to minimize NR pathways and enhance PL.

1.2.1 Struggling with Non-Radiative Decay

Similar to radiative processes (absorption, emission), the rate constants of NR processes depend on the overlap integral between the vibrational wave functions of the two electronic states involved (Franck-Condon factors).[61,62] To develop TMCs with photochemically exploitable ESs, it is thus essential to suppress rapid NR relaxation via low-energy, distorted ESs with strong vibronic coupling to the GS, i.e. ESs featuring different occupancy of antibonding MC orbitals relative to the GS.[50] However, for 3d TMCs, this presents a significant challenge in terms of ligand design, due to the weaker intrinsic LF strength compared to their heavier homologs.[54] This primogenic effect refers to the radial contraction of orbitals in the first p-, d-, and f-shell (2p, 3d, 4f), which lack nodes in the radial distribution function and are influenced by a higher effective nuclear charge.[63] As a result, the reduced overlap between the contracted 3d metal orbitals and ligand orbitals leads to weaker LF strength and lower MC state energies compared to analogous 4d/5d TMCs.[64] This is

exemplified by the photodynamics of the low spin d^6 complex $[Fe(bpy)_3]^{2+}$ and its heavier homologue $[Ru(bpy)_3]^{2+}$. While $[Ru(bpy)_3]^{2+}$ exhibits strong P from a ^{3}MLCT state (λ_P = 620 nm) with a long ES lifetime (LT) in the nanosecond range[65,66], $[Fe(bpy)_3]^{2+}$ is non-luminescent and suffers from fast NR decay via distorted low-energy $^{3/5}$MC states.[24,47,67–69]

While interconfigurational MC states typically promote NR pathways and are considered detrimental to PL in TMCs (such as MLCT systems), MC states can also be the source of PL.[70] In pseudooctahedral chromium(III) TMCs, the desired PL originates from intraconfigurational MC states of ^{2}E/^{2}T$_1$ parentage.[71] Since these spin-flip (SF) states are derived from the same t_{2g}^3 electron configuration as the GS (^{4}A$_2$), there is minimal change in the bonding situation during the transition, resulting in minor geometric reorganization.[72] Consequently, the SF states are nested, featuring relatively low vibrational overlap with the GS, which makes them less prone for NR decay via surface crossing (weak-coupling limit, Fig. 1.2a).[57,61]

However, interconfigurational MC states can also play a significant role in the dynamics of NR processes of excited chromium(III) TMCs. To allow slow P to compete kinetically, it is necessary that the LF-dependent ^{4}T$_2$ state is not energetically accessible from the nearly LF-independent ^{2}E/^{2}T$_1$ states. Due to the asymmetric occupation of (antibonding) orbitals, the ^{4}T$_2$ state undergoes Jahn-Teller (JT) distortion and has a rather flat ES potential surface with a minimum that is horizontally displaced from the GS.[72,73] This leads to substantial vibronic coupling with the GS, resulting in rapid NR deactivation (strong-coupling limit, Fig. 1.2b) or ligand dissociation.[57,61]

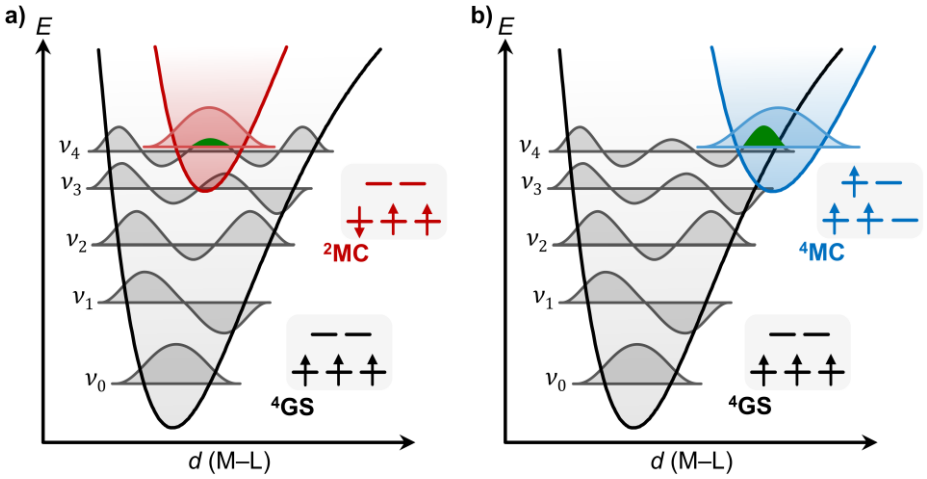

Fig. 1.2 Anharmonic potential energy wells with vibrational wave functions showing the a) the weak-coupling limit between a nested ^{2}MC state and the ^{4}GS and b) the strong-coupling limit between a distorted ^{4}MC state and the ^{4}GS.[61]

Even in chromium(III) TMCs with traditionally strong field ligands, such as $[Cr(tpy)_2]^{3+}$ (tpy = 2,2‘:6‘,2“-terpyridine), PL efficiency is poor due to an insufficient LF strength, which results in a small energy gap between the excited doublet and relaxed quartet states.[72,74] This enables thermally activated back-intersystem crossing (back-ISC) from the $^2E/^2T_1$ manifold to the $^4T_2$ state, facilitating NR decay via surface crossing and leading to low photostability in these TMCs (Fig. 1.3a).[70,75] Among chromium(III) polypyridyl TMCs incorporating five-ring chelates, $[Cr(phen)_3]^{3+}$ (phen = 1,10-phenanthroline) exhibits the highest quantum yield (QY) in deaerated solution (Φ_P = 1.2%, 1 M HCl).[74]

Another factor limiting PL in pseudooctahedral chromium(III) TMCs involves ES distortions within the emissive SF states caused by symmetry effects. In tris(bidentate) TMCs, such as $[Cr(bpy)_3]^{3+}$ and $[Cr(phen)_3]^{3+}$, local symmetry lowering from O_h to D_{3h} point group through trigonal distortion of the first coordination sphere in the doublet ESs mixes the $^4A_2$ (O_h) and the $^4T_2$ (O_h) states, giving a destabilized $^4E'$ (D_{3h}) GS and a stabilized $^4E''$ (D_{3h}) ES (Fig. 1.3b).[72,73] These states exhibit a reduced quartet-doublet energy gap and different relaxed geometries, facilitating efficient NR deactivation through surface crossing.[76,77]

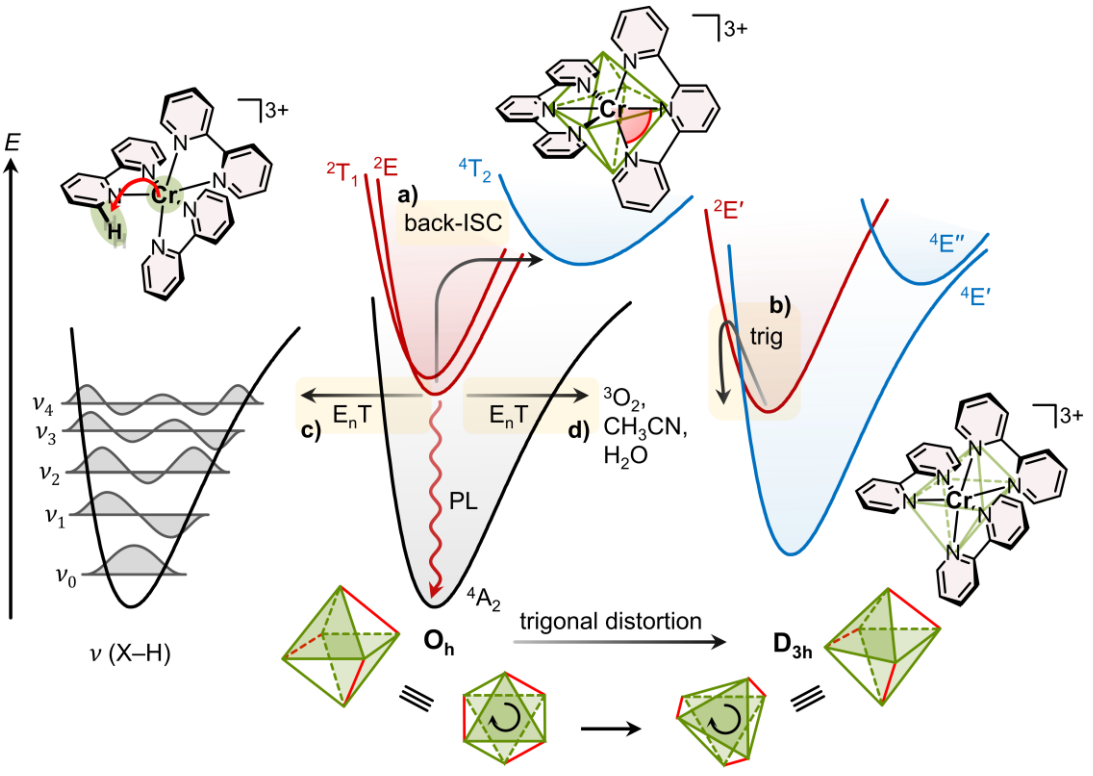

Fig. 1.3 Relevant decay pathways of excited chromium(III) complexes, including: a) thermally activated back-ISC to the distorted $^4T_2$ state, b) trigonal distortion leading to surface crossing with the GS, c) intramolecular E_NT to high-energy X-H oscillators, d) intermolecular E_NT to triplet oxygen and solvent molecules, and PL, along with representative TMC examples.[76]

Due to the local inversion symmetry in pseudooctahedral chromium(III) TMCs, their SF transition obeys both the spin selection rule and Laporte's rule[78], leading to low overall radiative rate constants.[79] As a result, SF states are highly sensitive to intermolecular and intramolecular quenching processes due to their long ES LT.[56,70] In contrast, ^{3}MLCT emitters, such as $[Ru(bpy)_3]^{2+}$, experience higher radiative rates, as their emission is limited solely by the spin selection rule, which is further weakened by the high spin-orbit coupling (SOC) of the heavy element.[24,65,80]

The relatively low emission energy of photoactive chromium(III) systems (typically 12,800–15,000 cm^{-1})[59] facilitates quenching via intramolecular energy transfer (E_NT) to vibrational overtones (fourth or fifth overtone) of X–H oscillators (X = C, N, O) with frequencies above 3000 cm^{-1} (Fig. 1.3c).[70,81] For this inductive resonant mechanism to be effective, the oscillators must be in the vicinity of the metal center, and the overtone (fourth or fifth) should exhibit substantial spectral overlap with the TMC's emission band.[73,82] Due to the distance dependence d^{-6} of the corresponding rate constant, the closest alpha C–H oscillators in chromium(III) complexes with pyridine ligands are typically the most relevant for the multiphonon relaxation.[76]

Solvent molecules, salt additives, counterions, or triplet oxygen can also significantly influence the PL properties of chromium(III) TMCs through intermolecular E_NT (Fig. 1.3d).[70,81] The quenching efficiency via solvent overtones or triplet oxygen depends on the accessibility of the metal center by the energy acceptor. Salt additives or counterions can protect the metal center by occupying binding pockets between the ligands or forming contact ion pairs.[83,84] Additionally, filled binding pockets can rigidify the system, inhibiting distortional NR pathways and improving PL efficiency.[85] Chromium(III) emitters are particularly susceptible to quenching via Dexter-type E_NT with triplet oxygen, a process facilitated by their long ES LT and favorable spin statistics, which predict that 4/6 (67%) of encounter complexes lead to productive singlet oxygen generation.[86,87]

1.2.2 Achieving Photoluminescence

To achieve strong PL in TMCs, it is essential to minimize NR processes, as outlined in Section 1.2.1, through structural design and environmental control. Addressing the inherent challenges of 3d TMCs, i.e. their intrinsically weaker LF strength, typically involves two primary strategies. The first strategy focuses on systems with $3d^0$ or $3d^{10}$ electronic configurations, where low-lying MC states are absent. The second approach, applicable to the other $3d^n$ configurations (n = 1–9), aims to generate a strong LF to raise the energy of detrimental MC states and to increase rigidity in order to minimize JT distortions.[88] The latter approach was successfully implemented in the complex

$[Cr(ddpd)_2]^{3+}$ (ddpd = *N*,*N*'-dimethyl-*N*,*N*'-di(pyridin-2-yl)pyridine-2,6-diamine, Fig. 1.5), representing a conceptual breakthrough in 3d metal photochemistry.[70] This system exhibtis exceptional photochemical properties, including strong P with a long ES LT (τ_P = 1120 µs) and a high QY (Φ_P = 13.7%) in deaerated solution.[84,87]

In $[Cr(ddpd)_2]^{3+}$, the strong LF necessary to separate the emissive $^2E/^2T_1$ states from the $^4T_2$ state is provided by the six-membered chelate rings formed by expanding the tpy-like ligand with NMe groups. The electron-rich ddpd ligand coordinates with nearly perfect octahedral local symmetry, featuring N–Cr–N bite angles close to 90°, resulting in optimized metal-ligand orbital overlap and strong Cr–N σ-bonds.[57,73] According to the Tanabe-Sugano (TS) diagram for an octahedral ML_6 system (Fig. 1.4), the LF strength reaches the second quartet-doublet crossing point ($^4T_2/^2T_2$), effectively preventing NR decay via thermally activated back-ISC.[89–91] The rigidity of the tridentate ddpd ligand, with its NMe-bridged architecture, further prevents trigonal distortion. These structural properties of $[Cr(ddpd)_2]^{3+}$ effectively suppress large-amplitude motions in the ESs, resulting in an exceptionally long ES LT.[79]

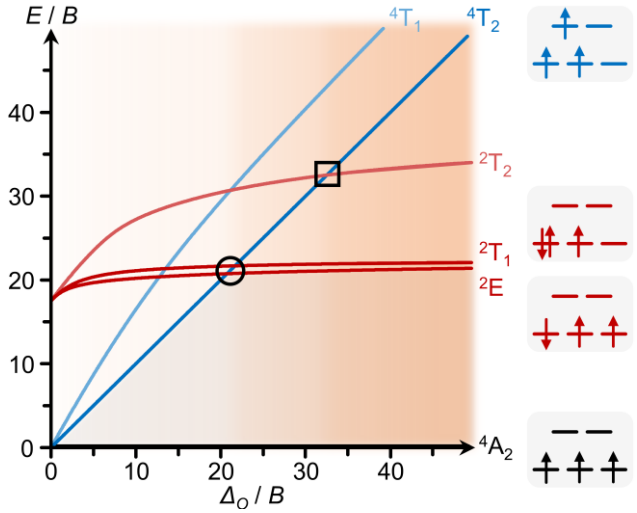

Fig. 1.4 Simplified TS diagram for octahedral complexes featuring d^3 electronic configuration (C/B = 4) with exemplary microstates showing the energy dependence of the MC states from the LF strength. Critical quartet-doublet crossing points are highlighted by a circle and a square, respectively.[90,91]

In addition to preventing the depopulation of photoactive states, it is crucial to ensure their efficient population while avoiding additional loss channels to achieve high overall PL efficiency. In $[Cr(ddpd)_2]^{3+}$, following excitation of the $^4T_2$ and ^{4}LMCT states in the visible region (λ_{exc} = 435 nm), this is realized through ultrafast ISC (τ_{ISC} < 200 fs) from vibrationally hot $^4T_2$ states to the $^2T_2$ state, effectively outcompeting F or nuclear distortions of the $^4T_2$ state (Fig. 1.5).[89] The rapid ISC is driven by the high density of doublet states near the second quartet-doublet crossing

point, coupled with SOC, enhanced by spin-vibronic interactions.[92] Following ISC, internal conversion (IC) and vibrational cooling (VC) within the doublet manifold occur ($\tau_{IC/VC}$ = 3.2 ps), both proceeding faster than the $^2T_2 \rightarrow {}^4T_2$ back-ISC, ensuring an efficient population of the emissive ES.[70]

The thermally equilibrated $^2T_1$ and ^2E derived ESs of $[Cr(ddpd)_2]^{3+}$ produce strong dual P in the near-infrared (NIR) spectral region (λ_P = 738, 775 nm, Fig. 1.5) at room temperature (RT). Because the *d*-electron configuration is preserved in the SF transitions, the involved states share a similar equilibrium geometry, resulting in sharp emission bands (FWHM = 420 cm^{-1}).[87] In addition to P, weak F (λ_F = 500 nm) with a relatively large Stokes shift (2400 cm^{-1})[93] originating from the distorted $^4T_2$ state is also observed in $[Cr(ddpd)_2]^{3+}$. The low QY of residual F (Φ_F = 0.01%) indicates efficient depopulation of the $^4T_2$ state by ultrafast ISC.[79]

The doublet states of $[Cr(ddpd)_2]^{3+}$ are also detectable via absorption spectroscopy (Fig. 1.5), revealing the lifting of degeneracy in the lower D_2 symmetry due to π-bonding of the pyridyl donors. The NIR absorption spectrum of $[Cr(ddpd)_2]^{3+}$ shows at least three weak bands (λ_{max} = 697, 736, 776 nm), attributable to five spin- and Laporte-forbidden $^4A_2 \rightarrow {}^2E/{}^2T_1$ transitions.[87] Multireference calculations with perturbation correction (CASSCF(7,12) NEVPT2) at the DFT-optimized $^4A_2$ geometry place the lowest $^2T_1(1)$ microstate below the lowest $^2E(1)$ microstate (contrary to the TS diagram for an octahedral d^3 system), likely due to the greater flexibility of the asymmetric occupation of the split t_{2g} orbital set in the $^2T_1$ microstate.[89]

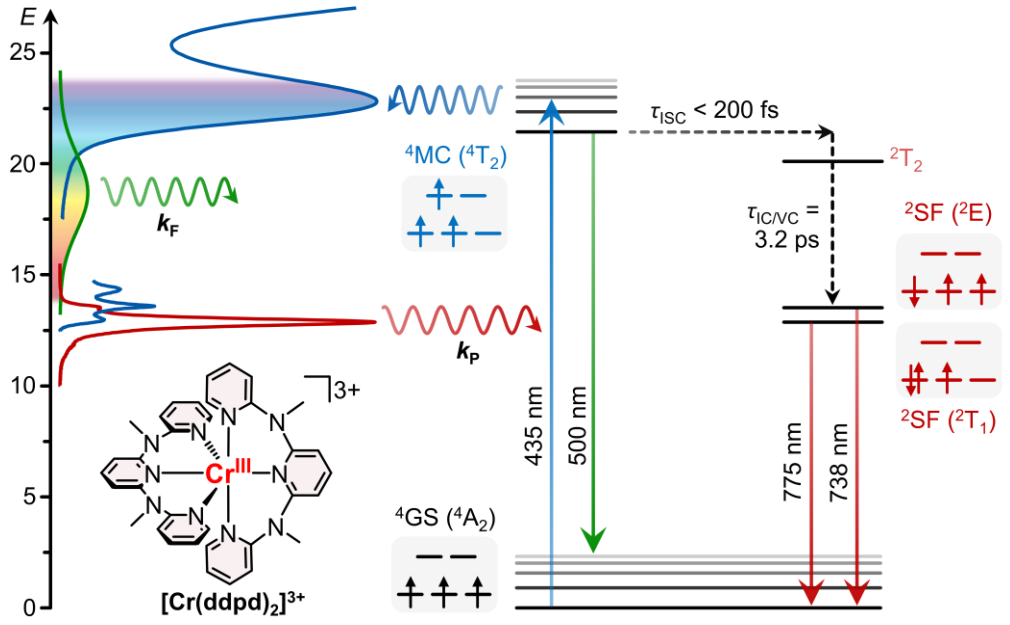

Fig. 1.5 Normalized (NIR) absorption (blue), P (red) and F (green) spectra of $[Cr(ddpd)_2]^{3+}$ with chemical structure and Jablonski-diagram, showing relevant relaxation pathways and exemplary microstate configurations of the involved electronic states.[94]

The PL performance of $[Cr(ddpd)_2]^{3+}$ can be significantly enhanced through quantitative deuteration of the ddpd ligand, which reduces the NR relaxation decay via multiphonon relaxation (τ_P = 1800 µs, Φ_P = 22.0%).[76] Replacing C–H oscillators (≈ 3100 cm^{-1}) with C–D oscillators (≈ 2300 cm^{-1}) lowers the fundamental vibrational mode, restricting resonant E_NT to higher vibrational overtones ($\nu_0 \rightarrow \nu_6$). The reduced extinction coefficient of the higher C–D overtone (ν^6), compared to possible C–H overtones ($\nu^4+\nu^5$), decreases the spectral overlap with the emission band, reducing PL quenching.[70] In deuterated solvents, intermolecular E_NT is further minimized, leading to record LTs and QYs (τ_P = 2300 µs, Φ_P = 30.1%).[76] The influence of the solvent depends on its stretching vibrations and the counterion of the complex salt.[73]

1.3 Nature of Excited States

The electronic nature of the emissive ESs has a decisive influence on the photophysical properties of TMCs, including their ES LT, emission bandwidths, tunability, photostability, and electron transfer efficiency.[94] Since different applications have varying requirements, CT and SF systems, with their fundamentally distinct ES characteristics, are suited for different uses. For instance, while longer ES LTs are generally preferred for photocatalysis to enhance quenching efficiency, shorter LTs are more desirable in imaging techniques and OLEDs to reduce photodegradation and optimize performance.[26,31,32,95] From an electronic perspective, CT transitions can be described as intramolecular redox processes, with the redistribution of electron density over large parts of the molecule, whereas SF transitions are rather localized at the metal center. Regardless of the electronic nature, both CT and SF complexes share two fundamental requirements for achieving PL: after spin-allowed excitation, efficient ISC/IC should facilitate the population of the photoactive ESs, while a strong LF should prevent their depopulation via low-energy, distorted MC states.

The next section elucidates the fundamental photochemical properties and distinctions between CT and SF emitters, supplemented by selected examples of 3d TMCs, and explores the specific challenges they face in meeting the summarized PL requirements. The photophysical advantages of both emitter classes are thoroughly compared, with a particular focus on tuning their ES properties. To provide a comprehensive comparison with $[Cr(ddpd)_2]^{3+}$ discussed in the previous section, the photophysics of the ^{3}MLCT benchmark system $[Ru(bpy)_3]^{2+}$ are introduced in detail.

1.3.1 Charge-Transfer Emitters

In CT transitions, the shift of electron density from weakly bonding to antibonding orbitals, combined with the Coulomb interaction between separated charges, results in weak geometric ES distortion. When projected onto a single distortional coordinate, this manifests as a (relatively small) horizontal displacement of the potential energy minimum relative to the GS, which enhances vibronic coupling and leads to broad absorption and emission bands (strong coupling limit).[94] Unlike SF transitions, CT transitions are parity-allowed and have larger transition dipole moments, leading to higher molar absorption coefficients ($\varepsilon = 10^2$–10^6 M^{-1} cm^{-1}) and higher radiative rates ($k_P = 10^4$–10^6 s^{-1}).[96,97] Strong absorption is advantageous for applications requiring high brightness (e.g., DSSCs) or high concentrations of the excited photosensitizer (e.g., photocatalysis).[26,34] Notably, CT emission can occur as both P and F, whereas SF emission is inherently linked to P. As exemplified later in LMCT emitters, rapid F offers a strategy to make PL competitive with NR processes.[51]

Prominent CT complexes, such as $[Ru(bpy)_3]^{2+}$ and *fac*-$Ir(ppy)_3$ are well-established in numerous applications including photocatalysis (Ru, Ir)[29,30], DSSCs (Ru)[34], and phosphorescent OLEDs (Ir)[31,33] due to their favorable optical properties.[57] Their heavy metal centers offer two advantages: they accelerate spin-forbidden processes (ISC, P) due to their large SOC and shift detrimental MC states to higher energies through their strong intrinsic LFs, thus enhancing overall photostability and efficiency.

In $[Ru(bpy)_3]^{2+}$, the pivotal photoactive ^{3}MLCT state is populated after ^{1}MLCT excitation using blue light (λ_{exc} = 450 nm), followed by ultrafast quantitative ISC ($\tau_{ISC} = 15 \pm 10$ fs, Fig. 1.6).[98,99] During and after VC ($\tau_{VC} < 300$ fs)[99–101] within the triplet manifold, red P (λ_P = 620 nm) is observed, with a high QY (Φ_P = 9.5%)[102] and ES LT (τ_P = 0.81 µs)[103]. At lower temperatures (77 K), the PL efficiency improves (τ_P = 5 µs), with the temperature dependence being attributed to thermally activated IC processes from the ^{3}MLCT state to the distorted and substitutionally labile $^3T_1$ state, followed by surface crossing to the GS.[68,104] Different JT isomers featuring, elongated Ru–N bonds, are related to the NR decay pathways through ^{3}ES/^{1}GS minimum energy crossing points (MECPs) and enable ES photochemical reactions.[105–107]

Analogous to SF systems, thermally activated NR relaxation via interconfigurational MC states becomes more relevant as LF strength decreases. For example, in $[Ru(tpy)_2]^{2+}$, being emissive only at lower temperatures, a lower-energy $^3T_1$ state goes hand in hand with a reduced activation barrier for IC (^{3}MLCT→$^3T_1$), facilitating NR deactivation.[69,108] Transitioning to a 3d metal in $[Fe(bpy)_3]^{2+}$, the LF is further weakened by the primogenic effect, resulting in $^{3/5}$MC states lower in energy than the ^{3}MLCT state. This opens up a fast relaxation cascade through IC into the ^{3}MC state,

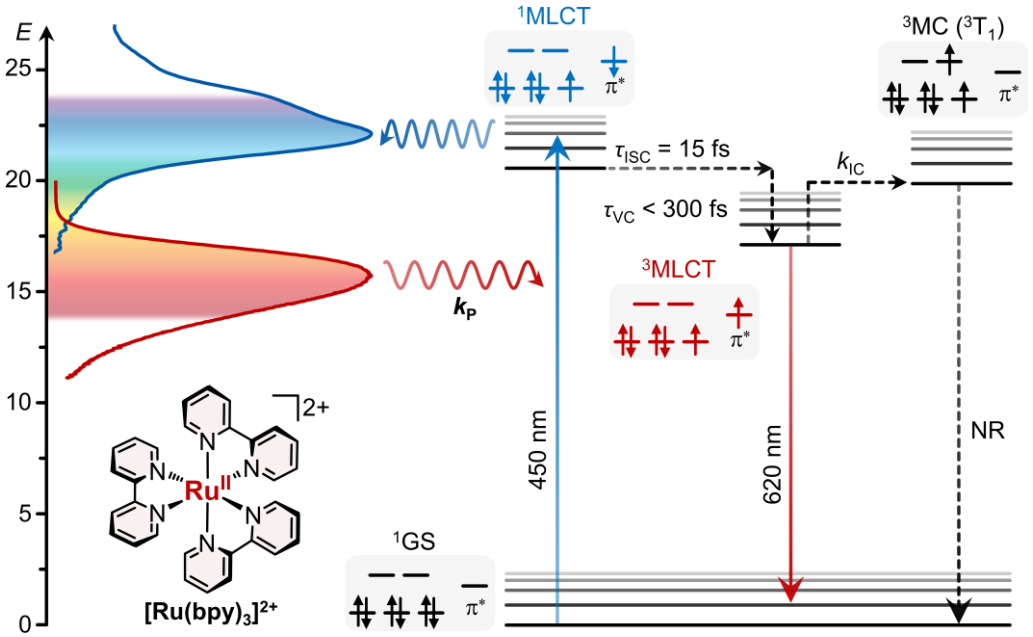

Fig. 1.6 Normalized absorption (blue) and P (red) spectra of $[Ru(bpy)_3]^{2+}$ with chemical structure and Jablonski-diagram, showing relevant relaxation pathways and exemplary microstate configurations of the involved electronic states.[94]

followed by ISC into the high-spin ^{5}MC state (<50 fs)[109,110], which decays via spin crossover to the GS with a temperature-dependent time constant (≈ 650 ps).[111,112]

In the pursuit of luminescent iron(II) TMCs, strongly σ-donating *N*-heterocyclic carbene (NHC) and σ-donating/π-accepting mesoionic carbene ligands have been used to raise the energy of detrimental $^{3/5}$MC states.[113–117] However, iron(II) TMCs such as $[Fe(pbmi)_2]^{2+}$ (τ_P = 9 ps, Fig. 1.7) and $[Fe(btz)_3]^{2+}$ (τ_P = 528 ps, Fig. 1.7) exhibit ES LTs sufficient for certain applications, such as DSSCs, yet do not show detectable PL.[118,119] The first emissive mononuclear iron(II) complex $Fe(pphen)_2$ (Fig. 1.7), incorporating a 9-phenylphenanthroline ligand, shows PL in the NIR II spectral range (λ_P = 1170–1230 nm, τ_P = 1 ns).[120]

CT complexes based on chromium(0) can also exhibit emission when stabilized by strong π-accepting ligands such as carbonyls or isocyanides.[52,121–123] The arylisocyanide ligand in $Cr(L^{NC,tBu})$ (Fig. 1.7) enables ^{3}MLCT emission with a notable LT (λ_P = 630 nm, Φ_P = 0.001%, τ_P = 2.2 ns), which is remarkable given that analogous iron(II) TMCs are generally nonluminescent.[124] The strong LF, pronounced metal-ligand bond covalency, and protection of the metal center by the sterically demanding ligand backbone, make PL a competitive relaxation process in the chromium(0) system.[125] The ES LT of the TMC is sufficient for bimolecular reactions, including E_NT for sensitizing triplet-triplet annihilation (TTA) upconversion (UC).[126]

This design concept, employing strong isocyanide ligands, has been extended to manganese(I), yielding $[Mn(L^{NC,bi})_3]^+$ (Fig. 1.7) and its tridentate analog, which

display blue-shifted PL (λ_P = 478, 525 nm) compared to chromium(0) systems due to the higher oxidation state.[127] Although the QYs are relatively low (Φ_P = 0.03, 0.05%) owing to energy dissipation via nuclear motions, the LTs are long enough for bimolecular E_NT reactions (τ_P = 0.74, 1.73 ns), including TTA UC.[51]

PL from LMCT states in 3d TMCs can be achieved upon formal oxidation of the aforementioned iron(II) complex to $[Fe(btz)_3]^{3+}$ (λ_F = 600 nm, Φ_F = 0.03%, τ_F = 100 ps, Fig. 1.7).[128] In this system, the interplay of a high radiative rate for spin-allowed F and a significantly large $^2LMCT \rightarrow {}^4T_1$ activation barrier, which hinders NR decay via ISC to the lower-energy, JT-distorted $^4T_1$ state, enables ^{2}LMCT emission. The more rigid anionic ligand in $[Fe(PhB(MeIm)_3)_2]^+$ (λ_F = 655 nm, Φ_F = 2%, τ_F = 2.0 ns, Fig. 1.7) induces an even stronger LF, further destabilizing the detrimental $^{4/6}$MC states and resulting in enhanced PL efficiency.[129]

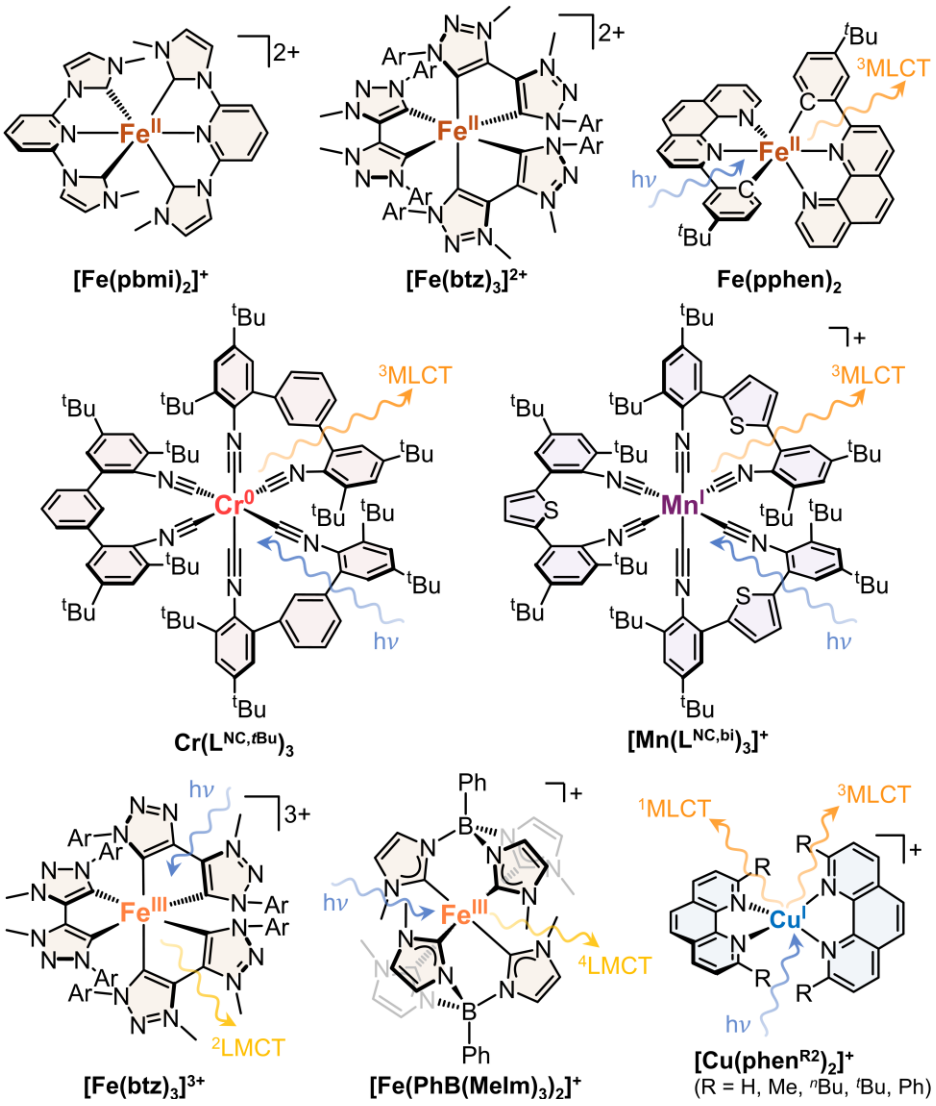

Fig. 1.7 Chemical structures of selected 3d metal based CT complexes with arrows indicating if PL is detectable.[118–120,124,127–131]

A common strategy for circumventing NR deactivation via MC states in CT complexes involves the use of d^0 or d^{10} electronic configurations with an empty or completely filled shell.[132–135] For 3d metals, MC states are absent in tetrahedral copper(I) complexes of the type $[Cu(phen^{R2})_2]^+$ (R = H, Me, ^{n}Bu, ^{t}Bu, Ph, Fig. 1.7).[130,131] In these systems, second-order JT distortions, including ES flattening driven by a formally oxidized copper(II) center in the MLCT state, become relevant alongside PL and can be sterically hindered by introducing rigid substituents.[136,137] With a small singlet-triplet energy gap (<1000 cm^{-1}) and a low P rate, these TMCs exhibits either ^{3}MLCT P or thermally activated delayed F (TADF) from a ^{1}MLCT state following back-ISC, depending on the temperature.[138,139]

1.3.2 Spin-Flip Emitters

SF transitions involve only a change in electron spin within a constant *d*-electron configuration, resulting in minimal alteration to the electronic structure. Compared to CT states, SF states exhibit less distortion, with potential wells that are nested with respect to the GS, which generally helps to decelerate NR processes.[94] As demonstrated in $[Cr(ddpd)_2]^{3+}$ (Section 1.2.2), this results in sharp emission bands due to dominant FC factors from lower vibronic levels.[73] In accordance with Laporte's Rule, SF transitions in centrosymmetric coordination environments exhibit low radiative rates (k_P = 20-200 s^{-1}).[59,70] Combined with low NR rates, this leads to long ES LTs, making SF emitters highly efficient for applications such as optical sensing and photocatalysis.[50,54,56,60]

The electronic occupation in SF states distinguishes between spin-unpaired and spin-paired microstates (of different ^{2}E or $^2T_1$ parentage for d^3 systems, Fig. 1.4). Spin-unpaired microstates are characterized by symmetric orbital occupation and differ from the GS only by a flipping of a single electron spin. Population of the more distorted spin-paired microstates with asymmetric orbital occupation may lead to ES JT distortion if the SF involves antibonding orbitals (e.g., in nickel(II) systems).[70] However, if the SF occurs in non-bonding orbitals, as in chromium(III) systems, the SF states exhibit only slight geometric distinctions.[79]

Pseudooctahedral chromium(III) TMCs, such as $[Cr(ddpd)_2]^{3+}$, represent the most extensively studied class of SF emitters and will be discussed further in Section 1.4. Generally, TMCs with d^2, d^3, d^4 or d^8 electronic configurations can give rise to SF ESs. However, these d-orbital occupancies pose challenges for certain metals in low or high oxidation states, as low-lying distorted CT states may come into play.[70] For example, vanadium(II) and manganese(IV) ions also exhibit d^3 electronic configuration, but PL efficiency is quite poor in most corresponding TMCs due to rapid deactivation via

MLCT and LMCT states, respectively.[140,141] Consequently, SF emitters beyond the d^3 electronic configuration and +III oxidation state remain rare. This issue has been addressed by using ligands with strong electron-donating or electron-withdrawing groups to shift detrimental CT states to higher energies.[50,54]

In the vanadium(II) complex *mer*-$[V(ddpd)_2]^{2+}$ (Fig. 1.8), the absence of SF emission is attributed to the mixing of low-energy ^{2}MLCT states with the SF states, leading to ES distortion and efficient NR relaxation. The system demonstrates that the LC π^* orbitals are even too low in energy when coordinating the electron-rich ddpd ligand on the electron-rich metal.[140]

The oxidized vanadium(III) complex *mer*-$[V(ddpd)_2]^{3+}$ (Fig. 1.8), with a d^2 electronic configuration, exhibits weak $^1E/^1T_2 \rightarrow {}^3T_1$ P in the NIR-II region (λ_P = 982, 1088, 1109 nm, Φ_P = 0.00018%), representing the first 3d TMC emitting in this spectral range (>1000 nm) at RT in solution.[142] Additionally, the TMC displays strong blue F (λ_P = 396 nm, Φ_F = 2.1%) from a ^{3}LMCT state under these conditions. The observation of dual emission is mechanistically explained by a high F rate and inefficient ISC from initially populated triplet ESs to the singlet ESs, allowing concurrent IC into the ^{3}LMCT state. While multiphonon relaxation slightly impacts the photodynamics of the TMC, the low ISC rate, due to a low density of singlet acceptor states in the triplet energy region, may account for the poor P efficiency.[70]

In comparison, the heteroleptic TMC *mer*-VCl_3(ddpd) (Fig. 1.8), with a higher ISC efficiency attributed to the heavy atom effect of chloride, exclusively shows P (λ_P = 1102, 1219, 1256 nm, τ_P = 0.5 μs).[143] Ligand deuteration further increases the ES LT (τ_P = 3.4 μs), indicating that multiphonon relaxation involving C–H oscillators is a significant NR pathway in this system. Additionally, a large GS splitting, as evidenced by the appearance of multiple $^1E/^1T_2 \rightarrow {}^3T_1$ emission band maxima, reduces the energy gap between the emissive ESs and the GS, thereby facilitating NR deactivation in agreement with the energy gap law.[61]

The hexacarbene manganese(IV) complex $[Mn(PhB(MeIm)_3)_2]^{2+}$ (Fig. 1.8) also exhibits both discussed PL types, showing long-lived $^2E/^2T_1 \rightarrow {}^4A_2$ P in the NIR (λ_P = 814 nm) and green ^{4}LMCT F (λ_F = 600–750 nm).[144] The red-shifted P compared to many chromium(III) emitters reflects the high degree of metal-ligand bond covalency between the highly charged metal ion and the anionic ligand.[51,70] The assignment of pure SF character to the P contrasts with the PL observed in the second NIR II emissive manganese(IV) complex $[Mn(dgpy)_2]^{4+}$ (Fig. 1.8), which has dominant ^{2}LMCT character with only a small SF contribution.[141]

SF emission from pseudooctahedral TMCs with low-spin d^4 electronic configuration has not been reported to date. Challenges for these systems include the need for a

high LF strength (Δ_O > 38 B)[90,91] as well as efficient population of the potentially emissive $^1T_2/^1E$ states. Since the ^3E state is rapidly deactivated through a relaxation cascade via the lower-lying ^5E state, analogous to iron(II) systems,[145] populating the emissive ES must follow an alternative excitation route (e.g., through CT states). Additionally, the degenerate $^3T_1$ GS can undergo JT distortion, similar to the d^2 electronic configuration in vanadium(III) systems, thereby facilitating NR decay.[70]

In pseudooctahedral TMCs with a d^8 electronic configuration, such as nickel(II) systems, the SF transition occurs in the antibonding e_g orbitals, giving rise to spin-paired and unpaired microstates of ^1E parentage. As previously discussed, the population of the JT distorted spin-paired microstate can facilitate NR relaxation to the $^3A_2$ GS. To date, SF emission with nickel(II) has not been achieved, primarily because the detrimental $^3T_2$ and ^1E state are not sufficiently separated by a strong LF (Δ_O = 17–18 B).[70] Moving to even stronger ligands than ddpd, such as CN^-, forces the d^8 system into a square planar coordination geometry in $[Ni(CN)_4]^{2-}$, where SF states are absent, rendering the TMC diamagnetic.[146]

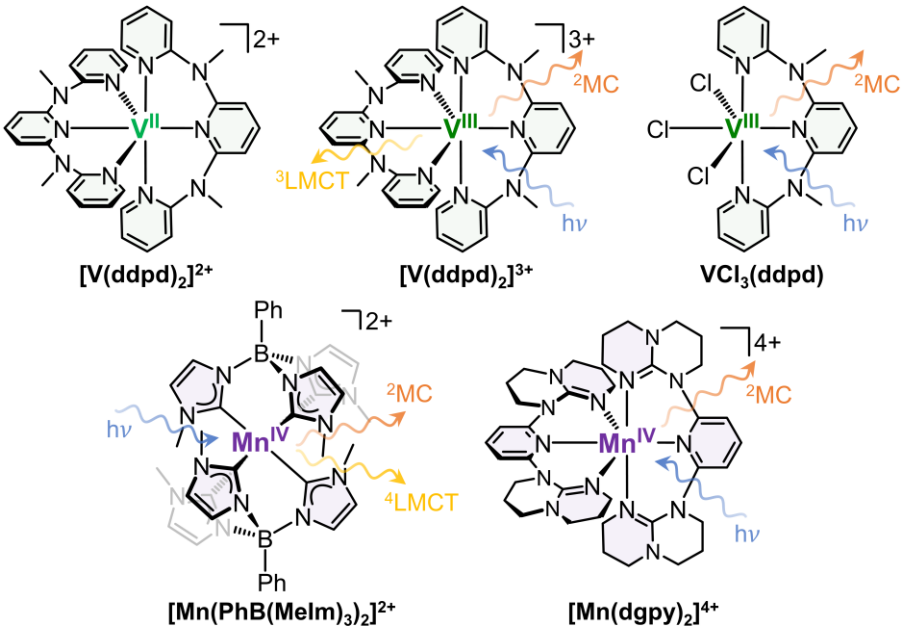

Fig. 1.8 Chemical structures of selected 3d metal based SF complexes with arrows indicating if PL is detectable.[140–144]

1.3.3 Emission Energy Tuning

The energy of the emissive ESs strongly correlates with ES dynamics and is a crucial parameter in determining the overall PL efficiency of a TMC. The example of photoactive $[Mn(PhB(MeIm)_3)_2]^{2+}$ (Fig. 1.8), which exhibits SF emission in the NIR (λ_P = 814 nm), demonstrates that relying solely on simple LF theory is insufficient for

deriving general emission energy trends.[144] Considering the Racah parameters for free Mn^{4+} (B_0 = 1064 cm^{-1}) and Cr^{3+} (B_0 = 918 cm^{-1}) ions,[147] one might expect higher PL energies for the manganese(IV) complex compared to most chromium(III) TMCs; however, the opposite is observed.[70] Indeed, metal-ligand bond covalency and interelectronic repulsion of *d*-electrons play a significant role for SF energies, factors that can theoretically be tuned to control PL properties. Depending on the electronic nature of the ESs, different approaches can be applied for tuning emission energies.[94]

To a first approximation, the energy of CT transitions depends on the energy difference between the MC and LC donor and acceptor orbitals, according to Koopmann's theorem.[148] CT energies can thus be adjusted by ligand design, such as incorporating electron-donating or electron-withdrawing groups or modifying the aromatic system.[149,150] Alternatively, changing the metal center alters the energies of the involved *d*-orbitals, thereby affecting CT energies.[151,152] For example, $[Os(bpy)_3]^{2+}$ (λ_P = 730 nm) shows red-shifted ^{3}MLCT P relative to $[Ru(bpy)_3]^{2+}$ due to higher-energy 5d donor orbitals, while *mer*–$Ir(ppy)_3$ (λ_P = 550 nm) exhibits blue-shifted ^{3}MLCT P owing to the higher metal charge and higher-energy π-accepting LC orbitals (Fig. 1.9).[30,153,154] In general, the electronic structures of the metal and ligand are coupled, such that ligand modifications also influence MC orbital energies and vice versa.[94,152] Additionally, in systems with high electron correlation, the transition energy can deviate significantly from the energy difference of the orbitals involved, complicating predictions based on orbital energies alone.[155–157] Owing to the charge-separated nature of CT states with dipole moments significantly different from the GS, CT energies can be influenced by the surrounding matrix (e.g., solvatochromism).[158–163] As a result of various tuning options available, the emission of CT emitters, such as iridium(III) TMCs, can be adjusted across a wide range of the visible spectrum.[40]

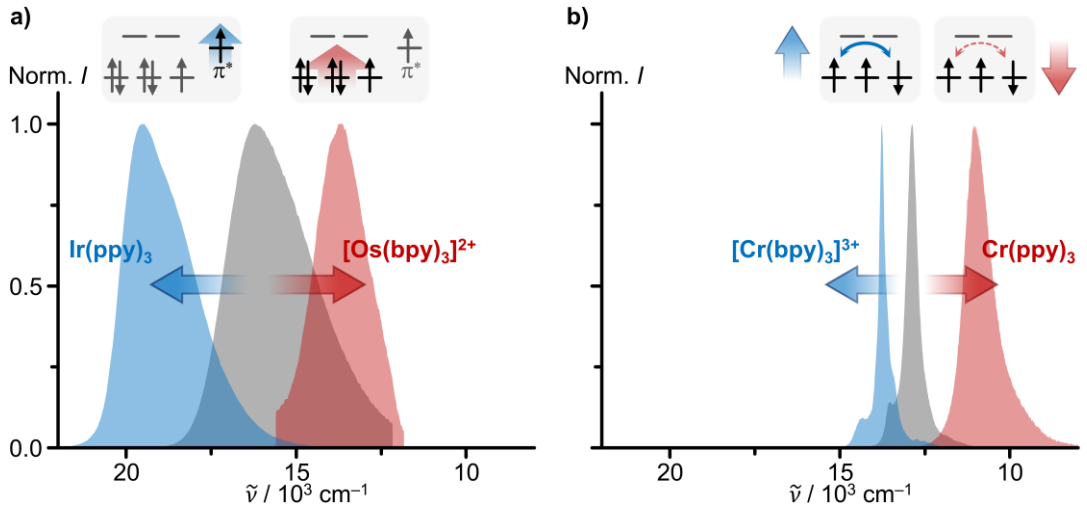

Fig. 1.9 Normalized emission spectra of selected a) CT and b) SF systems to illustrate strategies to shift emission energies relative to $[Ru(bpy)_3]^{2+}$ and $[Cr(ddpd)_2]^{3+}$ (gray).[94]

Tuning the energy of SF states is less straightforward than for CT states. Since SF transitions do not involve charge separation and the electronic structure changes only slightly, with localization at the metal center, traditional strategies such as ligand substitution or altering the solvent environment have minimal impact on SF energies. Instead, SF transition energies depend on varying exchange interactions between electrons in the involved states.[94] This non-classical interaction arises from the antisymmetry requirement for a fermionic wavefunction and is based on electronic Coulomb interaction. Classically, electrons in states with higher total spin avoid each other more effectively, resulting in a reduced interelectronic repulsion and lower energies compared to states of lower multiplicity but identical orbital occupancy (Hund's rule).[148] Thus, tuning SF transitions requires considering the effects of a so-called exchange term, which consistently stabilizes the GS relative to ESs of lower multiplicity, though to varying degrees.

In LF theory, interelectronic repulsion in the nearly degenerate *d*-orbitals of a TMC is quantified by the Racah parameters B and C, which account for Coulomb and exchange interactions. In a free ion in the gas phase, interelectronic repulsion is maximized due to the electrons occupying contracted *d*-orbitals resulting from a high effective nuclear charge, expressed by the highest value B_0 for the Racah parameter B. This situation often fails to predict SF energies of complexes or solids accurately. Upon forming a covalent bond with ligands, the *d*-orbitals expand due to ligand orbital admixture and the reduction in the effective nuclear charge through dative bonding. The resulting decrease in interelectronic repulsion and the Racah parameter B relative to the free metal ion is known as the nephelauxetic effect, understood as an expansion of the electron cloud onto the ligand (Fig. 1.10). This effect represents the transition from M–L bonds of an electrostatic nature in crystal field theory to more covalent

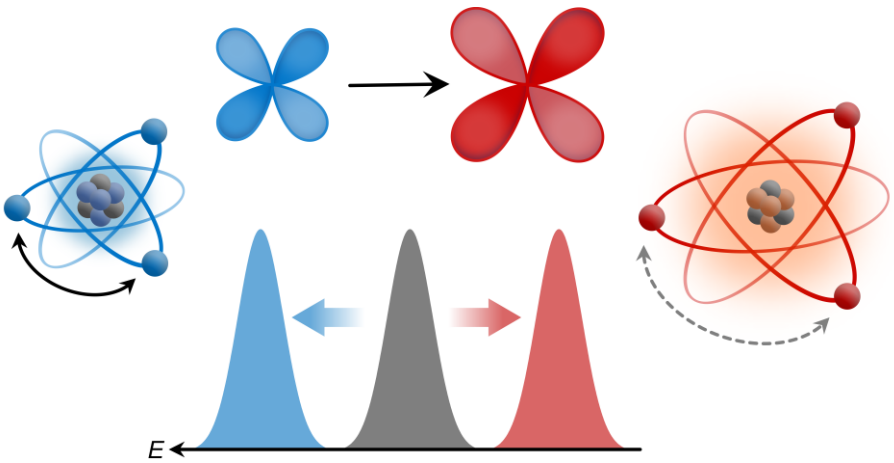

Fig. 1.10 Simplified illustration of the nephelauxetic effect, showing the expansion of a MC *d*-orbital, leading to reduced interelectronic interactions and a shift in SF bands.

bonding described in LF theory. The degree of this cloud-expanding effect, quantified by the nephelauxetic parameter β (ratio B/B_0), could be expressed in a nephelauxetic series of metals and simple ligands and depends on the effective nuclear charge of the metal ion and the electronegativity of the ligand donor atoms.[164–166] However, this data, based mainly on monodentate ligands, has limited predictive power when applied to photoactive TMCs with more complex multidentate ligand scaffolds.[88]

The key strategy for tuning SF energies in a TMC is to control the nephelauxetic effect by modifying M–L bond covalency and the size of the *d*-orbitals. Generally, the electronic structure of MC ESs in TMCs is determined by the ratio between LF splitting Δ_0 and the Racah parameter B.[166] Thus, the nephelauxetic effect can also be crucial for CT emitters, as it allows control over the relative energies of CT and interconfigurational MC states (e.g., chromium(0) and manganese(I) systems).[124,127] For stronger CT emission, an increase in M–L bond covalency, in addition to a stronger LF, can lift dark MC states above CT states, reducing NR processes.[88] In TMCs with π donor ligands, the competition between decreasing the LF and increasing the M–L bond covalency can destabilize MC ESs relative to CT ESs, though this effect is insufficient to significantly extend the LT of the latter.[167,168]

SF transitions are typically found in the NIR-I (750–1000 nm) to NIR-II (1000–1700 nm) spectral regions and are generally lower in energy than CT transitions.[52,70] Blue-shifting SF energies into the visible range is challenging compared to tuning CT energies. Metals in high oxidation states required for this purpose often give rise to closely lying dark LMCT states and/or form highly covalent M–L bonds, resulting in lower overall SF energies (e.g, manganese(IV)).[94,144] As will be discussed for chromium(III) TMCs, lowering SF energies by increasing the Racah parameter B can introduce challenges with the energy gap law and enhanced multiphonon relaxation, leading to low PL efficencies.[57,61]

The TS diagram for octahedral d^3 systems (Fig. 1.4) shows that MC states exhibit different functional dependencies on the ratio Δ_0/B.[90,91] While the energy of the lowest $^4T_2$ state corresponds to Δ_0, the SF states $^2E/^2T_1$ are only weakly dependent on Δ_0 and are primarily influenced by the Racah parameters B and C (eq. 1.1–1.3).[79] For perfectly octahedral chromium(III) systems ($B_0 = 918\ cm^{-1}$), assuming $C/B = 4$, LF theory predicts a theoretical emission energy maximum at 559 nm. Achieving a blue shift of SF emission towards this intrinsic upper limit into the red spectral region (>725 nm), however, has so far been achieved at the expense of PL efficiency.[70] In red-emissive complexes, such as $[Cr(en)_3]^{3+}$ ($\lambda_P = 670$ nm, Fig. 1.11), with ligands that predominantly influence the σ-system, the LF strength and the rigidity are too weak to suppress NR deactivation pathways.[169] Transitioning to σ-donating and π-accepting polypyridine ligands strengthens the emission by widening the $^4T_2$ to $^2E/^2T_1$ energy

gap but decreases the Racah parameter B.[88] The PL of the respective chromium(III) complexes typically falls within a relatively narrow spectral window in the NIR I (725–780 nm) because the first coordination sphere of six pyridines is largely preserved.

$$E(^4T_2) - E(^4A_2) = \Delta_O \tag{1.1}$$

$$E(^2T_1) - E(^4A_2) \approx 9B + 3C - 24\left(\frac{B^2}{\Delta_O}\right) \tag{1.2}$$

$$E(^2E) - E(^4A_2) \approx 9B + 3C - 50\left(\frac{B^2}{\Delta_O}\right) \tag{1.3}$$

Substitution of donor atoms by replacing three of the six pyridine units with stronger σ- and π-donating carbanionic phenyl rings, as in *fac*-Cr(ppy)$_3$ (λ_P = 910 nm, Φ_P = 0.03%, Fig. 1.11), creates a more covalent bonding situation (Fig. 1.9).[170] Despite the stronger LF compared to structurally related [Cr(bpy)$_3$]$^{3+}$ (λ_P = 727 nm, Φ_P = 0.09%), the PL efficiency of the neutral TMC is lower, attributed to enhanced multiphonon relaxation due to the lower emission energy, trigonal distortion, and self-quenching via intermolecular π–π and CH–π interactions.[70]

Further red-shifting of SF energies into the NIR-II region was achieved in [Cr(dpc)$_2$]$^+$ (λ_P = 1067 nm, Fig. 1.11) by incorporating the anionic dpc ligand with a carbazolato backbone.[171] Similar to *fac*-Cr(ppy)$_3$, the combination of π-accepting pyridines with π-donating amides/phenyls induces a push-pull effect of π density, increasing bond covalency compared to purely pyridine-based TMCs.[170] However, nearby ^{2}LMCT states cause ES distortion and likely enhanced multiphonon relaxation in [Cr(dpc)$_2$]$^+$, resulting in weak PL detectable only at low temperatures in frozen solution (Φ_P < 0.00089%).

The influence of ligand backbone substitutions on SF energies was investigated in a series of chromium(III) complexes [Cr(bpi^{R1,R2})]$^+$ (R^1 = H; R^2 = H, OMe and R^1 = Me, Et, OMe, NMe_2; R^2 = H, Fig. 1.11) with isoindoline-based ligands.[172,173] Upon substitution on the pyridine moieties, the PL of the TMCs could be tuned between 777 and 970 nm, with the PL efficiency strongly influenced by the energy gap law.[61] Despite some LMCT character, SF energies increase linearly with an increasing nephelauxetic parameter β, forming a consistent trend with the PL maxima of *fac*-Cr(ppy)$_3$ and [Cr(dpc)$_2$]$^+$.[88]

The aforementioned studies addressed the nephelauxtetic effect using pyridine, phenyl and amine ligands. In addition, the cyclometalated TMCs *fac*-Cr(C^N)$_3$ and *fac*-Cr(C^P)$_3$ (Fig. 1.11) adjusted M–L bond covalency by employing amine and

phosphine donors.[174] Both complexes exhibit SF emission in the NIR region (λ_P = 765, 866 nm), although NR deactivation via intermolecular interactions (solid state) and flexible chelate rings (solution) limit PL performance. Considering the SF energies of $[Cr(bpy)_3]^{3+}$ and *fac*-$Cr(ppy)_3$, these results establish a nephelauxetic series $NR_3 < PR_3 \cong py < Ph^-$ for chromium(III) TMCs.[169,170]

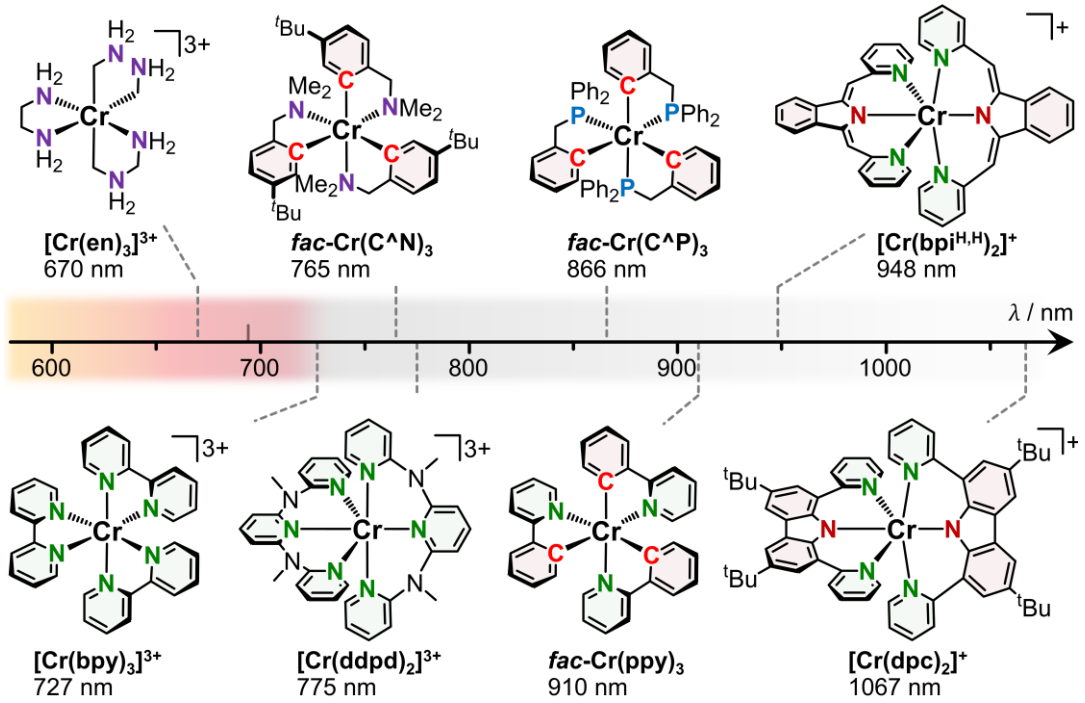

Fig. 1.11 Luminescent chromium(III) complexes arranged by increasing emission energy (low-energy maximum). The donor atoms of the ligands are color-coded based on their electronic properties (purple: σ-donor, blue and green: σ-donor/π-acceptor; red: σ-donor/π-donor).[87,169–174]

1.4 Innovation Molecular Rubies

Inspired by the gemstone ruby (Al_2O_3:Cr^{3+}), the most prominent example of a SF emitter, which led to the development of the first laser, pseudooctahedral chromium(III) TMCs have been proposed as promising photoactive complexes.[175] These molecular alternatives offer intrinsic advantages over their solid-state counterpart, including tunability, sensitivity, and solubility, making them suitable for applications in homogeneous photocatalysis, optical sensing, photon upconversion (UC) and circularly polarized luminescence.[50,56,60,70,79] However, as discussed in Section 1.2.1, the PL efficiency of many chromium(III) TMCs is limited by rapid NR decay (Φ_P < 0.15%), hindering their use in optical applications.[70,74] This limitation was overcome with the discovery of $[Cr(ddpd)_2]^{3+}$, which exhibits intense, sharp dual

SF emission with ES LTs and QYs an order of magnitude higher than previously reported chromium(III) compounds.[87] As highlighted in Section 1.2.2, the structural key to these exceptional photochemical properties lies in the design of the tridentate ddpd ligand, which prevents trigonal distortion and forms six-membered chelate rings with optimized N–Cr–N bite angles.[73] $[Cr(ddpd)_2]^{3+}$ demonstrates that the photochemical properties of a TMC can be controlled through a structure-property design approach.

Building on its remarkable optical properties, $[Cr(ddpd)_2]^{3+}$ became the first member of a family of strongly emissive chromium(III) TMCs featuring this structural motif, giving rise to the term "molecular rubies".[73,79] This chapter summarizes the progress in the field of molecular rubies, focusing on structure-property design concepts aimed at modifying their GS and ES characteristics. It concludes with an overview of selected emission- and quenching-based applications enabled by the unique properties of this innovative compound class, highlighting their untapped potential.

1.4.1 Advances in Ruby Design

To distinguish molecular rubies from other chromium(III) emitters, several key defining properties can be identified.[79] Structurally, molecular rubies incorporate rigid, tridentate six-membered chelators that form strong σ-bonds with the metal, creating a strong LF close to the second doublet/quartet crossing point in the TS diagram.[90,91] This configuration prevents the repopulation of the deactivating $^4T_2$ state and promotes effective population of the emissive $^2E/^2T_1$ states. Rapid ISC further ensures that the system does not remain in the detrimental $^4T_2$ state long enough for significant nuclear motion beyond the FC geometry. These structural and dynamic features result in strong PL with a long ES LT at RT, characterizing molecular rubies.

Introducing bulky substituents in the periphery of the ddpd ligand, as in the series $[Cr(ddpd^{5R})]^{3+}$ (R = Me, Mes, Tripp, Fig. 1.12), protects the chromium(III) center from triplet oxygen quenching via Dexter-type E_NT.[176] By incorporating sterically demanding aryl substituents, the PL performance under aerated conditions improves by nearly an order of magnitude (R = Tripp, Φ_P = 5.1%, τ_P = 518 us) compared to the parent compound $[Cr(ddpd)_2]^{3+}$ (Φ_P = 0.8%, τ_P = 52 us),[84] without affecting the PL energy. Due to the localized nature of SF states, shielding effects are easier to achieve in SF systems than in CT systems, where the ES character is more delocalized.

Another TMC that meets the criteria for molecular rubies, is $[Cr(H_2tpda)_2]^{3+}$ (H_2tpda = 2,6-bis(2-pyridylamino)pyridine, λ_P = 738, 782 nm, Fig. 1.12), which exhibits emission energies similar to $[Cr(ddpd)_2]^{3+}$.[87,177] Due to the short distances between the highly charged metal center and the bridging NH groups, this complex is acidic

(pK_a = 8.8) and can be reversibly deprotonated into a non-emissive species in solution. In the solid state, and presumably in solution, counterions coordinate to the NH groups via hydrogen bonds, reducing oxygen sensitivity by protecting the metal center. The pronounced acidity of $[Cr(H_2tpda)_2]^{3+}$ further facilitates rapid NH/ND exchange in D_2O, which enhances PL efficiency by reducing multiphonon relaxation.

In $[Cr(dqp)_2]^{3+}$ (dqp = 2,6-di(quinolin-8-yl)pyridine, λ_P = 724, 747 nm, Fig. 1.12), which features the rigid dqp ligand, the SF energies are more significantly modified than in the previous examples.[178] Due to the lower metal-ligand bond covalency, the two emission maxima are hypsochromically shifted relative to $[Cr(ddpd)_2]^{3+}$.[87] The differing impacts of LF strength Δ_0 and the Racah parameter B on the doublet energies (eq. 1.1–1.2) are reflected in the larger separation of the $^2E/^2T_1$ bands. Functionalizing the ligand periphery in $[Cr(dqp^R)_2]^{3+}$ (R = OMe, Br, CCH, Fig. 1.12), enhances the nephelauxetic effect relative to the unsubstituted TMC, with the methoxy group exerting the strongest influence on the π-system (λ_P = 727, 759 nm).[179]

In heteroleptic molecular rubies such as $[Cr(ddpd)(dqp)]^{3+}$ (λ_P = 728, 762 nm, Fig. 1.12) and $[Cr(dqp)(dqp^{OMe})]^{3+}$ (λ_P = 725, 752 nm, Fig. 1.12), the SF energies lie between those of their respective homoleptic counterparts.[180] Predicting PL energies

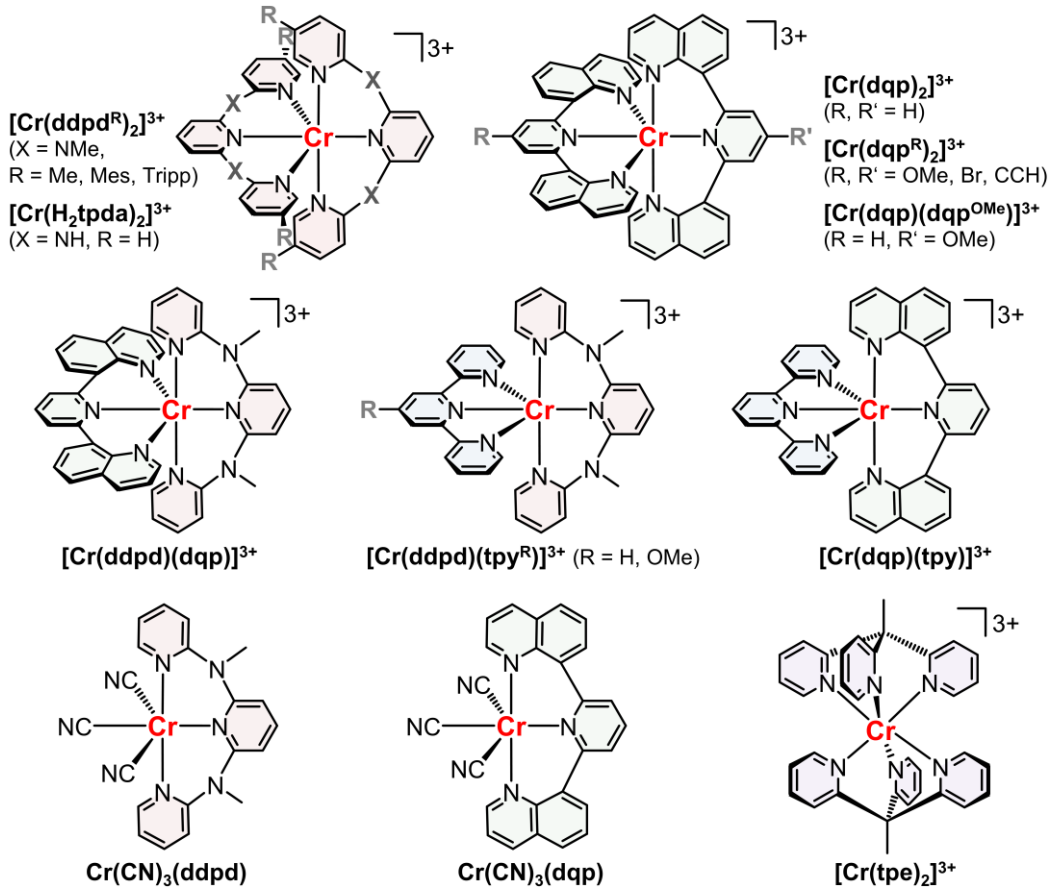

Fig. 1.12 Chemical structures of selected molecular rubies.

in these systems based on additive nephelauxetic effects of the ligands seems feasible, similar to the general approximation of LF strength in heteroleptic TMCs using increment rules derived from their homoleptic analogs.[166] Despite their lower symmetry, which should lift Laporte's rule, the radiative rates of the heteroleptic TMCs are not significantly increased, while NR rates are higher than in the homoleptic species.[79] In contrast, incorporating single six-membered chelators in $[Cr(ddpd)(tpy^{R})]^{3+}$ (R = H, COOEt, τ_P = 1000, 980 µs, Φ_P = 0.06, 0.14%, Fig. 1.12) and $[Cr(dqp)(tpy)]^{3+}$ (τ_P = 578 µs, Φ_P = 0.2%, Fig. 1.12) markedly enhances PL efficiency compared to the homoleptic five-membered chelating systems.[181]

The inclusion of monodentate ligands in $Cr(CN)_3(ddpd)$ (τ_P = 79 µs, Fig. 1.12) and $Cr(CN)_3(dqp)$ (τ_P = 13 µs, Fig. 1.12), which induce large Δ_0/B values, also results in PL, particularly at lower temperatures.[182] Replacing cyanide with halides as weaker ligands increases NR decay via back-ISC, making the emission undetectable at RT.

The introduction of an an inversion center in molecular rubies, as realized in $[Cr(tpe)_2]^{3+}$ (tpe = 1,1,1-tris(pyrid-2-yl)ethane), by using tripodal ligands, significantly reduces radiative rates (Fig. 1.12).[83] In the centrosymmetric complex, Laporte's rule applies more stringently compared to meridionally coordinated TMCs, resulting in an unprecedented ES LT (τ_P = 4500 µs). Due to the required activation of ungerade parity vibrational modes to allow PL, the emission band is asymmetric and features fine structure. However, the long ES LT and inversion symmetry go hand in hand with a high oxygen sensitivity of PL efficiency and low extinction coefficients for the $^4A_2 \rightarrow {}^4T_2$ MC absorption ($\varepsilon < 50$ cm^{-1}). Additionally, LMCT bands in $[Cr(tpe)_2]^{3+}$ are shifted to higher energies compared to $[Cr(ddpd)_2]^{3+}$.[87] Consequently, photocatalytic applications that rely on visible-light excitation to avoid substrate absorption require high efficiency, particularly at low catalyst concentrations and short optical path lengths.[183]

1.4.2 Emission based Applications

Molecular rubies are highly suitable for optical sensing applications due to their dual, sharp PL in the NIR region, characterized by long ES LTs, high QYs, excitability in the visible region, and excellent thermal and (photo)chemical stability.[60,70,79]

Given that the energy difference between the ^2E and $^2T_1$ states in $[Cr(ddpd)_2]^{3+}$ (ΔE = 660 cm^{-1}) lies within the thermal energy range, the intensity ratio of the two emission bands, reflecting a Boltzmann distribution, can be used for ratiometric optical temperature measurements in solution, nanoparticles, and micelles within the temperature range of 210 – 373 K (Fig. 1.13).[184] The narrow bandwidth, long ES LT, and large energy separation between excitation and emission simplify the spectral

distinction of scattered excitation light and background F and enable combination with other visible light-absorbing/emitting probes.

The high sensitivity of PL to the presence of triplet oxygen allows molecular rubies to function as oxygen sensors when the emission is quantified relative to an oxygen-insensitive emissive compound.[79] Nanosensors embedding $[Cr(ddpd)_2]^{3+}$ have successfully demonstrated simultaneous ratiometric optical measurement of temperature, oxygen partial pressure, and *p*H, covering biologically and physiologically relevant ranges.[185] For this purpose, biocompatible polystyrene nanocarriers doped with the molecular ruby and an inert reference dye were covalently labeled with *p*H-sensitive fluorescein, creating a sensing system that operates under single-wavelength excitation.

The emission bands of $[Cr(ddpd)_2]^{3+}$ and $[Cr(H_2tpda)_2]^{3+}$ exhibit a linear pressure-induced redshift in both solid state and solution (up to $-14.8\ cm^{-1}\ kbar^{-1}$), making them suitable for optical pressure sensing in various media (Fig. 1.13).[92] The pressure sensitivity of molecular rubies exceeds that of the traditional ruby ($-0.8\ cm^{-1}\ kbar^{-1}$), which can be attributed to the greater structural reorganization in molecular materials compared to the oxide.[186] Calculations on $[Cr(ddpd)_2]^{3+}$ indicate that the most significant structural changes under hydrostatic pressure are the compression of the CrN_6 coordination polyhedron and the planarization of the central pyridines.[187] Notably, the pressure response of the $^2T_1$ state is higher than that of the ^2E state (-14.1 and $-7.7\ cm^{-1}\ kbar^{-1}$, solid state), likely due to the stronger π interaction of the doubly occupied orbital with the pyridine donors.[79]

A structural feature of molecular rubies with meridionally coordinating ligands, which form 6-membered chelate rings, is their inherent helical chirality, leading to (*P*,*P*) and (*M*,*M*) enantiomers. The compound class holds significant potential for circularly polarized luminescence (CPL), as they exhibit a high excess of single-handed polarized light due to the magnetically dipole-allowed ($\Delta S \neq 0$) and electrically dipole-forbidden ($\Delta L = 0$) nature of their SF transitions.[79] To achieve chiral resolution, racemic mixtures of $[Cr(ddpd)_2]^{3+}$ and $[Cr(dqp^R)_2]^{3+}$ (R = H, OMe, Br, CCH) were separated into enantiopure materials using chiral high-performance liquid chromatography (HPLC).[178,179,188] The enantiomerically enriched samples display dual CPL with impressive dissymmetry factors ($|g_{lum}| \leq 0.2$), among the highest reported for d-block TMCs. Combined with their high QY and photochemical stability, molecular rubies are promising candidates for applications in chiral optoelectronics and photonics.

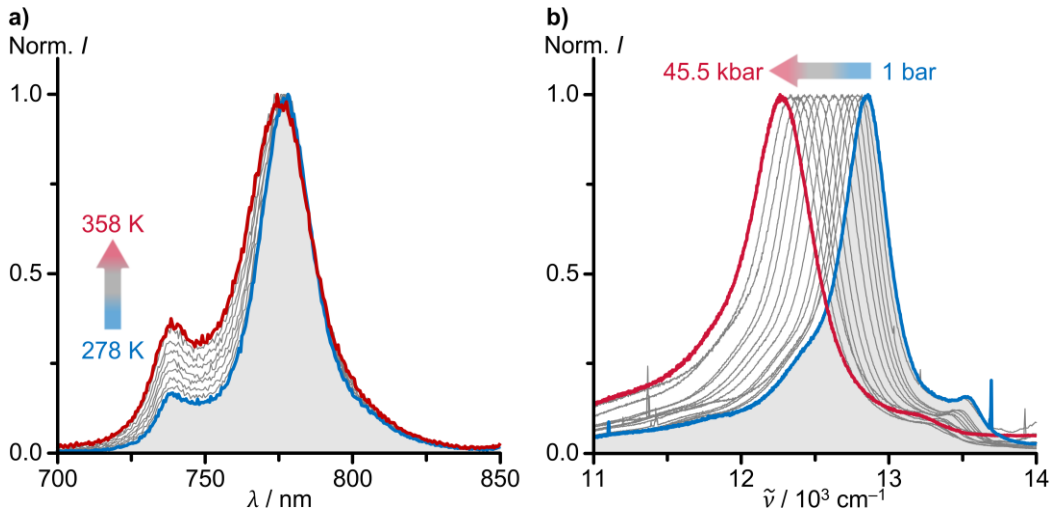

Fig. 1.13 Normalized variable-temperature emission spectra of $[Cr(ddpd)_2](BF_4)_3$ in air saturated H_2O and b) normalized pressure-dependent emission spectra of $[Cr(ddpd)_2](BF_4)_3$ x 3 CH_3CN for a solid sample.[92,184]

1.4.3 Quenching based Applications

Due to their long ES LTs, molecular rubies efficiently participate in homogeneous energy transfer (E_NT) or photoinduced electron transfer (PET) reactions, even at lower quenching rates.[56] The kinetic and thermodynamic preference for either quenching pathway depends on the relative rates, driving forces, and is determined by the ES energies for E_NT and GS/ES redox potentials (vs. FcH/FcH^+ in this work) for PET, as well as the reorganization energies of the donor/acceptor.[24,189]

For PET, the ES redox potential of the TMC is crucial and can be estimated from its GS redox potential and the transition energy between GS and ES at zero vibrational levels (Rehm-Weller equation).[61,62,190] While the ES redox properties of CT sensitizers can be understood using an electron/hole formalism, the potential in SF sensitizers with intraconfigurational ES nature is governed by electron exchange interactions.[191] Typically, an excited molecule acts as both a stronger oxidant and reductant; however, for molecular rubies, only the reductive pathway is relevant due to the unfeasibility of Cr^{IV}/Cr^{III} oxidation in typical ligand environment.[56] Since the lowest SF transitions of molecular rubies with pyridine ligands occur in a similar energy range, the GS potential primarily determines their oxidative strength in the ESs.[79] In PET catalysis, a MC reduction, as observed in $[Cr(ddpd)_2]^{3+}$ (E_0 = –1.11 V)[87], leading to a substitutionally labile high-spin chromium(II) species (at RT), is less favorable than a predominantly LC reduction, as enforced in $[Cr(dqp)_2]^{3+}$ (E_0 = –0.80 V)[178] and $[Cr(tpe)_2]^{3+}$ (E_0 = –0.88 V)[83], as the reduced species should be substitutionally stable under the catalytic conditions.

Centrosymmetric $[Cr(tpe)_2]^{3+}$ ($E^* = 0.87$ V) features a non-innocent ligand facilitating LC reduction by the coplanar orientation of the *trans*-coordinated pyridines.[83] The TMC catalyzes the visible-light-driven radical cation [4+2] cycloaddition of *trans*-anethole and 2,3-dimethyl-1,3-butadiene with quantitative conversion under aerated conditions (Fig. 1.14).[183] Surpassing the prominent photocatalyst $[Ru(bpz)_3]^{2+}$ in photostability, reversible redox chemistry, and ES LT, the molecular ruby demonstrates exceptional performance and reusability in this photoreaction. The mechanism is initiated by the reductive quenching of the excited sensitizer by *trans*-anethole. In the presence of oxygen as a redox mediator, non-geminate back ET is minimized due to rapid photocatalyst regeneration, while the lower E_NT quenching rate to triplet oxygen renders this side reaction negligible.

Similarly, under oxygenated conditions, $[Cr(dqp)_2]^{3+}$ ($E^* = 0.86$ V) catalyzes aerobic bromination of methoxyaryls, oxygenation of 1,1,2,2-tetraphenylethylene, and aerobic hydroxylation of arylboronic acids.[191] In contrast, the vinylation of *N*-phenylpyrrolidine proceeds without requiring oxygen in catalyst regeneration. The efficiency of these reactions generally benefit from the long ES LTs of the molecular rubies, which compensate for the relatively low thermodynamic driving force of PET.

Due to their relatively low SF energies, resulting in minimal spectral overlap, molecular rubies can sensitize only few substrates through dynamic E_NT.[56] However, substrate activation can be achieved indirectly after prior singlet oxygen formation via Dexter-type E_NT. Singlet oxygen sensitized by $[Cr(ddpd)_2]^{3+}$ can, for example, serve as a reagent for the α-cyanation of tertiary aliphatic amines with Me_3SiCN, yielding α-aminonitriles.[192] Since amine oxidation by $[Cr(ddpd)_2]^{3+}$ is thermodynamically unfeasible, the reaction proceeds with high selectivity via singlet oxygen sensitization, followed by selective C–H bond activation. The catalysis benefits from the high quantum efficiency of singlet oxygen formation ($\Phi(^1O_2) = 61\%$), with the long ES LT of the sensitizer more than compensating for the low oxygen quenching rate.[87]

Photon UC offers a solution to the challenge of low ES energies of energy donors to sensitize photoreactions, providing the acceptor has a sufficiently long ES LT. Molecular rubies like $[Cr(ddpd)_2]^{3+}$ meet this requirement and can also function as energy acceptors, making UC particularly feasible at short donor-acceptor distances.[79] The hetero-oligometallic sensitizer-activator assembly $[Cr(ddpd)_2][Yb(dpa)_3]$ exhibits chromium(III) SF emission in the solid state after excitation of two lanthanide ions ($^2F_{7/2} \rightarrow {}^2F_{5/2}$), followed by cooperative E_NT to the 3d TMC.[193] In this assembly, the biphotonic UC process is structurally facilitated by each activator cation being surrounded by five sensitizer anions, enabling efficient static E_NT. Additionally, the downshifting back-E_NT $^2E/{}^2T_1(Cr^{3+}) \rightarrow {}^2F_{5/2}(Yb^{3+})$ (Dexter and Förster mechanism) are diminished in this system through the spatial separation of the metal centers.

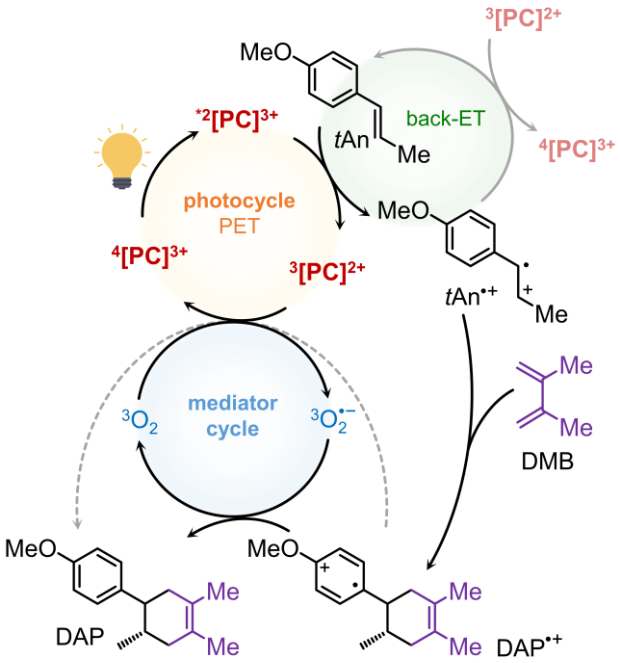

Fig. 1.14 Proposed mechanism for the visible light-driven radical cation [4+2] cycloaddition of *trans*-anethole (*t*An) and 2,3-dimethyl-1,3-butadiene (DMB) to the Diels-Alder product (DAP) using the photocatalyst $[Cr(tpe)_2]^{3+}$ (PC).[183]

2 Motivation and Aim of the Work

Molecular rubies possess remarkable photophysical properties, positioning them as promising candidates for applications in optical sensing, photocatalysis, photon upconversion and circularly polarized emission.[50,56,60,70] However, the relationship between these properties and their underlying geometric and electronic structure is not yet fully understood, a gap that must be addressed for the ongoing development and sustainable use of these 3d transition metal complexes. In particular, tuning emission energies across the high-energy NIR region, as well as deeper understanding of excited state dynamics remain underexplored.[88] Additionally, current representatives of the compound class exhibit limited diversity in their optical properties, such as emission in the non-visible range and the need for blue-light excitation, restricting their broader applicability.[79]

This research is motivated by the need to address these challenges and push the boundaries of molecular ruby design. The work is divided into six projects, each contributing to the overarching goal of controlling spin-flip energies and excited state redox potentials. The primary objectives are to develop new molecular rubies with enhanced photophysical properties, understand these properties through detailed structure-property analysis, and to increase accessibility by establishing new synthetic pathways. By integrating computational methods, this research ultimately aims to improve the predictive power for tuning photochemical properties, enabling targeted design of these photoactive compounds for a broader range of applications.

Enhancement of Photochemical Properties

Photoactive compounds based on rare metals like ruthenium(II) achieve strong red emission and are widely employed, particularly in biosensing.[61] However, no molecular example among the more abundant chromium(III) complexes has yet combined the benefits of spin-flip systems with strong visible light emission.[94] Existing molecular rubies typically emit in the NIR region due to a pronounced nephelauxetic effect, while visible-light emitting chromium(III) complexes suffer from poor quantum yields.[70,79] Guided by quantum chemical predictions, this work seeks to overcome this limitation by increasing spin-flip energies in molecular rubies while maintaining high luminescence efficiency (Fig. 2.1a, Section 3.2). Additionally, it aims to enhance electrochemical properties by designing an electron-poor complex with a high excited-state potential to expand the applicability of molecular rubies in photoredox catalysis.

First-row transition metal complexes are rarely used for photon upconversion compared to their heavier, less abundant counterparts, primarily due to lower emission energies and shorter excited-state lifetimes, resulting in inefficient energy transfer.[194,195] The developed molecular ruby, with its sufficient excited-state energy, is expected to enable the sensitization of anthracenes for triplet-triplet annihilation photon upconversion (Fig. 2.1b, Section 3.3). A follow-up project aims to efficiently convert low-energy green photons into anti-Stokes shifted blue photons via an underexplored energy transfer mechanism using a 3d metal complex. Besides appearing as delayed fluorescence, the upconverted energy is intended to drive chemical transformations of sterically less-hindered anthracenes.

For broader applications in photoredox catalysis, it is essential to diversify both the optical and electrochemical properties of molecular rubies.[56,60] This work focuses on modifying the ground state reduction potential of molecular rubies by introducing electron-donating or electron-withdrawing groups in the ligand periphery (Fig. 2.1c, Section 3.4). The goal is to determine to what extent their redox behaviour can be tuned independently of their luminescence properties enabling selective optimization for photoredox applications while preserving optical functionality.

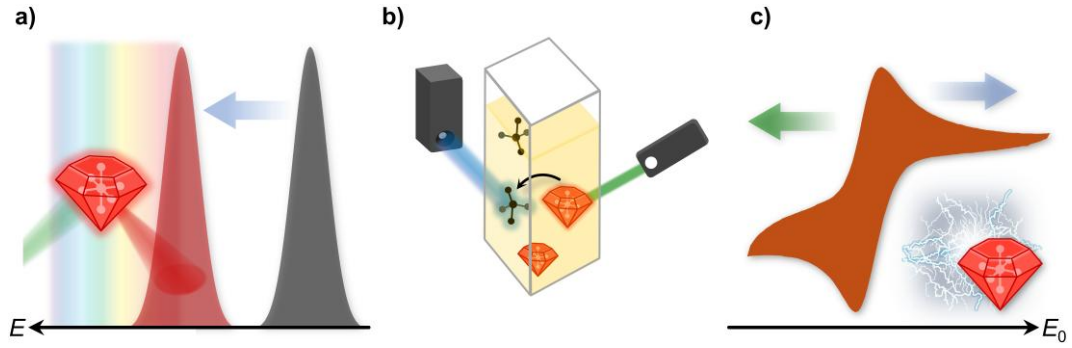

Fig. 2.1 Schematic illustration of aims of the work including a) achieving visible-light emission, b) upconverting light via sensitized triplet-triplet annihilation and c) modifying ground state redox potentials—all focused on molecular rubies.

Tuning of Photochemical Properties

A structure-based approach to control excited-state energies and dynamics is crucial for tailoring the properties of photoactive compounds to specific applications. Unlike charge-transfer energies with well-established correlations, tuning spin-flip energies presents a greater challenge due to the significant influence of Pauli repulsion and the nephelauxetic effect, and is hence less explored.[88,94] This work centers on analyzing structure-property relationships to uncover structural and electronic key factors governing the energies, population, and non-radiative decay of the emissive states in

molecular rubies (Fig. 2.2a, Section 3.5). The insights gained from the study of an isostructural series of chromium(III) complexes with tridentate ligands aim to provide a consistent picture of excited state dynamics and to inform future design strategies for optimizing the excited-state thermodynamics and kinetics of this compound class.

Beyond improving optical and electrochemical properties, expanding the accessibility of photoactive compounds is essential for their widespread application. However, particularly for heteroleptic molecular rubies, generalized synthetic methods are lacking, as key reagents are often incompatible with ligands of differing basicity.[180,181,196] Another objective of this work is the development and optimization of a versatile synthetic route allowing for the efficient preparation of heteroleptic molecular rubies (Fig. 2.2b, Section 3.6). Furthermore, it seeks to determine whether the spin-flip energies of heteroleptic chromium(III) complexes can be predicted from their respective homoleptic counterparts. Establishing semi-quantitative correlations would enable spin-flip energy tuning via strategic ligand combinations, thus broadening the availability of photoactive compounds with diverse optical properties.

A common limitation of many existing molecular rubies is their incompatibility with post-synthetic modifications to flexibly adjust photophysical properties.[56,79] This work further intend to explore the effect of adduct formation with electrophilic species, such as Lewis acids, on the doublet energies of molecular rubies with free electron pairs at the ligand periphery. Additionally, it seeks to enhance absorption properties by red-shifting the lowest-energy spin-allowed transitions, with the aim of broadening the applicability of molecular rubies in light-harvesting systems (Fig. 2.2c, Section 3.7).

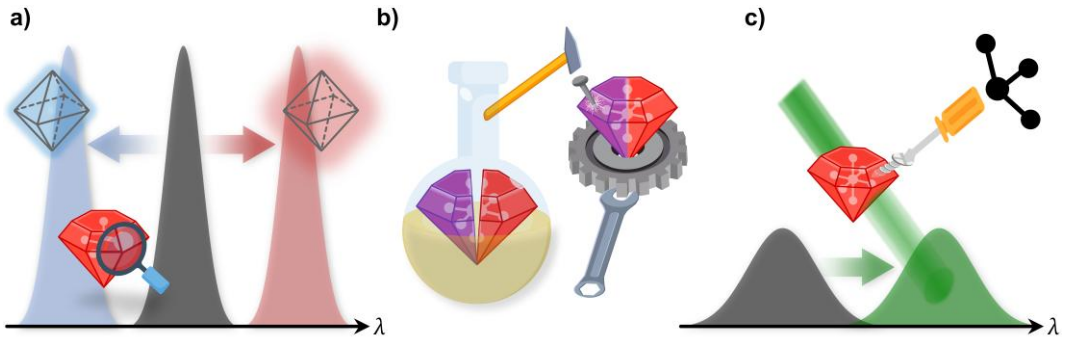

Fig. 2.2 Schematic illustration of aims of the work including a) investigating structure-property relationships, b) expanding accessibility and tuning optical properties and c) red-shifting absorption and post-synthetic tuning of optical properties—all focused on molecular rubies.

3 Results and Discussion

3.1 Overview

The majority of the research findings presented in this work have either been published or submitted to peer-reviewed scientific journals. In the subsequent sections, these publications are reprinted alongside discussion of unpublished results.

Molecular rubies, recognized for their exceptional luminescence performance, exhibit significant potential as optical materials, particularly in applications targeting non-visible emission.[92,178,179,184,185,188] The study *"Strongly Red-Emissive Molecular Ruby $[Cr(bpmp)_2]^{3+}$ surpasses $[Ru(bpy)_3]^{2+}$"* (Section 3.2) focuses on increasing spin-flip energies of molecular rubies by mitigating the nephelauxetic effect. Guided by quantum chemical design, this was achieved by developing $[Cr(bpmp)_2]^{3+}$ (bpmp = 2,6-bis(2-pyridylmethyl)pyridine, Fig. 3.1), wherein *N*-methyl groups were formally replaced by methylene bridges. The resulting complex displays red phosphorescence at 709 nm, with a record quantum yield of 16.0% and a lifetime of 1500 µs in acidic aqueous solution at room temperature. Emission from the lower-energy, weakly distorted $^2T_1$ state is observed upon cooling in the solid state, which is prone to non-radiative decay at room temperature. Deuteration at the pyridine α positions closest to the metal center further enhances the quantum yield and lifetime up to 25% and 2500 µs. In the presence of proton acceptors, the complex (pK_a = 8.6) is reversibly deprotonated to a non-emissive species, enabling environment-dependent switchable emission and ratiometric optical *p*H measurements when combined with a *p*H-independent emitter. The electron-deficient ligand facilitates ligand-centered reduction, giving the system strong excited-state oxidation power of 0.94 V vs. FcH/FcH^+, as demonstrated by emission quenching experiments with azulene. Additionally, dynamic anion coordination to the acidic bridges reduces quenching by oxygen via energy transfer, thus improving oxygen insensitivity. These features position $[Cr(bpmp)_2]^{3+}$ as an efficient, earth-abundant alternative to precious metal compounds, with promising applications in luminescent materials and photocatalysis.

Due to their long excited state lifetimes, molecular rubies are particularly appealing as sensitizers for energy transfer-driven reactions, primary for substrates excitable in the NIR range, such as triplet oxygen.[192,193,197] The study *"Efficient Triplet-Triplet Annihilation Upconversion Sensitized by a Chromium(III) Complex via an Underexplored*

Energy Transfer Mechanism" (Section 3.3), leverages the increased spin-flip energy of $[Cr(bpmp)_2]^{3+}$ to sensitize organic substrates for photon upconversion. This second-generation molecular ruby enables efficient green-to-blue upconversion with anthracenes as annihilators, achieving 12.0% efficiency with DPA (DPA = 9,10-diphenylanthracene, Fig. 3.1), thereby surpassing $[Ru(bpy)_3]^{2+}$ (Φ_{UC} = 0.9%).[198] The high efficiency is driven by an effective doublet-triplet energy transfer (Φ_{3DPA} = 92%), facilitated by matching donor emission/acceptor absorption and the long excited state lifetime of the molecular ruby, which compensates for the inherently low energy transfer rate. The long-lived excited spin-flip emitter and ^{3}DPA form an excited-state equilibrium, leading to both delayed annihilator fluorescence and delayed sensitizer phosphorescence. With sterically less-hindered anthracenes, the sensitizer facilitates [4+4] photodimerization under green light irradiation, a reaction typically requiring UV light excitation in the absence of a sensitizer. However, the low absorbance of the sensitizer necessitates high excitation power, limiting its efficiency at lower intensities. Overall, this study highlights the potential of chromium-based systems in challenging optical applications traditionally dominated by precious metal complexes.

The long excited-state lifetimes of molecular rubies make them highly effective for photoredox catalysis, with the excited-state redox potential being in principle tunable over a broad range through ligand design.[183,191,199,200] The study *"Decoupled Enhancement of Electrochemical Properties in Molecular Rubies"* (Section 3.4) addresses the influence of electron-donating or electron-withdrawing substituents in the ligand periphery on the electrochemical properties of molecular rubies. In the complex series $[Cr(ddpd^X)_2]^{3+}$ (Fig. 3.1), the potential for reversible ground-state reduction shifts by ±0.1 V relative to $[Cr(ddpd)_2]^{3+}$ (E_0 = –0.99, –1.11, –1.19 V vs. FcH/FcH^+, X = CF_3, H, OMe)[87], with reductions occurring predominantly ligand-centered as electron deficiency rises. In contrast, exclusively the electron-rich substituted complexes (X = OMe, NMe_2) show reduced emission energies (λ_{em} = 786, 809 nm) and luminescence efficiency with a more pronounced nephelauxetic effect. In these systems, the substituent with +M effect exert a dominant influence on the metal's t_{2g} orbitals, raising the ^{4}LMCT states and causing a hypsochromic shift in the lowest-energy spin-allowed absorption band. The findings underscore the potential of molecular rubies in photoredox applications, demonstrating that their electrochemical properties can be fine-tuned without compromising their optical properties.

Design principles based on ligand field strength and metal-ligand bond covalency provide general guidelines for enhancing luminescence efficiency or red-shifting the emission of chromium(III) systems.[88,170–174] The study "*Bridge Editing of Spin-Flip Emitters gives Insight into Excited State Energies and Dynamics*" (Section 3.5) disentangles the structural and electronic factors that govern the dynamics and spin-flip energies of molecular rubies. Investigation of the isostructural series

$[Cr(ddpd)_2]^{3+}$, $[Cr(bpmp)_2]^{3+}$, $[Cr(bpop)_2]^{3+}$ and $[Cr(bptp)_2]^{3+}$ (bpop = 2,6-bis(pyridin-2-yloxy)pyridine, bptp = 2,6-bis(pyridin-2-ylthio)pyridine, Fig. 3.1) revealed that the bridging groups between pyridines induce significant geometry variations in chelate ring conformation and pyridine orientation. As confirmed by computational bridging-group alteration at fixed geometries, these structural distinctions play a more substantial role in modulating spin-flip energies than primary electronic effects. Additional calculations on the reference system $[Cr(py)_6]^{3+}$ identified the Cr–N bond lengths as the dominant factor for the nephelauxetic effect. A comparison of spectroscopically deviated energies for all five lowest $^2E/^2T_1$-derived states with calculated values yielded a common scaling factor of 0.89, allowing for detailed doublet state assignments. While all complexes within the nephelauxetic series $[Cr(ddpd)_2]^{3+}$ > $[Cr(bpop)_2]^{3+}$ > $[Cr(bptp)_2]^{3+}$ > $[Cr(bpmp)_2]^{3+}$ undergo fast ISC to the doublet manifold, the sulfur-bridged system exhibits poor luminescence efficiency and photostability, likely due to facilitated thermally activated back-ISC to distorted quartet levels (internal heavy atom effect of sulfur) and enhanced multiphonon relaxation. This study combines dynamic considerations beyond Franck-Condon geometries with detailed structure-property analyses, providing a framework of future design concepts for molecular rubies with enhanced performance.

The synthetic options for molecular rubies are often system-specific due to the distinct electronic demands of the ligands and precursor compounds. Homoleptic complexes with electron-rich ligands can be prepared via labile chromium(II) species, while heteroleptic systems require formation of chromium(III) triflato intermediates using HOTf or AgOTf as halide abstraction agents from halido precursors.[83,87,178,180,181,196] The project "*Factorizing the Nephelauxetic Effect in Heteroleptic Molecular Rubies*" (Section 3.6) describes a versatile synthetic route for heteroleptic molecular rubies, tolerating polypyridine ligands with varying redox properties and basicities. Using this approach, polypyridine ligands could be coordinated to the metal center in any sequence, giving access to the product series $[CrL^XL^Y]^{3+}$ (L^X, L^Y = ddpd, bpmp, bptp, Fig. 3.1). Spectroscopic analysis revealed that the spin-flip emission and absorption energies of the structurally related heteroleptic complexes fall between those of their homoleptic counterparts, suggesting an additive nephelauxetic effect of the constituent ligands. Deconvolution fits allowed experimental determination of the five lowest doublet microstate energies, which are consistent with the calculated values, corrected by a common empirical scaling factor of 0.88. This study establishes semi-quantitative relationships for spin-flip emission energies in heteroleptic molecular rubies and strengthens confidence in computational predictions for these systems. It also broadens the experimental accessibility of molecular rubies with tunable photophysical properties through targeted ligand combinations.

Photoactive compounds with functional groups offer attractive prospects for flexible modification, enabling in situ tuning of optical and electrochemical properties.[47,201,202] The project "*Post-Synthetic Excited State Manipulation in Molecular Rubies*" (Section 3.7) explores the modification of excited state energies in molecular rubies via electrophilic additives. In the presented complex $[Cr(ddad)_2]^{3+}$ (ddad = *N*,*N*'-dimethyl-*N*,*N*'-di(pyridin-2-yl)pyrazine-2,6-diamine, Fig. 3.1), which incorporates a pyrazine moiety within the ligand framework, the Lewis acids BF_3 and $B(C_6F_5)_3$ do not alter the absorption and emission properties, due to the low basicity of pyrazine in the highly charged system. Independent multireference calculations suggest that adduct formation with H^+, CH_3^+ and BF_3, interacting primarily with the σ-system, has a negligible influence on the two lowest doublet energies. Both homoleptic $[Cr(ddad)_2]^{3+}$ and heteroleptic $[Cr(bptp)(ddad)]^{3+}$ (Fig. 3.1) exhibit intense red-shifted absorption bands with maxima at 491 (ε = 2050 M^{-1} cm^{-1}) and 502 nm (ε = 1250 M^{-1} cm^{-1}), respectively, corresponding to ILCT transitions into low-energy π^* orbitals of the pyrazine moiety. Electrochemically, $[Cr(ddad)_2]^{3+}$ undergoes quasi-reversible ligand-centered reduction at an elevated potential (E_0 = –0.87 V vs. FcH/FcH^+) relative to $[Cr(ddpd)_2]^{3+}$, though accompanied by potential side reactions such as proton-coupled electron transfer. This study presents a design strategy for lowering the energy of spin-allowed absorption of molecular rubies while enhancing their electrochemical properties for photocatalysis.

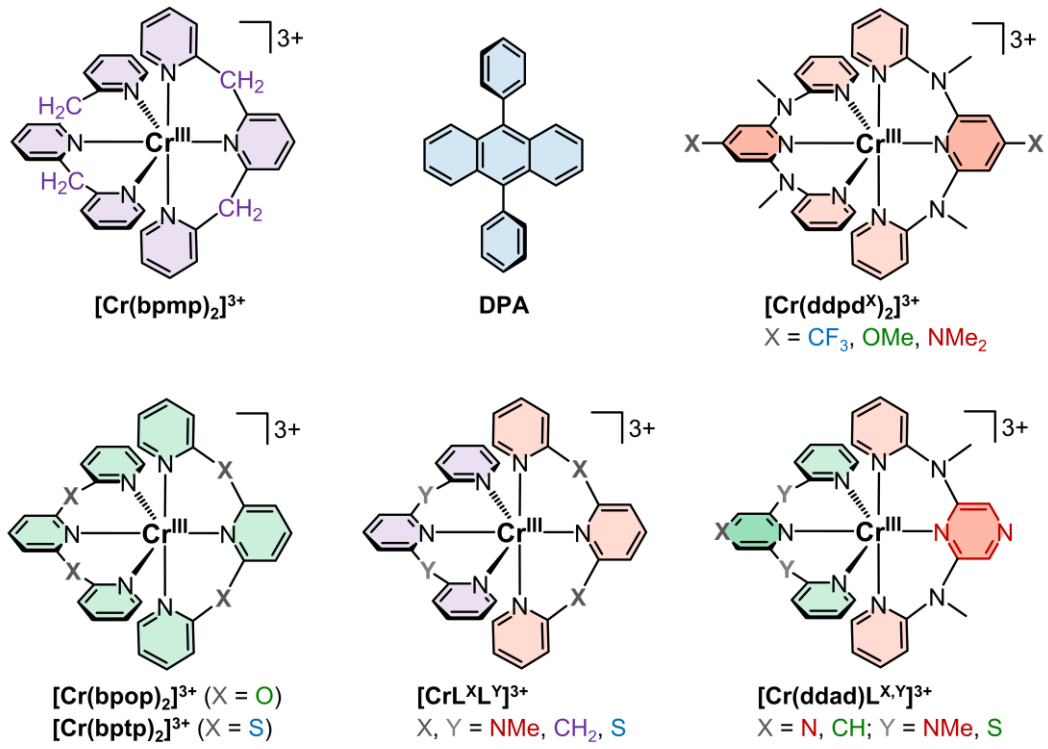

Fig. 3.1 Molecular structures of the compounds investigated in this work.

3.2 Strongly Red-Emissive Molecular Ruby $[Cr(bpmp)_2]^{3+}$ surpasses $[Ru(bpy)_3]^{2+}$

Authors: Florian Reichenauer, Cui Wang, Christoph Förster, Pit Boden, Naz Ugur, Ricardo Báez-Cruz, Jens Kalmbach, Luca M. Carrella, Eva Rentschler, Charusheela Ramanan, Gereon Niedner-Schatteburg, Markus Gerhards, Michael Seitz*, Ute Resch-Genger* and Katja Heinze*. * = Corresponding author.

J. Am. Chem. Soc. **2021**, *143*, 11843–11855. DOI: 10.1021/jacs.1c05971.

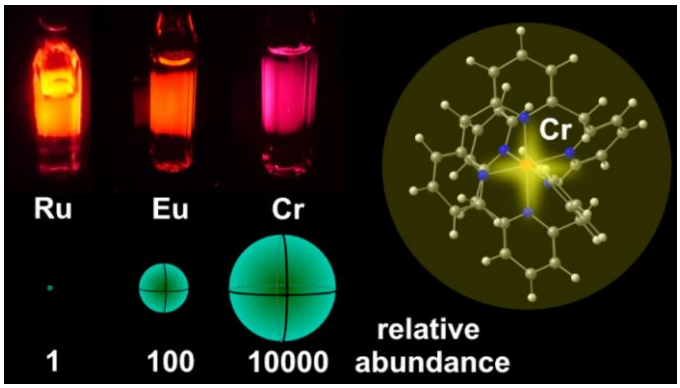

Achieving higher emission energies in spin-flip emitters, extending into the visible range, presents significant application potential in fields like biosensing and photocatalysis, yet remains challenging due to the need to address interelectronic repulsion and the nephelauxetic effect. Guided by quantum chemical predictions, targeted ligand design enabled red phosphorescence in a molecular chromium(III) complex, coupled with a record-breaking photoluminescence performance at room temperature in solution. The photophysical, electrochemical, and acid-base properties of the responsible molecular ruby $[Cr(bpmp)_2]^{3+}$ surpass those of traditional precious metal-based ruthenium(II) charge-transfer complexes, underscoring the bright future of this emerging class of compounds.

Authors Contributions

F. Reichenauer carried out the syntheses, characterization of ground state properties, steady-state spectroscopic experiments, and quantum chemical calculations. C. Wang and U. Resch-Genger conducted time-resolved emission and quantum yield measurements. C. Förster solved and refined the single crystal structures and contributed to the quantum chemical calculations. P. Boden, G. Niedner-Schatteburg and M. Gerhards recorded step-scan IR spectra and low-temperature emission spectra

in the solid state. N. Ugur, R. Báez-Cruz and C. Ramanan performed transient absorption measurements, while J. Kalmbach and M. Seitz did the overtone analysis. L. M. Carrella and E. Rentschler conducted magnetic measurements. K. Heinze conceived and supervised the project and wrote the manuscript with contributions from all authors.

Supporting Information

for this article can be found on pp. 129.

JACS
JOURNAL OF THE AMERICAN CHEMICAL SOCIETY
pubs.acs.org/JACS
Article

Strongly Red-Emissive Molecular Ruby $[Cr(bpmp)_2]^{3+}$ Surpasses $[Ru(bpy)_3]^{2+}$

Florian Reichenauer, Cui Wang, Christoph Förster, Pit Boden, Naz Ugur, Ricardo Báez-Cruz, Jens Kalmbach, Luca M. Carrella, Eva Rentschler, Charusheela Ramanan, Gereon Niedner-Schatteburg, Markus Gerhards, Michael Seitz,* Ute Resch-Genger,* and Katja Heinze*

Cite This: J. Am. Chem. Soc. 2021, 143, 11843−11855

Read Online

ACCESS | Metrics & More | Article Recommendations | Supporting Information

ABSTRACT: Gaining chemical control over the thermodynamics and kinetics of photoexcited states is paramount to an efficient and sustainable utilization of photoactive transition metal complexes in a plethora of technologies. In contrast to energies of charge transfer states described by spatially separated orbitals, the energies of spin-flip states cannot straightforwardly be predicted as Pauli repulsion and the nephelauxetic effect play key roles. Guided by multi-reference quantum chemical calculations, we report a novel highly luminescent spin-flip emitter with a quantum chemically predicted blue-shifted luminescence. The spin-flip emission band of the chromium complex $[Cr(bpmp)_2]^{3+}$ (bpmp = 2,6-bis(2-pyridyl-methyl)pyridine) shifted to higher energy from ca. 780 nm observed for known highly emissive chromium(III) complexes to 709 nm. The photoluminescence quantum yields climb to 20%, and very long excited state lifetimes in the millisecond range are achieved at room temperature in acidic D_2O solution. Partial ligand deuteration increases the quantum yield to 25%. The high excited state energy of $[Cr(bpmp)_2]^{3+}$ and its facile reduction to $[Cr(bpmp)_2]^{2+}$ result in a high excited state redox potential. The ligand's methylene bridge acts as a Brønsted acid quenching the luminescence at high pH. Combined with a pH-insensitive chromium(III) emitter, ratiometric optical pH sensing is achieved with single wavelength excitation. The photophysical and ground state properties (quantum yield, lifetime, redox potential, and acid/base) of this spin-flip complex incorporating an earth-abundant metal surpass those of the classical precious metal $[Ru(\alpha\text{-diimine})_3]^{2+}$ charge transfer complexes, which are commonly employed in optical sensing and photo(redox) catalysis, underlining the bright future of these molecular ruby analogues.

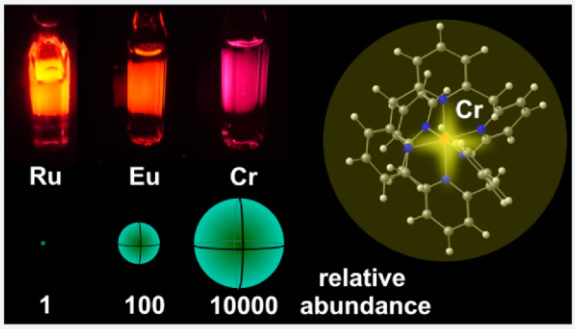

INTRODUCTION

In optical sensing, imaging, and photo(redox) chemistry, complexes with d^6 (e.g., Ru^{II}, Ir^{III}, Os^{II}, or Re^{I} and recently Mo^{0}),[1−13] d^8 (Pt^{II}, Au^{III}),[14] or d^{10} (Cu^{I})[15−22] electron configuration and electron deficient ligands are typically employed. Complexes of these metal ions with suitable electron accepting ligands such as 2,2′-bipyridine (bpy) or 2,2′:6′,2″-terpyridine (tpy) can possess favorable long-lived, luminescent, and/or redox active triplet metal-to-ligand charge transfer (^{3}MLCT) states. Such complexes are hence ubiquitous in photosensitized reactions, OLEDs, bioimaging probes, optical sensors, photodrugs, and dye-sensitized solar cells.[1−10] In the past few years, the substitution of precious metals by earth-abundant base metals has become a vivid and important research area aiming at sustainable photochemistry and photophysical applications.[23−40] Luminescent ligand-to-metal (LMCT) states of earth-abundant Fe^{III} and Co^{III} complexes have emerged very recently as alternative useful excited states of 3d transition metal complexes.[38−40] The highest quantum yields achieved so far with charge transfer (CT) emitters of MLCT or LMCT character based on earth-abundant 3d metals (except from the special case of copper(I)) are 0.001% (Cr^0),[33] 0.7% (Co^{III}),[40] and 2.1% (Fe^{III}).[38]

Fundamentally different from charge transfer states, which involve spatially separated metal and ligand frontier orbitals,[41] are metal-centered spin-flip states.[26,42−48] Such localized spin-flip states can be phosphorescent, in particular in the near-infrared spectral region.[26,44,49] These excited states could be useful for optical applications (sensing, imaging, and lasing) as well as excited state electron and energy transfer reactions. However, most transition metal complexes with a d^2 or d^3 electron configuration suitable for a spin-flip luminescence[50] are only weakly emissive ($\Phi \ll 0.15\%$).[44,49] With the development

Received: June 9, 2021
Published: July 23, 2021

https://doi.org/10.1021/jacs.1c05971
J. Am. Chem. Soc. 2021, 143, 11843−11855

of the so-called molecular ruby $[Cr(ddpd)_2]^{3+}$ (ddpd = *N*,*N*′-dimethyl-*N*,*N*′-dipyridine-2-ylpyridine-2,6-diamine[51,52]), we achieved record photoluminescence quantum yields of Φ = 11% (Φ = 30% with a partially deuterated ddpd ligand) of the NIR luminescence (λ_{em} = 775 nm).[53,54] Several applications in the fields of sensing, photocatalysis, upconversion, and circularly polarized luminescence already emerged in the past few years.[55−64] Variations of the ligand and the complex symmetry increased the lifetime of the luminescent excited spin-flip state up to the current record value of 4500 μs.[65] However, all these highly emissive chromium(III) complexes based on the molecular ruby motif emit in the near-infrared spectral region (≫700 nm; ≪1.77 eV) up to now (Scheme 1).[53−65]

Scheme 1. NIR-Emissive Chromium(III) Complexes and Classical Red-Emissive Complexes Based on Ruthenium(II) and Europium(III)

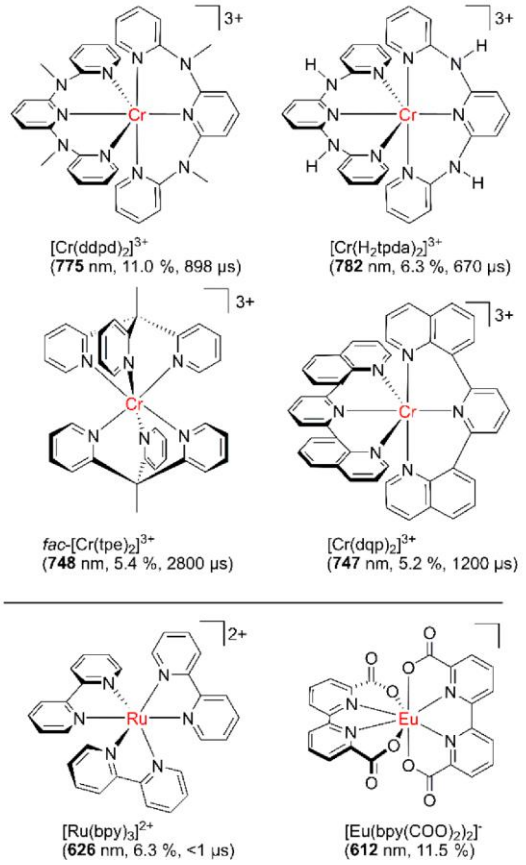

Red, long-lived emission (i.e., <≈700 nm) has been achieved by using europium(III)[66,67] and ruthenium(II) complexes (Scheme 1). Consequently, complexes of these metals are heavily exploited for example in biosensing.[68−70,48] However, these metals are dramatically less abundant than chromium by factors of ca. 100 and 10000. This scarcity is also reflected by the prices of ca. 30, 7300, and 16250 € mol^{-1} for $CrCl_3$, $EuCl_3$, and $RuCl_3$, respectively (based on the hydrated chlorides; commercial supplier, May 2021). Bright red emission from spin-flip excited states has only been realized in solid Cr^{III} materials such as ruby $Al_2O_3:Cr^{3+}$ itself (695 nm)[71−74] and in Mn^{IV}-doped solids, e.g., $K_2SiF_6:Mn^{4+}$ (630 nm),[75] but remained elusive for molecular chromium(III) complexes. Either the spin-flip states of previously reported molecular Cr^{III} complexes are at a too low energy as in the molecular rubies (Scheme 1),[53,57,64,65] or the quantum yields are extremely poor (0.024%−0.000005%).[49]

Unlike the straightforward and well-founded correlations elucidated for charge transfer complexes with MLCT, LMCT, or LL′CT excited states and organic emitters with donor−acceptor character, shifting of the excited doublet state levels of such spin-flip emitters and hence the emission color by chemical measures, such as donor atom variation or substitution patterns of the ligands, is extremely difficult to predict. A clear-cut correlation with ligand types for chromium(III) spin-flip emitters[49] remains elusive beyond the classical ligand field parameters of the covalently reduced d−d interelectronic repulsion (*B* and *C* ligand field parameters), that is, the nephelauxetic series of simple classical ligands such as halides.[76−78] The accurate description[79−82] of the relevant excited quartet *and* doublet states[83−86,58] is challenging due to the required consideration of interelectronic repulsion.[81] The localized spin-flip character instead of the charge transfer nature of the classical CT luminophores with separately addressable spatially distinct wave functions has furthermore precluded reliable predictions for spin-flip levels so far. However, recent method developments in quantum chemistry and coding suitable for open-shell complexes of realistic size in general and chromium(III) in particular conceptually tackled this challenge.[79−87]

In this study, we address the challenge to increase the energy of the spin-flip state in molecular chromium(III) complexes, while concomitantly maintaining a high quantum yield by providing a large enough energy gap between the detrimental metal centered quartet states and the emissive spin-flip level(s) using high-level quantum chemical calculations and the translation to synthesis, spectroscopy, and first applications of the resulting complex.

RESULTS AND DISCUSSION

Quantum Chemical Screening. To identify a ligand modification, which shifts the energy of the emissive spin-flip state(s) (^2E and $^2T_1$) of chromium(III) complexes to higher energy while maintaining a large enough quartet state energy ($^4T_2$), we screened six-coordinate chromium(III) complexes with several monodentate and chelate ligands (NH_3, CN^-, $acac^-$) and in particular pyridine-based ligands (py, bpy, tpy, ddpd) by high-level quantum chemical methods. As density functional theory (DFT) methods failed to give the correct ordering of doublet (^2E, $^2T_1$) and quartet excited states ($^4T_2$),[81] an ab initio multireference method was selected.[83−86] Complete active space self-consistent field (CASSCF) calculations combined with *N*-electron valence state perturbation theory (NEVPT2) to account for dynamic electron correlation based on a fully internally contracted (FIC) wave function have been successfully used for open-shell metal complexes.[83−86,58,44] This method was employed in the following for the complexes selected.

First, DFT calculations on the CPCM(acetonitrile)-UB3LYP-D3BJ-ZORA/def2-TZVPP level deliver the optimized geometries of the chromium(III) complexes in their respective $^4A_2$ ground states. Subsequently, CASSCF-FIC-NEVPT2 calculations with an active space comprising the five 3d orbitals and the three d electrons CAS(3,5) estimate the required excited state energies (Table S1, Supporting Information). These calcu-

https://doi.org/10.1021/jacs.1c05971
J. Am. Chem. Soc. 2021, 143, 11843−11855

lations were followed by an ab initio ligand field theory (AILFT) analysis to yield the Racah parameters B and C and the ligand field splitting Δ_0 (Table S2).[83,84]

This initial screening of DFT-optimized chromium(III) complexes coordinated by monodentate and chelate ligands $Cr(acac)_3$, $[Cr(NH_3)_6]^{3+}$, $[Cr(py)_6]^{3+}$, $[Cr(tpy)_2]^{3+}$, $[Cr(bpy)_3]^{3+}$, $[Cr(ddpd)_2]^{3+}$, and $[Cr(CN)_6]^{3-}$ yielded ligand field splittings Δ_0 ($^4T_2$ energies) increasing in the order of $acac^-$ < py < tpy < ddpd < NH_3 < bpy < CN^- (Table S1). The experimental spectrochemical series $acac^-$ < tpy < ddpd < bpy < CN^-, that is, the experimentally observed ligand field transitions $^4A_2 \rightarrow {}^4T_2$, confirms this approach. As the ligand field splitting Δ_0 of all these complexes is large enough to enable luminescence from doublet states, the decisive parameter is the Racah parameter B, which determines the energy of the doublet states. The calculated B values increase in the order CN^- (888 cm^{-1}) < tpy < ddpd < py < $acac^-$ ≈ bpy < NH_3 (988 cm^{-1}) (Table S2). Clearly, this nephelauxetic series is difficult to explain or even to predict based on simple guidelines. As the tridentate ddpd ligand performed well in previous luminescence studies of its chromium(III) complex due to its large enough Δ_0 and relative rigidity,[26,53,54] we attempted simple modifications of ddpd maintaining the tridentate ligation and the six-membered chelate rings.

Replacing the NMe groups of the ddpd ligand by CH_2 bridges provided a hit structure based on the two conditions of high energy doublet *and* high energy excited quartet levels. The chromium(III) complex $[Cr(bpmp)_2]^{3+}$ with the ligand 2,6-bis(2-pyridylmethyl)pyridine (bpmp) shows the highest calculated B = 1003 cm^{-1} in the series, while maintaining a large enough Δ_0 = 20882 cm^{-1} (Tables S1 and S2).

For $[Cr(bpmp)_2]^{3+}$ and its parent complex $[Cr(ddpd)_2]^{3+}$ the active space was then expanded to CAS(7,12) with the two filled Cr−N σ-bonding orbitals and a second d shell.[86,87] This methodology had proven to be sufficiently accurate to predict the relative energies of excited quartet and doublet states and even the energy gap between the two lowest doublet states for $[Cr(ddpd)_2]^{3+}$.[58]

The refined calculation of the doublet and quartet excited states of $[Cr(bpmp)_2]^{3+}$ using CASSCF(7,12)-FIC-NEVPT2 confirmed the relative doublet and quartet energies (Figure 1; Tables S1 and S3). Interestingly, one doublet microstate of $^2T_1$ parentage drops below the lowest energy doublet microstate of ^2E parentage in the CASSCF(7,12)-FIC-NEVPT2 calculation, similar to the doublet state ordering of the parent complex $[Cr(ddpd)_2]^{3+}$ (Figure 1 and Table S3).[58] The energy gap between the lowest doublet state and the lowest excited quartet level (from the $^4T_2$ set) in $[Cr(bpmp)_2]^{3+}$ amounts to 6010 cm^{-1} (>70 kJ mol^{-1}) on this level of theory. After excitation, intersystem crossing (ISC), and vibrational cooling (VC), this large gap prohibits back-intersystem crossing (back-ISC) at room temperature. Consequently, the detrimental nonradiative relaxation via the $^4T_2$ state is eliminated. Importantly, the calculated energy of the lowest emissive doublet level of $[Cr(bpmp)_2]^{3+}$ exceeds that calculated for $[Cr(ddpd)_2]^{3+}$ by 766 cm^{-1} at the same level of theory as desired (Figure 1 and Table S3).

Synthesis, Structure, and Ground State Reactivity of $[Cr(bpmp)_2]^{3+}$. Encouraged by the quantum chemical predictions and the facile synthesis of the proposed suitable ligand bpmp,[88] the corresponding chromium(III) complex $[Cr(bpmp)_2]^{3+}$ was prepared. However, unlike the straightforward synthesis of $[Cr(ddpd)_2]^{3+}$,[53] simple mixing of bpmp and

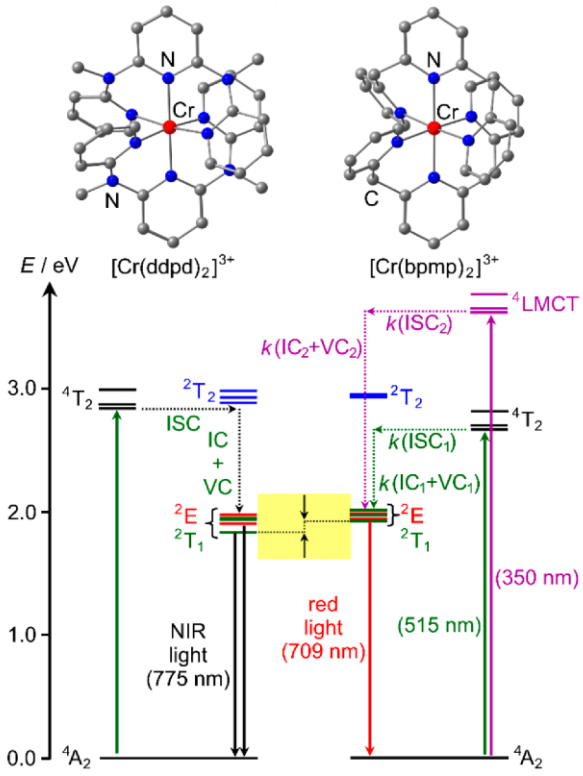

Figure 1. DFT-optimized geometries and Jablonski diagrams derived from CASSCF(7,12)-FIC-NEVPT2 calculations of $[Cr(ddpd)_2]^{3+}$ (left)[58] and $[Cr(bpmp)_2]^{3+}$ (right). The energy difference between the two lowest doublet levels of the complexes is indicated by arrows and highlighted in yellow. ISC = intersystem crossing, IC = internal conversion, and VC = vibrational cooling. Decay cascades starting from ^{4}LMCT and $^4T_2$ states are indicated with dotted purple and green arrows, respectively. The experimentally employed excitation and observed emission wavelengths are given in parentheses.

$CrCl_2$ resulted in redox reactions instead of the desired complexation. Consequently, a stepwise route starting from chromium(III) chloride[89,90] instead of chromium(II) chloride was applied (Figure 2a).

Refluxing the inexpensive starting material $CrCl_3 \cdot 6H_2O$ with 1 equiv of the ligand bpmp in isopropanol gives the green chlorido complex $Cr(bpmp)Cl_3$ in nearly quantitative yield (Figure 2a). The heteroleptic complex $Cr(bpmp)Cl_3$ was characterized by IR spectroscopy, mass spectrometry, and elemental analysis (Figures S1 and S2). Quantitative substitution of the three coordinated chlorido ligands of $Cr(bpmp)Cl_3$ by more labile triflates with triflic acid yields the red-brown complex $Cr(bpmp)(OTf)_3$ under release of gaseous HCl (Figure 2a). An analogous procedure starts from $CrBr_3 \cdot 6H_2O$ but gives no further advantage (Figures S3 and S4). The constitution of $Cr(bpmp)(OTf)_3$ is confirmed by IR spectroscopy, mass spectrometry, and single crystal X-ray diffraction (Figure 2b, Figures S5 and S6).

XRD analysis of a single crystal of $Cr(bpmp)(OTf)_3 \cdot {}^1/_4CH_3CN$ confirms the meridional configuration of the cation (Figure 2b). Interestingly, the triflato ligands form intra- and intermolecular CH···O hydrogen bonds to the methylene bridges of the bpmp ligand, indicating a significant

https://doi.org/10.1021/jacs.1c05971
J. Am. Chem. Soc. 2021, 143, 11843−11855

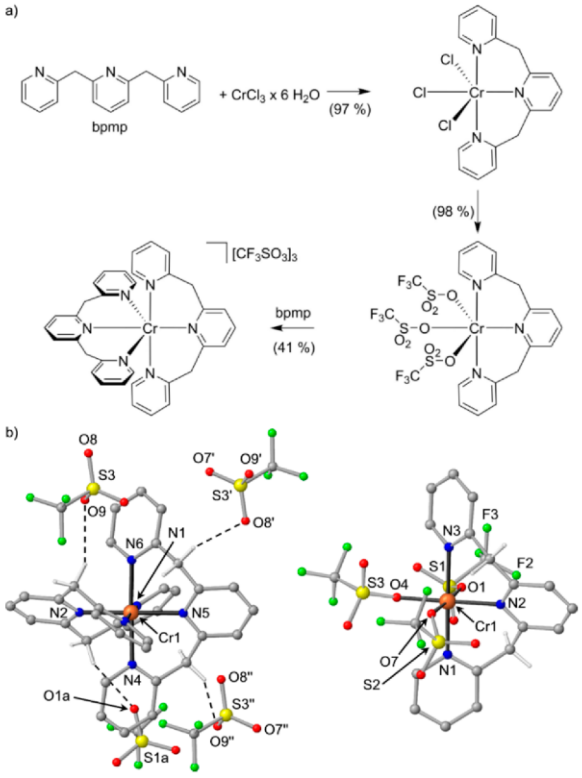

Figure 2. (a) Synthesis of $[Cr(bpmp)_2][OTf]_3$ via $Cr(bpmp)Cl_3$ and $Cr(bpmp)(OTf)_3$ and (b) molecular structures of the complexes in the solid state. Hydrogen bonding of triflate ions to the CH_2 groups is illustrated in $[Cr(bpmp)_2][OTf]_3$ by dashed lines. Hydrogen atoms (except for the CH_2 groups) are omitted.

CH acidity of the coordinated ligand (d(C···O_{intra}) = 3.00−3.36 Å; d(C···O_{inter}) = 3.52−3.56 Å). Ligand exchange by a further equivalent of bpmp furnishes the cationic paramagnetic orange complex as triflate salt $[Cr(bpmp)_2][OTf]_3$ (Figure 2a) substantiated by IR spectroscopy, mass spectrometry, elemental analysis, and SQUID magnetometry (Figures S7−S9). Its constitution and meridional configuration was confirmed by single crystal X-ray diffraction of $[Cr(bpmp)_2][OTf]_3 \cdot CH_3CH_2OH$ (Figure 2b and Table S6).

The experimental structure of the cation fits to the geometry calculated by DFT (Figures 1 and 2b, Table S6). Notably, the $[CrN_6]$ core is highly octahedral with balanced Cr−N distances and N−Cr−N angles close to 90°. This ensures a large Cr/N orbital overlap and consequently a large ligand field splitting and high energy excited quartet levels.

In the solid state, the methylene bridges of the bpmp ligands form CH···O hydrogen bonds with the triflate counterions (d(C···O) = 3.12−3.49 Å; Figure 2b) similar to $Cr(bpmp)(OTf)_3$. Exchange of the triflates could be achieved with $[^nBu_4N][BF_4]$, $[^nBu_4N][PF_6]$, or $[^nBu_4N][ClO_4]$ as shown by IR spectroscopy, mass spectrometry, elemental analysis, and single crystal XRD analysis of the tetrafluoroborate salt (Figures S10−S14). Hydrogen bonds of the ligand's CH_2 bridges to BF_4^- counterions are present with C···F distances between 2.90 and 3.70 Å in the solid state (Figure S14).

At pH above 7−8, $[Cr(bpmp)_2]^{3+}$ converts to a dark yellow to brown complex in solution (Video S1). Even a solid sample reacts with gaseous ammonia to the brown complex and back to starting material with gaseous HCl (Video S2). UV/vis spectroscopy in H_2O reveals intense broad bands at ca. 350, 455, 540, 615, and 730 nm tailing up to 950 nm (Figure S15). This reactivity is associated with the acidity of the bridging CH_2 units in the cationic complex, which is already reflected in the hydrogen bonding of the triflates to the CH_2 groups in the solid state (Figure 2b). Comparing the experimental UV/vis spectrum with the time-dependent (TD-)DFT calculated transitions for the corresponding base $[Cr(bpmp)(bpmp\text{-}H)]^{2+}$ supports this acid/base chemistry (Figure S15 and Table S7). Photometric titration yields a pK_a value of 8.6 (Figure S16). $[Cr(bpmp)_2]^{3+}$ is similarly acidic as the NH analogue $[Cr(H_2tpda)_2]^{3+}$ with NH bridging units (pK_a 8.8; Scheme 1).[57] The methylene bridge can be reversibly de- and reprotonated by NaOH and HCl_{aq} or HOTf, respectively, several times as demonstrated optically and photometrically (Figure S17). However, above ca. pH 10 further processes set in which are partially irreversible, as suggested by the optical spectra (Figure S17). ESI mass spectra of $[Cr(bpmp)_2][OTf]_3$ display peaks at mass-to-charge ratios of 191.4 (7%), 286.6 (13%), and 572.2 (100%), corresponding to $\{[Cr(bpmp)_2]\}^{3+}$, $\{[Cr(bpmp)_2]\text{-}H\}^{2+}$, and $\{[Cr(bpmp)_2]\text{-}2H\}^{+}$, respectively (Figure S7). The BF_4^- and PF_6^- salts exhibits similar mass spectroscopic patterns (Figures S10 and S12). This further underscores the high acidity of $[Cr(bpmp)_2]^{3+}$. To ensure full protonation of the bridge and prohibit any decomposition, pertinent optical measurements were performed in the presence of aqueous perchloric acid.

A reversible $[Cr(bpmp)_2]^{3+/2+}$ reduction wave appears at −0.81 V vs ferrocene in the cyclic voltammogram followed by the waves for the $[Cr(bpmp)_2]^{2+/+}$, $[Cr(bpmp)_2]^{+/0}$, and $[Cr(bpmp)_2]^{0/1-}$ couples at −1.80, −2.13, and −2.31 V, respectively (Figures S18 and S19). The $[Cr(bpmp)_2]^{3+/2+}$ wave is shifted anodically by 0.3 V compared to that of the $[Cr(ddpd)_2]^{3+/2+}$ couple.[53] The more electron-deficient nature of the bpmp ligand as compared to ddpd accounts for this redox potential shift. Indeed, DFT calculations of $[Cr(bpmp)_2]^{2+}$ suggest an electronic structure of a low-spin chromium(II) ion admixed with a chromium(III) ion antiferromagnetically coupled to a ligand-centered radical (Figure S20). With this assignment, the electronic structure of $[Cr(bpmp)_2]^{2+}$ is between a genuine chromium(II) ion as found for $[Cr(ddpd)_2]^{2+}$ [53,93] and a ligand-centered radical found for $[Cr(bpy)_3]^{2+}/[Cr(tpy)_2]^{2+}$ [91,92] and $[Cr(tpe)_2]^{2+}$ [65] complexes (Figure 1, tpe = 1,1,1-tris(pyrid-2-yl)ethane).

Excited State Properties and Dynamics. The absorption spectrum of $[Cr(bpmp)_2]^{3+}$ in solution (H_2O or CH_3CN) can be divided into three spectral regions (Figure 3a). According to TD-DFT calculations (Figure S21), bands at 239 and 270 nm are assigned to $\pi-\pi^*$ transitions of the ligand, the band at 340 nm to ^{4}LMCT transitions, and the weak band at 465 nm (ε = 60 M^{-1} cm^{-1}, Figure 3a) to Laporte-forbidden $^4A_2 \rightarrow {}^4T_2$ transitions.

The latter absorption band reflects the ligand field splitting ($\Delta_{0,exp} \approx 21500$ cm^{-1}). This splitting is somewhat smaller than that of $[Cr(ddpd)_2]^{3+}$ with $\Delta_{0,exp} \approx 22990$ cm^{-1}.[53] The CASSCF-NEVPT2 calculations confirm this smaller ligand field splitting (Figure 1). The splitting is still sufficiently large to prevent nonradiative decay via back-ISC. Yet, this lower energy for excitation might be beneficial for future applications. Excitation with 462 nm light gives rise to a very sharp emission band (FWHM 280 cm^{-1}) peaking at 709 nm (Figure 3a). This is at the lower energy side of the visible spectral region giving a

https://doi.org/10.1021/jacs.1c05971
J. Am. Chem. Soc. 2021, 143, 11843−11855

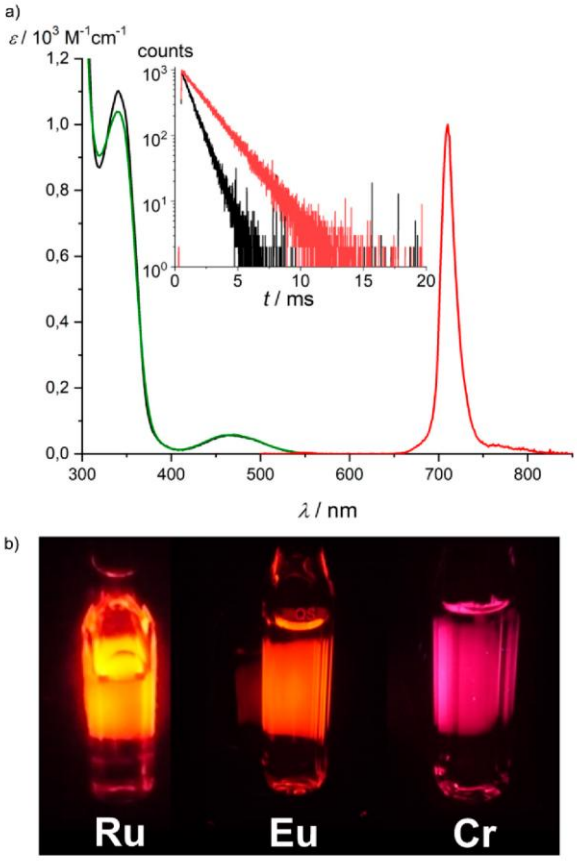

Figure 3. (a) UV/vis absorption spectrum (black), excitation spectrum (λ_{obs} = 709 nm, green), and emission spectrum (λ_{exc} = 462 nm, red) of $[Cr(bpmp)_2][OTf]_3$ in deaerated H_2O (0.1 M $HClO_4$) at room temperature; the inset shows the emission decay curves of $[Cr(bpmp)_2][OTf]_3$ in D_2O (0.1 M $DClO_4$) deaerated (red) and saturated with O_2 (black). b) Photographs of the red/orange emitters $[Ru(bpy)_3]^{2+}$, $[Eu(H_2O)(OTf)_2(tpy)_2]^+$, and the deep red emitter $[Cr(bpmp)_2]^{3+}$ in H_2O under irradiation with λ_{exc} = 340 nm.

deep red emission with CIE coordinates of x = 0.7326 and y = 0.2674 at the utmost corner of the CIE 1931 diagram (Figure 3b and Figure S22).[94]

The excitation spectrum (λ_{obs} = 709 nm) closely follows the absorption spectrum in the region of 300−600 nm. This confirms that the emission arises from the $[Cr(bpmp)_2]^{3+}$ chromophore. Furthermore, higher energy ^{4}LMCT states around 350 nm efficiently evolve to the luminescent state as well bypassing further loss channels (Figure 3a).

Gratifyingly, this emission band is higher in energy than that of $[Cr(ddpd)_2]^{3+}$[53] by 1200 cm^{-1}, in agreement with the predicted trend of the CASSCF-NEVPT2 calculations (Figure 1). The experimentally determined excited state energies (lowest excited quartet and doublet states) reflect the quantum chemically predicted trends and confirm the validity of our screening strategy. The most important aspect is the red emission of $[Cr(bpmp)_2]^{3+}$ which is readily detected with conventional detectors. Although only a fraction of the sharp emission band tails into the visible red region (Figure 3a), the red emission under illumination in solution can even be observed by the naked eye (Figure 3b).

Upon cooling, the emission band sharpens further with a FWHM = 230 cm^{-1} at 130 K in frozen butyronitrile solution. Fine structure appears at the lower energy side of the emission band at lower temperature. The pattern can be fitted by five Voigt functions centered at 14140, 14017, 13788, 13483, and 13099 cm^{-1} (Figure S23). At lower temperature, the intensity of the three lower energy bands increases relative to the prominent 709 nm band at room temperature. This behavior is similar to that of $[Cr(ddpd)_2]^{3+}$ describing a Boltzmann distribution between two equilibrating emissive states.[53,55] The higher energy state is more emissive, that is, less prone to thermally activated nonradiative decay. This is confirmed by the luminescence spectra of a KBr pellet of $[Cr(bpmp)_2][BF_4]_3$ cooled to 10 K. Below ca. 130 K the low-energy emission (719.5 nm; 13900 cm^{-1}) dramatically increases in intensity, suggesting less efficient nonradiative decay pathways for this state at low temperature (Figure 4). Concomitantly, the high-energy

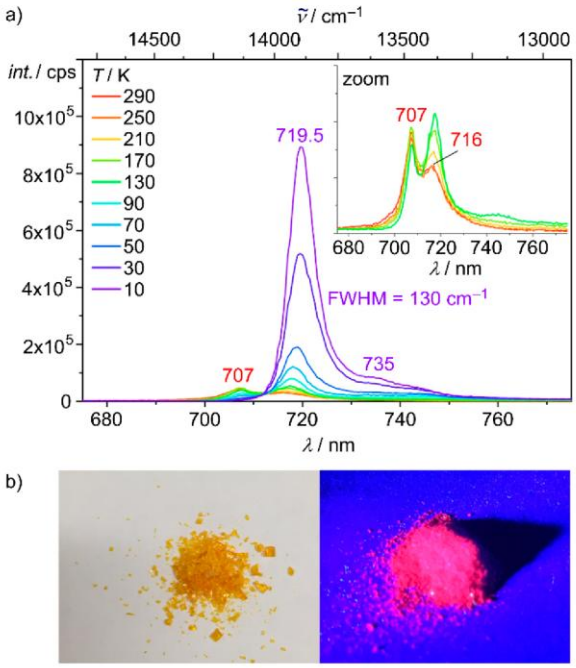

Figure 4. (a) Temperature-dependent luminescence spectra of $[Cr(bpmp)_2][BF_4]_3$ in a KBr matrix recorded between 10 K (purple) and 290 K (red) with λ_{exc} = 355 nm. The inset shows the spectra between 130 and 290 K. (b) Photographs of crystalline $[Cr(bpmp)_2][OTf]_3$ under ambient light and under irradiation with λ_{exc} = 340 nm.

emission (709 nm; 14105 cm^{-1}) vanishes. The energy difference is in the range predicted by the CASSCF(7,12)-NEVPT2 calculations for the two lowest doublet states (ΔE_{exp} = 245 cm^{-1}; ΔE_{CASSCF} = 154 cm^{-1}). The thermally activated nonradiative decay could be enabled by a surface crossing with the ground state, similar to the effects observed for $[Cr(tpe)_2]^{3+}$.[65] For this path to be operative, the lowest emissive state should be distorted relative to the ground state. This fits to a slightly distorted microstate of $^2T_1$ parentage which has been predicted by CASSCF(7,12)-NEVPT2 as the lowest doublet state. The presence of a vibrational fine structure of the low energy band confirms the distortion of this excited doublet state. Tentatively,

https://doi.org/10.1021/jacs.1c05971
J. Am. Chem. Soc. 2021, 143, 11843−11855

the vibrational progression of ca. 290 cm^{-1} could correspond to a Cr−N vibration (in the *xy*-plane) of the ground state according to the DFT calculations (308 cm^{-1}, scaled by 0.98:302 cm^{-1}; Figure S24). For $[Cr(NH_3)_6]^{3+}$, vibrations of odd symmetry $\delta(T_{1u}$, N−Cr−N) and $\nu(T_{1u}$, Cr−N) have been found at 267 and 458 cm^{-1}, respectively.[95]

The much higher integrated emission intensity upon cooling a sample of $[Cr(bpmp)_2][BF_4]_3$ in a KBr pellet from 290 to 10 K parallels an increase of the average photoluminescence lifetime from 38.0 to 1900 μs, respectively (Figure S25 and Table S8). The observed temperature dependence supports the model of reduced thermally available nonradiative decay pathways below ca. 130 K.

The photoluminescence quantum yield of $[Cr(bpmp)_2][OTf]_3$ reaches 12.3% at room temperature in deaerated H_2O solution (Table 1). This is similar to the quantum yield of the CD oscillators with Cr···H distances of 3.1−4.3 Å. Indeed, the quantum yield of $[Cr(bpmp)_2][OTf]_3$ increases from 15.8 to 19.6% by replacing $H_2O/HClO_4$ by $D_2O/DClO_4$ (Table 1). This gain results from the combined effect of the CH/CD replacement in the ligand methylene bridges and the OH/OD replacement in the aqueous solution. As the bridges rapidly exchange H/D in H_2O or D_2O, these first- and second-sphere isotope effects cannot be disentangled.

Table 1. Quantum Yields Φ and Luminescence Lifetimes τ of $[Cr(bpmp)_2][OTf]_3$ and $[Cr([D_2]\text{-bpmp})_2][OTf]_3$ in Various Environments at Room Temperature (λ_{exc} = 462 nm)

solvent	acid[a]	O_2[c]	Φ (%)	τ (μs)
		$[Cr(bpmp)_2]^{3+}$		
H_2O		−	12.3	1360
H_2O	$HClO_4$	−	15.8	1550
H_2O	$HClO_4$	+	9.8	880
D_2O	$DClO_4$[b]	−	19.6	1800
D_2O	$DClO_4$[b]	+	9.8	840
CH_3CN		−	0.8	840
CH_3CN	$HClO_4$	−	11.4	1290
CH_3CN	$HClO_4$	+	4.6	390
CD_3CN	$DClO_4$[b]	−	15.5	1340
CD_3CN	$DClO_4$[b]	+	4.3	380
PBS (pH 6.6)		−	1.4	600
PBS (pH 6.4)		+	1.4	470
		$[Cr([D_2]\text{-bpmp})_2]^{3+}$		
D_2O	$DClO_4$	−	24.6	2500
D_2O	$DClO_4$	+	9.5	990

[a]Final $HClO_4$ ($DClO_4$) concentration c = 0.1 M. [b]Under these conditions, H → D exchange at the methylene bridge is expected. [c]"+" refers to atmospheric conditions and "−" to inert conditions.

NIR emissive molecular ruby $[Cr(ddpd)_2]^{3+}$ and larger by several orders of magnitude compared to other reported chromium(III) emitters with emission in the red spectral region.[49] In pure and dry CH_3CN as well as in phosphate-buffered saline (PBS) buffer (0.1 M) the quantum yield drops below 2%, likely due to the deprotonation of the coordinated bpmp ligand in the ground state. Preventing CH_2 bridge deprotonation by adding $HClO_4$ increases the quantum yield to 15.8%. In the deuterated environments CD_3CN ($DClO_4$) and D_2O ($DClO_4$) the quantum yields increase to record numbers of 15.5% and 19.6%, respectively (Table 1). Other salts of $[Cr(bpmp)_2]^{3+}$ (ClO_4^-, PF_6^-, BF_4^-) show a similar behavior under acidic conditions (Table S9). The PF_6^- salt even reaches a quantum yield of 20% in $D_2O/DClO_4$ solution (Table S9). The acid/base chemistry and consequently the luminescence depend on the counterion in neutral to basic environments (Table S9).

In line with the above-mentioned acid/base chemistry, the CH acidic protons of the CH_2 bridges readily exchange with deuterium in D_2O (Figures S26 and S27). Replacement of CH by CD oscillators reduces the nonradiative excited state decay via multiphonon relaxation[54,57,96] involving the *aliphatic* CH/

$[Cr(ddpd)_2]^{3+}$ with a lower emission energy has some spectral overlap with the third *aromatic* CH vibrational overtone ν^4_{CH} at ≈11493 cm^{-1} with a comparably high extinction coefficient.[54] Deuteration of $[Cr(ddpd)_2]^{3+}$ to $[Cr([D_x]\text{-ddpd})_2]^{3+}$ (>95% D at the pyridine α-positions which are closest to the metal center) increased the quantum yield to 30% in CD_3CN.[54] The spectral overlap integral of the sharp $[Cr(bpmp)_2]^{3+}$ emission band at 14124 cm^{-1} with overtones of *aromatic* CH oscillators is rather small as the accepting energy level derives from the fourth vibrational overtone ν^5_{CH} at ≈14065 cm^{-1}.[54] This high overtone possesses a very small extinction coefficient.[54] To ascertain whether a further boost of the quantum yield could be achieved by deuteration of aromatic ligand protons, the ligand $[D_2]$-bpmp with the pyridine's α-positions deuterated and its chromium complex $[Cr([D_2]\text{-bpmp})_2]^{3+}$ were synthesized as detailed in the Supporting Information (Figures S28−S37). This deuteration at the α-position increases the luminescence quantum yield from Φ = 19.6% to Φ = 24.6% in $D_2O/DClO_4$ (Table 1). Concomitantly, the lifetime increases from 1800 to 2500 μs (Table 1). This substantial increase in luminescence efficiency can be traced back to the comparison of spectral overlap of the relevant isotopologic C−(H/D) overtones with the doublet emission of chromium (Figures S38−S43). The fourth CH overtone (ν^5_{CH}) shows good spectral overlap (Figure S42), leading to a substantial nonradiative relaxation, while CD oscillators have a much smaller spectral overlap (Figure S43), in addition to the generally decreased oscillator strength compared to CH oscillators.

The photophysical properties of $[Cr(bpmp)_2]^{3+}$ and $[Cr([D_2]\text{-bpmp})_2]^{3+}$ outperform the record NIR photoluminescence data of the molecular ruby $[Cr(ddpd)_2]^{3+}$[54] and the standard red-orange emitter $[Ru(bpy)_3]^{2+}$ ($\Phi(CH_3CN)$ = 9.5%; $\tau(CH_3CN)$ = 1.1 μs; $\Phi(H_2O)$ = 6.3%; $\tau(H_2O)$ = 0.65 μs; Scheme 1).[97−99]

In the solid state, the details of the photoluminescence quantum yield and lifetime depend on the counterion. The quantum yield increases in the series BF_4^-, ClO_4^-, PF_6^-, and OTf^- (Φ = 0.5, 1.7, 2.0, and 7.1%) under aerated conditions. The luminescence decay was fitted mono-, bi-, or triexponentially and follows the same increasing trend with 36 μs, 89/230 μs (52:48), 530/250/110 μs (13:66:21), and 1100/520/190 μs (54:41:5), respectively. Clearly, the different packing and possible counterion association modify the solid state luminescence. Counterion effects on solid state and solution luminescence and photoreactivity have been reported previously for MLCT emitters,[100,101] yet a clear structure−activity relationship of counterion and luminescence in general, and spin-flip luminescence in particular,[102] is still elusive and more data are required.

The very long lifetime of the emissive state(s) allowed recording step-scan FT-IR spectra[44,65,103−105] after excitation of $[Cr(bpmp)_2][BF_4]_3$ in a KBr pellet with 355 nm excitation at 290 and 20 K (Figure 5a and Figures S44−S49). This high energy pulse likely populates allowed ^{4}LMCT states with

https://doi.org/10.1021/jacs.1c05971
J. Am. Chem. Soc. 2021, 143, 11843−11855

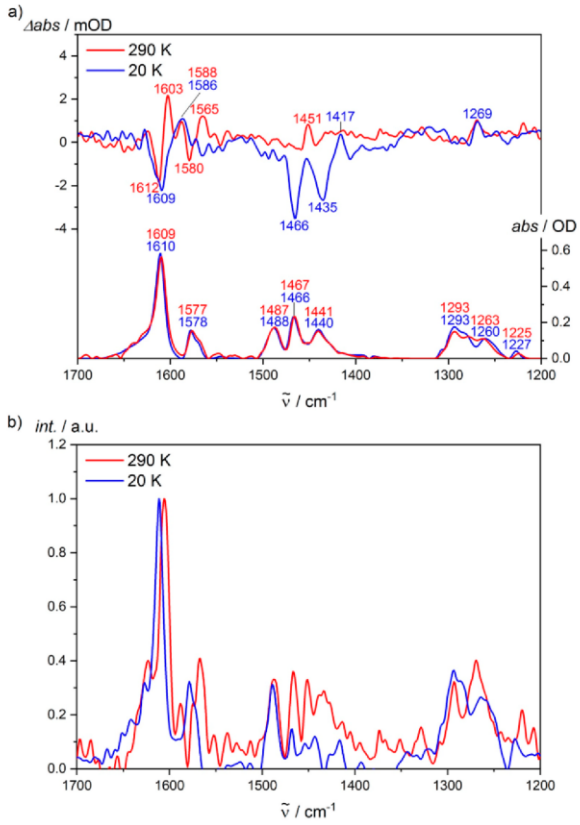

Figure 5. (a) Ground state (bottom) and step-scan FT-IR spectra (top, λ_{exc} = 355 nm; 0−1 μs) of $[Cr(bpmp)_2][BF_4]_3$ in a KBr pellet at 20 K (blue) and 290 K (red) and (b) excited state FT-IR spectra of $[Cr(bpmp)_2][BF_4]_3$ in a KBr pellet obtained from step-scan FT-IR spectra (λ_{exc} = 355 nm; 0−1 μs) (small contributions of 2% and 0.8% added to the respective ground state spectrum) at 20 K (blue) and 290 K (red). At 20 K, essentially the lowest doublet state is populated.

pyridine → t_{2g} CT character according to TD-DFT calculations (Figure 1 and Figure S21). The absorption and emission spectra are hardly affected by the matrix (solution, KBr pellet, thin film; Figures S50 and S51). The ground state FT-IR spectra are essentially superimposable at 290 and 20 K (Figure S44). On the other hand, the normalized excited state spectra show significant differences around 1600 cm^{-1}, 1550 cm^{-1}, and between 1400 and 1450 cm^{-1} at 290 and 20 K (Figure 5b). This is an indication for a temperature-dependent population of the contributing long-lived excited doublet states. With an estimated energy difference of the two lowest doublet microstates of $^2T_1$ and ^2E parentage of 245 cm^{-1} from the luminescence spectra (155 cm^{-1} from the CASSCF-NEVPT2 calculations), the derived Boltzmann population ratio amounts to 77:23 (CASSCF: 68:32) and 100:0 (CASSCF: 100:0) at 290 and 20 K, respectively. Consequently, only the lowest energy excited state is populated at 20 K. At 290 K, the rise and decay of the most prominent IR bands at 1612, 1603, 1588, and 1451 cm^{-1} were considered in a global fit to yield biexponential decays of 37 and 2.5 μs with contributions of 77% and 23%, respectively (Figure S48). This ratio matches the population ratio estimated from the luminescence energies. At 20 K, the higher doublet state is hardly populated. Indeed, the global fit of the IR bands yields a major time constant of 372 μs (96%) and a minor one of 13 μs (4%) (Figure S49). As thermal equilibration is not feasible at 20 K, the minor component might arise from the branching dynamics along the decay cascade after ^{4}LMCT excitation to the final excited $^2E/^2T_1$ states (Figure 1, purple arrows).

To experimentally probe the initial dynamics after excitation, subpicosecond transient absorption (TA) spectra of $[Cr(bpmp)_2][OTf]_3$ in CH_3CN ($HClO_4$) were recorded with excitation at 515 nm ($^4T_2$), 460 nm ($^4T_2$), and 350 nm (^{4}LMCT) (Figure 6 and Figures S52−S54). The TA spectra of

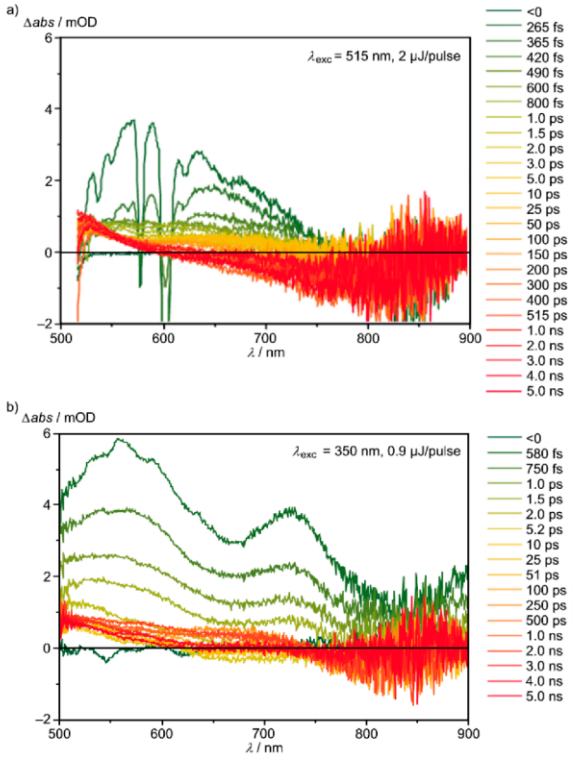

Figure 6. Transient absorption spectra of $[Cr(bpmp)_2][OTf]_3$ in CH_3CN ($HClO_4$) excited with femtosecond laser pulses (a) at 515 nm ($^4T_2$ states) and (b) at 350 nm (^{4}LMCT states).

the 515 and 460 nm excitation are very similar apart from the lower pump laser power at 460 nm, confirming that the same initial states are populated (Figure 6a and Figure S54). The TA spectra after $^4T_2$ excitation with 515 nm (Figure 6a) were fitted with three time constants $\tau^{515}{}_{1,2,3}$ of <200 fs, 300 ps, and a nondecaying component within the 8 ns time window, respectively. The fast decaying component $\tau^{515}{}_1$ is attributed to a coherent artifact necessary for the fit. The slow decaying component $\tau^{515}{}_3$ is straightforwardly assigned to the long-lived $^2E/^2T_1$ states. As the evolution-associated difference spectra (EADS) relating to τ_2 and τ_3 are similar lacking significant spectral shifts (Figure S52), they correspond to states of similar nature. A kinetic model assigns $\tau^{515}{}_2$ = 300 ps to internal conversion (IC) and vibrational cooling (VC) within doublet states $k(IC_1{+}VC_1)$ (Figure 1) while intersystem crossing (ISC) is faster than the instrument's time resolution ($\tau^{515}{}_1(ISC_1)$ < 200 fs). The combined ISC_1, IC_1, and VC_1 processes are slower than observed for $[Cr(ddpd)_2]^{3+}$ with 3.5 ps,[56] $Cr(acac)_3$ with 1.1 ps

https://doi.org/10.1021/jacs.1c05971
J. Am. Chem. Soc. 2021, 143, 11843−11855

(τ(ISC) < 100 fs),[107] Cr(*t*Buacac)$_3$ with 1.6 ps,[108] and $[Cr(CN)_6]^{3-}$ in a Cr^{III}–V^{III} Prussian blue analogue with τ(ISC) = 250 fs and τ(VC) = 1.1 ps[109] after $^4T_2$ excitation, while ISC occurs in the ultrafast time regime within hundreds of femtoseconds. The density of doublet states in the $^4T_2$ energy region and spin–orbit coupling (SOC) determine the ISC rates. For Cr(acac)$_3$ with nearly isoenergetic $^4T_2$ and $^2E/^2T_1$ states, SOC matrix elements between the $^4T_2$ and the $^2E/^2T_1$ states at geometries close to potential energy crossing points were calculated as 21–371 cm^{-1} (at the SOC-CASSCF(3,5) level of theory).[106] SOC-CASSCF(7,12)-NEVPT2 calculations for $[Cr(bpmp)_2]^{3+}$ (in the ground state geometry) deliver SOCs between the lowest quartet state $^4T_2(1)$ and the lowest doublet states derived from ^2E and $^2T_1$ states ranging from 6 to 97 cm^{-1} accounting for an ISC pathway from $^4T_2(1)$ to the doublet states, in particular the $^2E(1)$ state (Table S4). These values closely match those obtained for $[Cr(ddpd)_2]^{3+}$ (Table S4). The different SOCs for states of ^2E and $^2T_1$ parentage might account for the population of both $^2E(1)$ and states $^2T_1(1)$ at very low temperature without equilibration of these states.

The TA spectra after ^{4}LMCT excitation at 350 nm excitation (~Figure 6b) were fitted with three time constants $\tau^{350}{}_{1,2,3}$ of 540 fs, 75 ps, and a nondecaying component within the 8 ns time window. Again, $\tau^{350}{}_3$ is assigned to the lifetime of the $^2E/^2T_1$ states. The first EADS comprises a broad excited state absorption (ESA), with peaks at 560 and 740 nm (Figure S53). This decays in 540 fs to yield the second EADS, which shows an ESA at 525 nm. This evolves in 75 ps to the final EADS with a broad ESA, spanning 500–750 nm. The ESAs of the second and third EADS are rather similar and distinct from the first EADS. A plausible kinetic model assigns the fast component $\tau^{350}{}_1$ to ISC (and possibly electron redistribution) from ^{4}LMCT states to the metal-centered or charge-transfer doublet manifold [Figure 1; $\tau(ISC_2)$ = 540 fs] and the picosecond component $\tau^{350}{}_2$ to IC and VC within the doublets (Figure 1; $\tau(IC_2{+}VC_2)$ = 75 ps). ^{4}LMCT excitation of Cr(acac)$_3$ yielded a process of ~50 fs which had been tentatively assigned to the ^{4}LMCT to ^2E population transfer.[107] With these assignments, the conversion from the LMCT to the ligand field manifold is ~10 times slower in $[Cr(bpmp)_2]^{3+}$ than in Cr(acac)$_3$ which might be ascribed to a different density of (electronic and associated vibrational) doublet states in the respective CT energy regions and the very different ligand types.

Irrespective of the excitation energy and the decay pathway, the relaxed long-lived doublet state(s) of $[Cr(bpmp)_2]^{3+}$ are characterized by an ESA around 500–750 nm (Figure 6 and Figure S54), similar to the excited doublet states of $[Cr(ddpd)_2]^{3+}$ (530 nm)[56] and Cr(acac)$_3$ (510 nm).[108]

Singlet Oxygen Generation, Photoredox Chemistry, and Optical pH Sensing. The excited state reactivity of the long-lived doublet states of $[Cr(bpmp)_2][OTf]_3$ was probed by excited state quenching with oxygen in $H_2O/HClO_4$ and $CH_3CN/HClO_4$ (Table 1). In air-saturated solutions, the luminescence quantum yields were diminished by factors of 1.6 and 2.0, respectively. This is considerably less than observed for $[Cr(ddpd)_2][BF_4]_3$ with factors of 5.2 and 17, respectively.[53] The product of this reaction is singlet oxygen $^1O_2$ as confirmed by the observation of its characteristic emission at 1275 nm (Figure S55). Steady-state and time-resolved Stern–Volmer analyses yield Stern–Volmer constants $K_{SV} = 0.44 \times 10^4$ and 0.46×10^4 M^{-1}, respectively (Figures S56 and S57), demonstrating the dynamic character of the Dexter-type energy transfer quenching without significant static contributions.[110] With τ = 1550 μs, the bimolecular quenching rate constant k_q amounts to 0.29×10^7 M^{-1} s^{-1}. The longer lifetime of $[Cr(bpmp)_2]^{3+}$ and the lower K_{SV} as compared to those of $[Cr(ddpd)_2]^{3+}$[53] yield a lower bimolecular quenching rate constant k_q. The Stern–Volmer constants of the tetrafluoroborate salt are even lower than those of the triflate with $K_{SV} = 0.35 \times 10^4$ and 0.36×10^4 M^{-1} (intensity and lifetime based; Figures S58 and S59). The quenching rate constant was calculated to $k_q = 0.25 \times 10^7$ M^{-1} s^{-1} (τ = 1400 μs). The singlet oxygen quantum yields of $[Cr(bpmp)_2][X]_3$ were determined by using the comparative method as 55, 44, and 39% in DMF/$HClO_4$ for X^- = OTf^-, PF_6^-, and BF_4^-, respectively. These values are smaller than those of $[Cr(ddpd)_2][BF_4]_3$ in DMF (61%)[56] and in DMF/$HClO_4$ (86%) (Figure S55 and Table S5).

Although the driving force for energy transfer to oxygen is larger for $[Cr(bpmp)_2]^{3+}$ by 1200 cm^{-1} than for $[Cr(ddpd)_2]^{3+}$, and although the chromium center is somewhat less shielded by the CH_2 bridges than by the larger NCH_3 bridges of the ligands, $[Cr(bpmp)_2]^{3+}$ is less sensitive to oxygen than $[Cr(ddpd)_2]^{3+}$. A hypothesis for explaining this surprising result might be the dynamic association with the X^- counterions at the C–H acidic methylene bridges of the ligands, fully analogous to the coordination of triflates and tetrafluoroborates in the solid state structure (Figure 2b and Figure S14). Possibly, this dynamic coordination of the anions to the bridges in solution shields the chromium center in $[Cr(bpmp)_2]^{3+}$ from successful quenching encounters with O_2 more efficiently than the larger NCH_3 bridges which cannot hydrogen-bond to counterions. Consequently, the pockets spanned by the tridentate ligands are on average more often filled by counterions in the bpmp complex. These results might pave the way to successfully design *oxygen-insensitive* and *anion-sensitive* spin-flip emitters in the future.

Apart from excited state energy transfer, photoinduced single electron transfer could occur from suitable substrates to the excited chromium(III) complex. The favorable redox and excited state properties suggest the use of $[Cr(bpmp)_2][OTf]_3$ as photoredox sensitizer. The excited state is strongly oxidizing (0.94 V vs ferrocene), slightly more oxidizing than $*[Cr(tpe)_2]^{3+}/[Cr(tpe)_2]^{2+}$ (0.87 V vs ferrocene)[65] and significantly more oxidizing than $*[Ru(bpy)_3]^{2+}/[Ru(bpy)_3]^{+}$ (0.41 V vs ferrocene) or classical ground state ruthenium(III) oxidants $[Ru(bpy)_3]^{3+}$ (0.84 V vs ferrocene) and $[Ru(phen)_3]^{3+}$ (0.87 V vs ferrocene).[111]

In fact, azulene ($E_{1/2}$ = 0.50 V vs ferrocene)[112] quenches the emission of $[Cr(bpmp)_2]^{3+}$ ($K_{SV} = 3.73 \times 10^4$ M^{-1}; $k_q = 4.4 \times 10^7$ M^{-1} s^{-1} in CH_3CN; τ = 840 μs; Figure S60) slightly more efficiently than that of $[Cr(tpe)_2]^{3+}$ ($K_{SV} = 4.17 \times 10^4$ M^{-1}; $k_q = 1.4 \times 10^7$ M^{-1} s^{-1}). The larger driving force and hence a smaller activation barrier for the electron transfer between $*[Cr(bpmp)_2]^{3+}$ and azulene might account for this small difference. The small quenching rate constants of both complexes might be associated with a weak electronic coupling in the collision complex as a result of the metal-localized excited state and the formation of contact ion pairs with the counterions shielding the sensitizer. Unfortunately, photoinduced oxidation of amines as useful redox partners is not feasible due to the deprotonation of the CH_2 bridge of the coordinated ligand by amines already in the ground state (Figure 7). Yet, this intriguing feature can be turned into an advantage for sensing applications.

The reversible ground state acid/base chemistry forms dearomatized/rearomatized pyridine ligands.[113] Deprotonation at the methylene bridge leads to a coordinated nitrogen donor

https://doi.org/10.1021/jacs.1c05971
J. Am. Chem. Soc. 2021, 143, 11843–11855

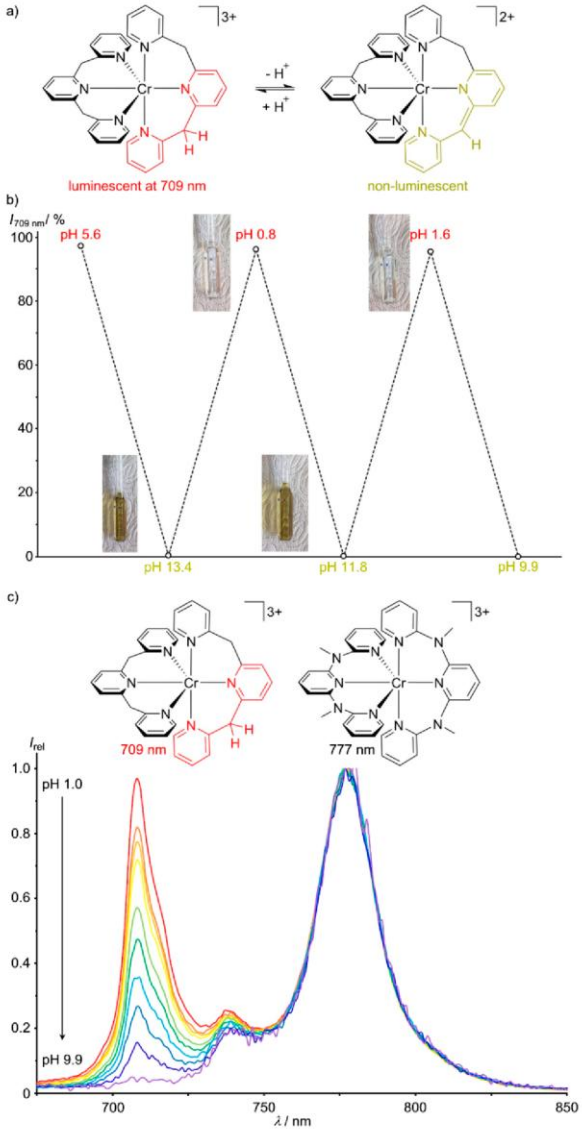

Figure 7. (a) Deprotonation/reprotonation equilibrium of an aqueous solution of $[Cr(bpmp)_2]^{3+}$ with concomitant dearomatization/rearomatization of a pyridine donor. (b) Intensity of the emission band at 709 nm during deprotonation/reprotonation cycles with NaOH and HOTf (λ_{exc} = 466 nm). (c) Normalized pH-dependent emission spectra of a mixture of $[Cr(bpmp)_2]^{3+}$ and $[Cr(ddpd)_2]^{3+}$ (molar fraction 25:2; λ_{exc} = 452 nm) in H_2O under ambient conditions. Note that dissolved O_2 reduces the quantum yield of both complexes especially at higher pH, and the nonemissive deprotonated complexes absorb strongly at the excitation wavelength. Both effects result in a poorer S/N ratio at high pH.

atom with enamide character dramatically changing the donor properties (Figure 7a). As a result, the luminescence of $[Cr(bpmp)_2]^{3+}$ at 709 nm is completely quenched at higher pH and reinstalled at lower pH (Figure 7b). As the emission of $[Cr(ddpd)_2]^{3+}$ at 777 nm is pH-insensitive, the combination of these two emitters gives a ratiometric optical pH sensor operating in the red to near-infrared spectral region with single-wavelength excitation in the blue (Figure 7c). The sharp emission bands of both complexes in the red/near-IR spectral region and the excitation with blue light would even allow combination with further luminophores utilizing the visible part of the spectral region.[60] Consequently, this luminophore combination will be further developed towards multicolor multianalyte optical probes in the future.[60]

CONCLUSIONS

On the basis of high-level computer-aided design, we developed the first molecular highly luminescent chromium(III) complex emitting in the red spectral region. After excitation of the $[Cr(bpmp)_2]^{3+}$ luminophore, ultrafast and efficient population transfer by intersystem crossing and vibrational cooling to the long-lived doublet states of $*[Cr(bpmp)_2]^{3+}$ occurs. These doublet states emit in the deep red spectral region with photoluminescence quantum yields up to 20% and excited state lifetimes up to 1800 μs. Deuteration of the α-positions of the terminal pyridines increases the quantum yield to 25% and the lifetime to 2500 μs. The key photophysical properties of the purely red-emissive molecular ruby $[Cr(bpmp)_2]^{3+}$ (emission color, photoluminescence quantum yield, excited state lifetime, and excited state redox potential) outperform those of the classical ruthenium(II) sensitizers and the often-used europium(III)-based red-emissive complexes. Furthermore, the reversible ground state (de)protonation of $[Cr(bpmp)_2]^{3+}$ coupled with an off/on luminescence enables ratiometric optical pH sensing. Future work will further exploit this novel red emitter with an earth-abundant chromium center in bioimaging, multicolor sensing (e.g., pH, O_2, and anions), photocatalysis, molecular upconversion,[61,114] and circularly polarized luminescence.[63,64,115−117]

ASSOCIATED CONTENT

Supporting Information

The Supporting Information is available free of charge at https://pubs.acs.org/doi/10.1021/jacs.1c05971.

Details of quantum chemical calculations, synthetic procedures, analytical and spectroscopic data of $Cr(bpmp)Cl_3$, $Cr(bpmp)Br_3$, $Cr(bpmp)(OTf)_3$, $[Cr(bpmp)_2][OTf]_3$, $[Cr(bpmp)_2][BF_4]_3$, $[Cr(bpmp)_2][PF_6]_3$, $[D_2]$-bpmp, $Cr([D_2]$-bpmp$)Cl_3$, $Cr([D_2]$-bpmp$)(OTf)_3$, and $[Cr([D_2]$-bpmp$)_2][OTf]_3$ (PDF)

Video S1 (MP4)

Video S2 (MP4)

Accession Codes

CCDC 1989536−1989537 and 2083757 contain the supplementary crystallographic data for this paper. These data can be obtained free of charge via www.ccdc.cam.ac.uk/data_request/cif, or by emailing data_request@ccdc.cam.ac.uk, or by contacting The Cambridge Crystallographic Data Centre, 12 Union Road, Cambridge CB2 1EZ, UK; fax: +44 1223 336033.

AUTHOR INFORMATION

Corresponding Authors

Katja Heinze − *Department of Chemistry, Johannes Gutenberg University of Mainz, 55128 Mainz, Germany;* orcid.org/0000-0003-1483-4156; Email: katja.heinze@uni-mainz.de

Ute Resch-Genger − *Division Biophotonics, Federal Institute for Materials Research and Testing (BAM), 12489 Berlin, Germany;* orcid.org/0000-0002-0944-1115; Email: ute.resch@bam.de

Michael Seitz − *Institute of Inorganic Chemistry, University of Tübingen, 72076 Tübingen, Germany;* orcid.org/0000-0002-9313-2779; Email: michael.seitz@uni-tuebingen.de

Authors

Florian Reichenauer − *Department of Chemistry, Johannes Gutenberg University of Mainz, 55128 Mainz, Germany*
Cui Wang − *Division Biophotonics, Federal Institute for Materials Research and Testing (BAM), 12489 Berlin, Germany; Institut für Chemie und Biochemie, Freie Universität Berlin, 14195 Berlin, Germany*
Christoph Förster − *Department of Chemistry, Johannes Gutenberg University of Mainz, 55128 Mainz, Germany*
Pit Boden − *Department of Chemistry and Research Center Optimas, University Kaiserslautern, 67663 Kaiserslautern, Germany*
Naz Ugur − *Max Planck Institute for Polymer Research, 55128 Mainz, Germany*
Ricardo Báez-Cruz − *Max Planck Institute for Polymer Research, 55128 Mainz, Germany*
Jens Kalmbach − *Institute of Inorganic Chemistry, University of Tübingen, 72076 Tübingen, Germany*
Luca M. Carrella − *Department of Chemistry, Johannes Gutenberg University of Mainz, 55128 Mainz, Germany*
Eva Rentschler − *Department of Chemistry, Johannes Gutenberg University of Mainz, 55128 Mainz, Germany;* orcid.org/0000-0003-1431-3641
Charusheela Ramanan − *Max Planck Institute for Polymer Research, 55128 Mainz, Germany*
Gereon Niedner-Schatteburg − *Department of Chemistry and Research Center Optimas, University Kaiserslautern, 67663 Kaiserslautern, Germany;* orcid.org/0000-0001-7240-6673
Markus Gerhards − *Department of Chemistry and Research Center Optimas, University Kaiserslautern, 67663 Kaiserslautern, Germany;* orcid.org/0000-0002-8748-2940

Complete contact information is available at: https://pubs.acs.org/10.1021/jacs.1c05971

Notes

The authors declare no competing financial interest.
During manuscript finalization, Prof. Markus Gerhards unexpectedly passed away on Dec 28th 2020.

■ ACKNOWLEDGMENTS

Financial support from the Deutsche Forschungsgemeinschaft [DFG, Priority Program SPP 2102 "Light-controlled reactivity of metal complexes" (GE 961/10-1, HE 2778/15-1, SE 1448/8-1] and RE 1203/23-1 is gratefully acknowledged. Parts of this research were conducted by using the supercomputer Mogon and advisory services offered by Johannes Gutenberg University Mainz (www.hpc.uni-mainz.de), which is a member of the AHRP and the Gauss Alliance e.V., and the supercomputer Elwetritsch and advisory services offered by the TU Kaiserslautern (https://elwe.rhrk.uni-kl.de), which is a member of the AHRP. We thank Marius Bauer and Leander Geske for assistance with photography and IR spectroscopy, respectively.

■ REFERENCES

(1) Baldo, M. A.; Thompson, M. E.; Forrest, S. R. High-Efficiency Fluorescent Organic Light-Emitting Devices using a Phosphorescent Sensitizer. *Nature* **2000**, *403*, 750−753.
(2) Li, A.; Turro, C.; Kodanko, J. J. Ru(II) Polypyridyl Complexes Derived from Tetradentate Ancillary Ligands for Effective Photocaging. *Acc. Chem. Res.* **2018**, *51*, 1415−1421.
(3) Mari, C.; Pierroz, V.; Ferrari, S.; Gasser, G. Combination of Ru(II) Complexes and Light: New Frontiers in Cancer Therapy. *Chem. Sci.* **2015**, *6*, 2660−2686.
(4) Hagfeldt, A.; Grätzel, M. Molecular Photovoltaics. *Acc. Chem. Res.* **2000**, *33*, 269−277.
(5) Yoon, T. P.; Ischay, M. A.; Du, J. N. Visible Light Photocatalysis as a Greener Approach to Photochemical Synthesis. *Nat. Chem.* **2010**, *2*, 527−532.
(6) Marzo, L.; Pagire, S. K.; Reiser, O.; König, B. Visible-light photocatalysis: does it make a difference in organic synthesis? *Angew. Chem., Int. Ed.* **2018**, *57*, 10034−10072.
(7) Romero, N. A.; Nicewicz, D. A. Organic photoredox catalysis. *Chem. Rev.* **2016**, *116*, 10075−10166.
(8) Skubi, K. L.; Blum, T. R.; Yoon, T. P. Dual Catalysis Strategies in Photochemical Synthesis. *Chem. Rev.* **2016**, *116*, 10035−10074.
(9) Shaw, M. H.; Twilton, J.; MacMillan, D. W. Photoredox catalysis in organic chemistry. *J. Org. Chem.* **2016**, *81*, 6898−926.
(10) Narayanam, J. M.; Stephenson, C. R. Visible light photoredox catalysis. Applications in organic synthesis. *Chem. Soc. Rev.* **2011**, *40*, 102−113.
(11) Herr, P.; Glaser, F.; Büldt, L. A.; Larsen, C. B.; Wenger, O. S. Long-Lived, Strongly Emissive, and Highly Reducing Excited States in Mo(0) Complexes with Chelating Isocyanides. *J. Am. Chem. Soc.* **2019**, *141*, 14394−14402.
(12) Büldt, L. A.; Wenger, O. S. Chromium(0), Molybdenum(0), and Tungsten(0) Isocyanide Complexes as Luminophores and Photosensitizers with Long-Lived Excited States. *Angew. Chem., Int. Ed.* **2017**, *56*, 5676−5682.
(13) Büldt, L. A.; Guo, X.; Prescimone, A.; Wenger, O. S. A Molybdenum(0) Isocyanide Analogue of $Ru(2,2\text{-Bipyridine})_3^{2+}$: A Strong Reductant for Photoredox Catalysis. *Angew. Chem., Int. Ed.* **2016**, *55*, 11247−11250.
(14) Yam, V. W.; Wong, K. M.-C. Luminescent metal complexes of d^6, d^8 and d^{10} transition metal centres. *Chem. Commun.* **2011**, *47*, 11579−11592.
(15) Hamze, R.; Peltier, J. L.; Sylvinson, D.; Jung, M.; Cardenas, J.; Haiges, R.; Soleilhavoup, M.; Jazzar, R.; Djurovich, P. I.; Bertrand, G.; Thompson, M. E. Eliminating Nonradiative Decay in Cu(I) Emitters: > 99% Quantum Efficiency and Microsecond Lifetime. *Science* **2019**, *363*, 601−606.
(16) Gernert, M.; Müller, U.; Haehnel, M.; Pflaum, J.; Steffen, A. A Cyclic Alkyl(amino)carbene as Two-Atom π-Chromophore Leading to the First Phosphorescent Linear Cu^I Complexes. *Chem. - Eur. J.* **2017**, *23*, 2206−2216.
(17) Di, D. W.; Romanov, A. S.; Yang, L.; Richter, J. M.; Rivett, J. P. H.; Jones, S.; Thomas, T. H.; Abdi Jalebi, M.; Friend, R. H.; Linnolahti, M.; Bochmann, M.; Credgington, D. High-Performance Light-Emitting Diodes based on Carbene-Metal-Amides. *Science* **2017**, *356*, 159−163.
(18) Hossain, A.; Bhattacharyya, A.; Reiser, O. Copper's Rapid Ascent in Visible-Light Photoredox Catalysis. *Science* **2019**, *364*, eaav9713.
(19) Hernandez-Perez, A. C.; Collins, S. K. Heteroleptic Cu-Based Sensitizers in Photoredox Catalysis. *Acc. Chem. Res.* **2016**, *49*, 1557−1565.
(20) Housecroft, C. E.; Constable, E. C. The emergence of copper(i)-based dye sensitized solar cells. *Chem. Soc. Rev.* **2015**, *44*, 8386−8398.
(21) Yersin, H.; Rausch, A. F.; Czerwieniec, R.; Hofbeck, T.; Fischer, T. The triplet state of organo-transition metal compounds. Triplet harvesting and singlet harvesting for efficient OLEDs. *Coord. Chem. Rev.* **2011**, *255*, 2622−2652.
(22) Zhang, Y.; Schulz, M.; Wächtler, M.; Karnahl, M.; Dietzek, B. Heteroleptic diimine−diphosphine Cu(I) complexes as an alternative towards noble-metal based photosensitizers: Design strategies, photophysical properties and perspective applications. *Coord. Chem. Rev.* **2018**, *356*, 127−146.

(23) Förster, C.; Heinze, K. Photophysics and photochemistry with Earth-abundant metals - fundamentals and concepts. *Chem. Soc. Rev.* **2020**, *49*, 1057−1070.
(24) Hockin, B. M.; Li, C.; Robertson, N.; Zysman-Colman, E. Photoredox catalysts based on earth-abundant metal complexes. *Catal. Sci. Technol.* **2019**, *9*, 889−915.
(25) Wenger, O. S. Photoactive Complexes with Earth-Abundant Metals. *J. Am. Chem. Soc.* **2018**, *140*, 13522−13533.
(26) Otto, S.; Dorn, M.; Förster, C.; Bauer, M.; Seitz, M.; Heinze, K. Understanding and Exploiting Long-lived Near-infrared Emission of a Molecular Ruby. *Coord. Chem. Rev.* **2018**, *359*, 102−111.
(27) Bizzarri, C.; Spuling, E.; Knoll, D. M.; Volz, D.; Bräse, S. Sustainable metal complexes for organic light-emitting diodes (OLEDs). *Coord. Chem. Rev.* **2018**, *373*, 49−82.
(28) Larsen, C. B.; Wenger, O. S. Photoredox Catalysis with Metal Complexes Made from Earth-Abundant Elements. *Chem. - Eur. J.* **2018**, *24*, 2039−2058.
(29) Bozic-Weber, B.; Constable, E. C.; Housecroft, C. E. Light harvesting with Earth abundant d-block metals: development of sensitizers in dye-sensitized solar cells (DSCs). *Coord. Chem. Rev.* **2013**, *257*, 3089−3106.
(30) Barbieri, A.; Accorsi, G.; Armaroli, N. Luminescent complexes beyond the platinum group: the d^{10} avenue. *Chem. Commun.* **2008**, 2185−2193.
(31) Harlang, T. C. B.; Liu, Y. Z.; Gordivska, O.; Fredin, L. A.; Ponseca, C. S.; Huang, P.; Chabera, P.; Kjaer, K. S.; Mateos, H.; Uhlig, J.; Lomoth, R.; Wallenberg, R.; Styring, S.; Persson, P.; Sundström, V.; Wärnmark, K. Iron Sensitizer Converts Light to Electrons with 92% Yield. *Nat. Chem.* **2015**, *7*, 883−889.
(32) Chábera, P.; Kjaer, K. S.; Prakash, O.; Honarfar, A.; Liu, Y. Z.; Fredin, L. A.; Harlang, T. C. B.; Lidin, S.; Uhlig, J.; Sundström, V.; Lomoth, R.; Persson, P.; Wärnmark, K. Fe^{II} Hexa N-Heterocyclic Carbene Complex with a 528 ps Metal-to-Ligand Charge-Transfer Excited-State Lifetime. *J. Phys. Chem. Lett.* **2018**, *9*, 459−463.
(33) Büldt, L. A.; Guo, X.; Vogel, R.; Prescimone, A.; Wenger, O. S. A Tris(diisocyanide)chromium(0) Complex Is a Luminescent Analog of $Fe(2,2'\text{-Bipyridine})_3^{2+}$. *J. Am. Chem. Soc.* **2017**, *139*, 985−992.
(34) Stevenson, S. M.; Shores, M. P.; Ferreira, E. M. Photooxidizing Chromium Catalysts for Promoting Radical Cation Cycloadditions. *Angew. Chem., Int. Ed.* **2015**, *54*, 6506−6510.
(35) Higgins, R. F.; Fatur, S. M.; Shepard, S. G.; Stevenson, S. M.; Boston, D. J.; Ferreira, E. M.; Damrauer, N. H.; Rappé, A. K.; Shores, M. P. Uncovering the Roles of Oxygen in Cr(III) Photoredox Catalysis. *J. Am. Chem. Soc.* **2016**, *138*, 5451−5464.
(36) Stevenson, S. M.; Higgins, R. F.; Shores, M. P.; Ferreira, E. M. Chromium photocatalysis: accessing structural complements to Diels−Alder adducts with electron-deficient dienophiles. *Chem. Sci.* **2017**, *8*, 654−660.
(37) Zhang, Y.; Lee, T. S.; Favale, J. M.; Leary, D. C.; Petersen, J. L.; Scholes, G. D.; Castellano, F. N.; Milsmann, C. Delayed fluorescence from a zirconium (iv) photosensitizer with ligand-to-metal charge-transfer excited states. *Nat. Chem.* **2020**, *12*, 345−352.
(38) Kjær, K. S.; Kaul, N.; Prakash, O.; Chábera, P.; Rosemann, N. W.; Honarfar, A.; Gordivska, O.; Fredin, L. A.; Bergquist, K. E.; Häggström, L.; Ericsson, T.; Lindh, L.; Yartsev, A.; Styring, S.; Huang, P.; Uhlig, J.; Bendix, J.; Strand, D.; Sundström, V.; Persson, P.; Lomoth, R.; Wärnmark, K. Luminescence and Reactivity of a Charge-Transfer Excited Iron Complex with Nanosecond Lifetime. *Science* **2019**, *363*, 249−253.
(39) Chábera, P.; Lindh, L.; Rosemann, N. W.; Prakash, O.; Uhlig, J.; Yartsev, A.; Wärnmark, K.; Sundström, V.; Persson, P. *Coord. Chem. Rev.* **2021**, *426*, 213517.
(40) Pal, A. K.; Li, C. F.; Hanan, G. S.; Zysman-Colman, E. Blue-Emissive Cobalt(III) Complexes and Their Use in the Photocatalytic Trifluoromethylation of Polycyclic Aromatic Hydrocarbons. *Angew. Chem., Int. Ed.* **2018**, *57*, 8027−8031.
(41) Yam, V. W.; Chan, A. K.; Hong, E. Y. Charge-transfer processes in metal complexes enable luminescence and memory functions. *Nat. Rev. Chem.* **2020**, *4*, 528−541.
(42) Jamieson, M. A.; Serpone, N.; Hoffman, M. Z. Advances in the photochemistry and photophysics of chromium(III) polypyridyl complexes in fluid media. *Coord. Chem. Rev.* **1981**, *39*, 121−179.
(43) Kirk, A. D. Photochemistry and Photophysics of Chromium(III) Complexes. *Chem. Rev.* **1999**, *99*, 1607−1640.
(44) Dorn, M.; Kalmbach, J.; Boden, P.; Päpcke, A.; Gómez, S.; Förster, C.; Kuczelinis, F.; Carrella, L. M.; Büldt, L.; Bings, N.; Rentschler, E.; Lochbrunner, S.; González, L.; Gerhards, M.; Seitz, M.; Heinze, K. A vanadium(III) complex with blue and NIR-II spin-flip luminescence in solution. *J. Am. Chem. Soc.* **2020**, *142*, 7947−7955.
(45) Forster, L. S. Thermal relaxation in excited electronic states of d^3 and d^6 metal complexes. *Coord. Chem. Rev.* **2002**, *227*, 59−92.
(46) Forster, L. S. Intersystem crossing in transition metal complexes. *Coord. Chem. Rev.* **2006**, *250*, 2023−2033.
(47) Kane-Maguire, N. A. P. Photochemistry and Photophysics of Coordination Compounds: Chromium. *Top. Curr. Chem.* **2007**, *280*, 37−67.
(48) Balzani, V.; Ceroni, P.; Juris, A.. *Photochemistry and Photophysics*; Wiley-VCH: Weinheim, 2014; pp 216−219.
(49) Xiang, H.; Cheng, J.; Ma, X.; Zhou, X.; Chruma, J. J. Near-infrared phosphorescence: materials and applications. *Chem. Soc. Rev.* **2013**, *42*, 6128−6185.
(50) Jørgenson, C. K. Recent Progress in Ligand Field Theory. *Struct. Bonding (Berlin)* **1966**, *1*, 3−31.
(51) Breivogel, A.; Förster, C.; Heinze, K. A Heteroleptic Bis(tridentate)ruthenium(II) Polypyridine Complex with Improved Photophysical Properties and Integrated Functionalizability. *Inorg. Chem.* **2010**, *49*, 7052−7056.
(52) Förster, C.; Dorn, M.; Reuter, T.; Otto, S.; Davarci, G.; Reich, T.; Carrella, L.; Rentschler, E.; Heinze, K. Ddpd as Expanded Terpyridine: Dramatic Effects of Symmetry and Electronic Properties in First Row Transition Metal Complexes. *Inorganics* **2018**, *6*, 86.
(53) Otto, S.; Grabolle, M.; Förster, C.; Kreitner, C.; Resch-Genger, U.; Heinze, K. $[Cr(ddpd)_2]^{3+}$: A molecular, water-soluble, highly NIR-emissive ruby analogue. *Angew. Chem., Int. Ed.* **2015**, *54*, 11572−11576.
(54) Wang, C.; Otto, S.; Dorn, M.; Kreidt, E.; Lebon, J.; Sršan, L.; Di Martino-Fumo, P.; Gerhards, M.; Resch-Genger, U.; Seitz, M.; Heinze, K. Deuterated Molecular Ruby with Record Luminescence Quantum Yield. *Angew. Chem., Int. Ed.* **2018**, *57*, 1112−1116.
(55) Otto, S.; Scholz, N.; Behnke, T.; Resch-Genger, U.; Heinze, K. Thermo-Chromium: A Contactless Optical Molecular Thermometer. *Chem. - Eur. J.* **2017**, *23*, 12131−12135.
(56) Otto, S.; Nauth, A. M.; Ermilov, E.; Scholz, N.; Friedrich, A.; Resch-Genger, U.; Lochbrunner, S.; Opatz, T.; Heinze, T. Photo-Chromium: Sensitizer for Visible Light-Induced Oxidative C-H Bond Functionalization − Electron or Energy Transfer? *ChemPhotoChem.* **2017**, *1*, 344−349.
(57) Otto, S.; Förster, C.; Wang, C.; Resch-Genger, U.; Heinze, K. A strongly luminescent chromium(III) complex acid. *Chem. - Eur. J.* **2018**, *24*, 12555−12563.
(58) Otto, S.; Harris, J.; Heinze, K.; Reber, C. Molecular ruby under pressure. *Angew. Chem., Int. Ed.* **2018**, *57*, 11069−11073.
(59) Basu, U.; Otto, S.; Heinze, K.; Gasser, G. Biological Evaluation of the NIR-Emissive Ruby Analogue $[Cr(ddpd)_2][BF_4]_3$ as a Photodynamic Therapy Photosensitizer. *Eur. J. Inorg. Chem.* **2019**, *2019*, 37−41.
(60) Wang, C.; Otto, S.; Dorn, M.; Heinze, K.; Resch-Genger, U. Luminescent TOP Nanosensors for Simultaneously Measuring Temperature, Oxygen, and pH at a Single Excitation Wavelength. *Anal. Chem.* **2019**, *91*, 2337−2344.
(61) Kalmbach, J.; Wang, C.; You, Y.; Förster, C.; Schubert, H.; Heinze, K.; Resch-Genger, U.; Seitz, M. Near-IR to Near-IR Upconversion Luminescence in Molecular Chromium Ytterbium Salts. *Angew. Chem., Int. Ed.* **2020**, *59*, 18804−18808.
(62) Jiménez, J.-R.; Doistau, B.; Besnard, C.; Piguet, C. Versatile heteroleptic bis-terdentate Cr(III) chromophores displaying room temperature millisecond excited state lifetimes. *Chem. Commun.* **2018**, *54*, 13228−13231.

https://doi.org/10.1021/jacs.1c05971
J. Am. Chem. Soc. 2021, 143, 11843−11855

(63) Jiménez, J. R.; Doistau, B.; Cruz, C. M.; Besnard, C.; Cuerva, J. M.; Campaña, A. G.; Piguet, C. Chiral Molecular Ruby $[Cr(dqp)_2]^{3+}$ with Long-Lived Circularly Polarized Luminescence. *J. Am. Chem. Soc.* **2019**, *141*, 13244−13252.
(64) Dee, C.; Zinna, F.; Kitzmann, W. R.; Pescitelli, G.; Heinze, K.; Di Bari, L.; Seitz, M. Strong Circularly Polarized Luminescence of an Octahedral Chromium(III) Complex. *Chem. Commun.* **2019**, *55*, 13078−13081.
(65) Treiling, S.; Wang, C.; Förster, C.; Reichenauer, F.; Kalmbach, J.; Boden, P.; Harris, J. P.; Carrella, L. M.; Rentschler, E.; Resch-Genger, U.; Reber, C.; Seitz, M.; Gerhards, M.; Heinze, K. Luminescence and Light-driven Energy and Electron Transfer from an Exceptionally Long-lived Excited State of a Non-innocent Chromium(III) Complex. *Angew. Chem., Int. Ed.* **2019**, *58*, 18075−18085.
(66) Bünzli, J.-C. G.; Charbonniere, L. J.; Ziessel, R. F. Structural and photophysical properties of Ln^{III} complexes with 2,2'-bipyridine-6,6'-dicarboxylic acid: surprising formation of a H-bonded network of bimetallic entities. *J. Chem. Soc., Dalton Trans.* **2000**, 1917−1923.
(67) Wahsner, J.; Seitz, M. Nonradiative Deactivation of Lanthanoid Excited States by Inner-Sphere Carboxylates. *Inorg. Chem.* **2015**, *54*, 10841−10848.
(68) Bünzli, J.-C. G. Lanthanide Luminescence for Biomedical Analyses and Imaging. *Chem. Rev.* **2010**, *110*, 2729−2755.
(69) Heffern, M. C.; Matosziuk, L. M.; Meade, T. J. Lanthanide Probes for Bioresponsive Imaging. *Chem. Rev.* **2014**, *114*, 4496−4539.
(70) Amoroso, A. J.; Pope, S. J. A. Using lanthanide ions in molecular bioimaging. *Chem. Soc. Rev.* **2015**, *44*, 4723−4742.
(71) Degli Esposti, C.; Bizzocchi, L. Absorption and Emission Spectroscopy of a Lasing Material: Ruby. *J. Chem. Educ.* **2007**, *84*, 1316−1318.
(72) Dominiak-Dzik, G.; Ryba-Romanowski, W.; Grinberg, M.; Beregi, E.; Kovacs, L. Excited-state relaxation dynamics of Cr^{3+}in $YAl_3(BO_3)_4$. *J. Phys.: Condens. Matter* **2002**, *14*, 5229−5237.
(73) Malysa, B.; Meijerink, A.; Jüstel, T. Temperature dependent luminescence Cr^{3+}-doped $GdAl_3(BO_3)_4$ and $YAl_3(BO_3)_4$. *J. Lumin.* **2016**, *171*, 246−253.
(74) Harris, J. P.; Sonneville, C.; Villain, O.; Calas, G.; Reber, C. Analytical fitting of temperature-dependent spin-flip transitions in absorption spectra of Cr^{3+}-doped silicate glasses. *Chem. Phys. Lett.: X* **2019**, *2*, 100003.
(75) Sijbom, H.; Verstraete, R.; Joos, J. J.; Poelman, D.; Smet, P. F. K_2SiF_6:Mn^{4+} as a red phosphor for displays and warm-white LEDs: a review of properties and perspectives. *Opt. Mater. Express* **2017**, *7*, 3332−3365.
(76) Ballhausen, C. J. *Introduction to Ligand Field Theory*; McGraw-Hill: New York, 1962; p 222.
(77) Ballhausen, C. J. *Molecular Electronic Structures of Transition Metal Complexes*; McGraw-Hill: New York, 1979; p 1.
(78) Avram, N. M., Brik, M. G., Eds.; *Optical Properties of 3d-Ions in Crystals: Spectroscopy and Crystal Field Analysis*; Springer: 2013; p 62.
(79) Daniel, C. Photochemistry and photophysics of transition metal complexes: quantum chemistry. *Coord. Chem. Rev.* **2015**, *282*−*283*, 19−32.
(80) Sousa, C.; Alías, M.; Domingo, A.; de Graaf, C. Deactivation of Excited States in Transition-Metal Complexes: Insight from Computational Chemistry. *Chem. - Eur. J.* **2019**, *25*, 1152−1164.
(81) Reinen, D.; Atanasov, M.; Köhler, P.; Babel, D. Jahn−Teller coupling and the influence of strain in T_g and E_g ground and excited states − A ligand field and DFT study on halide $M^{III}X_6$ model complexes [M = Ti^{III}−Cu^{III}; X = F^-, Cl^-]. *Coord. Chem. Rev.* **2010**, *254*, 2703−2754.
(82) Escudero, D. Photodeactivation Channels of Transition Metal Complexes: A Computational Chemistry Perspective. In *Transition Metals in Coordination Environments*; Broclawik, E., Borowski, T., Radoń, M., Eds; Challenges and Advances in Computational Chemistry and Physics; Springer: Cham, 2019; Vol. *29*.
(83) Atanasov, M.; Ganyushin, D.; Sivalingam, K.; Neese, F. A Modern First-Principles View on Ligand Field Theory Through the Eyes of Correlated Multireference Wavefunctions. *Struct. Bonding (Berlin, Ger.)* **2011**, *143*, 149−220.
(84) Singh, S. K.; Eng, J.; Atanasov, M.; Neese, F. Covalency and chemical bonding in transition metal complexes: An ab initio based ligand field perspective. *Coord. Chem. Rev.* **2017**, *344*, 2−25.
(85) Lang, L.; Atanasov, M.; Neese, F. Improvement of Ab Initio Ligand Field Theory by Means of Multistate Perturbation Theory. *J. Phys. Chem. A* **2020**, *124*, 1025−1037.
(86) Pierloot, K.; Vancoillie, S. Relative energy of the high-($^5T_{2g}$) and low-($^1A_{1g}$) spin states of $Fe(H_2O)_6]^{2+}$, $Fe(NH_3)_6]^{2+}$, and $[Fe(bpy)_3]^{2+}$: CASPT2 versus density functional theory. *J. Chem. Phys.* **2006**, *125*, 124303.
(87) Pierloot, K. Transition metals compounds: Outstanding challenges for multiconfigurational methods. *Int. J. Quantum Chem.* **2011**, *111*, 3291−3301.
(88) Dyker, G.; Muth, O. Synthesis of Methylene- and Methine-Bridged Oligopyridines. *Eur. J. Org. Chem.* **2004**, *2004*, 4319−4322.
(89) Constable, E. C.; Housecroft, C. E.; Neuburger, M.; Schönle, J.; Zampese, J. A. The surprising lability of bis(2,2':6',2"-terpyridine)-chromium(III) complexes. *Dalton Trans.* **2014**, *43*, 7227−7235.
(90) Zare, D.; Doistau, B.; Nozary, H.; Besnard, C.; Guénée, L.; Suffren, Y.; Pelé, A.-L.; Hauser, A.; Piguet, C. Cr^{III} as an alternative to Ru^{II} in metallo-supramolecular chemistry. *Dalton Trans.* **2017**, *46*, 8992−9009.
(91) Scarborough, C. C.; Sproules, S.; Weyhermüller, T.; DeBeer, S.; Wieghardt, K. Electronic and Molecular Structures of the Members of the Electron Transfer Series $[Cr(tbpy)_3]^n$ (n = 3+, 2+, 1+, 0): An X-ray Absorption Spectroscopic and Density Functional Theoretical Study. *Inorg. Chem.* **2011**, *50*, 12446−12462.
(92) Scarborough, C. C.; Lancaster, K. M.; DeBeer, S.; Weyhermüller, T.; Sproules, S.; Wieghardt, K. Experimental Fingerprints for Redox-Active Terpyridine in $[Cr(tpy)_2](PF_6)_n$ (n = 3−0), and the Remarkable Electronic Structure of $[Cr(tpy)_2]^{1-}$. *Inorg. Chem.* **2012**, *51*, 3718−3732.
(93) Becker, P. M.; Forster, C.; Carrella, L. M.; Boden, P.; Hunger, D.; Slageren, J.; Gerhards, M.; Rentschler, E.; Heinze, K. Spin Crossover and Long-lived Excited States in a Reduced Molecular Ruby. *Chem. - Eur. J.* **2020**, *26*, 7199−7204.
(94) CIE (1932). *Commission internationale de l'Eclairage proceedings*; Cambridge University Press: Cambridge, 1931.
(95) Eysel, H. H. Absorptions- und Lumineszenzspektrum von Hexamminchrom(III)-salzen. *Z. Phys. Chem.* **1970**, *72*, 82−90.
(96) Kreidt, E.; Kruck, C.; Seitz, M. *Handbook on the Physics and Chemistry of Rare Earths*; Bünzli, J. C.-G., Pecharsky, V. K., Eds.; Elsevier: Amsterdam, 2018; Vol. *53*, pp 35−79.
(97) Suzuki, K.; Kobayashi, A.; Kaneko, S.; Takehira, K.; Yoshihara, T.; Ishida, H.; Shiina, Y.; Oishi, S.; Tobita, S. Reevaluation of absolute luminescence quantum yields of standard solutions using a spectrometer with an integrating sphere and a back-thinned CCD detector. *Phys. Chem. Chem. Phys.* **2009**, *11*, 9850−9860.
(98) Young, R. C.; Meyer, T. J.; Whitten, D. G. Electron transfer quenching of excited states of metal complexes. *J. Am. Chem. Soc.* **1976**, *98*, 286−287.
(99) Juris, A.; Balzani, V.; Barigelletti, F.; Campagna, S.; Belser, P.; von Zelewsky, A. Ru(II) polypyridine complexes: photophysics, photochemistry, eletrochemistry, and chemiluminescence. *Coord. Chem. Rev.* **1988**, *84*, 85−277.
(100) Farney, E. P.; Chapman, S. J.; Swords, W. B.; Torelli, M. D.; Hamers, R. J.; Yoon, T. P. Discovery and Elucidation of Counteranion Dependence in Photoredox Catalysis. *J. Am. Chem. Soc.* **2019**, *141*, 6385−6391.
(101) Ma, D.; Duan, L.; Wei, Y.; He, L.; Wang, L.; Qiu, Y. Increased phosphorescent quantum yields of cationic iridium(III) complexes by wisely controlling the counter anions. *Chem. Commun.* **2014**, *50*, 530−532.
(102) Henry, M. S. Prolongation of the Lifetime of the ^2E State of Tris(2,2'-bipyridine)chromium(III) Ion by Anions in Aqueous Solution. *J. Am. Chem. Soc.* **1977**, *99*, 6138−6139.

https://doi.org/10.1021/jacs.1c05971
J. Am. Chem. Soc. 2021, 143, 11843−11855

(103) Schoonover, J. R.; Strouse, G. F.; Omberg, K. M.; Dyer, R. B. Application of transient vibrational spectroscopies to the excited states of metal polypyridyl complexes. *Comments Inorg. Chem.* **1996**, *18*, 165−188.
(104) Bäppler, F.; Zimmer, M.; Dietrich, F.; Grupe, M.; Wallesch, M.; Volz, D.; Bräse, S.; Gerhards, M.; Diller, R. Photophysical dynamics of a binuclear Cu(I)-emitter on the fs to μs timescale, in solid phase and in solution. *Phys. Chem. Chem. Phys.* **2017**, *19*, 29438−29448.
(105) Boden, P.; Di Martino-Fumo, P.; Otto, S.; Seidel, W.; Heinze, K.; Gerhards, M. Transient FTIR spectroscopy after pump/pump vs. pump/dump excitation and temperature dependent luminescence investigations on a highly luminescent chromium(III) complex. *Phys. Chem. Chem. Phys.* **2021**, *23*, 13808−13818.
(106) Ando, H.; Iuchi, S.; Sato, H. Theoretical study on ultrafast intersystem crossing of chromium(III) acetylacetonate. *Chem. Phys. Lett.* **2012**, *535*, 177−181.
(107) Juban, E. A.; McCusker, J. K. Ultrafast Dynamics of ^{2}E State Formation in $Cr(acac)_3$. *J. Am. Chem. Soc.* **2005**, *127*, 6857−6865.
(108) Schrauben, J. N.; Dillman, K. L.; Beck, W. F.; McCusker, J. K. Vibrational coherence in the excited state dynamics of $Cr(acac)_3$: probing the reaction coordinate for ultrafast intersystem crossing. *Chem. Sci.* **2010**, *1*, 405−410.
(109) Johansson, J. O.; Kim, J.-W.; Allwright, E.; Rogers, D. M.; Robertson, N.; Bigot, J.-Y. Directly probing spin dynamics in a molecular magnet with femtosecond time-resolution. *Chem. Sci.* **2016**, *7*, 7061−7067.
(110) Arias-Rotondo, D. A.; McCusker, J. K. The photophysics of photoredox catalysis: a roadmap for catalyst design. *Chem. Soc. Rev.* **2016**, *45*, 5803−5820.
(111) Connelly, N. G.; Geiger, W. E. Chemical Redox Agents for Organometallic Chemistry. *Chem. Rev.* **1996**, *96*, 877−910.
(112) Kurihara, T.; Suzuki, T.; Wakabayashi, H.; Ishikawa, S.; Shindo, K.; Shimada, Y.; Chiba, H.; Miyashi, T.; Yasunami, M.; Nozoe, T. Electronic Structures and Oxidation Potentials of Some Azulene Derivatives. *Bull. Chem. Soc. Jpn.* **1996**, *69*, 2003−2006.
(113) Khusnutdinova, J. R.; Milstein, D. Metal−Ligand Cooperation. *Angew. Chem., Int. Ed.* **2015**, *54*, 12236−12273.
(114) Aboshyan-Sorgho, L.; Besnard, C.; Pattison, P.; Kittilstved, K. R.; Aebischer, A.; Bünzli, J.-C. G.; Hauser, A.; Piguet, C. Near-InfraredVisible Light Upconversion in a Molecular Trinuclear d−f−d Complex. *Angew. Chem., Int. Ed.* **2011**, *50*, 4108−4112.
(115) Jimenez, J.; Cerdan, L.; Moreno, F.; Maroto, B. L.; García-Moreno, I.; Lunkley, J. L.; Muller, G.; de la Moya, S. Chiral Organic Dyes Endowed with Circularly Polarized Laser Emission. *J. Phys. Chem. C* **2017**, *121*, 5287−5292.
(116) Zhang, D.-W.; Li, M.; Chen, C.-F. Recent advances in circularly polarized electroluminescence based on organic light-emitting diodes. *Chem. Soc. Rev.* **2020**, *49*, 1331−1343.
(117) Jiménez, J.-R.; Poncet, M.; Míguez-Lago, S.; Grass, S.; Lacour, J.; Besnard, C.; Cuerva, J. M.; Campaña, A. G.; Piguet, C. Bright Long-Lived Circularly Polarized Luminescence in Chiral Chromium(III) Complexes. *Angew. Chem., Int. Ed.* **2021**, *60*, 10095−10102.

https://doi.org/10.1021/jacs.1c05971
J. Am. Chem. Soc. 2021, 143, 11843−11855

3.3 Efficient Triplet-Triplet Annihilation Upconversion Sensitized by a Chromium(III) Complex via an Underexplored Energy Transfer Mechanism

Authors: Cui Wang, Florian Reichenauer, Winald R. Kitzmann, Christoph Kerzig*, Katja Heinze*, Ute Resch-Genger*. * = Corresponding author.

Angew. Chem. Int. Ed. **2022**, *61*, e202202238. DOI: 10.1002/anie.202202238.
Angew. Chem. **2022**, *134*, e202202238. DOI: 10.1002/ange.202202238.

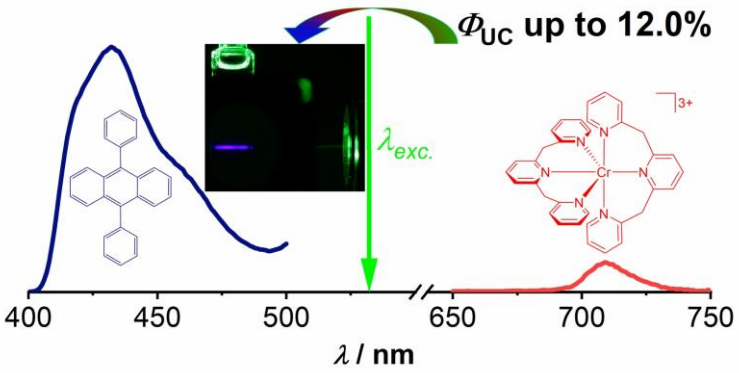

The application scope of triplet-triplet annihilation upconversion has, to date, been primarily limited to precious metal complexes due to insufficiently high excited-state energies or photoluminescence performance of many spin-flip complexes. Here, the blue-shifted emission, long excited-state lifetime, and green-light excitability of the molecular ruby $[Cr(bpmp)_2]^{3+}$ were harnessed for efficient sensitization of anthracenes via an underexplored doublet-triplet energy transfer, achieving green-to-blue photon upconversion. Furthermore, sterically accessible anthracenes undergo subsequent photochemical reactions, collectively underscoring the potential of earth-abundant metal complexes as versatile photocatalytic systems.

Authors Contributions

C. Wang and U. Resch-Genger conducted absorption as well as steady-state and time-resolved luminescence measurements. F. Reichenauer synthesized the photosensitizer, performed DFT calculations, and investigated the anthracene photoreaction via NMR spectroscopy. W. Kitzmann and F. Reichenauer prepared samples for the transient absorption studies and provided assistance during the measurements conducted by C. Kerzig. The project was conceptualized and designed

by C. Wang, K. Heinze and U. Resch-Genger, who wrote the manuscript with contributions of all authors.

Supporting Information

for this article can be found on pp. 199.

How to cite: *Angew. Chem. Int. Ed.* **2022**, *61*, e202202238
International Edition: doi.org/10.1002/anie.202202238
German Edition: doi.org/10.1002/ange.202202238

Upconversion Hot Paper

Efficient Triplet-Triplet Annihilation Upconversion Sensitized by a Chromium(III) Complex via an Underexplored Energy Transfer Mechanism

Cui Wang, Florian Reichenauer, Winald R. Kitzmann, Christoph Kerzig, Katja Heinze,* and Ute Resch-Genger**

Abstract: Sensitized triplet-triplet annihilation upconversion (sTTA-UC) mainly relies on precious metal complexes thanks to their high intersystem crossing (ISC) efficiencies, excited state energies, and lifetimes, while complexes of abundant first-row transition metals are only rarely utilized and with often moderate UC quantum yields. $[Cr(bpmp)_2]^{3+}$ (bpmp = 2,6-bis(2-pyridylmethyl)pyridine) containing earth-abundant chromium possesses an absorption band suitable for green light excitation, a doublet excited state energy matching the triplet energy of 9,10-diphenyl anthracene (DPA), a close to millisecond excited state lifetime, and high photostability. Combined ISC and doublet-triplet energy transfer from excited $[Cr(bpmp)_2]^{3+}$ to DPA gives ^{3}DPA with close-to-unity quantum yield. TTA of ^{3}DPA furnishes green-to-blue UC with a quantum yield of 12.0 % (close to the theoretical maximum). Sterically less-hindered anthracenes undergo a [4+4] cycloaddition with $[Cr(bpmp)_2]^{3+}$ and green light.

Introduction

Triplet-triplet annihilation-based sensitized photon upconversion (sTTA-UC) converts low-energy photons into anti-Stokes-shifted photons or allows demanding photochemical activation of substrates with low-energy light.[1] Typically, a sTTA-UC system consists of a strongly absorbing sensitizer with a long-lived excited triplet state and a highly fluorescent organic annihilator. Photoexcitation of the sensitizer, which is often a transition metal complex with a precious metal, from its singlet ground state to a singlet excited state (frequently a singlet metal-to-ligand charge-transfer state ^{1}MLCT), is followed by intersystem crossing (ISC) to populate its long-lived triplet state (often a ^{3}MLCT state). The electronically excited triplet photosensitizer engages in collisional triplet-triplet energy transfer (TTET) via a Dexter energy transfer mechanism with an acceptor possessing an appropriate triplet (T_1) energy. Interaction of two triplet excited acceptors leads to triplet-triplet annihilation (TTA), which yields one acceptor in its ground state S_0 and the second one in its excited singlet state S_1. The latter releases its energy by emitting delayed fluorescence at a shorter wavelength (higher energy) than the photons originally absorbed by the sensitizer.[1a–i] Alternatively, this S_1 state can be used for chemical transformations requiring more energy than a single low-energy photon.[1j–o]

$$\Phi_{UC} = \frac{f}{2}\Phi_{ISC}\Phi_{EnT}\Phi_{TTA}\Phi_F \quad (1)$$

Equation 1[2] describes the dependence of the upconversion quantum yield (Φ_{UC}) on the efficiencies of the involved processes, i.e., ISC of the sensitizer (Φ_{ISC}), energy transfer (EnT; often TTET from ^{3}MLCT states) from the excited sensitizer to the annihilator (Φ_{EnT}), TTA of the annihilator (Φ_{TTA}), and delayed annihilator fluorescence (Φ_F). f equals the spin-statistical factor for generating a singlet spin-state via TTA. The combination of two acceptors in their T_1 states in the TTA encounter complex generates nine spin states, namely one singlet, three triplet, and five quintet states. Depending on the energies of the annihilator's T_1, T_2, and S_1 states, the theoretical maximum of the spin-statistical factor f_{max} amounts to 11.1 %, 40 % or 100 % for all channels ($2E(T_1) > E(S_1)$; usually not accessible due to the too high energy of the quintet state), only singlet and triplet channels ($2E(T_1) > E(S_1)$ and $2E(T_1) > E(T_2)$), or only the singlet channel ($E(T_2) > 2E(T_1) > E(S_1)$) being open.[3] This leads to

[*] Dr. C. Wang, Dr. U. Resch-Genger
Division Biophotonics,
Federal Institute for Materials Research and Testing (BAM)
Richard-Willstätter-Strasse 11, 12489 Berlin (Germany)
E-mail: ute.resch@bam.de
Dr. C. Wang
Institute of Chemistry and Biochemistry,
Free University of Berlin
Arnimallee 22, 14195 Berlin (Germany)
F. Reichenauer, W. R. Kitzmann, Prof. Dr. C. Kerzig,
Prof. Dr. K. Heinze
Department of Chemistry,
Johannes Gutenberg University of Mainz
Duesbergweg 10–14, 55128 Mainz (Germany)
E-mail: ckerzig@uni-mainz.de
katja.heinze@uni-mainz.de

maximum UC quantum yields ($\Phi_{UC,max}$) of 5.55 %, 20 % or 50 %, respectively, for Φ_{ISC}, Φ_{EnT}, Φ_{TTA}, and Φ_F amounting to 100 %, taking the reaction stoichiometry into account.[2a,4] The excited states of the most often used blue fluorescent annihilator 9,10-diphenyl anthracene (DPA) allow both open singlet and triplet channels ($\Phi_{UC,max}=20$ % for $f_{max}=40$ %).[3a,5] Occasionally, Φ_{UC} values >20 % were observed as well,[6] as other factors like spin dynamics and shapes of the excited singlet and triplet energy surfaces of the annihilator can also affect the overall UC efficiency.[3a,7]

From the sensitizer perspective, both ISC and energy transfer—in most cases TTET—can be optimized. The ISC process is greatly accelerated in sensitizers with heavy metal ions, such as $[Ru(bpy)_3]^{2+}$ (bpy=2,2′-bipyridine) and its derivatives. This explains the ubiquitous utilization of noble metal complexes in sTTA-UC and other photochemical applications. Energy transfer processes from the excited sensitizer to the annihilator via the Dexter mechanism[8] require an overlap of the excited state wavefunction of the sensitizer and the annihilator's ground state wavefunction. Consequently, (triplet) charge-transfer excited states with a wavefunction extending onto the ligands are particularly well suited for Dexter energy transfer. This lays the basis for exploiting complexes such as $[Ru(bpy)_3]^{2+}$ and its derivatives with long-lived charge-transfer states (mostly ^{3}MLCT) in UC processes.[1h]

Most molecular triplet sensitizers featuring long-lived excited charge-transfer states contain precious second- or third-row transition metals, e.g. Ru^{II}, Ir^{III}, Re^{I}, Pt^{II}, Pd^{II} or Os^{II}.[9] Replacing precious metals with more earth-abundant transition metals, in particular first-row metals, opens non-radiative decay pathways via low-energy metal-centered (MC) excited states.[10] This can reduce their excited state lifetimes. Notable exceptions are Cu^{I} ^{3}MLCT and Zr^{IV} ^{3}LMCT sensitizers with $3d^{10}$ and $4d^0$ electron configurations that lack detrimental MC excited states,[6d,11] as well as Cr^0, Mn^{I}, and Mo^0 triplet sensitizers with a d^6 electron configuration in a strong ligand field.[11,12]

Fundamentally different from long-lived ^{3}MLCT (or ^{3}LMCT) excited states are intraconfigurational MC excited states which are characterized by a spin-flip within the lower-energy d orbitals (t_{2g} orbitals in octahedral symmetry).[13] Thanks to the spin-forbidden and often Laporte-forbidden character of these spin-flip transitions, the excited state lifetimes can even reach milliseconds.[13a,14] Certain Cr^{III} complexes are called "molecular rubies" owing to their excited state landscapes resembling that of the oxidic mineral ruby, and they possess extraordinarily long excited state lifetimes and record photoluminescence quantum yields.[13a,14] However, their excited state energies are very low.[13a,14a–d,f,15] This precludes their utilization in sTTA-UC due to the mismatch with the triplet energies of typical annihilators like DPA.[1h] Moreover, their electronic structure renders efficient excitation at wavelength >470 nm barely feasible. For these Cr^{III} complexes, energy transfer to triplet oxygen[14c,16] or to lanthanide ions with low energy excited states has been successfully demonstrated as well as UC luminescence (UCL) using $Cr^{III}\rightarrow Er^{III}$ energy transfer.[17] Energy transfer from Yb^{III} to Cr^{III} has also been reported to yield NIR-to-NIR upconverted photons.[18] Energy transfer from the π-π* states of appended anthracenyl substituents to Cr^{III} leads to quenching of the anthracene fluorescence and sensitized phosphorescence from the metal-centered doublet state.[19] The reverse process of sensitizing the triplet state of anthracenes or other organic dyes by electronically excited Cr^{III} complexes (doublet-triplet energy transfer, DTET), relevant for sTTA-UC, has not been observed so far due to the lack of Cr^{III} complexes with suitably high doublet state energies and long excited state lifetimes.[13a,14a–d,15] The recently reported second generation molecular ruby $[Cr(bpmp)_2]^{3+}$ has a comparably high doublet energy (1.75 eV) and a high excited spin-flip state lifetime in the low ms range (e.g., 1550 μs in $H_2O/HClO_4$) along with a comparably low-energy absorption band at 462 nm (bpmp=2,6-bis(2-pyridylmethyl)pyridine).[14e] This bands tails up to about 550 nm, enabling excitation with green light. These photophysical properties recommend $[Cr(bpmp)_2]^{3+}$ as potential sensitizer in sTTA-UC schemes.

We now report on unprecedented UC and photochemical cycloaddition reactions using the $[Cr(bpmp)_2]^{3+}$ sensitizer and green light excitation. The unique decisive DTET process from the excited Cr^{III} complex to anthracene acceptors is probed by steady-state and time-resolved photoluminescence spectroscopy and excitation power density (P) dependent luminescence studies, complemented by nanosecond transient absorption (TA) spectroscopy.

Results and Discussion

The key idea is to identify a suitable Cr^{III} based sensitizer which meets the sTTA-UC requirements of a low excitation energy, a doublet excited state energy matching the energy of the DPA annihilator in its triplet state T_1 ($E_T=1.72$–1.77 eV; Figure 1a),[3a,20] and a long excited state lifetime. To the best of our knowledge, out of the huge number of known Cr^{III} complexes, only the Cr^{III} complex $[Cr(bpmp)_2]^{3+}$ fulfills these requirements. $[Cr(bpmp)_2]^{3+}$ has an excitation energy of 2.33 eV (532 nm), a doublet excited state ($^2E/^2T_1$) energy of 1.75 eV, an excited state lifetime of $\tau_0=890$ μs independent of concentration (in deoxygenated DMF containing 0.1 M perchloric acid), and a high photostability (Figures 1a and 1b; Supporting Information, Figures S1, S2).[14e]

According to the intensity- and lifetime-based Stern–Volmer studies, DPA quenches the $[Cr(bpmp)_2]^{3+}$ phosphorescence at 709 nm with $K_{SV}=5.7\times10^4\,M^{-1}$ and $5.0\times10^4\,M^{-1}$, respectively (Figure S3). The similar K_{SV} values confirm dynamic quenching[21] of the $^2E/^2T_1$ states of $[Cr(bpmp)_2]^{3+}$ via DTET to DPA (Figure 1c)). The DTET rate constant $k_{DTET}=K_{SV}/\tau_0$ amounts to $(5.6\text{–}6.4)\times10^7\,M^{-1}s^{-1}$. This value is lower than the diffusion limit of bimolecular reactions in DMF ($830\times10^7\,M^{-1}s^{-1}$) at 25 °C[22] but similar to the rates of self-exchange reactions of Cr^{III} complexes involving doublet-doublet energy transfer.[23]

To visualize possible encounters of $[Cr(bpmp)_2]^{3+}$ and DPA and to estimate the distances involved in the Dexter-type DTET processes with Cr^{III} sensitizers, molecular

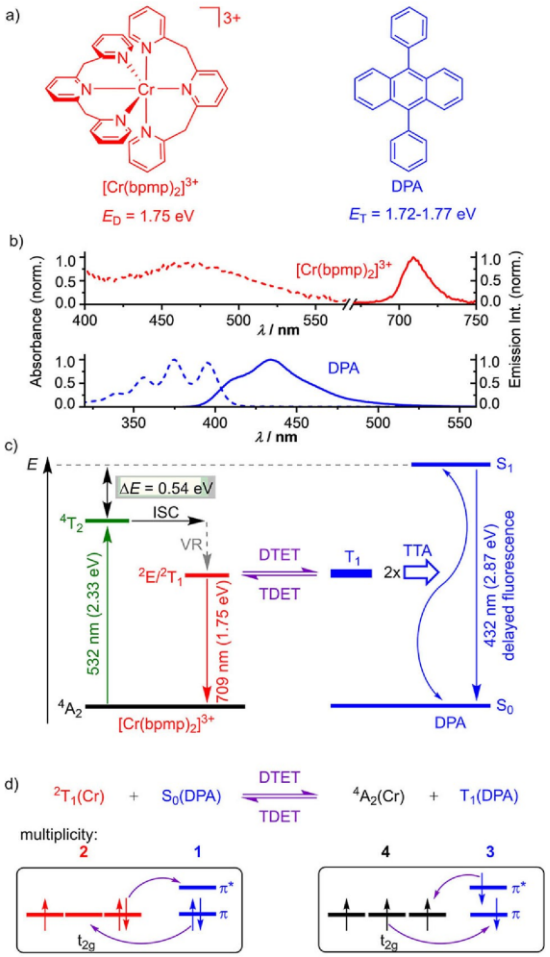

Figure 1. a) Structures and excited state energies of $[Cr(bpmp)_2]^{3+}$ and DPA, b) normalized absorption and emission spectra of $[Cr(bpmp)_2]^{3+}$ and DPA, c) Jablonski diagram illustrating the excitation of the sensitizer with green light, intersystem crossing (ISC) to its doublet states, vibrational relaxation (VR), doublet-triplet energy transfer (DTET), the reverse process triplet-doublet energy transfer (TDET), triplet-triplet annihilation (TTA) and delayed fluorescence, and d) illustration of the Dexter energy transfer between the excited $[Cr(bpmp)_2]^{3+}$ sensitizer and ground state DPA (DTET) and the reverse process TDET using relevant microstates. The multiplicities (spin degeneracies) of the involved states are highlighted.

models of anthracene as small DPA model and $[Cr(bpmp)_2]^{3+}$ in a solvent cage were optimized with Density Functional Theory calculations (CPCM(DMF)-RI-B3LYP-D3BJ-ZORA/def2-TZVPP; Figure S4). These qualitative models, which do not consider counter ions and solvent molecules, do not support a strong and static interaction between $[Cr(bpmp)_2]^{3+}$ and anthracene in agreement with the dynamic quenching of the doublet states. The models of the exemplary optimized collisional encounter complexes suggest shortest distances of 5.8–9.5 Å between the Cr^{III} ions to the centers of the anthracene rings. These distances are compatible with a Dexter mechanism[8] of the DTET process (Figure S4). Compared to sensitizers with triplet charge-transfer states,[11,6d,9–12] where the wavefunctions of the excited states extend onto the ligands, the metal-localized nature of the Cr^{III} spin-flip states[13] allows only for comparably weak sensitizer-annihilator orbital interactions in the encounter complexes. This—in addition to the small driving force for DTET (Figure 1c)—can explain the roughly 4.4–5.0 times lower energy transfer rate constant of $[Cr(bpmp)_2]^{3+}$/DPA as compared to, e.g. the triplet-triplet energy transfer (TTET) rate constant k_{TTET} of $28.2\times10^7\ M^{-1}s^{-1}$ reported by Castellano et al. for DPA and a Cu^{I}-based ^{3}MLCT sensitizer.[24]

The smaller k_{DTET} value of the $[Cr(bpmp)_2]^{3+}$/DPA pair is more than compensated by the very long excited state lifetime $\tau_0=890$ µs of $[Cr(bpmp)_2]^{3+}$. The DTET efficiencies $\Phi_{DTET}=1-\tau/\tau_0$ reach values of 84 % and >90 % for DPA concentrations of 100 µM and >300 µM (saturation), respectively. These values strongly exceed $\Phi_{DTET}=69$ % of the only other DTET process to an organic dye reported so far, that involved a luminescent doublet π-radical sensitizer with τ_0 of only 27 ns[25] and DPA (5 mM), as well as $\Phi_{TTET}=56$ % of the classical $[Ru(bpy)_3]^{2+}$/DPA pair ($\tau_0=935$ ns, Figure 2b). This underlines the importance of long sensitizer excited state lifetimes for these processes.

Formation of the T_1 state of DPA (^{3}DPA) was assessed by nanosecond TA spectroscopy for higher concentrations of $[Cr(bpmp)_2]^{3+}$ and DPA than those used for the luminescence studies. This yields the characteristic and essentially solvent independent 445 nm ^{3}DPA absorption band[11,22,26] (associated with electronic transitions from the long-lived lowest triplet state to higher triplet states of DPA) 10 µs after the excitation pulse (Figure 2, Figure S5; 2 mM $[Cr(bpmp)_2]^{3+}$/1 mM DPA) and confirms DTET from the excited Cr^{III} complex to DPA (Figure 2a, middle panel). The ISC process (Figure 1c) of the initially excited quartet state $^4T_2$ to the doublet states $^2E/^2T_1$ and vibrational relaxation (VR, Figure 1c) are much faster according to reported fs transient absorption spectroscopic data of $[Cr(bpmp)_2]^{3+}$.[14e] In the absence of DPA (Figure 2a, top panel), the TA spectrum of the relaxed doublet state is observed 100 ns after the excitation pulse. Due to the large energy gap between $^4T_2$ and $^2E/^2T_1$ states, back-ISC is thermodynamically unfeasible (Figure 1b). To gain a deeper insight into the formation efficiency of the DPA triplet and to quantify the involved processes, we performed quantitative TA studies with the $[Cr(bpmp)_2]^{3+}$/DPA pair utilizing $[Ru(bpy)_3]^{2+}$ as a reference sensitizer.[27] As TTET from $[Ru(bpy)_3]^{2+}$ to anthracenes proceeds without side reactions as demonstrated by the characteristic ^{3}DPA spectrum and the absence of DPA radical ion formation (indicated by the absence of additional absorption bands in the red spectral region in the lower panel of Figure 2a),[1j,l,28] this system is a suitable actinometer in laser flash photolysis (LFP) studies.[27] Thereby, the efficiency of the combined ISC and DTET processes of the $[Cr(bpmp)_2]^{3+}$ sensitizer was determined to $\Phi_{ISC+DTET}=(92\pm5)$ % using a TTET efficiency of $[Ru(bpy)_3]^{2+}$ of 56 % (Figure 2b; Supporting Information, Figure S6).

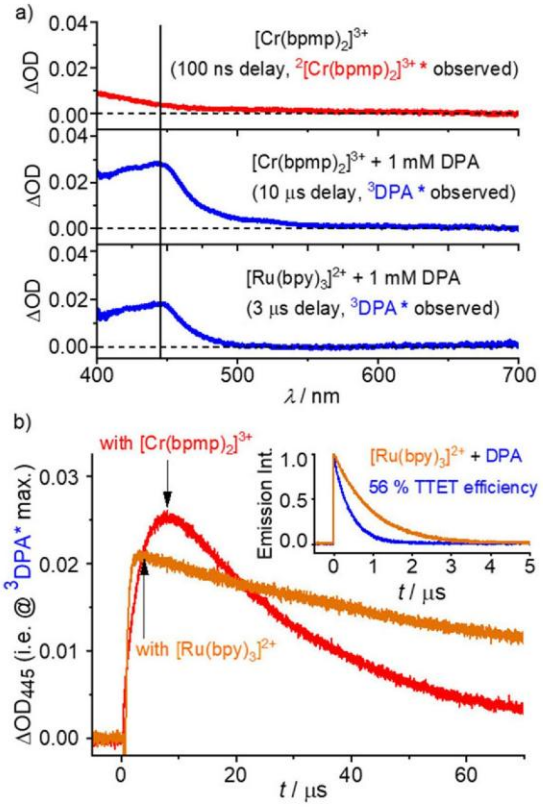

Figure 2. Transient absorption studies of the formation of ^{3}DPA upon sensitizer excitation with a 532 nm laser in Ar-saturated acidified DMF containing 1 mM of DPA. a) TA spectra of $[Cr(bpmp)_2]^{3+}$ (middle panel) and $[Ru(bpy)_3]^{2+}$ (bottom panel) in the presence of DPA integrated over 100 ns as well as control experiments with $[Cr(bpmp)_2]^{3+}$ (upper panel). b) Comparative TA traces monitoring the formation and decay of ^{3}DPA with $[Cr(bpmp)_2]^{3+}$ and $[Ru(bpy)_3]^{2+}$ under these conditions. The measurement of the $^3[Ru(bpy)_3]^{2+}$ TTET quenching efficiency is shown in the inset. The concentrations of $[Cr(bpmp)_2]^{3+}$ and $[Ru(bpy)_3]^{2+}$ were adjusted to matching absorbances of 0.027 ± 0.001 at 532 nm. The detection windows used for the measurement of the ^{3}DPA spectra are indicated with black arrows.

As shown in Figure 2b, the ^{3}DPA decay in the presence of $[Cr(bpmp)_2]^{3+}$ is faster than that observed for $[Ru(bpy)_3]^{2+}$.ek; This suggests a back-energy transfer process, namely triplet-doublet energy transfer (TDET) from ^{3}DPA to $[Cr(bpmp)_2]^{3+}$ in its $^4A_2$ ground state which is thermodynamically feasible (Figure 1c). TDET manifests itself also in the time-resolved luminescence spectra of $[Cr(bpmp)_2]^{3+}$ in the presence of DPA recorded with delays of 20 ns and 50 µs, revealing prompt and delayed $[Cr(bpmp)_2]^{3+}$ phosphorescence, respectively (Figure S7).

Beyond the small enthalpy difference between the $^2E/^2T_1$ manifold of $[Cr(bpmp)_2]^{3+}$ and the T_1 state of DPA (Figure 1c), entropy aspects can be relevant for this equilibrium.[29] Assuming that i) only the lowest microstate of the $^2E/^2T_1$ manifold of $[Cr(bpmp)_2]^{3+}$ is significantly populated (a $^2T_1$-derived microstate; Figure 1d[14e] and ii) the spin conservation rules[30] do merely affect the kinetic feasibility and not the thermodynamics, only the spin degeneracies play a role (Figure 1d). The number of degenerate states of the $[^4A_2(Cr) + T_1(DPA)]$ combination ($n = 4 \times 3 = 12$) then exceeds the number of the $[^2T_1(Cr) + S_0(DPA)]$ combinations ($n = 2 \times 1 = 2$) (Figure 1c). This yields an upper limit for the entropic contribution of $\Delta S = R \ln(12/2) = 15\ J\,mol^{-1}\,K^{-1}$, specific for Cr^{III} doublet sensitizer/triplet annihilator pairs and the DTET process. This adds an amount of $\approx 4.5\ kJ\,mol^{-1}$ to the driving force ΔG of the forward DTET at room temperature. In contrast, no entropic effects are expected for TTET with ^{3}MLCT sensitizers such as $[Ru(bpy)_3]^{2+}$. Even without such electronic entropy effects (i.e. for conventional TTET reactions), uphill energy transfer processes can occur at room temperature. This has been recently observed for an Ir^{III} ^{3}MLCT sensitizer and benzothiophenes (triplet energy difference of $24\ kJ\,mol^{-1}$).[31] The feasibility of this up-hill process was attributed to the thermal population of vibrational or rotational levels of the excited sensitizer or ground-state acceptor molecules which helped to overcome the thermodynamic energy gap.[31]

Consequently, $[Cr(bpmp)_2]^{3+}$ and DPA engage in an excited state equilibrium due to their long-excited state lifetimes, similar excited state energies, and the available thermal energy to overcome small energy gaps. As the doublet states, which can be reached by direct excitation of $[Cr(bpmp)_2]^{3+}$ and by repopulation via TDET, form an excited-state reservoir, no energy is lost. Hence, the TDET/DTET energy transfer pathways seem to barely affect the following TTA process (Figure 1c) and the overall UC process is very efficient despite the reduced lifetime of the ^{3}DPA state (see below).

Excitation of an oxygen-free acidified DMF solution of $[Cr(bpmp)_2]^{3+}$ and DPA with a 532 nm laser leads to strong blue DPA fluorescence at 432 nm (Figure 3a). The UCL maximum is blue shifted by 0.54 eV relative to the 532 nm excitation (Figure 1b, Figure 3a). In the absence of $[Cr(bpmp)_2]^{3+}$, no DPA fluorescence occurs under these conditions (Figure 1b; Figure S9). The integrated UCL intensity $I_{400-500}$ exceeds the residual emission of $[Cr(bpmp)_2]^{3+}$ ($I_{680-750}$) by a factor of about 45 indicating an efficient TTA-UC process. Even excitation at 532 nm with a significantly less intense xenon lamp ($\approx 1\ mW\,cm^{-2}$) leads to noticeable UCL of DPA (Figure S10).

Increasing the DPA concentration enhances the UCL signal, which gradually approaches saturation (Figure S11). The fluorescence lifetime of directly excited DPA equals 6.6 ns, while the lifetime of the DPA fluorescence fed by green light excitation of $[Cr(bpmp)_2]^{3+}$ and DTET/TTA amounts to 162 µs (Figure 3b). The T_1 state of DPA has a millisecond lifetime in the absence of non-radiative processes.[32] Consequently, the long UC fluorescence lifetime of 162 µs confirms its delayed nature caused by the intermediate population of the long-lived T_1 state of DPA (Figure 1c).

Time-resolved phosphorescence measurements of solutions of the $[Cr(bpmp)_2]^{3+}$/DPA pair (50 µM/1 mM; $\lambda_{exc} =$

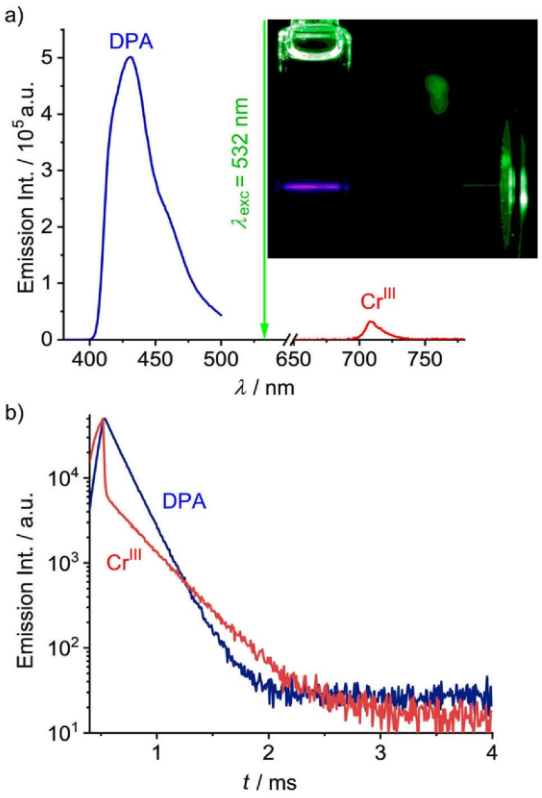

Figure 3. a) UCL spectrum (532 nm, cw, 1.5 W cm^{-2}) and b) UCL decay (532 nm, 250 Hz, pulse width 500 µs) of $[Cr(bpmp)_2]^{3+}$/DPA (blue/red). The red emission trace in (b) corresponds to the concomitant $[Cr(bpmp)_2]^{3+}$ phosphorescence decay. Inset: Photograph of the sample under 532 nm laser excitation (laser power ≈40 mW). The sensitizer and acceptor concentrations in deoxygenated acidified DMF were 50 µM and 1 mM.

532 nm, λ_{obs} = 709 nm) reveal biexponential decay kinetics with lifetimes τ_1 = 7 µs (15 %) and τ_2 = 303 µs (85 %), assigned to the prompt and delayed phosphorescence of $[Cr(bpmp)_2]^{3+}$, respectively (Figure 3b). The delayed signal arises from the doublet states of $[Cr(bpmp)_2]^{3+}$ which can be repopulated by TDET from the long-lived T_1 state of DPA (Figure 1c, d). An increase in the sensitizer concentration leads to a reduction in the delayed phosphorescence lifetime and an increase in its contribution to the luminescence decay (enlarged relative amplitude, see Supporting Information for details, Figure S8, Table S1). These data agree well with the assumed excited state equilibrium of $[Cr(bpmp)_2]^{3+}$ and DPA involving DTET/TDET processes (Figures 1c, d).[33] Under these conditions and using the lifetime of the prompt $[Cr(bpmp)_2]^{3+}$ phosphorescence τ_1 of 7 µs, the DTET yield amounts to $\Phi_{DTET} = 1-\tau_1/\tau_0 = 99.2$ % in agreement with the high DPA triplet quantum yield determined by quantitative TA spectroscopy. Notably, these values imply a lower limit for the ISC efficiency of $[Cr(bpmp)_2]^{3+}$ on the order of 90 %. This high value is remarkable considering that chromium is a first-row transition metal with a lower spin-orbit coupling constant compared to precious metals such as ruthenium.[34]

Due to the biphotonic nature of sTTA-UC, UCL from sensitizer/annihilator pairs nonlinearly depends on excitation power density and shows a slope factor (photonic order) of about two in the non-saturated regime which approaches one upon saturation. Increasing the excitation power density of the 532 nm laser (cw, 1.5 W cm^{-2}) drastically enhances the UCL of DPA (Figure 4a). The integrated UCL ($I_{400-500}$) of the $[Cr(bpmp)_2]^{3+}$/DPA pair shows a slope factor of 1.88 as expected for a biphotonic process. Yet, saturation is not reached up to power densities of 1.5 W cm^{-2} (Figure S12). To determine Φ_{UC} for the saturated system, we utilized a more intense 520 nm laser (cw, ca. 8 W cm^{-2}). Under these conditions, the integrated UCL nearly quadratically (slope factor of 1.91) depends on power density for power densities of up to about 2 W cm^{-2} and then starts to saturate as indicated by the linear slope of 1.03. The power density threshold value I_{th}, which indicates the turning point from a biphotonic to a linear (monophotonic) process reflecting UC saturation, amounts to about 1.56 W cm^{-2} (Figure 4b). This value, which is relatively high compared to I_{th} values of sTTA-UC systems reported for systems utilizing Zn^{II}, Zr^{IV}, and Cu^{I} sensitizers,[6d,11d,35] is ascribed to the very small absorption of $[Cr(bpmp)_2]^{3+}$ above 520 nm ($\varepsilon \approx 30$–$45\ M^{-1}cm^{-1}$).[14e] This leaves room for improvement of the sTTA-UC by further red shifting the absorption band the of the Cr^{III} sensitizer and/or increasing its molar absorption coefficient for green light excitation. The relative determination of Φ_{UC} (50 µM $[Cr(bpmp)_2]^{3+}$/1 mM DPA) give Φ_{UC} = 8.7 % for excitation with the 532 nm laser and Φ_{UC} = (12.0 ± 0.6) % for 520 nm excitation under saturated conditions (Figure 4c, Figure S12, S13). This value is amongst the highest UC efficiencies reported so far for sensitizers containing only earth-abundant elements.[11,6d,11d,35a]

With Φ_F of DPA of 82.8 % (measured in diluted, acidified DMF solution), $\Phi_{DTET+ISC}$ of about 90 % and a spin-statistical factor for DPA of f = 40 %, Equation (1) gives an upper limit of the sTTA-UC quantum yield Φ_{UC} of about 15 %. This value is close to the actual Φ_{UC} = (12.0 ± 0.6) % achieved with $[Cr(bpmp)_2]^{3+}$/DPA. The slight discrepancy is probably due to optical losses[2b] resulting from the higher DPA concentration. In addition to this relatively high sTTA-UC efficiency, the excellent photostability of $[Cr(bpmp)_2]^{3+}$ and DPA enable a constant UCL intensity under continuous laser illumination at 532 nm for more than two hours (Figure S14).

Sterically less-hindered anthracene derivatives form [4+4] cycloaddition products under UV illumination by the reaction of an anthracene in its S_1 state with a ground state anthracene.[36] Alternative to direct excitation with UV light, the S_1 state of these anthracenes can also be populated via sTTA-UC, e.g., by using $[Ru(bpy)_3]^{2+}$ derivatives as sensitizer and excitation with a 457.9 nm laser, yielding the respective anthracene dimer.[1i] To demonstrate that the $[Cr(bpmp)_2]^{3+}$ sensitizer can also initiate photochemical reactions via sTTA-UC, anthracene-9-propionic acid (APA), 9-anthracene carboxylic acid (ACA), and

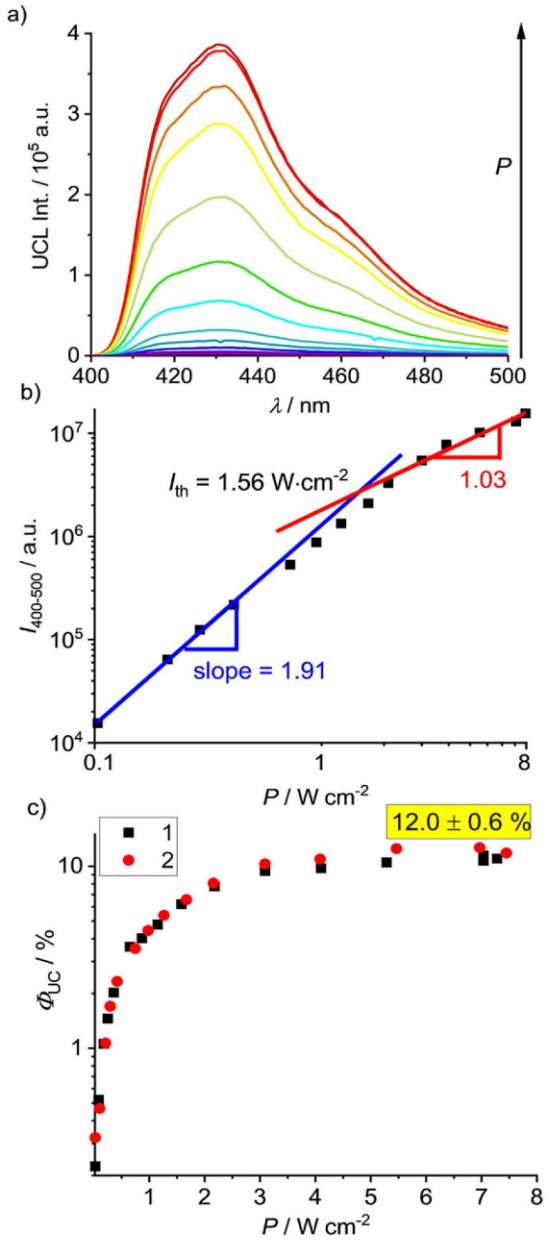

Figure 4. a) UCL spectra of $[Cr(bpmp)_2]^{3+}$/DPA (50 μM/1 mM in deoxygenated acidified DMF) as a function of excitation power density of a 520 nm laser (cw, ≈8 W cm^{-2}), b) excitation power density dependence of the integrated UCL ($I_{400-500}$) of DPA, c) relatively determined Φ_{UC} of the $[Cr(bpmp)_2]^{3+}$/DPA pair as a function of excitation power density of the 520 nm laser; the red and black symbols denote two independent experiments.

anthracene (An) were illuminated with 532 nm light in the presence of $[Cr(bpmp)_2]^{3+}$ in acidified deoxygenated DMF. All annihilators quench the $[Cr(bpmp)_2]^{3+}$ emission as expected from their T_1 energies, which are similar to that of DPA (Figure S15). UCL is observed in the steady-state and time-resolved spectra, showing the characteristic UC dependence on P (Figures S16–S21). Yet, the Φ_{UC} values obtained for APA, ACA, and An are much lower than Φ_{UC} of $[Cr(bpmp)_2]^{3+}$/DPA (Figure S22, Table S2). Photolysis at 532 nm in the presence of $[Cr(bpmp)_2]^{3+}$ leads to a decrease of the absorption bands and UCL of the anthracenes (Figures S23, S24). Exemplary for the $[Cr(bpmp)_2]^{3+}$/An pair, anthracene photodimerization was confirmed by proton NMR spectroscopy. The ^{1}H NMR spectra of $[Cr(bpmp)_2]^{3+}$/An in oxygen-free acidified d_7-DMF obtained during photolysis with a 525 nm Kessil LED indicated the formation of the [4+4] dimer on the basis of the increasing characteristic ^{1}H NMR resonance at $\delta = 4.47$ ppm for the bridgehead protons of the anthracene dimer (Figure S25).[ii]

Conclusion

The Cr^{III} complex $[Cr(bpmp)_2]^{3+}$ can replace classical ^{3}MLCT sensitizers, in particular $[Ru(bpy)_3]^{2+}$ derivatives, in sensitized triplet-triplet annihilation upconversion (sTTA-UC) processes with 9,10-diphenyl anthracene (DPA) as the annihilator generating upconverted blue photons from green photons. The key to success for efficient sTTA-UC with $[Cr(bpmp)_2]^{3+}$ lies in its comparably low excitation energy (2.33 eV), its relatively high doublet state energy (1.75 eV), its high photostability, and especially in its long doublet state lifetime of 890 μs. The latter can overcompensate the comparably lower doublet-triplet energy transfer rate, leading to high energy transfer efficiencies close to unity, thereby even outperforming $[Ru(bpy)_3]^{2+}$. This high energy transfer efficiency furnishes a UC quantum yield Φ_{UC} of (12.0 ± 0.6) %. For the sterically less-hindered anthracene derivatives anthracene-9-propionic acid, 9-anthracene carboxylic acid, and anthracene, the $[Cr(bpmp)_2]^{3+}$ sensitizer enables a [4+4] cycloaddition with green light that traditionally requires UV light.

Overall, this proof-of-concept study paves the way for novel sTTA-UC photosensitizers based on earth-abundant metal ions using long-lived spin-flip excited states instead of the traditionally employed precious metal sensitizers relying on charge-transfer excited states. To further lower the excitation power density threshold of sTTA-UC, on-going studies aim for increasing the absorptivity of the Cr^{III} sensitizers in the visible region.

Acknowledgements

This work was supported by the Deutsche Forschungsgemeinschaft (RE 1203/23-2, HE 2778/10-2, KE 2313/3-1). Parts of this research were conducted using the supercomputer Elwetritsch and advisory services offered by the TU Kaiserslautern (https://elwe.rhrk.uni-kl.de) which is a member of the Allianz für Hochleistungsrechnen Rheinland-Pfalz (AHRP). We thank Dr. Dipl.-Ing. Yi You from Division Instrumental Analytics of BAM (Berlin, Germany) for taking the photographs of the UC samples with 532 nm

laser and Dipl.-Ing. (FH) Arne Güttler for technical support for the UCL measurements. C.K. is grateful to the Chemical Industry Funds for a Liebig Fellowship. W.R.K. is grateful to the Chemical Industry Funds for a Kekulé Fellowship. Open Access funding enabled and organized by Projekt DEAL.

Conflict of Interest

The authors declare no conflict of interest.

Data Availability Statement

All experimental data, procedures for data analysis and pertinent data sets are provided in the Sup. Inform. document. Further raw data sets are available from the authors upon reasonable request.

Keywords: Chromium · Dexter Energy Transfer · Doublet-Triplet Energy Transfer · Triplet-Triplet Annihilation · Upconversion

[1] a) C. A. Parker, C. G. Hatchard, *Proc. R. Soc. London Ser. A* **1962**, *269*, 574–584; b) C. A. Parker, C. G. Hatchard, *Proc. Chem. Soc. London* **1962**, 386–387; c) C. A. Parker, C. G. Hatchard, T. A. Joyce, *Nature* **1965**, *205*, 1282–1284; d) P. Bharmoria, H. Bildirir, K. Moth-Poulsen, *Chem. Soc. Rev.* **2020**, *49*, 6529–6554; e) V. Gray, D. Dzebo, M. Abrahamsson, B. Albinsson, K. Moth-Poulsen, *Phys. Chem. Chem. Phys.* **2014**, *16*, 10345–10352; f) B. S. Richards, D. Hudry, D. Busko, A. Turshatov, I. A. Howard, *Chem. Rev.* **2021**, *121*, 9165–9195; g) V. Gray, K. Moth-Poulsen, B. Albinsson, M. Abrahamsson, *Coord. Chem. Rev.* **2018**, *362*, 54–71; h) T. N. Singh-Rachford, F. N. Castellano, *Coord. Chem. Rev.* **2010**, *254*, 2560–2573; i) R. R. Islangulov, F. N. Castellano, *Angew. Chem. Int. Ed.* **2006**, *45*, 5957–5959; *Angew. Chem.* **2006**, *118*, 6103–6105; j) C. Kerzig, O. S. Wenger, *Chem. Sci.* **2018**, *9*, 6670–6678; k) B. Pfund, D. M. Steffen, M. R. Schreier, M. S. Bertrams, C. Ye, K. Borjesson, O. S. Wenger, C. Kerzig, *J. Am. Chem. Soc.* **2020**, *142*, 10468–10476; l) J. B. Bilger, C. Kerzig, C. B. Larsen, O. S. Wenger, *J. Am. Chem. Soc.* **2021**, *143*, 1651–1663; m) J. Castellanos-Soriano, J. C. Herrera-Luna, D. Díaz Díaz, M. C. Jiménez, R. Pérez-Ruiz, *Org. Chem. Front.* **2020**, *7*, 1709–1716; n) M. Majek, U. Faltermeier, B. Dick, R. Perez-Ruiz, A. Jacobi von Wangelin, *Chem. Eur. J.* **2015**, *21*, 15496–15501; o) B. D. Ravetz, A. B. Pun, E. M. Churchill, D. N. Congreve, T. Rovis, L. M. Campos, *Nature* **2019**, *565*, 343–346.

[2] a) D. G. Bossanyi, Y. Sasaki, S. Wang, D. Chekulaev, N. Kimizuka, N. Yanai, J. Clark, *JACS Au* **2021**, *1*, 2188–2201; b) Y. Zhou, F. N. Castellano, T. W. Schmidt, K. Hanson, *ACS Energy Lett.* **2020**, *5*, 2322–2326.

[3] a) V. Gray, A. Dreos, P. Erhart, B. Albinsson, K. Moth-Poulsen, M. Abrahamsson, *Phys. Chem. Chem. Phys.* **2017**, *19*, 10931–10939; b) X. Wang, R. Tom, X. Liu, D. N. Congreve, N. Marom, *J. Mater. Chem. C* **2020**, *8*, 10816–10824; c) T. W. Schmidt, F. N. Castellano, *J. Phys. Chem. Lett.* **2014**, *5*, 4062–4072.

[4] a) Y. Y. Cheng, B. Fückel, T. Khoury, R. G. C. R. Clady, M. J. Y. Tayebjee, N. J. Ekins-Daukes, M. J. Crossley, T. W. Schmidt, *J. Phys. Chem. Lett.* **2010**, *1*, 1795–1799; b) J. Saltiel, G. R. March, W. K. Smothers, S. A. Stout, J. L. Charlton, *J. Am. Chem. Soc.* **1981**, *103*, 7159–7164.

[5] A. Monguzzi, R. Tubino, S. Hoseinkhani, M. Campione, F. Meinardi, *Phys. Chem. Chem. Phys.* **2012**, *14*, 4322–4332.

[6] a) C. Fan, L. Wei, T. Niu, M. Rao, G. Cheng, J. J. Chruma, W. Wu, C. Yang, *J. Am. Chem. Soc.* **2019**, *141*, 15070–15077; b) T. Ogawa, N. Yanai, A. Monguzzi, N. Kimizuka, *Sci. Rep.* **2015**, *5*, 10882; c) D. Dzebo, K. Moth-Poulsen, B. Albinsson, *Photochem. Photobiol. Sci.* **2017**, *16*, 1327–1334; d) M. Yang, S. Sheykhi, Y. Zhang, C. Milsmann, F. N. Castellano, *Chem. Sci.* **2021**, *12*, 9069–9077.

[7] K. Yokoyama, Y. Wakikawa, T. Miura, J. Fujimori, F. Ito, T. Ikoma, *J. Phys. Chem. B* **2015**, *119*, 15901–15908.

[8] a) S. S. Skourtis, C. Liu, P. Antoniou, A. M. Virshup, D. N. Beratan, *Proc. Natl. Acad. Sci. USA* **2016**, *113*, 8115–8120; b) F. Scandola, M. T. Indelli, C. Chiorboli, C. A. Bignozzi in *Photoinduced Electron and Energy Transfer in Polynuclear Complexes, Vol. 158* (Ed. J. Mattay), Springer, Berlin, **1990**; c) V. Balzani, G. Bergamini, S. Campagna, F. Puntoriero in *Photochemistry and Photophysics of Coordination Compounds: Overview and General Concepts., Vol. 280* (Eds.: V. Balzani, S. Campagna), Springer, Berlin, **2007**, pp. 1–36.

[9] a) R. R. Islangulov, D. V. Kozlov, F. N. Castellano, *Chem. Commun.* **2005**, 3776–3778; b) S. Gharaati, C. Wang, C. Förster, F. Weigert, U. Resch-Genger, K. Heinze, *Chem. Eur. J.* **2020**, *26*, 1003–1007; c) W. Zhao, F. N. Castellano, *J. Phys. Chem. A* **2006**, *110*, 11440–11445; d) Y. Wei, M. Zheng, L. Chen, X. Zhou, S. Liu, *Dalton Trans.* **2019**, *48*, 11763–11771; e) C. E. Elgar, H. Y. Otaif, X. Zhang, J. Zhao, P. N. Horton, S. J. Coles, J. M. Beames, S. J. A. Pope, *Chem. Eur. J.* **2021**, *27*, 3427–3439; f) W. Wu, S. Ji, W. Wu, J. Shao, H. Guo, T. D. James, J. Zhao, *Chem. Eur. J.* **2012**, *18*, 4953–4964; g) X. Yi, J. Zhao, J. Sun, S. Guo, H. Zhang, *Dalton Trans.* **2013**, *42*, 2062–2074; h) T. N. Singh-Rachford, F. N. Castellano, *J. Phys. Chem. Lett.* **2010**, *1*, 195–200; i) V. Yakutkin, S. Aleshchenkov, S. Chernov, T. Miteva, G. Nelles, A. Cheprakov, S. Baluschev, *Chem. Eur. J.* **2008**, *14*, 9846–9850; j) T. N. Singh-Rachford, F. N. Castellano, *Inorg. Chem.* **2009**, *48*, 2541–2548; k) S. Amemori, Y. Sasaki, N. Yanai, N. Kimizuka, *J. Am. Chem. Soc.* **2016**, *138*, 8702–8705; l) Y. Sasaki, S. Amemori, H. Kouno, N. Yanai, N. Kimizuka, *J. Mater. Chem. C* **2017**, *5*, 5063–5067.

[10] a) C. Förster, K. Heinze, *Chem. Soc. Rev.* **2020**, *49*, 1057–1070; b) J. K. McCusker, *Science* **2019**, *363*, 484–488.

[11] a) S. Garakyaraghi, P. D. Crapps, C. E. McCusker, F. N. Castellano, *Inorg. Chem.* **2016**, *55*, 10628–10636; b) S. Garakyaraghi, E. O. Danilov, C. E. McCusker, F. N. Castellano, *J. Phys. Chem. A* **2015**, *119*, 3181–3193; c) C. E. McCusker, F. N. Castellano, *Inorg. Chem.* **2015**, *54*, 6035–6042; d) Y. Zhang, J. L. Petersen, C. Milsmann, *J. Am. Chem. Soc.* **2016**, *138*, 13115–13118; e) Y. Zhang, T. S. Lee, J. L. Petersen, C. Milsmann, *J. Am. Chem. Soc.* **2018**, *140*, 5934–5947; f) Y. Zhang, T. S. Lee, J. M. Favale, D. C. Leary, J. L. Petersen, G. D. Scholes, F. N. Castellano, C. Milsmann, *Nat. Chem.* **2020**, *12*, 345–352.

[12] a) L. A. Büldt, O. S. Wenger, *Angew. Chem. Int. Ed.* **2017**, *56*, 5676–5682; *Angew. Chem.* **2017**, *129*, 5770–5776; b) L. A. Büldt, X. Guo, R. Vogel, A. Prescimone, O. S. Wenger, *J. Am. Chem. Soc.* **2017**, *139*, 985–992; c) P. Herr, C. Kerzig, C. B. Larsen, D. Häussinger, O. S. Wenger, *Nat. Chem.* **2021**, *13*, 956–962; d) K. Heinze, *Nat. Chem.* **2021**, *13*, 926–928; e) L. A. Büldt, X. Guo, A. Prescimone, O. S. Wenger, *Angew. Chem. Int. Ed.* **2016**, *55*, 11247–11250; *Angew. Chem.* **2016**, *128*, 11413–11417; f) P. Herr, F. Glaser, L. A. Büldt, C. B. Larsen, O. S. Wenger, *J. Am. Chem. Soc.* **2019**, *141*, 14394–14402.

[13] a) W. R. Kitzmann, J. Moll, K. Heinze, *Photochem. Photobiol. Sci.* **2022**, https://doi.org/10.1007/s43630-022-00186-3; b) S. Otto, M. Dorn, C. Förster, M. Bauer, M. Seitz, K. Heinze,

Coord. Chem. Rev. **2018**, *359*, 102–111; c) P. A. Scattergood in *Recent advances in chromium coordination chemistry: luminescent materials and photocatalysis, Vol. 43* Royal Society of Chemistry, Cambridge, **2020**, pp. 1–34.

[14] a) S. Otto, M. Grabolle, C. Förster, C. Kreitner, U. Resch-Genger, K. Heinze, *Angew. Chem. Int. Ed.* **2015**, *54*, 11572–11576; *Angew. Chem.* **2015**, *127*, 11735–11739; b) C. Wang, S. Otto, M. Dorn, E. Kreidt, J. Lebon, L. Srsan, P. Di Martino-Fumo, M. Gerhards, U. Resch-Genger, M. Seitz, K. Heinze, *Angew. Chem. Int. Ed.* **2018**, *57*, 1112–1116; *Angew. Chem.* **2018**, *130*, 1125–1130; c) S. Treiling, C. Wang, C. Förster, F. Reichenauer, J. Kalmbach, P. Boden, J. P. Harris, L. M. Carrella, E. Rentschler, U. Resch-Genger, C. Reber, M. Seitz, M. Gerhards, K. Heinze, *Angew. Chem. Int. Ed.* **2019**, *58*, 18075–18085; *Angew. Chem.* **2019**, *131*, 18243–18253; d) J.-R. Jiménez, B. Doistau, C. M. Cruz, C. Besnard, J. M. Cuerva, A. G. Campaña, C. Piguet, *J. Am. Chem. Soc.* **2019**, *141*, 13244–13252; e) F. Reichenauer, C. Wang, C. Förster, P. Boden, N. Ugur, R. Báez-Cruz, J. Kalmbach, L. M. Carrella, E. Rentschler, C. Ramanan, G. Niedner-Schatteburg, M. Gerhards, M. Seitz, U. Resch-Genger, K. Heinze, *J. Am. Chem. Soc.* **2021**, *143*, 11843–11855; f) C. Wang, W. R. Kitzmann, F. Weigert, C. Förster, X. Wang, K. Heinze, U. Resch-Genger, *ChemPhotoChem* **2022**, https://doi.org/10.1002/cptc.202100296.

[15] N. Sinha, J. R. Jimenez, B. Pfund, A. Prescimone, C. Piguet, O. S. Wenger, *Angew. Chem. Int. Ed.* **2021**, *60*, 23722–23728; *Angew. Chem.* **2021**, *133*, 23915–23921.

[16] a) S. Otto, A. M. Nauth, E. Ermilov, N. Scholz, A. Friedrich, U. Resch-Genger, S. Lochbrunner, T. Opatz, K. Heinze, *ChemPhotoChem* **2017**, *1*, 344–349; b) C. Wang, S. Otto, M. Dorn, K. Heinze, U. Resch-Genger, *Anal. Chem.* **2019**, *91*, 2337–2344.

[17] a) T. Lazarides, G. M. Davies, H. Adams, C. Sabatini, F. Barigelletti, A. Barbieri, S. J. Pope, S. Faulkner, M. D. Ward, *Photochem. Photobiol. Sci.* **2007**, *6*, 1152–1157; b) M. D. Ward, *Coord. Chem. Rev.* **2010**, *254*, 2634–2642; c) L. Aboshyan-Sorgho, M. Cantuel, S. Petoud, A. Hauser, C. Piguet, *Coord. Chem. Rev.* **2012**, *256*, 1644–1663; d) L. Aboshyan-Sorgho, H. Nozary, A. Aebischer, J. C. Bünzli, P. Y. Morgantini, K. R. Kittilstved, A. Hauser, S. V. Eliseeva, S. Petoud, C. Piguet, *J. Am. Chem. Soc.* **2012**, *134*, 12675–12684; e) L. Aboshyan-Sorgho, C. Besnard, P. Pattison, K. R. Kittilstved, A. Aebischer, J. C. Bünzli, A. Hauser, C. Piguet, *Angew. Chem. Int. Ed.* **2011**, *50*, 4108–4112; *Angew. Chem.* **2011**, *123*, 4194–4198; f) Y. Suffren, D. Zare, S. V. Eliseeva, L. Guénée, H. Nozary, T. Lathion, L. Aboshyan-Sorgho, S. Petoud, A. Hauser, C. Piguet, *J. Phys. Chem. C* **2013**, *117*, 26957–26963.

[18] J. Kalmbach, C. Wang, Y. You, C. Förster, H. Schubert, K. Heinze, U. Resch-Genger, M. Seitz, *Angew. Chem. Int. Ed.* **2020**, *59*, 18804–18808; *Angew. Chem.* **2020**, *132*, 18966–18970.

[19] F. DeRosa, X. Bu, K. Pohaku, P. C. Ford, *Inorg. Chem.* **2005**, *44*, 4166–4174.

[20] a) L. R. Faulkner, A. J. Bard, *J. Am. Chem. Soc.* **1969**, *91*, 209–210; b) T. Serevičius, R. Komskis, P. Adomėnas, O. Adomėnienė, G. Kreiza, V. Jankauskas, K. Kazlauskas, A. Miasojedovas, V. Jankus, A. Monkman, S. Juršėnas, *J. Phys. Chem. C* **2017**, *121*, 8515–8524; c) V. Gray, D. Dzebo, A. Lundin, J. Alborzpour, M. Abrahamsson, B. Albinsson, K. Moth-Poulsen, *J. Mater. Chem. C* **2015**, *3*, 11111–11121.

[21] D. M. Arias-Rotondo, J. K. McCusker, *Chem. Soc. Rev.* **2016**, *45*, 5803–5820.

[22] M. Montalti, A. Credi, L. Prodi, M. T. Gandolfi, *Handbook of Photochemistry*, CRC Taylor & Francis, Boca Raton, **2006**,.

[23] a) M. T. Vagnini, W. C. Rutledge, P. S. Wagenknecht, *Inorg. Chem.* **2010**, *49*, 833–838; b) P. S. Wagenknecht, N. A. P. Kane-Maguire, D. G. Speece, N. Helwic, *Inorg. Chem.* **2002**, *41*, 1229–1235.

[24] M. C. Rosko, K. A. Wells, C. E. Hauke, F. N. Castellano, *Inorg. Chem.* **2021**, *60*, 8394–8403.

[25] J. Han, Y. Jiang, A. Obolda, P. Duan, F. Li, M. Liu, *J. Phys. Chem. Lett.* **2017**, *8*, 5865–5870.

[26] S. K. Chattopadhyay, C. V. Kumar, P. K. Das, *Chem. Phys. Lett.* **1983**, *98*, 250–254.

[27] a) P. Müller, K. Brettel, *Photochem. Photobiol. Sci.* **2012**, *11*, 632–636; b) M. S. Bertrams, C. Kerzig, *Chem. Commun.* **2021**, *57*, 6752–6755.

[28] a) K. A. El Roz, F. N. Castellano, *Chem. Commun.* **2017**, *53*, 11705–11708; b) A. Yoshimura, M. Z. Hoffman, H. Sun, *J. Photochem. Photobiol. A* **1993**, *70*, 29–33.

[29] J. Isokuortti, S. R. Allu, A. Efimov, E. Vuorimaa-Laukkanen, N. V. Tkachenko, S. A. Vinogradov, T. Laaksonen, N. A. Durandin, *J. Phys. Chem. Lett.* **2020**, *11*, 318–324.

[30] D. Guo, T. E. Knight, J. K. McCusker, *Science* **2011**, *334*, 1684–1687.

[31] F. Strieth-Kalthoff, C. Henkel, M. Teders, A. Kahnt, W. Knolle, A. Gómez-Suárez, K. Dirian, W. Alex, K. Bergander, C. G. Daniliuc, B. Abel, D. M. Guldi, F. Glorius, *Chem* **2019**, *5*, 2183–2194.

[32] A. Olesund, V. Gray, J. Martensson, B. Albinsson, *J. Am. Chem. Soc.* **2021**, *143*, 5745–5754.

[33] a) D. Meroni, A. Monguzzi, F. Meinardi, *J. Chem. Phys.* **2020**, *153*, 114302; b) J. Perego, J. Pedrini, C. X. Bezuidenhout, P. E. Sozzani, F. Meinardi, S. Bracco, A. Comotti, A. Monguzzi, *Adv. Mater.* **2019**, *31*, 1903309; c) T. J. B. Zähringer, M.-S. Bertrams, C. Kerzig, *J. Mater. Chem. C* **2022**, *10*, 4568–4573.

[34] a) T. J. Penfold, E. Gindensperger, C. Daniel, C. M. Marian, *Chem. Rev.* **2018**, *118*, 6975–7025; b) C. M. Marian, *WIREs Comput. Mol. Sci.* **2012**, *2*, 187–203; c) T. M. Dunn, *Trans. Faraday Soc.* **1961**, *57*, 1441–1444.

[35] a) N. A. Durandin, J. Isokuortti, A. Efimov, E. Vuorimaa-Laukkanen, N. V. Tkachenko, T. Laaksonen, *Chem. Commun.* **2018**, *54*, 14029–14032; b) N. A. Durandin, J. Isokuortti, A. Efimov, E. Vuorimaa-Laukkanen, N. V. Tkachenko, T. Laaksonen, *J. Phys. Chem. C* **2019**, *123*, 22865–22872.

[36] P. Klán, J. Wirz, *Photochemistry of Organic Compounds: From Concepts to Practice*, Wiley, Hoboken, **2009**, pp. 46–60.

Manuscript received: February 10, 2022
Accepted manuscript online: March 28, 2022
Version of record online: May 9, 2022

3.4 Decoupled Enhancement of Electrochemical Properties in Molecular Rubies

Due to their long excited-state lifetimes, reaching up to the millisecond range, spin-flip (SF) chromium(III) complexes serve as efficient alternatives to ruthenium- and iridium-based systems as photooxidants.[50,56,59,60,79] Notable examples include complexes with bpy-type ligands, such as $[Cr(dmcbpy)_3]^{3+}$ or $[Cr(Ph_2phen)_3]^{3+}$, and molecular rubies with emission energies between 720 and 780 nm (Scheme 3.1).[183,191,199,200,205–208] Since the SF energies across these systems are rather similar, their ground-state potential becomes the key factor for applications in photoredox catalysis.[83,87,178,209] While the corresponding excited state potential in charge-transfer (CT) systems can be estimated using an electron/hole formalism, determining this parameter in SF systems is more challenging, as it primarily depends on variations in exchange interactions among the involved states.[191]

The electronic situation of the reduced chromium complex plays a crucial role in the thermodynamics and kinetics of the electron transfer process.[56] Among the relevant systems, the localization of spin density in the dicationic species varies significantly. Complexes with electron-rich ligands, such as $[Cr(ddpd)_2]^{3+}$, undergo metal-centered (MC) reduction, forming a labile high-spin chromium(II) species at room temperature.[87,210] In contrast, one-electron reductions of more electron-poor systems, like $[Cr(tpe)_2]^{3+}$ (Scheme 3.1), are ligand-centered (LC), resulting in an antiferromagnetically coupled chromium(III) and a ligand radical anion.[211–213] This extension of the excited-state wave function onto the ligand leads to strong electronic coupling between donor and acceptor, kinetically facilitating bimolecular reactions with substrates in solution.[214–217]

Unlike emission energy tuning, the ground-state potential in SF systems follows more predictable trends, allowing for systematic redox potential modification.[88,94] Substitution effects, as the introduction of electron-withdrawing groups can raise reduction potentials.[60] However, the ligand must not become excessively electron-poor, as this can hinder the formation of stable coordination bonds. Additionally, in a photoredox catalytic cycle, the sensitizer should be reoxidizable, a process that becomes increasingly challenging as the ground state potential rises.[56]

In CT systems, ligand substitutions inherently affect both electrochemical and optical properties due to the charge-separated excited state nature.[30,218] In contrast, in SF systems, featuring localized, MC excited states, the optical properties are less sensitive to structural modifications within the ligand peripherie.[94] This makes SF systems particularly suited for selectively enhancing electrochemical properties for photoredox catalysis, while leaving the optical characteristics, relevant for sensor applications,

largely unaffected. However, specifically for molecular rubies, the potential for independently enhancing the redox behavior remains largely untapped.

This study closes that gap by investigating how strongly ground-state redox properties in molecular rubies can be modified independently of their optical properties through peripheral ligand modification. Substituted complexes $[Cr(ddpd^{X})_2]^{3+}$ (X = CF_3, OMe, NMe_2, Scheme 3.1), structurally derived from the parent complex $[Cr(ddpd)_2]^{3+}$ (X = H), were synthesized and analyzed using UV/Vis/NIR absorption and emission spectroscopy, cyclic voltammetry and quantum chemical multireference calculations. The results provide quantitative insights into the systematic optimization of molecular rubies for both photoredox catalysis and optical applications.

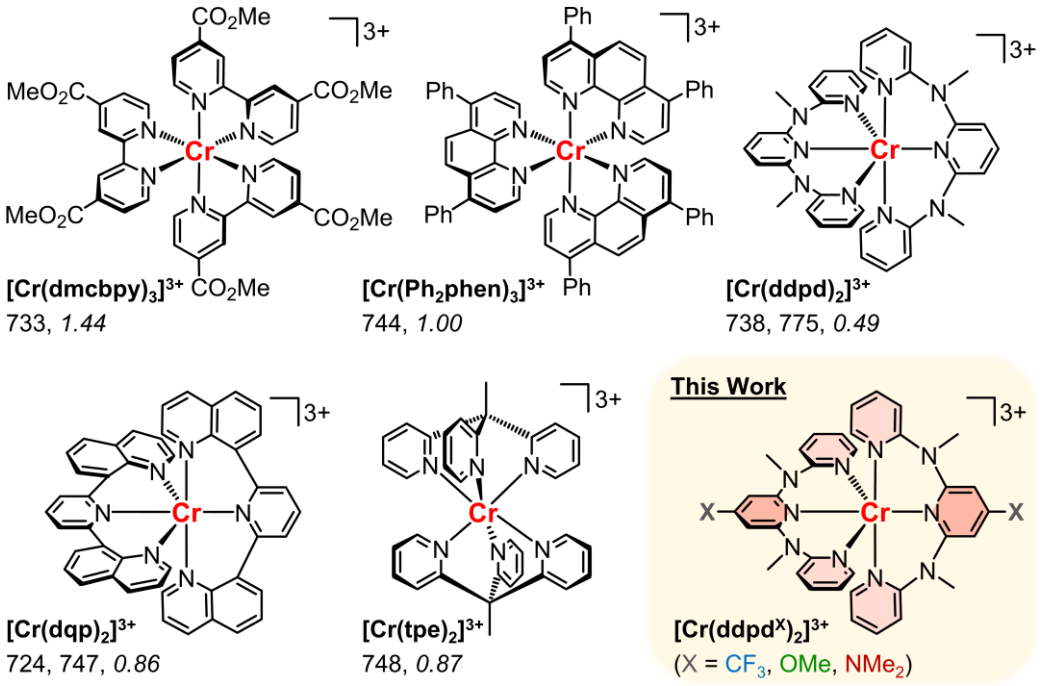

Scheme 3.1 Molecular structures of chromium(III) photo catalysts with emission wavelengths (nm) and excited state $[Cr]^{3+/2+}$ redox potentials (italic, V vs. FcH/FcH^+).[83,87,178,209]

This project incorporates parts of the bachelor thesis cited in ref. [219].
Supporting Information for this project can be found on pp. 229.

3.4.1 Synthesis and Characterization

The ligands $ddpd^{X}$ ($\mathbf{L}^{X}$, X = CF_3, OMe, NMe_2) substituted at the central pyridine were synthesized by reacting 2,6-dihalogenated-4-X-pyridines with 2-methylaminopyridine (Scheme 3.2). As expected, the efficiency of this reaction decreased with the declining electrophilicity of the 4-substituted pyridine (92%, 38%, <10%). To counteract the unfavorable electronic effects, $\mathbf{L}^{NMe2}$ was synthesized at elevated temperatures using

an excess of nucleophile and auxiliary base. However, due to purification issues, this ligand could not be isolated by chromatography in pure form. The three pincer ligands $\mathbf{L^X}$ were characterized by ESI$^+$ mass spectrometry (Fig. S1–3), ^{1}H/^{19}F/^{13}C NMR (Fig. S4–15), and IR spectroscopy (Fig. S16–18). The purity of the ligands $\mathbf{L^{CF3}}$ and $\mathbf{L^{OMe}}$ was additionally confirmed by elemental analysis.

The orange-colored complex salts [Cr(ddpd^X)$_2$](OTf)$_3$ ($\mathbf{[1^X](OTf)_3}$, X = CF$_3$, OMe, NMe$_2$) were synthesized by heating a solution of anhydrous chromium(III) triflate and the corresponding ligand $\mathbf{L^X}$ in 71%, 51%, and 32% yields, respectively (Scheme 3.2), thereby demonstrating the robustness of the known synthetic approach across ligands with varying electronic demands (Section 6.4). The composition and purity of the compounds were verified by ESI$^+$ mass spectrometry (Fig. S19–21), IR spectroscopy (Fig. S22–24), optical spectroscopy (Fig. S27–29) and elemental analysis (X = CF$_3$, OMe). Slow diffusion of diethyl ether into acetonitrile solutions of $\mathbf{[1^X](OTf)_3}$ (X = CF$_3$, OMe) at 5 °C produced single crystals suitable for XRD analysis. The structures confirmed the constitution and meridional configuration of the complex cations, with a highly octahedral CrN$_6$ core and N-Cr-N bond angles close to 90/180°, consistent with the unsubstituted parent compound $\mathbf{[1^H](OTf)_3}$.[84,87] Following the discussion of the syntheses, the effect of peripheral substitution on the optical and redox properties of the molecular rubies will be examined next.

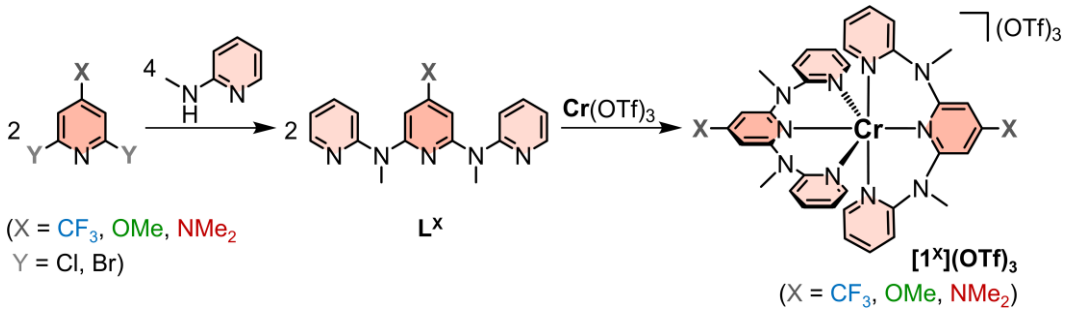

Scheme 3.2 Synthesis of the pyridine substituted ligands $\mathbf{L^X}$ and their corresponding homoleptic chromium(III) complexes $\mathbf{[1^X](OTf)_3}$.

3.4.2 Optical Properties

The absorption spectra of the complexes $\mathbf{[1^X]^{3+}}$ resemble those of $\mathbf{[1^H]^{3+}}$, characterized by intense LMCT and ILCT bands in the UV region (Fig. 3.2).[87] The lowest energy band in the visible range, corresponding to ^{4}A$_2$→^{4}LMCT and ^{4}A$_2$→^{4}T$_2$ transitions, shows a significant hypsochromic shift with increasing electron-donating properties of the substituents (450, 411, 392 nm, X = CF$_3$, OMe, NMe$_2$). Notably, in $\mathbf{[1^{CF3}]^{3+}}$, the lowest spin-allowed transitions contain large ^{4}A$_2$→^{4}ILCT (NMe→Py) contributions, confirming high electron deficiency of the substituted central pyridine.

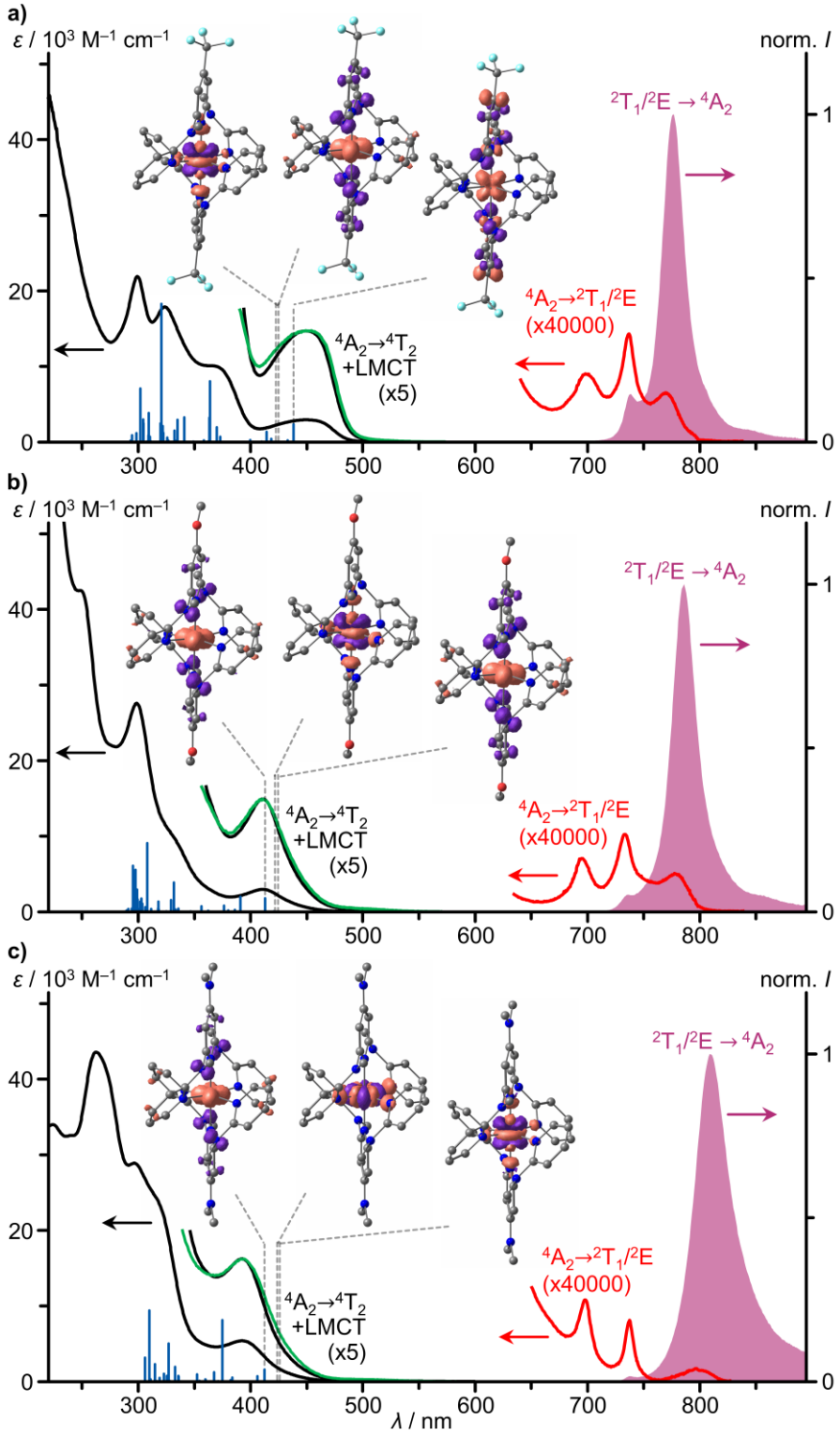

Fig. 3.2 UV/Vis/NIR absorption spectra (black, red), excitation spectra (λ_{em} = 776, 786 and 810 nm, green) and normalized emission spectra (λ_{exc} = 450, 411 and 392 nm, purple) of a) $[\mathbf{1}^{CF3}]^{3+}$, b) $[\mathbf{1}^{OMe}]^{3+}$ and c) $[\mathbf{1}^{NMe2}]^{3+}$ in deaerated CH_3CN at room temperature, TD-DFT calculated oscillator strengths (blue sticks) and difference electron densities of three low-energy transitions of ^{4}LMCT and ^{4}MC character. The regions of the spin-forbidden absorption bands, the lowest energy spin allowed/LMCT absorption band and the excitation spectrum are scaled with the indicated factors.

TD-DFT calculations further reveal that metal-ligand π-interactions in $[\mathbf{1}^{\mathbf{OMe}}]^{3+}$ and $[\mathbf{1}^{\mathbf{NMe2}}]^{3+}$ raise the LMCT states by increasing the energy of t_{2g} orbitals, compensating for the electron rich nature of the respective ligands (Fig. S27–29, Table S1–3). The weaker Laporte-forbidden MC transitions, largely obscured by LMCT/ILCT bands, exhibit less sensitivity to the substitution, with a slight bathochromic shift in $[\mathbf{1}^{\mathbf{NMe2}}]^{3+}$ attributed to π-backbonding. In the NIR region, three sharp, low-intensity bands at 770, 737, and 698 nm, 778, 734, and 695 nm, and 798, 738, and 698 nm for X = CF_3, OMe, and NMe_2, respectively, are detectable. These characteristic bands are assigned to the spin- and Laporte-forbidden $^4A_2 \rightarrow {}^2E/{}^2T_1$ transitions. The averaged energies of the SF bands indicate a more pronounced nephelauxetic effect in $[\mathbf{1}^{\mathbf{OMe}}]^{3+}$ and $[\mathbf{1}^{\mathbf{NMe2}}]^{3+}$, likely due to enhanced π-interactions between ligand and MC t_{2g} orbitals.

Excitation of acetonitrile solutions of $[\mathbf{1}^{\mathbf{X}}]^{3+}$ at room temperature results in strong dual emission peaking at 777/738, 786/736, and 809/739 nm for X = CF_3, OMe, and NMe_2, respectively (Fig. 3.2). The small Stokes shifts of the phosphorescence bands relative to the NIR absorption bands confirm minimal geometric reorganization of the respective states. The excitation spectra closely match the absorption spectra in the region of the lowest spin-allowed transitions, indicating efficient population transfer from the ^{4}LMCT/$^4T_2$ manifold to the emissive states via ISC and IC, with minimal loss channels. The variation in relative SF absorption and emission energies across the complex series suggest a symmetry-dependent influence of the peripheral substituent on doublet energies, which is also reflected in the intensity ratios of dual emission at room temperature.

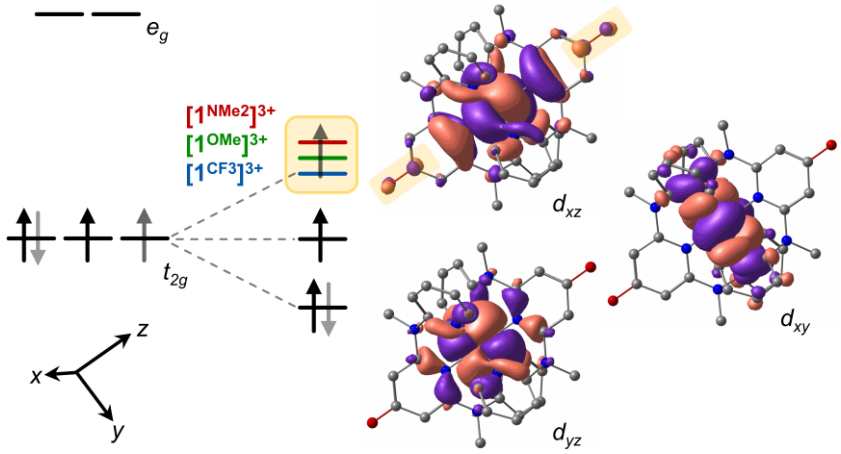

Fig. 3.3 Simplified (non-quantitative) MO diagram of the MC 3d orbitals in the complex series $[\mathbf{1}^{\mathbf{X}}]^{3+}$ (X = CF_3, OMe, NMe_2), illustrating that the spin-paired $^2T_1$ state (black and pale gray electrons) is relatively stabilized compared to the $^4A_2$ ground state (black and gray electrons) due to the energetic elevation of the d_{xz} orbital, resulting from antibonding π interactions with the central pyridines, which vary depending on the peripheral substituent.

CASSCF(7,12) calculations reproduced the doublet energy trends (Table S4), confirming lower averaged energies for $\mathbf{[1^{OMe}]^{3+}}$ and $\mathbf{[1^{NMe2}]^{3+}}$, with the largest energy separation between microstates in $\mathbf{[1^{NMe2}]^{3+}}$. According to the computation, the generally stronger influence of peripheral substituents on the energy of the spin-paired $^2T_1$ state is due to the highest t_{2g} orbital perpendicular to the central pyridines (Fig. 3.3). This orbital is energetically raised by π^* interactions with the +M substituents, which leads to a slight destabilization of the $^4A_2$ ground state relative to the $^2T_1$ state, in which this orbital is unoccupied.

The photoluminescence quantum yields and lifetimes for $\mathbf{[1^{X}]^{3+}}$ (X = CF_3, OMe) in deoxygenated acetonitrile at room temperature were determined to be 12.4% and 9.3%, and 1210 µs and 1040 µs, respectively. These high values are comparable to other molecular rubies, with $\mathbf{[1^{OMe}]^{3+}}$ showing a slightly higher non-radiative rate within the investigated complex series (Table 3.1), consistent with the energy gap law and increased multiphonon relaxation.[61,76,79] Overall, the spectroscopic data confirm that peripheral substitution exerts a smaller influence on the optical properties of these systems, with a maximum shift of 540 cm^{-1}, compared to modifications within the chelate ring (max. shift = 1200 cm^{-1}, Section 3.5).[176,178,220]

3.4.3 Electrochemical Properties

The electrochemical properties of the complexes $\mathbf{[1^{X}]^{3+}}$ (X = CF_3, OMe) were investigated using cyclic and square wave voltammetry (Fig. 3.4, Fig. S30-31). These measurements reveal reversible reduction waves at –0.99 V and –1.19 V vs. FcH/FcH^+, showing that the ground-state potential within this series can be shifted by approximately ±0.1 V relative to $\mathbf{[1^{H}]^{3+}}$ through simple ligand modification (Table 3.1). The data further confirm the expected trend based on the electron-donating and electron-withdrawing effects of the substituents. Similar to $\mathbf{[1^{H}]^{2+}}$, the calculated spin density of the reduced low-spin species $^3[1^{OMe}]^{2+}$ indicates a MC reduction of the corresponding tricationic complex.[210] In contrast, the spin density in $^3[1^{CF3}]^{2+}$ differs significantly (Fig. 3.4), suggesting an antiferromagnetically coupled chromium(III) center and a central pyridine delocalized radical anion. The reduction of the electron-deficient complex $\mathbf{[1^{CF3}]^{3+}}$ thus exhibits significant ligand character, similar to bpy-type chromium(III) systems.[211–213] This desirable electron density shift, along with the higher reduction potential relative to $\mathbf{[1^{H}]^{3+}}$, demonstrates that the electrochemical properties of molecular rubies can be systematically improved upon introducing peripheral substituents at the ligand.

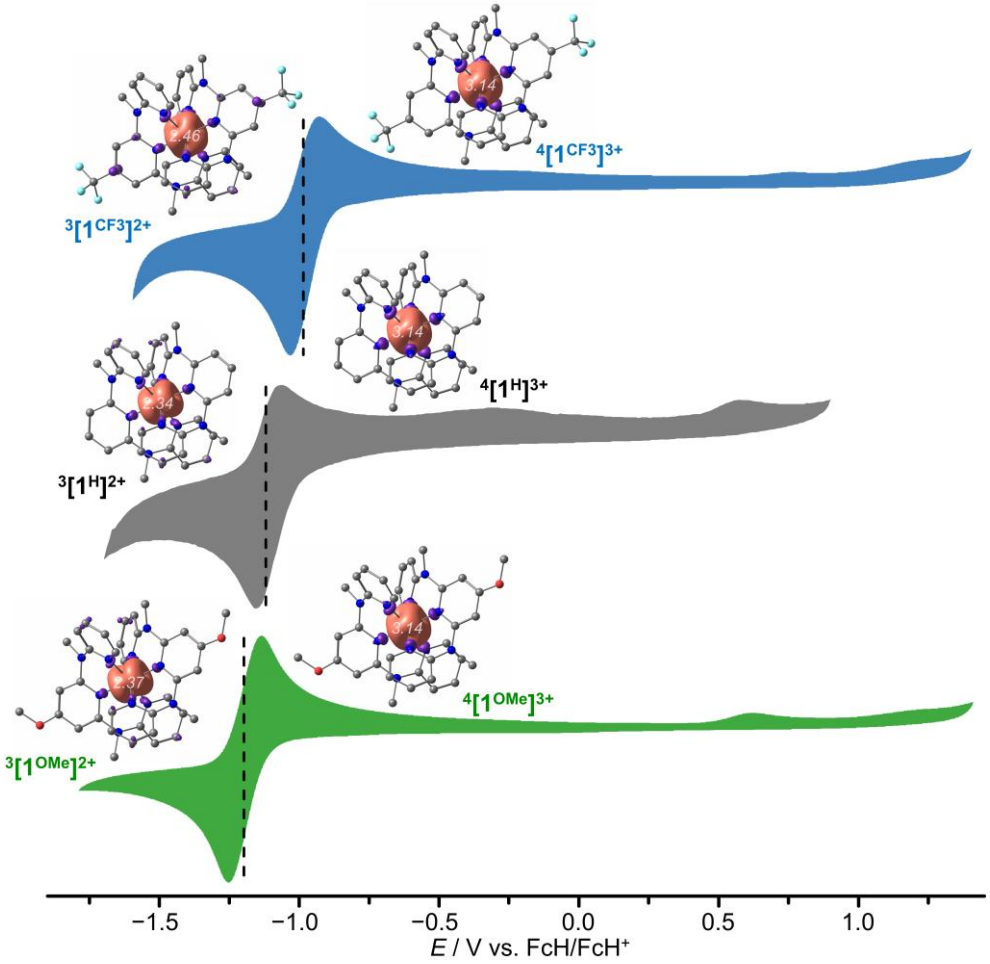

Fig. 3.4 Cyclic voltammograms of $[\mathbf{1}^{\mathbf{H}}]^{3+}$ (black)[87], $[\mathbf{1}^{\mathbf{CF3}}]^{3+}$ (blue) and $[\mathbf{1}^{\mathbf{OMe}}]^{3+}$ (green) in CH_3CN (peak potentials referenced against FcH/FcH^+) with calculated spin density plots (contour value: 0.005 a.u.) of the thermodynamically most stable dicationic and tricationic species and Mullikin spin populations at the metal center (italic).

3.4.4 Excited State Reactivity

The spectroscopic and voltammetric measurements clarify that the ground-state potentials (~0.20 V) within this complex series are more strongly influenced by ligand modification than the doublet energies (~0.02 eV). Based on these parameters, the excited-state potentials of $[\mathbf{1}^{\mathbf{CF3}}]^{3+}$ and $[\mathbf{1}^{\mathbf{OMe}}]^{3+}$ were estimated at 0.69 and 0.49 V vs. FcH/FcH^+, considering the maxima of the higher energy emission bands.[190] The bimolecular reactivities of the complexes $[\mathbf{1}^{\mathbf{X}}]^{3+}$ (X = H, CF_3, OMe) were assessed through emission quenching experiments with *trans*-anethole (E_0 = 0.73 V vs. FcH/FcH^+).[206] Due to the high triplet energy of the substrate (E_T = 2.52 eV),[221] energy transfer is thermodynamically unfeasible, but electron transfer via thermal activation of higher-energy states of $^2E/^2T_1$ parentage is plausible, particularly for $[\mathbf{1}^{\mathbf{CF3}}]^{3+}$. Stern-Volmer analysis revealed a significantly higher bimolecular quenching rate and Stern-

Volmer constant for $[\mathbf{1}^{CF3}]^{3+}$ compared to $[\mathbf{1}^{H}]^{3+}$ and $[\mathbf{1}^{OMe}]^{3+}$ (Table 3.1, Fig. S32), attributable to the increased thermodynamic driving force for electron transfer. However, the quenching efficiency is considerably lower than in $[Cr(tpe)_2]^{3+}$ and $[Cr(ddad)_2]^{3+}$ (Section 3.7 and 6.6), both of which exhibit increased excited-state potentials (E^* = 0.87 and 0.80 V vs. FcH/FcH^+).[83,183] Evidently, the potentially reactive higher-energy doublet states in the studied systems are insufficiently populated at room temperature to effectively contribute to the quenching process.

Table 3.1 Photo and redox properties of $[\mathbf{1}^{X}]^{3+}$ (X = H, CF_3, OMe) with wavelengths λ_{abs} for the lowest-energy spin-allowed and spin-forbidden absorption bands, emission wavelengths λ_{em}, photoluminescence lifetime τ and quantum yield Φ in CH_3CN under dearated conditions. Also listed are radiative and non-radiative rate constants k_r and k_{nr}, ground state and excited state reduction potentials E_0 and E^* and Stern-Volmer and bimolecular rate constants K_{SV} and k_q for quenching with *trans*-anethole.[79]

$[\mathbf{1}^{X}]^{3+}$	λ_{abs} / nm	λ_{em} / nm	τ / µs	Φ / %	k_r / s^{-1}	k_{nr} / s^{-1}	E_0 $[Cr]^{3+/2+}$ / V	E^* $[Cr]^{3+/2+}$ / V	K_{SV} / M^{-1}	k_q / 10^3 M^{-1} s^{-1}
$[\mathbf{1}^{H}]^{3+}$[87,183]	436, 697, 736, 771	738, 775	1140	13.7	120	760	–1.11	0.57	0.23	0.20
$[\mathbf{1}^{CF3}]^{3+}$	450, 770, 737, 698	738, 777	1210	12.4	100	730	–0.99	0.69	4.7	3.9
$[\mathbf{1}^{OMe}]^{3+}$	411, 695, 734, 778	736, 786	1040	9.3	90	870	–1.19	0.49	0.074	0.071

3.4.5 Conclusion and Outlook

To modulate the electrochemical properties of molecular rubies, the complex series $\mathbf{[1^X]^{3+}}$ (X = CF_3, OMe, NMe_2), incorporating electron-donating and electron-withdrawing groups, was investigated. The substituted ligands $\mathbf{L^X}$ and complex salts $\mathbf{[1^X](OTf)_3}$ were synthesized in an analogous manner, facilitating an efficient screening process. Spectroscopic measurements of the chromium(III) compounds showed that the doublet energies and luminescence efficiency were not significantly affected by the ligand modifications (Fig. 3.5a,b), with only minor deviations in emission energy (~0.02 eV) and comparable luminescence lifetimes and quantum yields for $\mathbf{[1^X]^{3+}}$ (X = CF_3, OMe) relative to the parent compound (X = H).[87] Notably, in $\mathbf{[1^{NMe2}]^{3+}}$, the low-energy spin-flip absorption and emission bands exhibit a stronger bathochromic shift (~0.07 eV) due to a pronounced nephelauxetic effect. High-level quantum chemical calculations clarified that the higher sensitivity of the $^2T_1$ energy, compared to the ^2E energy, to peripheral substitution can be attributed to the asymmetric orbital occupation, which leads to a slight stabilization of the $^2T_1$ state relative to both the ground and spin-unpaired ^2E states.

The redox properties of $\mathbf{[1^X]^{3+}}$ (X = H, CF_3, OMe) show a more substantial response to the peripheral substitution (Fig. 3.5c), with ground-state potentials shifting by approximately 0.20 V. Additionally, the reduction in the more electron-deficient system $\mathbf{[1^{CF3}]^{3+}}$ was found to be largely LC. Emission quenching experiments with *trans*-anethole demonstrated the varying oxidation power within the $\mathbf{[1^X]^{3+}}$ complex series (X = H, CF_3, OMe). While quenching efficiencies are relatively low, the study highlights the potential of peripheral substitution in molecular rubies as design strategy for photoredox catalysis. In this context, the effects of single and double substitution at the terminal pyridines could be considered and potentially exploited in future. However, the ability to enhance electrochemical properties largely independent of optical characteristics presents a promising pathway for optimizing these highly luminescent compounds for photocatalytic applications while preserving their optical functionality.

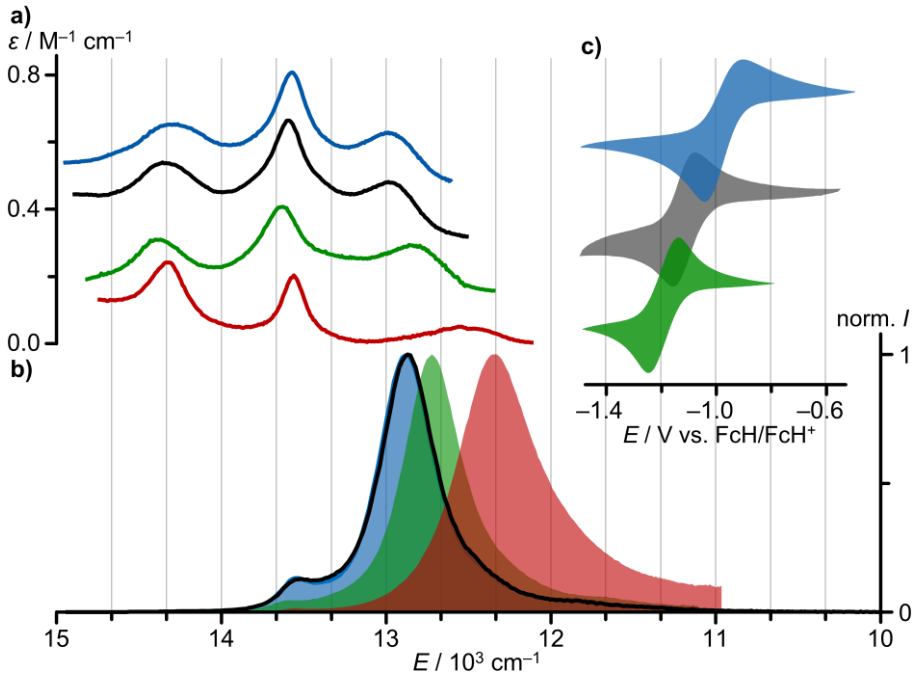

Fig. 3.5 Summarizing data showing a) NIR absorption spectra, b) normalized emission spectra (λ_{exc} = 450, 411 and 392 nm) and c) reduction waves of $[\mathbf{1^{H}}]^{3+}$ (black),[87] $[\mathbf{1^{CF3}}]^{3+}$ (blue), $[\mathbf{1^{OMe}}]^{3+}$ (green) and $[\mathbf{1^{NMe2}}]^{3+}$ (red) in deaerated CH_3CN at room temperature. For clarity, the absorption spectra of $[\mathbf{1^{X}}]^{3+}$ (X = OMe, H, CF_3) were shifted vertically by +0.15, +0.30 and +0.45 M^{-1} cm^{-1}, respectively.

3.5 Bridge Editing of Spin-Flip Emitters gives Insight into Excited State Energies and Dynamics

Authors: Florian Reichenauer, Robert Naumann, Christoph Förster, Winald R. Kitzmann, Antti-Pekka M. Reponen, Sascha Feldmann, Katja Heinze*.
* = Corresponding author.

Chem. Sci. **2024**, *143*, accepted. DOI: 10.1039/D4SC05860G.

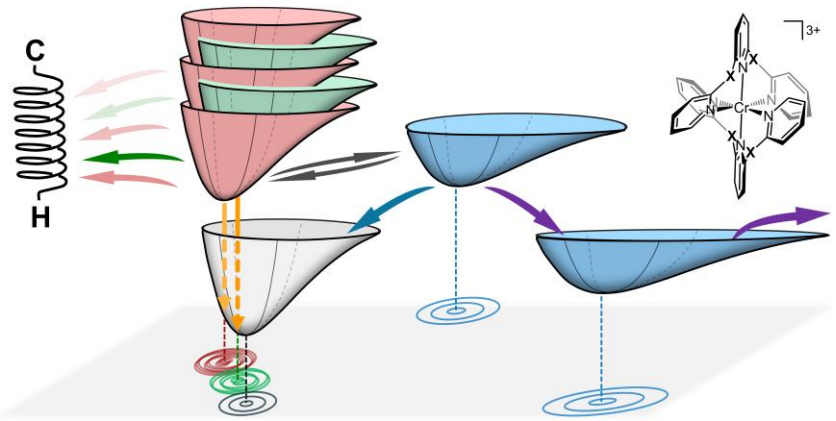

Although photoactive chromium(III) complexes now hold significant potential in optical sensing and photocatalysis, unlike charge-transfer complexes, they lack established design principles for tuning excited-state energies and dynamics. Investigation of a series of isostructural complexes goes beyond broad guidelines, isolating structural and electronic features that determine spin-flip energies and the nephelauxetic effect in molecular rubies. The computational supported analysis of structure-property relationships provides insights into non-radiative decay processes in these systems, influenced by spin-orbit coupling, excited-state Jahn-Teller distortions, and (thermally activated) multiphonon relaxation, thus supporting future design strategies for optimized molecular rubies.

Authors Contributions

F. Reichenauer performed the syntheses and spectroscopic characterization as well as the quantum chemical calculations. R. Naumann and F. Reichenauer measured and interpreted the emission data. C. Förster solved and refined the single crystal structures and assisted with the quantum chemical calculations. W. R. Kitzmann, A. M. Reponen and S. Feldmann conducted TA measurements. K. Heinze conceived and designed the project. F. Reichenauer and K. Heinze wrote the manuscript with

contributions of all authors. K. Heinze supervised and C. Förster co-supervised the project.

Supporting Information

for this article can be found on pp. 261.

View Article Online
DOI: 10.1039/D4SC05860G

ARTICLE

Bridge Editing of Spin-Flip Emitters gives Insight into Excited State Energies and Dynamics

Received 00th January 20xx,
Accepted 00th January 20xx

DOI: 10.1039/x0xx00000x

Florian Reichenauer,[a] Robert Naumann,[a] Christoph Förster,[a] Winald R. Kitzmann,[a] Antti-Pekka M. Reponen,[b] Sascha Feldmann[b] and Katja Heinze*[a]

Six-coordinate chromium(III) complexes with high spin-flip (SF) photoluminescence quantum yields and lifetimes (molecular rubies) have attracted huge interest in the past years due to their applicability in sensing, photocatalysis or circularly polarised emission. However, clearcut design rules for high quantum yields and lifetimes are still lacking due to the multidimensional problem of the non-radiative decay of the SF states. Based on an isostructural series of complexes differing in the ligand backbone, we disentangle decisive structural and electronic features for SF excited state energies and non-radiative decays promoted by spin-orbit coupling, Jahn-Teller distortions and (thermally activated) multiphonon relaxation. This analysis goes beyond the classical increasing of the ligand field strength or the metal-ligand covalency to reduce non-radiative decay or to tune the SF energy. The results underscore the utility of the combination of near-infrared absorption, variable temperature emission and fs-transient absorption spectroscopy as well as photolysis and high-level quantum chemical calculations to obtain a comprehensive picture of the excited dynamics on ultrafast and long timescales.

Introduction

Understanding and ultimately rationally modulating energies of metal-centered (MC) and charge-transfer (CT) excited states as well as their dynamics after light absorption are at the heart of contemporary design of transition metal complex photosensitisers and photocatalysts based on abundant elements.[1-14] Yet, design rules for MC states typically rely on qualitative arguments based on the ligand field splitting Δ_o, i.e. the energy gap between t_{2g} and e_g orbitals at the ground state geometry. This splitting is defined by the metal ion, the ligands and the coordination geometry according to well-known rules.[15-17] For CT excited states, ligand modification can shift the CT states to higher or lower energies based on clear-cut substituent effects, although this chemical modification might also indirectly affect the d orbital energies.[2-4] The dynamics of excited states[18-19] are in general governed by their relative energies, their different geometries and electronic couplings, yet in most cases a comprehensive picture for transition metal complexes is unavailable or still subject of debate.[20-23]

Tuning of excited state energies and dynamics of metal complexes with nested spin-flip (SF)[1,4,8,9] states as lowest energy excited states is even less understood. Yet, several high-performing $3d^3$-chromium(III) based complexes possessing high phosphorescence quantum yields and long excited state lifetimes have been developed in recent years.[24-30] Their useful excited state reactivities have been exploited in various applications, from sensing and photoredox catalysis to circularly polarised emission.[31-42]

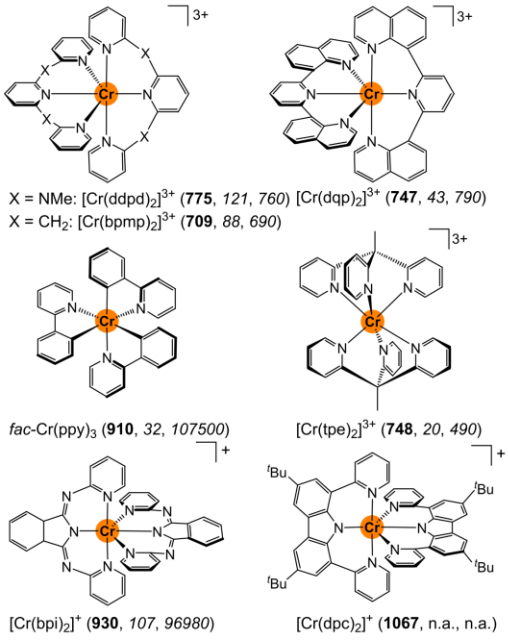

Scheme 1 Molecular structures of $[Cr(ddpd)_2]^{3+}$ (ddpd = *N,N'*-dimethyl-*N,N'*-dipyridine-2-yl-2,6-diamine),[24,25] $[Cr(bpmp)_2]^{3+}$ (bpmp = 2,6-bis(2-pyridylmethyl)pyridine),[29] $[Cr(dqp)_2]^{3+}$ (dqp = 2,6-di(quinoline-8-yl)pyridine),[28] *fac*-$Cr(ppy)_3$ (Hppy = 2-phenylpyridine),[47] $[Cr(tpe)_2]^{3+}$ (tpe = 1,1,1-tris(pyrid-2-yl)ethane),[27] $[Cr(bpi)_2]^{+}$ (Hbpi = 1,3-bis(2'-pyridylimino)-isoindoline),[50] and $[Cr(dpc)_2]^{+}$ (Hdpc = 3,6-di-*tert*-butyl-1,8-

[a] *Department of Chemistry, Johannes Gutenberg University Mainz, Duesbergweg 10-14, 55128 Mainz, Germany. E-Mail: Katja.Heinze@uni-mainz.de*
[b] *Rowland Institute, Harvard University, 100 Edwin H. Land Boulevard, Cambridge, MA 02142, USA.*
Electronic Supplementary Information (ESI) available: [Experimental procedures, spectroscopic details, quantum chemical results]. See DOI: 10.1039/x0xx00000x

View Article Online DOI: 10.1039/D4SC05666G

di(pyridine-2-yl)-carbazole),[46] along with their emission wavelengths (λ_{em} / nm) in bold and the radiative and non-radiative rate constants (k_r/s^{-1}, k_{nr}/s^{-1}) in italics in solution at room temperature (n.a. = not available).

The energies of the intraconfigurational excited states $^2E/^2T_1$ with t_{2g}^3 electron configuration in (pseudo-octahedral) transition metal complexes are essentially independent of Δ_o.[8,43,44] Their energies rather depend on the electron-electron repulsion as described by the Racah parameters *B* and *C* (with *C* being often approximated as multiple of *B*) in ligand field theory.[8,15,16] Qualitatively, these parameters can be related to the nephelauxetic (cloud-expanding) effect which describes the covalent vs. ionic character of the bonds between the metal and the ligands.[5,8] The expansion of the orbitals onto the ligands reduces the repulsion between individual d electrons and hence gives in principle a synthetic handle to modify SF state energies, although straightforward design rules are lacking.[45-52]

With pyridine and amine based ligands, chromium(III) complexes typically emit between ca. 680–780 nm (14700–12820 cm^{-1}).[1] π-Electron donating amido (carbazolato or isoindolinato) donors[46,50] and cyclometalating ligands[45,47] shift the ruby-like luminescence above 900 nm (Scheme 1).[1] Apart from changing the donors from amines/pyridines to anionic donors, even the bridging unit between coordinating pyridines affects the SF energies. In particular, the highly emissive polypyridyl chromium(III) complexes $[Cr(ddpd)_2]^{3+}$ (**[1^{NMe}]$^{3+}$**) and $[Cr(bpmp)_2]^{3+}$ (**[1^{CH2}]$^{3+}$**) (molecular rubies) with NMe and CH_2 bridges emit at 775/738 and 709 nm, respectively, although both complexes share a very similar six-fold pyridine coordination environment (Scheme 1).[24,29] While the correct energy level ordering of the two complexes could be predicted by high-level quantum chemical calculations, the underlying origin of the 1200 cm^{-1} emission energy difference remained unclear.[29] Under hydrostatic pressure, the emission energy of **[1^{NMe}]$^{3+}$** shifts by 13.9±0.9 cm^{-1} kbar^{-1} to lower energy slightly depending on the environment.[33] Compared to the pressure sensitivity of the ^2E emission of Al_2O_3:Cr with 0.7 cm^{-1} kbar^{-1}, this sensitivity is much more pronounced.[53] A compression of the Cr–N bonds and a co-planarisation of the central pyridine rings (Py_c) of the tridentate ligands leads to better overlap with ligand orbitals and thus to "cloud expansion".[54] The lowest doublet state is of $^2T_1$ parentage with two paired electrons in a t_{2g}-derived orbital showing the larger shift under pressure as compared to the classical lowest doublet states of ^2E parentage with singly occupied t_{2g} orbitals.[1,8,9]

Beyond the energies of the emissive SF states, the excited state dynamics are of particular importance for the overall performance of a SF luminescent complex. This includes the efficiency of the population of the doublet states via intersystem crossing (ISC),[55-57] as well as the radiative and non-radiative decay to the ground state (k_r and k_{nr}). The radiative rate constant k_r of the Laporte-forbidden[58] emission depends on the symmetry of the complex, with centrosymmetric complexes such as $[Cr(tpe)_2]^{3+}$ (Scheme 1) or $[Cr(CN)_6]^{3-}$ exhibiting very small radiative rate constants down to 20 and 0.4 s^{-1}, respectively.[1,27]

Several processes contribute to the non-radiative rate k_{nr}. One reason for the small k_{nr} is the comparably large Δ_o at the Franck-Condon geometry which likely mitigates back-ISC from the SF states to the non-emissive $^4T_2$ states with $t_{2g}^2e_g^1$ electron configuration. However, the relaxed $^4T_2$ states are strongly Jahn-Teller distorted and experience a huge stabilisation upon distortion.[59-61] Hence, for the excited state decay via back-ISC, distortional coordinates play major roles in addition to Δ_o at the ground state geometry. These back-ISC dynamics could be severely affected by subtle changes in the complex geometry and ligand properties, yet this has not been fully appreciated in the literature of molecular chromium(III) emitters. For ISC in general and the $^2E/^2T_1 \rightarrow {}^4T_2$ back-ISC processes in particular, spin-orbit coupling (SOC) and/or spin-vibronic coupling is required.[55,56]

A further non-radiative decay path of low-energy emitters is provided through overtones of nearby CH groups as energy acceptors.[62,63] This multiphonon relaxation depends on the distance of the CH oscillators to the metal confined excited state wave function and the spectral overlap integral of the luminescence bands with absorption bands of CH overtones.[62,63] For most chromium(III)-based SF emitters with pyridine ligands, the 4th aromatic CH overtone of a pyridine $\tilde{\nu}^4_{CH}$ = 14065 cm^{-1} is in the region of the emission energy providing a non-radiative decay path.[25]

In this study, we shed light on the specific factors that i) determine the SF state energies and ii) the population and decay (k_{nr}) of the SF states of molecular rubies. To this end, we expand the complex series **[1^{NMe}]$^{3+}$** and **[1^{CH2}]$^{3+}$** by two isolobal complexes with chalcogen bridges **[1^{O}]$^{3+}$** and **[1^{S}]$^{3+}$**. Elucidation of the ground state geometries by X-ray diffraction (XRD) analyses and excited state properties by UV/Vis/NIR absorption and emission spectroscopy is combined with high level quantum chemical modelling ((time-dependent) density functional theory, (TD)DFT and multi-reference, CASSCF-SC-NEVPT2). The excited state dynamics are probed by fs-transient absorption (TA) spectroscopy, variable-temperature (VT) emission spectroscopy, photolysis experiments and quantum chemical modelling of excited states. The combined information draw a consistent picture of excited state energies and dynamics of molecular rubies and informs about future design strategies to tune the thermodynamics and kinetics after light excitation.

Results and Discussion

1. Syntheses, structures and ground state properties

The known tridentate pyridyl thioether ligand bptp (2,6-bis(pyridine-2-ylthio)pyridine)[64,65] was prepared from 2-mercaptopyridine in 79% yield. Crystals suitable for single crystal XRD were obtained by crystallisation at low temperature. Expectedly, the C–S–C angle is with 102.7° much smaller than the angles observed at CH_2, NMe and O bridged pyridines with 111.7°, 122.9° and 120.3°, respectively.[66-68] (ESI, Fig. S1). The analogous synthetic route for the pyridyl ether ligand 2,6-bis(pyridine-2-yloxy)pyridine (bpop) starting from

2-hydroxypyridine (2-pyridone), however, yields mainly 2,6-bis(2-oxopyridin-1(2*H*)-yl)pyridine[69] due to the lower nucleophilicity of oxygen compared to sulphur and the higher resonance contribution of the keto form of the deprotonated 2-pyridone compared to its enolate form.[70,71] After extensive optimisation using various bases and solvents at different temperatures, the oxygen bridged ligand bpop could be obtained in low yields via substitution of 2,6-dihydroxypyridine with 2-bromopyridine besides 2,6-bis(2-oxopyridin-1(2*H*)-yl)pyridine as the major product. Both tripyridine pincer ligands bpop and bptp are fully characterised by elemental analyses, ESI$^+$ mass spectrometry (ESI, Fig. S2–S4), as well as ^{1}H/^{13}C NMR (ESI, Fig. S5–S15), IR (ESI, Fig. S16–S18) and optical spectroscopy (ESI, Fig. S19–S21).

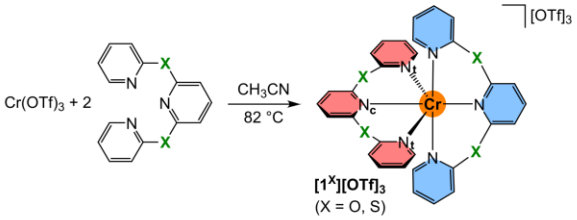

Scheme 2 Synthesis of chromium(III) complexes with tripyridine ligands with chalcogen atoms X = O, S in the six-membered chelate rings. Coordinating terminal and central pyridine nitrogen atoms are denoted N_t and N_c, respectively. The two tridentate ligands (1) and (2) are highlighted in red and blue, respectively.

The orange complex salts [Cr(bpop)$_2$][OTf]$_3$ **[1^O][OTf]$_3$** and [Cr(bptp)$_2$][OTf]$_3$ **[1^S][OTf]$_3$** were prepared in 24% and 31% isolated yields, respectively, by heating an acetonitrile solution of anhydrous chromium(III) triflate (see ESI for a convenient route and characterisation, Fig. S22–S24)[72] and the corresponding ligand (Scheme 1). The purity and composition of the complexes are confirmed by elemental analyses, ESI$^+$ mass spectrometry (ESI, Fig. S25–S26), IR spectroscopy (ESI, Fig. S27–S28), optical spectroscopy (ESI, Fig. S29–S32) and electrochemistry (ESI, Fig. S33–S36).

Electrochemical experiments reveal irreversible reduction waves at E_p = –0.48, –1.91 V and –0.40, –1.52 V vs. ferrocene for **[1^O]$^{3+}$** and **[1^S]$^{3+}$**, respectively (ESI, Fig. S33–S36), while **[1^{NMe}]$^{3+}$** and **[1^{CH2}]$^{3+}$** are reversibly reduced at –1.11 V and –0.81 V vs. ferrocene.[24,29] DFT calculations on the dications **[1^O]$^{2+}$** and **[1^S]$^{2+}$** and monocations **[1^O]$^+$** and **[1^S]$^+$** suggest a metal centered first reduction event forming chromium(II) species followed by a second reduction with significant ligand localisation. As chromium(II) complexes are typically very labile,[73,74] ligand loss or partial ligand dissociation leading to solvent coordination similar to analogous ruthenium(II) complexes might account for the irreversibility of the reduction processes.[65].

Single crystals of the complex salts **[1^O][OTf]$_3$** and **[1^S][OTf]$_3$** suitable for XRD were obtained from acetonitrile solutions at 5 °C confirming the constitution and meridional configuration (Fig. 1, ESI, Fig. S37–S38, Tables S1–S2). The [CrN$_6$] core of the complexes is highly octahedral with N–Cr–N bond angles close to 90°/180° and almost uniform Cr–N bond lengths analogous to **[1^{NMe}][BF$_4$]$_3$** (CCDC 1059802) and **[1^{CH2}][OTf]$_3$** (CCDC 1989537).[24,29] Distinct differences are apparent in the four complex cations **[1^X]$^{3+}$**, which arise from the different bridging units X. The sp^3-atom bridging units X = NMe, O, CH$_2$, S with their averaged C–X–C angles decreasing from 122°, 121°, 115° to 104° are responsible for the chelate ring conformations and the pyridine orientations.

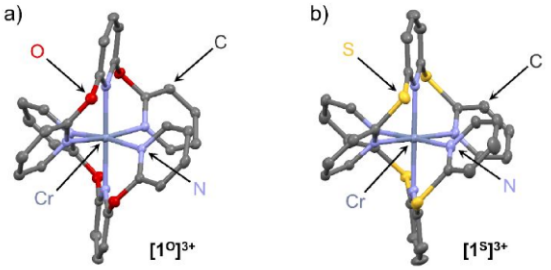

Fig. 1 Molecular structures of the trications of the chromium complexes a) **[1^O][OTf]$_3$** and b) **[1^S][OTf]$_3$** determined by XRD. Hydrogen atoms, counter ions and co-crystallised solvent molecules omitted. Thermal ellipsoids at 50% probability level.

For a detailed structure description, we denote the atoms of two tridentate ligands L^X of **[1^X]$^{3+}$** with (1) and (2) shown in red and blue, respectively (Scheme 2). The atoms of the central and terminal pyridines L^X are denoted with subscripts c and t, respectively (Scheme 2). The averaged Cr–N$_t$ distances d_{CrNt} (Table S1) increase from 2.042(4), 2.047(6) to 2.075(3)/2.076(3) Å for X = NMe, O, S, CH$_2$. The averaged Cr–N$_c$ distances d_{CrNc} increase from 2.038(3), 2.038(4), 2.069(2) to 2.094(2) Å for X = NMe, O, CH$_2$, S. The overall size of the [CrN$_6$] coordination polyhedron thus increases in the series **[1^X]$^{3+}$** with X = NMe, O, CH$_2$ and S. The N$_t$ atoms of the tridentate ligands in **[1^O]$^{3+}$** and **[1^{NMe}]$^{3+}$** form N$_t$(1)–Cr–N$_t$(1) angles α (Table S1) below 180° (α = 172.6(2) and 171.9(1)°), while α of **[1^S]$^{3+}$** and **[1^{CH2}]$^{3+}$** is closer to 180° (α = 177.8(1) and 177.6(1)°). The smallest N$_t$(1)–Cr–N$_t$(2) angle β between the N$_t$ atoms of the two different ligands (Table S1) is close to 90° for **[1^O]$^{3+}$** and **[1^{NMe}]$^{3+}$** (β = 89.7(2) and 89.8(1)°), but below 90° for **[1^S]$^{3+}$** and **[1^{CH2}]$^{3+}$** (β = 85.3(1) and 84.9(1)°). The angles between the planes of the terminal pyridines within a ligand are denoted by the torsion angles δ^1/δ^2 C^{alpha}–N$_t$(1)–N$_t$(1)–C^{alpha} and C^{alpha}–N$_t$(2)–N$_t$(2)–C^{alpha}, respectively (Table S2). These angles δ^1 and δ^2 increase from 73.5/69.8°, 72.3/71.2°, 79.1/80.6° to 81.7/86.3° for X = O, CH$_2$, NMe and S approaching a more orthogonal orientation. The angles between the planes of the central pyridines of the two ligands ϕ, described by the torsion angle C^{alpha}–N$_c$(1)–N$_c$(2)–C^{alpha} (Table S2), decrease from 29.5°, 21.8°, 18.5° to 18.3° for X = CH$_2$, O, S, NMe. The structural parameters d_{CrN}, α and β of the coordination polyhedron and the orientation of the pyridines $\delta^{1,2}$ and ϕ serve to identify the most relevant structural aspects for the SF state energies in the quantum chemical modeling. The optical properties and the excited state dynamics of the complexes will be discussed next.

2. Excited state energies

To understand the optical properties of the complexes, we first describe the properties of the chalcogen bridged pyridine ligands bpop and bptp (ESI, Fig. S19–S21). The $S_0 \rightarrow S_1$ absorption

View Article Online DOI: 10.1039/D4SC06866C

bands at λ_{max} = 267/308 nm and the corresponding broad $S_1 \rightarrow S_0$ fluorescence bands at λ_{emis} = 307/349 nm show large Stokes shifts of 4880 and 3810 cm^{-1}, respectively. This agrees with the X→pyridine CT character of the S_1 state assigned by TDDFT calculations (ESI, Fig. S19–S20) and the higher-energy sulphur lone pairs as compared to the oxygen lone pairs.

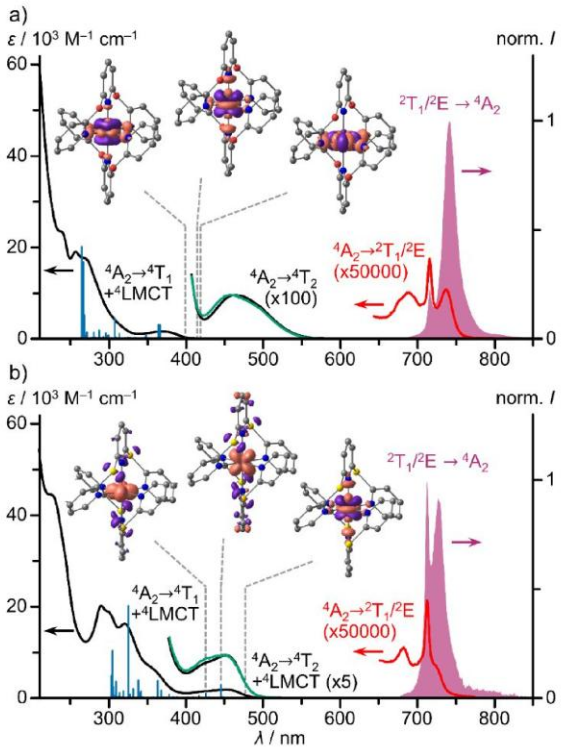

Fig. 2 UV/VIS/NIR absorption spectra (black, red), excitation spectra (λ_{em} = 714 and 742 nm, green) and emission spectra (λ_{exc} = 450 nm, purple) of a) $[\mathbf{1^O}]^{3+}$ and b) $[\mathbf{1^S}]^{3+}$ in deaerated acetonitrile at room temperature, TDDFT calculated oscillator strengths (blue sticks) and difference electron densities of three low-energy transitions of ^{4}LMCT and ^{4}MC character. The regions of the spin-forbidden absorption bands, the lowest energy spin allowed/LMCT absorption band and the excitation spectrum are scaled with the indicated factors.

In the absorption spectra of the chromium(III) complexes $[\mathbf{1^O}]^{3+}$ and $[\mathbf{1^S}]^{3+}$, high intensity bands of ^{4}LMCT/$^4(\pi\text{–}\pi^*)$ character, weak spin-allowed, Laporte-forbidden $^4A_2 \rightarrow {}^4T_2$ bands and very weak spin- and Laporte-forbidden $^4A_2 \rightarrow {}^2T_1/{}^2E$ bands are present in the UV, visible and NIR spectral regions, respectively (Fig. 2; ESI, Fig. S29–S30). The $^4A_2 \rightarrow {}^4T_2$ bands of $[\mathbf{1^O}]^{3+}$ appear isolated according to TDDFT calculations (ESI, Table S3) at 463 nm with ε = 100 M^{-1} cm^{-1} (Fig. 2a), similar to $^4A_2 \rightarrow {}^4T_2$ bands of $[\mathbf{1^{CH2}}]^{3+}$ (465 nm; ε = 70 M^{-1} cm^{-1}; ESI, Fig. S39).[29] In contrast, the analogous dd band of $[\mathbf{1^S}]^{3+}$ is hidden by low energy S→Cr LMCT transitions according to TDDFT calculations (ESI, Table S4), which increases the intensity of this band at 452 nm (Fig. 2b; ε = 1880 M^{-1} cm^{-1}). This is analogous to the NMe→Cr LMCT transition in $[\mathbf{1^{NMe}}]^{3+}$ at around 435 nm (ε = 4100 M^{-1} cm^{-1}) overlapping the $^4A_2 \rightarrow {}^4T_2$ dd transitions (ESI, Fig. S40).[9,24]

Due to the superimposed LMCT bands and the symmetry deviating from octahedral, the ligand field splitting Δ_o can only roughly be estimated from the dd bands as 21510, 21600, 22120 and 22990 cm^{-1} for $[\mathbf{1^X}]^{3+}$ with X = CH_2, O, S and NMe, respectively. For a more reliable ordering of the complexes in a spectrochemical series we resorted to quantum chemical calculations. TDDFT calculated lowest energy $^4A_2 \rightarrow {}^4T_2$ transitions at the optimised geometries, which can be assigned to the ligand field splitting Δ_o, increase from 20960, 23120, 23790 to 23870 cm^{-1} for $[\mathbf{1^X}]^{3+}$ with X = S, CH_2, NMe and O, respectively. CASSCF(7,12)-SC-NEVPT2 calculations at the same geometries deliver 20290, 21740, 22660 and 23220 cm^{-1} for $[\mathbf{1^X}]^{3+}$ with X = S, CH_2, O and NMe, respectively (ESI, Table S5, Fig. S41). Hence, we suggest a weaker ligand field in the $[\mathbf{1^S}]^{3+}$ derivative, a medium field in $[\mathbf{1^{CH2}}]^{3+}$ and stronger fields in the $[\mathbf{1^O}]^{3+}$/$[\mathbf{1^{NMe}}]^{3+}$ complexes. Yet, all ligand field strengths can be classified as very strong.

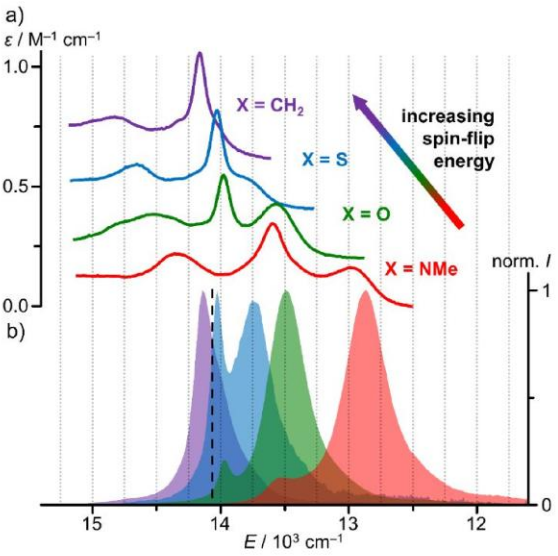

Fig. 3 a) NIR absorption spectra and b) normalised emission spectra of $[\mathbf{1^{CH2}}]^{3+}$ (purple, λ_{exc} = 460 nm), $[\mathbf{1^S}]^{3+}$ (blue, λ_{exc} = 450 nm), $[\mathbf{1^O}]^{3+}$ (green, λ_{exc} = 450 nm) and $[\mathbf{1^{NMe}}]^{3+}$ (red, λ_{exc} = 435 nm) in CH_3CN at room temperature. For clarity, the absorption spectra of $[\mathbf{1^X}]^{3+}$ with X = O, S, CH_2 were shifted vertically by +0.2, +0.4 and +0.6 M^{-1} cm^{-1}. The dashed black line marks the energy of the 4th pyridine CH overtone $\tilde{\nu}_{4_{CH}}$.[25]

The NIR spectral region shows a characteristic absorption band pattern consisting of three weak bands with discernible maxima at 689, 716, 737 nm and at 683, 713, 724 (sh) nm for $[\mathbf{1^O}]^{3+}$ and $[\mathbf{1^S}]^{3+}$, respectively. Similar absorption band patterns of 697, 736, 771 nm and 674, 699, 706 nm were found for $[\mathbf{1^{NMe}}]^{3+}$ and $[\mathbf{1^{CH2}}]^{3+}$, respectively (Fig. 3a, ESI, Fig. S39–S40).[24,29]

As the NIR absorption bands correspond to five SF transitions (^2E, $^2T_1$ in octahedral symmetry), we fitted the spectral patterns with five Voigt functions each (after baseline correction as described in the ESI; Fig. S42–S45). Indeed, these five Voigt functions excellently reproduce the experimental band patterns. The data is compiled in Table 1.

View Article Online
DOI: 10.1039/D4SC05600K

Table 1 Five band maxima / cm^{-1} from deconvoluted SF absorption bands of $[1^X]^{3+}$ (X = CH_2, S, O, NMe), CASSCF(7,12)-SC-NEVPT2 calculated transitions (in italics; scaled by 0.89) and assignment according to the calculations. Selected energy differences / cm^{-1}. [a] This is the band with a smaller experimental full width at half maximum (FWHM).

No.	#5	#4	#3	#2	#1	ΔE(#5–#1)	ΔE(#2–#1)
X = CH_2							
exp.	15060	14780	14320	14160	14050	1010	110
calcd.	*14660*	*14640*	*14430*	*14140*	*13970*	*690*	*170*
term	$^2T_1(3)$	$^2E(2)$	$^2T_1(2)$	$^2E(1)^{[a]}$	$^2T_1(1)$		
X = S							
exp.	14770	14630	14210	14030	13800	970	230
calcd.	*14750*	*14720*	*14500*	*14200*	*14000*	*750*	*200*
term	$^2T_1(3)$	$^2E(2)$	$^2T_1(2)$	$^2E(1)^{[a]}$	$^2T_1(1)$		
X = O							
exp.	14780	14520	14360	13980	13560	1220	420
calcd.	*14510*	*14420*	*14160*	*14000*	*13590*	*920*	*410*
term	$^2E(2)$	$^2T_1(3)$	$^2T_1(2)$	$^2E(1)^{[a]}$	$^2T_1(1)$		
X = NMe							
exp.	14430	14300	13600	13530	12960	1470	570
calcd.	*14400*	*14250*	*13880*	*14180*	*13400*	*1000*	*480*
term	$^2E(2)$	$^2T_1(3)$	**$^2E(1)^{[a]}$**	$^2T_1(2)$	$^2T_1(1)$		

From the CASSCF(7,12)-SC-NEVPT2 calculations of all $[1^X]^{3+}$ complexes at their respective DFT-optimised ground state geometries we obtained the five lowest doublet state energies (ESI, Table S5, Fig. S41). With a common scaling factor of 0.89 these energies excellently fit to the experimentally derived energies allowing a detailed assignment of the individual states (Table 1). Importantly, the calculations reproduce the experimental nephelauxetic series of the complexes $[1^X]^{3+}$ with X = CH_2, S, O and NMe derived from the SF energies, the increased lifting of the degeneracies ΔE(#5–#1) in the series CH_2/S < O < NMe and the energy difference of the two lowest energy SF absorptions ΔE(#2–#1) (Table 1). The very sharp central band (doublet state #3 for X = NMe, #2 for the other complexes) reflects a miniscule geometric distortion of an excited state and can most likely be assigned to a (0,0) transition of a nested, i.e. undistorted, microstate of ^2E character.[1,8] The tentative assignment of the SF state #2 as $^2E(1)$ is confirmed by the (7,12)-SC-NEVPT2 calculations (Table 1). Based on these agreements, we attest a high fidelity to the quantum chemical calculations and assignments. In all cases, the lowest doublet states #1 and #2 are of $^2T_1$ and ^2E character, respectively.

Irradiation of a solution of $[1^O]^{3+}$ and $[1^S]^{3+}$ at room temperature in acetonitrile with λ_{exc} = 450 nm gives rise to two sharp emission bands peaking at 716/741 nm and 713/727 nm with FWHM of 140/350 and 150/420 cm^{-1}, respectively (Fig. 3b, ESI, Fig. S31). The energies of the two phosphorescence bands of all complexes $[1^X]^{3+}$ match the energies of the two lowest-energy absorption bands (Fig. 3; ESI, Fig. S39–S40).[9,24,29] Small Stokes shifts of 80, 60, 70 and 70 cm^{-1} are observed for the lowest energy emission band ($^2T_1(1)\rightarrow{}^4A_2$), while even smaller Stokes shifts < 40 cm^{-1} are determined for the second lowest energy emission band ($^2E(1)\rightarrow{}^4A_2$) in agreement with slightly distorted $^2T_1(1)$ states and almost perfectly nested $^2E(1)$ states (Fig. 3).

Doublet states of ^2E and $^2T_1$ parentage could be localised by excited state geometry optimization via TDDFT. The Cr–N distances d_{CrN} slightly decrease from d_{CrNc}/d_{CrNt} = 2.051/2.071 Å ($^4A_2$ ground state) to 2.044/2.064 Å (^2E) and 2.042/2.057 Å ($^2T_1$) for X = O and from d_{CrNc}/d_{CrNt} = 2.140/2.118 Å ($^4A_2$ ground state) to 2.103/2.087 Å (^2E) and 2.098/2.079 Å ($^2T_1$) for X = S. In both cases, the compression is larger in the $^2T_1(1)$ excited states than in the $^2E(1)$ states. This further confirms that the broader low-energy bands with a larger Stokes shifts arise from the slightly more distorted $^2T_1(1)$ states.

In order to correlate structural effects of the hexapyridine chromium(III) complexes with their doublet state energies, we first disentangle primary electronic from secondary structural effects (d_{CrN}, α, β, $\delta^{1,2}$ and ϕ) of the bridging unit X. In a first series of calculations, the bridging unit was substituted by a different bridge while retaining the geometry (ESI, Fig. S46, Table S6). For example, the NMe unit of $[1^{NMe}]^{3+}$ was replaced by X = O and CH_2, while the original geometry of $[1^{NMe}]^{3+}$ was retained. According to the CASSCF(7,12)-SC-NEVPT2 calculations, NMe→O replacement increases the SF energy, while NMe→CH_2 replacement decreases it (ESI, Fig. S46, Table S6). The latter is at odds with the experiment, suggesting that electronic substituent effects (at the *ortho* positions) alone do not correctly describe the SF energy shifts. Furthermore, the energy variation at fixed geometries but with different X bridges is smaller than the energy variation due to geometric distortions (ESI, Fig. S46). Hence, the indirect effects of structural modification (d_{CrN}, α, β, $\delta^{1,2}$ and ϕ) exerted by the bridge X are more relevant for the SF energies than primary electronic effects.

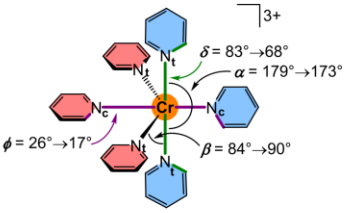

Scheme 3 Structure of the model system $[Cr(py)_6]^{3+}$ and the definition and relevant ranges of the bond angles α / β and the dihedral angles δ / ϕ.

To explore the effects of the geometry on the SF energies, we employed a model system $[Cr(py)_6]^{3+}$ where contributions from the bridging atoms are excluded (Scheme 3). The parameters d_{CrN}, α, β, δ and ϕ were varied within the value ranges as determined from XRD analyses and DFT optimisations and also extrapolated to smaller and larger values (ESI, Fig. S47–S57). Within this set of parameters, decreasing the Cr–N distances d_{CrNc} = 2.140→2.046 Å and d_{CrNt} = 2.118→2.058 Å shifts the SF energies to lower energy by 225 and 228 cm^{-1}, respectively, at fixed α, β, δ and ϕ angles in the calculations (Fig. S58). Hence, symmetric compression of the $[CrN_6]$ coordination polyhedron in local D_{4h} symmetry results in bathochromic shifts of the SF energies. This bathochromic shift is also observed for ruby[53] and molecular rubies under pressure (ESI, Fig. S48–S51).[35,54] Shorter Cr–N bonds enhance the covalency of the bonds, thereby

increasing the electron delocalization and hence the nephelauxetic effect resulting in lower SF energies. Expectedly the energetic order of the five individual SF microstates is essentially unaffected by the symmetrical Cr–N modes in the observed distance range. Decreasing the angle α in the model $[Cr(py)_6]^{3+}$ (ESI, Fig. S52) from 179° (as found in **[1^{S}]$^{3+}$**) to 173° (as found in **[1^{NMe}]$^{3+}$**) at fixed Cr–N distances and ϕ angles (β and δ had to be adjusted in order to avoid close H···H contacts) lowers the SF energy by 75 cm^{-1} (ESI, Fig. S58). This unsymmetrical distortion also changes the $^2T_1/^2E$ contributions to the individual microstates. Expansion of β from 84° (as found in **[1^{CH2}]$^{3+}$**) to 90° (as found in **[1^{O}]$^{3+}$**) lowers the SF energy by 28 cm^{-1} (ESI, Fig. S58). The torsional modes δ (ESI, Fig. S54–S55) and ϕ (ESI, Fig. S56–S57) exert weaker effects. Creating a less orthogonal orientation of terminal pyridines, i.e. adjusting δ = 83→68° (**[1^{S}]$^{3+}$** → **[1^{O}]$^{3+}$**) and more co-planar orientations of the central pyridines, i.e. adjusting ϕ = 26→17° (**[1^{CH2}]$^{3+}$** → **[1^{S}]$^{3+}$**) leads to very small bathochromic shifts of 9 and 5 cm^{-1}, respectively (ESI, Fig. S58).

Consequently within the present complex series **[1^{X}]$^{3+}$**, the bridging unit X indirectly affects both the average energy of the $^2T_1/^2E$ manifold and the relative energies of the five doublet microstates with $^2T_1$ and ^2E parentage. Bond compression exerts the largest bathochromic effect, followed by lowering the N_t–Cr–N_t bite angle α, although the angular modifications are not independent from each other in the chelate complexes. Having assigned the character of the lowest energy excited states and the structural origins of the relative energies, we now turn to the excited state dynamics.

3. Excited state dynamics

Excitation spectra of **[1^{O}]$^{3+}$** and **[1^{S}]$^{3+}$** (λ_{em} = 742 and 714 nm) closely follow the respective absorption spectra in the region of the lowest spin-allowed $^4A_2$→$^4T_2$ and ^{4}LMCT transitions (ca. 380–600 nm, Fig. 3). This substantiates that both types of quartet states efficiently populate the SF states via ISC without branching to other decay channels.

Femtosecond TA spectroscopy on **[1^{O}]$^{3+}$** and **[1^{S}]$^{3+}$** confirms that the vibrationally cold doublet states are populated within τ_1,τ_2 = 1.0, 47 ps and τ_1,τ_2 = 1.2, 90 ps (ESI, Fig. S59–S64) after excitation at 343 nm (**[1^{O}]$^{3+}$**) and 515 nm (**[1^{S}]$^{3+}$**), respectively. In both complexes **[1^{O}]$^{3+}$** and **[1^{S}]$^{3+}$**, ISC appears to occur on an ultrafast time scale. This rapid ISC likely arises from the high density of doublet states both for ^{4}LMCT (**[1^{O}]$^{3+}$**) and ^{4}MC/^{4}LMCT (**[1^{S}]$^{3+}$**) excitation. For example the $^2T_2$ derived states are close in energy to the $^4T_2$ states according to CASSCF calculations (ESI, Table S6, Fig. S41). No loss channels are apparent on the fast time scale and hence the decisive non-radiative and radiative decay occurs from the lowest energy SF states, similar to **[1^{NMe}]$^{3+}$** and **[1^{CH2}]$^{3+}$**.[24,29]

The photoluminescence quantum yield Φ = 11.5% and SF excited state lifetime τ_P = 836 µs of **[1^{O}]$^{3+}$** in deaerated CH_3CN are in very high ranges, similar to the record values of **[1^{NMe}]$^{3+}$** and **[1^{CH2}]$^{3+}$**.[24,29] The observed excited state lifetime corresponds to the common lifetime of the equilibrating emissive lowest energy doublet states $^2T_1(1)$ and $^2E(1)$.[31] The radiative and non-radiative rate constants k_r = 138 s^{-1} and k_{nr} = 1059 s^{-1} are similar to the values of **[1^{NMe}]$^{3+}$** and **[1^{CH2}]$^{3+}$** (Scheme 1). On the other hand, the values of the sulphur derivative **[1^{S}]$^{3+}$** are lower by orders of magnitude with Φ = 0.01% and τ_P = 1.65 µs. This gives a somewhat smaller k_r = 61 s^{-1}, while the non-radiative rate constant k_{nr} = 606000 s^{-1} increased by orders of magnitude.

As this huge difference of k_{nr} is completely unexpected in light of the similar ground state geometries and excited state energies, we investigated the excited decay of **[1^{O}]$^{3+}$** and **[1^{S}]$^{3+}$** by variable-temperature (time-resolved) emission spectroscopy in order to identify thermally accessible loss channels. Emission spectra and lifetimes of **[1^{O}]$^{3+}$** and **[1^{S}]$^{3+}$** were determined between 293 and 77 K in ethanol/methanol (3:2 *v*/*v*) solution, which freezes around 130 K (Fig. 4).

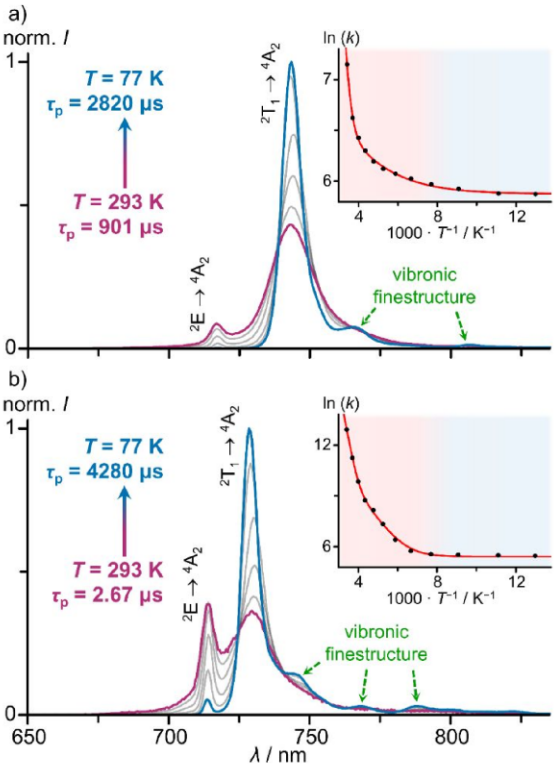

Fig. 4 Integration area normalised low temperature emission spectra (λ_{exc} = 450 nm) of a) **[1^{O}]$^{3+}$** and b) **[1^{S}]$^{3+}$** in a mixture of ethanol/methanol (3:2 *v*/*v*) between 77 and 293 K under deaerated conditions. Insets show corresponding Arrhenius plots of the photoluminescence rate constants $k(T)$ with fit and coloured backgrounds for temperature ranges of liquid (red) and frozen solvent mixture (blue).

Temperature-dependent emission spectra clearly reveal thermal population of the two lowest energy SF states for all complexes under study and even population of the next higher energy SF state #3 $^2T_1(2)$ to a small degree (ESI, Fig. S65–S68). At lower temperatures, the lowest SF state $^2T_1(1)$ is increasingly populated at the expense of the other SF states. The $^2T_1(1)$→$^4A_2$ emission bands develop vibrational fine structure at lower temperature with maxima centred at 13050, 12390, 12210, 11830 cm^{-1} and 13440, 13020, 12690, 12480, 12150 cm^{-1} for

[1^{O}]$^{3+}$ and **[1^{S}]$^{3+}$**, respectively (ESI, Fig. S65–S66). Similar vibrational progressions have been reported for **[1^{NMe}]$^{3+}$** and **[1^{CH2}]$^{3+}$** (ESI, Fig. S67–S68).[24,29] The energy differences are compatible with Cr–N vibrational modes.[75]

Cooling the solution of **[1^{O}]$^{3+}$** from 293 K to 77 K sharpens the low-energy $^2T_1(1)\rightarrow{}^4A_2$ band (FWHM = 350 → 150 cm^{-1}) and increases the lifetime τ_P = 901 → 2820 µs (Fig. 4a; ESI, Fig. S69). At 250 K, the quantum yield reaches approximately Φ = 22%. Similarly, cooling a solution of **[1^{S}]$^{3+}$** from 293 K to 77 K sharpens the low-energy $^2T_1(1)\rightarrow{}^4A_2$ band (FWHM = 420→140 cm^{-1}) and drastically increases the lifetime τ_P = 2.67 → 4280 µs (Fig. 4b, ESI, Fig. S70). Concomitantly, the integrated luminescence intensity increases 900-fold, i.e. approaching approximate values of Φ = 9% at 77 K (assuming a temperature independent absorbance at the excitation energy).

The thermally activated decay of **[1^{O}]$^{3+}$** and **[1^{S}]$^{3+}$** was successfully modelled with an Arrhenius-like behaviour according to eq. 1 (Fig. 4). The photoluminescence rate constants $k(T) = 1/\tau_p(T)$ of the complexes (ESI, Fig. S69–S70) were fitted as a sum of a T-independent rate constant k_0, describing non-thermally activated radiative and non-radiative processes, and two T-dependent rate constants $k_1(T)$ and $k_2(T)$ (eq. 1).

$$k(T) = k_0 + k_1(T) + k_2(T) = k_0 + A_1 e^{-\frac{E_{a1}}{RT}} + A_2 e^{-\frac{E_{a2}}{RT}} \qquad \text{(eq. 1)}$$

Two thermally activated processes (A_1, E_{a1}; A_2, E_{a2}) were required to satisfactorily fit the experimental data (Table 2). k_1 (A_1, E_{a1}) and k_2 (A_2, E_{a2}) dominate the high and low temperature regions, respectively.

Table 2 Fit parameters for the emission decays of solutions of **[1^{O}]$^{3+}$** and **[1^{S}]$^{3+}$** obtained from Arrhenius plots according to eq. 1.

	[1^{O}]$^{3+}$	**[1^{S}]$^{3+}$**
k_0 / s^{-1}	356	225
E_{a1} / cm^{-1} (eV)	3360 (0.417)	4320 (0.536)
E_{a2} / cm^{-1} (eV)	370 (0.046)	1090 (0.135)
A_1 / s^{-1}	9.18×10^9	6.27×10^{14}
A_2 / s^{-1}	1.80×10^3	4.65×10^6

Based on the two experimentally determined barriers E_{a1} and E_{a2} for thermally activated decay pathways with high and small frequency factors A_1 and A_2 (Table 2), we now propose a kinetic model with physical assignments to the processes. The larger barriers E_{a1} of 3360 and 4320 cm^{-1} for **[1^{O}]$^{3+}$** and **[1^{S}]$^{3+}$** are likely associated with the thermally activated back-ISC from the $^2T_1(1)/^2E(1)$ levels to the quartet levels, possibly along several conceivable Jahn-Teller modes associated with the $^4T_2$ or ^{4}LMCT states similar to ^{3}MC states of d^6 metal complexes such as [Ru(bpy)$_3$]$^{2+}$ (bpy = 2,2'-bipyridine).[76-79]

Excited state geometry optimisations of the complex cations by TDDFT (ESI, Table S7) delivered quartet excited states with $^4T_2$ character and one or two elongated Cr–N$_c$ distances. The symmetric N$_c$–Cr–N$_c$ breathing elongation amounts to 9% and 6-8% for **[1^{O}]$^{3+}$** and **[1^{S}]$^{3+}$**, while the more asymmetric Cr–N$_c$ elongation reaches 22% and 13% for **[1^{O}]$^{3+}$** and **[1^{S}]$^{3+}$**, respectively. Asymmetric $^4T_2$ states were also localised for X = **[1^{CH2}]$^{3+}$** and **[1^{NMe}]$^{3+}$** where a single Cr–N$_c$ bond is elongated by 20% and 13%, respectively. In addition to the distorted metal-centered $^4T_2$ states of **[1^{S}]$^{3+}$**, two distorted ^{4}LMCT states are located at similar energies. One optimised ^{4}LMCT coordination polyhedron is elongated along the symmetric N$_c$–Cr–N$_c$ breathing mode (10–15% elongation) and the other optimised state exhibits a pincer-like deformation with a 14% increase of two Cr-N$_t$ bond lengths of a single bptp ligand. In essence, all complexes **[1^{X}]$^{3+}$** possess low-energy distorted metal-centered quartet states, while **[1^{S}]$^{3+}$** additionally possesses distorted low-energy ^{4}LMCT states with significant S→Cr CT character.

The experimental barrier E_{a1} of the oxygen derivative **[1^{O}]$^{3+}$** is smaller than that of the sulphur derivative **[1^{S}]$^{3+}$**. This suggests favoured thermally activated non-radiative decay for **[1^{O}]$^{3+}$**, which is at odds with the experimentally observed lower k_{nr} of **[1^{O}]$^{3+}$** at first sight. However, the frequency factor A_1 determined for **[1^{S}]$^{3+}$** is higher than that for **[1^{O}]$^{3+}$** by orders of magnitude, which overcompensates the somewhat higher barrier of **[1^{S}]$^{3+}$** (Table 2). In a picture of semi-classical Marcus theory, larger frequency factors are associated with a stronger electronic coupling of the involved states.[80] In other words, although **[1^{O}]$^{3+}$** has smaller barriers, its electronic coupling is much weaker leading to a smaller ISC transition probability. For **[1^{S}]$^{3+}$**, the large frequency factor A_1 enables rapid excited state decay. The larger A_1 might arise from a higher density of accessible distorted quartet states in **[1^{S}]$^{3+}$** (Table S7) and/or higher SOC, i.e. higher electronic coupling. We hypothesise that the heavier sulphur atoms invoke larger SOCs[16,81] as compared to the lighter bridging carbon, nitrogen or oxygen atoms of **[1^{CH2}]$^{3+}$**, **[1^{NMe}]$^{3+}$** and **[1^{O}]$^{3+}$** and hence promote the $^2T_1(1)/^2E(1)\rightarrow{}^4T_2/^4$LMCT back-ISC process via the heavy atom effect.[82-85] The sulphur orbital contributions to the ^{4}LMCT state could further assist the $^2T_1(1)/^2E(1)\rightarrow{}^4$LMCT back-ISC process via SOC.[55,56]

Following this simple argument, the lower Φ of **[1^{S}]$^{3+}$** at room temperature is associated with a heavy-atom promoted thermally activated back-ISC to $^4T_2/^4$LMCT levels. As these distorted $^4T_2/^4$LMCT states can cross the $^4A_2$ ground state potential surface or can lead to ligand dissociation (see below), this back-ISC process can be irreversible.

The second barriers E_{a2} of a few hundred wavenumbers might be associated with the thermal population of the five lowest doublet states (Table 1, Fig. 4). This reversible equilibration of doublet states, however, should not promote non-radiative decay *per se* as these doublet states are essentially nested states. Yet, multiphonon relaxation, which requires a resonant energy transfer to a vibrational overtone, might become relevant upon populating higher energy SF states. The 4th aromatic CH overtone of a pyridine of $\tilde{\nu}^4_{CH}$ = 14065 cm^{-1} is in the region of the SF states for both complexes (Table 1, Fig. 3b).[25] Accidentally, the ^{2}E(1) state of **[1^{S}]$^{3+}$** is even almost resonant with $\tilde{\nu}^4_{CH}$. Hence, a diminished ^{2}E(1) population of **[1^{S}]$^{3+}$** at lower temperature will mitigate this pathway significantly. Inspection of Fig. 4b shows that the $^2E(1)\rightarrow{}^4A_2$ emission band of **[1^{S}]$^{3+}$** dramatically diminishes in intensity at 77 K relative to the $^2T_1(1)\rightarrow{}^4A_2$ emission band. This effect is much less pronounced for **[1^{O}]$^{3+}$** due to its larger $E(^2E(1)–{}^2T_1(1))$ energy difference (Table 1). In addition, its ^{2}E(1) emission band

has a much smaller spectral overlap integral with the CH overtone anyway thanks to the larger energy gap $E(^2E(1)–\tilde{\nu}^4_{CH})$. Consequently, we propose that multiphonon relaxation via CH overtones is more relevant for $[1^S]^{3+}$ and that this pathway is *T*-dependent due to thermally activated population of its (accidentally resonant) $^2E(1)$ state.

The extremely efficient non-radiative decay of $[1^S]^{3+}$ with $k_{nr}(293\ K) = 606000\ s^{-1}$ via the $^4T_2/^4LMCT$ and $^2E(1)$ levels is strongly diminished at 77 K with $k_{nr}(77\ K) = 213\ s^{-1}$. The first decay path is associated with the presence of a sulphur atom with larger SOC for the $^2T_1(1)/^2E(1)\rightarrow{}^4T_2/^4LMCT$ ISC (internal heavy atom effect) and the second decay path is associated with the thermally populated $^2E(1)$ level that is accidentally resonant with a CH overtone (thermally activated multiphonon relaxation).

4. Excited state reactivity

The photostability of the complexes $[1^X]^{3+}$ was probed by irradiating them in deaerated CH_3CN (X = CH_2, S, O, NMe). High light intensities are required for significant photochemical responses which is why we used a 460 nm UHP-LED with an output power of 1.1 W for these experiments. Under these conditions, which also might include a rise in temperature, the absorption spectra change and the luminescence intensities decrease in all cases (Fig. S71–S74). The resulting spectra are compatible with (partial) ligand dissociation with the dissociated tripyridine ligands possibly undergoing follow-up reactions such as protonation (from the environment) or oxidation by excited chromium complexes.[67]

The ligand photodissociation is not very efficient for $[1^O]^{3+}$, $[1^{NMe}]^{3+}$ and $[1^{CH2}]^{3+}$, but appears more efficient for $[1^S]^{3+}$, although the rates are not entirely comparable due to the different absorption changes during the photolysis. As discussed above, the heavy-atom effect of sulphur[82-85] and the higher density of states might again be made responsible for the more efficient $^2E/^2T_1\rightarrow{}^4T_2(1)/^4LMCT$ back-ISC of $[1^S]^{3+}$ and hence the more efficient unimolecular ligand dissociation. A potentially dissociative state could be the ^4LMCT state with a pincer-like deformation of one bptp ligand (ESI, Table S7).

For all complexes, the excited state lifetimes are sufficiently high (> 1.5 µs) at room temperature to allow for bimolecular quenching. The doublet states of all sensitisers $[1^X]^{3+}$ are quenched by Dexter energy transfer to triplet oxygen with rate constants $k_q = 0.17\times10^7\ M^{-1}\ s^{-1}$, $0.29\times10^7\ M^{-1}\ s^{-1}$,[29] $1.77\times10^7\ M^{-1}\ s^{-1}$,[36] $8.55\times10^7\ M^{-1}\ s^{-1}$ for X = O, CH_2, NMe, S, respectively (Fig. S75–S76). This series might be associated with the different accessibility of the Cr centre by O_2 due to the different bridges X. Singlet oxygen quantum yields were already reported for $[1^{NMe}]^{3+}$ and $[1^{CH2}]^{3+}$ as 61% (DMF) and 55% ($DMF/HClO_4$), respectively.[32,29]

Based on the high excited state reduction potentials of $[1^O]^{3+}$ and $[1^S]^{3+}$ of $E(^*[1^X]^{3+}/[1^X]^{2+}) = 1.25$ and 1.34 V (derived from the $^2E(1)$ energies at 293 K), these sensitisers should react with suitable redox-active quenchers. Anthracene ($E_{1/2} = 0.69$ V vs. ferrocene, $E_T = 1.85$ eV)[86,87] and *trans*-stilbene ($E_{1/2} = 1.03$ V vs. ferrocene, $E_T = 2.14$ eV)[86,87] should quench excited $[1^O]^{3+}$ and $[1^S]^{3+}$ exclusively by electron transfer, but not by energy transfer due to their high triplet energies E_T. The larger driving force for the oxidation of anthracene compared to *trans*-stilbene gives quenching rate constants $k_q(\text{anthracene}) = 7.21\times10^8/44\times10^8\ M^{-1}\ s^{-1}$ larger by two orders of magnitude than for *trans*-stilbene with $k_q(\text{trans-stilbene}) = 2.06\times10^6/27.3\times10^6\ M^{-1}\ s^{-1}$ for $[1^O]^{3+}$ and $[1^S]^{3+}$, respectively (Fig. S77–S80). Both quenchers react faster with the sulphur derivative $[1^S]^{3+}$ than with $[1^O]^{3+}$ due to the higher excited state potential of $[1^S]^{3+}$ in agreement with Marcus theory.

Conclusions

Two new molecular rubies $[1^X]^{3+}$ with X = O, S bridging atoms in the tripyridine ligands were structurally and spectroscopically characterised complementing the analogous known spin-flip emitters with X = NMe, CH_2. This series allows an unprecedented insight into excited state energies and dynamics. The energies of all five lowest doublet levels derived from $^2E/^2T_1$ terms in octahedral symmetry of all complexes were experimentally identified by absorption spectroscopy for the first time. High-level quantum chemical calculations reproduced these doublet state energies very well. Calculations on model systems revealed the underlying structure-property relationship with the dominant parameter for the emission energy being the Cr–N distances: shorter distances lead to bathochromic shifts, which can be explained on the basis of the nephelauxetic effect.

All four molecular rubies $[1^X]^{3+}$ undergo ultrafast ISC to the doublet manifold. The excited state dynamics of $[1^X]^{3+}$ with X = O, CH_2, NMe on longer times scales are similar and high quantum yields and lifetimes are obtained. The sulphur derivative $[1^S]^{3+}$, however, experiences extremely rapid non-radiative decay via two pathways at room temperature: The first decay path is likely associated with stronger spin-orbit coupling caused by the sulphur atoms leading to faster doublet-quartet back-intersystem crossing (internal heavy atom effect). The second decay pathway is opened by thermal population of the $^2E(1)$ level that is accidentally resonant with a CH overtone enabling multiphonon relaxation. The efficient population of the distorted quartet states in $[1^S]^{3+}$ furthermore promotes more facile ligand dissociation. All sensitisers $[1^X]^{3+}$ engage in photoinduced energy and electron transfer reactions from their doublet levels thanks to their microsecond excited state lifetime.

Key results from this study are as follows: i) the Cr–L distances appear as the most important parameter to tune the luminescence energies of spin-flip emitters (nephelauxetic effect); ii) with a large ligand field splitting, the density of doublet states at the Franck-Condon geometry is high, which enables efficient ISC without requiring SOC by further heavy atoms; iii) heavy atoms should indeed be avoided as they can promote thermally activated back-ISC to the quartet levels along Jahn-Teller modes, increasing k_{nr} (heavy atom effect); iv) Jahn-Teller distortions in $^4T_2/^4LMCT$ states are responsible for photodissociation and v) CH overtones of the ligands (in particular CH oscillators those close to the metal centre) can

define spectral regions of the luminescence with higher and lower non-radiative decay via (thermally activated) multiphonon relaxation. These key aspects will aid in future design concepts of improved molecular rubies.

Author Contributions

F.R. performed the syntheses and spectroscopic characterization as well as the quantum chemical calculations. R.N. and F.R. measured and interpreted the emission data. C.F. solved and refined the single crystal structures and assisted with the quantum chemical calculations. W.R.K., A.M.R. and S.F. conducted TA measurements. K.H. conceived and designed the project. F.R. and K.H. wrote the manuscript with contributions of all authors. K.H. supervised and C.F. co-supervised the project.

Conflicts of interest

There are no conflicts to declare.

Acknowledgements

This work has been financially supported by the Deutsche Forschungsgemeinschaft (DFG) under grants INST 247/1018-1, HE2778/10-2 and HE2778/15-2. W.R.K. is thankful for the support from the German Academic Scholarship Foundation and financial support from the Max Planck Graduate Center (MPGC) with the Johannes Gutenberg University of Mainz. Parts of this research were conducted using the supercomputer Elwetritsch and advisory services offered by the RPTU Kaiserslautern-Landau (https://elwe.rhrk.uni-kl.de), which is a member of the AHRP. We thank Dr. Dieter Schollmeyer and Dr. Luca M. Carrella for collecting the XRD data.

Notes and references

[1] C. Förster and K. Heinze, The Photophysics and Applications of Molecular Rubies, *Adv. Inorg. Chem.*, 2024, **83**, 111–159.

[2] A. M. May and J, L. Dempsey, A new era of LMCT: leveraging ligand-to-metal charge transfer excited states for photochemical reactions, *Chem. Sci.*, 2024, **15**, 6661–6678.

[3] N. Sinha and O. S. Wenger, Photoactive Metal-to-Ligand Charge Transfer Excited States in $3d^6$ Complexes with Cr^0, Mn^I, Fe^{II}, and Co^{III}, *J. Am. Chem. Soc.*, 2023, **145**, 4903–4920.

[4] W. R. Kitzmann and K. Heinze, Charge-Transfer and Spin-Flip States: Thriving as Complements, *Angew. Chem. Int. Ed.*, 2023, **62**, e202213207.

[5] N. Sinha, P. Yaltseva and O. S. Wenger, The Nephelauxetic Effect Becomes an Important Design Factor for Photoactive First-Row Transition Metal Complexes, *Angew. Chem. Int. Ed.*, 2023, **62**, e202303864.

[6] C. Förster and K. Heinze, Bimolecular Reactivity of 3d Metal-Centered Excited States (Cr, Mn, Fe, Co), *Chem. Phys. Rev.*, 2022, **3**, 041302.

[7] P. Dierks, Y. Vukadinovic and M. Bauer, Photoactive iron complexes: more sustainable, but still a challenge, *Inorg. Chem. Front.*, 2022, **9**, 206–220.

[8] W. R. Kitzmann, J. Moll and K. Heinze, Spin-Flip Luminescence, *Photochem. Photobiol. Sci.*, 2022, **21**, 1309–1331.

[9] W. R. Kitzmann, C. Ramanan, R. Naumann and K. Heinze, Molecular Ruby: Exploring the Excited State Landscape, *Dalton Trans.*, 2022, **51**, 6519-6525.

[10] C. Wegeberg and O. S. Wenger, Luminescent First-Row Transition Metal Complexes, *JACS Au*, 2021, **1**, 1860–1876.

[11] C. Förster and K. Heinze, Photophysics and photochemistry with Earth-abundant metals – fundamentals and concepts, *Chem. Soc. Rev.*, 2020, **49**, 1057–1070.

[12] O. S. Wenger, Photoactive Complexes with Earth-Abundant Metals, *J. Am. Chem. Soc.*, 2018, **140**, 13522−13533.

[13] L. A. Büldt and O. S. Wenger, Chromium complexes for luminescence, solar cells, photoredox catalysis, upconversion, and phototriggered NO release, *Chem. Sci.*, 2017, **8**, 7359–7367.

[14] Y. Liu, P. Persson, V. Sundström and K. Wärnmark, Fe N-Heterocyclic Carbene Complexes as Promising Photosensitizers, *Acc. Chem. Res.*, 2016, **49**, 1477–1485.

[15] B. N. Figgis and M. A. Hitchman, Ligand field theory and its applications, 2000, Wiley, Chichester.

[16] A. B. P. Lever and E. I. Solomon, Ligand Field Theory and the Properties of Transition Metal Complexes in Inorganic Electronic Structure and Spectroscopy, 1999, Vol. I, (Ed. E. I. Solomon, A. B. P. Lever), 1–91, John Wiley & Sons, Inc.

[17] J. K. McCusker, Electronic structure in the transition metal block and its implications for light harvesting, *Science*, 2019, **363**, 484–488.

[18] P. M. Kraus, M. Zürch, S. K. Cushing, D. M. Neumark and S. R. Leone, The ultrafast X-ray spectroscopic revolution in chemical dynamics, *Nat. Rev. Chem.*, 2018, **2**, 82–94.

[19] K. J. Gaffney, Capturing photochemical and photophysical transformations in iron complexes with ultrafast X-ray spectroscopy and scattering, *Chem. Sci.*, 2021, **12**, 8010–8025.

[20] L. Lindh, T. Pascher, S. Persson, Y. Goriya, K. Wärnmark, J. Uhlig, P. Chábera, P. Persson, A. Yartsev, Multifaceted Deactivation Dynamics of Fe(II) N-Heterocyclic Carbene Photosensitizers, *J. Phys. Chem. A*, 2023, **127**, 10210–10222.

[21] M. E. Reinhard, B. K. Sidhu, I. B. Lozada, N. Powers-Riggs, R. J. Ortiz, H. Lim, R. Nickel, J. van Lierop, R. Alonso-Mori, M. Chollet, L. B. Gee, P. L. Kramer, T. Kroll, S. L. Raj, T. B. van Driel, A. A. Cordones, D. Sokaras, D. E. Herbert and K. J. Gaffney, Time-Resolved X-ray Emission Spectroscopy and Synthetic High-Spin Model Complexes Resolve Ambiguities in Excited-State Assignments of Transition-Metal Chromophores: A Case

Study of Fe-Amido Complexes, *J. Am. Chem. Soc.*, 2024, **146**, 17908–17916.

[22] J. N. Schrauben, K. L. Dillman, W. F. Beck and J. K. McCusker, Vibrational coherence in the excited state dynamics of $Cr(acac)_3$: probing the reaction coordinate for ultrafast intersystem crossing, *Chem. Sci.*, 2010, **1**, 405–410.

[23] B. C. Paulus and J. K. McCusker, On the use of vibronic coherence to identify reaction coordinates for ultrafast excited-state dynamics of transition metal-based chromophores. *Faraday Discuss.*, 2022, **237**, 274–299.

[24] S. Otto, M. Grabolle, C. Förster, C. Kreitner, U. Resch-Genger and K. Heinze, $[Cr(ddpd)_2]^{3+}$: a molecular, water-soluble, highly NIR-emissive ruby analogue, *Angew. Chem. Int. Ed.*, 2015, **54**, 11572–11576.

[25] C. Wang, S. Otto, M. Dorn, E. Kreidt, J. Lebon, L. Sršan, P. Di Martino-Fumo, M. Gerhards, U. Resch-Genger, M. Seitz and K. Heinze, Deuterated Molecular Ruby with Record Luminescence Quantum Yield, *Angew. Chem. Int. Ed.*, 2018, **57**, 1112–1116.

[26] S. Otto, C. Förster, C. Wang, U. Resch-Genger and K. Heinze, A strongly luminescent chromium(III) complex acid, *Chem. Eur. J.*, 2018, **24**, 12555–12563.

[27] S. Treiling, C. Wang, C. Förster, F. Reichenauer, J. Kalmbach, P. Boden, J. P. Harris, L. Carrella, E. Rentschler, U. Resch-Genger, C. Reber, M. Seitz, M. Gerhards and K. Heinze, Luminescence and Light-driven Energy and Electron Transfer from an Exceptionally Long-lived Excited State of a Non-innocent Chromium(III) Complex, *Angew. Chem. Int. Ed.*, 2019, **58**, 18075–18085.

[28] J.-R. Jiménez, B. Doistau, C. M. Cruz, C. Besnard, J. M. Cuerva, A. G. Campaña and C. Piguet, Chiral Molecular Ruby $[Cr(dqp)_2]^{3+}$ with Long-Lived Circularly Polarized Luminescence, *J. Am. Chem. Soc.*, 2019, **141**, 13244.

[29] F. Reichenauer, C. Wang, C. Förster, P. Boden, N. Ugur, R. Báez-Cruz, J. Kalmbach, L. M. Carrella, E. Rentschler, C. Ramanan, G. Niedner-Schatteburg, M. Gerhards, M. Seitz, U. Resch-Genger and K. Heinze, Strongly Red-Emissive Molecular Ruby $[Cr(bpmp)_2]^{3+}$ surpasses $[Ru(bpy)_3]^{2+}$, *J. Am. Chem. Soc.*, 2021, **143**, 11843–11855.

[30] J.-R. Jiménez, M. Poncet, S. Míguez-Lago, S. Grass, J. Lacour, C. Besnard, J. M. Cuerva, A. G Campaña and C. Piguet, Bright Long-Lived Circularly Polarized Luminescence in Chiral Chromium(III) Complexes, *Angew. Chem. Int. Ed.*, 2021, **60**, 10095–10102.

[31] S. Otto, N. Scholz, T. Behnke, U. Resch-Genger and K. Heinze, Thermo-Chromium: A Contactless Optical Molecular Thermometer, *Chem. Eur. J.*, 2017, **23**, 12131–12135.

[32] S. Otto, A. M. Nauth, E. Ermilov, N. Scholz, A. Friedrich, U. Resch-Genger, S. Lochbrunner, T. Opatz and K. Heinze, Photo-Chromium: Sensitizer for Visible Light-Induced Oxidative C-H Bond Functionalization – Electron or Energy Transfer? *ChemPhotoChem*, 2017, **1**, 344–349.

[33] S. Otto, J. Harris, K. Heinze and C. Reber, Molecular ruby under pressure, *Angew. Chem. Int Ed.*, 2018, **57**, 11069–11073.

[34] C. Wang, S. Otto, M. Dorn, K. Heinze and U. Resch-Genger, Luminescent TOP Nanosensors for Simultaneously Measuring Temperature, Oxygen, and pH at a Single Excitation Wavelength, *Anal. Chem.*, 2019, **91**, 2337–2344.

[35] C. Dee, F. Zinna, W. R. Kitzmann, G. Pescitelli, K. Heinze, L. Di Bari and M. Seitz, Strong Circularly Polarized Luminescence of an Octahedral Chromium(III) Complex, *Chem. Commun.*, 2019, **55**, 13078–13081.

[36] L. Stein, C. Wang, C. Förster, U. Resch-Genger and K. Heinze, Bulky Ligands protect Molecular Ruby from Oxygen Quenching, *Dalton Trans.*, 2022, **51**, 17664–17670.

[37] C. Wang, W. R. Kitzmann, F. Weigert, C. Förster, X. Wang, K. Heinze and U. Resch-Genger, Matrix Effects on Photoluminescence and Oxygen Sensitivity of a Molecular Ruby, *ChemPhotoChem*, 2022, **6**, e202100296.

[38] C. Wang, F. Reichenauer, W. R. Kitzmann, C. Kerzig, K. Heinze and U. Resch-Genger, Efficient Triplet-Triplet Annihilation Upconversion Sensitized by a Chromium(III) Complex via an Underexplored Energy Transfer Mechanism, *Angew. Chem. Int. Ed.*, 2022, **61**, e202202238.

[39] T. H. Bürgin, F. Glaser, O. S. Wenger, Shedding Light on the Oxidizing Properties of Spin-Flip Excited States in a Cr^{III} Polypyridine Complex and Their Use in Photoredox Catalysis, *J. Am. Chem. Soc.*, 2022, **144**, 14181–14194.

[40] S. Sittel, R. Naumann and K. Heinze, Molecular Rubies in Photoredox Catalysis, *Front. Chem.*, 2022, **10**, 887439.

[41] S. Sittel, A. C. Sell, K. Hofman, C. Wiedemann, J. P. Nau, C. Kerzig, G. Manolikakes, K. Heinze, Visible-Light Induced Fixation of SO2 into Organic Molecules with Polypyridine Chromium(III) Complexes, *Chem. Cat. Chem.*, 2023, **15**, e202201562.

[42] C. Wang, H. Li, T. H. Bürgin and O. S. Wenger, Cage escape governs photoredox reaction rates and quantum yields. *Nat. Chem.*, 2024, **16**, 1151–1159.

[43] Y. Tanabe and S. Sugano, On the Absorption Spectra of Complex Ions. I, *J. Phys. Soc. Jpn.*, 1954, **9**, 753–766.

[44] Y. Tanabe and S. Sugano, On the Absorption Spectra of Complex Ions. II, *J. Phys. Soc. Jpn.*, 1954, **9**, 766–779.

[45] J.-R. Jiménez, M. Poncet, B. Doistau, C. Besnard and C. Piguet, Luminescent polypyridyl heteroleptic Cr^{III} complexes with high quantum yields and long excited state lifetimes, *Dalton Trans.*, 2020, **49**, 13528–13532.

[46] N. Sinha, J.-R. Jiménez, B. Pfund, A. Prescimone, C. Piguet and O. S. Wenger, A Near-Infrared-II Emissive Chromium(III) Complex, *Angew. Chem. Int. Ed.*, 2021, **60**, 23722–23728.

[47] L. Stein, P. Boden, R. Naumann, C. Förster, G. Niedner-Schatteburg and K. Heinze, The overlooked NIR luminescence of $Cr(ppy)_3$, *Chem. Commun.*, 2022, **58**, 3701–3704.

[48] N. Sawicka, C. J. Craze, P. N. Horton, S. J. Coles, E. Richards and S. J. A. Pope, Long-lived, near-IR emission from Cr(III) under ambient conditions, *Chem. Commun.*, 2022, **58**, 5733–5736.

[49] J. Chong, C. Besnard, C. M. Cruz, C. Piguet and J.-R. Jiménez Heteroleptic mer-[Cr(N∩N∩N)(CN)$_3$] complexes: synthetic challenge, structural characterization and photophysical properties, *Dalton Trans.*, 2022, **51**, 4297–4309.

[50] Y. Cheng, Q. Yang, J. He, W. Zou, K. Liao, X. Chang, C. Zou and W. Lu, The energy gap law for NIR-phosphorescent Cr(III) complexes. *Dalton Trans.*, 2023, **52**, 2561–2565.

[51] L. Stein, C. Förster and K. Heinze, Luminescent Cyclometalated Chromium(III) Complexes, *Organometallics*, 2024, **43**, 1766–1774.

[52] R. W. Jones, R. A. Cowin, I. I. Ivalo. D. Chekulaev, T. M. Roseveare, C. R. Rice, J. A. Weinstein, P. I. P. Elliott and P. A. Scattergood, A Near-Infrared Luminescent Cr(III) N-Heterocyclic Carbene Complex, *Inorg. Chem.*, 2024, **63**, 8526–8530.

[53] R. A. Forman, G. J. Piermarini, J. D. Barnett, S. Block, Pressure Measurement Made by the Utilization of Ruby Sharp-Line Luminescence. *Science*, 1972, **176**, 284–285.

[54] C. Förster, H. Osthues, D. Schwab, N. L. Doltsinis and K. Heinze, Quantum Chemical Study of the Pressure-dependent Phosphorescence of [Cr(ddpd)$_2$]$^{3+}$ in the Solid State, *ChemPhysChem*, 2023, **24**, e202300165.

[55] C. M. Marian, Understanding and Controlling Intersystem Crossing in Molecules, *Annu. Rev. Phys. Chem.*, 2021, **72**, 617–640.

[56] T. J. Penfold, E. Gindensperger, C. Daniel and C. M. Marian, Spin-Vibronic Mechanism for Intersystem Crossing, *Chem. Rev.*, 2018, **118**, 6975–7025.

[57] R. W. Jones, A. J. Auty, G. Wu, P. Persson, M. V. Appleby, D. Chekulaev, C. R. Rice, J. A. Weinstein, P. I. P. Elliott and P. A. Scattergood, Direct Determination of the Rate of Intersystem Crossing in a Near-IR Luminescent Cr(III) Triazolyl Complex, *J. Am. Chem. Soc.*, 2023, **145**, 12081–12092.

[58] O. Laporte and W. F. Meggers, Some rules of spectral structure, *J. Opt. Soc. Am.*, 1925, **11**, 459–463.

[59] H. U. Guedel and T. R. Snellgrove, Jahn-Teller effect in the $^4T_{2g}$ state of chromium(III) in dicesium sodium indium(III) hexachloride, *Inorg. Chem.*, 1978, **17**, 1617–1620.

[60] R. B. Wilson and E. I. Solomon, Spectroscopic Studies of the Photoactive $^4T_{2g}$ Excited State of Hexaamminechromium(III). *Inorg. Chem.*, 1978, **17**, 1729–1736.

[61] I. B. Bersuker, Pseudo-Jahn–Teller Effect—A Two-State Paradigm in Formation, Deformation, and Transformation of Molecular Systems and Solids, *Chem. Rev.*, 2013, **113**, 1351–1390.

[62] V. L. Ermolaev and E. B. Sveshnikova, The application of luminescence-kinetic methods in the study of the formation of lanthanide ion complexes in solution, *Russ. Chem. Rev.*, 1994, **63**, 905–922.

[63] E. Kreidt, C. Kruck, M. Seitz, Nonradiative Deactivation of Lanthanoid Luminescence by Multiphonon Relaxation in Molecular Complexes, *Handbook on the Physics and Chemistry of Rare Earths*, 2018, **53**, 35–79, Elsevier.

[64] S. Balamurugan, S. Ganesan, S. Kamaraj, V. Mathew, J. Kim, N. Arumugam and A. I. Almansour, Effect of poly (ethylene glycol) gel polymer electrolyte consist of novel heteroleptic cobalt redox shuttle and pyridine based organic additive on performance of dye sensitized solar cells, *Optical Materials*, 2022, **125**, 112082.

[65] C. M. Brown, N. E. Arsenault, T. N. K. Cross, D. Hean, Z. Xu and M. O. Wolf, Structural, electrochemical and photophysical behavior of Ru(II) complexes with large bite angle sulfur-bridged terpyridyl ligands, *Inorg. Chem. Front.*, 2020, **7**, 117–127.

[66] M. Nieger, E. Niecke and C. Volkholz CCDC 258237: Experimental Crystal Structure Determination, 2005, DOI: 10.5517/cc8nq7v.

[67] C. Förster, M. Dorn, T. Reuter, S. Otto, G. Davarci, T. Reich, L. Carrella, E. Rentschler and K. Heinze, Ddpd as expanded terpyridine: dramatic effects of symmetry and electronic properties in first row transition metal complexes, *Inorganics*, 2018, **6**, 86.

[68] S. J. Dunne, E. I. von Nagy-Felsobuki and M. F. Mackay, 2,2'-Oxybispyridine and 2,2'-Selenobispyridine. *Acta Cryst.*, 1995, **C51**, 1454–1457.

[69] P.-S. Wang, C.-K. Liang and M.-k. Leung, An improved Ullmann–Ukita–Buchwald–Li conditions for CuI-catalyzed coupling reaction of 2-pyridones with aryl halides, *Tetrahedron*, 2005, **61**, 2931–2939.

[70] M. J. Cook, A. R. Katritzky, P. Linda and R. D. Tack, Aromaticity and Tautomerism. Part 1. The Aromatic Resonance Energy of 2-Pyridone and the Related Thione, Methide, and Imine, *J. Chem. Soc., Perkin Trans., 2*, 1972, 1295–1301.

[71] S. Millefiori and A. Millefiori, On Tautomerism and Self-Association of 2-Pyridinol/2-Pyridone System, *Bull. Chem. Soc. Jpn.*, 1990, **63**, 2981–2984.

[72] R. D. Köhn, A. G. N. Coxon, S. Chunawat, C. Heron, S. Mihan, C. L. Lyall, S. B. Reeksting and G. Kociok-Köhn, Triazacyclohexane chromium triflate complexes as precursors for the catalytic selective olefin trimerisation and its investigation by mass spectrometry, *Polyhedron*, 2020, **185**, 114572.

[73] P. M. Becker, C. Förster, L. M. Carrella, P. Boden, D. Hunger, J. van Slageren, M. Gerhards, E. Rentschler and K. Heinze, Spin Crossover and Long-lived Excited States in a Reduced Molecular Ruby, *Chem. Eur. J.*, 2020, **26**, 7199–7204.

[74] M. Kranz, A.Witkowska, J. T. Yoke, Preparation of Labile Compounds Under Protective Conditions. Chromium(II) Salts, *Inorg. Synth.*, 2007, **6**, 144–146.

[75] R. Acevedo, G. Díaz and C. D. Flint, Normal coordinate analysis of the 25-atom system Cr(NH$_3$)$_6^{3+}$ octahedral symmetry, *Spectrochimica Acta*, 1985, **41**, 1397-1403.

[76] A. Soupart, F. Alary, J.-L. Heully, P. I.P. Elliott, I. M. Dixon, Recent progress in ligand photorelease reaction mechanisms: Theoretical insights focusing on Ru(II) ^{3}MC states, *Coord. Chem. Rev.*, 2020, **408**, 213184.

[77] A. Soupart, F. Alary, J.-L. Heully, P. I. P. Elliott, I. M. Dixon, Theoretical Study of the Full Photosolvolysis Mechanism of $[Ru(bpy)_3]^{2+}$: Providing a General Mechanistic Roadmap for the Photochemistry of $[Ru(N^N)_3]^{2+}$-Type Complexes toward Both Cis and Trans Photoproducts, *Inorg. Chem.*, 2020, **59**, 14679–14695.

[78] K. Eastham, P. A. Scattergood, D. Chu, R. Z. Boota, A. Soupart, F. Alary, I. M. Dixon, C. R. Rice, S. J. O. Hardman, P. I. P. Elliott, Not All ^3MC States Are the Same: The Role of $^3MC_{cis}$ States in the Photochemical NΛN Ligand Release from $[Ru(bpy)_2(NΛN)]^{2+}$ Complexes, *Inorg. Chem.*, 2022, **61**, 19907–19924.

[79] D. Hernández-Castillo, R. E. P. Nau, M.-A. Schmid, S. Tschierlei, S. Rau, L. González, Multiple Triplet Metal-Centered Jahn-Teller Isomers Determine Temperature-Dependent Luminescence Lifetimes in $[Ru(bpy)_3]^{2+}$, *Angew. Chem. Int. Ed.*, 2023, **62**, e202308803.

[80] M. C. Carey, S. L. Adelman and J. K. McCusker, Insights into the excited state dynamics of Fe(II) polypyridyl complexes from variable-temperature ultrafast spectroscopy, *Chem. Sci.*, 2019, **10**, 134–144.

[81] M. Blume and R. E. Watson, Theory of spin-orbit coupling in atoms II. Comparison of theory with experiment, *Proc. R. Soc. Lond. A*, 1963, **271**, 565–578.

[82] M. Mitra, O. Mrózek, M. Putscher, J. Guhl, B. Hupp, A. Belyaev, C. M. Marian and A. Steffen, Structural Control of Highly Efficient Thermally Activated Delayed Fluorescence in Carbene Zinc(II) Dithiolates, *Angew. Chem. Int. Ed.*, 2024, **63**, e202316300.

[83] S. D. Ezquerra Riega, M. E. Gutierrez Suburu, H. B. Rodríguez, B. Lantaño, M. Kleinschmidt, C. M. Marian and C. A. Strassert, A Case-Study on the Photophysics of Chalcogen-Substituted Zinc(II) Phthalocyanines, *Chem. Eur. J.*, 2024, **30**, e202304083.

[84] W. Sang-aroon, M. E. Alberto, M. Toscano and N. Russo, Chalcogen atom effect on the intersystem crossing kinetic constant of oxygen- and sulfur disubstituted heteroporphyrins, *J. Comput. Chem.*, 2024, **45**, 1322–1328.

[85] M. Mońka, D. Grzywacz, E. Hoffman, V. Ievtukhov, K. Kozakiewicz, R. Rogowski, A. Kubickia, B. Liberek, P. Bojarski and I. E. Serdiuk, Decisive role of heavy-atom orientation for efficient enhancement of spin–orbit coupling in organic thermally activated delayed fluorescence emitters, *J. Mater. Chem. C*, 2022, **10**, 11719–11729.

[86] F. Strieth-Kalthoff, M. J. James, M. Teders, L. Pitzer and F. Glorius, Energy transfer catalysis mediated by visible light: principles, applications, directions, *Chem. Soc. Rev.*, 2018, **47**, 7190–7202.

[87] M. Montalti, A. Credi, L. Prodi, M. T. Gandolfi, J. Michl and V. Balzani, *Handbook of photochemistry*, 2020, CRC/Taylor & Francis, Boca Raton.

View Article Online
DOI: 10.1039/D4SC05860G

View Article Online
DOI: 10.1039/D4SC05860G

The data supporting this article have been included as part of the ESI.

3.6 Factorizing the Nephelauxetic Effect in Heteroleptic Molecular Rubies

Authors: Florian Reichenauer, Dimitri Zorn, Robert Naumann, Christoph Förster, Katja Heinze*. * = Corresponding author.

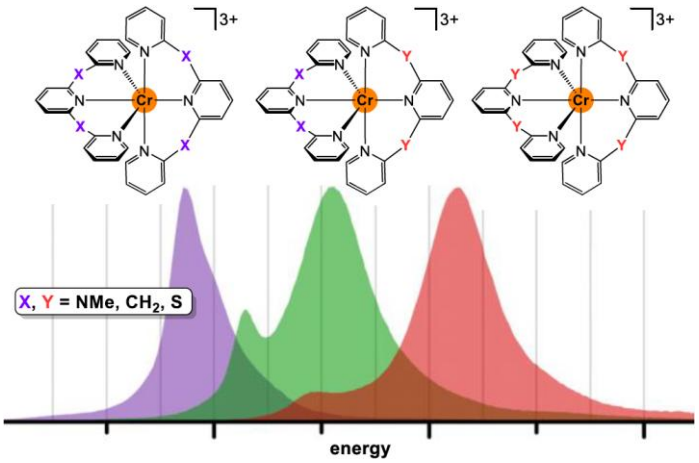

With the growing interest in luminescent chromium(III) complexes as efficient red-to-near-infrared spin-flip emitters and photocatalysts, the demand for diverse photochemical properties has also increased. The optical property tuning of spin-flip emitters was explored through a series of heteroleptic molecular rubies prepared via a novel synthetic approach. The spin-flip energies of these three complexes, when compared to their homoleptic counterparts, support the presence of an additive nephelauxetic effect among ligands in chromium(III) complexes, providing a foundation for systematic predictions of emission energies in related systems.

Authors Contributions

F. Reichenauer performed the syntheses and spectroscopic characterizations as well as the quantum chemical calculations. D. Zorn optimized and performed the HPLC purifications. F. Reichenauer and R. Naumann measured and interpreted the emission data. C. Förster solved and refined the single crystal structures and assisted with the quantum chemical calculations. K. Heinze conceived and designed the project. K. Heinze wrote the manuscript with contributions of all authors. K. Heinze supervised and C. Förster co-supervised the project.

Supporting Information

for this article can be found on pp. 321.

Factorizing the Nephelauxetic Effect in Heteroleptic Molecular Rubies

Florian Reichenauer, Dimitri Zorn, Robert Naumann, Christoph Förster and Katja Heinze*

Department of Chemistry, Johannes Gutenberg University Mainz, Duesbergweg 10-14, 55128 Mainz (Germany)

Keywords: chromium, ligand field theory, nephelauxetic effect, photophysics, spin-flip luminescence

ABSTRACT: The interest in chromium(III) complexes has been renewed over the last decade for the design of efficient earth-abundant phosphorescent red to near-infrared spin-flip emitters and photocatalysts with long excited state lifetimes. In this context, we report the energy tuning of spin-flip excited states based on heteroleptic bis(tridentate) polypyridine chromium(III) complexes $[\mathbf{3}^{X,Y}]^{3+}$, namely $[\mathbf{3}^{NMe,CH_2}]^{3+}$, $[\mathbf{3}^{NMe,S}]^{3+}$ and $[\mathbf{3}^{CH_2,S}]^{3+}$ with the tridentate ligands L^X and L^Y (X/Y = NMe, *N*,*N*'-dimethyl-*N*,*N*'-dipyridin-2-ylpyridine-2,6-diamine; X/Y = CH_2, 2,6-bis(2-pyridylmethyl)pyridine and X/Y = S, 2,6-bis(pyridine-2-ylthio)pyridine). The heteroleptic complexes $[\mathbf{3}^{X,Y}]^{3+}$ are obtained via a novel synthetic approach towards the required intermediate labile triflato complexes $Cr(L^X)(OTf)_3$ $\mathbf{2}^X$ from the respective chlorido precursors $CrCl_3(L^X)$ $\mathbf{1}^X$ using trimethylsilyl trifluoromethanesulfonate. Spin-flip energies were experimentally detected by Vis/NIR absorption and emission spectroscopy as well as computationally derived by multi-reference calculations. Together with the known homoleptic molecular ruby complexes, the three resulting series of luminescent complexes $[\mathbf{3}^{X,X}]^{3+}/[\mathbf{3}^{X,Y}]^{3+}/[\mathbf{3}^{Y,Y}]^{3+}$ allow delineating an additive nephelauxetic effect of the ligands with chromium(III) ions and thus predicting spin-flip emission energies of derived molecular rubies.

INTRODUCTION

Pseudo-octahedral polypyridine chromium(III) complexes exhibit interesting photophysical and photochemical properties and stand out among the photoactive first row transition metal complexes with a partially filled d shell.[1-9] Chromium(III) ions in a strong ligand field possess doublet excited states (of ^2E and $^2T_1$ parentage in octahedral symmetry), which can display long-lived red to near infrared spin-flip (SF) emission.[5-9] With the breakthrough development of strongly emissive chromium(III) complexes (molecular rubies),[10-16] this field has been revitalized and a wealth of applications ranging from sensing, upconversion, circularly polarized luminescence and photocatalysis has already been reported in the last decade.[14-29]

While temperature or the environment (solid, solution) has only a negligible influence on SF state energies,[17,24] shifting the $^2E/^2T_1$ excited states to lower energy by pressure has been demonstrated[19,30] exploiting the nephelauxetic ("cloud-expanding") effect[31] as described in ligand field theory by the Racah parameters.[32-35] The nephelauxetic effect describes the expansion of the electron cloud around the metal center relative to the free metal ion due to covalent bonding with the ligand.[32,33] This reduces interelectronic repulsion and diminishes the impact of exchange interactions across states of different multiplicities. In chromium(III) complexes, for example, this effect results in consistent but variable stabilization of the $^4A_2$ ground state relative to the ^2E and $^2T_1$ excited states modulating transition energies. Expectedly, different metal ions such as vanadium or molybdenum instead of chromium strongly shift the SF energies to the NIR-II spectral region.[8,36-38] Similarly but less strongly, carbon- and anionic nitrogen-based donors (cyanide, aryl, carbene, amide, carbazolate) shift the chromium(III) SF emission bands to lower energy compared to pyridine donors. This has been ascribed to the different covalency of the chromium-ligand bonds.[39-46] Heteroleptic complexes comprising strongfield tpy, ddpd, dqp and cyanido ligands (Scheme 1; tpy = 2,2';6',2''-terpyridine, ddpd = *N*,*N*'-dimethyl-*N*,*N*'-dipyridin-2-ylpyridine-2,6-diamine, dqp = 2,6-di(quinolin-8-yl)pyridine) appear to have intermediate SF emission energies with respect to their homoleptic counterparts.[39,43,47]

Scheme 1. Luminescent heteroleptic chromium(III) complexes with strongfield ligands.[39,43,47]

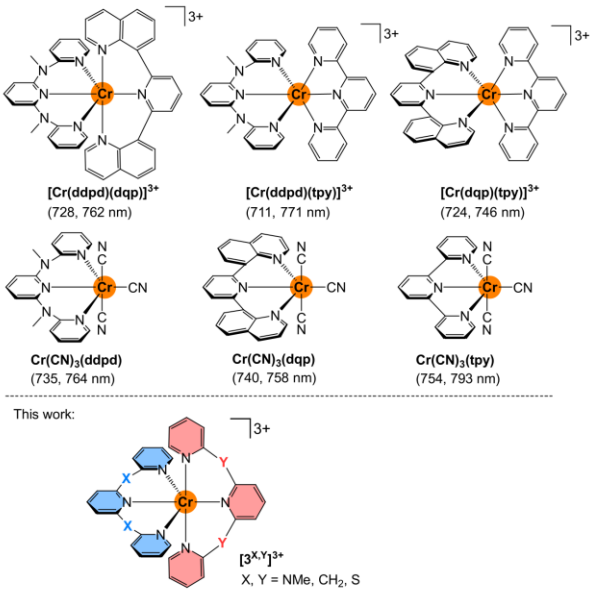

However, heteroleptic complexes with tpy or cyanides display only small photoluminescence quantum yields reducing their applicability.[7] Furthermore, the photoluminescence energy of these heteroleptic complexes cannot be predicted from the data of the homoleptic complexes.[39,43,47] The emission energy of the ddpd/dqp complex $[Cr(ddpd)(dqp)]^{3+}$ [39] (Scheme 1) on the other hand is close to the average emission energy of the homoleptic complexes $[Cr(ddpd)_2]^{3+}$ and $[Cr(dqp)_2]^{3+}$.[10,14] We had previously shown that the rather remote bridging unit between pyridines affects the SF state energies of molecular rubies mainly via geometrical rather than electronic effects.[10,15,48] Semi-quantitative correlations for the SF emission energy of heteroleptic molecular rubies have not yet been delineated.

In order to identify whether the SF energies of a heteroleptic chromium(III) complex can be predicted from the SF energies of the parent homoleptic complexes within a structurally similar series, we developed a synthetic route to heteroleptic chromium(III) complexes based on the molecular ruby motif. The tridentate ligands L^X merely differ in the bridging units between coordinating pyridines but share the same pyridine bonding mode to chromium(III) ions. With the tridentate ligands L^X (ddpd, X = NMe;[24,49] bpmp = 2,6-bis(2-pyridylmethyl)pyridine, X = CH_2;[50] bptp = 2,6-bis(pyridine-2-ylthio)pyridine, X = S[51,52]) and their previously reported homoleptic complexes $[\mathbf{3}^{X,X}]^{3+}$ ($[Cr(ddpd)_2]^{3+}$ [10], $[Cr(bpmp)_2]^{3+}$ [15] and $[Cr(bptp)_2]^{3+}$ [48]) spanning SF emission maxima from 709–775 nm (14100–12900 cm^{-1}), we now discuss the photoluminescence properties of the three possible heteroleptic complexes $[\mathbf{3}^{XY}]^{3+}$ giving three series of molecular rubies $[\mathbf{3}^{XX}]^{3+}/[\mathbf{3}^{XY}]^{3+}/[\mathbf{3}^{YY}]^{3+}$ with X/Y = NMe, CH_2 and S. The experimental data on the SF states are substantiated by quantum chemical multi-reference calculations. Furthermore, we describe a novel general approach towards heteroleptic chromium(III) complexes avoiding AgOTf or HOTf, which are typically employed reagents for halide abstraction to form triflate intermediate complexes[53,54] on the way to heteroleptic chromium(III) complexes.[55-61]

RESULTS AND DISCUSSION

Synthesis and Characterization of the heteroleptic chromium(III) complexes. Coordination of a single tridentate pyridine ligand L^X to chromium(III) is straightforward starting from $CrCl_3{\times}6H_2O$ or $CrBr_3{\times}6H_2O$ and L^X, which has been reported previously for tpy,[54] L^{NMe},[43,61] and L^{CH_2}.[15] The green chlorido intermediates $CrCl_3(L^X)$ $\mathbf{1}^X$ form in yields above 80% (Scheme 2; X = NMe, CH_2, S). Sequential coordination of different tridentate pyridine ligands to chromium(III) relies on the formation of labile chromium(III) triflato intermediates. These can be obtained from the halido complexes as pioneered by Kane-Maguire for heteroleptic tris(bidentate) chromium(III) complexes using AgOTf and/or HOTf as halide scavengers.[53,54] This strategy for heteroleptic chromium(III) complexes has also been adapted by the groups of Damrauer,[55] Constable[56-58] and Piguet.[43,39,47,59-61] While chromium(III) halido complexes such as CrX_3(tpy) and CrX_3(bpmp) can be treated with HOTf to form $Cr(OTf)_3$(tpy/bpmp) and HCl, more basic polypyridine ligands like ddpd require AgOTf for halide abstraction.[39,47,61] Yet, silver salts are occasionally incompatible with other pyridine ligands such as bpmp,[15] require the absence of light during handling and the formed silver halides are sometimes tedious to remove completely. Hence, no general and straightforward synthetic access to $Cr(L)(OTf)_3$ is available.

Here, we establish trimethylsilyl trifluoromethanesulfonate TMSOTf as generally applicable chloride abstracting agent forming trimethylsilyl chloride as volatile by-product (b.p. 66°C[62]). The desired triflato complexes $Cr(L^X)(OTf)_3$ $\mathbf{2}^X$ were straightforwardly isolated as analytically pure powders in over 80% yields (X = NMe, CH2, S). All chlorido and triflato complexes $\mathbf{1}^X$ and $\mathbf{2}^X$ were characterized by mass spectrometry, IR spectroscopy and elemental analyses (Supporting Information, Figures S1–S12). $\mathbf{2}^{NMe}$ was additionally characterized by single-crystal XRD confirming the coordination of the triflato ligands in a meridional fashion similar to $\mathbf{2}^{CH_2}$ prepared via the HOTf method[15] (Supporting Information, Figure S13).

Scheme 2. Synthesis of heteroleptic chromium(III) complexes containing tripyridine ligands with X = CH_2, NMe and S bridging units.

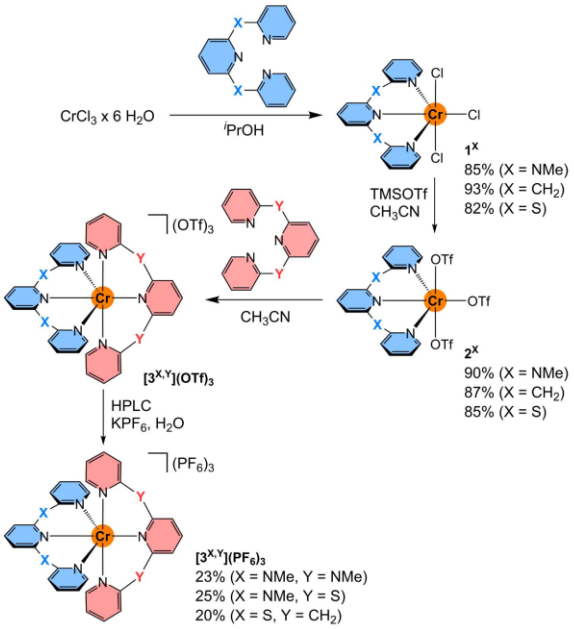

Stirring $\mathbf{2}^{X}$ with a tridentate ligand $\mathbf{L}^{Y}$ at 60°C substitutes the triflato ligands and gives the heteroleptic complexes $[\mathbf{3}^{X,Y}]^{3+}$ as triflate salts (Scheme 2). Crystals of $[\mathbf{3}^{NMe,CH_2}](\mathbf{OTf})_3$ were suitable for XRD confirming the meridional bis(tridentate) coordination of the different chelate ligands L^{NMe} and L^{CH_2} (Experimental Section, Supporting Information, Figure S20). However, emission spectroscopic analysis (see below) suggested the presence of traces of the respective homoleptic complexes in the bulk material. The amount of homoleptic complexes formed differs slightly when reversing the sequence of the coordination of the tridentate ligands L^{X} and L^{Y} (see Experimental Section). The analytically pure heteroleptic complexes were finally obtained after purification by HPLC, salt metathesis and recrystallization as hexafluorophosphate salts $[\mathbf{3}^{X,Y}](\mathbf{PF_6})_3$ (Scheme 2; Supporting Information, Figures S14–S19, S21). These carefully purified materials were used for analytical and spectroscopic characterization.

Optical characterization of the heteroleptic chromium(III) complexes. UV/Vis/NIR absorption, excitation and emission spectra of the three heteroleptic complexes $[\mathbf{3}^{X,Y}](\mathbf{PF_6})_3$ in CH_3CN are depicted in Figure 1. Absorption maxima at 446, 463 and 422 nm with $\varepsilon = 1540$, 1660 and 760 $M^{-1}\,cm^{-1}$ are observed in the visible spectral region for $[\mathbf{3}^{NMe,CH_2}]^{3+}$, $[\mathbf{3}^{NMe,S}]^{3+}$ and $[\mathbf{3}^{CH_2,S}]^{3+}$, respectively.

These bands comprise spin-allowed ligand field transitions ($^4A_2 \rightarrow {}^4T_2$; metal-centered, MC) and spin-allowed ligand-to-metal charge transfer (^{4}LMCT) transitions, according to time-dependent density functional theory (TD-DFT) calculations and charge transfer number analyses of homo- and heteroleptic complexes (Figure 1, Supporting Information, Figures S22–S27; Tables S1–S3). Energy and intensity of these bands are dominated by the LMCT component with L^{NMe} and L^{S} ligands providing bands with lower energy and higher intensity due to LMCT transitions with bridge→Cr contributions.

Three maxima including shoulders of the (five) spin-forbidden NIR absorption bands of $^4A_2 \rightarrow {}^2E$ and $^4A_2 \rightarrow {}^2T_1$ character are detected at 734/722/689 nm, 748/727/693 nm and 714/707/673 nm for $[\mathbf{3}^{NMe,CH_2}]^{3+}$, $[\mathbf{3}^{NMe,S}]^{3+}$ and $[\mathbf{3}^{CH_2,S}]^{3+}$, respectively (Figure 1, Experimental Section). The molar absorption coefficients ε are below 0.5 $M^{-1}\,cm^{-1}$ due to the spin- and Laporte-forbidden[63] nature of the transitions. Excitation at the ^{4}LMCT/^{4}MC absorption maxima and throughout the visible spectral region (green excitation spectra in Figure 1) yields SF emission bands coincident with the lowest energy absorption bands, i.e. corresponding to transitions with $^2E \rightarrow {}^4A_2$ and $^2T_1 \rightarrow {}^4A_2$ character (Figure 1).

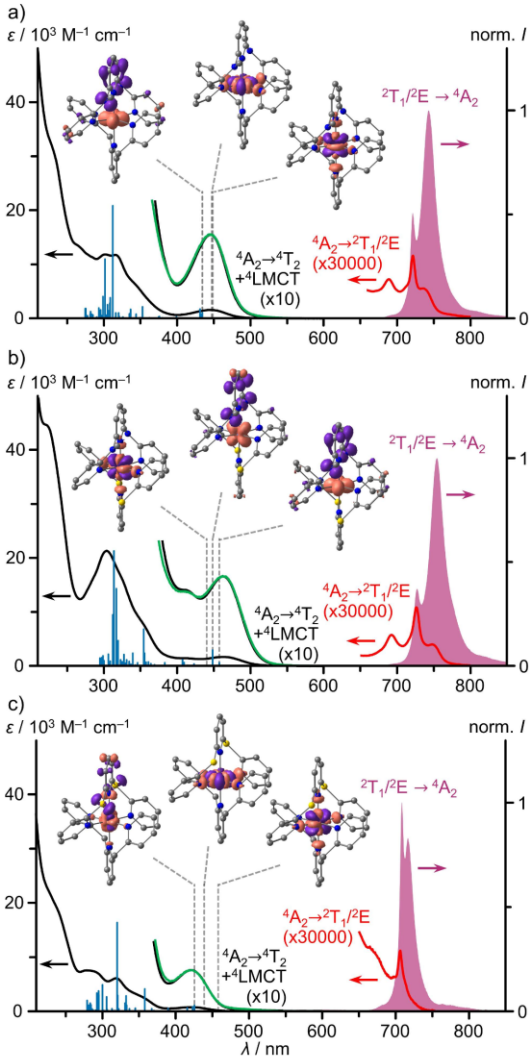

Figure 1. UV/Vis/NIR absorption spectra (black, red), excitation spectra (λ_{em} = 745, 755 and 709 nm, green) and emission spectra (λ_{exc} = 446, 463 and 422 nm, purple) of a) $[\mathbf{3}^{NMe,CH_2}]^{3+}$, b) $[\mathbf{3}^{NMe,S}]^{3+}$ and c) $[\mathbf{3}^{CH_2,S}]^{3+}$ in deaerated acetonitrile at room temperature, TD-DFT calculated oscillator strengths (blue bars) and difference electron densities of three low-energy transitions of ^{4}LMCT and ^{4}MC

character. The regions of the spin-forbidden absorption bands, the lowest energy spin allowed/LMCT absorption band and the excitation spectrum are scaled with the indicated factors.

In all three cases, the photoluminescence lifetimes $\tau^{X,Y}$ = 1170 µs, 111 µs and 8.03 µs of the heteroleptic complexes $[3^{NMe,CH2}]^{3+}$, $[3^{NMe,S}]^{3+}$ and $[3^{CH2,S}]^{3+}$ fall in between the lifetimes $\tau^{X,X}$ = 1136 µs, 1290 µs and 1.65 µs of the respective homoleptic complexes $[3^{NMe,NMe}]^{3+}$,[10,23] $[3^{CH2,CH2}]^{3+}$, [15] and $[3^{S,S}]^{3+}$ [48] (Table 1, Supporting Information, Figure S28). The photoluminescence quantum yields decrease in the series $[3^{NMe,CH2}]^{3+}$, $[3^{NMe,S}]^{3+}$ and $[3^{CH2,S}]^{3+}$ from 16.2% over 1.3% to 0.1%. While the radiative rate constants are rather similar with k_r = 140, 115 and 125 s^{-1} and comparable to those of the homoleptic complexes, the rate constants for non-radiative decay increase strongly with k_{nr} = 715, 8890 and 124410 s^{-1} in the series $[3^{NMe,CH2}]^{3+}$, $[3^{NMe,S}]^{3+}$ and $[3^{CH2,S}]^{3+}$. Hence, the radiative decay seems to be comparably independent from the bridging unit of the tridentate ligands, while the non-radiative decay is strongly affected by the type of the bridge. The effects of the bridge on k_{nr} are not linear as would have been expected if merely the energy difference between ground and emissive states would be responsible for the non-radiative decay in the present series (energy-gap law44) (Supporting Information, Figure S29). This non-linearity is expected due to the multidimensional decay pathways, comprising back-intersystem crossing to distorted excited quartet states[64-66] and multiphonon relaxation via resonant energy transfer to high energy oscillators,[11,48,67,68] and the effects of heavy-atoms (sulfur) on all non-radiative decay rates from the doublet states to the quartet ground state.[48,69-72] It is interesting to note, that the heavy atom sulfur does not seem to affect the radiative decay rate, but merely the non-radiative decay rate.

Table 1: Optical properties of homo- and heteroleptic molecular rubies $[1^{X,X}]^{3+}$ and $[1^{X,Y}]^{3+}$ in deaerated acetonitrile at room temperature.[10,15,48]

Complex	λ_{abs} / nm	λ_{em} / nm	τ_{RT} / µs	Φ_{RT} / %	k_r / s^{-1}	k_{nr} / s^{-1}
$[3^{NMe,NMe}]^{3+}$	436	738, 775	1136	13.7	120	760
$[3^{CH2,CH2}]^{3+}$	465	709	1290	11.4	90	685
$[3^{S,S}]^{3+}$	452	713, 727	1.65	0.01	60	606000
$[3^{NMe,CH2}]^{3+}$	446	722, 743	1170	16.2	140	715
$[3^{NMe,S}]^{3+}$	463	727, 755	111	1.3	115	8890
$[3^{CH2,S}]^{3+}$	422	709, 717	8.03	0.1	125	124410

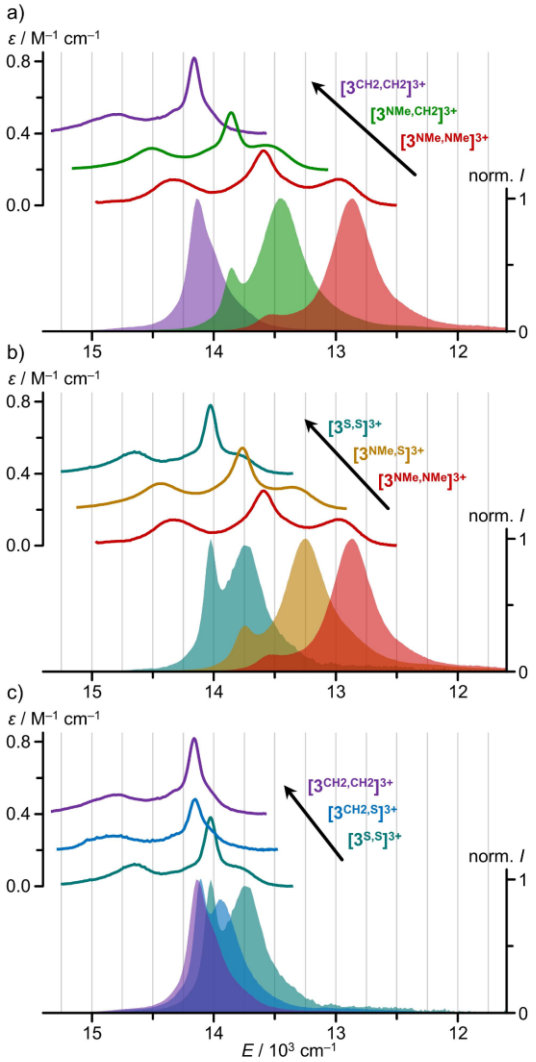

Figure 2. Baseline corrected Vis/NIR absorption spectra and normalized emission spectra of a) $[3^{NMe,CH2}]^{3+}$ (green), b) $[3^{NMe,S}]^{3+}$ (orange) and c) $[3^{CH2,S}]^{3+}$ (blue) along with the spectra of the respective homoleptic complexes in CH_3CN at room temperature. For clarity, the absorption spectra of $[3^{X,Y}]^{3+}$ and of one parent $[3^{X,X}]^{3+}$ complex were shifted vertically by +0.2 and +0.4 M^{-1} cm^{-1}, respectively.

The emission and Vis/NIR absorption energies of the heteroleptic complexes $[3^{NMe,CH2}]^{3+}$, $[3^{NMe,S}]^{3+}$ and $[3^{CH2,S}]^{3+}$ lie in between the emission/absorption energies of the respective homoleptic complexes $[3^{NMe,NMe}]^{3+}$,[10] $[3^{CH2,CH2}]^{3+}$,[15] and $[3^{S,S}]^{3+}$ [48] (Figure 2). In fact, the observable SF state energies of the structurally very similar heteroleptic complexes $[3^{X,Y}]^{3+}$ are well described by the average of the SF state energies of the parent complexes $[3^{X,X}]^{3+}$ and $[3^{Y,Y}]^{3+}$ with a maximum deviation of 85 cm^{-1}. This semi-quantitative correlation suggests an additive nephelauxetic effect of the present polypyridine ligands L^X coordinated to chromium(III) centers.

Quantum chemical calculations of SF states. Experimentally, the energies of all five lowest-energy SF states of the heteroleptic complexes $[3^{X,Y}]^{3+}$ derived from ^2E and $^2T_1$

terms were obtained from baseline-corrected Vis/NIR absorption spectra followed by a fit of the SF band pattern to five Voigt functions (Supporting Information, Figures S30–S32). A comparison of absorption and emission spectra with a logarithmic intensity axis is shown in the Supporting Information (Figures S33–S35). An analogous procedure had been reported for the homoleptic complexes $[\mathbf{3}^{X,X}]^{3+}$.[48] Computationally, the energies and characters of the lowest energy SF states of all complexes $[\mathbf{3}^{X,Y}]^{3+}$ were assessed by CASSCF(7,12)-SC/NEVPT2 calculations at the same level of theory at the DFT-optimized ground state geometries (B3LYP, TZVPP, ZORA, CPCM, D3BJ; identical ORCA software version; Supporting Information, Table S4). This method had been successfully employed previously for chromium(III) complexes and their almost nested doublet states.[15,48] With a common empirical scaling factor of 0.88, the five calculated doublet state energies match well to the experimentally derived ones (Supporting Information, Table S5, Figures S36–S38). In particular, the energy differences between the two lowest energy SF states and the energy differences between the lowest and highest energy SF states are reproduced very well by the calculations (Supporting Information, Table S5). These correlations give us confidence that – at least in the series of polypyridine chromium(III) complexes – the nephelauxetic effect and hence the SF state energies can be predicted with sufficient accuracy by multi-reference methods at this level of theory in reasonable amounts of time.

SUMMARY AND CONCLUSIONS

This study describes the synthesis and optical properties of heteroleptic molecular rubies, i.e. chromium(III) complexes with tridentate strong-field ligands L^X and long spin-flip excited state lifetimes of 1170 µs, 111 µs and 8.03 µs at room temperature in solution. The heteroleptic chromium(III) complexes $[Cr(L^X)(L^Y)]^{3+}$ $[\mathbf{3}^{X,Y}]^{3+}$ are prepared via triflato intermediates $Cr(L^X)(OTf)_3$, which are conveniently obtained from the parent chlorido precursors $CrCl_3(L^X)$ using trimethylsilyl trifluoromethanesulfonate as chloride scavenger instead of the commonly employed triflic acid or silver triflate. The resulting heteroleptic tricationic complexes $[\mathbf{3}^{X,Y}]^{3+}$ were purified by HPLC for accurate and reliable spectroscopic measurements. Detailed spectroscopic and computational analyses suggest that the energies of the lowest energy spin-flip states are described by additive nephelauxetic effects of the respective ligands. Within this structurally similar series of chromium(III) complexes, the nephelauxtic effects of the ligands L^X/L^Y even add up in a semi-quantitative fashion. Quantum chemical multi-reference methods fully corroborate the spectroscopic data. These findings will allow quantum chemical predictions of the spin-flip energies of strongly emissive molecular rubies in the future. In the present complex series, the radiative rate constants are independent from the bridging units while the non-radiative rate constants are strongly affected. Combination of the ligands of the most emissive parent homoleptic molecular rubies delivers the heteroleptic complex with the highest quantum yield of 16.2% at room temperature in solution.

EXPERIMENTAL SECTION

General procedures. Unless otherwise noted, all reactions and sample preparations were performed under an argon atmosphere. Gloveboxes (UniLab/MBraun – Ar 5.0, O_2 < 1 ppm, H_2O < 0.1 ppm) were used to store and weight sensitive compounds for synthesis as well as to prepare samples that require the absence of oxygen and/or water. Reagents and dry ethanol were purchased from commercial suppliers (Acros Organics, Fischer Scientific and Sigma Aldrich) and used without further purification. Acetonitrile and petroleum ether were dried and distilled from CaH_2. The tridentate ligands L^X (X = $NMe^{24,49}$, CH_2^{50}, $S^{51,52}$) were prepared according to literature procedures. For spectroscopic measurements bis(tridendate) complexes containing the bpmp ligand were handled in 0.01 M $HClO_4$ acetonitrile solution to prevent deprotonation at the methylene bridge.[15]

HPLC purification was carried out using a setup consisting of a Jasco LC-NetII/ADC control unit, two Jasco PU-2087 Plus pumps, a Jasco CO-4060 column oven and a Jasco UV-2075 Plus absorption detector. Fractions were collected utilizing an Advantec CHF122SC fraction collector. Eluents were degassed by a Gastorr AG-42 degassing unit and subsequently mixed with a high pressure mixing unit. Analytical runs were conducted on a Macherey-Nagel EC Nucleodur HILIC column (5 µm, 4.6×250 mm), while semi-preparative separations were performed on a Macherey-Nagel VP Nucleodur HILIC column (5 µM, 21×250 mm). **IR spectra** were recorded with a Bruker Alpha FTIR spectrometer with an ATR unit containing a diamond crystal. **ESI^+ mass spectra** were measured on an Agilent 6545 HPLC-ESI-QTOF-MS spectrometer at a temperature of 275 °C for the precursor complexes and 150 °C for the bis(tridentate) complexes. The bis(tridentate) complexes were directly injected into the ion source (without HPLC) and the spectra were corrected using a background measurement of the pure solvent. **Elemental analyses** were conducted by the central analytic service of the Department of Chemistry of the Johannes Gutenberg University Mainz using an Elementar vario EL Cube (precursors) or by the Mikroanalytisches Labor Kolbe, c/o Fraunhofer Institut UMSICHT, Oberhausen, Germany (bis(tridentate) complexes). **Absorption spectra** were measured on an Agilent Cary 5000 spectrometer in acetonitrile (Optima® LC/MS grade, Fisher Scientific) at room temperature. Measurements from 1000–200 nm were conducted using 1.00 cm path length cuvettes, while measurements of the Vis/NIR bands within 900-600 nm were performed using a 10.0 cm path length cuvette. Extinction coefficients are given at maximum absorption and for shoulders (highlighted as sh). For deconvolution of the Vis/NIR absorption band patterns, the spectra were baseline corrected using a biexponential function to model the tailing of higher energy bands:

$$\varepsilon(\tilde{\nu}) = \varepsilon_0 + A_1 e^{\frac{\tilde{\nu}-\tilde{\nu}_0}{t_1}} + A_2 e^{\frac{\tilde{\nu}-\tilde{\nu}_0}{t_2}}$$

Deconvolution of the baseline corrected spectra was achieved with five Voigt functions using the Origin94 software package. **Steady-state emission and excitation spectra** were recorded with a spectrofluorometer FS5 from

Edinburgh Instruments equipped with a cooled photomultiplier detector and a xenon arc lamp Xe2 (150 W) or with a FLS1000 spectrometer from Edinburgh Instruments equipped with a cooled photomultiplier detector PMT-980 and a xenon arc lamp Xe2 (450 W) under an argon atmosphere in acetonitrile (Optima® LC/MS grade, Fisher Scientific) at room temperature. The FS5 spectrofluorometer war also used for reaction monitoring and identification of HPLC fractions. **Time-resolved luminescence experiments** were conducted with the FLS1000 spectrometer using a pulsed diode laser VPL-450 as excitation source. Absolute luminescence quantum yields Φ were determined using an integrating sphere from Edinburgh Instruments with a relative uncertainty of Φ estimated as ±10%. **DFT calculations** were performed using the quantum computing suite ORCA 5.0.4.[73] Geometry optimization was performed using unrestricted Kohn-Sham orbitals DFT (UKS) and the B3LYP functional[74-76] in combination with Ahlrich's split valance triple-zeta basis set ZORA-def2-TZVPP[77] and the SARC/J auxiliary basis set for all atoms. Tight convergence criteria were chosen for DFT calculations (keywords *tightscf* and *tightopt*). All DFT calculations make use of the resolution of identity (Split-RI-J) approach for the Coulomb term in combination with the chain-of-spheres approximation for the exchange term (keyword *RIJCOSX*).[78,79] The zeroth order regular approximation was used to describe relativistic effects in all calculations (keyword *ZORA*).[80-82] To account for solvent effects, a conductor-like screening model (keyword *CPCM(acetonitrile)*) modelling acetonitrile was used in all calculations.[83,84] Atom-pairwise dispersion correction was performed with the Becke-Johnson damping scheme (keyword *D3BJ*).[85,86] A numerical frequency calculation confirmed that the optimized geometry corresponds to a minimum structure. Explicit counter ions and/or solvent molecules were neglected. Fifty vertical spin-allowed transitions were calculated by TD-DFT. The charge transfer number analyses of the TD-DFT calculated transitions were done using TheoDORE 2.4.[87,88] All calculations were computed on the Elwetritsch supercomputer at RPTU Kaiserslautern-Landau (hpc.rz.rptu.de). This is a member of the AHRP (Alliance for High Performance Computing Rhineland-Palatinate). **CASSCF(x,y)-SC-NEVPT2 calculations** with respect to pure metal-centered states were performed using the complete-active-space self-consistent field (CASSCF) method[89,90] in conjunction with the strongly contracted N electron valence perturbation theory to second order (SC-NEVPT2)[91-93] in order to recover missing dynamic electron correlation. All electronic states are classified by irreducible representations of the O point group, in spite of the lower actual symmetry of the considered complexes. The active space (7,12) comprising of five d-orbitals, two occupied σ bonding orbitals and five unoccupied d orbitals of a second d-shell[94] was considered for all CASSCF calculations including ten quartet and ten doublet roots. The geometries of the DFT optimized $^4A_2$ states were used for the calculations. For quantitative comparison with the experimental doublet energies derived from the deconvoluted Vis/NIR absorption bands, the calculated energies were scaled using a common empirical scaling factor of 0.884, which was obtained by averaging the ratios of the maxima of the Voigt functions to the calculated SF state energies. Intensity data for **crystal structure determinations** were collected with a STOE IPDS-2T diffractometer from STOE & CIE GmbH with an Oxford cooling using Mo-K_α radiation (λ = 0.71073 Å). The diffraction frames were integrated using the STOE X-Area software package[95] and were corrected for absorption with MULABS[96] of the PLATON software package.[97] The structures were solved with SHELXT[98] and refined by the full-matrix method based on F^2 using SHELXL[99] of the SHELX[100] software package and the ShelXle[101] graphical interface. All non-hydrogen atoms were refined anisotropically, while the positions of all hydrogen atoms were generated with appropriate geometric constraints and allowed to ride on their respective parent atoms with fixed isotropic thermal parameters. Crystallographic data for the structures reported in this paper have been deposited with the Cambridge Crystallographic Data Centre as supplementary publication no. CCDC-2386545 for $\mathbf{2}^{\mathbf{NMe}}$ and no. CCDC-2386546 for $[\mathbf{3}^{\mathbf{CH_2,NMe}}](\mathbf{OTf})_3$.

Synthesis of chlorido complexes $CrCl_3(L^X)$ $\mathbf{1}^X$ (procedure adapted from ref. 47): Under ambient conditions, a pale yellow solution of the ligand L^X (18.8 mmol, 1.0 eq.) in isopropanol (100 mL) was combined with a deep green solution of chromium(III) chloride hexahydrate (5.00 g, 18.8 mmol, 1.0 eq.) in isopropanol (200 mL). Upon heating the mixture to 60–70 °C, a green solid precipitated within 15 minutes. The green suspension was then heated at 82 °C for 16 hours. After cooling to room temperature, the suspension was filtered and washed with isopropanol (3×50 mL), methanol (3×50 mL), acetonitrile (50 mL) and diethyl ether (2×50 mL). The green powder $\mathbf{1}^X$ was dried under reduced pressure.

$CrCl_3(\mathbf{1}^{NMe})$: The single crystal XRD of this complex had been reported before.[61] Ligand L^{NMe} (5.47 g, 18.8 mmol) yielded green powder $\mathbf{1}^{NMe}$ (7.19 g, 16.0 mmol, 85%). MS (ESI$^+$, CH_3CN): *m/z* (%) = 413.03 (91) $[\mathbf{1}^{NMe}–Cl]^+$, 468.03 (9) $[\mathbf{1}^{NMe}+NH_4]^+$, 472.98 (28) $[\mathbf{1}^{NMe}+Na]^+$, 488.96 (9) $[\mathbf{1}^{NMe}+K]^+$, 863.02 (5) $[(\mathbf{1}^{NMe})_2–Cl]^+$, 916.02 (28) $[(\mathbf{1}^{NMe})_2+NH_4]^+$, 920.98 (100) $[(\mathbf{1}^{NMe})_2+Na]^+$, 936.95 (20) $[(\mathbf{1}^{NMe})_2+K]^+$. IR (ATR): $\tilde{\nu}_{max}$ = 3123 (w), 2973 (w), 1595 (s), 1584 (s), 1568 (s), 1494 (s), 1470 (m), 1444 (vs), 1429 (vs), 1376 (w), 1363 (w), 1347 (s), 1316 (w), 1252 (w), 1235 (w), 1193 (w), 1165 (m), 1141 (m), 1129 (s), 1099 (m), 1087 (w), 1065 (w), 1024 (w), 1003 (w), 983 (w), 951 (m), 886 (w), 867 (w), 796 (vs), 776 (vs), 751 (s), 734 (s), 715 (w), 653 (w), 623 (w), 586 (s), 507 (w), 459 (m), 447 (m), 433 (m), 414 (w) cm^{-1}. Elemental analysis calcd. for $C_{17}H_{17}Cl_3CrN_5$: C, 45.40; H, 3.81; N, 15.57. Found: C, 46.25; H, 4.33; N, 14.85.

$CrCl_3(L^{CH_2})$ ($\mathbf{1}^{CH_2}$): Ligand L^{CH_2} (4.90 g, 18.8 mmol) yielded a dark green powder $\mathbf{1}^{CH_2}$ (7.35 g, 17.5 mmol, 93%). MS (ESI$^+$, CH_3CN): *m/z* (%) = 383.00 (33) $[\mathbf{1}^{CH_2}–Cl]^+$, 424.03 (100) $[\mathbf{1}^{CH_2}+CH_3CN]^+$, 438.01 (2) $[\mathbf{1}^{CH_2}+NH4]^+$, 440.96 (13) $[\mathbf{1}^{CH_2}+Na]^+$, 456.94 (5) $[\mathbf{1}^{CH_2}+K]^+$, 842.97 (4) $[(\mathbf{1}^{CH_2})_2–Cl+CH_3CN]^+$, 855.98 (2) $[(\mathbf{1}^{CH_2})_2+NH_4]^+$, 860.93 (13) $[(\mathbf{1}^{CH_2})_2+Na]^+$, 876.91 (4) $[(\mathbf{1}^{CH_2})_2+K]^+$. IR (ATR): $\tilde{\nu}_{max}$ = 3113

(w), 3088 (w), 2890 (w), 1604 (s), 1577 (m), 1566 (m), 1484 (m), 1458 (s), 1432 (s), 1417 (s), 1291 (m), 1238 (w), 1221 (w), 1172 (w), 1156 (w), 1131 (w), 1106 (w), 1060 (m), 1024 (m), 977 (w), 937 (m), 887 (w), 850 (m), 792 (m), 770 (vs), 739 (m), 667 (w), 651 (m), 621 (s), 604 (w), 593 (w), 555 (w), 474 (m), 458 (w), 443 (vs), 413 (m) cm^{-1}. Elemental analysis calcd. for $C_{17}H_{15}Cl_3CrN_3$: C, 48.65; H, 3.60; N, 10.01. Found: C, 49.49; H, 4.00; N, 9.46.

$CrCl_3(L^S)$ ($\mathbf{1}^S$): Ligand L^S (5.58 g, 18.8 mmol) yielded the light green powder 1^S (7.02 g, 15.4 mmol, 82%). MS (ESI$^+$, CH_3CN): *m/z* (%) = 418.92 (47) [$\mathbf{1}^S$–Cl]$^+$, 478.88 (15) [$\mathbf{1}^S$+Na]$^+$, 494.85 (6) [$\mathbf{1}^S$+K]$^+$, 934.76 (2) [($\mathbf{1}^S$)2+Na]$^+$. IR (ATR): $\tilde{\nu}_{max}$ = 3107 (w), 3064 (w), 3051 (w), 1590 (m), 1573 (w), 1559 (w), 1542 (w), 1500 (w), 1466 (m), 1436 (w), 1418 (s), 1348 (w), 1288 (w), 1207 (m), 1189 (m), 1157 (s), 1130 (s), 1100 (w), 1055 (m), 1016 (m), 1005 (m), 881 (w), 810 (w), 727 (vs), 737 (w), 725 (s), 691 (w), 635 (w), 550 (w), 521 (w), 489 (w), 445 (m), 433 (m) cm^{-1}. Elemental analysis calcd. for $C_{15}H_{11}Cl_3CrN_3S_2$: C, 39.53; H, 2.43; N, 9.22. Found: C, 39.19; H, 2.82; N, 8.84.

Synthesis of triflato complexes $Cr(L^X)(OTf)_3$ $\mathbf{2}^X$: Trimethylsilyl trifluoromethanesulfonate (10 mL, 55.3 mmol, 20 eq.) was added to a green suspension of $\mathbf{1}^X$ (2.76 mmol, 1.0 eq.) in dry acetonitrile (100 mL). Depending on the tridentate ligand L^X, a color change was observed immediately (X = NMe: yellow-brown) or upon heating the suspension (X = CH_2: purple-brown; X = S: green-brown). The mixture was heated at 82 °C for three days, then allowed to cool to room temperature. The solvent was removed using a water bath under reduced pressure (0.3 mbar, 30 °C). The crude residue was dried under reduced pressure (0.02 mbar) for 16 hours and washed with dry ethanol (2×60 mL), each time stirring for one hour, followed by decantation. The product was suspended in dry ethanol (60 mL), filtered, and the solid was washed with dry petroleum ether (2×40 mL). Drying under reduced pressure (0.02 mbar) for 24 hours yielded $\mathbf{2}^X$ as a powder.

$Cr(L^{NMe})(OTf)_3$ ($\mathbf{2}^{NMe}$): Complex $\mathbf{1}^{NMe}$ (1.24 g, 2.76 mmol) yielded the yellow powder $\mathbf{2}^{NMe}$ (1.96 g, 2.48 mmol, 90%). Yellow crystals with diffraction quality could be obtained by cooling a concentrated acetonitrile solution of $\mathbf{2}^{NMe}$ diluted with the same volume of diethyl ether to –18 °C. MS (ESI$^+$, CH_3CN): *m/z* (%) = 640.99 (73) [$\mathbf{2}^{NMe}$–OTf]$^+$, 682.02 (16) [$\mathbf{2}^{NMe}$–OTf+CH_3CN]+, 807.98 (75) [$\mathbf{2}^{NMe}$+NH_4]$^+$, 812.93 (100) [$\mathbf{2}^{NMe}$+Na]$^+$, 828.91 (31) [$\mathbf{2}^{NMe}$+K]$^+$. IR (ATR): $\tilde{\nu}_{max}$ = 2300 (w), 1606 (s), 1589 (m), 1575 (m), 1500 (s), 1451 (s), 1436 (vs), 1340 (s), 1281 (w), 1236 (s), 1201 (vs), 1140 (m), 1097 (w), 1069 (w), 999 (s), 952 (w), 869 (w), 779 (m), 749 (w), 659 (w), 632 (vs), 586 (w), 510 (w), 460 (w), 437 (w) cm^{-1}. Elemental analysis calcd. for $C_{20}H_{17}CrF_9N_3O_9S_3$: C, 30.39; H, 2.17; N, 8.86. Found: C, 30.36; H, 2.83; N, 8.78.

$Cr(L^{CH_2})(OTf)_3$ ($\mathbf{2}^{CH_2}$): Complex $\mathbf{1}^{CH_2}$ (1.16 g, 2.76 mmol) yielded the grey powder $\mathbf{2}^{CH_2}$ (1.82 g, 2.39 mmol, 87%). MS (ESI$^+$, CH_3CN): *m/z* (%) = 610.97 (42) [$\mathbf{2}^{CH_2}$–OTf]$^+$, 652.00 (11) [$\mathbf{2}^{CH_2}$–OTf+CH_3CN]$^+$, 777.96 (100) [$\mathbf{2}^{CH_2}$+NH_4]$^+$, 782.91 (58) [$\mathbf{2}^{CH_2}$+Na]$^+$, 798.89 (18) [$\mathbf{2}^{CH_2}$+K]$^+$. IR (ATR): $\tilde{\nu}_{max}$ = 1612 (w), 1581 (w), 1494 (w), 1463 (w), 1439 (w), 1427 (w), 1343 (vs), 1302 (w), 1235 (s), 1200 (vs) 1185 (vs), 1168 (s), 1157 (s), 1128 (w), 1114 (w), 1070 (w), 991 (vs), 944 (w), 931 (w), 894 (w), 850 (w), 795 (m), 780 (m), 737 (m), 658 (m), 631 (vs), 602 (w), 593 (w), 568 (w), 511 (m), 458 (m), 439 (m), 425 (m), 406 (w) cm^{-1}. Elemental analysis calcd. for $C_{20}H_{15}CrF_9N_3O_9S_3$: C, 31.59; H, 1.99; N, 5.53. Found: C, 31.49; H, 2.73; N, 5.59.

$Cr(L^S)(OTf)_3$ ($\mathbf{2}^S$): Complex $\mathbf{1}^S$ (1.26 g, 2.76 mmol) yielded the green powder $\mathbf{2}^S$ (1.87 g, 2.35 mmol, 85%). MS (ESI$^+$, CH_3CN): *m/z* (%) = 646.88 (100) [$\mathbf{2}^S$–OTf]$^+$, 687.91 (17) [$\mathbf{2}^S$–OTf+CH_3CN]$^+$. IR (ATR): $\tilde{\nu}_{max}$ = 3123 (w), 2327 (w), 2299 (w), 2253 (w), 1597 (m), 1563 (w), 1547 (w), 1474 (w), 1419 (m), 1343 (s), 1276 (m), 1234 (s), 1194 (vs), 1155 (vs), 1097 (w), 1067 (w), 1026 (vs), 979 (vs), 809 (w), 770 (s), 742 (w), 727 (m), 693 (w), 629 (vs), 595 (m), 572 (m), 511 (s), 472 (w), 450 (m), 432 (m) cm^{-1}. Elemental analysis calcd. for $C_{18}H_{11}CrF_9N_3O_9S_5$: C, 27.14; H, 1.39; N, 5.28. Found: C, 26.92; H, 1.83; N, 5.22.

Synthesis of heteroleptic complexes $[Cr(L^X)(L^Y)](PF_6)_3$ ($[\mathbf{3}^{X,Y}](PF_6)_3$): A solution of the tridentate ligand L^Y (1.00 mmol, 1.0 eq.) in dry acetonitrile (20 mL) was added dropwise to a solution of the triflato complex $\mathbf{2}^X$ (1.00 mmol, 1.0 eq.) in dry acetonitrile (100 mL). The mixture was heated at 60 °C for 16 hours, changing the solution color to orange-red. After cooling to room temperature, the solvent was removed under reduced pressure (180 mbar, 40 °C), and the residue was dried under reduced pressure (0.02 mbar) for five hours. The red-brown crude product was stirred as suspension in THF (100 mL) for ten hours, yielding a yellow solid and a red solution. The solvent was decanted and the solid residue was washed with THF (2×100 mL), each time stirring for one hour, followed by decantation. Finally, the yellow powder was filtered as a suspension in THF (50 mL), washed with diethyl ether (2×50 mL), and dried under reduced pressure (0.02 mbar) for three hours. For each ligand combination L^X/L^Y, two reaction pathways (path 1, path 2, see below) provide access to the heteroleptic complexes, both yielding a mixture of $[\mathbf{3}^{X,Y}](OTf)_3$ (main product) and the corresponding homoleptic complexes (by-products). The mixture with the higher estimated fraction of the heteroleptic complex (reaction monitoring by emission spectroscopy) was subjected to HPLC for final purification. The combined HPLC fractions were concentrated under reduced pressure to approximately 10 mL (30 mbar, 40 °C). Adding a saturated solution of potassium hexafluorophosphate in water (20 mL) precipitated a yellow solid. The powdery product $[\mathbf{3}^{X,Y}](PF_6)_3$ was filtered, washed with cooled water (10 mL) and diethyl ether (2×10 mL) and dried under reduced pressure (0.02 mbar).

$[Cr(L^{NMe})(L^{CH_2})](PF_6)_3$ ($[\mathbf{3}^{NMe,CH_2}](PF_6)_3$): Path 1: Reaction of L^{CH_2} (261 mg, 1.00 mmol) with $\mathbf{2}^{NMe}$ (791 mg, 1.00 mmol) yielded a yellow powder (352 mg). Path 2: Reaction of L^{NMe} (291 mg, 1.00 mmol) with $\mathbf{2}^{CH_2}$ (761 mg, 1.00 mmol) yielded a yellow powder (325 mg). Slow diffusion of cooled diethyl ether (fridge) into a concentrated acetonitrile solution of this mixture gave yellow crystals of $[\mathbf{3}^{NMe,CH_2}](OTf)_3$ with

diffraction quality. The product mixture of path 2 was purified by HPLC (H_2O/CH_3CN (35:65), 300 mM $[NH_4][HCO_2]$, 0.1% HCO_2H, R_t = 11.4 min). Subsequent anion metathesis yielded $[\mathbf{3}^{\mathbf{NMe,CH_2}}](\mathbf{PF_6})_3$ (236 mg, 0.23 mmol, 23%) as yellow powder. MS (ESI$^+$, CH_3CN): m/z (%) = 201.41 (68) $[\mathbf{3}^{\mathbf{NMe,CH_2}}]^{3+}$, 301.61 (15) $[\mathbf{3}^{\mathbf{NMe,CH_2}}–H]^{2+}$, 374.59 (42) $[\mathbf{3}^{\mathbf{NMe,CH_2}}+PF_6]^{2+}$, 748.18 (100) $[\mathbf{3}^{\mathbf{NMe,CH_2}}–H+PF_6]^+$, 894.15 (69) $[\mathbf{3}^{\mathbf{NMe,CH_2}}+2\times PF_6]^+$, 1062.10 (2) $[\mathbf{3}^{\mathbf{NMe,CH_2}}+3\times PF_6+Na]^+$, 1078.07 (7) $[\mathbf{3}^{\mathbf{NMe,CH_2}}+3\times PF_6+K]^+$. IR (ATR): $\tilde{\nu}_{max}$ = 3667 (w), 1609 (s), 1585 (m), 1570 (w), 1496 (m), 1451 (m), 1437 (s), 1371 (w), 1346 (w), 1298 (w), 1242 (w), 1203 (w), 1177 (w), 1141 (w), 1094 (w), 1071 (w), 1029 (w), 951 (w), 830 (vs), 805 (m), 779 (m), 751 (w), 740 (w), 658 (w), 623 (w), 584 (w), 557 (vs), 459 (w), 440 (w), 413 (w) cm^{-1}. UV/Vis/NIR (0.01 M $HClO_4$, CH_3CN): λ_{max} (ε) = 734 (0.18), 722 (0.38), 689 (0.24), 446 (1540), 342 (6440, sh), 316 (11720), 302 (11820), 265 (13460, sh), 229 (32110, sh) nm (M^{-1} cm^{-1}). Emission (0.01 M $HClO_4$, CH_3CN, room temperature): λ_{max} = 743, 722 nm (λ_{exc} = 446 nm); Φ = 16.2%. Elemental analysis calcd. for $C_{34}H_{32}CrF_{18}N_8P_3$: C, 39.28; H, 3.10; N, 10.78. Found: C, 38.93; H, 3.12; N, 10.68.

$[Cr(^{LNMe})(L^S)](PF_6)_3$ ($[\mathbf{3}^{\mathbf{NMe,S}}](\mathbf{PF_6})_3$): Path 1: Reaction of L^S (297 mg, 1.00 mmol) with $\mathbf{2}^{\mathbf{NMe}}$ (791 mg, 1.00 mmol) yielded a yellow powder (313 mg). Path 2: Reaction of L^{NMe} (291 mg, 1.00 mmol) with $\mathbf{2}^{\mathbf{S}}$ (797 mg, 1.00 mmol) yielded a yellow powder (372 mg). The product mixture of path 1 was purified by HPLC (H_2O/CH_3CN (50:50), 300 mM $[NH_4][HCO_2]$, R_t = 10.3 min). Subsequent anion metathesis yielded $[\mathbf{3}^{\mathbf{NMe,S}}](\mathbf{PF_6})_3$ (267 mg, 0.25 mmol, 25%) as yellow powder. MS (ESI$^+$, CH_3CN): m/z (%) = 213.38 (32) $[\mathbf{3}^{\mathbf{NMe,S}}]^{3+}$, 392.55 (59) $[\mathbf{3}^{\mathbf{NMe,S}}+PF_6]^{2+}$, 930.06 (100) $[\mathbf{3}^{\mathbf{NMe,S}}+2\times PF_6]^+$, 1098.01 (2) $[\mathbf{3}^{\mathbf{NMe,S}}+3\times PF_6+Na]^+$, 1113.98 (4) $[\mathbf{3}^{\mathbf{NMe,S}}+3\times PF_6+K]^+$. IR (ATR): $\tilde{\nu}_{max}$ = 2253 (w), 1605 (m), 1594 (m), 1585 (m), 1569 (m), 1545 (w), 1495 (s), 1468 (w), 1448 (m), 1433 (s), 1421 (s), 1369 (w), 1343 (m), 1320 (w), 1290 (w), 1260 (w), 1241 (w), 1204 (w), 1182 (w), 1168 (w), 1139 (m), 1094 (w), 1068 (w), 1021 (m), 950 (w), 921 (w), 879 (w), 818 (vs), 767 (vs), 750 (s), 726 (s), 689 (w), 659 (w), 650 (w), 627 (w), 584 (m), 554 (vs), 526 (s), 470 (w), 451 (w), 438 (m), 412 (w) cm^{-1}. UV/Vis/NIR (CH_3CN): λ_{max} (ε) = 748 (0.13), 727 (0.36), 693 (0.19), 463 (1660), 413 (1410, sh), 353 (7950, sh), 324 (16410, sh), 304 (21270), 222 (44580, sh) nm (M^{-1} cm^{-1}). Emission (CH_3CN, room temperature): λ_{max} = 755, 727 nm (λ_{exc} = 463 nm); Φ = 1.30%. Elemental analysis calcd. for $C_{32}H_{28}CrF_{18}N_8P_3S_2$: C, 35.73; H, 2.62; N, 10.42; S, 5.96. Found: C, 35.55; H, 2.67; N, 10.36; S, 5.93.

$[Cr(L^{CH_2})(L^S)](PF_6)_3$ ($[\mathbf{3}^{\mathbf{CH_2,S}}](\mathbf{PF_6})_3$): Path 1: Reaction of L^S (297 mg, 1.00 mmol) with $\mathbf{2}^{\mathbf{CH_2}}$ (761 mg, 1.00 mmol) yielded a yellow powder (295 mg). Path 2: Reaction of L^{CH_2} (261 mg, 1.00 mmol) with $\mathbf{2}^{\mathbf{S}}$ (797 mg, 1.00 mmol) yielded a yellow powder (335 mg). The product mixture of path 2 was purified by HPLC (H_2O/CH_3CN (35:65), 300 mM $[NH_4][HCO_2]$, 0.1% HCO_2H, R_t = 12.1 min). Subsequent anion metathesis yielded $[\mathbf{3}^{\mathbf{CH_2,S}}](\mathbf{PF_6})_3$ (206 mg, 0.20 mmol, 20%) as yellow powder. MS (ESI$^+$, CH_3CN): m/z (%) = 203.37 (13) $[\mathbf{3}^{\mathbf{CH_2,S}}]^{3+}$, 304.55 (38) $[\mathbf{3}^{\mathbf{CH_2,S}}–H]^{2+}$, 377.54 (4) $[\mathbf{3}^{\mathbf{CH_2,S}}+PF_6]^{2+}$, 754.06 (36) $[\mathbf{3}^{\mathbf{CH_2,S}}–H+PF_6]^+$, 900.03 (100) $[\mathbf{3}^{\mathbf{CH_2,S}}+2\times PF_6]^+$, 1067.98 (4) $[\mathbf{3}^{\mathbf{CH_2,S}}+3\times PF_6+Na]^+$, 1083.96 (11) $[\mathbf{3}^{\mathbf{CH_2,S}}+3\times PF_6+K]^+$. IR (ATR): $\tilde{\nu}_{max}$ = 2252 (w), 1611 (w), 1594 (w), 1577 (w), 1545 (w), 1492 (w), 1466 (w), 1420 (m), 1290 (w), 1229 (w), 1171 (w), 1135 (w), 1112 (w), 1069 (w), 1029 (w), 827 (vs), 773 (s), 741 (m), 727 (m), 689 (w), 658 (w), 622 (w), 556 (vs), 472 (w), 439 (w) cm^{-1}. UV/Vis/NIR (CH_3CN): λ_{max} (ε) = 714 (0.16, sh), 707 (0.37), 673 (0.35), 422 (760), 355 (2620, sh), 319 (6100), 290 (7300), 280 (7540), 230 (21390, sh) nm (M^{-1} cm^{-1}). Emission (CH_3CN, room temperature): λ_{max} = 717, 709 nm (λ_{exc} = 422 nm); Φ = 0.1%. Elemental analysis calcd. for $C_{32}H_{26}CrF_{18}N_6P_3S_2$: C, 36.76; H, 2.51; N, 8.04; S, 6.13. Found: C, 36.11; H, 2.55; N, 7.90; S, 6.09.

ASSOCIATED CONTENT

Supporting Information

The Supporting Information is available free of charge at xx.
Analytical and spectroscopic data, results of quantum chemical calculations (PDF)
Cartesian coordinates of optimized geometries from quantum-chemical calculations (XYZ)

AUTHOR INFORMATION

Corresponding Author

***Katja Heinze** – Department of Chemistry, Johannes Gutenberg University Mainz, Duesbergweg 10-14, 55128 Mainz (Germany); orcid.org/0000-0003-1483-4156; E-Mail: katja.heinze@uni-mainz.de

Authors

Florian Reichenauer – Department of Chemistry, Johannes Gutenberg University Mainz, Duesbergweg 10-14, 55128 Mainz (Germany)
Dimitri Zorn – Department of Chemistry, Johannes Gutenberg University Mainz, Duesbergweg 10-14, 55128 Mainz (Germany)
Robert Naumann – Department of Chemistry, Johannes Gutenberg University Mainz, Duesbergweg 10-14, 55128 Mainz (Germany); orcid.org/0000-0002-0912-7644.
Christoph Förster – Department of Chemistry, Johannes Gutenberg University Mainz, Duesbergweg 10-14, 55128 Mainz (Germany); orcid.org/0000-0003-4971-5368.
Complete contact information is available at xx

Author Contributions

F.R. performed the syntheses and spectroscopic characterizations as well as the quantum chemical calculations. D.Z. optimized and performed the HPLC purifications. F.R. and R.N. measured and interpreted the emission data. C.F. solved and refined the single crystal structures and assisted with the quantum chemical calculations. K.H. conceived and designed the project. K.H. wrote the manuscript with contributions of all authors. K.H. supervised and C.F. co-supervised the project.

Notes

The authors declare no conflict of interest.

ACKNOWLEDGMENTS

This work has been financially supported by the Deutsche Forschungsgemeinschaft (DFG) under grants INST 247/1018-1 and HE2778/10-2. Parts of this research were conducted using the supercomputer Elwetritsch and advisory services offered by the RPTU Kaiserslautern-Landau (https://elwe.rhrk.uni-kl.de), which is a member of the AHRP. We thank Dr. Dieter Schollmeyer for collecting the XRD data (CCDC no. 2386545 and 2386546) and Pascal Schmidt for collecting numerous ESI mass spectra.

REFERENCES

(1) Dorn, M.; East, N. R.; Förster, C.; Kitzmann, W. R.; Moll, J.; Reichenauer, F.; Reuter, T.; Stein, L.; Heinze, K. d-d and Charge Transfer Photochemistry of 3d Metal Complexes in Comprehensive Inorganic Chemistry III (Section Ed. V. W.-W. Yam) **2023**, 707-788. DOI: 10.1016/B978-0-12-823144-9.00063-7.

(2) Förster, C.; Heinze, K. Bimolecular Reactivity of 3d Metal-Centered Excited States (Cr, Mn, Fe, Co), *Chem. Phys. Rev.* **2022**, *3*, 041302. DOI: 10.1063/5.0112531.

(3) Wegeberg, C.; Wenger, O. S., Luminescent First-Row Transition Metal Complexes, *JACS Au* **2021**, *1*, 1860–1876. DOI: 10.1021/jacsau.1c00353.

(4) Förster, C.; Heinze, K. Photophysics and photochemistry with Earth-abundant metals – fundamentals and concepts, *Chem. Soc. Rev.* **2020**, *49*, 1057–1070. DOI: 10.1039/c9cs00573k.

(5) Wenger, O. S. Photoactive Complexes with Earth-Abundant Metals, *J. Am. Chem. Soc.* **2018**, *140*, 13522−13533. DOI: 10.1021/jacs.8b08822.

(6) Büldt, L. A.; Wenger, O. S. Chromium complexes for luminescence, solar cells, photoredox catalysis, upconversion, and phototriggered NO release, *Chem. Sci.* **2017**, *8*, 7359–7367. DOI: 10.1039/C7SC03372A.

(7) Förster, C.; Heinze, K. The Photophysics and Applications of Molecular Rubies, *Adv. Inorg. Chem.* **2024**, *83*, 111–159. DOI: 10.1016/bs.adioch.2024.01.002.

(8) Kitzmann, W. R.; Moll, J.; Heinze, K. Spin-Flip Luminescence, *Photochem. Photobiol. Sci.* **2022**, *21*, 1309–1331. DOI: 10.1007/s43630-022-00186-3.

(9) Kitzmann, W. R.; Ramanan, C.; Naumann, R.; Heinze, K. Molecular Ruby: Exploring the Excited State Landscape, *Dalton Trans.* **2022**, *51*, 6519-6525. DOI: 10.1039/D2DT00569G.

(10) Otto, S.; Grabolle, M.; Förster, C.; Kreitner, C.; Resch-Genger, U.; Heinze, K. $[Cr(ddpd)_2]^{3+}$: a molecular, water-soluble, highly NIR-emissive ruby analogue, *Angew. Chem. Int. Ed.* **2015**, *54*, 11572–11576. DOI: 10.1002/anie.201504894.

(11) Wang, C.; Otto, S.; Dorn, M.; Kreidt, E.; Lebon, J.; Sršan, L.; Di Martino-Fumo, P.; Gerhards, M.; Resch-Genger, U.; Seitz, M.; Heinze, K. Deuterated Molecular Ruby with Record Luminescence Quantum Yield, *Angew. Chem. Int. Ed.* **2018**, *57*, 1112–1116. DOI: 10.1002/anie.201711350.

(12) Otto, S.; Förster, C.; Wang, C.; Resch-Genger, U.; Heinze, K. A strongly luminescent chromium(III) complex acid, *Chem. Eur. J.* **2018**, *24*, 12555–12563. DOI: 10.1002/chem.201802797.

(13) Treiling, S.; Wang, C.; Förster, C.; Reichenauer, F.; Kalmbach, J.; Boden, P.; Harris, J. P.; Carrella, L. M.; Rentschler, E.; Resch-Genger, U.; Reber, C.; Seitz, M.; Gerhards, M.; Heinze, K. Luminescence and Light-driven Energy and Electron Transfer from an Exceptionally Long-lived Excited State of a Non-innocent Chromium(III) Complex, *Angew. Chem. Int. Ed.* **2019**, *58*, 18075–18085. DOI: 10.1002/anie.201909325.

(14) Jiménez, J.-R.; Doistau, B.; Cruz, C. M.; Besnard, C.; Cuerva, J. M.; Campaña, A. G.; Piguet, C. Chiral Molecular Ruby $[Cr(dqp)_2]^{3+}$ with Long-Lived Circularly Polarized Luminescence, *J. Am. Chem. Soc.* **2019**, *141*, 13244–13252. DOI: 10.1021/jacs.9b06524.

(15) Reichenauer, F.; Wang, C.; Förster, C.; Boden, P.; Ugur, N.; Báez-Cruz, R.; Kalmbach, J.; Carrella, L. M.; Rentschler, E.; Ramanan, C.; Niedner-Schatteburg, G.; Gerhards, M.; Seitz, M.; Resch-Genger, U.; Heinze, K. Strongly Red-Emissive Molecular Ruby $[Cr(bpmp)_2]^{3+}$ surpasses $[Ru(bpy)_3]^{2+}$, *J. Am. Chem. Soc.* **2021**, *143*, 11843–11855. DOI: 10.1021/jacs.1c05971.

(16) Jiménez, J.-R.; Poncet, M.; Míguez-Lago, S.; Grass, S.; Lacour, J.; Besnard, C.; Cuerva, J. M.; Campaña, A. G.; Piguet, C. Bright Long-Lived Circularly Polarized Luminescence in Chiral Chromium(III) Complexes, *Angew. Chem. Int. Ed.* **2021**, *60*, 10095–10102. DOI: 10.1002/anie.202101158.

(17) Otto, S.; Scholz, N.; Behnke, T.; Resch-Genger, U.; Heinze, K. Thermo-Chromium: A Contactless Optical Molecular Thermometer, *Chem. Eur. J.* **2017**, *23*, 12131–12135. DOI: 10.1002/chem.201701726.

(18) Otto, S.; Nauth, A. M.; Ermilov, E.; Scholz, N.; Friedrich, A.; Resch-Genger, U.; Lochbrunner, S.; Opatz, T.; Heinze, K. Photo-Chromium: Sensitizer for Visible Light-Induced Oxidative C-H Bond Functionalization – Electron or Energy Transfer? *ChemPhotoChem* **2017**, *1*, 344–349. DOI: 10.1002/cptc.201700077.

(19) Otto, S.; Harris, J. P.; Heinze, K.; Reber, C. Molecular ruby under pressure, *Angew. Chem. Int Ed.* **2018**, *57*, 11069–11073. DOI: 10.1002/anie.201806755.

(20) Wang, C.; Otto, S.; Dorn, M.; Heinze, K.; Resch-Genger, U. Luminescent TOP Nanosensors for Simultaneously Measuring Temperature, Oxygen, and pH at a Single Excitation Wavelength, *Anal. Chem.* **2019**, *91*, 2337–2344. DOI: 10.1021/acs.analchem.8b05060.

(21) Dee, C.; Zinna, F.; Kitzmann, W. R.; Pescitelli, G.; Heinze, K.; Di Bari, L.; Seitz, M. Strong Circularly Polarized Luminescence of an Octahedral Chromium(III) Complex, *Chem. Commun.* **2019**, *55*, 13078–13081. DOI: 10.1039/c9cc06909g.

(22) Kalmbach, J.; Wang, C.; You, Y.; Förster, C.; Schubert, H.; Heinze, K.; Resch-Genger, U.; Seitz, M. Near-IR to Near-IR Upconversion Luminescence in Molecular Chromium Ytterbium Salts. *Angew. Chem. Int. Ed.* **2020**, *59*, 18804–18808. DOI: 10.1002/anie.202007200.

(23) Stein, L.; Wang, C.; Förster, C.; Resch-Genger, U.; Heinze, K Bulky Ligands protect Molecular Ruby from Oxygen Quenching, *Dalton Trans.* **2022**, *51*, 17664–17670. DOI: 10.1039/d2dt02950b.

(24) Wang, C.; Kitzmann, W. R.; Weigert, F.; Förster, C.; Wang, X.; Heinze, K.; Resch-Genger, U. Matrix Effects on Photoluminescence and Oxygen Sensitivity of a Molecular Ruby, *ChemPhotoChem* **2022**, *6*, e202100296. DOI: 10.1002/cptc.202100296.

(25) Wang, C.; Reichenauer, F.; Kitzmann, W. R.; Kerzig, C.; Heinze, K.; Resch-Genger, U. Efficient Triplet-Triplet Annihilation Upconversion Sensitized by a Chromium(III) Complex via an Underexplored Energy Transfer Mechanism, *Angew. Chem. Int. Ed.* **2022**, *61*, e202202238. DOI: 10.1002/anie.202202238.

(26) Bürgin, T. H.; Glaser, F.; Wenger, O. S. Shedding Light on the Oxidizing Properties of Spin-Flip Excited States in a Cr^{III} Polypyridine Complex and Their Use in Photoredox Catalysis, *J. Am. Chem. Soc.* **2022**, *144*, 14181–14194. DOI: 10.1021/jacs.2c04465.

(27) Sittel, S.; Naumann, R.; Heinze, K. Molecular Rubies in Photoredox Catalysis, *Front. Chem.* **2022**, *10*, 887439. DOI: 10.3389/fchem.2022.887439.

(28) Sittel, S.; Sell, A. C.; Hofman, K.; Wiedemann, C.; Nau, J. P.; Kerzig, C.; Manolikakes, G.; Heinze, K. Visible-Light Induced Fixation of SO_2 into Organic Molecules with Polypyridine Chromium(III) Complexes, *Chem. Cat. Chem.* **2023**, *15*, e202201562. DOI: 10.1002/cctc.202201562.

(29) Wang, C.; Li, H.; Bürgin, T. H.; Wenger, O. S. Cage escape governs photoredox reaction rates and quantum yields. *Nat. Chem.* **2024**, *16*, 1151–1159. DOI: 10.1038/s41557-024-01482-4.

(30) Förster, C.; Osthues, H.; Schwab, D.; Doltsinis, N. L.; Heinze, K. Quantum Chemical Study of the Pressure-dependent Phosphorescence of $[Cr(ddpd)_2]^{3+}$ in the Solid State, *Chem. Phys. Chem.* **2023**, *24*, e202300165. DOI: 10.1002/cphc.202300165.

(31) Sinha, N.; Yaltseva, P.; Wenger, O. S. The Nephelauxetic Effect Becomes an Important Design Factor for Photoactive First-Row Transition Metal Complexes, *Angew. Chem. Int. Ed.* **2023**, *62*, e202303864. DOI: 10.1002/anie.202303864

(32) Figgis, B. N.; Hitchman, M. A. Ligand field theory and its applications. Wiley, Chichester (2000).

(33) Lever, A. B. P.; Solomon, E. I. Ligand Field Theory and the Properties of Transition Metal Complexes in Inorganic Electronic Structure and Spectroscopy, 1999, Vol. I, (Ed. E. I. Solomon, A. B. P. Lever), 1–91, John Wiley & Sons, Inc.

(34) Tanabe, Y.; Sugano, S. On the Absorption Spectra of Complex Ions. I, *J. Phys. Soc. Jpn.* **1954**, *9*, 753–766. DOI: 10.1143/JPSJ.9.753.

(35) Tanabe, Y.; Sugano, S. On the Absorption Spectra of Complex Ions. II, *J. Phys. Soc. Jpn.* **1954**, *9*, 766–779. DOI: 10.1143/JPSJ.9.766.

(36) Kitzmann, W. R.; Hunger, D.; Reponen, A.-P. M.; Förster, C.; Schoch, R.; Bauer, M.; Feldmann, S.; van Slageren, J.; Heinze, K. Electronic Structure and Excited State Dynamics of the NIR-II Emissive Molybdenum(III) Analog to the Molecular Ruby. *Inorg. Chem.* **2023**, *62*, 15797-15808. DOI: 10.1021/acs.inorgchem.3c02186.

(37) Dorn, M.; Kalmbach, J.; Boden, P.; Kruse, A.; Dab, C.; Reber, C.; Niedner-Schatteburg, G.; Lochbrunner, S.; Gerhards, M.; Seitz, M.; Heinze, K. Ultrafast and long-time excited state kinetics of an NIR-emissive vanadium(III) complex I: Synthesis, spectroscopy and static quantum chemistry. *Chem. Sci.* **2021**, *12*, 10780–10790. DOI: 10.1039/D1SC02137K.

(38) Dorn, M.; Kalmbach, J.; Boden, P.; Päpcke, A.; Gómez, S.; Förster, C.; Kuczelinis, F.; Carrella, L. M.; Büldt, L. A.; Bings, N. H.; Rentschler, E.; Lochbrunner, S.; González, L.; Gerhards, M.; Seitz, M.; Heinze, K. A vanadium(III) complex with blue and NIR-II spin-flip luminescence in solution. *J. Am. Chem. Soc.* **2020**, *142*, 7947–7955. DOI: 10.1021/jacs.0c02122.

(39) Jiménez, J.-R.; Poncet, M.; Doistau, B.; Besnard, C.; Piguet, C. Luminescent polypyridyl heteroleptic Cr^{III} complexes with high quantum yields and long excited state lifetimes, *Dalton Trans.* **2020**, *49*, 13528–13532. DOI: 10.1039/d0dt02872j.

(40) Sinha, N.; Jiménez, J.-R.; Pfund, B.; Prescimone, A.; Piguet, C.; Wenger, O. S. A Near-Infrared-II Emissive Chromium(III) Complex, *Angew. Chem. Int. Ed.* **2021**, *60*, 23722–23728. DOI: 10.1002/anie.202106398.
(41) Stein, L.; Boden, P.; Naumann, R.; Förster, C.; Niedner-Schatteburg, G.; Heinze, K. The overlooked NIR luminescence of $Cr(ppy)_3$, *Chem. Commun.* **2022**, *58*, 3701–3704. DOI: 10.1039/D2CC00680D.
(42) Sawicka, N.; Craze, C. J.; Horton, P. N.; Coles, S. J.; Richards, E.; Pope, S. J. A. Long-lived, near-IR emission from Cr(III) under ambient conditions, *Chem. Commun.* **2022**, *58*, 5733−5736. DOI: 10.1039/D2CC01434C.
(43) Chong, J.; Besnard, C.; Cruz, C. M.; Piguet, C.; Jiménez, J.-R. Heteroleptic mer-$[Cr(N\cap N\cap N)(CN)_3]$ complexes: synthetic challenge, structural characterization and photophysical properties, *Dalton Trans.* **2022**, *51*, 4297–4309. DOI: 10.1039/d2dt00126h.
(44) Cheng, Y.; Yang, Q.; He, J.; Zou, W.; Liao, K.; Chang, X.; Zou, C.; Lu, W. The energy gap law for NIR-phosphorescent Cr(III) complexes. *Dalton Trans.* **2023**, *52*, 2561−2565. DOI: 10.1039/D2DT02872G.
(45) Stein, L.; Förster, C.; Heinze, K. Luminescent Cyclometalated Chromium(III) Complexes, *Organometallics* **2024**, *43*, 1766–1774. DOI: 10.1021/acs.organomet.4c00075.
(46) Jones, R. W.; Cowin, R. A.; Ivalo I. I.; Chekulaev, D.; Roseveare, T. M.; Rice, C. R.; Weinstein, J. A.; Elliott, P. I. P.; Scattergood, P. A. A Near-Infrared Luminescent Cr(III) N-Heterocyclic Carbene Complex, *Inorg. Chem.* **2024**, *63*, 8526–8530. DOI: 10.1021/acs.inorgchem.4c01270.
(47) Jiménez, J.-R.; Doistau, B.; Besnard, C.; Piguet, C. Versatile heteroleptic bis-terdentate Cr(III) chromophores displaying room temperature millisecond excited state lifetimes. *Chem. Commun.* **2018**, *54*, 13228–13231. DOI: 10.1039/c8cc07671e.
(48) Reichenauer, F.; Naumann, R.; Förster, C.; Kitzmann, W. R.; Reponen, A.-P. M.; Feldmann, S.; Heinze, K. Bridge Editing of Spin-Flip Emitters gives Insight into Excited State Energies and Dynamics, *Chem. Sci.*, under revision.
(49) Breivogel, A.; Förster, C.; Heinze, K. A Heteroleptic Bis(tridentate)ruthenium(II) Polypyridine Complex with Improved Photophysical Properties and Integrated Functionalizability. *Inorg. Chem.* **2010**, *49*, 7052–7056. DOI: 10.1021/ic1007236.
(50) Dyker, G.; Muth, O. Synthesis of Methylene- and Methine-Bridged Oligopyridines. *Eur. J. Org. Chem.* **2004**, *2004*, 4319–4322. DOI: 10.1002/ejoc.200400435.
(51) Balamurugan, S.; Ganesan, S.; Kamaraj, S.; Mathew, V.; Kim, J.; Arumugam, N.; Almansour, A. I. Effect of poly (ethylene glycol) gel polymer electrolyte consist of novel heteroleptic cobalt redox shuttle and pyridine based organic additive on performance of dye sensitized solar cells, *Optical Materials* **2022**, *125*, 112082. DOI: 10.1016/j.optmat.2022.112082.
(52) Brown, C. M.; Arsenault, N. E.; Cross, T. N. K.; Hean, D.; Xu, Z.; Wolf, M. O. Structural, electrochemical and photophysical behavior of Ru(II) complexes with large bite angle sulfur-bridged terpyridyl ligands, *Inorg. Chem. Front.* **2020**, *7*, 117–127. DOI: 10.1039/C9QI01009B.
(53) Barker, K. D.; Barnett, K. A.; Connel, S. M.; Glaeser, J. W.; Wallace, A. J.; Wildsmith, J.; Herbert, B. J.; Wheeler, J. F.; Kane-Maguire, N. A. P. Synthesis and characterization of heteroleptic $Cr(diimine)_3^{3+}$ complexes. *Inorg. Chim. Acta* **2001**, *316*, 41–49. DOI: 10.1016/S0020-1693(01)00377-2.
(54) Donnay, E. G.; Schaeper, J. P.; Brooksbank, R. D.; Fox, J. L.; Potts, R. G.; Davidson, R. M.; Wheeler, J. F.; Kane-Maguire, N. A. P. Synthesis and characterization of tris(heteroleptic) diimine complexes of chromium(III). *Inorg. Chim. Acta* **2007**, *360*, 3272–3280. DOI: 10.1016/j.ica.2007.03.055.
(55) McDaniel, A. M.; Tseng, H.-W.; Damrauer, H. H.; Shores, M. P. Synthesis and Solution Phase Characterization of Strongly Photooxidizing Heteroleptic Cr(III) Tris-Dipyridyl Complexes. *Inorg. Chem.* **2010**, *49*, 7981–7991. DOI: 10.1021/ic1009972.
(56) Constable, E. C.; Housecroft, C. E.; Neuburger, M.; Schönle, J.; Zampese, J. A. The surprising lability of bis(2,2′:6′,2″-terpyridine)chromium(iii) complexes. *Dalton Trans.* **2014**, *43*, 7227–7235. DOI: 10.1039/C4DT00200H.
(57) Schönle, J.; Constable, E. C.; Housecroft, C. E.; Neuburger, M.; Zampese, J. A. Heteroleptic chromium(III) tris(diimine) $[Cr(N\text{^}N)_2(N'\text{^}N')]^{3+}$ complexes. *Inorg. Chem. Commun.* **2015**, *51*, 75–77. DOI: 10.1016/j.inoche.2014.11.012.
(58) Schönle, J.; Constable, E. C.; Housecroft, C. E.; Prescimone, A.; Zampese, J. A. Homoleptic and heteroleptic complexes of chromium(III) containing 4'-diphenylamino-2,2':6',2''-terpyridine ligands. *Polyhedron* **2015**, *89*, 182–188. DOI: 10.1016/j.poly.2015.01.015.
(59) Doistau, B.; Jiménez, J.-R.; Guerra, S.; Besnard, C.; Piguet, C. Key Strategy for the Rational Incorporation of Long-Lived NIR Emissive Cr(III) Chromophores into Polymetallic Architectures. *Inorg. Chem.* **2020**, *59*, 1424−1435. DOI: 10.1021/acs.inorgchem.9b03163.
(60) Doistau, B.; Collet, G.; Bolomey, E. A.; Sadat-Noorbakhsh, V.; Besnard, C.; Piguet, C. Heteroleptic Ter-Bidentate Cr(III) Complexes as Tunable Optical Sensitizers. *Inorg. Chem.* **2018**, *57*, 14362−14373. DOI: 10.1021/acs.inorgchem.8b02530.
(61) Zare, D.; Doistau, B.; Nozary, H.; Besnard, C.; Guénée, L.; Suffren, Y.; Pelé, A.-P.; Hauser, A.; Piguet, C. Cr^{III} as an alternative to Ru^{II} in metallo-supramolecular chemistry. *Dalton Trans.* **2017**, *46*, 8992–9009. DOI: 10.1039/c7dt01747b.
(62) Rösch, L.; John, P.; Reitmeier, R. Silicon Compounds, Organic. In Ullmann's Encyclopedia of Industrial Chemistry, (Ed.). **2000**. DOI: 10.1002/14356007.a24_021.
(63) Laporte, O.; Meggers, W. F. Some rules of spectral structure, *J. Opt. Soc. Am.* **1925**, *11*, 459–463. DOI: 10.1364/JOSA.11.000459.
(64) Guedel, H. U.; Snellgrove, T. R. Jahn-Teller effect in the $4T_{2g}$ state of chromium(III) in dicesium sodium indium(III) hexachloride, *Inorg. Chem.* **1978**, *17*, 1617–1620. DOI: 10.1021/ic50184a045.
(65) Wenger, O. S.; Güdel, H. U. Optical spectroscopy of $CrCl_6^{3-}$ doped $Cs_2NaScCl_6$: Broadband near-infrared luminescence and Jahn-Teller effect, *J. Chem. Phys.* **2001**, *114*, 5832–5841. DOI: 10.1063/1.1352730.
(66) Bersuker, I. B. Pseudo-Jahn–Teller Effect—A Two-State Paradigm in Formation, Deformation, and Transformation of Molecular Systems and Solids, *Chem. Rev.* **2013**, *113*, 1351–1390. DOI: 10.1021/cr300279n.
(67) Ermolaev, V. L.; Sveshnikova, E. B. The application of luminescence-kinetic methods in the study of the formation of lanthanide ion complexes in solution, *Russ. Chem. Rev.* **1994**, *63*, 905–922. DOI: 10.1070/RC1994v063n11ABEH000125.
(68) Kreidt, E.; Kruck, C.; Seitz, M. Nonradiative Deactivation of Lanthanoid Luminescence by Multiphonon Relaxation in Molecular Complexes, *Handbook on the Physics and Chemistry of Rare Earths*, chapter 300, Elsevier, **2018**, *53*, 35–79. DOI: 10.1016/bs.hpcre.2018.04.001.
(69) Mitra, M.; Mrózek, O.; Putscher, M.; Guhl, J.; Hupp, B.; Belyaev, A.; Marian, C. M.; Steffen, A. Structural Control of Highly Efficient Thermally Activated Delayed Fluorescence in Carbene Zinc(II) Dithiolates, *Angew. Chem. Int. Ed.* **2024**, *63*, e202316300. DOI: 10.1002/anie.202316300.
(70) Ezquerra Riega, S. D.; Gutierrez Suburu, M. E.; Rodríguez, H. B.; Lantaño, B.; Kleinschmidt, M.; Marian, C. M.; Strassert, C. A. A Case-Study on the Photophysics of Chalcogen-Substituted Zinc(II) Phthalocyanines, *Chem. Eur. J.* **2024**, *30*, e202304083. DOI: 10.1002/chem.202304083.
(71) Sang-aroon, W.; Alberto, M. E.; Toscano, M.; Russo, N. Chalcogen atom effect on the intersystem crossing kinetic constant of oxygen- and sulfur disubstituted heteroporphyrins, *J. Comput. Chem.* **2024**, *45*, 1322–1328. DOI: 10.1002/jcc.27331.
(72) Mońka, M.; Grzywacz, D.; Hoffman, E.; Ievtukhov, V.; Kozakiewicz, K.; Rogowski, R.; Kubickia, A.; Liberek, B.; Bojarski, P.; Serdiuk, I. E. Decisive role of heavy-atom orientation for efficient enhancement of spin–orbit coupling in organic thermally activated delayed fluorescence emitters, *J. Mater. Chem. C* **2022**, *10*, 11719–11729. DOI: 10.1039/D2TC01729F.
(73) Neese, F. Software update: The ORCA program system—Version 5.0. *Wiley Interdiscip. Rev. Comput Mol Sci.* **2022**, *12*, e1606. DOI: 10.1002/wcms.1606.
(74) Lee, C.; Yang, W.; Parr, R. G. Development of the Colle-Salvetti correlation-energy formula into a functional of the electron density. *Phys. Rev. B: Condens. Matter Mater Phys.* **1988**, *37*, 785–789. DOI: 10.1103/PhysRevB.37.785.
(75) Miehlich, B.; Savin, A.; Stoll, H.; Preuss, H. Results obtained with the correlation energy density functionals of becke and Lee, Yang and Parr. *Chem. Phys. Lett.* **1989**, *157*, 200–206. DOI: 10.1016/0009-2614(89)87234-3.
(76) Becke, A. D. Density-functional thermochemistry. III. The role of exact exchange. *J. Chem. Phys.* **1993**, *98*, 5648–5652. DOI: 10.1063/1.464913.
(77) Weigend, F.; Ahlrichs, R. Balanced basis sets of split valence, triple zeta valence and quadruple zeta valence quality for H to Rn: Design and assessment of accuracy. *Phys. Chem. Chem. Phys.* **2005**, *7*, 3297–3305. DOI: 10.1039/B508541A.
(78) Neese, F.; Wennmohs, F.; Hansen, A.; Becker, U. Efficient, approximate and parallel Hartree–Fock and hybrid DFT calculations. A 'chain-of-spheres' algorithm for the Hartree–Fock exchange. *Chem. Phys.* **2009**, *356*, 98–109. DOI: 10.1016/j.chemphys.2008.10.036.

(79) Izsák, R.; Neese, F. An overlap fitted chain of spheres exchange method. *J. Chem. Phys.* **2011**, *135*, 144105. DOI: 10.1063/1.3646921.
(80) Weigend, F. Accurate Coulomb-fitting basis sets for H to Rn. *Phys. Chem. Chem. Phys.* **2006**, *8*, 1057–1065. DOI: 10.1039/B515623H.
(81) van Wüllen, C. Molecular density functional calculations in the regular relativistic approximation: Method, application to coinage metal diatomics, hydrides, fluorides and chlorides, and comparison with first-order relativistic calculations. *J. Chem. Phys.* **1998**, *109*, 392–399. DOI: 10.1063/1.476576.
(82) van Lenthe, E. ; Baerends, E. J.; Snijders, J. G. Relativistic regular two-component Hamiltonians. *J. Chem. Phys.* **1993**, *99*, 4597–4610. DOI: 10.1063/1.466059.
(83) Miertuš, S.; Scrocco, E.; Tomasi, J. Electrostatic interaction of a solute with a continuum. A direct utilization of AB initio molecular potentials for the prevision of solvent effects. *Chem. Phys.* **1981**, *55*, 117–129. DOI: 10.1016/0301-0104(81)85090-2.
(84) Barone, V.; Cossi, M. Quantum Calculation of Molecular Energies and Energy Gradients in Solution by a Conductor Solvent Model. *J. Phys. Chem. A* **1998**, *102*, 1995–2001. DOI: 10.1021/jp9716997.
(85) Grimme, S.; Antony, J.; Ehrlich, S.; Krieg, H. A consistent and accurate ab initio parametrization of density functional dispersion correction (DFT-D) for the 94 elements H-Pu. *J. Chem. Phys.* **2010**, *132*, 154104. DOI: 10.1063/1.3382344.
(86) Grimme, S.; Ehrlich, S.; Goerigk, L. Effect of the Damping Function in Dispersion Corrected Density Functional Theory. *J. Comput. Chem.* **2011**, *32*, 1456–1465. DOI: 10.1002/jcc.21759.
(87) Plasser, F. TheoDORE: A toolbox for a detailed and automated analysis of electronic excited state computations. *J. Chem. Phys.* **2020**, *152*, 84108. DOI: 10.1063/1.5143076.
(88) Mai, S.; Plasser, F.; Dorn, J.; Fumanal, M.; Daniel, C.; González, L. Quantitative wave function analysis for excited states of transition metal complexes. *Coord. Chem. Rev.* **2018**, *361*, 74–97. DOI: 10.1016/j.ccr.2018.01.019.
(89) Roos, B. O.; Taylor, P. R.; Sigbahn, P. E. M. A complete active space SCF method (CASSCF) using a density matrix formulated super-CI approach. *Chem. Phys.* **1980**, *48*, 157–173. DOI: 10.1016/0301-0104(80)80045-0.
(90) Siegbahn, P. E. M.; Almlöf, J.; Heiberg, A.; Roos, B. O. The complete active space SCF (CASSCF) method in a Newton–Raphson formulation with application to the HNO molecule. *J. Chem. Phys.* **1981**, *74*, 2384–2396. DOI: 10.1063/1.441359.
(91) Angeli, C.; Cimiraglia, R.; Evangelisti, S.; Leininger, T.; Malrieu, J.-P. Introduction of n-electron valence states for multireference perturbation theory. *J. Chem. Phys.* **2001**, *114*, 10252–10264. DOI: 10.1063/1.1361246.
(92) Angeli, C.; Cimiraglia, R.; Malrieu, J.-P. N-electron valence state perturbation theory: a fast implementation of the strongly contracted variant. *Chem. Phys. Lett.* **2001**, *350*, 297–305. DOI: 10.1016/S0009-2614(01)01303-3.
(93) Angeli, C.; Cimiraglia, R.; Malrieu, J.-P. n-electron valence state perturbation theory: A spinless formulation and an efficient implementation of the strongly contracted and of the partially contracted variants. *J. Chem. Phys.* **2002**, *117*, 9138–9153. DOI: 10.1063/1.1515317.
(94) Pierloot, K. Transition metals compounds: Outstanding challenges for multiconfigurational methods. *Int. J. Quantum Chem.* **2011**, *111*, 3291–3301. DOI: 10.1002/qua.23029.
(95) STOE & Cie, X-Area; STOE & Cie GmbH: Darmstadt, Germany
(96) Blessing, R. H. An empirical correction for absorption anisotropy. *Acta Crystallogr., Sect. A* **1995**, *51*, 33–38. DOI: 10.1107/S0108767394005726.
(97) Spek, A. L. Structure validation in chemical crystallography. *Acta Crystallogr., Sect. D* **2009**, *65*, 148–155. DOI: 10.1107/S090744490804362X.
(98) Sheldrick, G. M. SHELXT - integrated space-group and crystal-structure determination. *Acta Crystallogr., Sect. A* **2015**, *71*, 3–8. DOI: 10.1107/S2053273314026370.
(99) Sheldrick, G. M. Crystal structure refinement with SHELXL. *Acta Crystallogr., Sect. C* **2015**, *71*, 3–8. DOI: 10.1107/S2053229614024218.
(100) Sheldrick, G. M. A short history of SHELX. *Acta Crystallogr., Sect. A* **2008**, *64*, 112–122. DOI: 10.1107/S0108767307043930.
(101) Hübschle, C. B.; Sheldrick, G. M.; Dittrich, B. ShelXle: a Qt graphical user interface for SHELXL. *J. Appl. Crystallogr.* **2011**, *44*, 1281–1284. DOI: 10.1107/S0021889811043202.

For Table of Contents Only

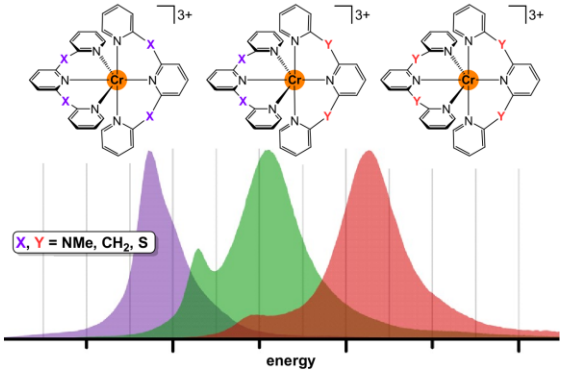

Heteroleptic pseudo-octahedral chromium(III) complexes were obtained via triflato intermediates prepared from chlorido precursors and trimethylsilyl trifluoromethanesulfonate. Near-infrared absorption and emission spectroscopic analyses provided the spin-flip state energies, which were reproduced well quantum chemically. Together with the respective homoleptic complexes, the series of luminescent complexes allow delineating an additive nephelauxetic effect of the ligands.

3.7 Post-Synthetic Excited State Manipulation in Molecular Rubies

The design principle of molecular rubies provide a reliable framework for developing highly emissive, earth-abundant chromium(III) complexes with diverse optical and electrochemical properties.[79,87] Based on this concept, numerous molecular rubies with promising application potential in photocatalysis, sensing, upconversion and circularly polarized emission have been developed.[92,178,179,183–185,188,191–193,199,200] The remarkable photoluminescence efficiency of these compounds is significantly influenced by external factors, such as the solvent or oxygen presence.[76,83,84,176] In contrast, their emission energies, due to the localized spin-flip (SF) nature, are less sensitive to environmental conditions (solid or solution) compared to charge transfer (CT) transitions, which involve a large change in the electric dipole moment.[94,159]

Nevertheless, the energies of SF states in molecular rubies can be modulated not only through modifications in the primary coordination sphere but also by external factors, such as thermodynamic variables.[88] While temperature effects primarily influence the population of closely lying doublet states, $[Cr(ddpd)_2]^{3+}$ (Scheme 3.3) has demonstrated a bathochromic shift in SF emission bands under hydrostatic pressure.[92,184] This effect is more pronounced than in the gemstone ruby and is attributed to more sensitive pressure-induced changes in the coordination geometry and metal-ligand π-overlap, affecting bond covalency and the nephelauxetic effect.[187]

Beyond ligand-based control of emission energies, which has gained considerable attention over the last decade, the second coordination sphere can also impact the optical properties of molecular rubies.[88] Counterions, salt additives and acids can shield the metal center from triplet oxygen or solvent molecules, thereby enhancing luminescence performance, as demonstrated for acidic $[Cr(H_2tpda)_2]^{3+}$ and $[Cr(tpe)_2]^{3+}$ (Scheme 3.3).[83,177] Switching counterions in $[Cr(ddpd)_2]^{3+}$ affects oxygen sensitivity as well as quantum yield and lifetime under oxygen-free conditions in different matrix environments.[84] However, this effect is less pronounced compared to iridium(III) ^{3}MLCT emitters due to the MC excited state nature.[223] Post-synthetic excited-state tuning through manipulations of a coordinated functional ligand in the second coordination sphere using (Lewis) acids has, in contrast to CT systems, not yet been explored in this compound class.[224] Given that known molecular rubies are coordinatively saturated, it is unlikely they can leverage acid-base adduct formation to modify photophysical properties for optical applications.

In addition to emission properties, absorption characteristics play a critical role for the applicability of photoactive compounds, particularly in catalytic systems.[25,225–227] For a strong required absorption in the visible range, pseudo-octahedral molecular rubies

like $[Cr(dqp)_2]^{3+}$ (Scheme 3.3) rely on LMCT excitation, as their Laporte-forbidden MC transitions suffer from low extinction coefficients.[83,87,178] However, in most electron-rich representatives, the corresponding LMCT bands are lying in the deep blue spectral region, thus strongly overlapping with the absorption of many relevant organic substrates, limiting their potential in photocatalysis.[56,79]

This study explores whether the optical properties of molecular rubies can be tuned through in situ binding of additives in first coordination sphere. Moreover, it addresses the challenge of achieving bathochromic shifts in absorption maxima in these compounds by ligand design, extending into the green spectral region. To this end, the complexes $[Cr(ddad)_2]^{3+}$ and $[Cr(bptp)(ddad)]^{3+}$ (Scheme 3.3), featuring potential coordination sites at the central pyrazine unit, were synthesized and characterized electrochemically and spectroscopically in the absence and presence of Lewis acids. The results, obtained through UV/Vis/NIR absorption, emission, and (spectro)-electrochemical measurements, as well as quantum chemical multireference calculations aim to elucidate external SF energy tuning effects and advance design strategies for these promising transition metal complexes.

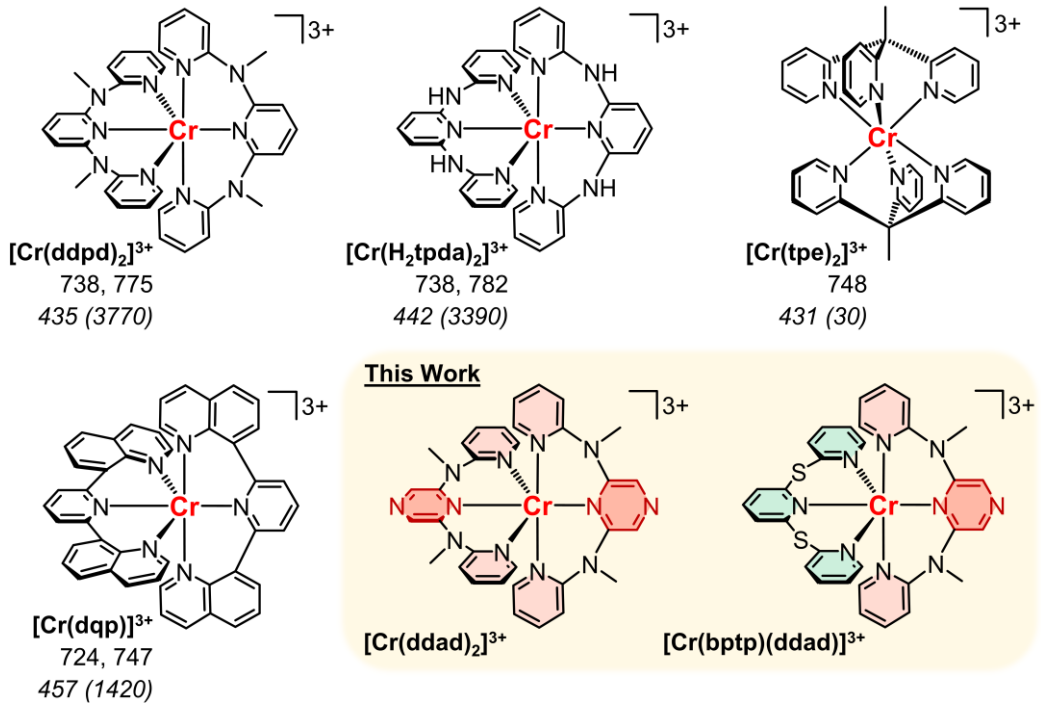

Scheme 3.3 Molecular structures of selected highly emissive chromium(III) complexes with emission (nm) and absorption wavelengths (italic, nm) with molar extinction coefficients (in brackets, italic, M^{-1} cm^{-1}).[83,87,177,178]

This project incorporates parts of the bachelor thesis cited in ref. [228].
Supporting Information for this project can be found on pp. 351.

3.7.1 Synthesis and Characterization

The tridentate ligand ddad ($\mathbf{L^N}$) was prepared analogously to the known pincer ligand ddpd ($\mathbf{L^{NMe}}$) by reacting electrophilic 2,6-dichloropyrazine with 2-methylamino-pyridine, yielding 64% (Scheme 3.4).[229] The pyrazine-based compound was fully characterized using elemental analysis, ESI^+ mass spectrometry (Fig. S1), $^1H/^{13}C$ NMR (Fig. S2–6), IR (Fig. S7) and optical spectroscopy (Fig. S9) as well as single-crystal X-ray diffraction (Fig. S8). As expected, the crystallographic data revealed structural parameters similar to those of $\mathbf{L^{NMe}}$, with C–NMe–C angles of 122.7° (122.9°), however, both ligands crystallize in different space groups.[73]

The homoleptic complex salt $[Cr(ddad)_2](OTf)_3$ ($\mathbf{[3^N](OTf)_3}$) was synthesized according to an established procedure (Section 6.4) in 63% yield, using anhydrous chromium(III) triflate as the precursor (Scheme 3.4a). For preparation of the heteroleptic complex salt $[Cr(bptp)(ddad)](OTf)_3$ ($\mathbf{[3^{N,S}](OTf)_3}$), a stepwise synthesis route (analogous to Section 6.5) was followed, passing the intermediates $CrCl_3(ddad)$ ($\mathbf{1^N}$, 81%) and $Cr(ddad)(OTf)_3$ ($\mathbf{2^N}$, 89%) (Scheme 3.4b). These neutral complexes were analyzed by ESI^+ mass spectrometry (Fig. S.10–11), IR spectroscopy (Fig. S12–13), and single crystal X-ray diffraction (Fig. S14–15), which revealed meridional coordination of the monodentate ligands around the metal center, preorganizing the configuration of the heteroleptic bis(tridentate) complex. The target complex was obtained by heating a precursor solution with the known ligand bptp ($\mathbf{L^S}$) in 30% yield. The composition of $\mathbf{[3^{N,S}](OTf)_3}$ and $\mathbf{[3^N](OTf)_3}$ was verified by ESI^+ mass spectrometry (Fig. S16–17), IR (Fig. S18–19), and optical spectroscopy (Fig. S23–24), and the purity of the latter was further evidenced by elemental analysis. No contamination by homoleptic complexes was detected in bulk material of $\mathbf{[3^{N,S}](OTf)_3}$.

X-ray diffraction analysis of single crystals (Fig. S20–21), obtained from acetonitrile solutions at 5 °C, reveals structural differences between the complex cations $\mathbf{[3^N]^{3+}}$, $\mathbf{[3^{N,S}]^{3+}}$ and $[Cr(bptp)_2]^{3+}$ ($\mathbf{[1^S]^{3+}}$, Section 3.5) (Fig. S22, Table S1). The average Cr–N bond distances in $\mathbf{[3^{N,S}]^{3+}}$ (2.063 Å) fall between those of the homoleptic systems $\mathbf{[3^N]^{3+}}$ (2.035 Å) and $\mathbf{[1^S]^{3+}}$ (2.081 Å). However, the Cr–N bond lengths *d* within the CrN_6 core of $\mathbf{[3^{N,S}]^{3+}}$ are not uniform, being longer toward the ligand $\mathbf{L^S}$ (2.087 A) than toward $\mathbf{L^N}$ (2.039 A), consistent with the homoleptic complexes. Additionally, the intraligand N–Cr–N angles α and γ of 171.2/179.0° (*trans*) and 85.6/89.5° (*cis*) for the donor atoms of the ligands $\mathbf{L^N/L^S}$ in $\mathbf{[3^{N,S}]^{3+}}$ closely resemble those of $\mathbf{[3^N]^{3+}}$ (170.4 and 85.3°) and $\mathbf{[1^S]^{3+}}$ (177.8 and 89.6°). Thus, the geometry of the heteroleptic complex can be seen as superposition of the respective homoleptic counterparts, with the ligands behaving structurally independently. As known from structure-property investigations (Section 3.5), the geometric distinctions of molecular rubies play a crucial role for their optical properties, which are discussed next.

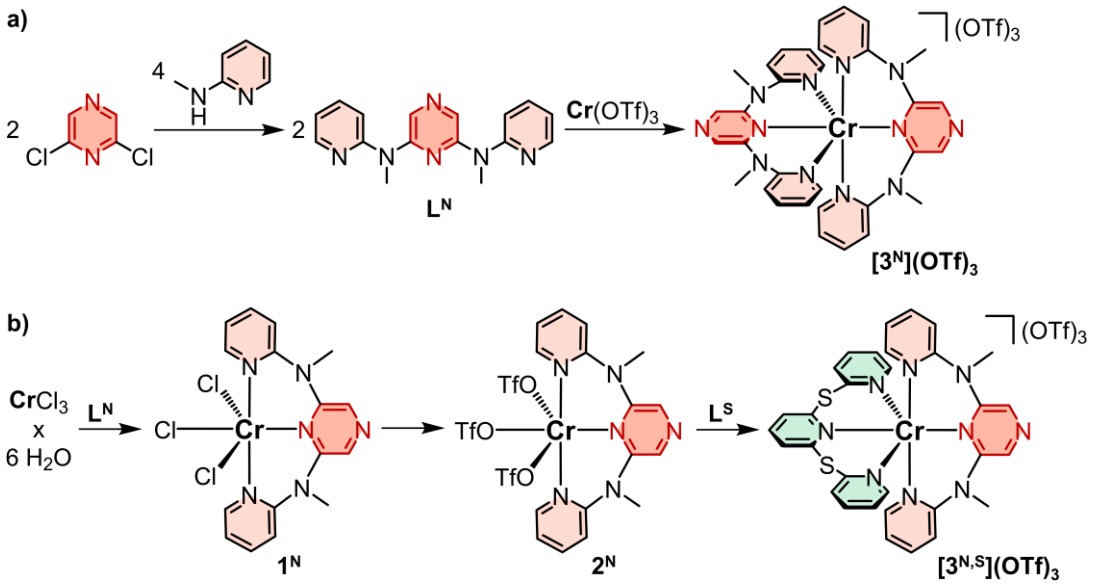

Scheme 3.4 Synthesis of the pyrazine-based ligand $\mathbf{L^N}$ and its corresponding a) homoleptic and b) heteroleptic chromium(III) complexes $\mathbf{[3^N](OTf)_3}$ and $\mathbf{[3^{N,S}](OTf)_3}$, the latter incorporating the ligand $\mathbf{L^S}$.

3.7.2 Excited State Properties

To better understand the absorption properties of the chromium(III) complexes, the optical properties of the ligand $\mathbf{L^N}$ were examined (Fig. S9). The compound exhibits a weak low-energy $S_0 \rightarrow S_1$ absorption band around 442 nm (10 M^{-1} cm^{-1}) with mixed NMe→pyrazine CT and pyrazine-localized π-π^* character, as indicated by TD-DFT calculations. Excitation into these bands more efficiently leads to broad $S_1 \rightarrow S_0$ emission peaking at 535 nm, compared to higher-energy excitations. These optical data confirm the presence of low-lying π^* orbitals in the pyrazine unit, which are also expected to contribute to the low-energy region of the respective molecular rubies.

Indeed, the UV/Vis/NIR absorption spectra of $\mathbf{[3^N]^{3+}}$ and $\mathbf{[3^{N,S}]^{3+}}$ are characterized by low-energy spin-allowed absorption bands at 491 (2050 M^{-1} cm^{-1}) and 502 nm (1250 M^{-1} cm^{-1}), tailing into the green spectral region (Fig. 3.6). These maxima are bathochromically shifted on average by 2300 and 2800 cm^{-1} relative to the absorption of $[Cr(ddpd)_2]^{3+}$[87], $[Cr(tpe)_2]^{3+}$[83] and $[Cr(dqp)_2]^{3+}$[178] employed in photocatalysis (Scheme 3.3) and are primarily ascribable to $^4A_2 \rightarrow {}^4$ILCT (NMe/Pz→Pz) transitions into pyrazine π^* orbitals (Fig. S23–24, Table S2–3). At higher energies, TD-DFT calculations locate the lowest $^4A_2 \rightarrow {}^4$LMCT and MC $^4A_2 \rightarrow {}^4T_2$ transitions for $\mathbf{[3^N]^{3+}}$ (434.6 and 420.2 nm) and $\mathbf{[3^{N,S}]^{3+}}$ (452.7 and 438.5 nm), which are rather similar to $[Cr(ddpd)_2]^{3+}$ ($\mathbf{[1^H]^{3+}}$, 434.6 and 420.3 nm). Thus, the ligand field strength in this complex series remains largely unaffected by the π-donor/π-acceptor properties of the pyrazine unit and is only reduced in presence of the weaker ligand $\mathbf{L^S}$.

In the NIR region, the absorption spectra show three characteristic SF bands corresponding to Laporte- and spin-forbidden $^4A_2 \rightarrow {}^2E/{}^2T_1$ transitions at 773, 742, and 703 nm for $\mathbf{[3^N]^{3+}}$, and 749, 729, and 691 nm for $\mathbf{[3^{N,S}]^{3+}}$ (Fig. 3.6). To extract the energies of the five lowest-energy doublet states, the baseline-corrected spectral bands were fitted with five Voigt functions (Fig. S25–26, Section 3.5). The experimentally derived energies align well with the microstate energies obtained from CASSCF(7,12) calculations after correction with a common empirical scaling factor of 0.88 (Table S3–4). Additionally, the calculations accurately reproduce the relative energy trends, including the lifting of the degeneracy ($\Delta E(\#5–\#1)$) and the differences between the highest SF states ($\Delta E(\#2–\#1)$). Based on the consistency between experiment and theory, the SF energies of structurally related molecular rubies can be reliably predicted at this level of theory (Section 3.6).

Upon irradiation at room temperature, acetonitrile solutions of $\mathbf{[3^N]^{3+}}$ and $\mathbf{[3^{N,S}]^{3+}}$ exhibit dual $^2E/{}^2T_1 \rightarrow {}^4A_2$ phosphorescence with maxima at 779/743 nm and 756/730 nm, respectively (Fig. 3.6). The emission maxima closely match the energies of the SF absorption bands, aside from small Stokes shifts of 100/20 cm^{-1} and 120/20 cm^{-1} ($^2E/{}^2T_1$). The minimal discrepancy between the lower-energy emission and the second-lowest absorption band supports the assignment of these sharp bands to genuine SF transitions of ^2E parentage. According to the excitation spectra, the emissive states of both complexes can be efficiently populated by low-energy $^4A_2 \rightarrow {}^4$ILCT excitation as well as higher-energy UV absorption.

Notably, the spectroscopic measurements demonstrate that the metal-ligand bond covalency in $\mathbf{[3^N]^{3+}}$, relative to $\mathbf{[1^{NMe}]^{3+}}$, is not significantly affected by the pyridine/pyrazine exchange, analogous to the ligand field strength. However, modification of the bridging group in $\mathbf{[3^{N,S}]^{3+}}$ results in a significant shift in SF energies, falling almost exactly between those of the homoleptic counterparts. For the investigated complex series, this semi-quantitative correlation supports the assumption of an additive nephelauxetic effect of the ligands, likely due to the structural independence of the individual polypyridine ligands (Section 3.6).

The photoluminescence lifetime and quantum yield of $\mathbf{[3^{N,S}]^{3+}}$ (τ = 21.9 µs, Φ = 0.22%) are also intermediate between those of $\mathbf{[3^N]^{3+}}$ and $\mathbf{[1^S]^{3+}}$ (τ = 966 and 1.65 µs, Φ = 12.5 and 0.01%). While the radiative rates are similar across the complex series (k_r = 130, 100, 60 cm^{-1}), the non-radiative rates (k_{nr} = 910, 45560, 606000 cm^{-1}) are strongly influenced by the type of bridging unit. Analogous to other molecular rubies, the increased non-radiative decay can be attributed to back-intersystem crossing to distorted excited quartet states promoted by heavier atoms (sulfur) and multiphonon relaxation via resonant energy transfer (Section 3.5).

To assess the photostability of pyrazine-bearing $[\mathbf{3}^{\mathbf{N}}]^{3+}$ relative to $[\mathbf{1}^{\mathbf{H}}]^{3+}$, solutions of the complexes in deoxygenated water and acetonitrile were irradiated at 460 nm under high light intensities. Under these conditions, $[\mathbf{3}^{\mathbf{N}}]^{3+}$ shows significant photolysis, particularly in water, as evidenced by changes in absorption, emission, and excitation spectra (Fig. S27). The changes in the absorption profile, including the rise of bands at 363/267 nm and the decrease in luminescence intensity, are consistent with dissociation of the ddad ligand. In contrast, the optical properties of $[\mathbf{1}^{\mathbf{H}}]^{3+}$ show a weaker response after identical irradiation periods in both solvents. However, the photoreaction rates of the investigated complexes are not directly comparable due to differing changes in absorption during the experiment.

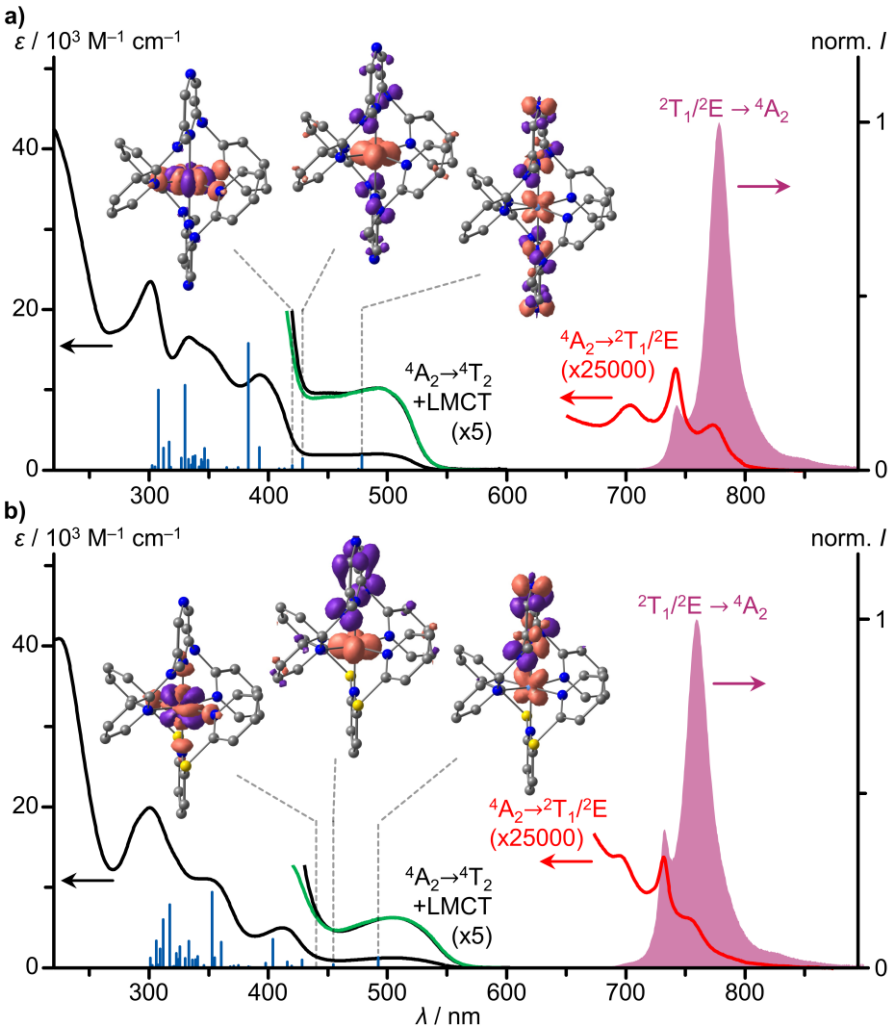

Fig. 3.6 UV/Vis/NIR absorption spectra (black, red), excitation spectra (λ_{em} = 778 and 756 nm, green) and normalized emission spectra (λ_{exc} = 493 and 503 nm, purple) of a) $[\mathbf{3}^{\mathbf{N}}]^{3+}$ and b) $[\mathbf{3}^{\mathbf{N,S}}]^{3+}$ in deaerated CH_3CN at room temperature, TD-DFT calculated oscillator strengths (blue sticks) and difference electron densities of three low-energy transitions of ^{4}ILCT, ^{4}LMCT and ^{4}MC character. The regions of the spin-forbidden absorption bands, the lowest energy spin allowed/LMCT absorption band and the excitation spectrum are scaled with the indicated factors.

3.7.3 Ground State Redox Properties

The influence of pyrazine incorporation on the electrochemical properties of molecular rubies was investigated for $\mathbf{[3^N]^{3+}}$ using cyclic voltammetry (Fig. S28) and square-wave voltammetry (Fig. S29). These measurements reveal a higher ground-state potential of –0.87 V vs. FcH/FcH^+ compared to $\mathbf{[1^H]^{3+}}$ (E_0 = –1.11 V vs. FcH/FcH^+) and its substituted homologues (Section 3.4). The TD-DFT calculated spin density of low-spin $\mathbf{[3^N]^{2+}}$ shows that the anodically shifted reversible reduction occurs ligand-centered, attributed to low-energy π^* orbitals of the pyrazine unit. The increased excited-state potential (E^* = 0.80 V vs. FcH/FcH^+) was probed via quenching experiments using *trans*-anethol as substrate, giving a Stern-Volmer constant of 64 M^{-1} and a bimolecular quenching rate of 67 x 10^3 M^{-1} s^{-1} (Section 3.4).

To experimentally confirm the reduction site in $\mathbf{[3^N]^{3+}}$, spectro-electrochemical measurements were performed in the range of the reduction wave from 0.3 to –1.0 V. Most notably, with decreasing potential, broad low-energy absorption bands emerge in the red region around 600 nm and in the NIR, ranging from 700 nm to beyond 1000 nm (measuring limit) (Fig. 3.7a). These bands are assignable to π-π^* transitions of the coordinated (pyrazine) radical ligands, analogous to those observed in $[Cr(tpe)_2]^{3+}$ and $[Cr(dqp)_2]^{3+}$.[83,191] TD-DFT-calculated transitions of geometry-optimized $^3[3^N]^{2+}$ satisfactorily reproduce the obtained (estimated) absorption maxima, further supporting the ligand-centered reduction hypothesis.

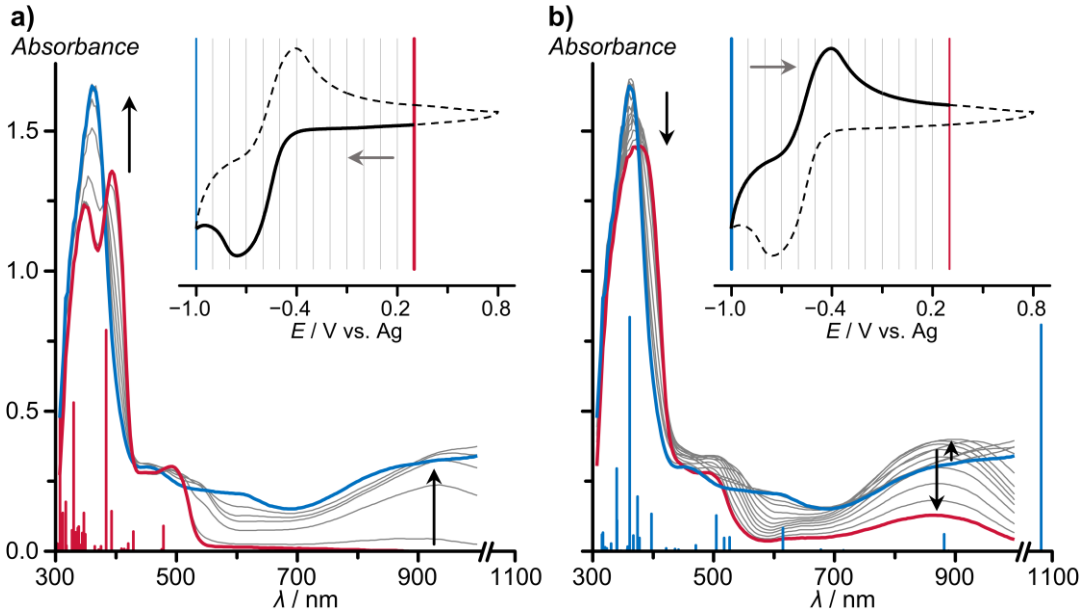

Fig. 3.7 UV/Vis/NIR absorption spectra of $\mathbf{[3^N]^{3+}}$ in deaerated CH_3CN during electroreduction within the potential ranges of a) 0.3 to –1.0 V and b) –1.0 to 0.3 V (vs. Ag pseudo-reference), with TD-DFT calculated oscillator strengths for species a) $^4[3^N]^{3+}$ (red sticks) and b) $^3[3^N]^{2+}$ (blue sticks). Insets show the cyclic voltammogram with the corresponding potential ranges and step width (±0.1 V).

Upon reoxidation, the long-wavelength absorption tail diminishes in favor of a band at 880 nm, which subsequently decreases with increasing potential (Fig. 3.7b). The appearance of these intermediate absorption bands and the absence of isosbestic points indicate side product formation. A proton-coupled electron transfer mechanism, as suggested for iridium complexes with bpy ligands substituted in the *para*-position to the donor atoms, might be a plausible explanation for these observations.[230] The original spectrum of $\mathbf{[3^N]^{3+}}$ is only partially restored after a redox cycle, supporting that follow-up reactions are involved in the electroreduction process.

3.7.4 Excited State Energy Tuning

The post-synthetic tuning of excited state energies was investigated by titrating solutions of BF_3 and $B(C_6F_5)_3$ in deaerated acetonitrile into a solution of $\mathbf{[3^N]^{3+}}$ in the same solvent. The effect of the Lewis acids on the optical properties of the complex was monitored using UV/Vis/NIR absorption, emission, and excitation spectroscopy (Fig. 3.8). Even after the addition of 100 equivalents of the additives, no significant changes in the normalized spectra were observed. Since coordination of the pyrazine unit to the electrophiles is expected to induce a noticeable shift in the low-energy ILCT absorption band, the spectra suggest that no adduct formation occurs between the Lewis acids and the complex under dynamic solution conditions. This is likely due to the reduced nucleophilicity of the free pyrazine donor atom, a consequence of the electron-withdrawing effect of the highly charged chromium(III) cation.

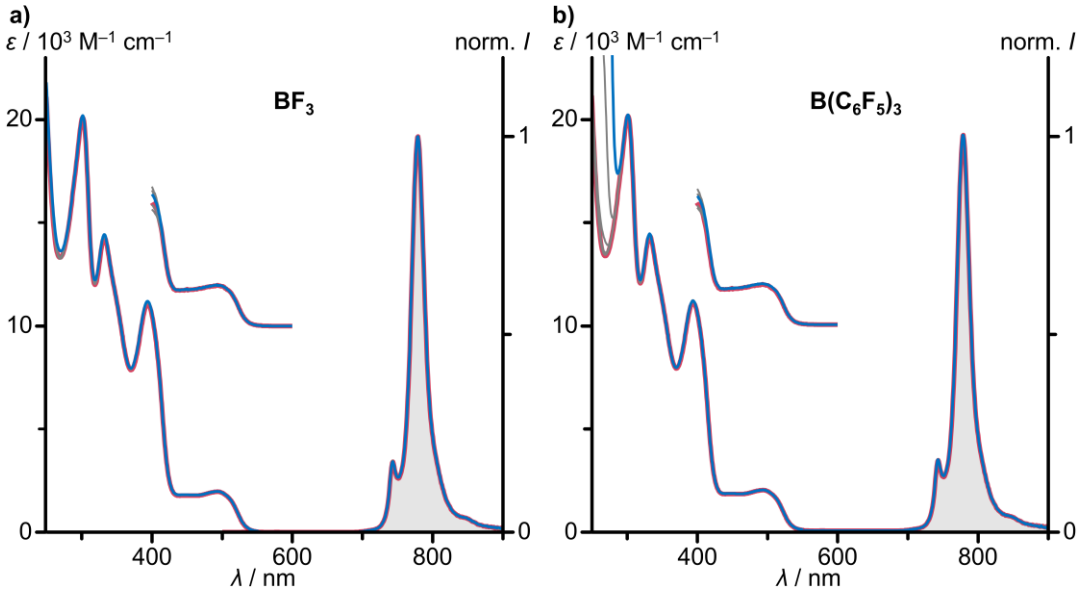

Fig. 3.8 UV/Vis/NIR absorption spectra, excitation spectra (λ_{em} = 779 nm) and emission spectra (λ_{exc} = 493 nm) of $\mathbf{[3^N]^{3+}}$ in deaerated CH_3CN during titration with a) BF_3 and b) $B(C_6F_5)_3$ solutions, recorded before (red) and after addition of 0.01, 0.1, 1, 10 (each gray) and 100 (blue) equivalents of the Lewis acids.

To evaluate the general influence of dative pyrazine bonding on the doublet state energies of $\mathbf{[3^{N}]^{3+}}$ and $\mathbf{[3^{N,S}]^{3+}}$, CASCF(7,12) calculations were conducted for various adducts with H^+, CH_3^+ and BF_3. The screening results indicate that the energies of the two lowest microstates ($^2T_1/^2E$ parentage), corresponding to the dual emission bands, are altered by a maximum of 10 cm^{-1} due to BF_3 binding in the ligand periphery (Table S3), while the higher-energy microstates are more strongly affected, with shifts between 10 and 100 cm^{-1}. Covalent bonding with the cationic species H^+ and CH_3^+, results in shifts of 10–40 cm^{-1} in the lowest doublet energies, which is thus predicted to be slightly higher than the effect of the neutral Lewis acid BF_3. These computational findings demonstrate that the localized SF states of molecular rubies are minimally affected by functional groups that interact exclusively through the σ-system, in contrast to the more significant influence of substituents with +M effect (Section 3.4).

3.7.5 Conclusion and Outlook

To improve the optical excitability of molecular rubies under low-energy light and to investigate the effect of Lewis acid-base adduct formation on their spin-flip energies, the complexes $\mathbf{[3^{N}]^{3+}}$ and $\mathbf{[3^{N,S}]^{3+}}$ were prepared. Structural analysis of the complex cations reveals that the geometry of $\mathbf{[3^{N,S}]^{3+}}$ can be interpreted as a superposition of its homoleptic parent complexes, including the Cr–N bond lengths, which primarily govern the nephelauxetic effect. These structural features are reflected in the NIR absorption and emission spectra, with spin-flip energies of $\mathbf{[3^{N,S}]^{3+}}$ close to the average of those of $\mathbf{[3^{N}]^{3+}}$ and $\mathbf{[1^{S}]^{3+}}$ (Fig. 3.9a,b). The deconvoluted energies of the five spin-flip states of $^2E/^2T_1$ parentage for both molecular rubies align well with the theoretical values, with discrepancies similar to those observed in structurally related complexes (Sections 3.5 and 3.6). The derived correlations allow for correct scaling of calculated emission energies of analogue systems and hence for reliable predictions.

Importantly, the lowest intense spin-allowed absorption bands of $\mathbf{[3^{N}]^{3+}}$ and $\mathbf{[3^{N,S}]^{3+}}$, at 492 and 502 nm respectively, are significantly red-shifted compared to other molecular rubies (Fig. 3.9c), corresponding to ILCT transitions into pyrazine π^* orbitals.[83,87,177,178] However, the excited state energies of $\mathbf{[3^{N}]^{3+}}$ in solution could not be tuned with the Lewis acids BF_3 or $B(C_6F_5)_3$, likely due to the absence of adduct formation, attributed to the low basicity of the pyrazine donor. Electrochemical studies of $\mathbf{[3^{N}]^{3+}}$ indicate that incorporating an electron-poor pyrazine heteroaromatic unit in the ligand framework induces a more pronounced anodic shift in the ground-state potential than ligand backbone substitution (Section 3.4). The reduction may involve side reactions like proton-coupled electron transfer. Overall, this work offers valuable insights and design concepts for the development of photoactive systems with enhanced photophysical properties for broader application in photocatalysis.

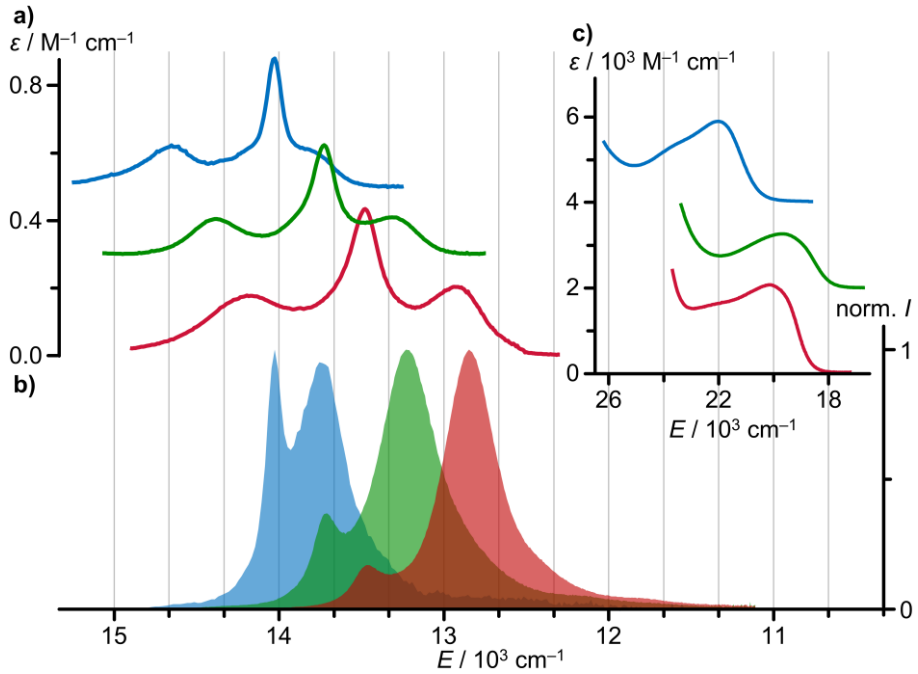

Fig. 3.9 Summarizing data showing a) baseline corrected NIR absorption spectra, b) normalized emission spectra (λ_{exc} = 450, 493 and 503 nm) and c) UV/Vis absorption spectra of $[\mathbf{1}^{S}]^{3+}$ (blue, Section 3.5), $[\mathbf{3}^{N}]^{3+}$ (red) and $[\mathbf{3}^{N,S}]^{3+}$ (green) in deaerated CH_3CN at room temperature. For clarity, the NIR and UV/Vis absorption spectra of $[\mathbf{3}^{N,S}]^{3+}$ and $[\mathbf{1}^{S}]^{3+}$ were shifted vertically by +0.30 and +2000, and +0.50 and +4000 M^{-1} cm^{-1}, respectively.

4 Conclusion and Outlook

Highly luminescent chromium(III) complexes present a competitive and complementary alternative to charge-transfer complexes based on precious or noble metals, such as ruthenium(II), for applications in optical sensing, circularly polarized emission and photocatalysis.[50,56,60,70,79] Extensive research has aimed to understand and improve their photophysical properties, addressing initial applications, yet has encountered intrinsic disadvantages of spin-flip systems compared to charge-transfer systems.[94] The findings of this work provide strategies to bridge this gap for molecular rubies, broadening their application potential by enhancing and diversifying their photochemical properties, deepening the understanding of spin-flip energy tuning and excited state dynamics, and improving synthetic accessibility.

Each project in this work involves detailed spectroscopic, electrochemical, and computational characterization of the synthesized molecular rubies to establish a clear comprehension of the relationship between their underlying structure and (enhanced) photophysical properties (Section 3.1). The insights gained from this work offer future studies design strategies for developing sustainable 3d transition metal complexes with targeted photophysical properties for a variety of advanced technologies.

Enhancement of Photochemical Properties

Enhancing the photochemical properties of chromium(III) complexes by increasing emission energies has been challenging due to the lack of established design principles for spin-flip states.[88,94] This work demonstrates that quantum chemical predictions of spin-flip energies enable the targeted design of molecular rubies emitting in the red spectral region (Section 3.2). The blue-shifted phosphorescence of $[Cr(bpmp)_2]^{3+}$ at 709 nm highlights that the nephelauxetic effect in structurally related systems can be effectively addressed through bridging group modification (Fig. 4.1a). The impact of partial deuteration further confirms that isotopic substitution of key oscillators is a viable strategy for improving the luminescence efficiency of photoactive compounds. The first study underscores the potential of chromium(III) complexes, particularly $[Cr(bpmp)_2]^{3+}$, as sustainable alternatives to ruthenium(II) systems in photoredox catalysis, offering superior photophysical properties, including high redox potential, strong red luminescence, and long excited state lifetimes. Although reversible ground-state deprotonation enables ratiometric optical *p*H sensing, the *p*H sensitivity limits $[Cr(bpmp)_2]^{3+}$ to neutral and acidic environments. This limitation can be addressed

through ligand design, i.e. substituting the methylene bridges with carbonyl groups, thereby expanding the applicability of these systems to more diverse conditions.

The increased emission energy of $[Cr(bpmp)_2]^{3+}$ highlights its potential for direct activation of organic substrates via energy transfer, while other molecular rubies rely on this mechanism to generate singlet oxygen as a reaction initiator (Section 3.4).[192] The complex efficiently sensitizes anthracenes for triplet-triplet annihilation upconversion, reinforcing the ability of first-row transition metals to replace precious metals like ruthenium in photocatalytic processes. Green-to-blue photon upconversion with a quantum yield of 12.0% was achieved using diphenylanthracene as the annihilator, with efficient doublet-triplet energy transfer being the key to this high performance (Fig. 4.1b). These results emphasize the advantage of long excited-state lifetimes, which compensate for low energy transfer rates in photocatalytic systems. Furthermore, $[Cr(bpmp)_2]^{3+}$ successfully initiates [4+4] cycloaddition reactions of sterically less-hindered anthracenes under green light excitation. The high power densities required for efficient upconversion necessitate improvements in sensitizer absorbance, i.e. through incorporating low-energy LMCT states. Overall, this study provides compelling evidence for the use of earth-abundant metals in advanced photochemical applications, reducing reliance on precious metals.

The excited-state potential of a photosensitizer is the crucial parameter of a photoredox catalytic cycle.[56] Modulating this thermodynamic quantity in charge transfer systems through ligand functionalization is well-established, typically affecting emission energies.[30,218] This work demonstrates the significant potential of molecular rubies in photochemical applications, showing that their electrochemical properties can be tuned largely independently of their spin-flip energies (Section 3.4). Peripheral substitution in the series $[Cr(ddpd^X)_2]^{3+}$ shifts the ground-state potential by ± 0.1 V (X = CF_3, OMe) relative to $[Cr(ddpd)_2]^{3+}$ (Fig. 4.1c), with reductions becoming increasingly ligand-centered as electron deficiency rises. In contrast, the spin-flip energies and luminescence efficiency are only slightly affected by the substituents with +M effect (X = OMe, NMe_2), underscoring the robustness of the molecular ruby design. Importantly, ligands and complexes can be synthesized in an analogous fashion, which allows for efficient screening. This study highlights the versatility of molecular rubies, demonstrating their capacity for selective optimization in photoredox applications without compromising optical functionality.

Tuning of Photochemical Properties

Optimizing the optical properties of photoactive compounds for specific applications fundamentally depends on controlling the thermodynamics and kinetics of their excited states. While previous studies provided general guidelines for reducing non-

radiative decay or bathochromically shifting emission bands in molecular rubies, this work offers unprecedented insights into spin-flip energy tuning and excited-state dynamics in these systems (Section 3.5).[76,84,88,171,172] By examining the nephelauxetic series $[Cr(ddpd)_2]^{3+} > [Cr(bpop)_2]^{3+} > [Cr(bptp)_2]^{3+} > [Cr(bpmp)_2]^{3+}$, this work elucidates how structural and electronic features of the ligand backbone precisely modulate the photophysical properties of molecular rubies. The first experimental determination of the energies of the five lowest $^2T_1/^2E$-derived states enables straightforward scaling of computational values, facilitating reliable predictions in these systems (Fig. 4.1d). A structure-property analysis on the reference system $[Cr(py)_6]^{3+}$ identified Cr–N bond lengths as the key factor in controlling the nephelauxetic effect. Additionally, this project highlights the detrimental effects of multiphonon relaxation and heavy atoms on luminescence efficiency and photostability, emphasizing the importance of considering dynamic effects beyond Franck-Condon geometries when designing new photoactive systems.

The differing electronic demands of polypyridine ligands have historically limited the transferability of synthetic routes across molecular rubies, leaving the optical properties of heteroleptic representatives largely unexplored.[180–182,196] This work developed a versatile synthetic route, giving access to heteroleptic molecular rubies with unique optical properties (Section 3.6). The complexes $[CrL^XL^Y]^{3+}$ (L^X, L^Y = ddpd, bpmp, bptp) were prepared sequentially from both possible reaction paths via tris(triflato) chromium(III) intermediates, conveniently formed by introducing TMSOTf as a halide scavenger for the parent trichlorido chromium(III) precursors. The spin-flip energies of the heteroleptic complexes, which fall between those of their homoleptic counterparts, demonstrate that the nephelauxetic effects of the present ligands add up in a semi-quantitative fashion (Fig. 4.1e), analogous to ligand field strength correlations using increment rules.[166] Computational analysis, corrected by a common empirical scaling factor, accurately reproduced the experimental results, providing a reliable framework for predicting spin-flip energies in molecular rubies. This work expands accessibility to molecular rubies with diverse photophysical properties, offering new opportunities for optical and photocatalytic applications through strategic ligand combinations.

The concept of modifying the photophysical properties of molecular rubies post-synthetically is particularly valuable, as it eliminates the need for developing new synthetic routes for ligands (Section 3.7). In $[Cr(ddad)_2]^{3+}$, the excited state energies remain unaffected by the presence of Lewis acids BF_3 and $B(C_6F_5)_3$, likely due to the reduced donor ability of the pyrazine unit, demonstrating the significant electronic influence exerted by the charged metal center. Both $[Cr(ddad)_2]^{3+}$ and $[Cr(bptp)(ddad)]^{3+}$ exhibit intense absorption bands at 491 and 502 nm, respectively, corresponding to ILCT transitions into low-energy π^* orbitals of the pyrazine

(Fig. 4.1f). This work thus gives a design strategy at hand for achieving red-shifted, spin-allowed absorption in molecular rubies, beneficial for photocatalysis and light-harvesting applications.[25,225–227] The geometry of $[Cr(bptp)(ddad)]^{3+}$ reflects the additive effect of combining structurally related ligands, resulting in intermediate spin-flip energies with respect to the homoleptic complexes. This demonstrates that the structural independence of the ligands translates into an additive influence on electronic properties, such as the nephelauxetic effect.

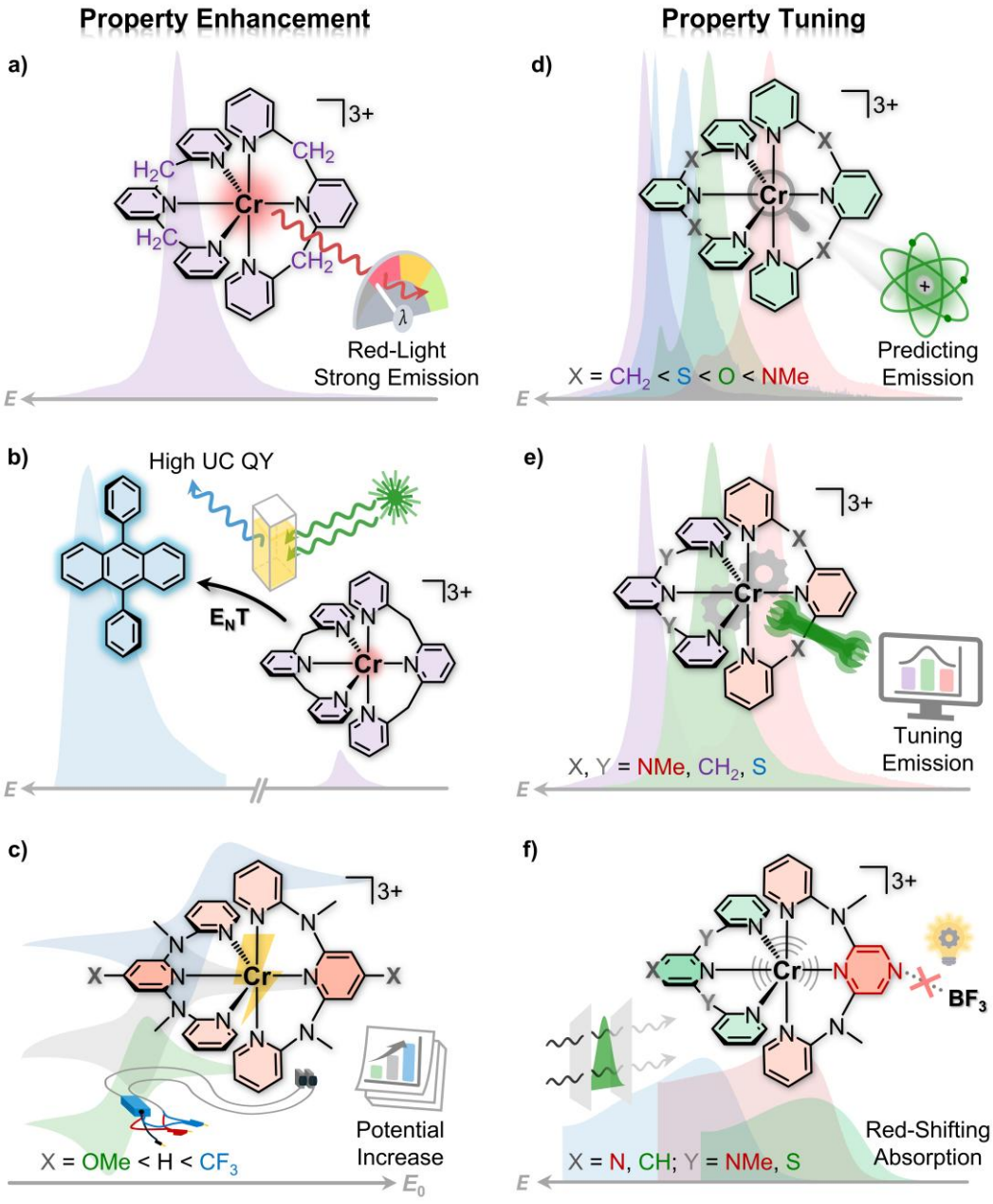

Fig. 4.1 Overview of the results from this work, covering the chemical structures of the investigated compounds, key spectra and voltammograms in the background, and a schematic representation of the main findings.

References

5

[1] J. Rockström, W. Steffen, K. Noone, A. Persson, F. S. Chapin, E. F. Lambin, T. M. Lenton, M. Scheffer, C. Folke, H. J. Schellnhuber, B. Nykvist, C. A. de Wit, T. Hughes, S. van der Leeuw, H. Rodhe, S. Sörlin, P. K. Snyder, R. Costanza, U. Svedin, M. Falkenmark, L. Karlberg, R. W. Corell, V. J. Fabry, J. Hansen, B. Walker, D. Liverman, K. Richardson, P. Crutzen, J. A. Foley, *Nature* **2009**, *461*, 472–475.

[2] W. Steffen, K. Richardson, J. Rockström, S. E. Cornell, I. Fetzer, E. M. Bennett, R. Biggs, S. R. Carpenter, W. de Vries, C. A. de Wit, C. Folke, D. Gerten, J. Heinke, G. M. Mace, L. M. Persson, V. Ramanathan, B. Reyers, S. Sörlin, *Science (N. Y.)* **2015**, *347*, 1259855.

[3] N. Armaroli, V. Balzani, *Chem. - Asian J.* **2011**, *6*, 768–784.

[4] International Energy Agency, *World Energy Outlook 2023*, Paris, **2023**.

[5] D. Zhang, C. Rong, T. Ahmad, H. Xie, H. Zhu, X. Li, T. Wu, *Eng. Rep.* **2022**, e12584.

[6] Intergovernmental Panel on Climate Change, *Climate Change 2022 – Impacts, Adaptation and Vulnerability*, Cambridge University Press, **2023**.

[7] U. N. Environment, *Global Environment Outlook – GEO-6: Healthy Planet, Healthy People*, Cambridge University Press, **2019**.

[8] United Nations, *Sustainable Development Goals*, New York, **2015**.

[9] N. S. Lewis, D. G. Nocera, *Proc. Natl. Acad. Sci. U. S. A.* **2006**, *103*, 15729–15735.

[10] N. Armaroli, V. Balzani, *Angew. Chem. Int. Ed.* **2007**, *46*, 52–66.

[11] P. K. Nayak, S. Mahesh, H. J. Snaith, D. Cahen, *Nat. Rev. Mater.* **2019**, *4*, 269–285.

[12] S. D. Tilley, M. Cornuz, K. Sivula, M. Grätzel, *Angew. Chem. Int. Ed.* **2010**, *49*, 6405–6408.

[13] N. J. Turro, V. Ramamurthy, J. C. Scaiano, *Principles of Molecular Photochemistry*. *An Introduction*, University Science Books, Sausalito, Calif., **2009**.

[14] J. Twilton, C. Le, P. Zhang, M. H. Shaw, R. W. Evans, D. W. C. MacMillan, *Nat. Rev. Chem.* **2017**, *1*, 572.

[15] D. G. Nocera, *Acc. Chem. Res.* **2012**, *45*, 767–776.

[16] D. Gust, T. A. Moore, A. L. Moore, *Acc. Chem. Res.* **2009**, *42*, 1890–1898.

[17] H. Yersin, *Highly Efficient OLEDs with Phosphorescent Materials*, Wiley, Hoboken, **2007**.

[18] V. Balzani, A. Juris, M. Venturi, S. Campagna, S. Serroni, *Chem. Rev.* **1996**, *96*, 759–834.

[19] L. C.-C. Lee, K. K.-W. Lo, *Chem. Rev.* **2024**, *124*, 8825–9014.

[20] F. Puntoriero, G. La Ganga, A. M. Cancelliere, S. Campagna, *Curr. Opin. Green Sustainable Chem.* **2022**, *36*, 100636.

[21] M. DeRosa, *Coord. Chem. Rev.* **2002**, *233-234*, 351–371.

[22] H. Kumagai, Y. Tamaki, O. Ishitani, *Acc. Chem. Res.* **2022**, *55*, 978–990.

[23] J. K. McCusker, *Acc. Chem. Res.* **2003**, *36*, 876–887.

[24] A. Juris, V. Balzani, F. Barigelletti, S. Campagna, P. Belser, A. von Zelewsky, *Coord. Chem. Rev.* **1988**, *84*, 85–277.

[25] K. Kalyanasundaram, *Coord. Chem. Rev.* **1982**, *46*, 159–244.

[26] F. Glaser, O. S. Wenger, *Coord. Chem. Rev.* **2020**, *405*, 213129.

[27] C. K. Prier, D. A. Rankic, D. W. C. MacMillan, *Chem. Rev.* **2013**, *113*, 5322–5363.

[28] W.-M. Cheng, R. Shang, *ACS Catal.* **2020**, *10*, 9170–9196.

[29] L. Marzo, S. K. Pagire, O. Reiser, B. König, *Angew. Chem. Int. Ed.* **2018**, *57*, 10034–10072.

[30] D. M. Arias-Rotondo, J. K. McCusker, *Chem. Soc. Rev.* **2016**, *45*, 5803–5820.

[31] H. Xu, R. Chen, Q. Sun, W. Lai, Q. Su, W. Huang, X. Liu, *Chem. Soc. Rev.* **2014**, *43*, 3259–3302.

[32] J.-H. Lee, C.-H. Chen, P.-H. Lee, H.-Y. Lin, M.-k. Leung, T.-L. Chiu, C.-F. Lin, *J. Mater. Chem. C* **2019**, *7*, 5874–5888.

[33] H. Yersin, A. F. Rausch, R. Czerwieniec, T. Hofbeck, T. Fischer, *Coord. Chem. Rev.* **2011**, *255*, 2622–2652.

[34] S. Zhang, X. Yang, Y. Numata, L. Han, *Energy Environ. Sci.* **2013**, *6*, 1443.

[35] M. K. Nazeeruddin, E. Baranoff, M. Grätzel, *Solar Energy* **2011**, *85*, 1172–1178.

[36] A. S. Polo, M. K. Itokazu, N. Y. Murakami Iha, *Coord. Chem. Rev.* **2004**, *248*, 1343–1361.

[37] L. C.-C. Lee, K. K.-W. Lo, *J. Am. Chem. Soc.* **2022**, *144*, 14420–14440.

[38] K. K.-W. Lo, *Acc. Chem. Res.* **2020**, *53*, 32–44.

[39] X.-D. Bi, R. Yang, Y.-C. Zhou, D. Chen, G.-K. Li, Y.-X. Guo, M.-F. Wang, D. Liu, F. Gao, *Inorg. Chem.* **2020**, *59*, 14920–14931.

[40] Y. You, S. Cho, W. Nam, *Inorg. Chem.* **2014**, *53*, 1804–1815.

[41] R. M. Izatt, S. R. Izatt, R. L. Bruening, N. E. Izatt, B. A. Moyer, *Chem. Soc. Rev.* **2014**, *43*, 2451–2475.

[42] M. Lancaster, *Green Chemistry*, Royal Society of Chemistry, Cambridge, **2007**.

[43] U.S. Geological Survey, *Mineral Commodity Summaries 2024*, Reston, **2024**.

[44] N. Haque, A. Hughes, S. Lim, C. Vernon, *Resources* **2014**, *3*, 614–635.

[45] S. E. Manahan, *Environmental chemistry*, CRC Press Taylor & Francis Group, Boca Raton, London, New York, **2017**.

[46] C. Bizzarri, E. Spuling, D. M. Knoll, D. Volz, S. Bräse, *Coord. Chem. Rev.* **2018**, *373*, 49–82.

[47] J. K. McCusker, *Science (N.Y.)* **2019**, *363*, 484–488.

[48] C. B. Larsen, O. S. Wenger, *Chem. Eur. J.* **2018**, *24*, 2039–2058.

[49] B. M. Hockin, C. Li, N. Robertson, E. Zysman-Colman, *Catal. Sci. Technol.* **2019**, *9*, 889–915.

[50] O. S. Wenger, *J. Am. Chem. Soc.* **2018**, *140*, 13522–13533.

[51] C. Wegeberg, O. S. Wenger, *JACS Au* **2021**, *1*, 1860–1876.

[52] N. Sinha, O. S. Wenger, *J. Am. Chem. Soc.* **2023**, *145*, 4903–4920.

[53] R. Mondal, A. K. Guin, G. Chakraborty, N. D. Paul, *Org. Biomol. Chem.* **2022**, *20*, 296–328.

[54] M. Dorn, N. R. East, C. Förster, W. R. Kitzmann, J. Moll, F. Reichenauer, T. Reuter, L. Stein, K. Heinze in *Comprehensive Inorganic Chemistry III*, Elsevier, Amsterdam, **2023**, S. 707–788.

[55] X. Li, Y. Xie, Z. Li, *Chem. - Asian J.* **2021**, *16*, 2817–2829.

[56] C. Förster, K. Heinze, *Chem. Phys. Rev.* **2022**, *3*, 1543.

[57] C. Förster, K. Heinze, *Chem. Soc. Rev.* **2020**, *49*, 1057–1070.

[58] J.-R. Jiménez, B. Doistau, M. Poncet, C. Piguet, *Coord. Chem. Rev.* **2021**, *434*, 213750.

[59] P. A. Scattergood in *Organometallic Chemistry* (Eds.: N. J. Patmore, P. I. P. Elliott), Royal Society of Chemistry, Cambridge, **2020**, S. 1–34.

[60] L. A. Büldt, O. S. Wenger, *Chem. Sci.* **2017**, *8*, 7359–7367.

[61] V. Balzani, P. Ceroni, A. Juris, *Photochemistry and Photophysics*. *Concepts, Research, Applications*, Wiley-VCH, Weinheim, **2014**.

[62] V. Balzani, S. Campagna, *Photochemistry and Photophysics of Coordination Compounds I*, Springer, Berlin, Heidelberg, **2007**.

[63] P. Pyykko, *Chem. Rev.* **1988**, *88*, 563–594.

[64] M. Kaupp, *J. Comput. Chem.* **2007**, *28*, 320–325.

[65] P. Dongare, B. D.B. Myron, L. Wang, D. W. Thompson, T. J. Meyer, *Coord. Chem. Rev.* **2017**, *345*, 86–107.

[66] H. Ishida, S. Tobita, Y. Hasegawa, R. Katoh, K. Nozaki, *Coord. Chem. Rev.* **2010**, *254*, 2449–2458.

[67] O. S. Wenger, *Chem. Eur. J.* **2019**, *25*, 6043–6052.

[68] Q. Sun, S. Mosquera-Vazquez, Y. Suffren, J. Hankache, N. Amstutz, L. M. Lawson Daku, E. Vauthey, A. Hauser, *Coord. Chem. Rev.* **2015**, *282-283*, 87–99.

[69] A. Soupart, I. M. Dixon, F. Alary, J.-L. Heully, *Theor. Chem. Acc.* **2018**, *137*, 159.

[70] W. R. Kitzmann, J. Moll, K. Heinze, *Photochem. Photobiol. Sci.* **2022**, *21*, 1309–1331.

[71] C. Degli Esposti, L. Bizzocchi, *J. Chem. Educ.* **2007**, *84*, 1316.

[72] P. S. Wagenknecht, P. C. Ford, *Coord. Chem. Rev.* **2011**, *255*, 591–616.

[73] S. Otto, M. Dorn, C. Förster, M. Bauer, M. Seitz, K. Heinze, *Coord. Chem. Rev.* **2018**, *359*, 102–111.

[74] N. Serpone, M. A. Jamieson, M. S. Henry, M. Z. Hoffman, F. Bolletta, M. Maestri, *J. Am. Chem. Soc.* **1979**, *101*, 2907–2916.

[75] R. Ballardini, G. Varani, H. F. Wasgestian, L. Moggi, V. Balzani, *J. Phys. Chem.* **1973**, *77*, 2947–2951.

[76] C. Wang, S. Otto, M. Dorn, E. Kreidt, J. Lebon, L. Sršan, P. Di Martino-Fumo, M. Gerhards, U. Resch-Genger, M. Seitz, K. Heinze, *Angew. Chem. Int. Ed.* **2018**, *57*, 1112–1116.

[77] M. W. Perkovic, M. J. Heeg, J. F. Endicott, *Inorg. Chem.* **1991**, *30*, 3140–3147.

[78] O. Laporte, W. F. Meggers, *J. Opt. Soc. Am.* **1925**, *11*, 459.

[79] C. Förster, K. Heinze, *Adv. Inorg. Chem.* **2024**, *83*, 111–159.

[80] G. D. Hager, G. A. Crosby, *J. Am. Chem. Soc.* **1975**, *97*, 7031–7037.

[81] E. Kreidt, C. Kruck, M. Seitz in *Handbook on the Physics and Chemistry of Rare Earths*, Elsevier, Amsterdam, **2018**, S. 35–79.

[82] E. B. Sveshnikova, V. L. Ermolaev, *Opt. Spectrosc.* **2011**, *111*, 34–50.

[83] S. Treiling, C. Wang, C. Förster, F. Reichenauer, J. Kalmbach, P. Boden, J. P. Harris, L. M. Carrella, E. Rentschler, U. Resch-Genger, C. Reber, M. Seitz, M. Gerhards, K. Heinze, *Angew. Chem. Int. Ed.* **2019**, *58*, 18075–18085.

[84] C. Wang, W. R. Kitzmann, F. Weigert, C. Förster, X. Wang, K. Heinze, U. Resch-Genger, *ChemPhotoChem* **2022**, *6*, 113.

[85] M. S. Henry, *J. Am. Chem. Soc.* **1977**, *99*, 6138–6139.

[86] M. Z. Hoffman, F. Bolletta, L. Moggi, G. L. Hug, *J. Phys. Chem. Rev. Data* **1989**, *18*, 219–543.

[87] S. Otto, M. Grabolle, C. Förster, C. Kreitner, U. Resch-Genger, K. Heinze, *Angew. Chem. Int. Ed.* **2015**, *54*, 11572–11576.

[88] N. Sinha, P. Yaltseva, O. S. Wenger, *Angew. Chem. Int. Ed.* **2023**, *62*, e202303864.

[89] W. R. Kitzmann, C. Ramanan, R. Naumann, K. Heinze, *Dalton Trans.* **2022**, *51*, 6519–6525.

[90] Y. Tanabe, S. Sugano, *J. Phys. Soc. Jpn.* **1954**, *9*, 766–779.

[91] Y. Tanabe, S. Sugano, *J. Phys. Soc. Jpn.* **1954**, *9*, 753–766.

[92] S. Otto, J. P. Harris, K. Heinze, C. Reber, *Angew. Chem. Int. Ed.* **2018**, *57*, 11069–11073.

[93] S. Lenz, H. Bamberger, P. P. Hallmen, Y. Thiebes, S. Otto, K. Heinze, J. van Slageren, *Phys. Chem. Chem. Phys.* **2019**, *21*, 6976–6983.

[94] W. R. Kitzmann, K. Heinze, *Angew. Chem. Int. Ed.* **2023**, *62*, e202213207.

[95] A. C. Sell, J. C. Wetzel, M. Schmitz, A. W. Maijenburg, G. Woltersdorf, R. Naumann, C. Kerzig, *Dalton Trans.* **2022**, *51*, 10799–10808.

[96] G. Baryshnikov, B. Minaev, H. Ågren, *Chem. Rev.* **2017**, *117*, 6500–6537.

[97] D. M. Roundhill, *Photochemistry and Photophysics of Metal Complexes*, Springer, Boston, MA, **1994**.

[98] J. N. Demas, D. G. Taylor, *Inorg. Chem.* **1979**, *18*, 3177–3179.

[99] A. Cannizzo, F. van Mourik, W. Gawelda, G. Zgrablic, C. Bressler, M. Chergui, *Angew. Chem.* **2006**, *118*, 3246–3248.

[100] N. H. Damrauer, G. Cerullo, A. Yeh, T. R. Boussie, C. V. Shank, J. K. McCusker, *Science (N. Y.)* **1997**, *275*, 54–57.

[101] A. T. Yeh, C. V. Shank, J. K. McCusker, *Science (N. Y.)* **2000**, *289*, 935–938.

[102] K. Suzuki, A. Kobayashi, S. Kaneko, K. Takehira, T. Yoshihara, H. Ishida, Y. Shiina, S. Oishi, S. Tobita, *Phys. Chem. Chem. Phys.* **2009**, *11*, 9850–9860.

[103] Z. Fang, A. Ito, S. Keinan, Z. Chen, Z. Watson, J. Rochette, Y. Kanai, D. Taylor, K. S. Schanze, T. J. Meyer, *Inorg. Chem.* **2013**, *52*, 8511–8520.

[104] L. S. Forster, *Coord. Chem. Rev.* **2002**, *227*, 59–92.

[105] A. Soupart, F. Alary, J.-L. Heully, P. I. P. Elliott, I. M. Dixon, *Inorg. Chem.* **2020**, *59*, 14679–14695.

[106] C. Kreitner, K. Heinze, *Dalton Trans.* **2016**, *45*, 13631–13647.

[107] D. Hernández-Castillo, R. E. P. Nau, M.-A. Schmid, S. Tschierlei, S. Rau, L. González, *Angew. Chem. Int. Ed.* **2023**, *62*, e202308803.

[108] A. Amini, A. Harriman, A. Mayeux, *Phys. Chem. Chem. Phys.* **2004**, *6*, 1157–1164.

[109] W. Zhang, R. Alonso-Mori, U. Bergmann, C. Bressler, M. Chollet, A. Galler, W. Gawelda, R. G. Hadt, R. W. Hartsock, T. Kroll, K. S. Kjær, K. Kubiček, H. T. Lemke, H. W. Liang, D. A. Meyer, M. M. Nielsen, C. Purser, J. S. Robinson, E. I. Solomon, Z. Sun, D. Sokaras, T. B. van Driel, G. Vankó, T.-C. Weng, D. Zhu, K. J. Gaffney, *Nature* **2014**, *509*, 345–348.

[110] G. Auböck, M. Chergui, *Nat. Chem.* **2015**, *7*, 629–633.

[111] A. Cannizzo, C. J. Milne, C. Consani, W. Gawelda, C. Bressler, F. van Mourik, M. Chergui, *Coord. Chem. Rev.* **2010**, *254*, 2677–2686.

[112] M. C. Carey, S. L. Adelman, J. K. McCusker, *Chem. Sci.* **2019**, *10*, 134–144.

[113] L. Liu, T. Duchanois, T. Etienne, A. Monari, M. Beley, X. Assfeld, S. Haacke, P. C. Gros, *Phys. Chem. Chem. Phys.* **2016**, *18*, 12550–12556.

[114] T. Duchanois, T. Etienne, C. Cebrián, L. Liu, A. Monari, M. Beley, X. Assfeld, S. Haacke, P. C. Gros, *Eur. J. Inorg. Chem.* **2015**, *2015*, 2469–2477.

[115] T. C. B. Harlang, Y. Liu, O. Gordivska, L. A. Fredin, C. S. Ponseca, P. Huang, P. Chábera, K. S. Kjaer, H. Mateos, J. Uhlig, R. Lomoth, R. Wallenberg, S. Styring, P. Persson, V. Sundström, K. Wärnmark, *Nat. Chem.* **2015**, *7*, 883–889.

[116] P. Zimmer, L. Burkhardt, A. Friedrich, J. Steube, A. Neuba, R. Schepper, P. Müller, U. Flörke, M. Huber, S. Lochbrunner, M. Bauer, *Inorg. Chem.* **2018**, *57*, 360–373.

[117] D. Leshchev, T. C. B. Harlang, L. A. Fredin, D. Khakhulin, Y. Liu, E. Biasin, M. G. Laursen, G. E. Newby, K. Haldrup, M. M. Nielsen, K. Wärnmark, V. Sundström, P. Persson, K. S. Kjær, M. Wulff, *Chem. Sci.* **2018**, *9*, 405–414.

[118] P. Chábera, K. S. Kjaer, O. Prakash, A. Honarfar, Y. Liu, L. A. Fredin, T. C. B. Harlang, S. Lidin, J. Uhlig, V. Sundström, R. Lomoth, P. Persson, K. Wärnmark, *J. Phys. Chem. Lett.* **2018**, *9*, 459–463.

[119] Y. Liu, T. Harlang, S. E. Canton, P. Chábera, K. Suárez-Alcántara, A. Fleckhaus, D. A. Vithanage, E. Göransson, A. Corani, R. Lomoth, V. Sundström, K. Wärnmark, *Chem. Commun.* **2013**, *49*, 6412–6414.

[120] W. Leis, M. A. Argüello Cordero, S. Lochbrunner, H. Schubert, A. Berkefeld, *J. Am. Chem. Soc.* **2022**, *144*, 1169–1173.

[121] D. M. Manuta, A. J. Lees, *Inorg. Chem.* **1986**, *25*, 1354–1359.

[122] A. J. Lees, *Chem. Rev.* **1987**, *87*, 711–743.

[123] I. R. Farrell, P. Matousek, M. Towrie, A. W. Parker, D. C. Grills, M. W. George, A. Vlcek, *Inorg. Chem.* **2002**, *41*, 4318–4323.

[124] L. A. Büldt, X. Guo, R. Vogel, A. Prescimone, O. S. Wenger, *J. Am. Chem. Soc.* **2017**, *139*, 985–992.

[125] L. A. Büldt, O. S. Wenger, *Angew. Chem. Int. Ed.* **2017**, *56*, 5676–5682.

[126] P. Herr, F. Glaser, L. A. Büldt, C. B. Larsen, O. S. Wenger, *J. Am. Chem. Soc.* **2019**, *141*, 14394–14402.

[127] P. Herr, C. Kerzig, C. B. Larsen, D. Häussinger, O. S. Wenger, *Nat. Chem.* **2021**, *13*, 956–962.

[128] P. Chábera, Y. Liu, O. Prakash, E. Thyrhaug, A. E. Nahhas, A. Honarfar, S. Essén, L. A. Fredin, T. C. B. Harlang, K. S. Kjær, K. Handrup, F. Ericson, H. Tatsuno, K. Morgan, J. Schnadt, L. Häggström, T. Ericsson, A. Sobkowiak, S. Lidin, P. Huang, S. Styring, J. Uhlig, J. Bendix, R. Lomoth, V. Sundström, P. Persson, K. Wärnmark, *Nature* **2017**, *543*, 695–699.

[129] K. S. Kjær, N. Kaul, O. Prakash, P. Chábera, N. W. Rosemann, A. Honarfar, O. Gordivska, L. A. Fredin, K.-E. Bergquist, L. Häggström, T. Ericsson, L. Lindh, A. Yartsev, S. Styring, P. Huang, J. Uhlig, J. Bendix, D. Strand, V. Sundström, P. Persson, R. Lomoth, K. Wärnmark, *Science (N. Y.)* **2019**, *363*, 249–253.

[130] Y. Zhang, M. Schulz, M. Wächtler, M. Karnahl, B. Dietzek, *Coord. Chem. Rev.* **2018**, *356*, 127–146.

[131] M. W. Mara, K. A. Fransted, L. X. Chen, *Coord. Chem. Rev.* **2015**, *282-283*, 2–18.

[132] Y. Zhang, T. S. Lee, J. L. Petersen, C. Milsmann, *J. Am. Chem. Soc.* **2018**, *140*, 5934–5947.

[133] Y. Zhang, J. L. Petersen, C. Milsmann, *J. Am. Chem. Soc.* **2016**, *138*, 13115–13118.

[134] Y. Zhang, N. G. Akhmedov, J. L. Petersen, C. Milsmann, *Chem. Eur. J.* **2019**, *25*, 3042–3052.

[135] Y. Zhang, J. L. Petersen, C. Milsmann, *Organometallics* **2018**, *37*, 4488–4499.

[136] M. Iwamura, S. Takeuchi, T. Tahara, *Acc. Chem. Res.* **2015**, *48*, 782–791.

[137] L. Gimeno, B. T. Phelan, E. A. Sprague-Klein, T. Roisnel, E. Blart, C. Gourlaouen, L. X. Chen, Y. Pellegrin, *Inorg. Chem.* **2022**, *61*, 7296–7307.

[138] R. Czerwieniec, M. J. Leitl, H. H.H. Homeier, H. Yersin, *Coord. Chem. Rev.* **2016**, *325*, 2–28.

[139] H. Yersin, R. Czerwieniec, M. Z. Shafikov, A. F. Suleymanova, *ChemPhysChem* **2017**, *18*, 3508–3535.

[140] M. Dorn, D. Hunger, C. Förster, R. Naumann, J. van Slageren, K. Heinze, *Chem. Eur. J.* **2023**, *29*, e202202898.

[141] N. R. East, R. Naumann, C. Förster, C. Ramanan, G. Diezemann, K. Heinze, *Nat. Chem.* **2024**, *16*, 827–834.

[142] M. Dorn, J. Kalmbach, P. Boden, A. Päpcke, S. Gómez, C. Förster, F. Kuczelinis, L. M. Carrella, L. A. Büldt, N. H. Bings, E. Rentschler, S. Lochbrunner, L. González, M. Gerhards, M. Seitz, K. Heinze, *J. Am. Chem. Soc.* **2020**, *142*, 7947–7955.

[143] M. Dorn, J. Kalmbach, P. Boden, A. Kruse, C. Dab, C. Reber, G. Niedner-Schatteburg, S. Lochbrunner, M. Gerhards, M. Seitz, K. Heinze, *Chem. Sci.* **2021**, *12*, 10780–10790.

[144] J. P. Harris, C. Reber, H. E. Colmer, T. A. Jackson, A. P. Forshaw, J. M. Smith, R. A. Kinney, J. Telser, *Can. J. Chem.* **2017**, *95*, 547–552.

[145] P. Dierks, Y. Vukadinovic, M. Bauer, *Inorg. Chem. Front.* **2022**, *9*, 206–220.

[146] J. J. Oppenheim, B. J. McNicholas, J. Miller, H. B. Gray, *Inorg. Chem.* **2019**, *58*, 15202–15206.

[147] A. B. P. Lever, A. B. P. Lever, *Inorganic Electronic Spectroscopy,* 2. Aufl., Elsevier, Amsterdam, **1984**.

[148] P. W. Atkins, R. Friedman, *Molecular Quantum Mechanics,* 5. Aufl., Oxford University Press, Oxford, New York, **2011**.

[149] D. B. Nemez, I. B. Lozada, J. D. Braun, J. A. G. Williams, D. E. Herbert, *Inorg. Chem.* **2022**, *61*, 13386–13398.

[150] T. M. Stonelake, K. A. Phillips, H. Y. Otaif, Z. C. Edwardson, P. N. Horton, S. J. Coles, J. M. Beames, S. J. A. Pope, *Inorg. Chem.* **2020**, *59*, 2266–2277.

[151] H. Xiang, J. Cheng, X. Ma, X. Zhou, J. J. Chruma, *Chem. Soc. Rev.* **2013**, *42*, 6128–6185.

[152] J. A. Treadway, G. F. Strouse, R. R. Ruminski, T. J. Meyer, *Inorg. Chem.* **2001**, *40*, 4508–4509.

[153] S. Sun, W. Sun, D. Mu, N. Jiang, X. Peng, *Chem. Commun.* **2015**, *51*, 2529–2531.

[154] M. S. Mehata, Y. Yang, Z.-J. Qu, J.-S. Chen, F.-J. Zhao, K.-L. Han, *RSC Adv.* **2015**, *5*, 34094–34099.

[155] C. J. Cramer, *Essentials of Computational Chemistry,* 2. Aufl., Wiley-VCH, Chichester, **2004**.

[156] K. Pierloot, S. Vancoillie, *J. Chem. Phys.* **2008**, *128*, 34104.

[157] M. Reiher, A. Wolf, *Relativistic Quantum Chemistry*. *The Fundamental Theory of Molecular Science,* 2. Aufl., Wiley-VCH, Weinheim, **2015**.

[158] W. R. Kitzmann, M.-S. Bertrams, P. Boden, A. C. Fischer, R. Klauer, J. Sutter, R. Naumann, C. Förster, G. Niedner-Schatteburg, N. H. Bings, J. Hunger, C. Kerzig, K. Heinze, *J. Am. Chem. Soc.* **2023**, *145*, 16597–16609.

[159] P. Chen, T. J. Meyer, *Chem. Rev.* **1998**, *98*, 1439–1478.

[160] S. D. Helland, A. S. Chang, K. W. Lee, P. S. Hutchison, W. W. Brennessel, W. T. Eckenhoff, *Inorg. Chem.* **2020**, *59*, 705–716.

[161] N. M. Ali, V. L. MacLeod, P. Jennison, I. V. Sazanovich, C. A. Hunter, J. A. Weinstein, M. D. Ward, *Dalton Trans.* **2012**, *41*, 2408.

[162] E. M. Kober, B. P. Sullivan, T. J. Meyer, *Inorg. Chem.* **1984**, *23*, 2098–2104.

[163] W. Kaim, S. Kohlmann, S. Ernst, B. Olbrich-Deussner, C. Bessenbacher, A. Schulz, *J. Org. Chem.* **1987**, *321*, 215–226.

[164] C. E. Housecroft, A. G. Sharpe, *Inorganic Chemistry,* 4. Aufl., Pearson, London, **2012**.

[165] J. E. Huheey, R. Keiter, E. A. Keiter, *Anorganische Chemie*, De Gruyter, Berlin, **2003**.

[166] L. H. Gade, *Koordinationschemie*, John Wiley & Sons, Hoboken, **2012**.

[167] C. B. Larsen, J. D. Braun, I. B. Lozada, K. Kunnus, E. Biasin, C. Kolodziej, C. Burda, A. A. Cordones, K. J. Gaffney, D. E. Herbert, *J. Am. Chem. Soc.* **2021**, *143*, 20645–20656.

[168] M. E. Reinhard, B. K. Sidhu, I. B. Lozada, N. Powers-Riggs, R. J. Ortiz, H. Lim, R. Nickel, J. van Lierop, R. Alonso-Mori, M. Chollet, L. B. Gee, P. L. Kramer, T. Kroll, S. L. Raj, T. B. van Driel, A. A. Cordones, D. Sokaras, D. E. Herbert, K. J. Gaffney, *J. Am. Chem. Soc.* **2024**, *146*, 17908–17916.

[169] A. D. Kirk, G. B. Porter, *J. Phys. Chem.* **1980**, *84*, 887–891.

[170] L. Stein, P. Boden, R. Naumann, C. Förster, G. Niedner-Schatteburg, K. Heinze, *Chem. Commun.* **2022**, *58*, 3701–3704.

[171] N. Sinha, J.-R. Jiménez, B. Pfund, A. Prescimone, C. Piguet, O. S. Wenger, *Angew. Chem. Int. Ed.* **2021**, *60*, 23722–23728.

[172] N. Sawicka, C. J. Craze, P. N. Horton, S. J. Coles, E. Richards, S. J. A. Pope, *Chem. Commun.* **2022**, *58*, 5733–5736.

[173] Y. Cheng, Q. Yang, J. He, W. Zou, K. Liao, X. Chang, C. Zou, W. Lu, *Dalton Trans.* **2023**, *52*, 2561–2565.

[174] L. Stein, C. Förster, K. Heinze, *Organometallics* **2024**, *43*, 1766–1774.

[175] T. H. Maiman, *Nature* **1960**, *187*, 493–494.

[176] L. Stein, C. Wang, C. Förster, U. Resch-Genger, K. Heinze, *Dalton Trans.* **2022**, *51*, 17664–17670.

[177] S. Otto, C. Förster, C. Wang, U. Resch-Genger, K. Heinze, *Chem. Eur. J.* **2018**, *24*, 12555–12563.

[178] J.-R. Jiménez, B. Doistau, C. M. Cruz, C. Besnard, J. M. Cuerva, A. G. Campaña, C. Piguet, *J. Am. Chem. Soc.* **2019**, *141*, 13244–13252.

[179] J.-R. Jiménez, M. Poncet, S. Míguez-Lago, S. Grass, J. Lacour, C. Besnard, J. M. Cuerva, A. G. Campaña, C. Piguet, *Angew. Chem. Int. Ed.* **2021**, *60*, 10095–10102.

[180] J.-R. Jiménez, M. Poncet, B. Doistau, C. Besnard, C. Piguet, *Dalton Trans.* **2020**, *49*, 13528–13532.

[181] J.-R. Jiménez, B. Doistau, C. Besnard, C. Piguet, *Chem. Commun.* **2018**, *54*, 13228–13231.

[182] J. Chong, C. Besnard, C. M. Cruz, C. Piguet, J.-R. Jiménez, *Dalton Trans.* **2022**, *51*, 4297–4309.

[183] S. Sittel, R. Naumann, K. Heinze, *Front. Chem.* **2022**, *10*, 887439.

[184] S. Otto, N. Scholz, T. Behnke, U. Resch-Genger, K. Heinze, *Chem. Eur. J.* **2017**, *23*, 12131–12135.

[185] C. Wang, S. Otto, M. Dorn, K. Heinze, U. Resch-Genger, *Anal. Chem.* **2019**, *91*, 2337–2344.

[186] R. A. Forman, G. J. Piermarini, J. D. Barnett, S. Block, *Science (N. Y.)* **1972**, *176*, 284–285.

[187] C. Förster, H. Osthues, D. Schwab, N. L. Doltsinis, K. Heinze, *ChemPhysChem* **2023**, *24*, e202300165.

[188] C. Dee, F. Zinna, W. R. Kitzmann, G. Pescitelli, K. Heinze, L. Di Bari, M. Seitz, *Chem. Commun.* **2019**, *55*, 13078–13081.

[189] M. T. Indelli, F. Scandola, *J. Phys. Chem.* **1993**, *97*, 3328–3332.

[190] D. Rehm, A. Weller, *Isr. J. Chem.* **1970**, *8*, 259–271.

[191] T. H. Bürgin, F. Glaser, O. S. Wenger, *J. Am. Chem. Soc.* **2022**, *144*, 14181–14194.

[192] S. Otto, A. M. Nauth, E. Ermilov, N. Scholz, A. Friedrich, U. Resch-Genger, S. Lochbrunner, T. Opatz, K. Heinze, *ChemPhotoChem* **2017**, *1*, 344–349.

[193] J. Kalmbach, C. Wang, Y. You, C. Förster, H. Schubert, K. Heinze, U. Resch-Genger, M. Seitz, *Angew. Chem. Int. Ed.* **2020**, *59*, 18804–18808.

[194] T. N. Singh-Rachford, F. N. Castellano, *Coord. Chem. Rev.* **2010**, *254*, 2560–2573.

[195] V. Gray in *Photochemistry* (Eds.: A. Albini, S. Protti), Royal Society of Chemistry, Cambridge, **2019**, S. 404–420.

[196] D. Zare, B. Doistau, H. Nozary, C. Besnard, L. Guénée, Y. Suffren, A.-L. Pelé, A. Hauser, C. Piguet, *Dalton Trans.* **2017**, *46*, 8992–9009.

[197] U. Basu, S. Otto, K. Heinze, G. Gasser, *Eur. J. Inorg. Chem.* **2019**, *2019*, 37–41.

[198] S. Ji, W. Wu, W. Wu, H. Guo, J. Zhao, *Angew. Chem. Int. Ed.* **2011**, *50*, 1626–1629.

[199] S. Sittel, A. C. Sell, K. Hofmann, C. Wiedemann, J. P. Nau, C. Kerzig, G. Manolikakes, K. Heinze, *ChemCatChem* **2023**, *15*, 75.

[200] C. Wang, H. Li, T. H. Bürgin, O. S. Wenger, *Nat. Chem.* **2024**, *16*, 1151–1159.

[201] K. Kalyanasundaram, *Coord. Chem. Rev.* **1998**, *177*, 347–414.

[202] R. D. Costa, E. Ortí, H. J. Bolink, F. Monti, G. Accorsi, N. Armaroli, *Angew. Chem. Int. Ed.* **2012**, *51*, 8178–8211.

[203] F. Reichenauer, C. Wang, C. Förster, P. Boden, N. Ugur, R. Báez-Cruz, J. Kalmbach, L. M. Carrella, E. Rentschler, C. Ramanan, G. Niedner-Schatteburg, M. Gerhards, M. Seitz, U. Resch-Genger, K. Heinze, *J. Am. Chem. Soc.* **2021**, *143*, 11843–11855.

[204] C. Wang, F. Reichenauer, W. R. Kitzmann, C. Kerzig, K. Heinze, U. Resch-Genger, *Angew. Chem. Int. Ed.* **2022**, *61*, e202202238.

[205] R. F. Higgins, S. M. Fatur, S. G. Shepard, S. M. Stevenson, D. J. Boston, E. M. Ferreira, N. H. Damrauer, A. K. Rappé, M. P. Shores, *J. Am. Chem. Soc.* **2016**, *138*, 5451–5464.

[206] S. M. Stevenson, M. P. Shores, E. M. Ferreira, *Angew. Chem. Int. Ed.* **2015**, *54*, 6506–6510.

[207] R. F. Higgins, S. M. Fatur, N. H. Damrauer, E. M. Ferreira, A. K. Rappé, M. P. Shores, *ACS Catal.* **2018**, *8*, 9216–9225.

[208] S. M. Stevenson, R. F. Higgins, M. P. Shores, E. M. Ferreira, *Chem. Sci.* **2017**, *8*, 654–660.

[209] A. M. McDaniel, H.-W. Tseng, N. H. Damrauer, M. P. Shores, *Inorg. Chem.* **2010**, *49*, 7981–7991.

[210] P. M. Becker, C. Förster, L. M. Carrella, P. Boden, D. Hunger, J. van Slageren, M. Gerhards, E. Rentschler, K. Heinze, *Chem. Eur. J.* **2020**, *26*, 7199–7204.

[211] C. C. Scarborough, S. Sproules, T. Weyhermüller, S. DeBeer, K. Wieghardt, *Inorg. Chem.* **2011**, *50*, 12446–12462.

[212] M. Wang, T. Weyhermüller, K. Wieghardt, *Eur. J. Inorg. Chem.* **2015**, *2015*, 3246–3254.

[213] C. C. Scarborough, K. M. Lancaster, S. DeBeer, T. Weyhermüller, S. Sproules, K. Wieghardt, *Inorg. Chem.* **2012**, *51*, 3718–3732.

[214] E. J. Piechota, G. J. Meyer, *J. Chem. Educ.* **2019**, *96*, 2450–2466.

[215] R. A. Marcus, *Angew. Chem. Int. Ed. Engl.* **1993**, *32*, 1111–1121.

[216] C. C. Moser, J. M. Keske, K. Warncke, R. S. Farid, P. L. Dutton, *Nature* **1992**, *355*, 796–802.

[217] R. A. Marcus, N. Sutin, *Biochim. Biophys. Acta, Bioener.* **1985**, *811*, 265–322.

[218] N. Kandoth, J. Pérez Hernández, E. Palomares, J. Lloret-Fillol, *Sustainable Energy Fuels* **2021**, *5*, 638–665.

[219] A. P. Busch, *Bachelorarbeit*, Johannes Gutenberg-Universität Mainz, Mainz, **2024**.

[220] R. W. Jones, A. J. Auty, G. Wu, P. Persson, M. V. Appleby, D. Chekulaev, C. R. Rice, J. A. Weinstein, P. I. P. Elliott, P. A. Scattergood, *J. Am. Chem. Soc.* **2023**, *145*, 12081–12092.

[221] M. Korff, T. O. Paulisch, F. Glorius, N. L. Doltsinis, B. Wünsch, *Molecules* **2022**, *27*.

[222] F. Reichenauer, R. Naumann, C. Förster, W. R. R. Kitzmann, A.-P. M. Reponen, S. Feldmann, K. Heinze, *Chem. Sci.* **2024**.

[223] D. Ma, L. Duan, Y. Wei, L. He, L. Wang, Y. Qiu, *Chem. Commun.* **2014**, *50*, 530–532.

[224] K. Witas, S. S. Nair, T. Maisuradze, L. Zedler, H. Schmidt, P. Garcia-Porta, A. S. J. Rein, T. Bolter, S. Rau, S. Kupfer, B. Dietzek-Ivanšić, D. U. Sorsche, *J. Am. Chem. Soc.* **2024**, *146*, 19710–19719.

[225] X. Zhang, Y. Hou, X. Xiao, X. Chen, M. Hu, X. Geng, Z. Wang, J. Zhao, *Coord. Chem. Rev.* **2020**, *417*, 213371.

[226] T. J. Meyer, *Acc. Chem. Res.* **1989**, *22*, 163–170.

[227] T. Mirkovic, E. E. Ostroumov, J. M. Anna, R. van Grondelle, Govindjee, G. D. Scholes, *Chem. Rev.* **2017**, *117*, 249–293.

[228] L. Leuschner, *Bachelorarbeit*, Johannes Gutenberg-Universität Mainz, Mainz, **2021**.

[229] A. Breivogel, C. Förster, K. Heinze, *Inorg. Chem.* **2010**, *49*, 7052–7056.

[230] T. U. Connell, C. L. Fraser, M. L. Czyz, Z. M. Smith, D. J. Hayne, E. H. Doeven, J. Agugiaro, D. J. D. Wilson, J. L. Adcock, A. D. Scully, D. E. Gómez, N. W. Barnett, A. Polyzos, P. S. Francis, *J. Am. Chem. Soc.* **2019**, *141*, 17646–17658.

6 Appendix

6.1 Supporting Information: Strongly Red-Emissive Molecular Ruby $[Cr(bpmp)_2]^{3+}$ surpasses $[Ru(bpy)_3]^{2+}$

Strongly Red-Emissive Molecular Ruby $[Cr(bpmp)_2]^{3+}$ surpasses $[Ru(bpy)_3]^{2+}$

Florian Reichenauer[a], Cui Wang[b,c], Christoph Förster[a], Pit Boden[d], Naz Ugur[e], Ricardo Báez-Cruz[e], Jens Kalmbach[f], Luca M. Carrella[a], Eva Rentschler[a], Charusheela Ramanan[e], Gereon Niedner-Schatteburg[d], Markus Gerhards[d†], Michael Seitz[f,*], Ute Resch-Genger[b,*] and Katja Heinze[a,*]

[a] Department of Chemistry, Johannes Gutenberg University of Mainz, Duesbergweg 10-14, 55128 Mainz, Germany

[b] Federal Institute for Materials Research and Testing (BAM), Division Biophotonics, Richard-Willstätter-Str. 11, 12489 Berlin, Germany

[c] Institut für Chemie und Biochemie, Freie Universität Berlin, Arnimallee 22, 14195 Berlin, Germany

[d] Department of Chemistry and Research Center Optimas, University Kaiserslautern, Erwin-Schrödinger-Straße, 67663 Kaiserslautern, Germany

[e] Max Planck Institute for Polymer Research, Ackermannweg 10, 55128 Mainz, Germany

[f] Institute of Inorganic Chemistry, University of Tübingen, Auf der Morgenstelle 18, 72076 Tübingen, Germany.

† During manuscript finalization, Prof. Markus Gerhards unexpectedly passed away on Dec. 28th 2020.

Supporting Information

Contents

Quantum Chemical Screening and Refinement

Static unrestricted Kohn-Sham orbitals DFT (UKS): All calculations were performed using the quantum computing suite ORCA 4.0.1.[1] Geometry optimization was performed using unrestricted Kohn-Sham orbitals DFT (UKS) and the B3LYP functional[2] in combination with Ahlrichs' split-valence triple-ζ basis set def2-TZVPP for all atoms.[3,4] Tight convergence criteria were chosen for DFT-UKS calculations (keywords *tightscf* and *tightopt*). All DFT-UKS calculations make use of the resolution of identity (Split-RI-J) approach for the Coulomb term in combination with the chain-of-spheres approximation for the exchange term (*COSX*).[5,6] The zero order relativistic approximation was used to describe relativistic effects in all calculations (keyword *ZORA*).[7,8] Grimme's empirical dispersion correction D3(BJ) was employed (keyword *D3BJ*).[9,10] To account for solvent effects, a conductor-like screening model (keyword *CPCM* acetonitrile) modeling acetonitrile was used in all calculations.[11] Explicit counter ions and/or solvent molecules were neglected.

SOC-CASSCF(x,y)-FIC-NEVPT2: Calculations of ground and excited state properties with respect to metal-centered (MC) states were performed using the complete-active-space self-consistent field method including spin-orbit coupling (SOC-CASSCF)[12,13] in conjunction with the fully internally contracted N-electron valence perturbation theory to second order (FIC-NEVPT2)[14,15] in order to recover missing dynamic electron correlation. All electronic states are classified by irreducible representations of the *O* point group, in spite of the lower actual symmetries of the considered complexes. In the screening procedure, a small active space of the three d electrons and five d orbitals was selected CAS(3,5) (Table S1). In order to accurately model the ligand field of the hit structure and the reference structure, the active space was expanded to encompass the dominant bonding/antibonding orbitals formed between chromium and the ligand. In addition to the minimal active space of (3,5), two occupied Cr–N σ bonding orbitals and a second d shell[16] were included in these calculations giving an active space of (7,12) (Table S3). 7 quartet and 9 doublet roots were calculated with this active space. 10 quartet and 40 doublet roots were calculated to invoke an ab initio ligand field theory (AILFT)[17,18] analysis from CASSCF(3,5)-NEVPT results (keyword *actorbs dorbs*) (Table S2). SOC was treated through the mean-field (SOMF) approximation[19,20], and the effective Hamiltonian approach[21-23] was used to compute the spin-Hamiltonian parameters (Table S4). From these SOC matrix elements, we obtain an approximate guess of conceivable ISC processes at the Franck-Condon geometry, i.e. before vibrational cooling in the excited quartet state.

Table S1. CASSCF(3,5)-NEVPT results; energies in cm^{-1} (bold values indicate the lowest state of each multiplicity).

	$^2E(1)$	$^2E(2)$	$^2T_1(1)$	$^2T_1(2)$	$^2T_1(3)$	$^2T_2(1)$	$^2T_2(2)$	$^2T_2(3)$	$^4T_2(1)$	$^4T_2(2)$	$^4T_2(3)$
$Cr(acac)_3$	**16577**	16630	17290	17564	17598	24793	24874	25479	**19006**	19427	19526
$[Cr(NH_3)_6]^{3+}$	**16784**	16786	17554	17605	17698	25608	25841	25953	**22731**	22789	22823
$[Cr(py)_6]^{3+}$	**16589**	16589	17428	17432	17445	25159	25192	25202	**20213**	20245	2026
$[Cr(tpy)_2]^{3+}$	**16021**	16087	16819	16820	16911	24694	24738	24739	**20386**	23113	23119
$[Cr(bpy)_3]^{3+}$	**16278**	16288	16817	17210	17233	24810	24864	25762	**23300**	23440	23539
$[Cr(ddpd)_2]^{3+}$	**15605**	16269	16804	16919	17089	25069	25423	25781	**22448**	22767	23907
$[Cr(bpmp)_2]^{3+}$	**16299**	16515	17096	17354	17391	25246	25440	25488	**20882**	21203	22186
$[Cr(CN)_6]^{3-}$	**15623**	15624	16332	16333	16333	24651	24653	24653	**28470**	28483	28484

Table S2. LFT parameters from CASSCF(3,5)-NEVPT results; *B*, *C* in cm^{-1}.

	B	*C*	*C*/*B*
$Cr(acac)_3$	982	3116	3.17
$[Cr(NH_3)_6]^{3+}$	988	3053	3.09
$[Cr(py)_6]^{3+}$	976	3011	3.08
$[Cr(tpy)_2]^{3+}$	947	2962	3.13
$[Cr(bpy)_3]^{3+}$	982	2942	2.99
$[Cr(ddpd)_2]^{3+}$	964	2972	3.08
$[Cr(bpmp)_2]^{3+}$	1003	2937	2.93
$[Cr(CN)_6]^{3-}$	888	2939	3.31

Table S3. CASSCF(7,12)-NEVPT results of $[Cr(ddpd)_2]^{3+}$ and $[Cr(bpmp)_2]^{3+}$; energies in cm^{-1} (bold values indicate the lowest state of each multiplicity).

	$^2E(1)$	$^2E(2)$	$^2T_1(1)$	$^2T_1(2)$	$^2T_1(3)$	$^2T_2(1)$	$^2T_2(2)$	$^2T_3(3)$	$^4T_2(1)$	$^4T_2(2)$	$^4T_2(3)$
$[Cr(ddpd)_2]^{3+}$	15355	15916	**14769**	15647	15719	23328	23600	24033	**22899**	23230	24174
$[Cr(bpmp)_2]^{3+}$	15689	16225	**15535**	16000	16245	23649	23670	23848	**21546**	21822	22733

Table S4. Root-mean-squared spin-orbit coupling (SOC)[a] matrix elements / cm^{-1} between the lowest excited quartet $^4T_2(1)$ and the 8 lowest doublet states of $[Cr(ddpd)_2]^{3+}$ and $[Cr(bpmp)_2]^{3+}$ at their ground state geometry (the Franck-Condon point) from SOC-CASSCF(7,12)-NEVPT results.

	$^2E(1)$	$^2E(2)$	$^2T_1(1)$	$^2T_1(2)$	$^2T_1(3)$	$^2T_2(1)$	$^2T_2(2)$	$^2T_3(3)$
$[Cr(ddpd)_2]^{3+}$	97	10	1	45	36	32	42	3
$[Cr(bpmp)_2]^{3+}$	98	12	6	46	40	32	38	4

[a] The listed SOC values are root-mean-square values for SOC matrix elements over all possible M_S states.

Methods and Synthetic Procedures

General procedures

Acetonitrile was distilled over calcium hydride and butyronitrile over Na_2CO_3/$KMnO_4$. Ethanol, isopropanol, tetrahydrofuran, diethyl ether, $CrCl_3 \times 6H_2O$ and $CrBr_3 \times 6H_2O$ (Alfa Aesar), D_2O (99.9 % D, Deutero or Sigma Aldrich), CD_3CN (99 % D, abcr), triflic acid (Alfa Aesar), deuterated triflic acid (98 % D, Sigma Aldrich), tetrafluoroboric acid diethyl ether complex (Sigma Aldrich), tetra-*n*-butylammonium hexafluorophosphate (TCI), tetra-*n*-butylammonium tetrafluoroborate (Acros), tetra-*n*-butylammonium perchlorate (Aldrich), $HClO_4$ (70 %, Merck), $DClO_4$ (99 % D, Bernd Kraft), 2-bromo-6-methylpyridine (abcr) and 2,6-difluoropyridine (abcr) were used as received. The ligand bpmp[24] and $[Cr(ddpd)_2][BF_4]_3$[25] were prepared according to reported procedures. NMR spectroscopic and mass spectrometric data match the literature values. Column chromatography was performed using aluminum oxide (neutral, Brockmann I). Analytical thin layer chromatography (TLC) was done on aluminum oxide F254 (Macherey-Nagel, coated on polyester sheets). A glovebox (UniLab/MBraun, Ar 4.8, $O_2 < 1$ ppm, $H_2O < 0.1$ ppm) was used for storage and weighing of sensitive compounds.

NMR spectra were recorded on a Bruker Avance DRX 400 or AVII+400 NMR spectrometer at 400.31 MHz (^1H). All resonances are reported in ppm versus the solvent signal as internal standard.[26]

IR spectra were recorded with a Bruker Alpha FTIR spectrometer with an ATR unit containing a diamond crystal.

ESI$^+$ mass spectra were recorded on a Micromass Q-TOF-Ultima spectrometer by the central analytical facility of the Department of Chemistry (University of Mainz).

APCI mass spectra were recorded on an Advion expressIon-L CMS spectrometer by the central analytical facility of the Department of Chemistry (University of Mainz).

DC magnetic studies were performed with a Quantum Design MPMS-XL-7 SQUID magnetometer on powdered microcrystalline samples. Experimental susceptibility data were corrected for the underlying diamagnetism using Pascal's constants. The temperature dependent magnetic contribution of the holder and of the embedding eicosane matrix was experimentally determined and subtracted from the measured susceptibility data. Variable temperature susceptibility data were collected in a temperature range of 2 – 300 K under an applied field of 0.1 Tesla.

Electrochemical experiments were carried out on a BioLogic SP-200 voltammetric analyzer using platinum wires as counter and working electrodes and a 0.01 M Ag/Ag[NO_3] electrode as reference electrode. Cyclic voltammetry and square wave measurements were carried out at scan rates of 50–200 mV s^{-1} using 0.1 M [^{n}Bu$_4$N][PF_6] in CH_3CN as supporting electrolyte. Potentials are referenced against the ferrocene/ferrocenium couple.

UV/Vis/NIR spectra were recorded on a Varian Cary 5000 spectrometer using 1.0 cm cells.

Luminescence experiments. Luminescence emission spectra and luminescence decay kinetics in solution were obtained with a calibrated spectrofluorometer FSP 920 from Edinburgh Instruments. For the measurement of the emission spectra, a CW xenon lamp was applied as excitation light source, while the time-resolved luminescence measurements were performed with a µs xenon flashlamp and single photon counting detection in a multi-channel scaling mode. Emission spectra of singlet oxygen were obtained with the FSP 920 spectrometer as well, yet with a cooled NIR-detector (R5509P PMT). All measurements were performed at magic angle conditions using polarizers in the excitation and emission channel set to 0° and 54.7°, respectively. The luminescence decays in solution were analyzed by fitting the obtained decay curves with the program FAST (Fluorescence Analysis Software Technology, Edinburgh Instruments Ltd.). The luminescence quantum yields in solution were determined absolutely using an Ulbricht integrating sphere

setup (Quantaurus-QY C11347-11, Hamamatsu). Relative uncertainties are estimated to be ±5 %. pH- and *T*-dependent emission spectra in solution and Stern-Volmer analyses with azulene were recorded on a Varian Cary Eclipse fluorescence spectrometer.

Stern-Volmer studies with oxygen were carried out by measuring the luminescence response (emission intensity and lifetime) of complex solutions to oxygen at different oxygen concentrations. The general procedure was achieved by following the measuring order: oxygen concentration determination of the sample – luminescence emission spectra and lifetimes measurements – control the oxygen concentration in the sample. The oxygen concentration was taken from the average value of the oxygen concentrations before and after the luminescent measurements cycle to minimize the effect of oxygen diffusion during the measurements. Determination of the oxygen partial pressure $p(O_2)$ in solution was completed with a commercial fiber-optic oxygen meter Firesting O_2 from *PyroScience* and a solvent-resistant oxygen probe tip (OXSOLVPT) from the manufacturer.

Luminescence emission spectra and decays in KBr pellets at variable temperature (20 – 290 K at the sample) were recorded in the solid state with a FluoroMax-2 (Horiba Jobin-Yvon) spectrometer using a closed cycle helium cryostat (ARS Model DE-202A). The cryo cooler was equipped with a copper pellet holder and CaF_2 windows. KBr pellets of $[Cr(bpmp)_2][BF_4]_3$ (ca. 0.7 mg) were prepared by mixing with dry KBr (ca. 200 mg, stored in a compartment dryer at 80 °C, purchased from Merck) and grinding to a homogeneous mixture. Neat films were prepared by spraying a solution of the compound in CH_3CN on a CaF_2 substrate (13 mm diameter, 1 mm thick), followed by evaporation of the solvent. The luminescence lifetimes were determined with the time-correlated single photon counting technique (TCSPC). Data were recorded with a DeltaFlex (Horiba Scientific) spectrometer. The sample was excited with short light pulses of a SpectraLED (390 nm) and the emission monochromator was set to 707 – 720 nm. The emitted light was detected with a picosecond photon counting (PPT) detection module. In all the static and time-resolved luminescence experiments, a long pass filter (600 nm) was mounted between the sample and the emission monochromator to prevent scattered excitation light from reaching the detector.

Time-resolved FTIR experiments were performed with an FTIR spectrometer Bruker Vertex 80v, operated in the step-scan mode. Temperature dependent measurements were performed at 290 K and 20 K by the use of KBr pellets and the cryostat described above. The strongest peak in the ground state spectrum at 1610 cm^{-1} showed an absorption of about 0.6 OD with the mentioned concentration. A liquid-nitrogen-cooled mercury cadmium telluride (MCT) detector (Kolmar Tech., Model KV100-1-B-7/190) with a rise time of 25 ns, connected to a fast preamplifier and a 14-bit transient recorder board (Spectrum Germany, M3I4142, 400 MS s^{-1}), was used for signal detection and processing. The laser setup includes a Q-switched Nd:YAG laser (Innolas SpitLight Evo I) generating pulses with a band-width of 6 ns at a repetition rate of 100 Hz. The third harmonic (355 nm) of the Nd:YAG laser was used for sample excitation. The UV pump beam was attenuated to about 2.0 mJ per shot at a diameter of 9 mm. The beam was directed onto the sample and adjusted to have a maximal overlap with the IR beam of the spectrometer. The sample chamber was equipped with anti-reflection-coated germanium filters to prevent the entrance of laser radiation into the detector and interferometer compartments. The time delay between the start of the experiment and the UV laser pulse was controlled with a Stanford Research Systems DG535 delay generator and the time where the laser pulse reached the sample was set as zero point in all spectra. The temporal resolution was set to 50 ns at 290 K and 100 ns at 20 K. A total of 4000 and 4400 coadditions were recorded at each interferogram point at 290 K and 20 K, respectively. The spectral region was limited by undersampling to 988 – 1975 cm^{-1} with a spectral resolution of 4 cm^{-1} resulting in 555 interferogram points. An IR broad band filter (850 – 1750 cm^{-1}) and the CaF_2 windows (no IR transmission < 1000 cm^{-1}) of the cryostat prevented problems when performing a Fourier transformation (*i.e.* no IR intensity outside the measured region should be observed). FTIR ground state spectra were recorded systematically to check for sample degradation. A more detailed description of the step-scan setup is given here.[27-29]

Transient absorption spectra were measured using a Helios-Fire pump-probe setup (Ultrafast systems) paired with a regeneratively amplified 1030 nm laser (Pharos, Light Conversion, 1030 nm, 200 fs, 200 µJ). The effective laser repetition rate of 1 kHz was set via an internal pulse picker. A small portion of the 1030 nm fundamental is directed to the optical delay line and is subsequently used to generate broadband probe light by focusing onto a sapphire crystal. The pump pulse is generated with an optical parametric amplifier (Orpheus-F, Light Conversion). The pump fluence at the sample was 0.9–2 µJ/pulse, as noted in the respective experiments. The experiments were run with 5 seconds of averaging at each time delay. Samples were measured in 2 mm path length cuvettes, with an OD of ~1 at 500 nm. Global analysis of the TA data was done using the R-package TIMP software[30] with the graphical interface Glotaran 1.5.1.[31]

Singlet oxygen quantum yields were determined optically using the reference $[Cr(ddpd)_2][BF_4]_3$ with a known $^1O_2$ quantum yield (0.61 in DMF).[32] Samples and reference were excited at the same wavelength (462 nm) and measured under the same conditions, i.e. using the same fluorimeter settings. $\Phi[^1O_2]$ was calculated using the following equation:

$$\Phi_S\left[\,^1O_2\right] = \Phi_{Ref}\left[\,^1O_2\right] * \frac{I_S}{I_{Ref}} * \frac{A_{Ref}}{A_S}$$

Here $\Phi_{Ref}\left[\,^1O_2\right]$, I_{Ref} and A_{Ref} are assigned to the singlet oxygen quantum yield, the integrated emission intensity (λ = 1240 – 1360 nm) and the absorbance of the reference compound in DMF solution, respectively; I_S and A_S denote the integrated emission intensity and absorbance of the sample, respectively. As the $[Cr(bpmp)_2]^{3+}$ complexes tend to deprotonate in pure DMF, an acidic environment was provided by adding 2 µL $HClO_4$ (70 – 72 %) to 3 mL DMF solution, achieving a final $HClO_4$ concentration of ca. 0.01 M. The singlet oxygen quantum yield of $[Cr(ddpd)_2][BF_4]_3$ was determined in DMF/$HClO_4$ (0.01 M), which was then used as a reference for the $[Cr(bpmp)_2]^{3+}$ complexes in DMF/$HClO_4$ (0.01 M).

Table S5. $^1O_2$ quantum yields.

	solvent	Φ / %
$[Cr(ddpd)_3][BF_4]_3$	DMF	61
$[Cr(ddpd)_3][BF_4]_3$	DMF/$HClO_4$	86
$[Cr(bpmp)_3][OTf]_3$	DMF/$HClO_4$	55
$[Cr(bpmp)_3][PF_6]_3$	DMF/$HClO_4$	44
$[Cr(bpmp)_3][BF_4]_3$	DMF/$HClO_4$	39

Elemental analyses were conducted by the microanalytical laboratory of the department of chemistry of the University of Mainz.

Caution! Although we have not experienced any problems in handling the perchlorate *solutions*, all materials should be handled with extreme care. Especially, we avoided isolation of *dried perchlorate salts*.

Crystal structure determinations. Intensity data were collected with a STOE STADIVARI diffractometer with an Oxford cooling using Mo-K_α radiation (λ = 0.71073 Å). The diffraction frames were integrated using the STOE X-Area software package[33] and most were corrected for absorption with MULABS[34] of the PLATON software package[35] or with STOE LANA[36,37]. The structures were solved by direct methods and refined by the full-matrix method based on F^2 using the SHELX software package[38] using the ShelXle graphical interface[39]. All non-hydrogen atoms were refined anisotropically while the positions of all hydrogen atoms were generated with appropriate geometric constraints and allowed to ride on their respective parent atoms with fixed isotropic thermal parameters. CCDC 1989536 (Cr(bpmp)(OTf)$_3$), 1989537 ([Cr(bpmp)$_2$][OTf]$_3$×CH_3CH_2OH) and 2083757 ([Cr(bpmp)$_2$][BF_4]$_3$×$^5/_3CH_3CN$) contain the supplementary crystallographic data for this paper. These data are provided free of charge by The Cambridge Crystallographic Data Centre.

Crystallographic Data of *mer*-Cr(bpmp)(OTf)$_3$×0.25CH_3CN. $C_{20}H_{15}CrF_9N_3O_9S_3$×0.25$CH_3CN$ (770.79); triclinic; $P\bar{1}$; a = 9.872(2) Å, b = 10.578(2) Å, c = 15.838(3) Å, α = 70.84(3)°, β = 86.05(3)°, γ = 66.13(3)°; V = 1424.7(7) Å^3; Z = 2; density, calcd. = 1.797 g cm^{-3}, T = 120(2) K, μ = 0.736 mm^{-1}; F(000) = 773; crystal size 0.240 × 0.214 × 0.200 mm; θ = 2.198 to 30.701 deg.; –14≤h≤13, –14≤k≤13, –22≤l≤21; rfln collected = 28517; rfln unique = 7881 [R(int) = 0.0349]; completeness to θ = 25.242 deg. = 99.9 %; semi empirical absorption correction from equivalents; max. and min. transmission 1.07582 and 0.94806; data 7881; restraints 24, parameters 434; goodness-of-fit on F^2 = 1.031; final indices [I > 2σ(I)] R_1 = 0.0313, wR_2 = 0.0854; R indices (all data) R_1 = 0.0391, wR_2 = 0.0882; largest diff. peak and hole 0.562 and –0.656 e Å^{-3}.

Crystallographic Data of *mer*-[Cr(bpmp)$_2$][OTf]$_3$×CH_3CH_2OH. $C_{37}H_{30}CrF_3N_6O_3S$×CH_3CH_2OH (1067.92); triclinic; $P\bar{1}$; a = 10.550(2) Å, b = 12.178(2) Å, c = 16.714(3) Å, α = 81.77(3)°, β = 78.79(3)°, γ = 85.55(3)°; V = 2082.0(7) Å^3; Z = 2; density, calcd. = 1.465 g cm^{-3}, T = 120(2) K, μ = 0.533 mm^{-1}; F(000) = 1090; crystal size 0.370 × 0.250 × 0.120 mm; θ = 1.969 to 30.985 deg.; –15≤h≤15, –17≤k≤17, –23≤l≤24; rfln collected = 42354; rfln unique = 11665 [R(int) = 0.0486]; completeness to θ = 25.242 deg. = 100.0 %; semi empirical absorption correction from equivalents; max. and min. transmission 1.16976 and 0.90213; data 11665; restraints 774, parameters 689; goodness-of-fit on F^2 = 1.018; final indices [I > 2σ(I)] R_1 = 0.0340, wR_2 = 0.0908; R indices (all data) R_1 = 0.0430, wR_2 = 0.0937; largest diff. peak and hole 0.637 and –0.806 e Å^{-3}.

Crystallographic Data of *mer*-[Cr(bpmp)$_2$][BF_4]$_3$×$^5/_3CH_3CN$. $C_{34}H_{30}B_3CrF_{12}N_6$×$^5/_3CH_3CN$ (903.49); trigonal; P-3c1; a = b = 19.2795(3) Å, c = 38.1826(8) Å, α = β = 90°, γ = 120°; V = 12291.0(5) Å^3; Z = 12; density, calcd. = 1.704 g cm^{-3}, T = 173(2) K, μ = 0.373 mm^{-1}; F(000) = 5516; crystal size 0.480 × 0.245 × 0.056 mm; θ = 2.113 to 24.992 deg.; –20≤h≤21, –20≤k≤21, –42≤l≤37; rfln collected = 54247; rfln unique = 6527 [R(int) = 0.0283]; completeness to θ = 24.992 deg. = 90.3 %; semi empirical absorption correction from equivalents; max. and min. transmission 0.9949 and 0.2028; data 6527; restraints 276, parameters 688; goodness-of-fit on F^2 = 1.111; final indices [I > 2σ(I)] R_1 = 0.0463, wR_2 = 0.0685; R indices (all data) R_1 = 0.1339, wR_2 = 0.1395; largest diff. peak and hole 1.553 and –0.711 e Å^{-3}.

Synthesis of Cr(bpmp)Cl_3 (procedure adapted from ref. 40). A pale yellow solution of bpmp (2.07 g, 7.92 mmol) in isopropanol (50 mL) was added to a green solution of chromium(III) chloride hexahydrate (2.11 g, 7.92 mmol) in isopropanol (150 mL). The green mixture was heated to 82 °C for 15 hours yielding a dark green precipitate. After cooling, the suspension was filtered and the solid was washed with warm ethanol (2 x 50 mL) and diethyl ether (2 x 70 mL). The dark green product was dried under reduced pressure. Yield: 3.22 g (7.67 mmol, 97 %). MS (ESI^+, CH_3CN): *m/z* (%) = 383.00 (100) $[Cr(bpmp)Cl_3–Cl]^+$. IR (ATR): $\tilde{\nu}$ = 2890 (w), 1604 (s), 1577 (m), 1566 (w), 1483 (m), 1459 (s), 1432 (s), 1416 (m), 1292 (m), 1238 (vw), 1221 (vw), 1172 (w), 1156 (vw), 1131 (vw), 1107 (w), 1060 (m), 1025 (m), 1004 (vw), 977 (vw), 930 (m), 913 (vw), 887 (vw), 849 (m), 792 (m), 771 (vs), 739 (m), 724 (vw), 667 (vw), 651 (m), 621 (s), 604 (w), 594 (w), 554 (vw), 474 (m), 458 (w), 443 (s), 413 (m) cm^{-1}. Elemental analysis calcd. (%) for $C_{17}H_{15}Cl_3CrN_3$ (419.68): C 48.65 H 3.60, N 10.01; found C 48.45, H 3.31 N 9.31.

Synthesis of Cr(bpmp)Br_3 (procedure adapted from ref. 40). A pale yellow solution of bpmp (2.52 g, 9.64 mmol) in isopropanol (50 mL) was added to a green solution of chromium(III) bromide hexahydrate (3.85 g, 9.64 mmol) in isopropanol (200 mL). The green mixture was heated to 82 °C for 15 hours yielding a green precipitate. After cooling, the suspension was filtered and the solid was washed with warm ethanol (2 x 50 mL) and diethyl ether (2 x 70 mL). The green product was dried under reduced pressure. Yield: 5.01 g (9.06 mmol, 94 %). MS (ESI^+, CH_3CN): *m/z* (%) = 450.01 (100) $[Cr(bpmp)Br_3–2Br+OH+CH_3CN]^+$, 472.90 (51) $[Cr(bpmp)Br_3–Br]^+$, 513.93 (28) $[Cr(bpmp)Br_3–Br+CH_3CN]^+$. IR (ATR): $\tilde{\nu}$ = 2873 (w), 1604 (s), 1576 (m), 1565 (w), 1483 (m), 1458 (s), 1431 (m), 1412 (m), 1292 (m), 1276 (vw), 1237 (vw), 1219 (vw), 1172 (w), 1157 (vw), 1131 (vw), 1107 (w), 1062 (m), 1023 (m), 1001 (vw), 974 (vw), 927 (m), 885 (vw), 849 (m), 789 (m), 769 (vs), 737 (m), 649 (m), 621 (s), 604 (w), 594 (w), 553 (vw), 517 (vw), 472 (m), 454 (w), 441 (s), 421 (vw), 408 (m) cm^{-1}. Elemental analysis calcd. (%) for $C_{17}H_{15}Br_3CrN_3$ (553.03): C 36.92 H 2.73, N 7.60; found C 36.38, H 2.81 N 7.13.

Synthesis of Cr(bpmp)$(OTf)_3$ (procedure adapted from ref. 41). Anhydrous triflic acid (6.0 mL, 68.4 mmol) was added under argon atmosphere to Cr(bpmp)Cl_3 (2.15 g, 5.12 mmol) or [Cr(bpmp)Br_3] (2.83 g, 5.12 mmol), respectively. The reaction mixture turned dark red immediately together with gas evolution. The HCl (HBr) was detected by bubbling the gas into an aqueous solution of silver nitrate. After stirring at room temperature for four hours, the solution was cooled with ice and dry diethylether (400 mL) was added. The precipitate was collected by filtration, washed with dry diethyl ether (2 x 80 mL) and dried under reduced pressure. Yield: 3.82 g (5.02 mmol, 98 %) (from Cr(bpmp)Cl_3) and 3.67 g (4.8 mmol, 94 %) (from Cr(bpmp)Br_3). Cooling a concentrated solution of Cr(bpmp)$(OTf)_3$ in acetonitrile yielded dichroic green/purple single crystals of Cr(bpmp)$(OTf)_3 \times {}^1/_4 CH_3CN$ suitable for single crystal XRD. MS (APCI, CH_3CN): *m/z* (%) = 610.97 (100) $[Cr(bpmp)(OTf)_3–OTf]^+$, 628.98 (14) $[Cr(bpmp)(OTf)_3–OTf+H_2O]^+$, 652.00 (66) $[Cr(bpmp)(OTf)_3–OTf+CH_3CN]^+$. IR (ATR): $\tilde{\nu}$ = 3094 (vw), 2936 (vw), 1613 (m), 1580 (w), 1496 (w), 1465 (m), 1441 (m), 1347 (s), 1260 (m), 1236 (s), 1201 (vs), 1114 (w), 1073 (w), 1031 (s), 986 (s), 931 (w), 850 (w), 769 (m), 738 (vw), 660 (w), 634 (s), 594 (w), 572 (w), 513 (m), 458 (w), 441 (m), 416 (w) cm^{-1}.

Synthesis of $[Cr(bpmp)_2][OTf]_3$. A pale yellow solution of bpmp (1.38 g, 5.28 mmol) in dry acetonitrile (20 mL) was added to a dark green solution of Cr(bpmp)$(OTf)_3$ (2.01 g, 2.64 mmol) in dry acetonitrile (80 mL). The solution was heated at 60 °C for 20 hours. The solvent of the resulting dark yellow/brown solution was removed under reduced pressure. The residue was heated in tetrahydrofuran (200 mL) and the insoluble yellow solid was collected by filtration, washed with THF (50 mL) and diethyl ether (50 mL) und dried under reduced pressure. Diffusion of diethyl ether into a concentrated solution of $[Cr(bpmp)_2](OTf)_3$ in ethanol/anhydrous triflic acid (100:1) yielded orange diffraction quality crystals of $[Cr(bpmp)_2](OTf)_3 \times C_2H_5OH$. Yield: 1.11 g (1.09 mmol, 41 %). MS (ESI^+, CH_3CN): *m/z* (%) = 191.73 (4) $[Cr(bpmp)_2]^{3+}$, 286.59 (13) $[Cr(bpmp)_2–H]^{2+}$, 572.18 (100) $[Cr(bpmp)_2–2H]^+$. IR (ATR): $\tilde{\nu}$ = 3554 (w), 3091 (vw), 1610 (s), 1578 (m), 1491 (m), 1466 (m), 1442 (m), 1259 (vs), 1225 (s), 1157 (s), 1112 (w), 1073 (w), 1029 (vs), 929 (vw), 847 (w), 776 (m), 737 (vw), 657 (m), 637 (s), 592 (w), 574 (m), 518 (m), 445 (m) cm^{-1}. Elemental analysis calcd. (%) for $C_{37}H_{30}CrN_6O_9F_9S_3$ (1021.85): C 43.49 H 2.96, N 8.22; found C 43.68, H 2.47 N 7.84.

Synthesis of $[Cr(bpmp)_2][PF_6]_3$. A dark yellow solution of **$[Cr(bpmp)_2](O_3SCF_3)_3$** (0.50 g, 0.489 mmol) in ethanol (200 mL) was acidified with two drops of triflic acid resulting in a pale yellow solution. A solution of tetra-*n*-butylammonium hexafluorophosphate (1.14 g, 2.94 mmol) in ethanol (80 mL) was added while stirring. A yellow solid precipitated immediately. After stirring for one hour, the suspension was filtered. The collected solid was washed with ethanol (3 × 20 ml) and diethyl ether (3 × 20 ml) and dried under reduced pressure. Yield: 0.29 g (0.287 mmol, 59 %). MS (ESI^+, CH_3CN): *m/z* (%) = 191.40 (1) $[Cr(bpmp)_2]^{3+}$, 286.59 (10) $[Cr(bpmp)_2–H]^{2+}$, 572.18 (100) $[Cr(bpmp)_2–2H]^+$, 718.15 (41) $[Cr(bpmp)_2–H+PF_6]^+$. IR (ATR): $\tilde{\nu}$ = 3103 (vw), 1608 (s), 1576 (m), 1490 (m), 1463 (m), 1444 (m), 1410 (m), 1296 (m), 1243 (w), 1220 (w), 1173 (m), 1124 (w), 1112 (w), 1074 (m), 1028 (s), 928 (w), 888 (m), 824 (vs, PF), 771 (s), 656 (m), 620 (m), 593 (w), 554 (vs, PF), 471 (m), 440 (s) cm^{-1}. Elemental analysis calcd. (%) for $C_{34}H_{30}CrN_6F_{18}P_3$ (1009.53): C 40.45 H 3.00, N 8.32; found C 40.12, H 2.93 N 8.16.

Synthesis of $[Cr(bpmp)_2][BF_4]_3$. A dark yellow solution of **$[Cr(bpmp)_2](O_3SCF_3)_3$** (0.50 g, 0.489 mmol) in ethanol (200 mL) was acidified with two drops of tetrafluoroboric acid diethyl ether complex resulting in a pale yellow solution. A solution of tetra-*n*-butylammonium tetrafluoroborate (0.97 g, 2.94 mmol) in ethanol (20 ml) was added while stirring. A yellow solid precipitated immediately. After stirring for one hour, the suspension was filtered. The collected solid was washed with ethanol (3 × 20 ml) and diethyl ether (3 × 20 ml) and dried under reduced pressure. Diffusion of diethyl ether into a concentrated solution of the complex in acetonitrile/tetrafluoroboric acid diethyl ether complex (100:1) yielded orange diffraction quality crystals of $[Cr(bpmp)_2](BF_4)_3×3CH_3CN$. Yield: 0.28 g (0.335 mmol, 69 %). MS (ESI^+, CH_3CN): *m/z* (%) = 191.40 (1) $[Cr(bpmp)_2]^{3+}$, 286.59 (8) $[Cr(bpmp)_2–H]^{2+}$, 572.18 (100) $[Cr(bpmp)_2–2H]^+$, 660.19 (15) $[Cr(bpmp)_2–H+BF_4]^+$. IR (ATR): $\tilde{\nu}$ = 1610 (s), 1578 (m), 1491 (m), 1464 (m), 1438 (m), 1422 (m), 1296 (m), 1171 (w), 1054 (vs, B-F), 1026 (vs, B-F), 928 (m), 845 (m), 773 (s, -B-F), 695 (w), 657 (m), 637 (m), 619 (m), 594 (m), 543 (w), 564 (w), 519 (s), 474 (m), 456 (s), 440 (s), 430 (m), 412 (s) cm^{-1}. Elemental analysis calcd. (%) for $C_{34}H_{30}CrN_6F_{12}B_3$ (835.05)×3H_2O: C 45.93 H 4.08, N 9.45; found C 46.02, H 3.25 N 9.46.

Synthesis of $[Cr(bpmp)_2][ClO_4]_3$. The synthesis of this salt is in principle analogous to the preparation of the PF_6^- and BF_4^- salts. However, the *dried* perchlorate salt can be explosive and we do not wish to report its isolation and full characterization as dried material. Instead, we merely report some photophysical data in solution obtained from the *non-dried complex*.

Synthesis of $[Cr([D_4]\text{-}bpmp)_2][PF_6]_3$. $[Cr(bpmp)_2](PF_6)_3$ (200 mg, 0.20 mmol) was suspended in D_2O (8 mL, NMR grade, 99.9 % D) and stirred under argon for 10 h. The solvent was removed under reduced pressure. This procedure was repeated twice. Diffusion of diethyl ether into a solution of the complex in CH_3OD yielded crystals of **$[Cr([D_4]\text{-}bpmp)_2][PF_6]_3$** (142 mg, 0.14 mmol, 70 %) as orange needles. MS (ESI^+, CH_3CN): *m/z* (%) = 193.07 (5), 289.11 (21), 576.20 (100), 723.18 (88) (partial H/D exchange at the methylene groups occurs in the mass spectrometer). IR (ATR): $\tilde{\nu}$ = 1611 (s), 1577 (m), 1491 (m), 1464 (m), 1438 (m), 1266 (m), 1171 (m), 1113 (w), 1074 (w), 1029 (s), 836 (vs, PF), 765 (s), 740 (m), 656 (m), 639 (s), 621 (w), 556 (vs, PF), 518 (m), 457 (m), 437 (s) cm^{-1}.

Synthesis of 6-deutero-2-methylpyridine: A solution of *n*-butyllithium in hexane (56 mL, 2.5 M) was added dropwise within half an hour to a solution of 2-bromo-6-methylpyridine (15.9 mL, 140 mmol) in dry diethyl ether (600 mL) while cooling to −70 °C (ethanol/dry ice). The orange reaction mixture was stirred for three hours at −70 °C and then warmed to −10 °C. Deuterium oxide (100 mL, 99.9 % D) was added dropwise within half an hour. After phase separation, the aqueous phase was extracted with diethylether (3 × 100 mL). The combined organic phases were dried with sodium sulfate and the solvent was removed under reduced pressure. The colorless to yellow product was isolated by distillation (128°C, ambient pressure). Yield: 11.49 g (122 mmol, 87 %). C_5H_6DNBr (162.03). ^1H NMR (400 MHz, $CDCl_3$): δ = 7.50 (t, $^3J_{HH}$ = 7.7 Hz, 1H, H^4), 7.09 (d, $^3J_{HH}$ = 7.8 Hz, 1H, H^5), 7.02 (d, $^3J_{HH}$ = 7.5 Hz, 1H, H^3), 2.50 (s, 3H, CH_3).

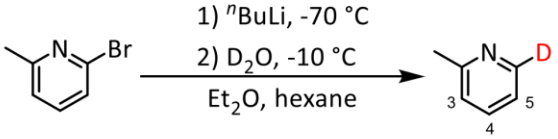

Synthesis of [D$_2$]-bpmp (analogous to the synthesis of the non-deuterated ligand, ref. 24): A solution of *n*-butyllithium in hexane (48 mL, 2.5 M) was added dropwise within half an hour to a pale yellow solution of 6-deutero-2-methylpyridine (11.33 g, 120 mmol) in dried tetrahydrofuran (80 mL) while cooling to −70 °C (ethanol/dry ice). The orange mixture was stirred at −70 °C for two hours and then warmed to −20 °C. 2,6-Difluoropyridine (1.09 mL, 12.0 mmol) was added and the mixture was heated to reflux at 60 °C for 24 hours. After cooling to room temperature, water (50 mL) was added dropwise and the phases were separated. The aqueous phase was extracted with dichloromethane (3 × 50 mL), the combined organic layers were dried with sodium sulfate and the solvents were removed under reduced pressure. The product was purified by column chromatography (Alox, 1:1 cyclohexane/ethyl acetate) yielding a yellow oil (R_f = 0.32). Yield: 0.80 g (3.04 mmol, 25 %). $C_{17}H_{13}D_2N_3$ (263.33). ^{1}H NMR (400 MHz, CD_2Cl_2): δ = 7.59 (t, $^3J_{HH}$ = 7.6 Hz, 2H, H^7), 7.52 (t, $^3J_{HH}$ = 7.7 Hz, 1H, H^1), 7.23 (d, $^3J_{HH}$ = 7.8 Hz, 2H, H^6), 7.12 (d, $^3J_{HH}$ = 7.5 Hz, 2H, H^8), 7.06 (d, $^3J_{HH}$ = 7.7 Hz, 2H, H^2), 4.27 (s, 4H, H^4). MS (ESI$^+$, CH_3CN): *m/z* (%) = 264.1 (100) [[D$_2$]-bpmp+H]$^+$, 286.1 (41) [[D$_2$]-bpmp+Na]$^+$, 326.1 (21) [[D$_2$]-bpmp+Cu]$^+$, 550.3 (43) [2x[D$_2$]-bpmp+Na]$^+$.

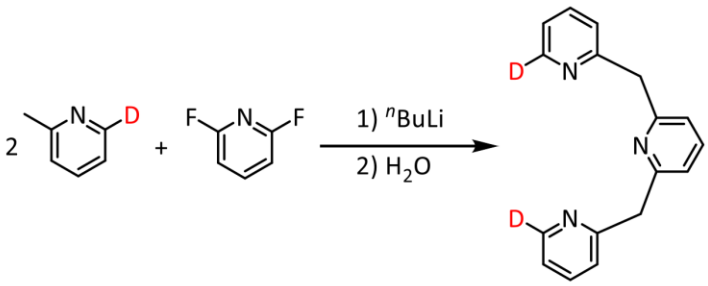

Synthesis of Cr([D$_2$]-bpmp)Cl$_3$: A pale yellow solution of [D$_2$]-bpmp (0.30 g, 1.14 mmol) in isopropanol (8 mL) was added to a green solution of chromium(III) chloride hexahydrate (0.30 g, 1.14 mmol) in isopropanol (25 mL). The reaction mixture was heated for 15 hours to 82 °C yielding a dark green precipitate. After cooling to room temperature, the solution was decanted and the solid was washed with warm ethanol (2 × 10 mL) and diethyl ether (2 × 10 mL). The dark green product was dried under reduced pressure. Yield: 0.47 g (1.11 mmol, 98 %). MS (ESI$^+$, CH_3CN): *m/z* (%) = 385.0 (33) [Cr([D$_2$]-bpmp)Cl$_3$–Cl]$^+$, 426.0 (100) [Cr([D$_2$]-bpmp)Cl$_3$–Cl+CH_3CN]$^+$, 445.0 (24) [Cr([D$_2$]-bpmp)Cl$_3$+Na]$^+$, 867.0 (56) [2x Cr([D$_2$]-bpmp)Cl$_3$+Na]$^+$. MS (APCI, CH_3CN): *m/z* (%) = 385.0 (100) [Cr([D$_2$]-bpmp)Cl$_3$–Cl]$^+$. IR (ATR): $\tilde{\nu}$ = 3088 (w), 2975 (vw), 2982 (m), 1597 (s), 1577 (m), 1562 (m), 1461 (s), 1447 (s), 1420 (s), 1286 (vw), 1237 (m), 1167 (m), 1132 (w), 1099 (m), 1061 (w), 1026 (m), 938 (m), 915 (m), 876 (w), 865 (w), 838 (m), 825 (m), 794 (m), 774 (m), 757 (s), 701 (m), 605 (s), 555 (w), 458 (m), 443 (m), 424 (vs), 410 (m) cm^{-1}.

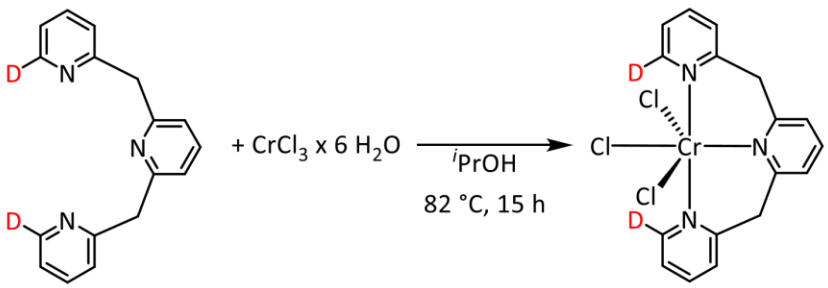

Synthesis of Cr([D$_2$]-bpmp)(O$_3$SCF$_3$)$_3$: Anhydrous deuterated triflic acid (0.76 mL, 8.54 mmol, 98 % D) was added under inert conditions to Cr([D$_2$]-bpmp)Cl$_3$ (0.24 g, 0.569 mmol). The reaction mixture turned dark red immediately together with evolution of hydrogen chloride gas. After stirring at room temperature for two hours, dry diethylether (10 mL) was added giving a red brown solid. After decanting, the product was washed with dried diethyl ether (2 × 10 mL) and dried under reduced pressure. Yield: 0.42 g (0.551 mmol, 97 %). MS (ESI$^+$, CH$_3$CN): *m/z* (%) = 613.0 (4) [Cr([D$_2$]-bpmp)(OTf)$_3$–OTf]$^+$, 654.0 (2) [Cr([D$_2$]-bpmp)(OTf)$_3$–OTf+CH$_3$CN]$^+$. MS (APCI, CH$_3$CN): *m/z* (%) = 613.0 (100) [Cr([D$_2$]-bpmp)(OTf)$_3$–OTf]$^+$, 631.0 (10) [Cr([D$_2$]-bpmp)(OTf)$_3$–OTf+H$_2$O]$^+$, 654.0 (49) [Cr([D$_2$]-bpmp)(OTf)$_3$–OTf+CH$_3$CN]$^+$. IR (ATR): $\tilde{\nu}$ = 3107 (w), 2939 (w), 1633 (m), 1609 (m), 1536 (vw), 1464 (vw), 1345 (s), 1286 (m), 1235 (vs), 1199 (vs), 1028 (s), 997 (s), 843 (vw), 764 (w), 634 (vs), 574 (m), 516 (m), 426 (m) cm^{-1}.

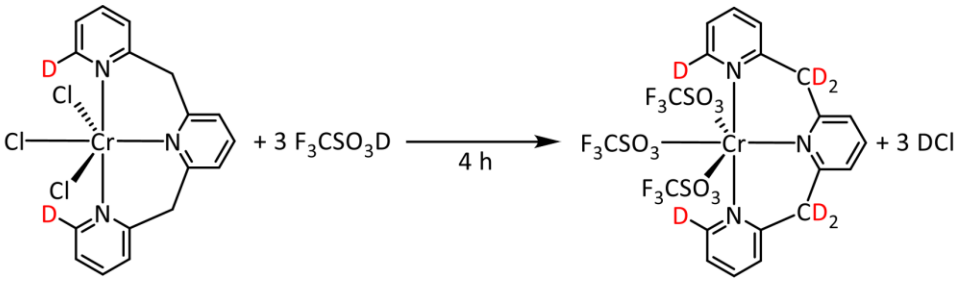

Synthesis of [Cr([D$_2$/D$_6$]-bpmp)$_2$](O$_3$SCF$_3$)$_3$: A pale yellow solution of [D$_2$]-bpmp (0.28 g, 1.05 mmol) in dry acetonitrile (4 mL) was added dropwise to a green solution of Cr([D$_2$]-bpmp)(O$_3$SCF$_3$)$_3$ (0.40 g, 0.525 mmol) in dry acetonitrile (16 mL). The initially dark green solution was heated for 20 hours to 60 °C, resulting in a dark yellow to brown mixture. The solvent was removed under reduced pressure and the residue was heated in tetrahydrofuran (50 mL). After cooling to room temperature, the solvent was decanted and the yellow solid was washed with tetrahydrofuran (20 mL) and diethyl ether (20 mL) and dried under reduced pressure. Yield: 0.23 g (0.224 mmol, 43 %). MS (ESI$^+$, CH$_3$CN): *m/z* (%) = 193.1 (5) [Cr([D$_2$]-bpmp)$_2$]$^{3+}$, 289.1 (12) [[Cr([D$_2$]-bpmp)$_2$]–H]$^{2+}$, 577.2 (100) [[Cr([D$_2$]-bpmp)$_2$]–2H]$^+$. MS (APCI, CH$_3$CN): *m/z* (%) = 576.2 (100) [[Cr([D$_2$]-bpmp)$_2$]–2H]$^+$, 617.2 (3) [[Cr([D$_2$]-bpmp)$_2$]–2H+CH$_3$CN]$^+$. Partial H/D exchange at the methylene groups occurs in the mass spectrometer. IR (ATR): $\tilde{\nu}$ = 3091 (vw), 2998 (vw), 1604 (s), 1577 (m), 1465 (m), 1432 (m), 1258 (vs), 1224 (s), 1155 (s), 1107 (m), 1029 (vs), 934 (vw), 917 (w), 839 (m), 785 (m), 755 (m), 700 (vw), 636 (vs), 606 (m), 573 (m), 517 (m), 455 (m), 430 (m) cm^{-1}.

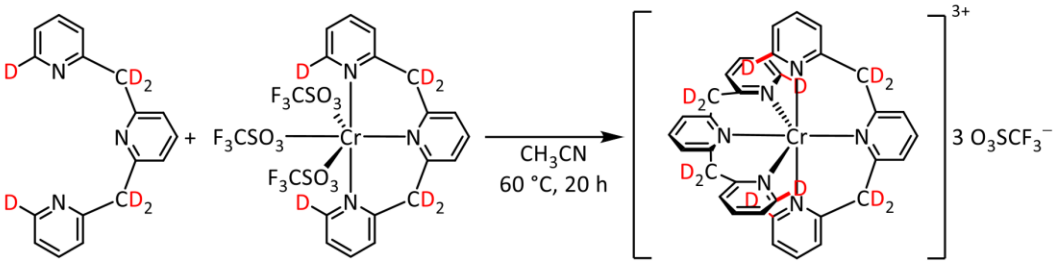

pH sensing with [Cr(bpmp)$_2$][O$_3$SCF$_3$]$_3$ and [Cr(ddpd)$_2$][BF$_4$]$_3$. An aqueous solution of [Cr(bpmp)$_2$][O$_3$SCF$_3$]$_3$ and [Cr(ddpd)$_2$][BF$_4$]$_3$ (25:2 molar ratio) was set to various pH values under ambient conditions. Luminescence spectra were obtained using λ_{exc} = 452 nm and normalized to the emission band at ca. 777 nm.

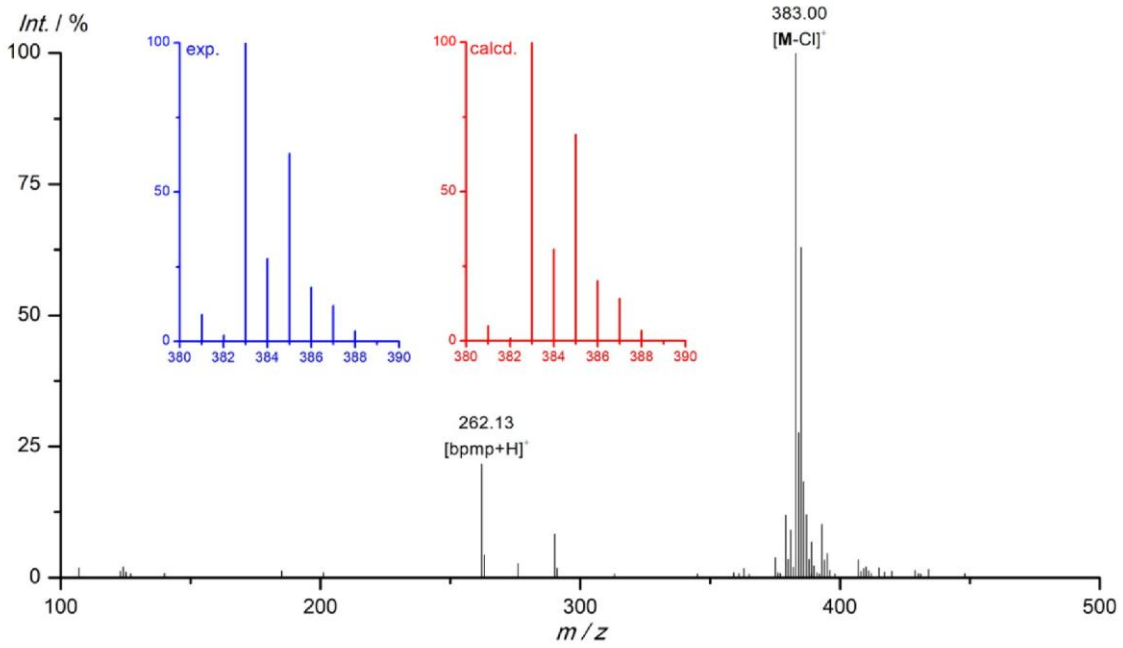

Figure S1. ESI^+ mass spectrum of $Cr(bpmp)Cl_3$ in CH_3CN. The insets depict the experimental (blue) and calculated (red) isotopic pattern of the peak at *m/z* 383 ($[Cr(bpmp)Cl_3–Cl]^+$).

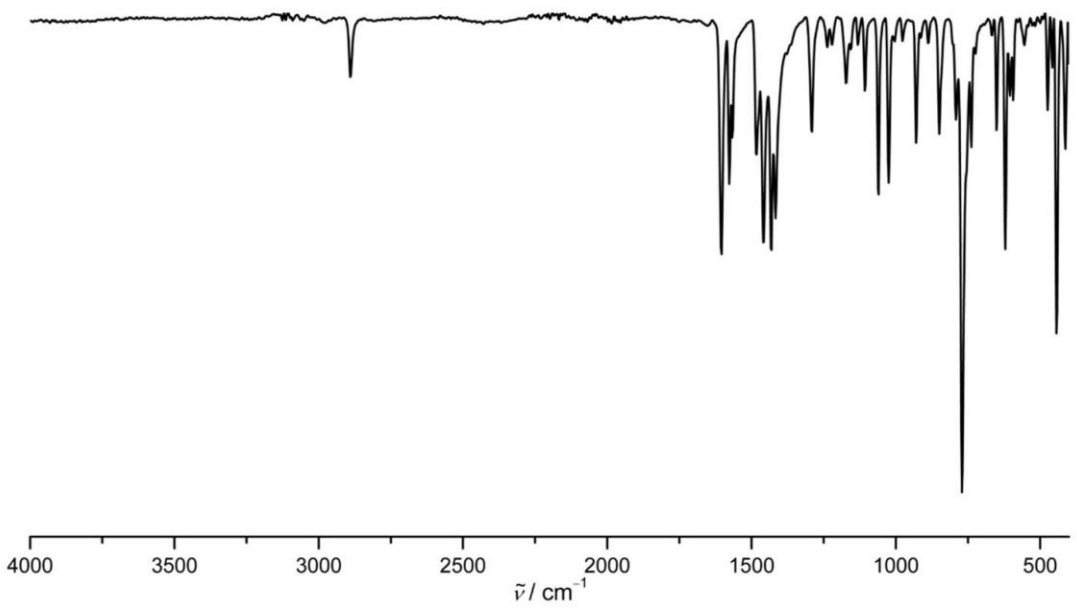

Figure S2. ATR-IR spectrum of $Cr(bpmp)Cl_3$.

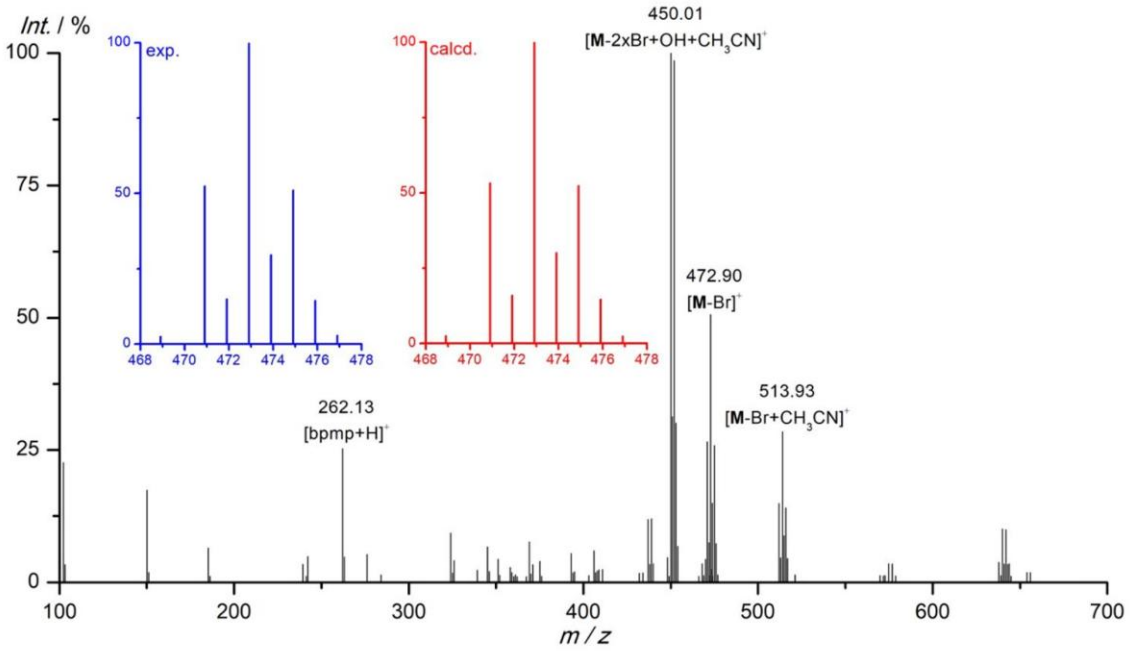

Figure S3. ESI^+ mass spectrum of $Cr(bpmp)Br_3$ in CH_3CN. The insets depict the experimental (blue) and calculated (red) isotopic pattern of the peak at *m/z* 473 ($[Cr(bpmp)Br_3–Br]^+$).

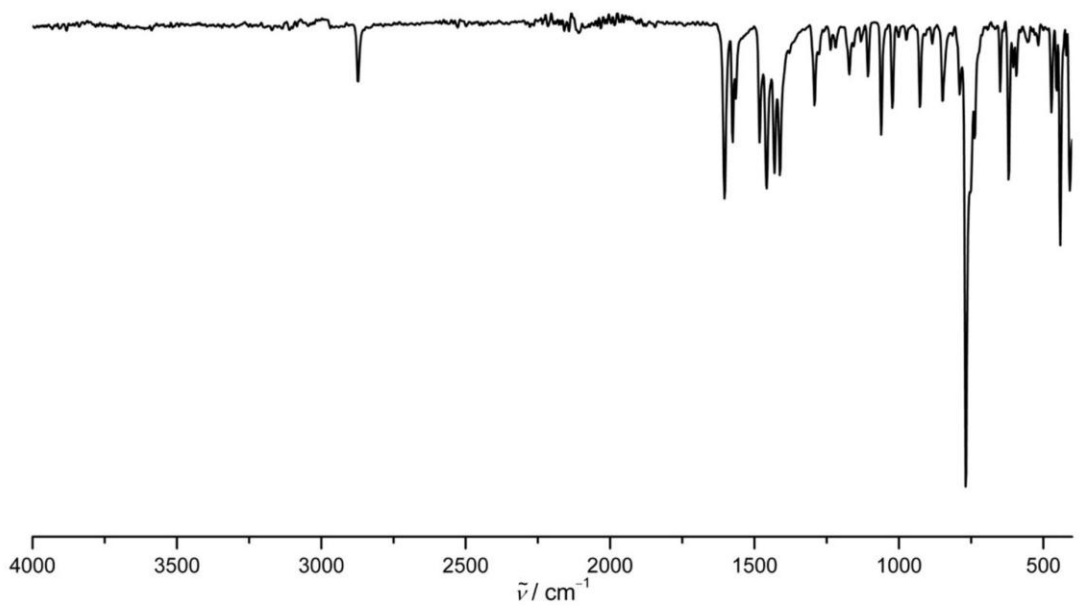

Figure S4. ATR-IR spectrum of $Cr(bpmp)Br_3$.

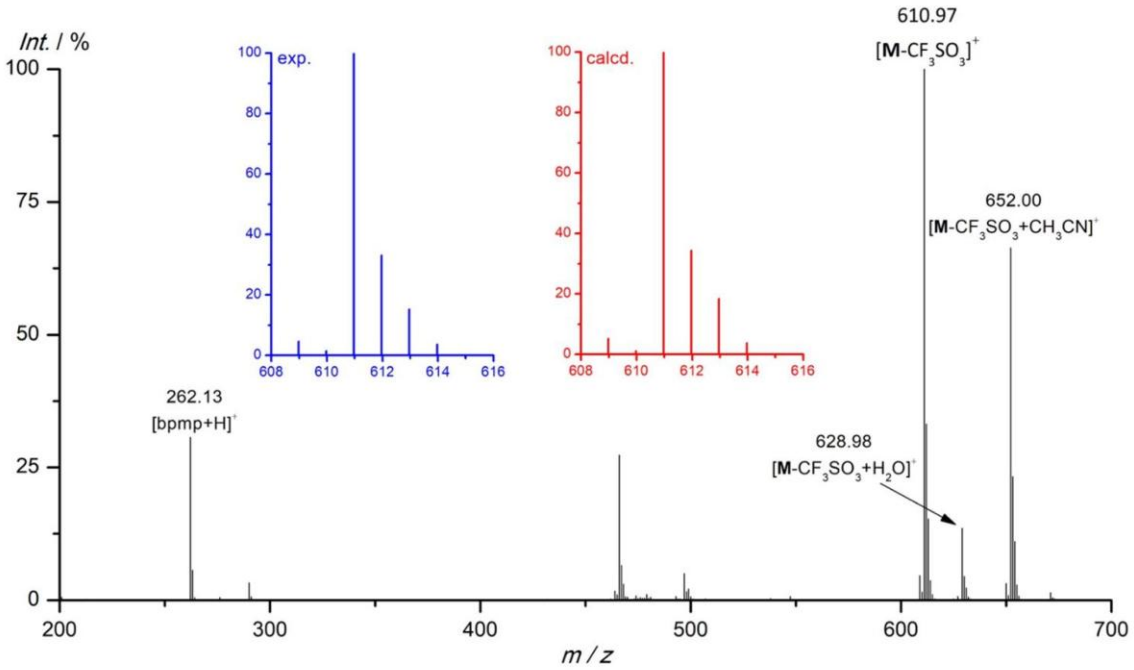

Figure S5. APCI mass spectrum of Cr(bpmp)(OTf)$_3$. The insets depict the experimental (blue) and calculated (red) isotopic pattern of the peak at *m/z* 611 ([Cr(bpmp)(OTf)$_3$–OTf]$^+$).

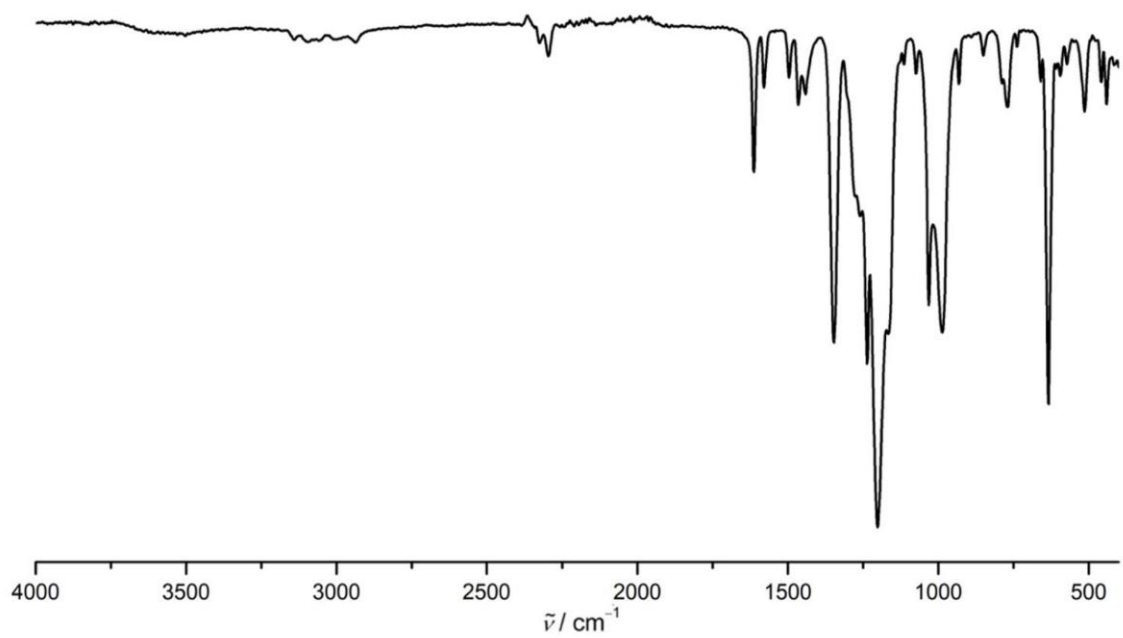

Figure S6. ATR-IR spectrum of Cr(bpmp)(OTf)$_3$.

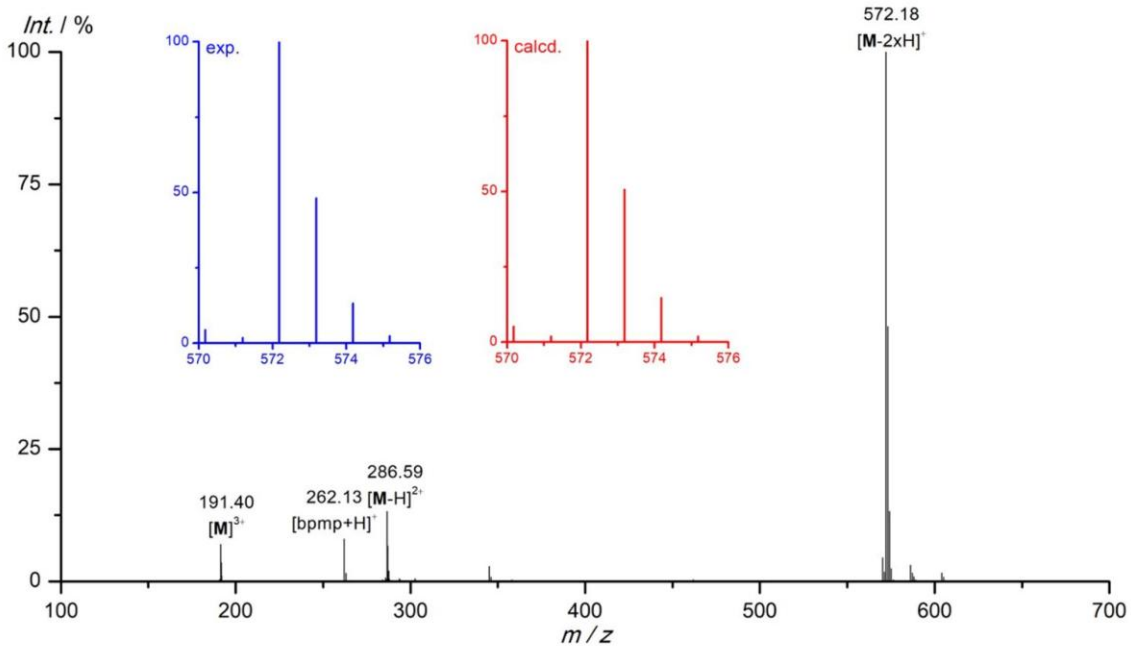

Figure S7. ESI^+ mass spectrum of $[Cr(bpmp)_2][OTf]_3$ in CH_3CN. The insets depict the experimental (blue) and calculated (red) isotopic pattern of the peak at *m/z* 572 ($[Cr(bpmp)_2–2H]^+$).

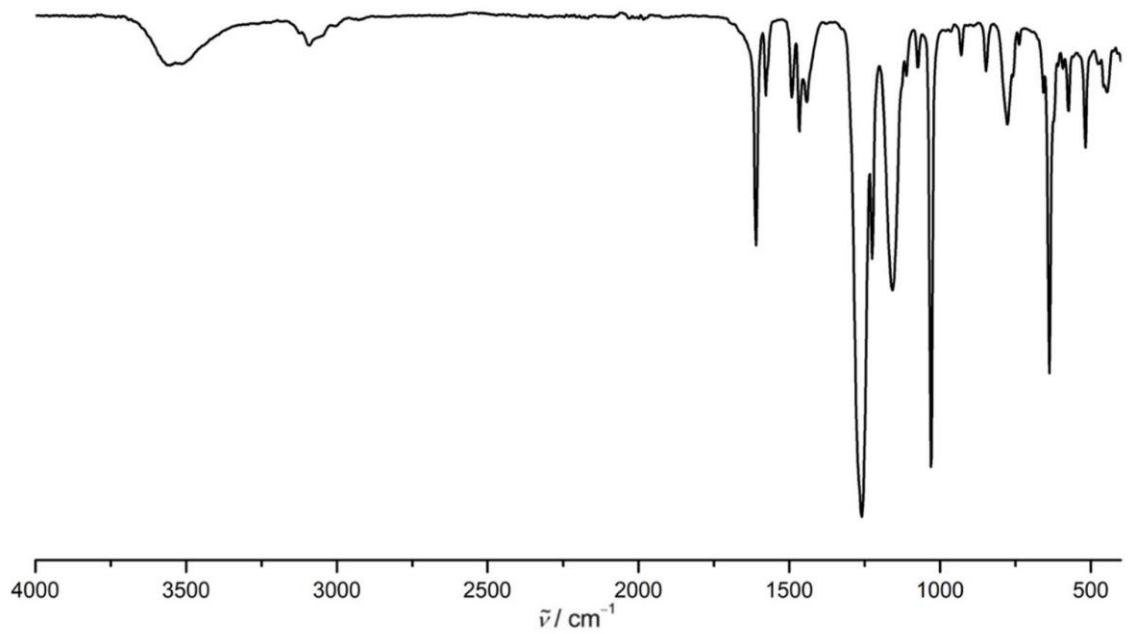

Figure S8. ATR-IR spectrum of $[Cr(bpmp)_2][OTf]_3$.

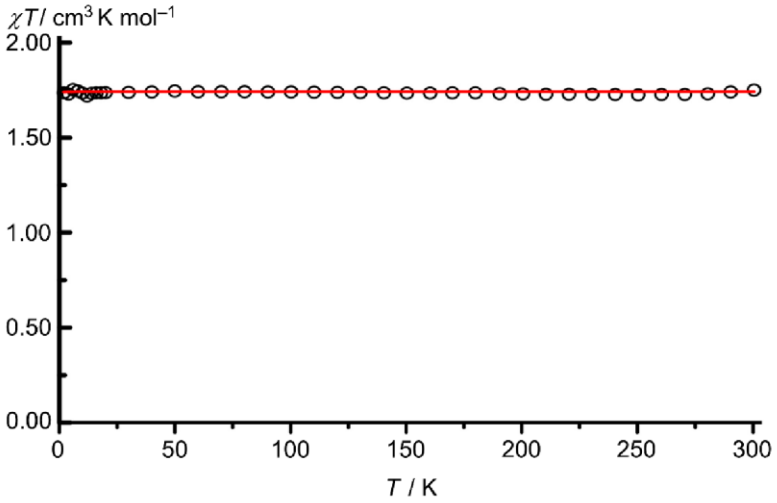

Figure S9. Temperature-dependence of $\chi_M T$ of $[Cr(bpmp)_2][BF_4]_3$ (black circles) with fit (red line, g = 1.972).

Table S6. Bond lengths [Å] and angles [deg] of $[Cr(bpmp)_2]^{3+}$ from XRD measurements of $[Cr(bpmp)_2][OTf]_3$ and $[Cr(bpmp)_2][BF_4]_3$ and DFT calculations of $[Cr(bpmp)_2]^{3+}$.

	$[Cr(bpmp)_2][OTf]_3$	$[Cr(bpmp)_2][BF_4]_3$	DFT
Cr1–N1	2.0755(13)	2.069(2)	2.1233
Cr1–N2	2.0599(13)	2.083(2)	2.1183
Cr1–N3	2.0691(13)	2.061(2)	2.1174
Cr1–N4	2.0703(13)	2.073(2)	2.1089
Cr1–N5	2.0771(13)	2.078(3)	2.0996
Cr1–N6	2.0886(13)	2.084(2)	2.1075
N1–Cr1–N2	89.55(5)	88.72(9)	88.46
N1–Cr1–N3	177.65(4)	176.71(10)	176.85
N1–Cr1–N4	93.04(5)	94.93(9)	96.50
N1–Cr1–N5	89.11(5)	92.85(9)	91.39
N1–Cr1–N6	85.08(5)	84.85(9)	84.14
N2–Cr1–N3	90.11(5)	88.01(10)	88.53
N2–Cr1–N4	91.00(5)	91.97(9)	90.81
N2–Cr1–N5	178.58(4)	178.42(9)	179.41
N2–Cr1–N6	90.68(5)	92.05(10)	91.77
N3–Cr1–N4	84.63(5)	85.54(9)	84.45
N3–Cr1–N5	91.20(5)	90.42(10)	91.64
N3–Cr1–N6	97.25(5)	94.91(9)	95.05
N4–Cr1–N5	88.59(5)	87.72(10)	88.64
N4–Cr1–N6	177.47(4)	175.97(10)	177.35
N5–Cr1–N6	89.69(5)	88.27(10)	88.78
S(OC-6)[42]	0.16	0.20	0.21

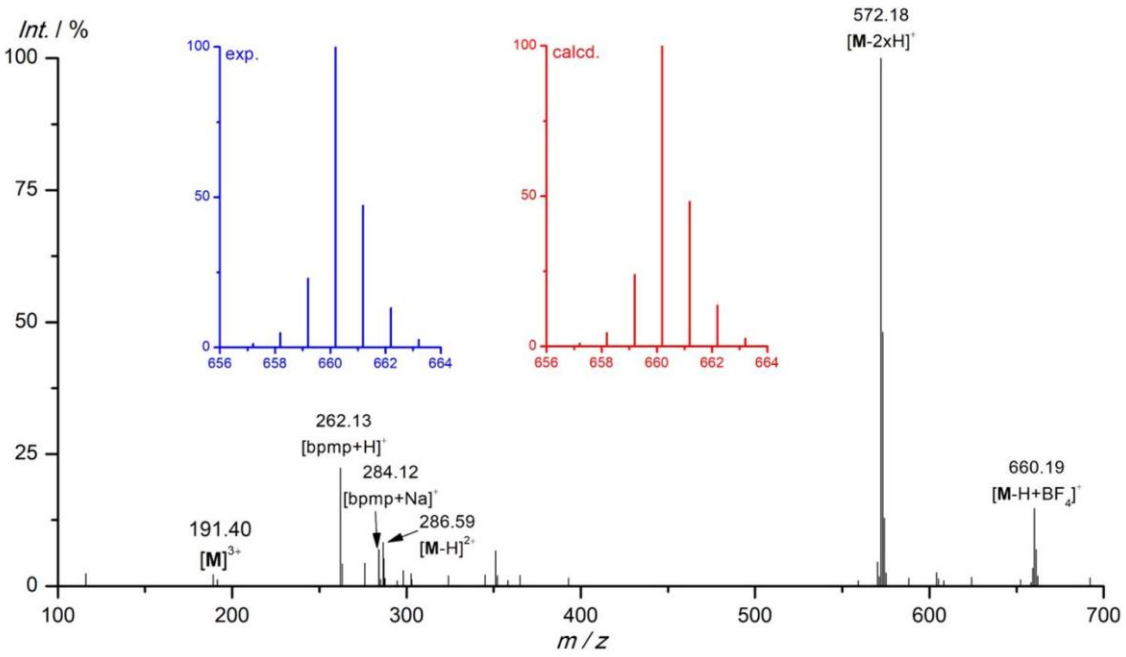

Figure S10. ESI^+ mass spectrum of $[Cr(bpmp)_2][BF_4]_3$ in CH_3CN. The insets depict the experimental (blue) and calculated (red) isotopic pattern of the peak at *m/z* 660 ($[Cr(bpmp)_2–H+BF_4]^+$).

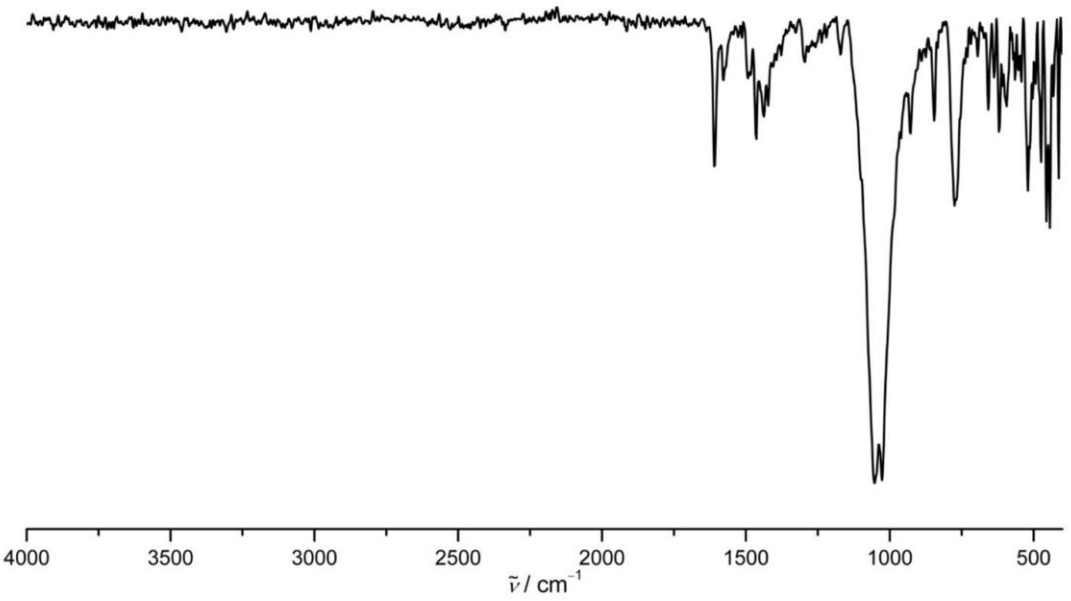

Figure S11. ATR-IR spectrum of $[Cr(bpmp)_2][BF_4]_3$.

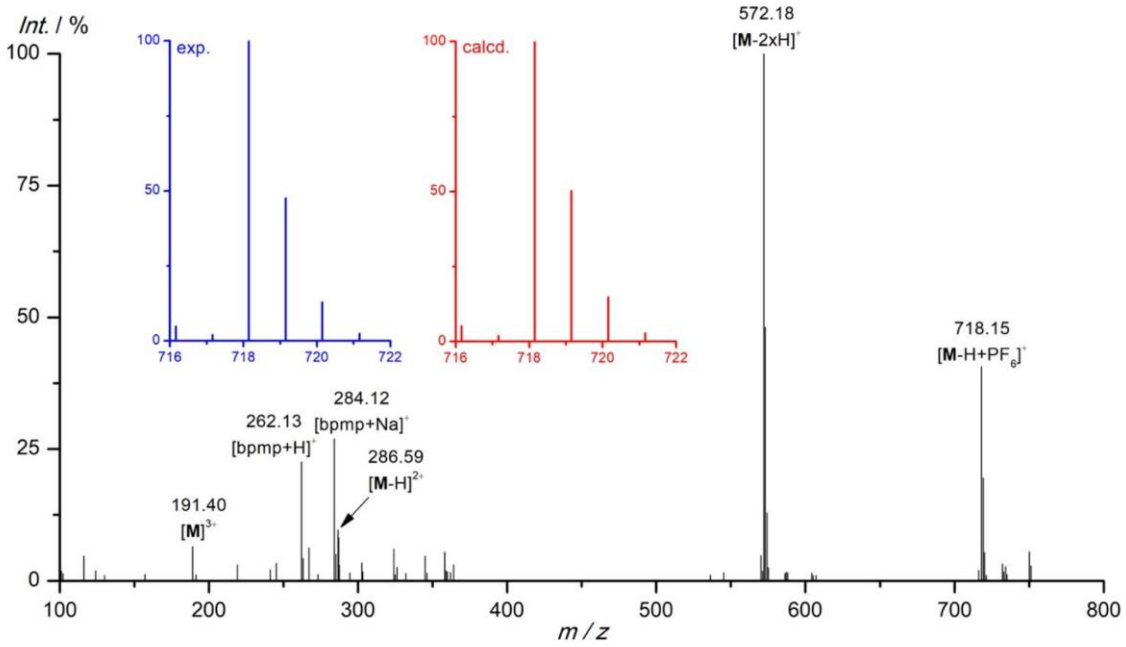

Figure S12. ESI$^+$ mass spectrum of $[Cr(bpmp)_2][PF_6]_3$ in CH_3CN. The insets depict the experimental (blue) and calculated (red) isotopic pattern of the peak at *m/z* 718 ($[Cr(bpmp)_2–H+PF_6]^+$).

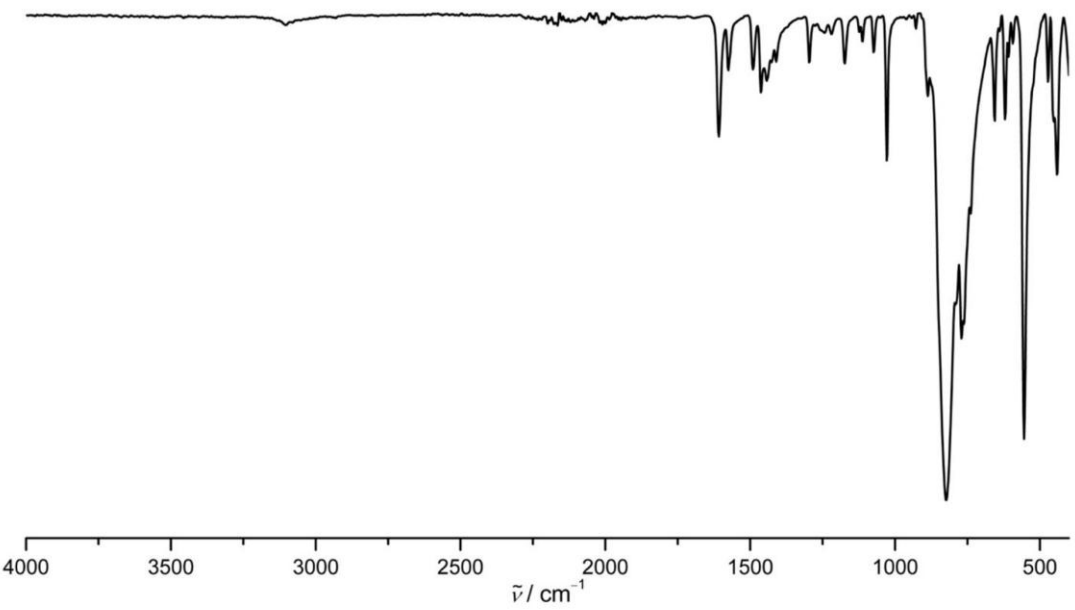

Figure S13. ATR-IR spectrum of $[Cr(bpmp)_2][PF_6]_3$.

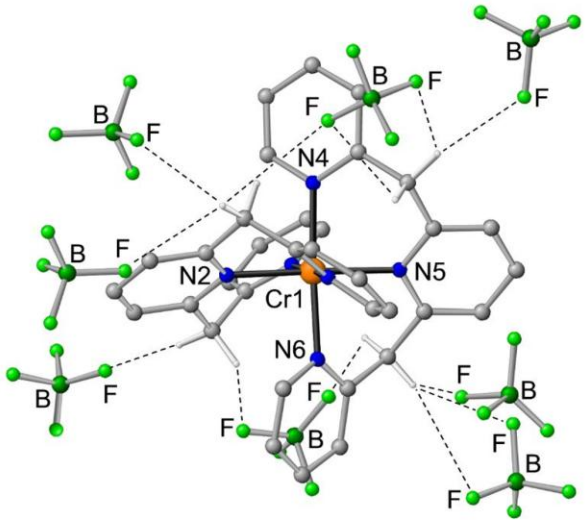

Figure S14. Molecular structure of $[Cr(bpmp)_2][BF_4]_3$ in the solid state. Hydrogen bonding of the tetrafluoroborate ions to the CH_2 groups is illustrated by dashed lines. Hydrogen atoms (except for the CH_2 groups) are omitted.

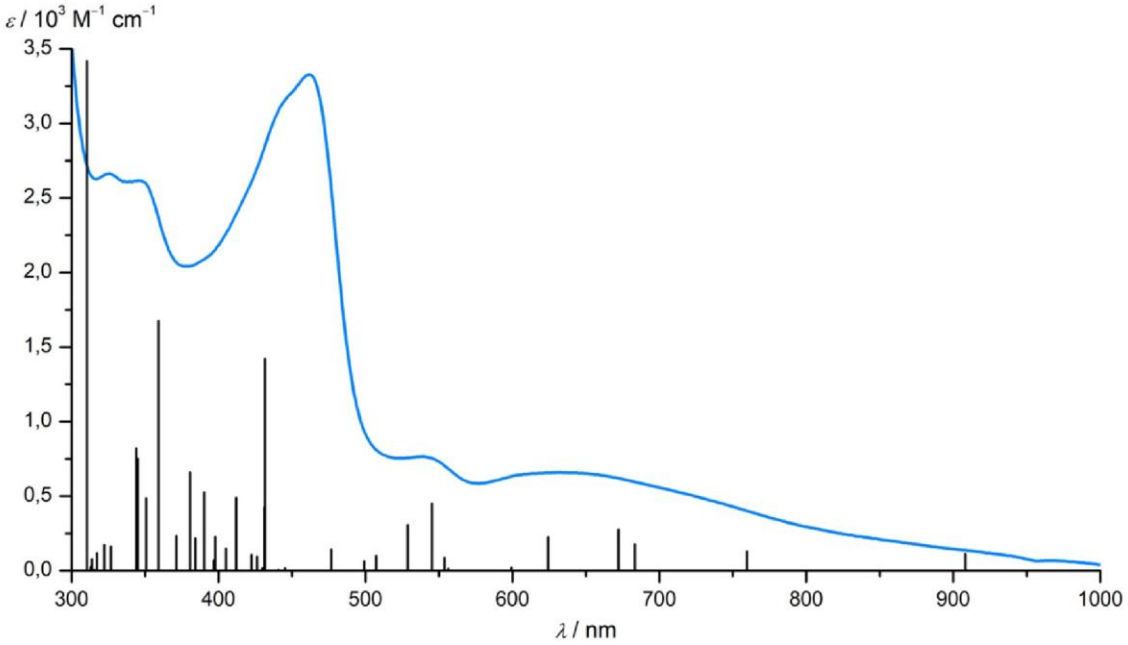

Figure S15. Absorption spectrum of $[Cr(bpmp)_2][OTf]_3$ in H_2O at pH 9.9 and TD-DFT calculated oscillator strengths of $[Cr(bpmp)(bpmp\text{-}H)]^{2+}$.

Table S7. TD-DFT calculated transitions of $[Cr(bpmp\text{-}H)(bpmp)]^{2+}$.

#	λ / nm	oscillator strength	character	from	to	difference electron density (purple = electron loss; orange = electron gain)
1	908.3	0.004200695	LMCT + LL'CT	p (CH) + p (py)	t_{2g} (d_{xz}) + p (py)	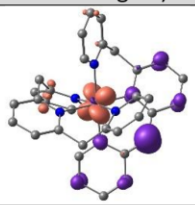
2	759.5	0.004813556	LMCT + LL'CT	p (CH) + p (py)	t_{2g} (d_{xz}+d_{yz}) + p (py)	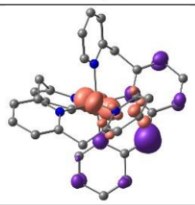
3	683.4	0.006631138	LMCT	p (CH) + p (py)	t_{2g} (d_{xy}) + e_g (d_{z2})	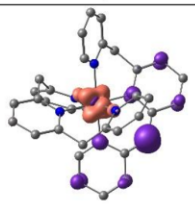
4	672.2	0.010283469	LMCT	p (CH) + p (py)	e_g (d_{z2})	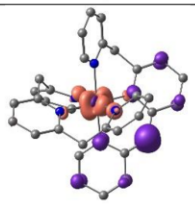
5	624.3	0.008371426	LMCT + MC	p (CH) + p (py) + t_{2g} (d_{xy})	e_g ($d_{x2\text{-}y2}$)	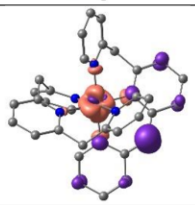
6	599.3	0.000772506	LL'CT + LMCT + MC	p (CH) + p (py) + t_{2g} (d_{xy})	p (py) + e_g ($d_{x2\text{-}y2}$)	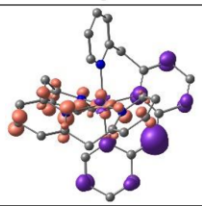
7	556.3	0.000436185	LMCT + LL'CT + MC	p (CH) + p (py) + t_{2g} (d_{xy})	e_g ($d_{x2\text{-}y2}$) + p (py)	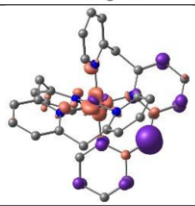

8	554	0.003206402	LL'CT + MC	p (CH) + p (py)+ t_{2g} (d_{xz}+d_{yz})	p (py) + e_g (d_{x2-y2}+d_{z2})	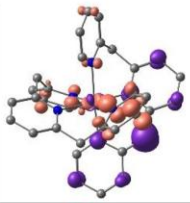
9	545.4	0.016762453	ILCT + LL'CT	p (CH) + p (py)	p (py)	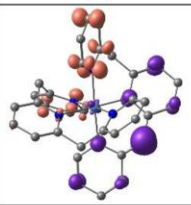
10	528.9	0.011456804	LL'CT	p (CH) + p (py)	p (py)	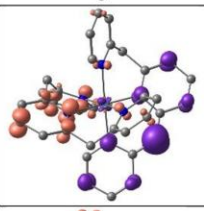
11	507.4	0.003737418	ILCT	p (CH) + p (py)	p (py)	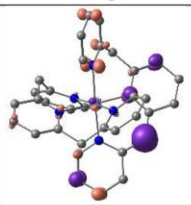
12	499.2	0.00234963	ILCT + MC	p (CH) + p (py) + t_{2g} (d_{yz})	p (py) + e_g (d_{x2-y2}+d_{z2})	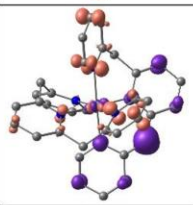
13	476.8	0.005313119	LL'CT + MC	p (CH) + p (py) + t_{2g} (d_{xy})	p (py) + t_{2g} (d_{yz})	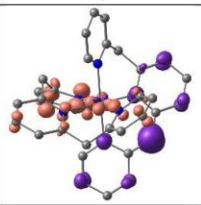
14	445.2	0.000607987	LL'CT	p (CH) + p (py)	p (py)	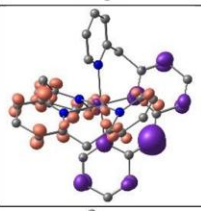
15	440.8	0.000222206	MC	t_{2g} (d_{xz})	e_g (d_{z2})	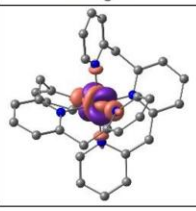

16	431.7	0.05277057	ILCT + MC	p (CH) + p (py) + t_{2g} (d_{xy})	p (py) + t_{2g} (d_{xy}+d_{xz})	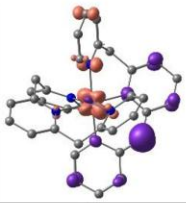
17	431.3	0.015787377	LMCT + LL'CT	p (CH) + p (py)	t_{2g} (d_{xy}+d_{xz}+d_{yz}) + p (py)	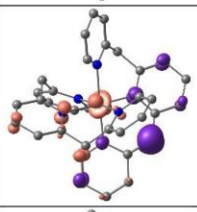
18	430	0.000617098	MC + LMCT	t_{2g} (d_{yz}) + p (CH)	e_g (d_{x2-y2}+d_{z2})	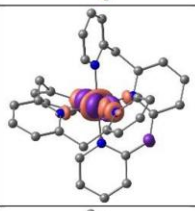
19	426.4	0.003518558	ILCT	p (CH) + p (py)	p (py)	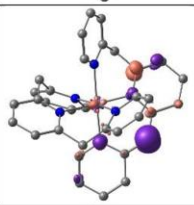
20	422.4	0.003935425	ILCT + LL'CT + LMCT	p (CH) + p (py)	p (py) + t_{2g} (d_{xy}+d_{yz})	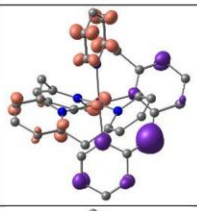
21	412.1	0.018123465	LL'CT + MC	p (CH) + p (py) + t_{2g} (d_{xy})	p (py) + e_g (d_{x2-y2})	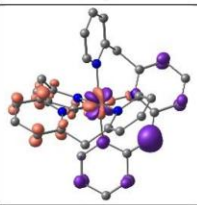
22	405.1	0.005534688	LL'CT + MC	p (CH) + p (py) + t_{2g} (d_{xy})	p (py) + e_g (d_{x2-y2}+d_{z2})	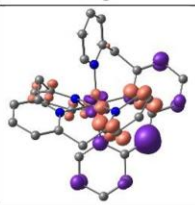
23	397.7	0.008474711	MC + LMCT	t_{2g} (d_{xy}) + p (CH)	e_g (d_{x2-y2})	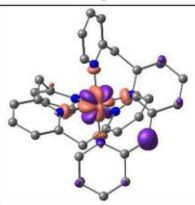

24	396.7	0.002528534	ILCT + LL'CT + MC	p (CH) + p (py) + t_{2g} (d_{xy})	p (py) + e_g (d_{x2-y2}+d_{z2})	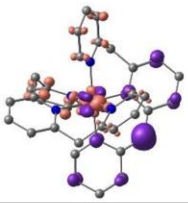
25	390.3	0.019580503	ILCT + MC	p (CH) + p (py) + t_{2g} (d_{xy})	p (py) + e_g (d_{x2-y2}+d_{z2})	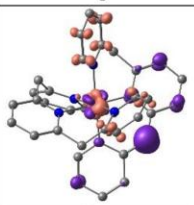
26	384.3	0.008136465	LL'CT + ILCT + MC	p (CH) + p (py) + t_{2g} (d_{xy})	p (py) + e_g (d_{x2-y2}+d_{z2})	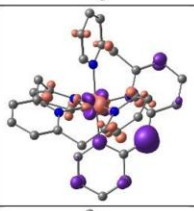
27	380.5	0.024575727	LL'CT + MC	p (CH) + p (py) + t_{2g} (d_{xy})	p (py) + e_g (d_{x2-y2}+d_{z2})	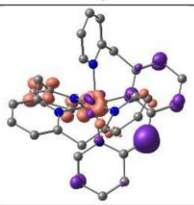
28	371.4	0.008661558	LL'CT + MC	p (CH) + p (py) + t_{2g} (d_{xy})	p (py) + e_g (d_{x2-y2}+d_{z2})	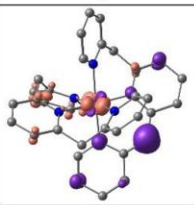
29	359.2	0.062219373	ILCT + MC	p (CH) + p (py) + t_{2g} (d_{xy}+d_{xz}+d_{yz})	p (py) + e_g (d_{x2-y2}+d_{z2})	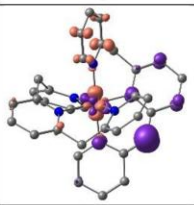
30	350.7	0.000959514	MC	t_{2g} (d_{xz})	e_g (d_{x2-y2})	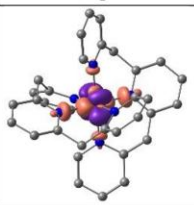
31	350.7	0.01803702	LMCT + ILCT	p (CH) + p (py)	e_g (d_{x2-y2}+d_{z2}) + p (py)	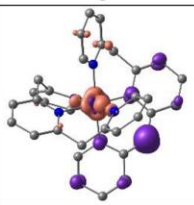

S24

32	345.1	0.027927026	LL'CT + LMCT	p (CH) + p (py)	p (py) + e_g (d_{x2-y2}+d_{z2})	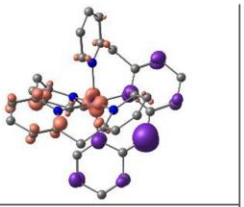
33	343.9	0.030471736	MC + LMCT	t_{2g} (d_{yz}) + p (CH)	e_g (d_{x2-y2}+d_{z2})	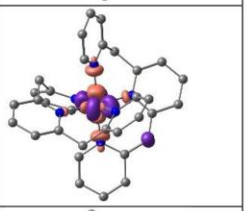
34	326.7	0.006043994	LMCT	p (CH) + p (py)	e_g (d_{x2-y2})	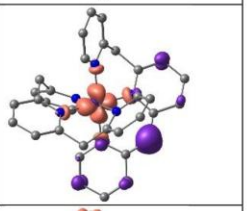
35	322.2	0.006409311	LMCT + ILCT	p (py)	t_{2g} (d_{xz}) + p (py)	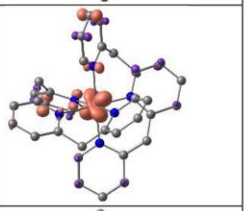
36	317.3	0.004341205	ILCT + LMCT	p (py)	p (py) + t_{2g} (d_{xy}+d_{xz}+d_{yz})	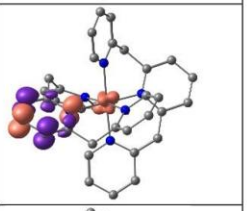
37	315.5	0.000239335	ILCT + LMCT	p (py)	p (py) + t_{2g} (d_{xz})	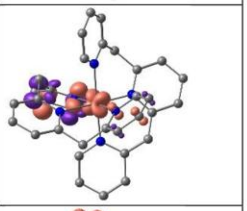
38	313.9	0.002920282	ILCT + LMCT	p (py)	p (py) + t_{2g} (d_{xz})	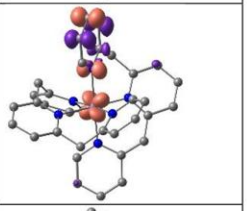
39	312.9	0.000853879	ILCT + LMCT	p (py)	p (py) + t_{2g} (d_{yz})	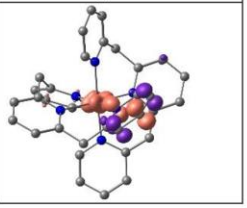

40	310.4	0.127030531	ILCT + LMCT	p (py) + p (CH)	p (py) + t_{2g} (d_{xy}+d_{yz})	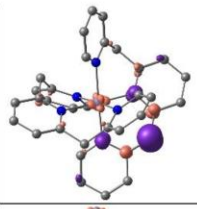
41	299.9	0.003619984	LMCT	p (py)	t_{2g} (d_{xz})	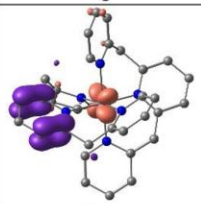
42	293.3	0.015512516	LMCT + LL'CT	p (py)	t_{2g} (d_{xz}+d_{yz}) + p (py)	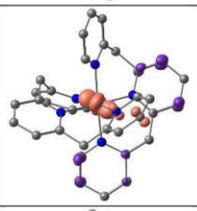
43	293	0.02365423	ILCT + LMCT	p (py)	p (py) + t_{2g} (d_{xy}+d_{xz}+d_{yz})	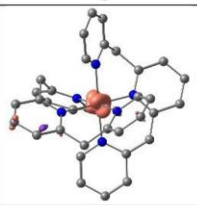
44	290.3	0.002589746	ILCT + LMCT	p (py)	p (py) + t_{2g} (d_{xy})	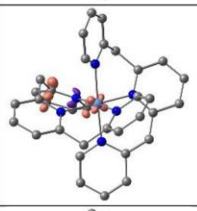
45	290.1	0.021949923	LMCT	p (py)	t_{2g} (d_{xy})	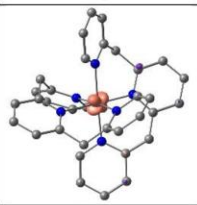
46	289.8	0.001517601	ILCT + LMCT	p (py)	p (py) + t_{2g} (d_{xy})	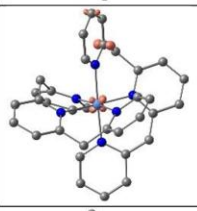
47	288.4	0.000490673	ILCT	p (py)	p (py)	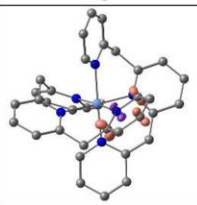

48	287.6	0.005138237	LMCT + ILCT	p (py)	t_{2g} (d_{xy}+d_{xz}+d_{yz}) + p (py)	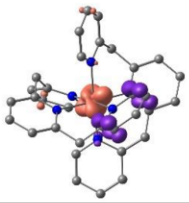
49	285.1	0.007037636	LMCT	p (CH) + p (py)	t_{2g} (d_{xy}+d_{yz})	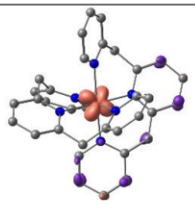
50	279.2	0.005036221	LMCT + ILCT	p (py)	t_{2g} (d_{xy}+d_{xz}) + p (py)	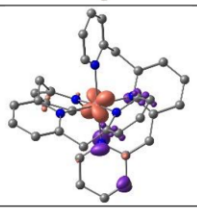

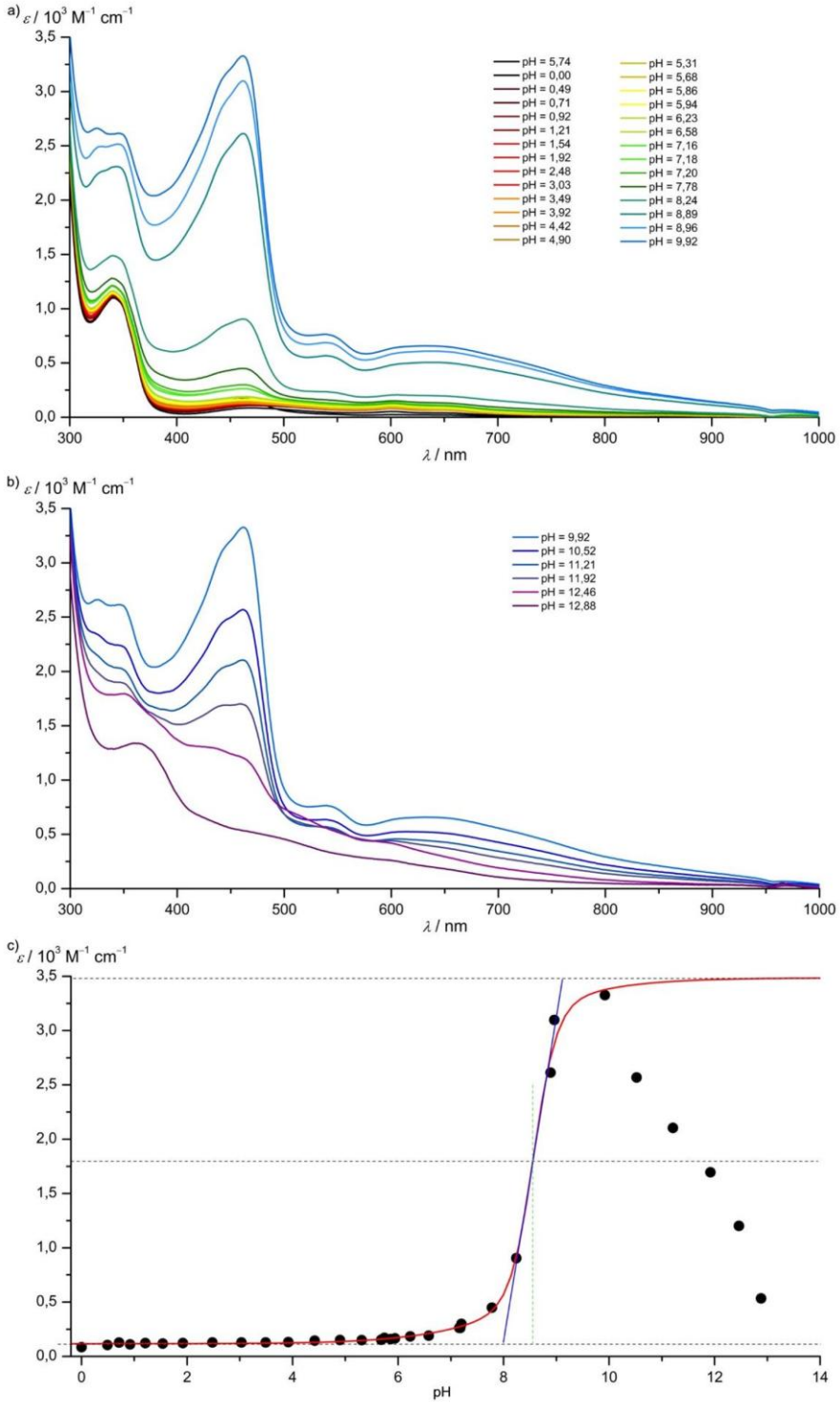

Figure S16. Photometric titration of $[Cr(bpmp)_2][OTf]_3$ in H_2O a) pH 0 – 9.9; b) pH 9.9 – 12.9 and c) pK_a determination at 445 nm.

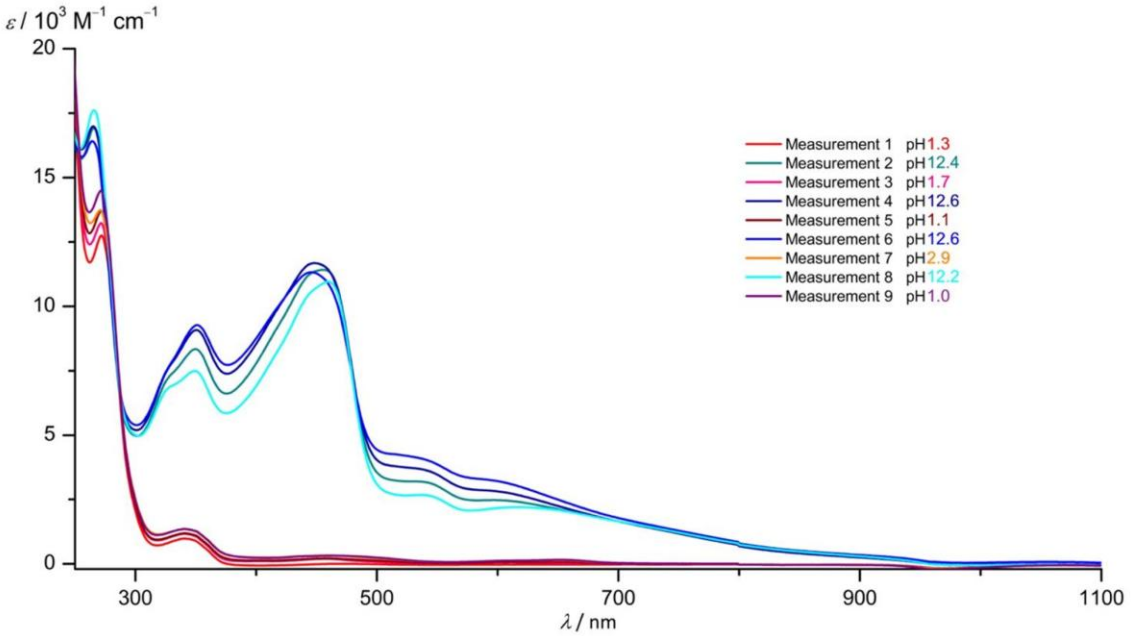

Figure S17. Absorption spectra of $[Cr(bpmp)_2][OTf]_3$ in H_2O cycling between pH ≈ 1.5 and pH > 12. pH > 12 causes some degradation.

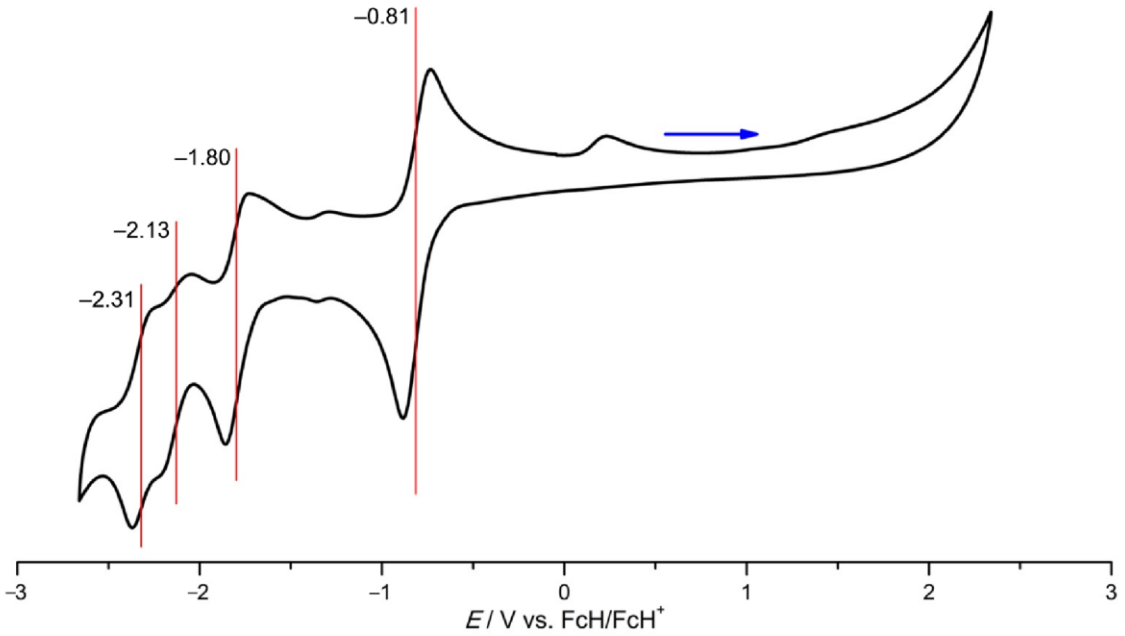

Figure S18. Cyclic voltammogram of $[Cr(bpmp)_2][PF_6]_3$ in $CH_3CN/[^nBu_4N][PF_6]$.

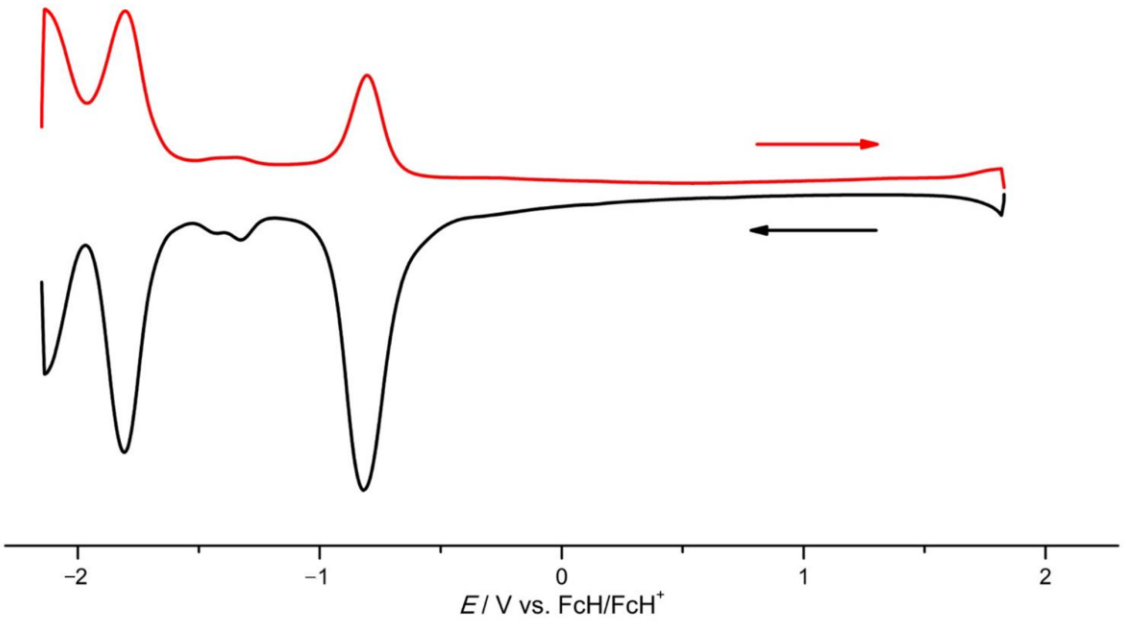

Figure S19. Square wave voltammogram of $[Cr(bpmp)_2][PF_6]_3$ in $CH_3CN/[^nBu_4N][PF_6]$.

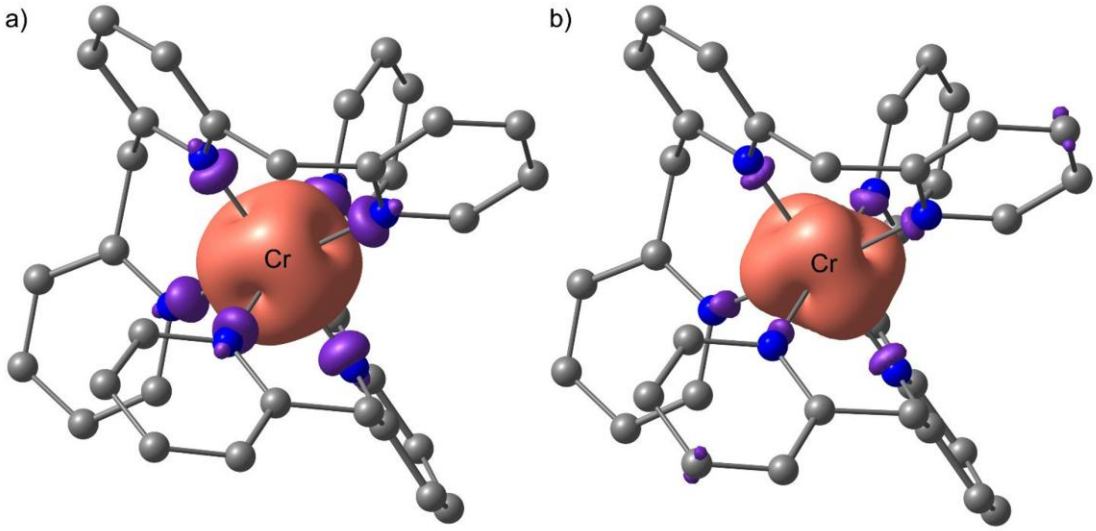

Figure S20. DFT optimized geometries of a) $[Cr(bpmp)_2]^{3+}$ (quartet state) and b) $[Cr(bpmp)_2]^{2+}$ (triplet state), and corresponding Mulliken spin densities plotted at 0.006 a.u. with the α spin in orange and the β spin in purple.

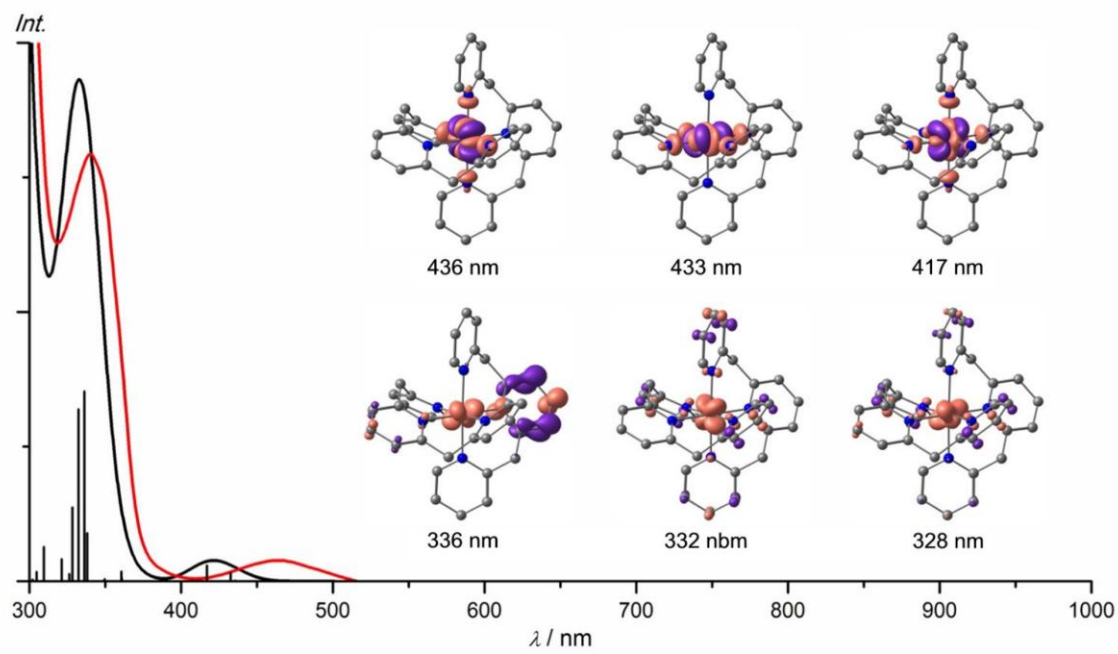

Figure S21. Experimental (red) and TD-DFT calculated absorption spectrum (black) of $[Cr(bpmp)_2]^{3+}$ and difference electron densities of the major transitions of ^{4}LMCT and $^4T_2$ character calculated by TD-DFT.

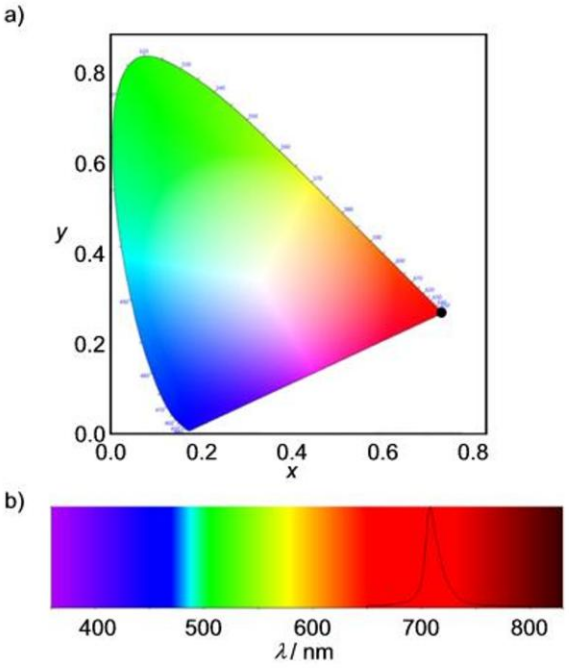

Figure S22. a) CIE 1931 diagram and CIE coordinates of $[Cr(bpmp)_2]^{3+}$ (0.7326, 0.2674) and b) emission spectrum plotted with a background colored with the visible spectral region.

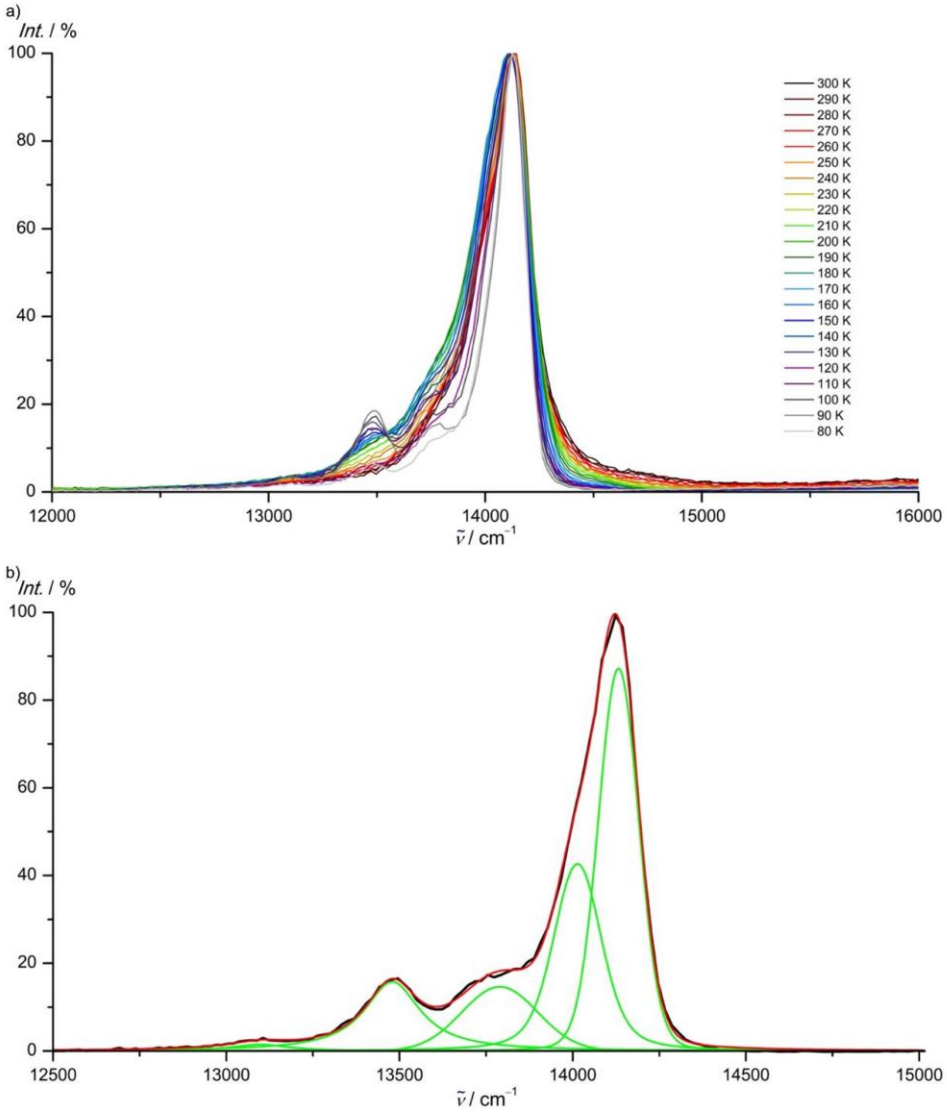

Figure S23. a) Normalized emission spectra of $[Cr(bpmp)_2][OTf]_3$ in butyronitrile at 300 – 80 K and b) emission spectrum of $[Cr(bpmp)_2][OTf]_3$ in butyronitrile at 100 K (black) fitted with five Voigt functions (green; peak centers at 14140, 14017, 13788, 13483 and 13099 cm^{-1}).

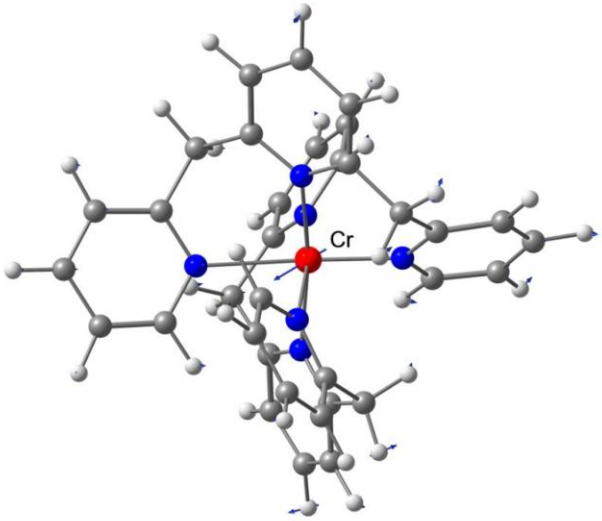

Figure S24. Illustration of the 308 cm^{-1} vibrational mode of $[Cr(bpmp)_2]^{3+}$ calculated by DFT. Scaled displacement vectors are shown as blue arrows.

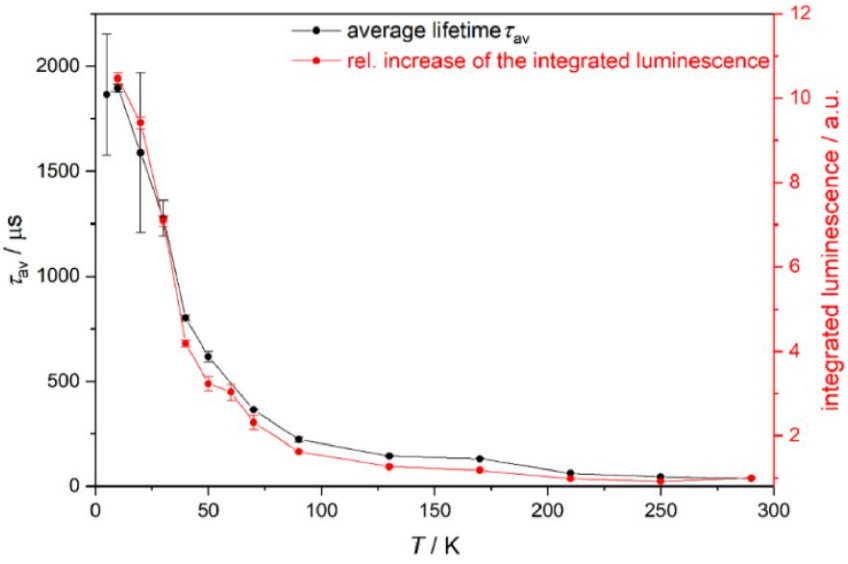

Figure S25. Plot of the average luminescence lifetime τ_{av} of $[Cr(bpmp)_2][BF_4]_3$ and the integrated luminescence (normalized to 290 K) versus temperature.

Table S8. Temperature-dependent luminescence lifetimes of $[Cr(bpmp)_2][BF_4]_3$ measured by TCSPC (KBr pellet, λ_{exc} = 390 nm)

T / K	λ_{em} / nm	τ_1 / µs	τ_2 / µs	τ_{av} / µs [a]
290	707	5.17 ± 0.07 (20%)	46.0 ± 0.3 (80%)	38.0 ± 0.3
	716	5.37 ± 0.09 (19%)	46.6 ± 0.3 (81%)	38.6 ± 0.3
250	707	6.00 ± 0.08 (19%)	55.4 ± 0.4 (81%)	45.8 ± 0.4
	717	7.6 ± 0.2 (14%)	63.4 ± 0.7 (86%)	55.3 ± 0.6
210	707	11.1 ± 0.1 (25%)	80.0 ± 0.5 (75%)	62.5 ± 0.4
	717	12.5 ± 0.1 (24%)	90.0 ± 0.7 (76%)	71.2 ± 0.5
170	707	21.7 ± 0.2 (21%)	160 ± 1 (79%)	131 ± 1
	718	29.5 ± 0.2 (24%)	200 ± 2 (76%)	159 ± 1
130	708	55.0 ± 0.5 (68%)	339 ± 13 (32%)	145 ± 4
	718	41.9 ± 0.3 (56%)	225 ± 3 (44%)	122 ± 2
90	718	120 ± 2 (79%)	600 ± 50 (21%)	220 ± 10
70	718	160 ± 2 (66%)	770 ± 40 (34%)	365 ± 1
50	719	300 ± 6 (60%)	1100 ± 60 (40%)	620 ± 30
40	719	273 ± 3 (49%)	1300 ± 20 (51%)	800 ± 10
30	720	420 ± 30 (33%)	1700 ± 100 (67%)	1300 ± 80
20	720	640 ± 200 (28%)	2000 ± 400 (72%)	1600 ± 400
10	720	680 ± 20 (28%)	2150 ± 20 (72%)	1900 ± 20
5	720	550 ± 60 (15%)	2050 ± 50 (85%)	1900 ± 300

[a] The average lifetime was calculated by considering the relative contributions of the time constants τ_1 and τ_2 to get an impression of the sharp increase of the emission lifetimes at low temperatures (especially below 70 K). However, one should be aware of the fact that τ_{av} is indicated here for illustration and does not correspond directly to the decay of an excited state. The biexponential decay of the luminescence over the whole temperature range of 290 – 5 K is assigned to contributions of at least two different emissive doublet microstates. Additionally, different microenvironments in the KBr matrix (e.g. $[Cr(bpmp)_2]^{3+}$ with differently close contacts to counter ions or co-crystallized solvent molecules in the microcrystalline state) might contribute to the multiexponential decay.

Table S9. Quantum yields Φ and luminescence lifetimes τ of $[Cr(bpmp)_2][ClO_4]_3$, $[Cr(bpmp)_2][PF_6]_3$, $[Cr(bpmp)_2][BF_4]_3$ in various environments at room temperature (λ_{exc} = 462 nm).

X	solvent	acid[a]	oxygen	Φ / %	τ / µs
ClO_4	H_2O	–	–	12.9	1500
ClO_4	H_2O	$HClO_4$	–	12.0	1500
ClO_4	H_2O	$HClO_4$	+	6.2	820
ClO_4	D_2O	$DClO_4$	–	15.7	1800
ClO_4	D_2O	$DClO_4$	+	8.0	810
ClO_4	CH_3CN	–	–	9.1	1000
ClO_4	CH_3CN	$HClO_4$	–	10.6	1200
ClO_4	CH_3CN	$HClO_4$	+	3.7	380
ClO_4	CD_3CN	$DClO_4$	–	9.7	1200
ClO_4	CD_3CN	$DClO_4$	+	2.8	370
ClO_4	PBS (pH 6.9)[b]	–	–	0.9	310
ClO_4	PBS (pH 6.5)[b]	–	–	1.7	570
PF_6	H_2O	–	–	0.3	220
PF_6	H_2O	$HClO_4$	–	16.0	1500
PF_6	H_2O	$HClO_4$	+	9.2	870
PF_6	D_2O	$DClO_4$	–	20.0	1800
PF_6	D_2O	$DClO_4$	+	9.2	860
PF_6	CH_3CN	–	–	0.5	550
PF_6	CH_3CN	$HClO_4$	–	11.1	1000
PF_6	CH_3CN	$HClO_4$	+	4.0	380
PF_6	CD_3CN	$DClO_4$	–	15.6	1300
PF_6	CD_3CN	$DClO_4$	+	4.8	410
PF_6	PBS (pH 6.9)[b]	–	–	0.5	310
PF_6	PBS (pH 6.5)[b]	–	–	3.2	800
BF_4	H_2O	–	–	0.4	480
BF_4	H_2O	$HClO_4$	–	12.0	1400
BF_4	H_2O	$HClO_4$	+	7.6	840
BF_4	D_2O	$DClO_4$	–	13.4	1500
BF_4	D_2O	$DClO_4$	+	7.4	840
BF_4	CH_3CN	–	–	0.6	950
BF_4	CH_3CN	$HClO_4$	–	10.4	1100
BF_4	CH_3CN	$HClO_4$	+	3.8	390
BF_4	CD_3CN	$DClO_4$	–	11.2	1200
BF_4	CD_3CN	$DClO_4$	+	4.2	400
BF_4	PBS (pH 6.9)[b]	–	–	0.4	480
BF_4	PBS (pH 6.5)[b]	–	–	3.2	860

[a] final $HClO_4$ ($DClO_4$) concentration c = 0.1 M. [b] PBS = phosphate buffered saline (0.1 M).

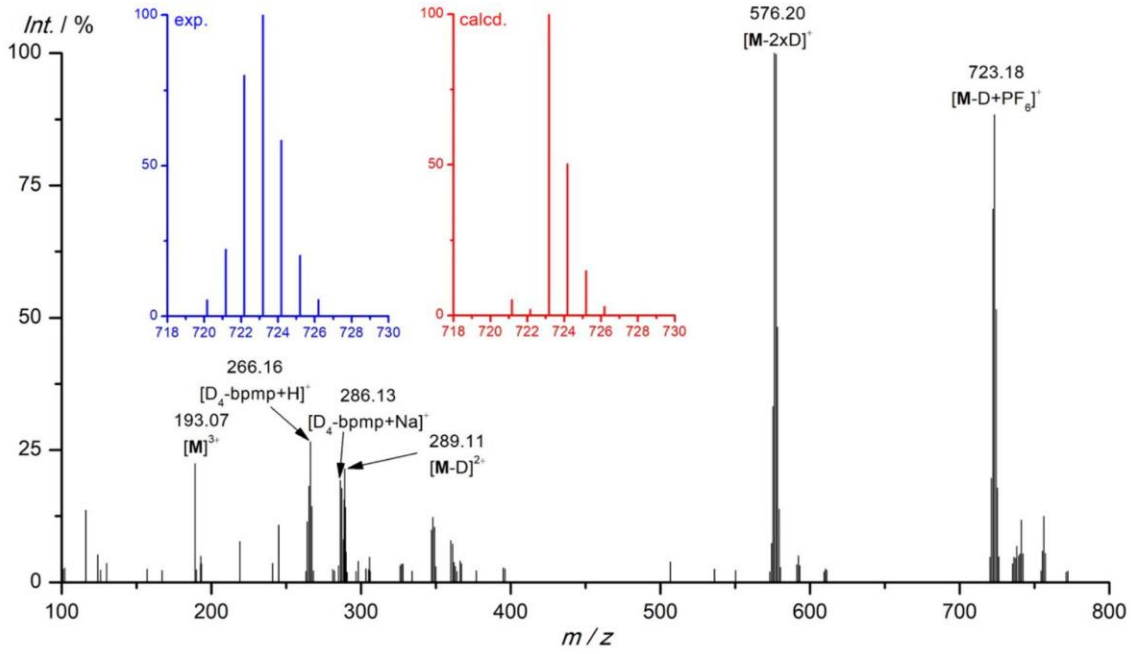

Figure S26. ESI$^+$ mass spectrum of $[Cr([D_4]\text{-bpmp})_2][PF_6]_3$ in CH_3CN. The insets depict the experimental (blue) isotopic pattern of the peak at *m/z* 723 and calculated isotopic patterns of the D_6 (red) and D_8 (black) isotopologues for illustration.

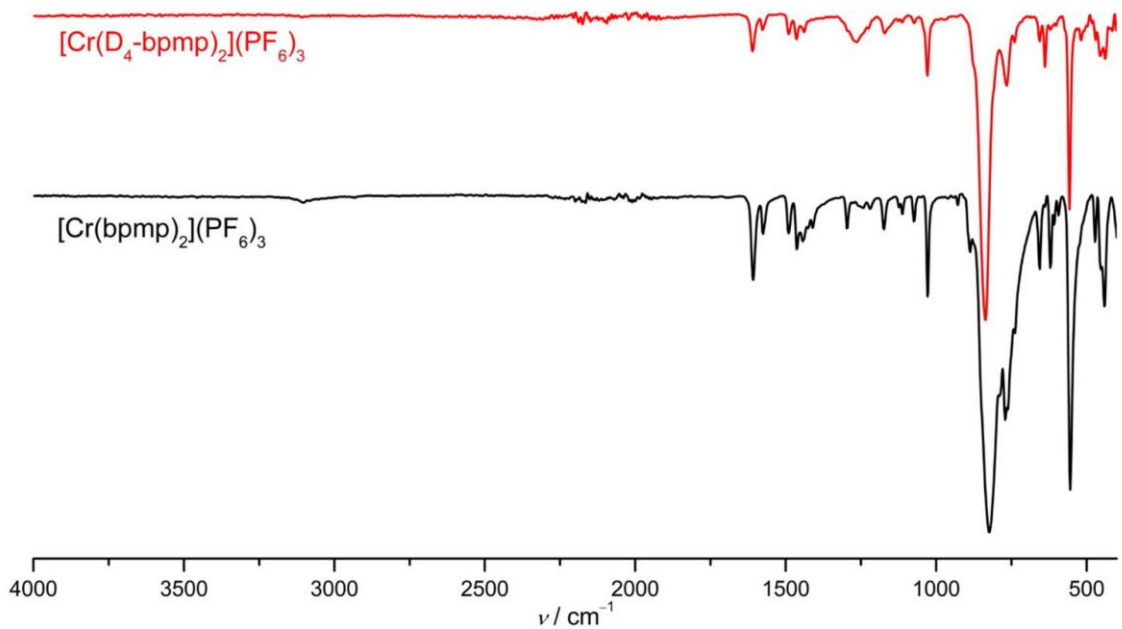

Figure S27. ATR-IR spectra of $[Cr([D_4]\text{-bpmp})_2][PF_6]_3$ with deuterated methylene bridges (red) and $[Cr(bpmp)_2][PF_6]_3$ (black).

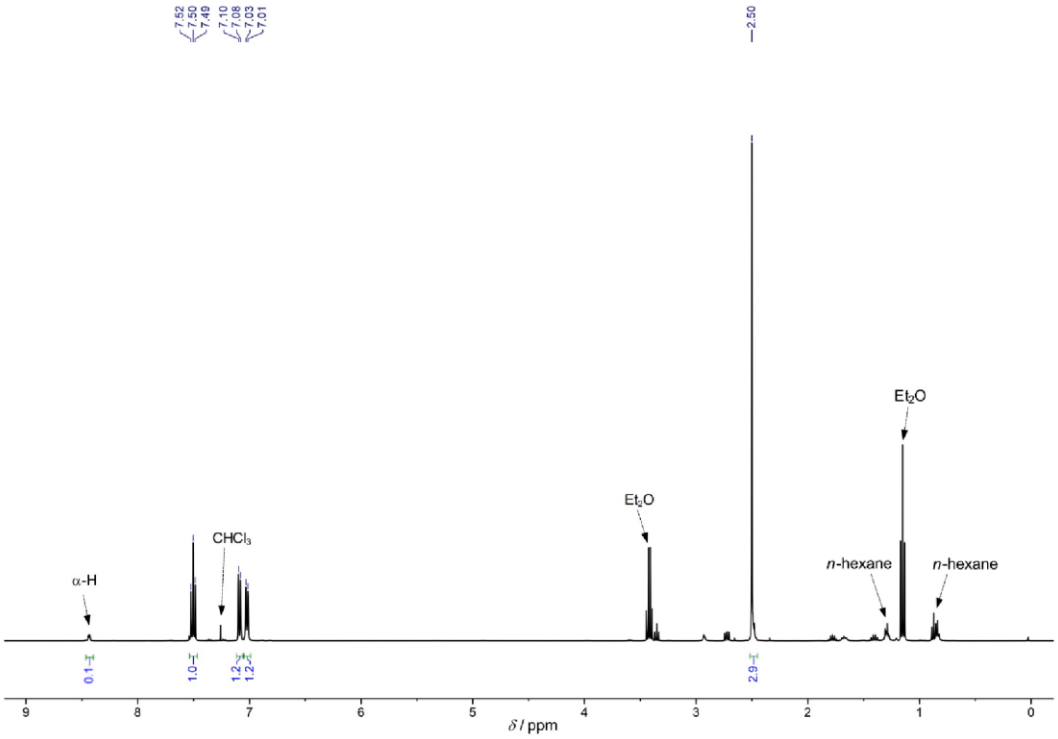

Figure S28. ^{1}H NMR spectrum of 6-deutero-2-methylpyridine in $CDCl_3$.

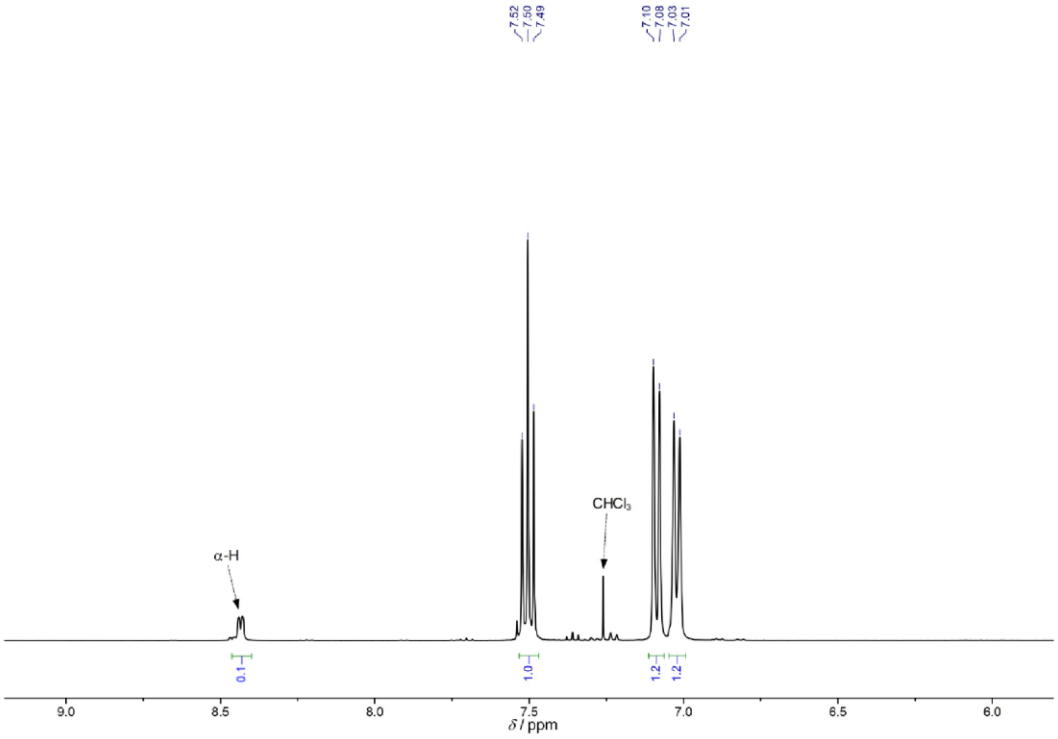

Figure S29. Zoom into the aromatic region of the ^{1}H NMR spectrum of 6-deutero-2-methylpyridine in $CDCl_3$.

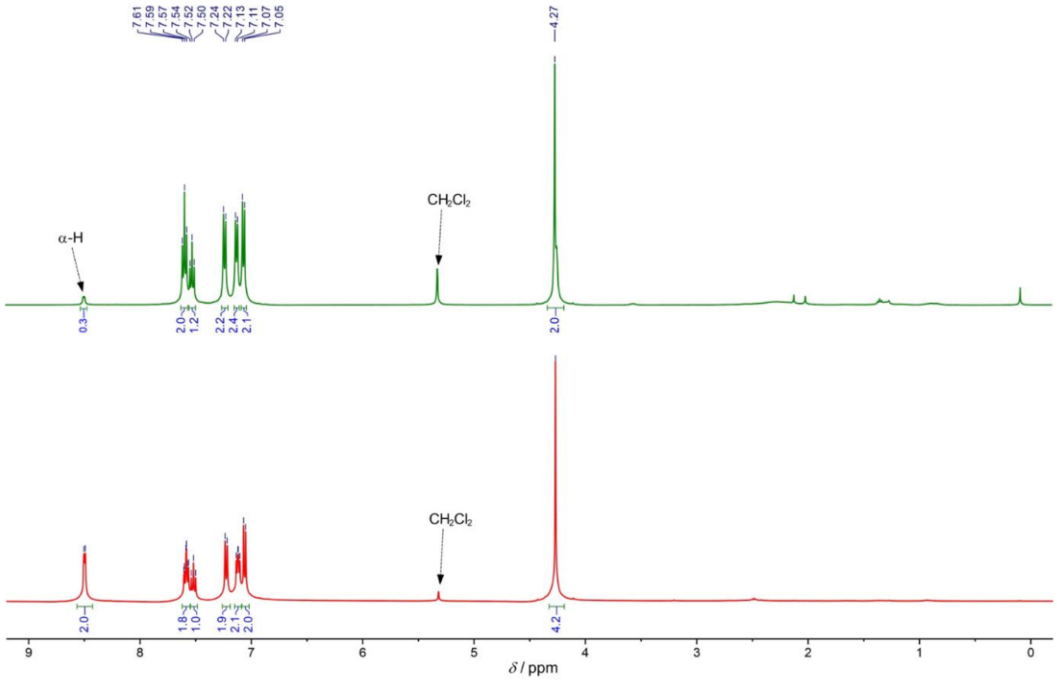

Figure S30. ^{1}H NMR spectra of [$D_{2/4}$]-bpmp (green) and bpmp (red) in CD_2Cl_2.

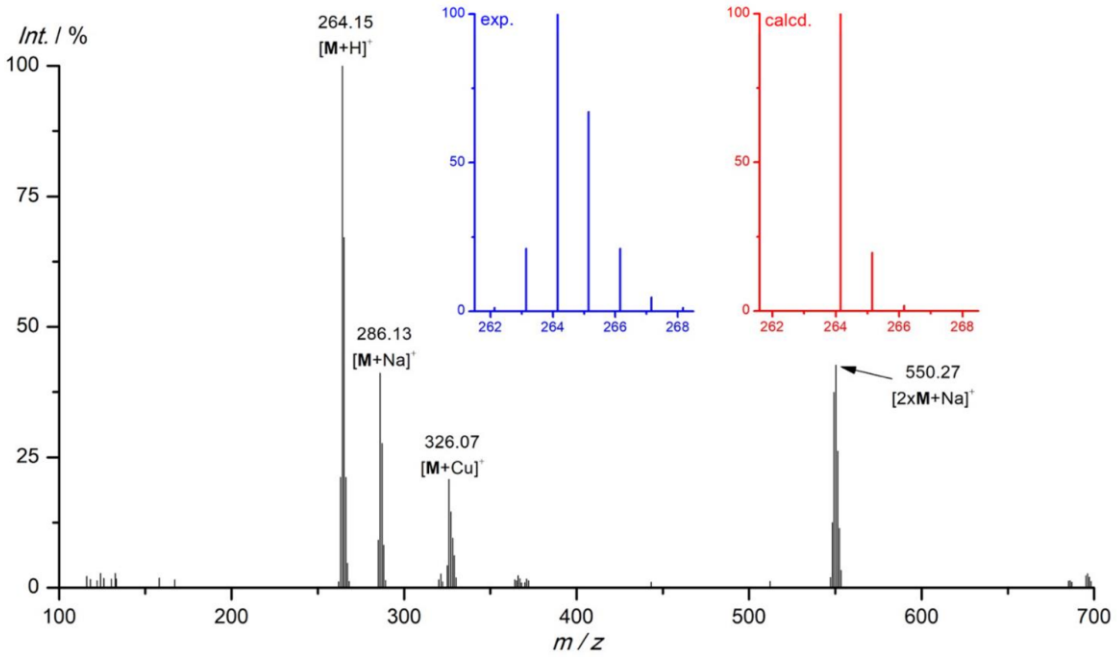

Figure S31. ESI^{+} mass spectrum of [D_2]-bpmp in CH_3CN. The insets depict the experimental (blue) and calculated (red) isotopic pattern of the peak at *m/z* 264.

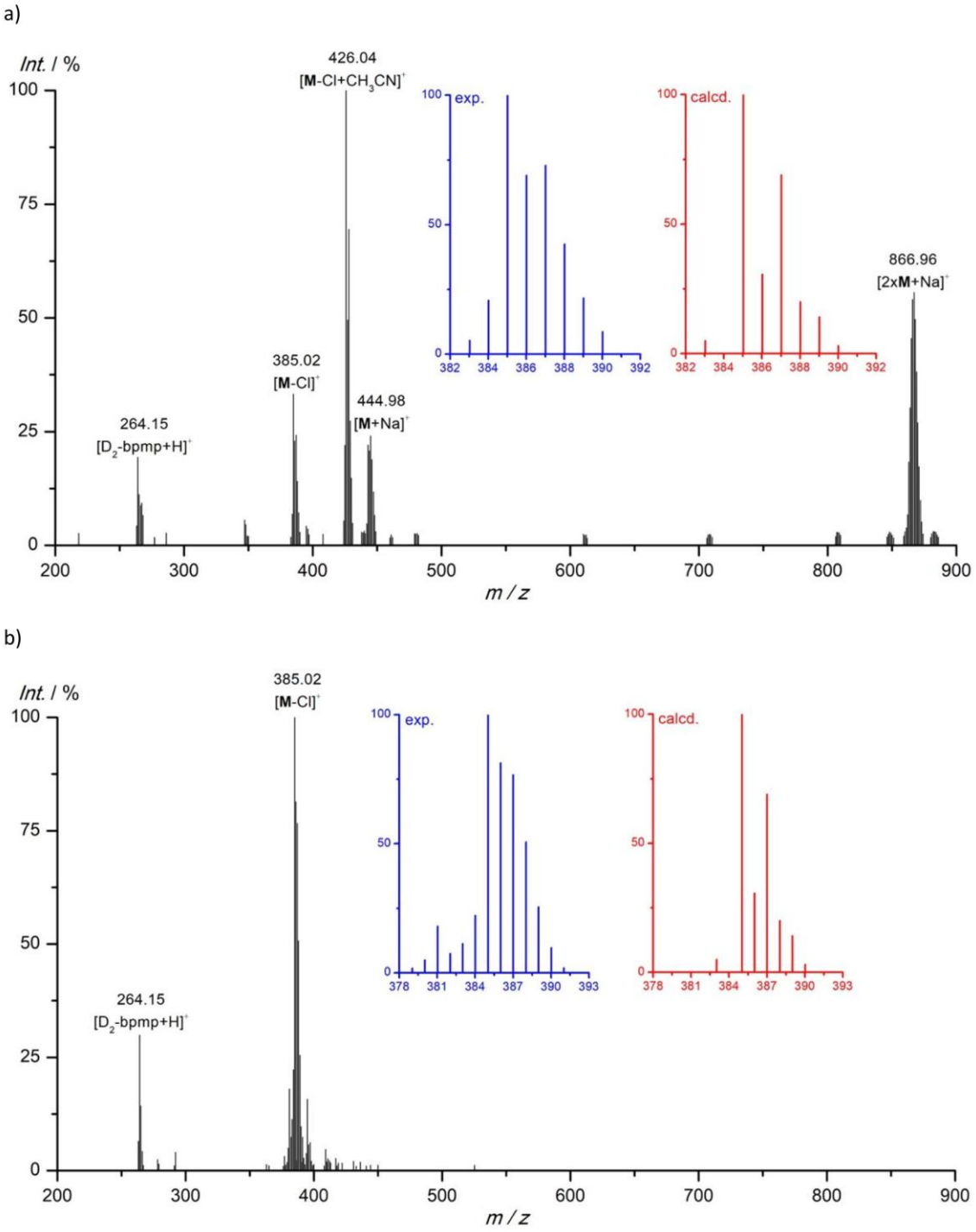

Figure S32. a) ESI^+ mass spectrum of $Cr([D_2]\text{-bpmp})Cl_3$ in CH_3CN. The insets depict the experimental (blue) and calculated (red) isotopic pattern of the peak at *m/z* 385. b) APCI mass spectrum of $Cr([D_2]\text{-bpmp})Cl_3$. The insets depict the experimental (blue) and calculated (red) isotopic pattern of the peak at *m/z* 385.

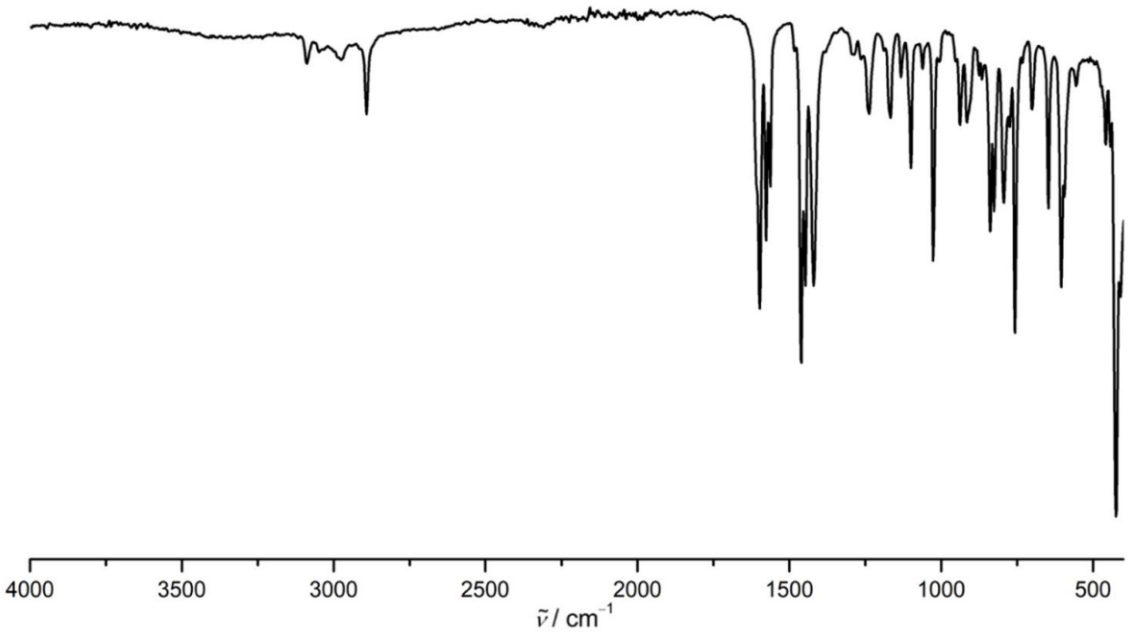

Figure S33. ATR-IR spectrum of Cr([D_2]-bpmp)Cl_3.

a)

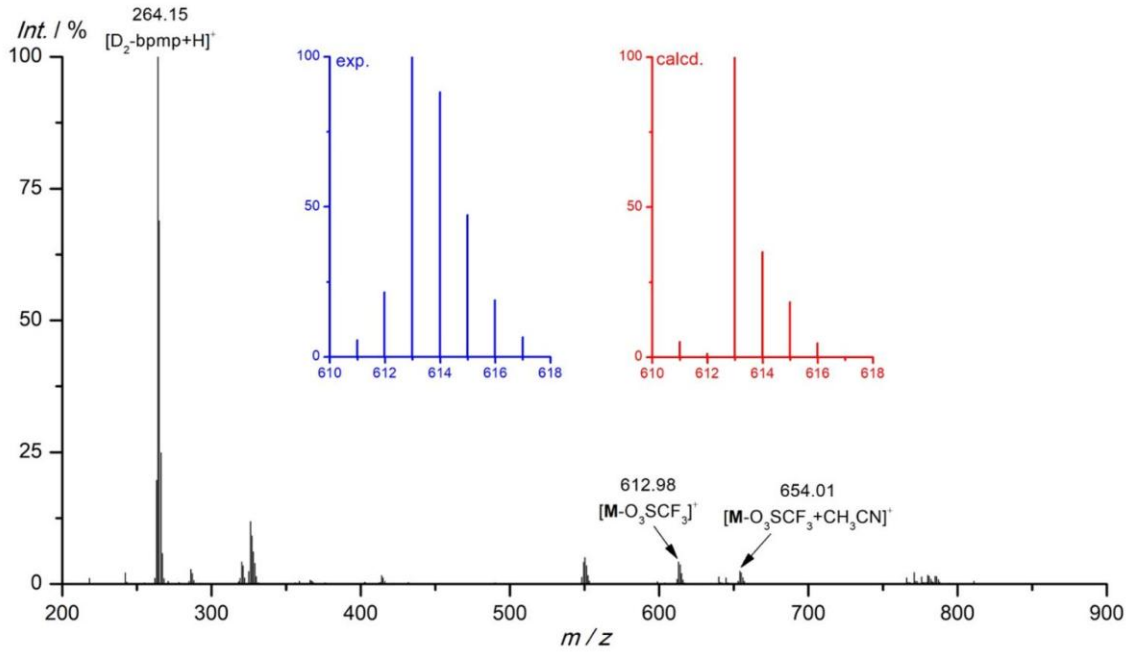

b)

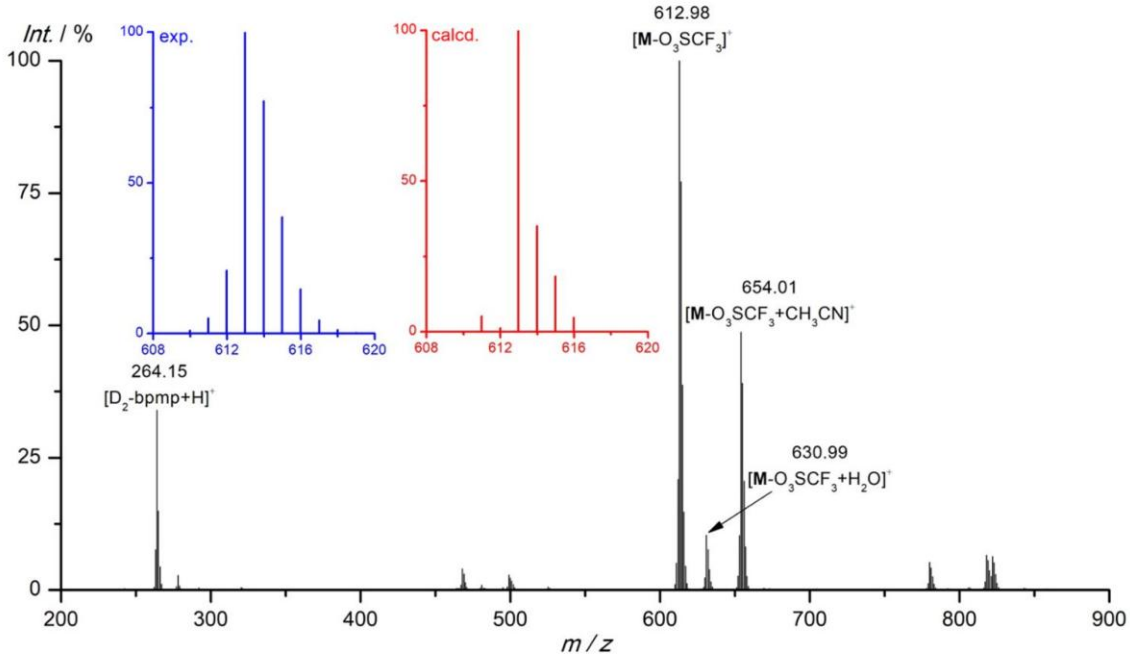

Figure S34. a) ESI$^+$ mass spectrum of Cr([D_2]-bpmp)$(OTf)_3$ in CH_3CN. The insets depict the experimental (blue) and calculated (red) isotopic pattern of the peak at *m/z* 613. b) APCI mass spectrum of Cr([D_2]-bpmp)$(OTf)_3$. The insets depict the experimental (blue) and calculated (red) isotopic pattern of the peak at *m/z* 613.

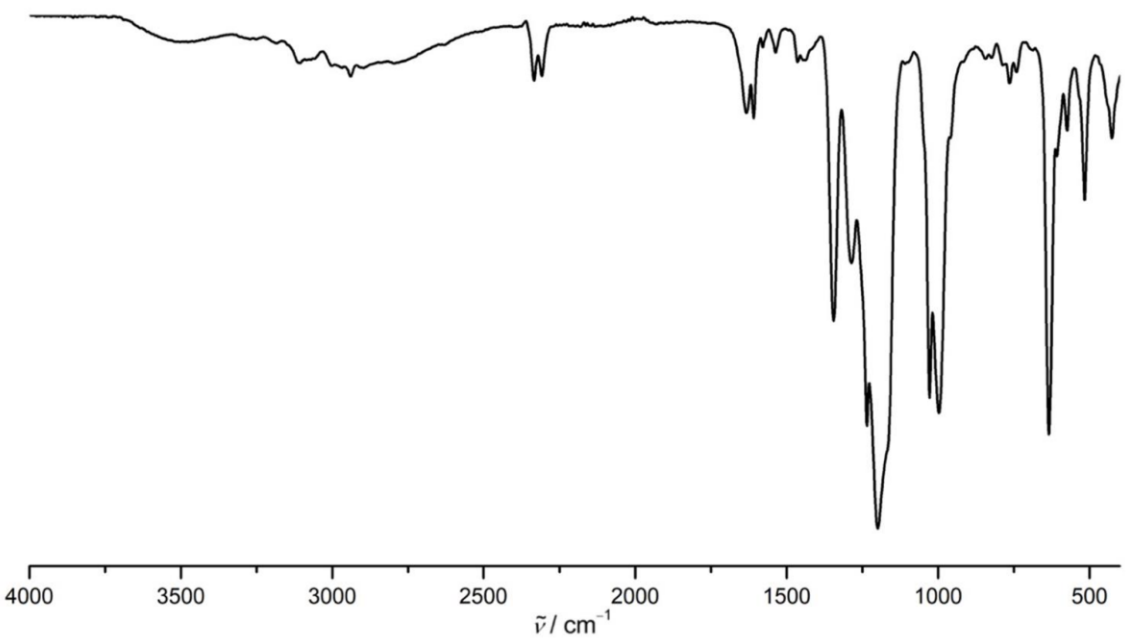

Figure S35. ATR-IR spectrum of Cr([D_2]-bpmp)$(OTf)_3$.

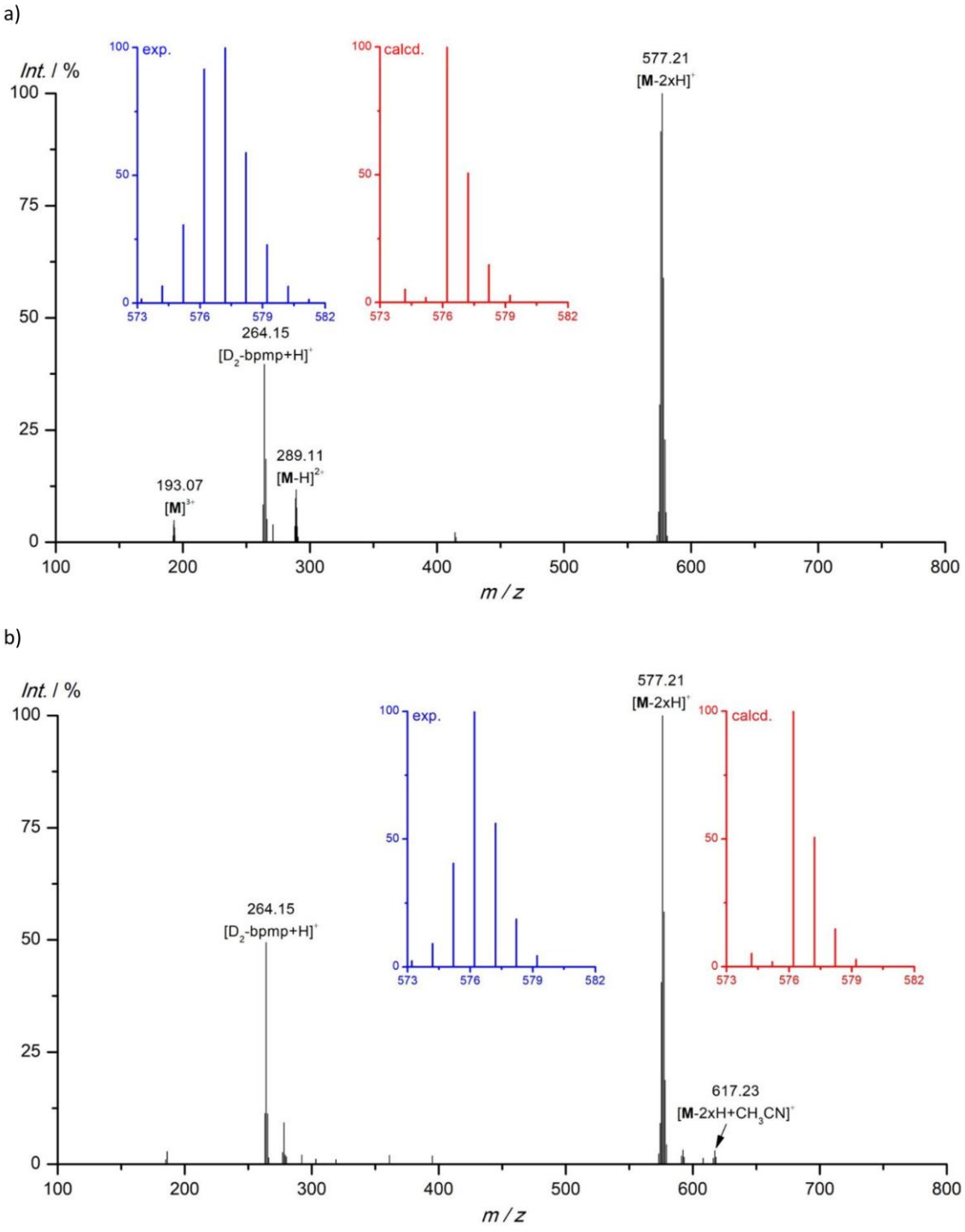

Figure S36. a) ESI^+ mass spectrum of $[Cr([D_2]\text{-bpmp})_2][OTf]_3$ in CH_3CN. The insets depict the experimental (blue) and calculated (red) isotopic pattern of the peak at *m/z* 576. b) APCI mass spectrum of $[Cr([D_2]\text{-bpmp})_2][OTf]_3$. The insets depict the experimental (blue) and calculated (red) isotopic pattern of the peak at *m/z* 576.

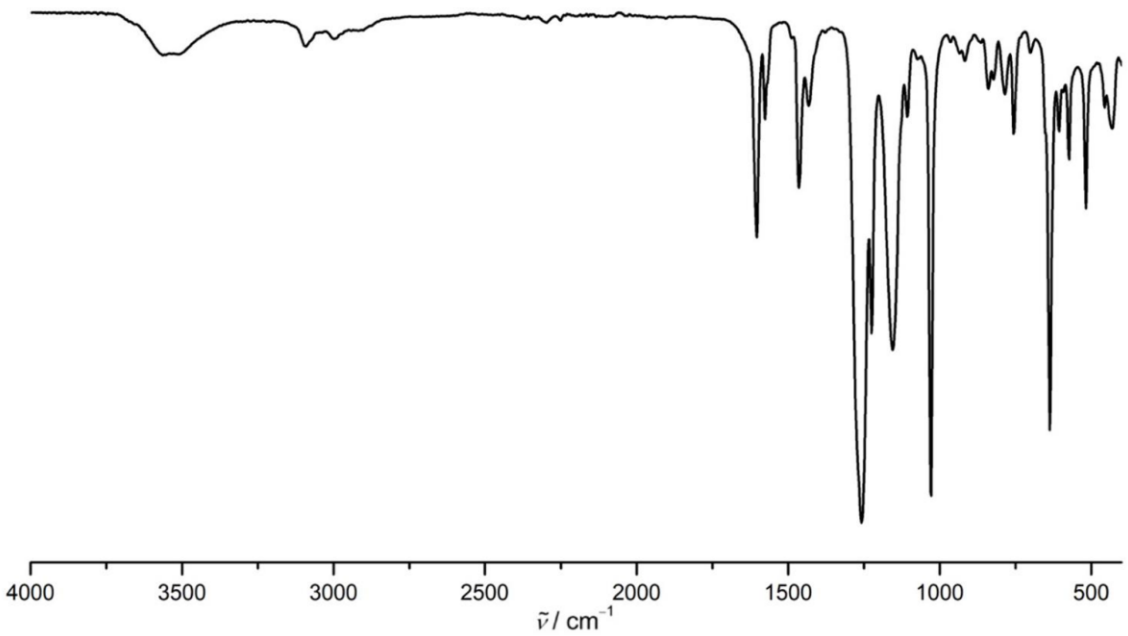

Figure S37. ATR-IR spectrum of $[Cr([D_2]\text{-bpmp})_2][OTf]_3$.

NIR Absorption Spectroscopy / Vibrational Overtone Analysis

Since the isotopologic chromium(III) complexes were not available in sufficient quantities, the analysis of the position and intensity of the C–H and C–D vibrational overtones for the chromium complexes was carried out on simpler pyridine-containing model compounds. The vibrational signatures of the methylene groups in **bpmp** were not investigated. Previously, the vibrational overtone data from the isotopologues of 6,6'-dimethyl-2,2'-bipyridine (**Me_2-bpy** and **[D_{12}]-Me_2-bpy**, Figure Sx) proved to be a successful model system for the very similar **ddpd** ligand (Figure S38).[43]

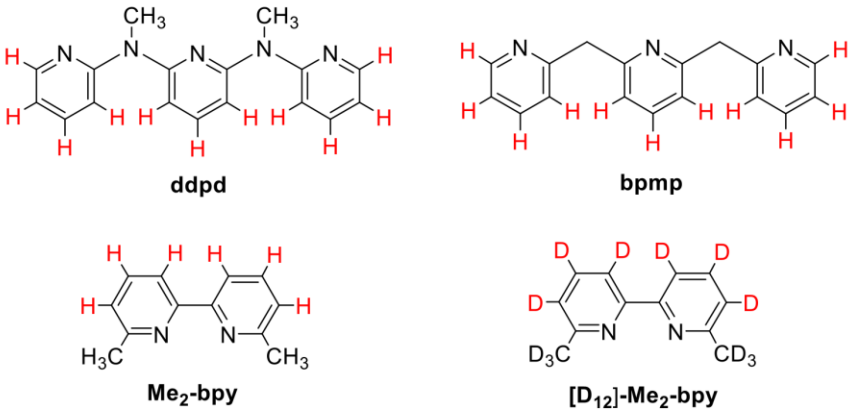

Figure S38. Top row: pyridine-based ligands in luminescent chromium complexes. Bottom row: model compounds used for the analysis of vibrational CH and CD overtones.

In order to verify if **Me_2-bpy** and **[D_{12}]-Me_2-bpy** are also good model compounds for the isotopologues of **bpmp**, we measured the aromatic C–H overtone energies of **bpmp** up to the third overtone (ν = 4) and compared them to the previously obtained overtone data from **Me_2-bpy** (Figure S39). The C–H overtones of **bpmp** showed a well-behaved Morse progression and could reasonably well be fitted with Gaussian functions of the form $y(x) = A * \exp(-0.5*((x-x_c)/\sigma)^2)$, defined by amplitude A, center wavenumber x_c, and Gaussian width σ. Despite the structural differences of **Me_2-bpy** and **bpmp** the Gaussian functions of the aromatic C–H vibrational overtones were very similar and confirmed the validity of **Me_2-bpy** as our model system.

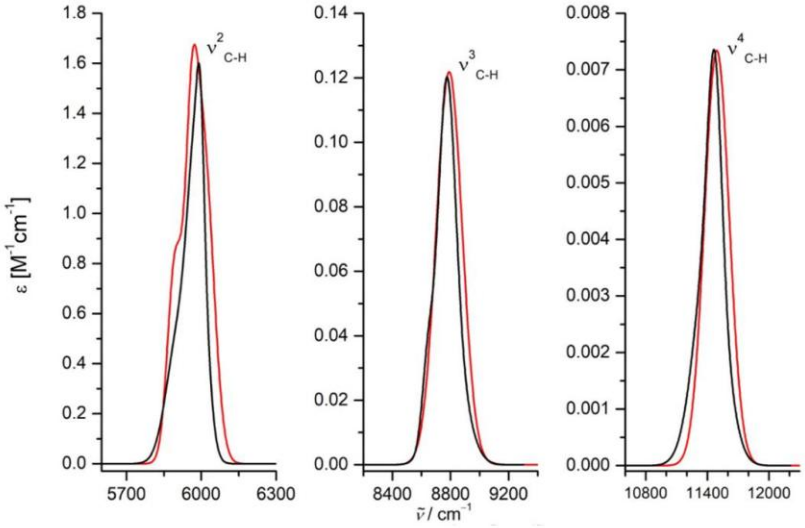

Figure S39. NIR absorption bands of the aromatic C–H vibrational overtones of **Me$_2$bpy** (black) and **bpmp** (red) in $CDCl_3$ in the region ν = 2 (left), ν = 3 (middle), and ν = 4 (right). Due to the smaller number of aromatic C–H oscillators in **Me$_2$bpy** (**6**) compared to **bpmp** (**11**) the Gaussians of **Me$_2$bpy** have been scaled by a factor of 11/6.

Hence, we exploited the earlier calculated Gaussians of the aromatic C–(H/D) overtones[43] of **Me$_2$-bpy** and **[D$_{12}$]-Me$_2$-bpy** for the SOI calculations. The integrand functions for the SOIs between the chromium complex emission and the relevant C–(H/D) overtones were constructed according to the mathematical definition of the SOIs:

$$\text{SOI} = \int I_{\text{norm}}(\tilde{\nu}) \cdot \varepsilon_{\text{vib}}(\tilde{\nu}) \cdot \tilde{\nu}^{-4} d\tilde{\nu}$$

with I_{norm} being the chromium emission spectrum (normalized to unit area) and ε the molar vibrational extinction coefficient (extracted and extrapolated absorption spectra of the relevant overtones), both expressed in the wavenumber scale $\tilde{\nu}$. The integrand functions were generated with a set of data points with a step size of 1 cm^{-1}. Numerical integration (OriginPro 9.0) gave the corresponding values for SOI.

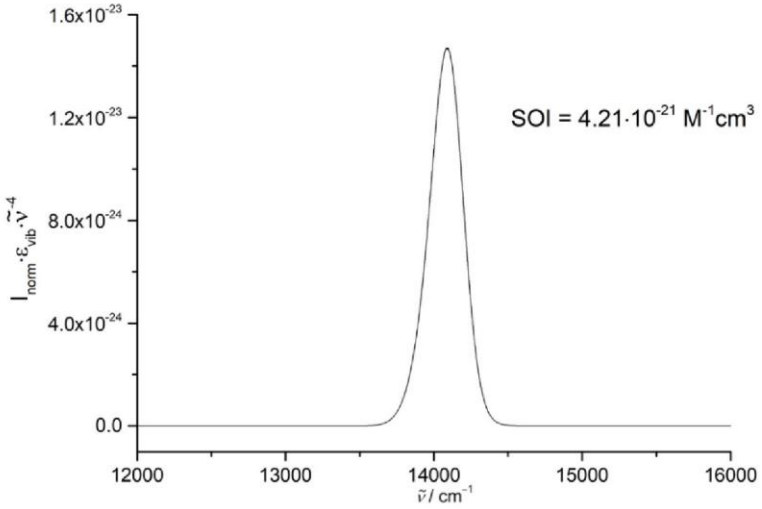

Figure S40. Integrand function of the spectral overlap integral (SOI) for the chromium emission band in **[Cr(bpmp)$_2$]$^{3+}$** and the fourth aromatic C–H (ν = 5) oscillators in **Me$_2$-bpy**.

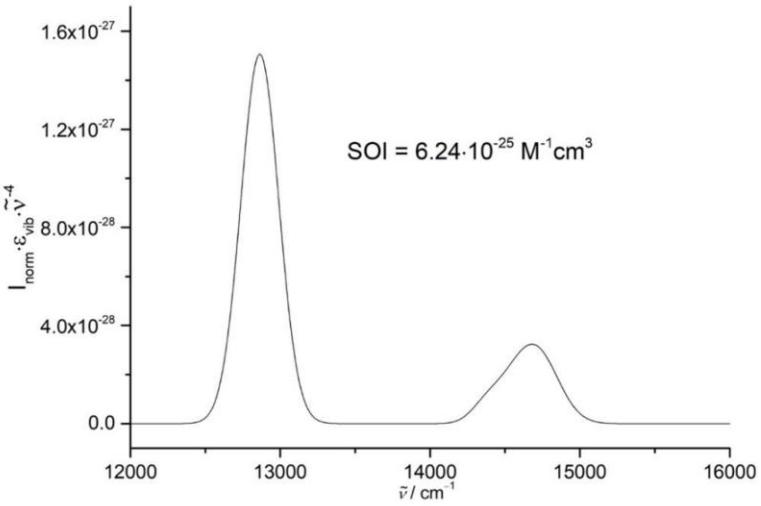

Figure S41. Integrand function of the spectral overlap integral (SOI) for the chromium emission band in **[Cr(bpmp)$_2$]$^{3+}$** and the fifth (ν = 6) and sixth (ν = 7) aromatic C–D oscillators in **[D$_{12}$]-Me$_2$-bpy**.

Based on the obtained SOIs, the ratio of the non-radiative deactivation rates of chromium excited states from **[Cr(bpmp)$_2$]$^{3+}$** and fully deuterated **[Cr(bpmp)$_2$]$^{3+}$** is estimated as:

$$\frac{k_{nr}(C\text{-}H)}{k_{nr}(C\text{-}D)} = \frac{SOI(C\text{-}H)}{SOI(C\text{-}D)} = \frac{4.21 \cdot 10^{-21}\ M^{-1}cm^3}{6.24 \cdot 10^{-25}\ M^{-1}cm^3} = 6.75 \cdot 10^3$$

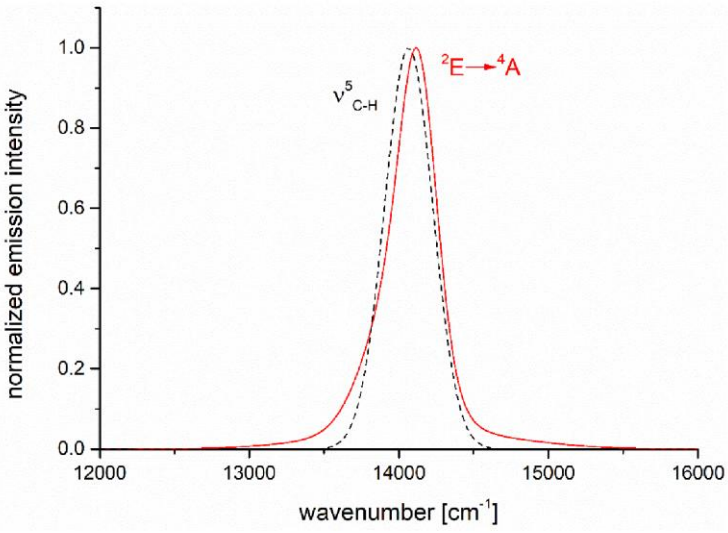

Figure S42. Normalized spectra for the chromium ^{2}E emission of **[Cr(bpmp)$_2$]$^{3+}$** (red) and the relevant vibrational aromatic C–H overtone absorption band (dashed black).

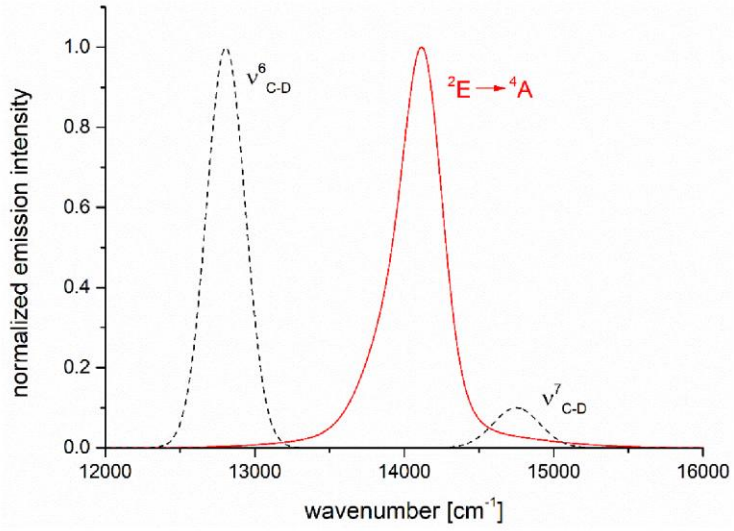

Figure S43. Spectra for the chromium ^{2}E emission of **[Cr(bpmp)$_2$]$^{3+}$** (red) and the relevant vibrational aromatic C–D overtone absorption bands (dashed black). The overtone intensities are shown with their actual intensity ratios.

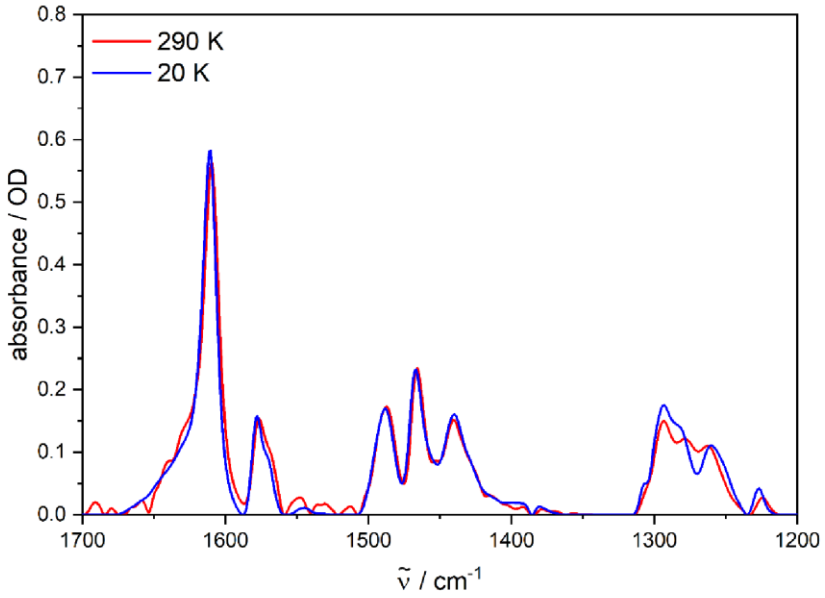

Figure S44. FTIR spectra of $[Cr(bpmp)_2][BF_4]_3$ as KBr pellets at 290 K (red) and 20 K (blue).

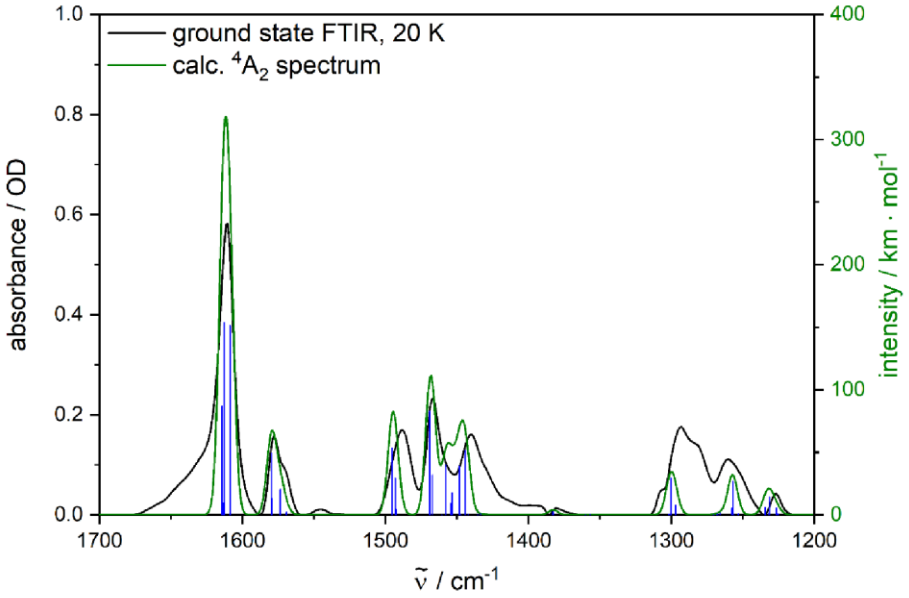

Figure S45. Ground state FTIR spectrum of $[Cr(bpmp)_2][BF_4]_3$ (KBr pellet, 20 K) (black) and calculated IR frequencies (blue sticks) and calculated IR spectrum (green) of $[Cr(bpmp)_2]^{3+}$ (scaled by 0.98, FWHM = 8 cm^{-1}, pseudo-Voigt profile) (DFT/B3LYP/def2-TZVP/D3-BJ).

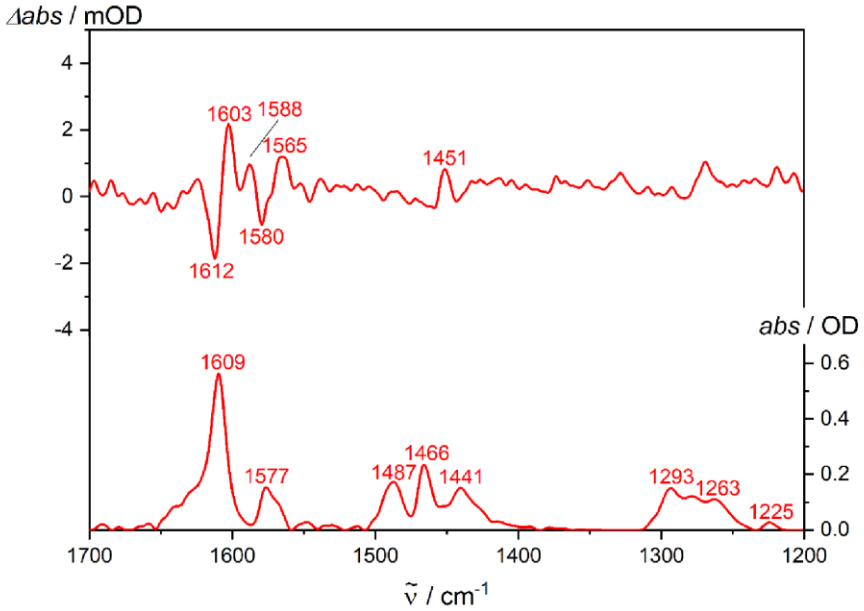

Figure S46. FTIR ground state spectrum (bottom) and step-scan spectra difference spectrum (top) of $[Cr(bpmp)_2][BF_4]_3$ (KBr pellet) recorded 0 – 1 µs after laser excitation at 355 nm (T = 290 K).

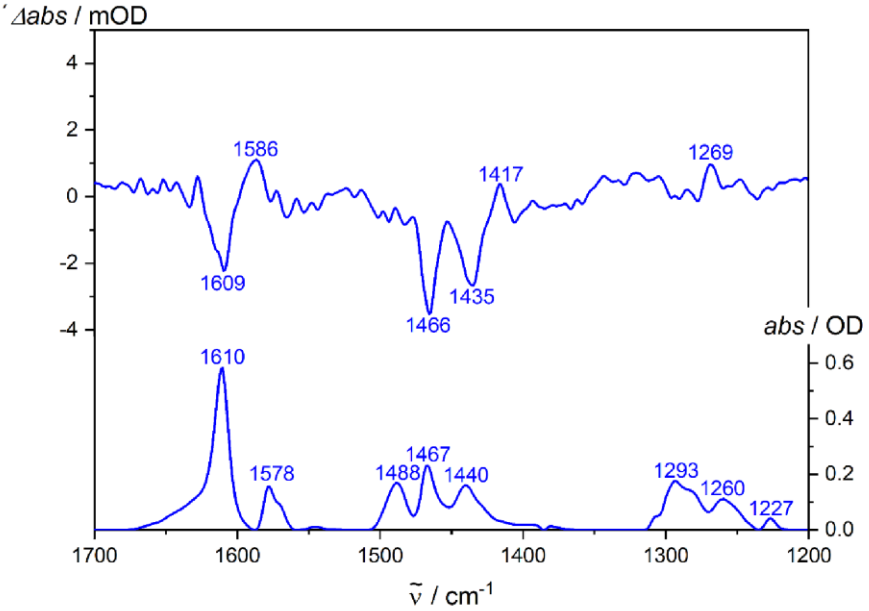

Figure S47. FTIR ground state spectrum (bottom) and step-scan spectra difference spectrum (top) of $[Cr(bpmp)_2][BF_4]_3$ (KBr pellet) recorded 0 – 1 µs after laser excitation at 355 nm (T = 20 K).

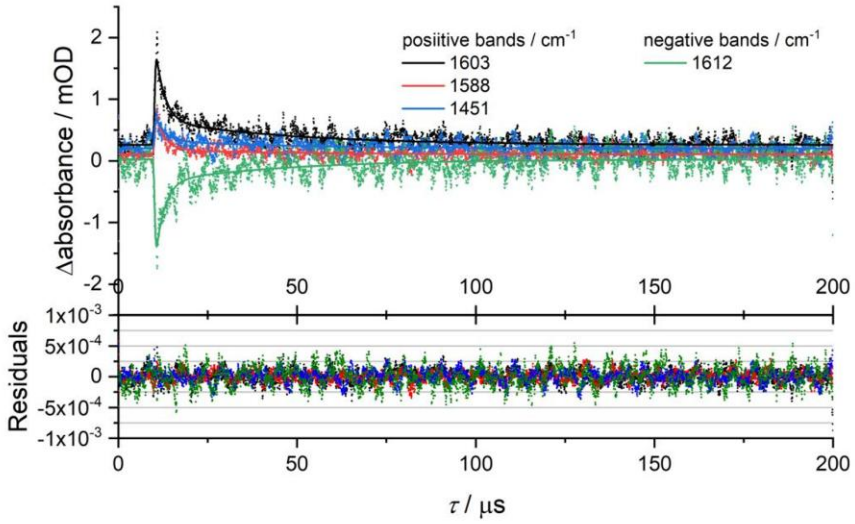

Figure S48. Global biexponential fit and residuals of $[Cr(bpmp)_2][BF_4]_3$ (KBr pellet) at 290 K.

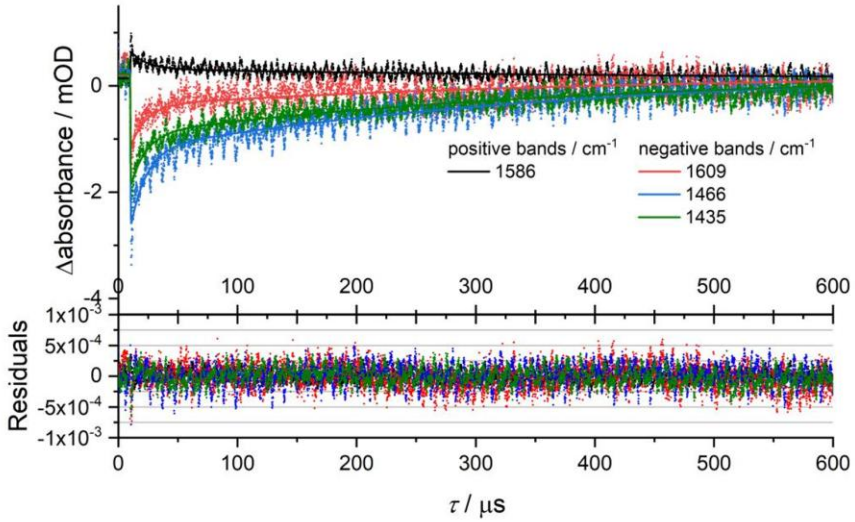

Figure S49. Global biexponential fit and residuals of $[Cr(bpmp)_2][BF_4]_3$ (KBr pellet) at 20 K.

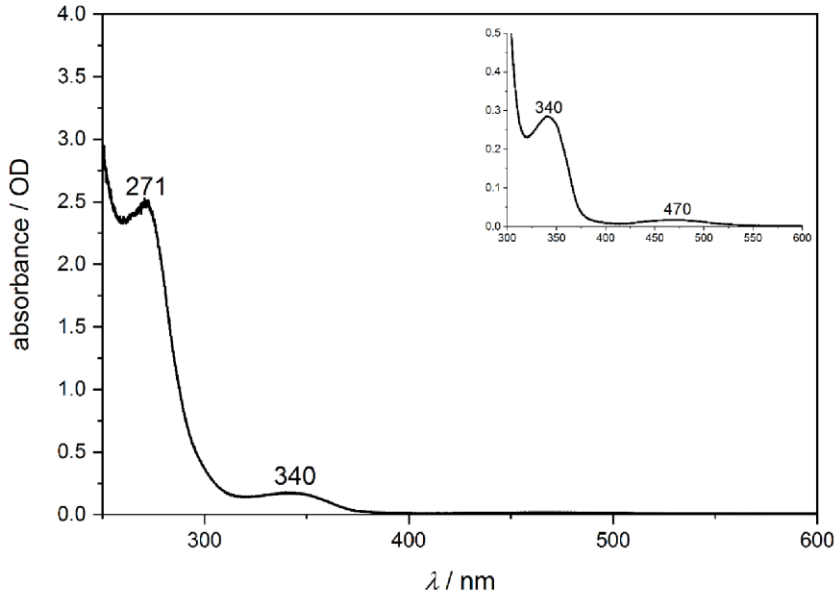

Figure S50. UV/Vis absorption spectrum of $[Cr(bpmp)_2][BF_4]_3$ (thin film) at 290 K.

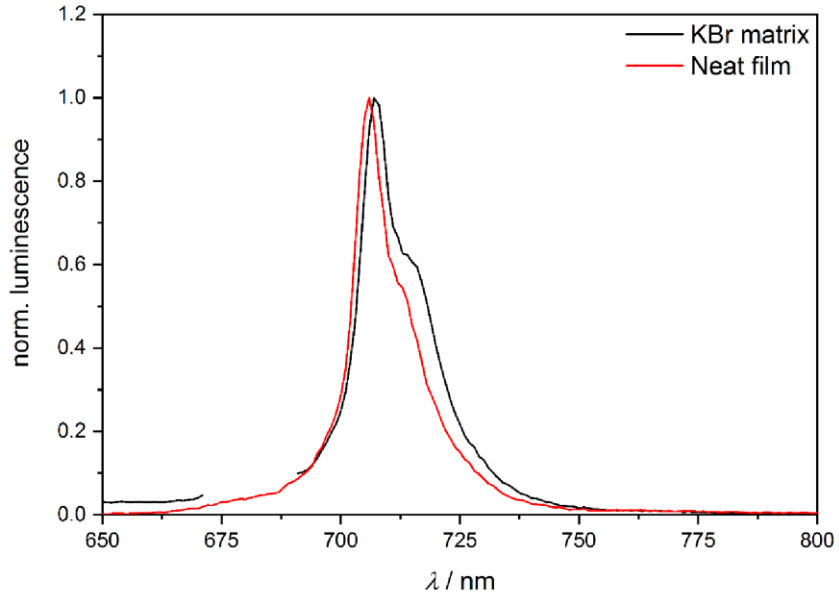

Figure S51. Luminescence spectrum of $[Cr(bpmp)_2][BF_4]_3$ (thin film and KBr pellet) at 290 K, λ_{exc} = 340 nm.

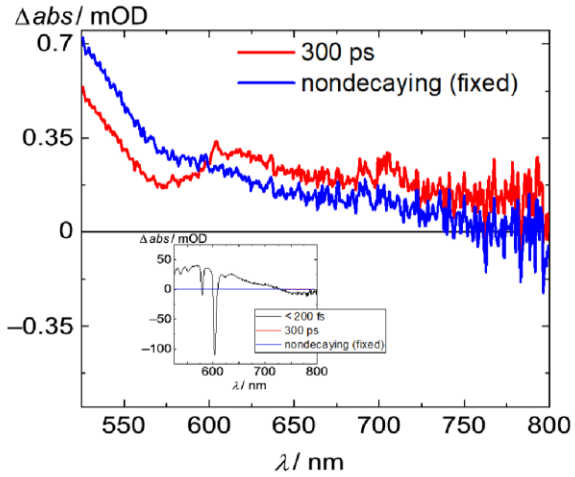

Figure S52. EADS of $[Cr(bpmp)_2][OTf]_3$ in $CH_3CN/HClO_4$ excited with λ_{exc} = 515 nm at 290 K. The inset displays the EADS of the very short component included in the fit, which is probably a coherent artefact.

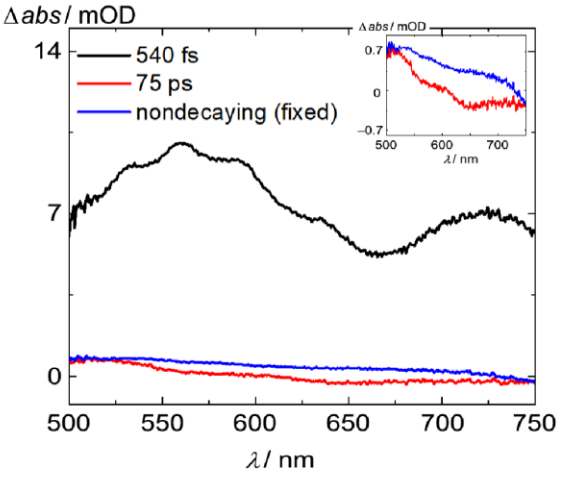

Figure S53. EADS of $[Cr(bpmp)_2][OTf]_3$ in $CH_3CN/HClO_4$ excited with λ_{exc} = 350 nm at 290 K. The inset displays the EADS of the longer components for better comparison.

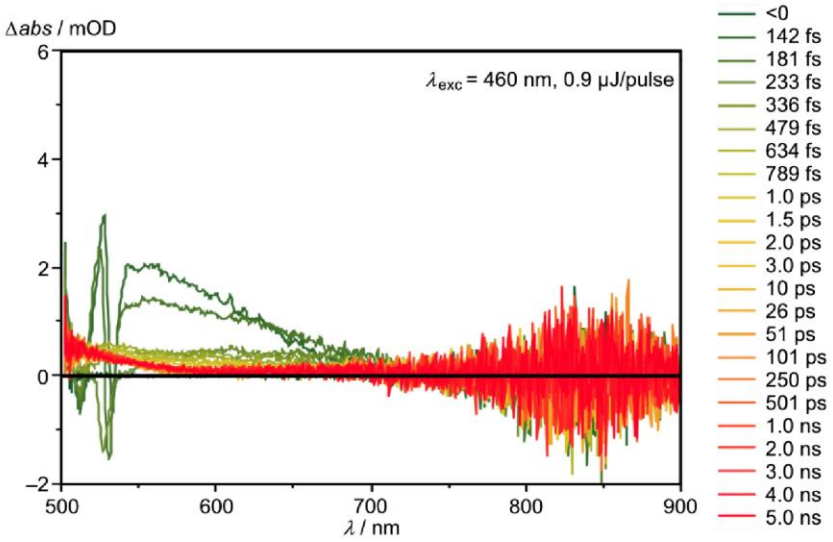

Figure S54. Transient absorption spectra of $[Cr(bpmp)_2][OTf]_3$ in CH_3CN ($HClO_4$) excited with fs laser pulses at 460 nm ($^4T_2$ states). The TA spectra are very similar to the ones obtained with 515 nm excitation shown in Fig. 6a ($^4T_2$ states), only the pump laser power is lower.

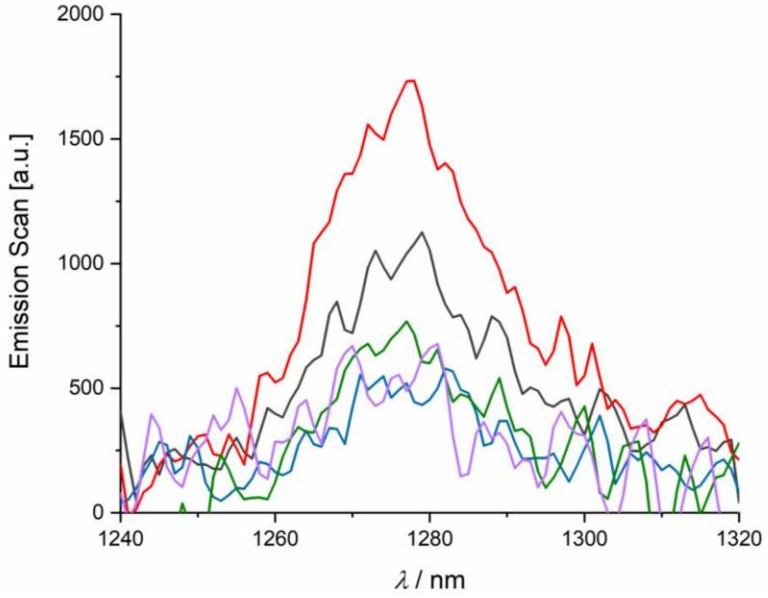

Figure S55. $^1O_2$ emission sensitized by $[Cr(ddpd)_2][BF_4]_3$ in DMF (black), $[Cr(ddpd)_2][BF_4]_3$ in DMF/$HClO_4$ (red), $[Cr(bpmp)_2][BF_4]_3$ in DMF/$HClO_4$ (green), $[Cr(bpmp)_2][PF_6]_3$ in DMF/$HClO_4$ (blue) and $[Cr(bpmp)_2][OTf]_3$ in DMF/$HClO_4$ (purple).

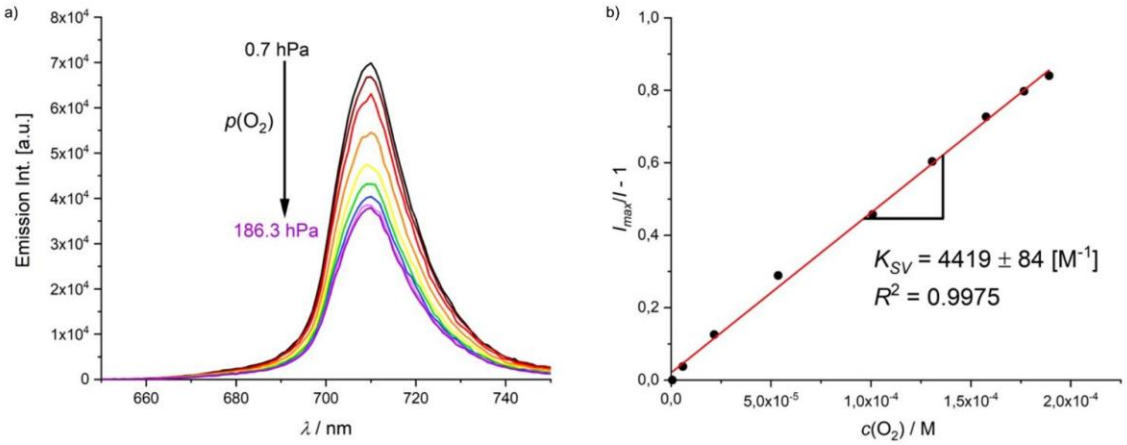

Figure S56. A) Emission spectra of $[Cr(bpmp)_2][OTf]_3$ with O_2 in $H_2O/HClO_4$ and b) corresponding steady-state Stern-Volmer plot. Steady-state implies that the emission intensities at different oxygen concentration/partial pressure were exploited for the Stern-Volmer plot.

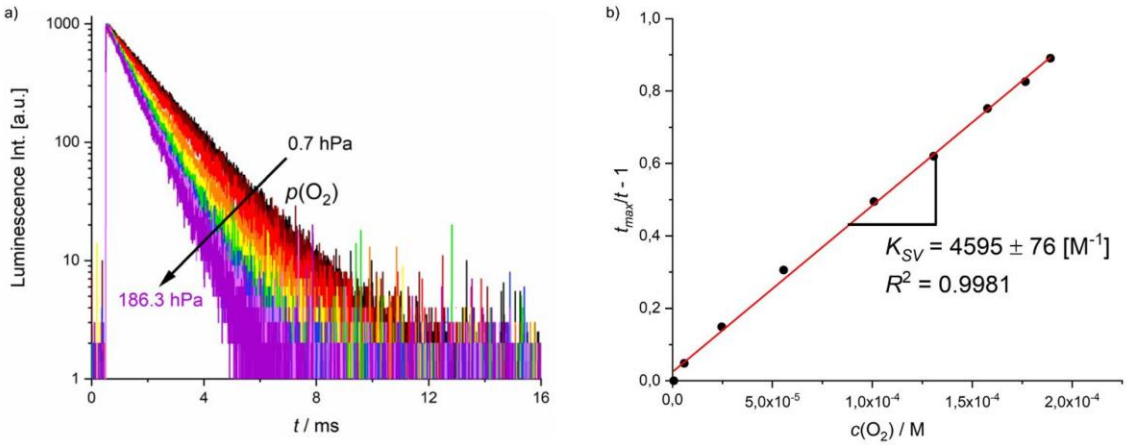

Figure S57. A) Luminescence decays of $[Cr(bpmp)_2][OTf]_3$ with O_2 in $H_2O/HClO_4$ and b) corresponding time-resolved Stern-Volmer plot. Time-resolved implies that the oxygen concentration/partial pressure-dependent luminescence lifetimes were utilized for the Stern-Volmer plot.

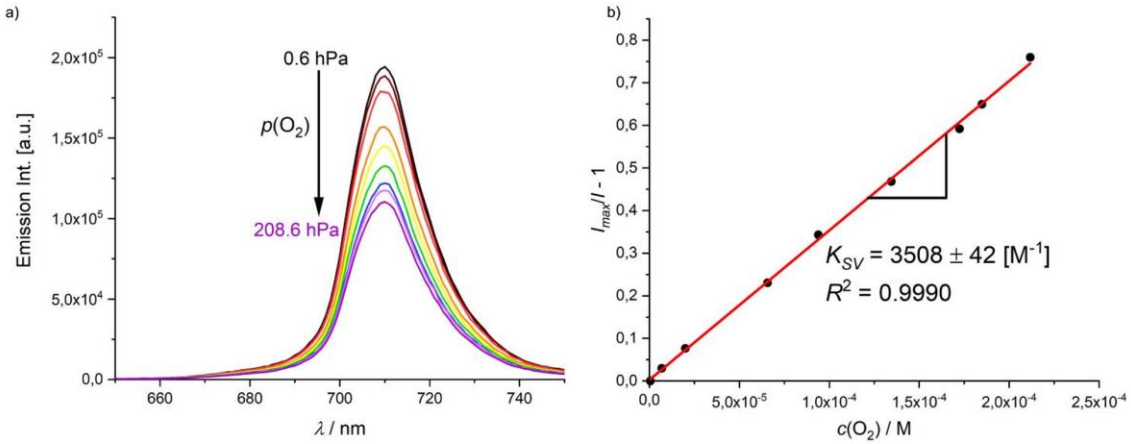

Figure S58. A) Emission spectra of $[Cr(bpmp)_2][BF_4]_3$ with O_2 in $H_2O/HClO_4$ and b) corresponding steady-state Stern-Volmer plot.

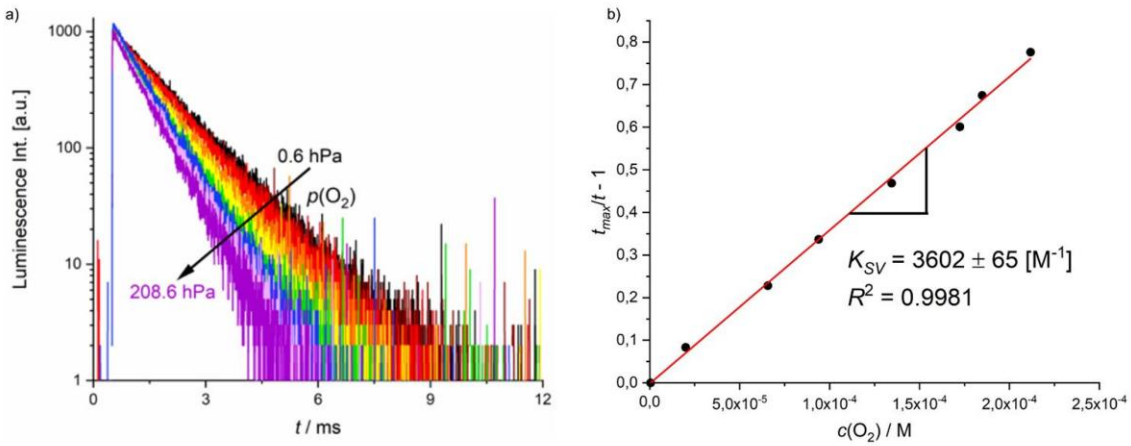

Figure S59. A) Luminescence decays of of $[Cr(bpmp)_2][BF_4]_3$ with O_2 in $H_2O/HClO_4$ and b) corresponding time-resolved Stern-Volmer plot.

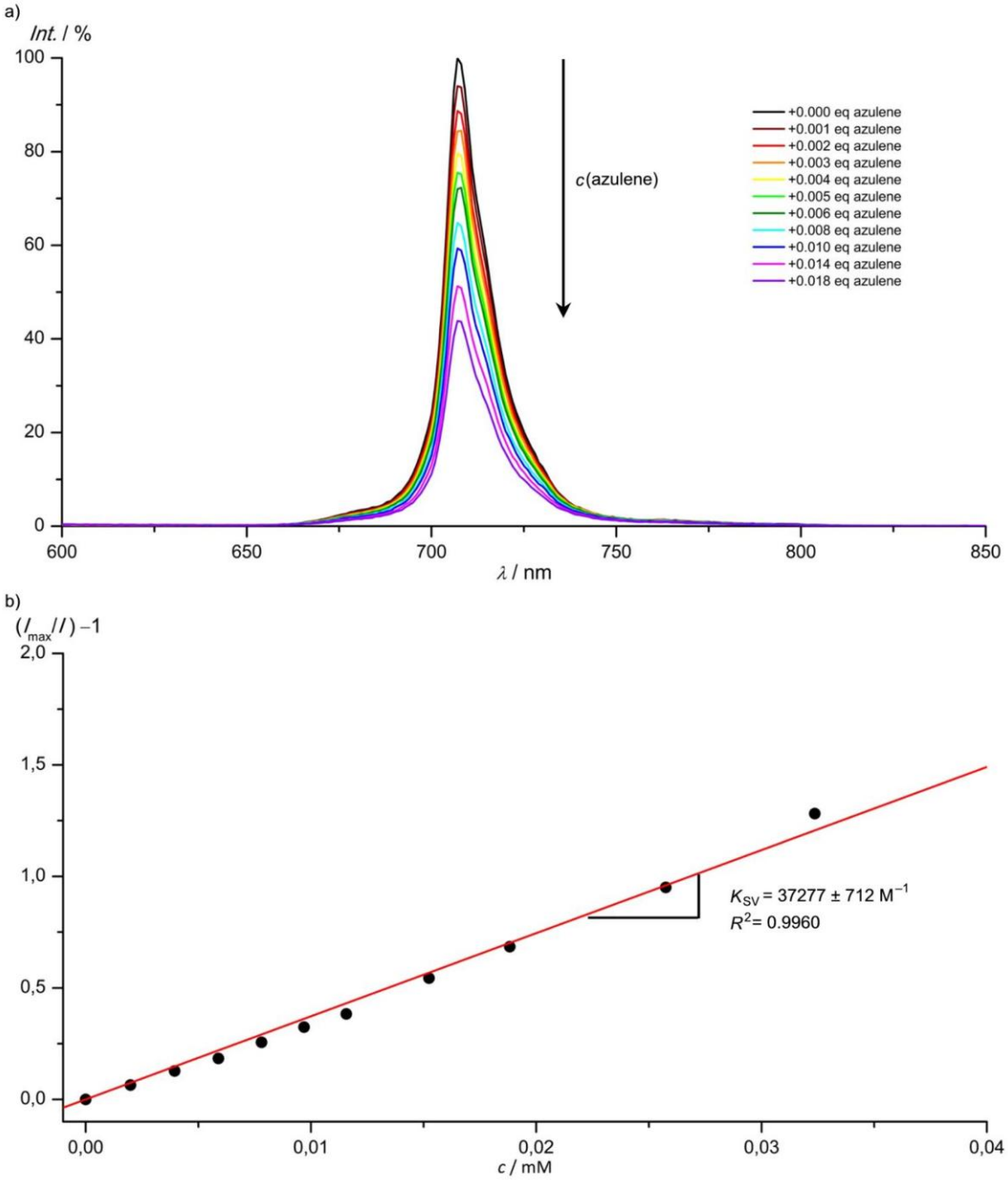

Figure S60. a) Emission spectra of $[Cr(bpmp)_2][OTf]_3$ with azulene in CH_3CN (undried) and b) corresponding steady-state Stern-Volmer plot.

Table S10. Cartesian Coordinates of $Cr(acac)_3$.

Cr	0.000000000	0.000000000	0.000000000
O	-0.022906000	-1.969601000	-0.066881000
O	-1.971782000	0.056768000	-0.002074000
O	0.011129000	0.052367000	-1.969159000
O	-0.005106000	1.966505000	0.081395000
O	1.966312000	-0.057809000	-0.013742000
O	-0.010053000	-0.066892000	1.975939000
C	-1.051048000	-2.724883000	-0.079372000
C	-2.376728000	-2.278140000	-0.085234000
C	-2.770453000	-0.936376000	-0.047183000
C	-0.765137000	-4.198436000	-0.091748000
C	-4.231243000	-0.588549000	-0.059373000
C	-0.063182000	1.084986000	-2.713430000
C	-0.141584000	2.401685000	-2.246987000
C	-0.125870000	2.774644000	-0.899266000
C	-0.060632000	0.816813000	-4.190593000
C	-0.258150000	4.222767000	-0.527713000
C	2.738957000	-0.263327000	0.982412000
C	2.320424000	-0.355348000	2.310252000
C	0.995437000	-0.227544000	2.742092000
C	4.197337000	-0.394310000	0.654941000
C	0.716124000	-0.248095000	4.216787000
H	-3.154083000	-3.025199000	-0.108143000
H	-0.259288000	-4.456022000	-1.025142000
H	-1.669226000	-4.794112000	0.004008000
H	-0.080774000	-4.439653000	0.722425000
H	-4.470502000	-0.094166000	-1.004380000
H	-4.442706000	0.123083000	0.738760000
H	-4.862982000	-1.465668000	0.056289000
H	-0.225569000	3.186994000	-2.981303000
H	-0.805246000	0.055568000	-4.424322000
H	0.914170000	0.413550000	-4.475920000
H	-0.261766000	1.714041000	-4.770565000
H	0.641720000	4.544244000	0.000677000
H	-1.095036000	4.338584000	0.162882000
H	-0.415980000	4.857717000	-1.395687000
H	3.074145000	-0.516258000	3.064868000
H	4.327671000	-1.139188000	-0.130812000
H	4.786518000	-0.676116000	1.524144000
H	4.562961000	0.557746000	0.263648000
H	-0.296773000	-0.598801000	4.407357000
H	0.810193000	0.769648000	4.605286000
H	1.431805000	-0.871080000	4.748294000

Table S11. Cartesian Coordinates of $[Cr(NH_3)_6]^{3+}$.

Cr	0.000000000	0.000000000	0.000000000
N	2.084661000	-0.001066000	0.088882000
N	-0.126719000	-2.082829000	-0.000893000
N	0.015485000	-0.018989000	2.087142000
N	0.005971000	2.088989000	0.009490000
N	-2.082726000	0.119048000	-0.106566000
N	0.109070000	-0.109220000	-2.081182000
H	2.479028000	-0.909872000	0.318912000
H	2.515444000	0.280562000	-0.788707000
H	2.446079000	0.637492000	0.792248000
H	0.762272000	-2.540808000	-0.185501000
H	-0.457776000	-2.456845000	0.885271000
H	-0.766331000	-2.436450000	-0.707662000
H	0.672545000	-0.701032000	2.457898000
H	-0.885179000	-0.247722000	2.500335000
H	0.290883000	0.874962000	2.486888000

H	0.915772000	2.494086000	0.214334000
H	-0.280992000	2.486218000	-0.882097000
H	-0.633674000	2.476835000	0.698455000
H	-2.533743000	-0.773598000	-0.289232000
H	-2.501852000	0.472458000	0.750337000
H	-2.397187000	0.746622000	-0.842460000
H	0.755324000	-0.829633000	-2.394150000
H	-0.784967000	-0.334458000	-2.510740000
H	0.423193000	0.753526000	-2.518408000

Table S12. Cartesian Coordinates of $[Cr(py)_6]^{3+}$.

Cr	0.000000000	0.000000000	0.000000000
N	-2.128157000	-0.000639000	0.006060000
N	2.127862000	0.000000000	-0.006692000
N	0.000000000	0.000000000	-2.128537000
N	0.000032000	0.000498000	2.127814000
N	0.004339000	-2.127702000	-0.002536000
N	-0.004570000	2.127760000	0.003554000
C	0.016073000	-2.827904000	1.151995000
C	-2.826117000	-1.156555000	-0.005645000
C	-1.151369000	-0.026928000	2.832796000
C	-0.012058000	2.827726000	-1.151180000
C	1.151656000	-0.017657000	-2.833418000
C	2.825580000	1.155856000	-0.031102000
C	-2.831111000	1.152082000	0.026873000
C	-1.156952000	0.014097000	-2.824792000
C	-0.002975000	2.828678000	1.157713000
C	1.156781000	0.028974000	2.823806000
C	2.830987000	-1.152691000	0.009183000
C	-0.002586000	-2.828424000	-1.156805000
C	-4.211623000	1.185456000	0.037962000
C	-4.206385000	-1.196599000	0.004417000
C	-1.182330000	-0.026877000	4.213392000
C	1.199194000	0.029965000	4.204023000
C	-0.008649000	4.209160000	1.193596000
C	-0.018699000	4.208089000	-1.188626000
C	4.205860000	1.195831000	-0.041216000
C	4.211491000	-1.186118000	0.000259000
C	-1.199245000	0.009604000	-4.204979000
C	1.182739000	-0.021906000	-4.214023000
C	0.002200000	-4.208868000	-1.193105000
C	0.020981000	-4.208322000	1.189034000
C	-0.011016000	-0.008749000	-4.920873000
C	-4.920321000	-0.007270000	0.027196000
C	-0.016803000	4.919998000	0.002144000
C	0.011304000	0.001523000	4.920036000
C	0.014068000	-4.919979000	-0.001845000
C	4.919986000	0.006471000	-0.025669000
H	-4.712325000	2.141860000	0.055463000
H	-2.277234000	2.071867000	0.035017000
H	-2.268184000	-2.073729000	-0.023990000
H	-4.702792000	-2.155284000	-0.006396000
H	-6.001018000	-0.009685000	0.035644000
H	0.023382000	-2.272160000	2.070720000
H	0.029673000	-4.706701000	2.146722000
H	0.017446000	-6.000708000	-0.001769000
H	-0.003653000	-4.707745000	-2.150596000
H	-0.013340000	-2.272856000	-2.075603000
H	-2.073311000	0.031530000	-2.265510000
H	2.072731000	-0.030969000	-2.281481000
H	2.138408000	-0.036915000	-4.716196000
H	-0.014996000	-0.012243000	-6.001643000
H	-2.158745000	0.021830000	-4.699837000

H	2.277157000	-2.072333000	0.030261000
H	4.712364000	-2.142495000	0.014216000
H	6.000688000	0.008791000	-0.033090000
H	4.702103000	2.154454000	-0.061328000
H	2.267418000	2.072984000	-0.043458000
H	2.072936000	0.054163000	2.264491000
H	2.158540000	0.053357000	4.698788000
H	0.015402000	0.001395000	6.000817000
H	-2.137753000	-0.050347000	4.715709000
H	-2.072241000	-0.051267000	2.280869000
H	0.001180000	2.273418000	2.076769000
H	-0.007336000	4.708258000	2.150991000
H	-0.021287000	6.000721000	0.001831000
H	-0.023856000	4.706225000	-2.146464000
H	-0.011904000	2.271439000	-2.069540000

Table S13. Cartesian Coordinates of $[Cr(tpy)_2]^{3+}$.

Cr	0.000000000	0.000000000	0.000000000
N	2.028840000	-0.000772000	-0.385480000
N	-2.020130000	0.000000000	-0.429392000
N	0.021555000	0.000000000	-1.991949000
N	-0.023487000	0.000225000	1.991915000
N	-0.004933000	2.024790000	0.407330000
N	-0.005317000	-2.024705000	0.407594000
C	-0.022593000	2.337991000	1.731200000
C	2.995918000	-0.001775000	0.535806000
C	-0.031204000	1.179762000	2.635961000
C	-0.022151000	-2.337718000	1.731524000
C	-1.150982000	0.000259000	-2.648866000
C	-3.006834000	-0.000227000	0.470826000
C	2.356330000	-0.000683000	-1.705998000
C	1.207967000	0.000124000	-2.623272000
C	0.003893000	-3.001819000	-0.503000000
C	-0.030990000	-1.179302000	2.636121000
C	-2.318969000	-0.000202000	-1.756654000
C	0.004493000	3.001780000	-0.503401000
C	3.678707000	-0.001635000	-2.114408000
C	4.337335000	-0.002778000	0.189683000
C	-0.046491000	1.208758000	4.023086000
C	-0.046220000	-1.208220000	4.023189000
C	-0.004103000	-4.339347000	-0.142249000
C	-0.031404000	-3.655538000	2.154347000
C	-4.340457000	-0.001035000	0.095835000
C	-3.632204000	-0.000885000	-2.193511000
C	1.251800000	0.000870000	-4.010076000
C	-1.165053000	0.000959000	-4.036263000
C	-0.004021000	4.339366000	-0.142880000
C	-0.032206000	3.655879000	2.153793000
C	0.050843000	0.001357000	-4.710610000
C	4.681832000	-0.002690000	-1.153438000
C	-0.022422000	-4.669130000	1.204458000
C	-0.053933000	0.000318000	4.710550000
C	-0.023004000	4.669340000	1.203761000
C	-4.655857000	-0.001398000	-1.254447000
H	3.926582000	-0.001632000	-3.164632000
H	2.688054000	-0.001626000	1.571038000
H	5.087287000	-0.003609000	0.965580000
H	5.719046000	-0.003484000	-1.455865000
H	-0.047218000	3.892256000	3.206526000
H	-0.031251000	5.703242000	1.517286000
H	0.003621000	5.097585000	-0.910634000
H	0.018165000	2.705186000	-1.541730000
H	-2.094204000	0.001264000	-4.583341000

H	0.062663000	0.001994000	-5.791022000
H	2.192537000	0.001087000	-4.537181000
H	-3.857173000	-0.001089000	-3.248913000
H	-5.686315000	-0.002038000	-1.579183000
H	-5.107104000	-0.001322000	0.855227000
H	-2.721046000	0.000401000	1.512212000
H	-0.051752000	-2.143210000	4.560194000
H	-0.066391000	0.000349000	5.790958000
H	-0.052454000	2.143782000	4.560064000
H	0.017518000	-2.705258000	-1.541309000
H	0.003387000	-5.097728000	-0.909850000
H	-0.030316000	-5.702989000	1.518130000
H	-0.046089000	-3.891729000	3.207143000

Table S14. Cartesian Coordinates of $[Cr(bpy)_3]^{3+}$.

Cr	0.000000000	0.000000000	0.000000000
N	-0.001798000	-0.044487000	2.056062000
N	-0.223854000	0.178612000	-2.033802000
N	-2.016505000	-0.183910000	0.367197000
N	2.043434000	0.043541000	-0.195510000
N	0.415985000	-2.011844000	-0.027069000
N	-0.217731000	2.032906000	-0.167822000
C	1.733579000	-2.320624000	-0.117371000
C	1.088377000	0.000762000	2.833332000
C	2.783879000	1.154797000	-0.304360000
C	-0.395965000	2.483714000	-1.433034000
C	-2.975838000	-0.197317000	-0.567352000
C	-0.414761000	1.446386000	-2.474100000
C	-1.224711000	-0.203483000	2.619399000
C	-2.353286000	-0.237774000	1.678457000
C	-0.177754000	2.901378000	0.850799000
C	2.640805000	-1.171685000	-0.243039000
C	-0.223407000	-0.837458000	-2.906317000
C	-0.492185000	-2.989809000	0.085497000
C	-1.363568000	-0.321197000	3.994184000
C	1.013334000	-0.112148000	4.208817000
C	4.156725000	1.109689000	-0.460602000
C	4.014798000	-1.281173000	-0.400919000
C	-0.301771000	4.264371000	0.656443000
C	-0.535004000	3.839488000	-1.689850000
C	-0.617777000	1.706388000	-3.821345000
C	-0.431142000	-0.642084000	-4.259242000
C	-3.682892000	-0.311001000	2.067793000
C	-4.317348000	-0.270127000	-0.242109000
C	-0.130235000	-4.324078000	0.115362000
C	2.157117000	-3.640778000	-0.087966000
C	-4.674547000	-0.327719000	1.096973000
C	-0.232531000	-0.278005000	4.796667000
C	-0.482460000	4.739059000	-0.634633000
C	4.780213000	-0.128307000	-0.509592000
C	1.215003000	-4.652497000	0.029935000
C	-0.633918000	0.650440000	-4.721484000
H	-2.338228000	-0.450839000	4.436170000
H	2.037673000	0.133716000	2.339739000
H	1.917547000	-0.071696000	4.796249000
H	-0.327318000	-0.373981000	5.868756000
H	3.206280000	-3.881137000	-0.152976000
H	1.532499000	-5.684949000	0.054412000
H	-0.893657000	-5.081334000	0.205324000
H	-1.527273000	-2.692532000	0.146981000
H	-2.659400000	-0.149186000	-1.596505000
H	-5.056149000	-0.280352000	-1.028483000
H	-5.713761000	-0.383851000	1.387983000

H	-3.945470000	-0.350349000	3.112785000
H	-0.060012000	-1.825342000	-2.506980000
H	-0.432633000	-1.490730000	-4.925695000
H	-0.802605000	0.839193000	-5.772021000
H	-0.770641000	2.716290000	-4.166771000
H	4.485978000	-2.250103000	-0.441053000
H	5.851361000	-0.201115000	-0.632487000
H	4.714214000	2.030073000	-0.541860000
H	2.263726000	2.097650000	-0.260671000
H	-0.034497000	2.492042000	1.838067000
H	-0.257278000	4.929321000	1.505072000
H	-0.582651000	5.798306000	-0.823042000
H	-0.674496000	4.192383000	-2.698831000

Table S15. Cartesian Coordinates of $[Cr(ddpd)_2]^{3+}$.

Cr	0.000000000	0.000000000	0.000000000
N	-0.063391000	-0.002063000	-2.040076000
N	0.056068000	-0.000994000	2.038359000
N	0.064332000	-2.053516000	-0.125516000
N	-0.071070000	2.051921000	-0.126429000
N	-2.047138000	-0.015009000	0.187929000
N	2.054912000	0.018135000	0.066023000
C	-0.735201000	-0.977917000	-2.697787000
C	-0.791085000	-1.002697000	-4.084742000
C	-0.154503000	-0.002615000	-4.797532000
C	0.526743000	0.998473000	-4.128816000
C	0.561329000	0.974650000	-2.741247000
H	-1.298855000	-1.803721000	-4.594691000
H	1.001586000	1.798527000	-4.671143000
C	0.747183000	-2.758791000	0.803969000
C	0.540327000	-4.097421000	1.015670000
C	-0.407385000	-4.748227000	0.225803000
C	-1.065763000	-4.052616000	-0.766696000
C	-0.788549000	-2.691905000	-0.948813000
H	-0.620473000	-5.797416000	0.375083000
H	1.447927000	-2.200083000	1.403603000
H	1.092680000	-4.613868000	1.785038000
H	-1.762206000	-4.559507000	-1.412479000
C	0.735855000	2.686747000	-0.997181000
C	1.039765000	4.043142000	-0.822327000
C	0.454724000	4.736329000	0.216761000
C	-0.451178000	4.090750000	1.058474000
C	-0.685946000	2.756496000	0.849851000
H	0.689534000	5.781495000	0.361338000
H	1.700565000	4.547933000	-1.506013000
H	-0.949287000	4.607438000	1.863740000
H	-1.355041000	2.199876000	1.486294000
C	-0.875782000	-0.687987000	2.743373000
C	-0.865985000	-0.693405000	4.131454000
C	0.122631000	0.009893000	4.796334000
C	1.076681000	0.708922000	4.079242000
C	1.020883000	0.690875000	2.692169000
H	-1.632110000	-1.216777000	4.678044000
H	1.867638000	1.236123000	4.584955000
C	-2.801365000	0.604412000	-0.747257000
C	-4.124725000	0.306810000	-0.944237000
C	-4.702333000	-0.674120000	-0.138079000
C	-3.960557000	-1.265375000	0.863117000
C	-2.620815000	-0.890693000	1.034620000
H	-5.733896000	-0.963598000	-0.280687000
H	-2.291678000	1.327427000	-1.363457000
H	-4.682502000	0.810589000	-1.717938000
H	-4.416257000	-1.986125000	1.520025000

C	2.681739000	0.870214000	0.898936000
C	4.024275000	1.209565000	0.686192000
C	4.715225000	0.612709000	-0.347854000
C	4.080598000	-0.335597000	-1.149640000
C	2.758275000	-0.603861000	-0.906574000
H	5.750347000	0.872480000	-0.519171000
H	4.522993000	1.905019000	1.339234000
H	4.596123000	-0.842135000	-1.950375000
H	2.209945000	-1.307182000	-1.512568000
N	-1.852228000	-1.426352000	2.058636000
C	-2.345035000	-2.646295000	2.718646000
H	-3.160065000	-2.446771000	3.414351000
H	-2.684548000	-3.336134000	1.952013000
H	-1.517735000	-3.102620000	3.251073000
N	1.963881000	1.420574000	1.953716000
C	2.502594000	2.635170000	2.586193000
H	3.335913000	2.426638000	3.257387000
H	2.830835000	3.311243000	1.802696000
H	1.702267000	3.112556000	3.141118000
N	-1.403815000	-1.966791000	-1.961860000
N	1.276591000	1.964143000	-2.052445000
C	-2.613215000	-2.539223000	-2.573577000
H	-2.389962000	-3.339101000	-3.279253000
H	-3.247451000	-2.924060000	-1.780923000
H	-3.143418000	-1.742928000	-3.084565000
C	2.451206000	2.527552000	-2.735704000
H	2.192694000	3.339239000	-3.415511000
H	3.141866000	2.893365000	-1.981626000
H	2.935799000	1.731051000	-3.290315000
H	-0.189922000	-0.003594000	-5.877783000
H	0.149669000	0.013581000	5.876821000

Table S16. Cartesian Coordinates of $[Cr(bpmp)_2]^{3+}$.

Cr	0.0000000000	0.0000000000	0.0000000000
N	-0.2392231150	-2.1091667910	-0.0513686530
N	2.1082842930	0.0000000000	0.0499894260
N	0.0000000000	0.0000000000	2.0996350620
N	-2.1069259780	0.0212638970	0.0450142550
N	0.2063853300	2.1064869570	-0.0604850260
C	-2.7913533870	-0.6749825610	-0.8873822620
C	-2.7834471940	0.6672820620	1.0141205650
C	-4.1662740780	-0.7375001930	-0.9034745460
C	-4.1719785930	0.6345219000	1.0536648770
C	-4.8737485900	-0.0666915060	0.0874396440
N	0.0201332680	-0.0081525660	-2.1181372370
C	-0.9527232910	0.6773031080	2.7849439450
C	0.9722827730	-0.6584638400	2.7774931060
C	-0.9503471600	0.7082687700	4.1698782490
C	1.0197583430	-0.6333371500	4.1609687800
C	0.0499852550	0.0552595590	4.8686549340
C	2.7863310940	-0.6619628030	1.0073501620
C	2.7918381000	0.7174001540	-0.8665231350
C	4.1745144010	-0.6295498400	1.0489474310
C	4.1668980980	0.7850116810	-0.8773936150
C	4.8756268060	0.0933443900	0.0979595550
C	-0.5266830220	1.0191819110	-2.8114667000
C	0.5857662100	-1.0377685650	-2.7930259750
C	-0.5051752450	1.0431914230	-4.1956300990
C	0.6083548660	-1.0637791970	-4.1770181680
C	0.0637676360	-0.0099867610	-4.8907552180
C	0.2531851980	-2.8410746360	-1.0696000460
C	-1.0665160750	-2.6954509720	0.8393386210
C	-0.1042445890	-4.1727895350	-1.2299554840

C	-1.4493884940	-4.0144732890	0.7385237060
C	-0.9707074110	-4.7667653800	-0.3269955960
C	-0.3113948450	2.8341824500	-1.0700356540
C	0.9874342950	2.7172098220	0.8551550510
C	1.2829682200	4.0608589770	0.8011335900
C	-0.0427696380	4.1913284600	-1.1811850640
C	0.7636226970	4.8146329920	-0.2440894000
H	1.3857612200	2.1007930270	1.6441661350
H	-0.4668693550	4.7430091350	-2.0065858600
H	-4.6876897650	1.1567406070	1.8456970550
H	-2.2090897110	-1.1875904110	-1.6354346450
H	2.2110828090	1.2423933270	-1.6066756760
H	4.6895758750	-1.1682267760	1.8302272190
H	0.2989510310	-4.7273103670	-2.0639726010
H	-1.4343117740	-2.0786872400	1.6428336160
H	0.0743190890	0.0826250500	5.9486312630
H	-1.7275472780	1.2512583650	4.6856502690
H	1.8156804510	-1.1549496100	4.6699689960
H	-0.9442542810	1.8823638640	-4.7128771720
H	1.0577064660	-1.9064255110	-4.6795756660
H	0.0788456730	-0.0118507470	-5.9713888320
C	-1.1912027560	2.1471192680	-2.0711314390
H	-1.5311318230	2.8766166080	-2.7981808610
H	-2.0837308350	1.7781968650	-1.5672104070
C	1.1981278680	-2.1798420600	-2.0282246760
H	2.0748207900	-1.8326056730	-1.4834787620
H	1.5517757440	-2.9165823950	-2.7414554490
C	2.0114992390	-1.4463028840	2.0256325920
H	2.7100331780	-1.8570091780	2.7459896290
H	1.5405343030	-2.3000632400	1.5370549470
C	-2.0160501290	1.4438707110	2.0438777230
H	-1.5664733800	2.3161886430	1.5668196700
H	-2.7195365140	1.8303277720	2.7731175500
H	-2.1186362280	-4.4313591760	1.4752787580
H	-1.2660559490	-5.7986159990	-0.4518416570
H	-4.6650010010	-1.3023014470	-1.6763548640
H	-5.9540480990	-0.0960103720	0.1098276680
H	4.6650790790	1.3674743680	-1.6374875930
H	5.9559241870	0.1230833800	0.1200063550
H	0.9853253720	5.8687323310	-0.3297031160
H	1.9148958170	4.4976615750	1.5588958720

Table S17. Cartesian Coordinates of $[Cr(CN)_6]^{3-}$.

Cr	0.000000000	0.000000000	0.000000000
C	-0.000058000	-2.084352000	-0.000015000
C	-2.084493000	0.000004000	-0.000212000
C	-0.000053000	2.084346000	-0.000005000
C	2.084479000	0.000007000	0.000233000
C	0.000078000	-0.000030000	2.084189000
C	-0.000216000	-0.000033000	-2.084186000
N	3.245160000	0.000011000	0.000206000
N	-0.000119000	-3.245041000	-0.000026000
N	0.000112000	-0.000050000	3.244873000
N	-3.245173000	0.000005000	-0.000165000
N	-0.000114000	3.245036000	-0.000011000
N	-0.000357000	-0.000070000	-3.244871000

References

1. Neese, F. The ORCA program system. *WIREs Comput. Mol. Sci.* **2012**, *2*, 73–78.
2. a) Becke, A. D. Density-functional thermochemistry. III. The role of exact exchange. *J. Chem. Phys.* **1993**, *98*, 5648–5652. b) Lee, C.; Yang, W.; Parr, R. G. *Phys. Rev. B* **1988**, *37*, 785–789. c) Miehlich, B.; Savin, A.; Stoll, H.; Preuss., H. *Chem. Phys. Lett.* **1989**, *157*, 200–206.
3. Weigend, F.; Ahlrichs, R. Balanced basis sets of split valence, triple zeta valence and quadruple zeta valence quality for H to Rn: Design and assessment of accuracy. *Phys. Chem. Chem. Phys.* **2005**, *7*, 3297–3305.
4. Weigend, F. Accurate Coulomb-fitting basis sets for H to Rn. *Phys. Chem. Chem. Phys.* **2006**, *8*, 1057–1065.
5. Neese, F.; Wennmohs, F.; Hansen, A.; Becker, U. Efficient, approximate and parallel Hartree–Fock and hybrid DFT calculations. A 'chain-of-spheres' algorithm for the Hartree–Fock exchange. *Chem. Phys.* **2009**, *356*, 98–109.
6. Izsák, R.; Neese, F. An overlap fitted chain of spheres exchange method. *J. Chem. Phys.* **2011**, *135*, 144105.
7. Pantazis, D. A.; Chen, X.-Y.; Landis, C. R.; Neese, F. All-Electron Scalar Relativistic Basis Sets for Third-Row Transition Metal Atoms. *J. Chem. Theory Comput.* **2008**, *4*, 908–919.
8. a) van Lenthe, E.; Baerends, E. J.; Snijders, J. G. Relativistic regular two-component Hamiltonians. *J. Chem. Phys.* **1993**, *99*, 4597–4610; b) van Wüllen, C. *J. Chem. Phys.* **1998**, *109*, 392–399.
9. Grimme, S.; Antony, J.; Ehrlich, S.; Krieg, H. A consistent and accurate ab initio parametrization of density functional dispersion correction (DFT-D) for the 94 elements H-Pu. *J. Chem. Phys.* **2010**, *132*, 154104.
10. Grimme, S.; Ehrlich, S.; Goerigk, L. Effect of the damping function in dispersion corrected density functional theory. *J. Comput. Chem.* **2011**, *32*, 1456–1465.
11. Barone, V.; Cossi, M. Quantum Calculation of Molecular Energies and Energy Gradients in Solution by a Conductor Solvent Model. *J. Phys. Chem. A* **1998**, *102*, 1995–2001.
12. Roos, B. O.; Taylor, P. R.; Siegbahn, P. E. M. A Complete Active Space SCF Method (CASSCF) Using a Density-Matrix Formulated Super-CI Approach. *Chem. Phys.* **1980**, *48*, 157−173.
13. Siegbahn, P. E. M.; Almlof, J., Heiberg, A.; Roos, B. O. The Complete Active Space Scf (CASSCF) Method in a Newton-Raphson Formulation with Application to the HNO Molecule. *J. Chem. Phys.* **1981**, *74*, 2384−2396.
14. Angeli, C.; Cimiraglia, R.; Evangelisti, S.; Leininger, T.; Malrieu, J.-P. Introduction of n-electron valence states for multireference perturbation theory. *J. Chem. Phys.* **2001**, *114*, 10252−10264.
15. Angeli, C.; Cimiraglia, R.; Malrieu, J.-P. *J. Chem. Phys.* **2002**, *117*, 9138–9153.
16. Pierloot, K. Transition metals compounds: Outstanding challenges for multiconfigurational methods. *Int. J. Quantum Chem.* **2011**, *111*, 3291–3301.
17. Atanasov, M.; Ganyushin, D.; Sivalingam, K.; Neese, F. A Modern First-Principles View on Ligand Field Theory Through the Eyes of Correlated Multireference Wavefunctions. *Struct. Bond.* **2012**, *143*, 149-220.
18. Singh, S. K.; Eng, J.; Atanasov, M.; Neese, F. Covalency and chemical bonding in transition metal complexes: An ab initio based ligand field perspective. *Coord. Chem. Rev.* **2017**, *344*, 2-25.
19. Neese, F. Efficient and accurate approximations to the molecular spin-orbit coupling operator and their use in molecular g-tensor calculations. *J. Chem. Phys.* **2005**, *122*, 34107.
20. Hess, B. A.; Marian, C. M. In Computational Molecular Spectroscopy; Jensen, P. B., Ed.; Wiley: New York, 2000; p. 169ff.
21. Cahier, B.; Maurice, R.; Bolvin, H.; Mallah, T.; Guihéry, N. Tools for Predicting the Nature and Magnitude of Magnetic Anisotropy in Transition Metal Complexes: Application to Co(II) Complexes. *Magnetochemistry* **2016**, *2*, 31−45.
22. Roos, B. O.; Malmqvist, P.-Å. Relativistic quantum chemistry: the multiconfigurational approach. *Phys. Chem. Chem. Phys.* **2004**, *6*, 2919−2927.
23. Durand, P.; Malrieu, J.-P. In Advances in Chemical Physics: Ab Initio Methods in Quantum Chemistry; Lawley, K. P., Ed.; John Wiley & Sons Ltd.: Hoboken, NJ, 1987; Vol. 67, Part 1, pp 321−412.

S66

24. Dyker, G.; Muth, O. Synthesis of Methylene- and Methine-Bridged Oligopyridines. *Eur. J. Org. Chem.* **2004**, 4319–4322.
25. Otto, S.; Grabolle, M.; Förster, C.; Kreitner, C.; Resch-Genger, U.; Heinze, K. $[Cr(ddpd)_2]^{3+}$: A molecular, water-soluble, highly NIR-emissive ruby analogue. *Angew. Chem., Int. Ed.* **2015**, *54*, 11572–11576.
26. Fulmer, G. R.; Miller, A. J. M.; Sherden, N. H.; Gottlieb, H. E.; Nudelman, A.; Stoltz, B. M.; Bercaw, J. E.; Goldberg, K. I. NMR Chemical Shifts of Trace Impurities: Common Laboratory Solvents, Organics, and Gases in Deuterated Solvents Relevant to the Organometallic Chemist. *Organometallics* **2010**, *29*, 2176–2179.
27. Zimmer, M.; Rupp, F.; Singer, P.; Walz, F.; Breher, F.; Klopper, W.; Diller, R.; Gerhards, M. Time-resolved IR spectroscopy of a trinuclear palladium complex in solution. *Phys. Chem. Chem. Phys.* **2015**, *17*, 14138–14144.
28. Bäppler, F.; Zimmer, M.; Dietrich, F.; Gruppe, M.; Wallesch, M.; Volz, D.; Bräse, S.; Gerhards, M.; Diller, R. Photophysical dynamics of a binuclear Cu(I)-emitter on the fs to µs timescale, in solid phase and in solution. *Phys. Chem. Chem. Phys.* **2017**, *19*, 29438–29448.
29. Zimmer, M.; Dietrich, F.; Volz, D.; Bräse, S.; Gerhards, M. Solid-State Step-Scan FTIR Spectroscopy of Binuclear Copper(I) Complexes. *ChemPhysChem* **2017**, *18*, 3023–3029.
30. Mullen, K. M.; van Stokkum, I. H. M. TIMP: An R Package for Modeling Multi-Way Spectroscopic Measurements. *J. Stat. Softw.* **2007**, *18*, 1–46.
31. Snellenburg, J. J.; Laptenok, S. P.; Seger, R.; Mullen, K. M.; van Stokkum, I. H. M. Glotaran: a Java-based Graphical User Interface for the R-package TIMP. *J. Stat. Softw.* **2012**, *49*, 1–22.
32. Otto, S.; Nauth, A. M.; Ermilov, E.; Scholz, N.; Friedrich, A.; Resch-Genger, U.; Lochbrunner, S.; Opatz, T.; Heinze, T. Photo-Chromium: Sensitizer for Visible Light-Induced Oxidative C-H Bond Functionalization – Electron or Energy Transfer? *ChemPhotoChem* **2017**, *1*, 344–349.
33. STOE & Cie, X-Area, STOE & Cie, Darmstadt, Germany.
34. Blessing, R. H. An empirical correction for absorption anisotropy. *Acta Crystallogr. Sect. A* **1995**, *51*, 33–38.
35. Spek, A. L. Structure validation in chemical crystallography. *Acta Crystallogr. Sect. D* **2009**, *65*, 148–55.
36. STOE & Cie, LANA, STOE & Cie, Darmstadt, Germany.
37. Koziskova, J.; Hahn, F.; Richter, J.; Kozisek, J. Comparison of different absorption corrections on the model structure of tetrakis(μ_2-acetato)-diaqua-di-copper(II). *Acta Chim. Slov.* **2016**, 9, 136–140.
38. a) Sheldrick, G. M. SHELXT – Integrated space-group and crystal-structure determination. *Acta Crystallogr. Sect. A* **2015**, *71*, 3–8. b) Sheldrick, G. M. SHELXL-2018/3, University of Göttingen, Göttingen, Germany, 2018.
39. Hübsche, C. B.; Sheldrick, G. M.; Dittrich, B. *J. Appl. Cryst.* **2011**, *44*, 1281–1284.
40. Jiménez, J.-R.; Doistau, B.; Besnard, C.; Piguet, C. Versatile heteroleptic bis-terdentate Cr(III) chromophores displaying room temperature millisecond excited state lifetimes. *Chem. Commun.* **2018**, *54*, 13228–13231.
41. Zare, D.; Doistau, B.; Nozary, H.; Besnard, C.; Guénée, L.; Suffren, Y.; Pelé, A.-L.; Hauser, A.; Piguet, C. Cr^{III} as an alternative to Ru^{II} in metallo-supramolecular chemistry. *Dalton Trans.* **2017**, *46*, 8992–9009.
42. Alemany, P.; Casanova, D.; Alvarez, S.; Dryzun, C.; Avnir, D. Continuous Symmetry Measures: A New Tool in Quantum Chemistry In *Reviews in Computational Chemistry*, John Wiley & Sons, Hoboken, NJ, USA, 2017, pp 289–352.
43. Wang, C.; Otto, S.; Dorn, M.; Kreidt, E.; Lebon, J.; Srsan, L.; Di Martino-Fumo, P.; Gerhards, M.; Resch-Genger, U.; Seitz, M.; Heinze, K. Deuterated Molecular Ruby with Record Luminescence Quantum Yield. *Angew. Chem. Int. Ed.* **2018**, *57*, 1112–1116.

6.2 Supporting Information: Efficient Triplet-Triplet Annihilation Upconversion Sensitized by a Chromium(III) Complex via an Underexplored Energy Transfer Mechanism

Angewandte Chemie
Eine Zeitschrift der Gesellschaft Deutscher Chemiker

Supporting Information

Efficient Triplet-Triplet Annihilation Upconversion Sensitized by a Chromium(III) Complex via an Underexplored Energy Transfer Mechanism

C. Wang, F. Reichenauer, W. R. Kitzmann, C. Kerzig, K. Heinze*, U. Resch-Genger**

Supporting Information

Content

1. Materials and methods

$[Cr(bpmp)_2][PF_6]_3$ was synthesized according to a reported procedure.[1] The anthracene derivatives were commercially obtained: 9,10-diphenylanthrace (DPA, Thermo Fisher Scientific), anthracene-9-propionic acid (APA, abcr), 9-anthracene carboxylic acid (ACA, Sigma-Aldrich), and anthracene (An, Sigma-Aldrich or Acros Organics). *N*,*N*-Dimethylformamide (DMF, anhydrous, 99.8%**,** Sigma-Aldrich), acetonitrile (ACN, HPLC grad**,** Sigma-Aldrich) and D_7-DMF (99.5 % D, Deutero), perchloric acid (70 % aq. soln., Alfa Aesar or Bernd Kraft) and $[Ru(bpy)_3][PF_6]_2$ (Sigma-Aldrich) were used as received from commercial suppliers.
To exclude the oxygen influence, all sample solutions for spectroscopic measurements were purged with argon for ca. 30 min in a sealed long-neck quartz cuvette.

UV/Vis absorption spectra were recorded with the Varian Cary 5000 spectrometer using 1.0 cm cells. Particularly, as the absorbance of the low-concentrated chromium complex is very low, absorption spectra for the Φ_{UC} determination were collected with very low measuring speed (0.1 nm/0.2 s) to suppress the influence from the noise and background.

Luminescence measurements (direct excitation): Phosphorescence spectra and decays of the $[Cr(bpmp)_2][PF_6]_3$ (sensitizer) were obtained with a calibrated spectrofluorometer FSP 920 from Edinburgh Instruments. For the measurement of the emission spectra, a CW xenon lamp was used as the excitation light source, while the time-resolved luminescence measurements were performed with a µs xenon flashlamp (100 Hz) and single photon counting detection in a multi-channel scaling mode. Fluorescence spectra and decays of the anthracene derivatives (acceptors) were measured on a calibrated spectrofluorometer FLS 920 from Edinburgh Instruments. The emission spectra were obtained with a CW xenon lamp as the excitation light source, while the decay kinetics were measured under direct excitation of DPA (395 nm), APA (375 nm), ACA (375 nm), and An (368 nm) with a supercontinuum laser (NKT FIU 15) (9.7 MHz) as the light source and a microchannel plate photomultiplier tube (MCP-PMT; R3809U50) (Figure S1).

UC luminescence measurements: UCL emission spectra were obtained with the calibrated spectrofluorometer FLS 920 equipped with a 532 nm CW laser (62 mW, Sunshine electronics, Shenzhen, CN) and a 520 nm CW laser (800 mW, Roithner Lasertechnik GmbH, Austria). One 532 nm notch filter was placed between the sample holder and the detector to suppress the excitation signal observed on the detector for the UC measurements using the 532 nm laser, while a metal filter (3926B, 9.12% transmission) was set between the sample and detector to reduce the too strong UC signal excited by the 520 nm laser. To take into account the various responses of the detector in different spectral regions, the emission of the UC signal (380-500 nm) and of the sensitizer (650-800 nm) were obtained with the corrective curve under strictly identical conditions (exc. and em. slit of 6 nm, using polarizers in the excitation and emission channel set to 0° and 54.7°, respectively). For excitation power density (*P*) dependent UCL emission measurements, the laser power was varied with a tunable OD filter and determined with a power meter (Newport 841-PE Powermeter) during the measurements. The laser spot size at the sample position was determined to be ca. 4 mm^2 (532 nm laser, basically identical spot sizes at different powers) and 5-8 mm^2 (520 nm laser, spot size differs a bit at different power) with a laser beam profiler (Newport, LBP2-HR-VIS). To exclude the different size effect on the calculated power density, the 520 nm-laser spot size was measured at each used laser power ranging from 0.3 mW to ca. 590 mW. The laser power density was calculated by dividing the measured laser power by the determined spot size.

UC luminescence decays of the annihilators were obtained on a calibrated spectrofluorometer FS5 from Edinburgh Instruments equipped with the same 532 nm laser (62 mW) and single photon counting detection in a multi-channel scaling mode. The laser was modulated in a pulsed mode (250 Hz, pulse width 500 µs) by a function generator (SRS, model DS345).

Φ_{PL} and Φ_F measurements: The photoluminescence quantum yields of the sensitizer (50 µM, in deaerated DMF containing 0.1 M $HClO_4$) and the annihilators (10-15 µM, in air-saturated DMF containing 0.1 M $HClO_4$) were determined absolutely using a calibrated Ulbricht integrating sphere setup (Quantaurus-QY C11347-11, Hamamatsu). These measurements were carried out by direct excitation of $[Cr(bpmp)_2][PF_6]_3$ (462 nm), DPA (395 nm), APA (375 nm), ACA (375 nm), and An (368 nm), respectively, with the excitation wavelengths being given in brackets. For DPA, fluorescence quantum yield measurements in air-saturated and deoxygenated acidified DMF revealed only a very small influence of oxygen under these conditions that was not further quantified. The relative uncertainties of these measurements are estimated to be ±5 %.[2]

Φ_{UC} determination: Φ_{UC} of UC samples containing 50 µM $[Cr(bpmp)_2][PF_6]_3$ and 1 mM anthracenes was determined relatively using a $[Cr(bpmp)_2][PF_6]_3$ (50 µM) solution without annihilator as reference.[3] Φ_{UC} was calculated according to Eq. S1.[4] In Eq. S1, A_{Ref} and A_{UC} stand for the absorbances of the reference solution and the UC sample at the excitation wavelength. The absorbance readouts at 532 and 520 nm were averaged by taking values from 533 to 531 nm and from 517 to 520 nm, respectively. I_{UC} and I_{Ref} represent the integrated intensities of the UCL and the reference emission, respectively. Φ_{Ref}, which equals the phosphorescence quantum yield of $[Cr(bpmp)_2][PF_6]_3$ in deaerated acidified DMF solution at room temperature, is 9.2%. Both reference and UC samples were prepared and measured twice and independently on different days.

$$\Phi_{UC} = \Phi_{Ref} \times \frac{A_{Ref}}{A_{UC}} \times \frac{I_{UC}}{I_{Ref}} \qquad \text{(Eq. S1)}$$

To confirm the linear power density dependence of the $[Cr(bpmp)_2][PF_6]_3$ phosphorescence, the corrected emission spectra of the reference solution were measured as a function of increasing power densities of the 520 nm and the 532 nm laser used as excitation light sources, respectively (Figure S13).

UC luminescence decays of the annihilators were obtained on a calibrated spectrofluorometer FS5 from Edinburgh Instruments equipped with the same 532 nm laser (62 mW) and single photon counting detection in a multi-channel scaling mode. The laser was modulated in a pulsed mode (250 Hz, pulse width 500 µs) by a function generator (SRS, model DS345).

Stern-Volmer studies with DPA and other anthracenes were performed by measuring the phosphorescence intensity (I_{709}) and lifetime (τ_{709}) of the deaerated $[Cr(bpmp)_2][PF_6]_3$ solutions (0.5 mM in acidified DMF) in the presence of the anthracene annihilators of different concentrations (0 – 1 mM), respectively.

Laser flash photolysis (LFP) experiments were carried out with an LP980KS apparatus from Edinburgh Instruments, monitoring either transient absorption or emission signals. A frequency-doubled Nd:YAG laser from Litron (Nano LG 300-10) was used for selective excitation of the sensitizers with laser pulses of ~5 ns duration. The excitation intensity at 532 nm was adjusted by a step-motor driven attenuator. Typical laser pulse energies were 40 mJ and the laser output stability was confirmed by several control experiments during each series of experiments. Detection of transient absorption and time-gated emission spectra occurred on an iCCD camera from Andor with precisely adjustable detection delay time (relative to the laser pulse) and integration time. Kinetic

traces at selected wavelengths were recorded using a photomultiplier tube. All LFP experiments were performed at 293 K with a cuvette holder allowing temperature control. The DMF solutions for these experiments were prepared in long neck cuvettes with an air-tight teflon screwcap in an Ar-filled glove box (MBraun Unilab Eco, <5 ppm oxygen).

NMR spectra were recorded on a Bruker Avance DRX 400 spectrometer at 400.31 MHz (^{1}H). Resonances are reported in ppm versus the solvent signal as internal standard.

Photolysis of anthracene in the presence of $[Cr(bpmp)_2][PF_6]_3$. A 0.1 M solution of D_7-DMF (99.5 % D, Deutero) and perchloric acid (70 % aq. soln.) was de-oxygenated by six freeze-pump-thaw cycles under pressures of less than 5×10^{-2} mbar. A 0.1 M solution of anthracene and 0.005 M solution of $[Cr(bpmp)_2][PF_6]_3$ in this solvent mixture was irradiated in an NMR tube with a Kessil LED (Kessil Science, PR160L, 525 nm (max. 44 W), 100-240 VAC, 352 mW cm^{-2} measured at 1 cm distance; www.kessil.com). ^{1}H NMR spectra were recorded after 0 min, 5 min, 15 min, 80 min, 5 h and 8 h of irradiation.

2. Optical characterization of the sensitizer and the annihilators

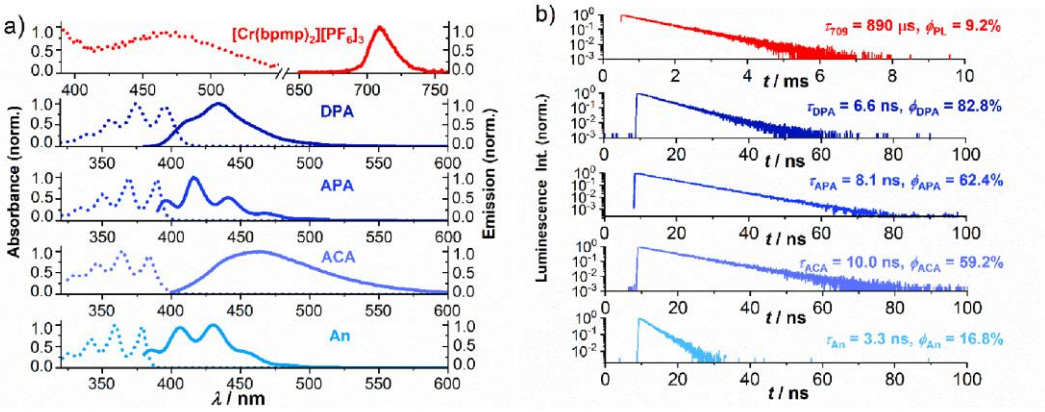

Figure S1: a) Absorption (dotted lines) and emission spectra (solid lines) of $[Cr(bpmp)_2][PF_6]_3$ (50 µM) and the annihilators DPA, APA, ACA, and An in acidified DMF (10 – 15 µM) at room temperature; The broad red-shifted emission spectrum of ACA observed in this solvent is ascribed to the formation of a linear-type ACA dimer bridged by hydrogen-bonds involving the COOH groups;[5] b) corresponding luminescence decays and quantum yields obtained for direct excitation at 462 nm, 395 nm, 375 nm, 375 nm, and 368 nm, respectively.

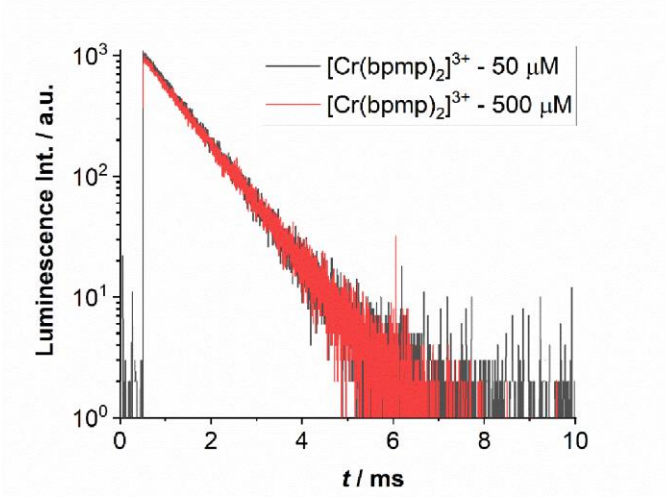

Figure S2: Phosphorescence decay kinetics of $[Cr(bpmp)_2][PF_6]_3$ at 709 nm in deaerated acidified DMF solution at room temperature obtained with concentrations of 50 µM (black) and 500 µM (red) of $[Cr(bpmp)_2][PF_6]_3$. Excitation was set at 532 nm with a xenon flash lamp.

3. Stern-Volmer studies

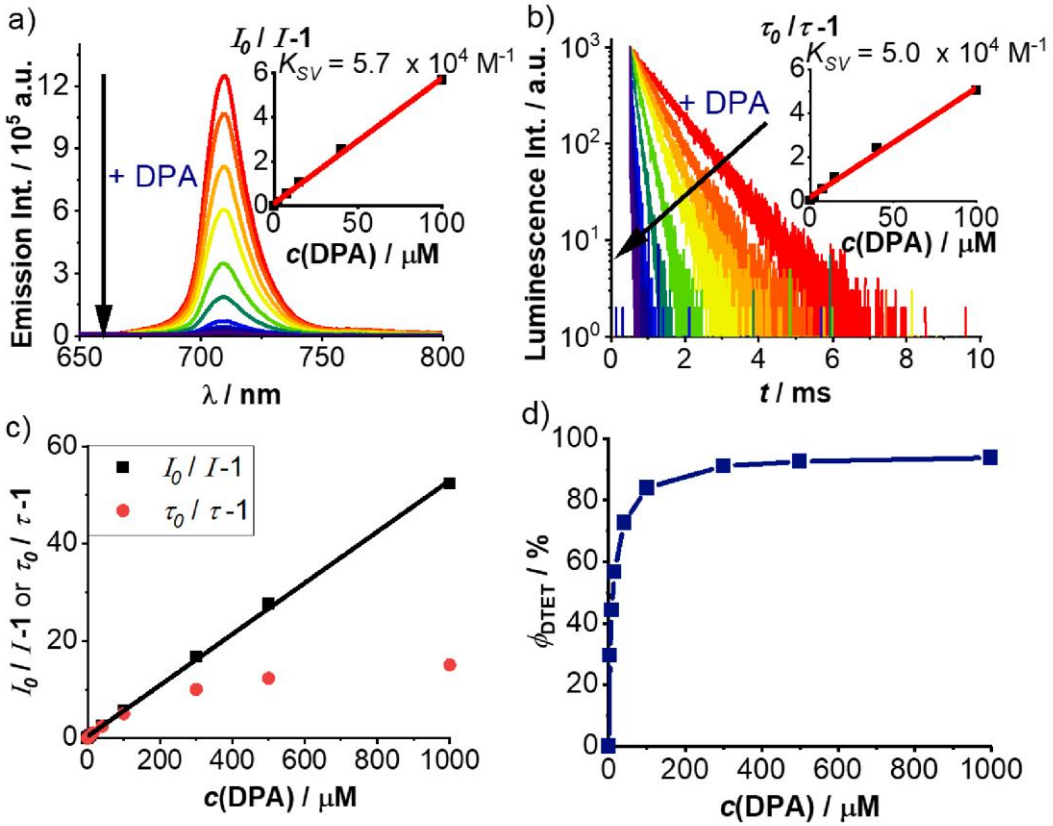

Figure S3: Stern-Volmer (SV) studies of $[Cr(bpmp)_2][PF_6]_3$ (0.5 mM) in acidified DMF in the presence of increasing concentrations of DPA: a) Phosphorescence intensity and b) Decay kinetics of $[Cr(bpmp)_2][PF_6]_3$ as a function of DPA concentration ((exc. 532 nm, em. 709 nm). The resulting SV plots up to a DPA concentration of 100 µM are given in the insets. c) SV plot derived from measurements of the phosphorescence intensity (dotted lines) and lifetime (solid lines) of $[Cr(bpmp)_2][PF_6]_3$ in the presence of increasing concentrations of DPA up to 1 mM; d) Φ_{DTET} derived from the sensitizer lifetimes plotted as a function of the DPA concentration.

Possible explanations for the deviations between the lifetime- and intensity-based SV plots could be static energy transfer and/or aggregation induced emission quenching, which does not yield the desired photoproduct. To address the observed deviations between lifetime- and intensity-based SV plots, transient absorption spectroscopic measurements (Figure S5 – S7) and luminescence lifetime measurements of the delayed phosphorescence of the sensitizer (Figure S8, Table S1) were performed. These data confirm the purely dynamic nature of the DTET process for the $[Cr(bpmp)_2][PF_6]_3$/DPA pair. More details follow in Sections 5 and 6.

4. Density functional theory calculations

All calculations were performed using the quantum computing suite ORCA 4.2.1.[6] Geometry optimization with DFT-methodology was performed using unrestricted Kohn-Sham orbitals DFT (UKS), the restricted Kohn-Sham (RKS) orbitals (for the anthracene derivatives in S_0 state), and the B3LYP functional[7] in combination with Ahlrichs' split-valence triple-ζ basis set def2-TZVPP for all atoms.[8] Tight convergence criteria were chosen for DFT-(U)KS calculations (keywords tightscf and tightopt). All DFT-(U)KS calculations make use of the resolution of identity (Split-RI-J) approach for the Coulomb term in combination with the chain-of-spheres approximation for the exchange term (COSX).[9] The zero order relativistic approximation was used to describe relativistic effects in all calculations (keyword ZORA).[10] Grimme's empirical dispersion correction D3(BJ) was employed (keyword D3BJ).[11] To account for solvent effects, a conductor-like screening model (keyword CPCM (DMF)) modeling DMF was used in all calculations.[12] Explicit counter ions and/or solvent molecules were neglected.

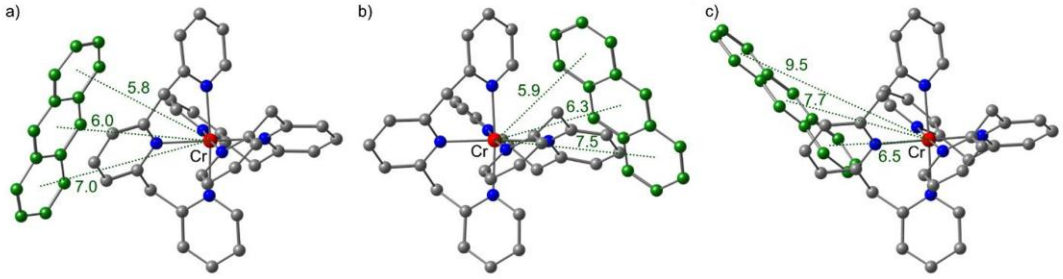

Figure S4: Geometries of $^4[[Cr(bpmp)_2]^{3+}$ + An] in three different arrangements optimized at the CPCM(DMF)-RI-B3LYP-D3BJ-ZORA/def2-TZVPP basis of theory. The anthracene acceptor is marked in green. The distances from Cr to the centers of the anthracene are given in Å. Hydrogen atoms are omitted for clarity.

Coordinates of DFT calculated geometries

^{4}[[Cr(bpmp)$_2$]$^{3+}$ + An]; orientation a); CPCM(DMF)-RI-B3LYP-D3BJ-ZORA/def2-TZVPP

24	-0.551561000	-0.171258000	0.523864000
7	-0.875026000	0.047765000	-1.558937000
7	-2.515539000	0.424947000	1.016303000
7	0.023703000	1.854078000	0.716366000
7	1.449136000	-0.594084000	0.002525000
7	-0.325913000	-0.541436000	2.586221000
6	1.697056000	-1.510733000	-0.955299000
6	2.483402000	0.033479000	0.596178000
6	2.972760000	-1.858886000	-1.333496000
6	3.794143000	-0.274301000	0.256000000
6	4.046974000	-1.235245000	-0.709662000
7	-1.007998000	-2.223221000	0.306823000
6	1.260030000	2.164599000	1.177448000
6	-0.811644000	2.847572000	0.328147000
6	1.690482000	3.479107000	1.241550000
6	-0.421594000	4.175637000	0.386800000
6	0.844238000	4.498822000	0.842077000
6	-3.013565000	1.621541000	0.652605000
6	-3.265594000	-0.393348000	1.783432000
6	-4.285162000	2.014225000	1.050914000
6	-4.530517000	-0.059548000	2.207709000
6	-5.055078000	1.172281000	1.834052000
6	-0.252770000	-3.143840000	0.949674000
6	-1.794404000	-2.614953000	-0.728204000
6	-0.208638000	-4.459660000	0.518073000
6	-1.756295000	-3.909159000	-1.207758000
6	-0.934678000	-4.840618000	-0.594767000
6	-1.887216000	-0.591122000	-2.180912000
6	-0.088882000	0.882346000	-2.270375000
6	-2.168533000	-0.351259000	-3.517794000
6	-0.310447000	1.149838000	-3.602976000
6	-1.382966000	0.534232000	-4.237867000
6	0.118934000	-1.722196000	3.058006000
6	-0.729374000	0.406222000	3.460506000
6	-0.705518000	0.216576000	4.823384000
6	0.160504000	-1.971529000	4.423865000
6	-0.249949000	-0.999188000	5.318694000
6	0.628790000	-2.757229000	2.105054000
6	-2.677434000	-1.599645000	-1.396352000
6	-2.181567000	2.525624000	-0.206014000
6	2.187363000	1.072427000	1.638025000
9	-2.189427000	-6.088050000	2.716619000
9	-3.129233000	-5.594464000	1.766322000
9	-3.422979000	-6.284233000	0.590848000
9	-3.749892000	-4.317925000	2.006276000
9	-4.599260000	-3.782574000	1.037950000
9	-4.850772000	-4.448971000	-0.162056000
9	-4.262687000	-5.743101000	-0.383763000
9	-1.892156000	-5.377059000	3.842860000
9	-3.451429000	-3.635100000	3.220601000
9	-5.639179000	-3.867208000	-1.195551000
9	-4.504496000	-6.398818000	-1.625284000
9	-5.261019000	-5.804856000	-2.593797000
9	-5.829290000	-4.518875000	-2.379359000
9	-2.543345000	-4.140611000	4.104715000

^{4}[[Cr(bpmp)$_2$]$^{3+}$ + An]; orientation b); CPCM(DMF)-RI-B3LYP-D3BJ-ZORA/def2-TZVPP

24	-0.236839000	-0.226109000	-0.207425000
7	0.128359000	1.367329000	-1.539357000
7	-2.261617000	0.296555000	0.084963000
7	0.230958000	0.965543000	1.485125000
7	1.838770000	-0.610360000	-0.390528000
7	-0.650020000	-1.911129000	0.977363000
6	2.396461000	-0.666181000	-1.617908000
6	2.629700000	-0.728878000	0.694160000
6	3.746930000	-0.847397000	-1.811005000
6	4.000634000	-0.903945000	0.563249000
6	4.569482000	-0.966302000	-0.697474000
7	-0.605727000	-1.448113000	-1.885214000
6	1.235802000	0.600201000	2.317898000
6	-0.456937000	2.105481000	1.736538000
6	1.580757000	1.374280000	3.412700000
6	-0.149276000	2.904427000	2.825814000
6	0.884561000	2.542157000	3.672153000
6	-2.617903000	1.511102000	0.547457000
6	-3.220635000	-0.624917000	-0.148727000
6	-3.951412000	1.826027000	0.773336000
6	-4.556584000	-0.366952000	0.053087000
6	-4.933282000	0.884525000	0.522892000
6	-0.133866000	-2.718149000	-1.915036000
6	-1.152250000	-0.914101000	-3.005867000
6	-0.141347000	-3.452353000	-3.089177000
6	-1.224931000	-1.636764000	-4.183978000
6	-0.697232000	-2.914555000	-4.235327000
6	-0.572153000	1.506304000	-2.683012000
6	1.113074000	2.247267000	-1.258475000
6	-0.296034000	2.541005000	-3.567243000
6	1.427525000	3.296202000	-2.092210000
6	0.707593000	3.449368000	-3.271408000
6	-0.264312000	-3.149423000	0.612351000
6	-1.294053000	-1.737613000	2.151774000
6	-1.557254000	-2.778040000	3.012778000
6	-0.491764000	-4.234647000	1.448410000
6	-1.137631000	-4.054297000	2.658640000
6	0.461411000	-3.352303000	-0.684899000
6	-1.651145000	0.504147000	-2.986192000
6	-1.556768000	2.538421000	0.806370000
6	2.002736000	-0.665871000	2.054913000
9	-3.703305000	-4.729060000	-0.106477000
9	-3.119588000	-5.149691000	-1.336580000
9	-1.991380000	-5.969208000	-1.383341000
9	-3.733295000	-4.729731000	-2.569298000
9	-3.193520000	-5.161588000	-3.779953000
9	-2.067518000	-5.984321000	-3.825699000
9	-1.445663000	-6.394035000	-2.594079000
9	-4.828441000	-3.957941000	-0.093020000
9	-4.893038000	-3.902244000	-2.510159000
9	-1.481134000	-6.397204000	-5.056188000
9	-0.262113000	-7.186509000	-2.653392000
9	0.281104000	-7.540742000	-3.853937000
9	-0.338767000	-7.143995000	-5.071275000
9	-5.431978000	-3.538915000	-1.311006000

^{4}[[Cr(bpmp)$_2$]$^{3+}$ + An]; orientation c); CPCM(DMF)-RI-B3LYP-D3BJ-ZORA/def2-TZVPP

24	-0.063554000	-0.281434000	0.184843000
7	0.549493000	1.085623000	-1.320630000
7	-2.153985000	-0.060594000	-0.079397000
7	-0.125134000	1.268388000	1.607037000
7	2.002650000	-0.459480000	0.542986000
7	-0.643020000	-1.713381000	1.631621000
6	2.829754000	-0.724042000	-0.490657000
6	2.529525000	-0.226681000	1.761427000
6	4.198569000	-0.771044000	-0.353156000
6	3.903580000	-0.258556000	1.960771000
6	4.749816000	-0.533712000	0.900514000
7	-0.005056000	-1.826650000	-1.254738000
6	0.684125000	1.234408000	2.693121000
6	-0.972056000	2.313506000	1.439406000
6	0.671728000	2.257128000	3.627654000
6	-1.015519000	3.353400000	2.352099000
6	-0.184337000	3.330529000	3.458516000
6	-2.751967000	1.135169000	0.101876000
6	-2.920978000	-1.161920000	-0.221559000
6	-4.134243000	1.237593000	0.171841000
6	-4.296081000	-1.122742000	-0.158881000
6	-4.917748000	0.100860000	0.051406000
6	0.374765000	-3.078752000	-0.907098000
6	-0.337911000	-1.566503000	-2.541956000
6	0.415171000	-4.101695000	-1.841131000
6	-0.283416000	-2.551707000	-3.512232000
6	0.090643000	-3.837948000	-3.159741000
6	0.203843000	0.892706000	-2.607893000
6	1.423610000	2.068216000	-1.017962000
6	0.743450000	1.669582000	-3.622521000
6	1.985208000	2.880010000	-1.979158000
6	1.647577000	2.671641000	-3.310616000
6	-0.249475000	-2.998571000	1.541865000
6	-1.542970000	-1.366922000	2.576939000
6	-2.085341000	-2.279063000	3.453792000
6	-0.772358000	-3.966827000	2.388387000
6	-1.701354000	-3.610605000	3.352074000
6	0.777415000	-3.366528000	0.512367000
6	-0.790807000	-0.183723000	-2.916975000
6	-1.881207000	2.349946000	0.239919000
6	1.607296000	0.066196000	2.906588000
9	-4.185299000	-1.280890000	-3.530644000
9	-5.317925000	-2.131050000	-3.365282000
9	-5.214185000	-3.522775000	-3.371184000
9	-6.613107000	-1.523883000	-3.200599000
9	-7.738347000	-2.339938000	-3.086407000
9	-7.638237000	-3.731628000	-3.118033000
9	-6.339738000	-4.340353000	-3.250200000
9	-4.319151000	0.076566000	-3.522287000
9	-6.704224000	-0.101025000	-3.175382000
9	-8.785047000	-4.574382000	-3.032993000
9	-6.253464000	-5.764267000	-3.269341000
9	-7.376822000	-6.535222000	-3.182805000
9	-8.660212000	-5.932652000	-3.067700000
9	-5.593248000	0.675567000	-3.329085000

5. Transient absorption measurements of ^{3}DPA

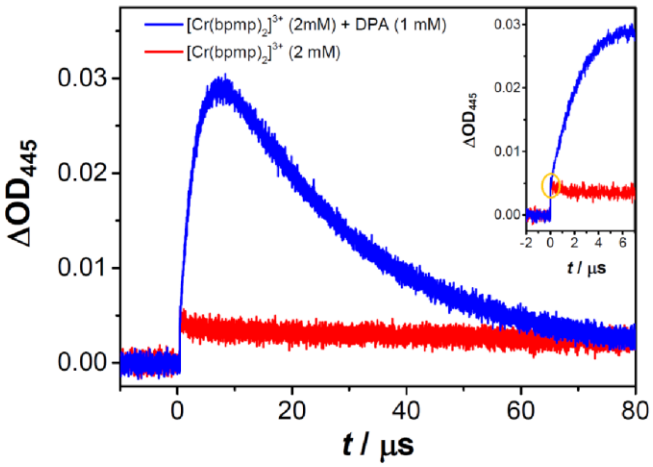

Figure S5: Transient absorption traces upon 532 nm laser excitation (~45 mJ pulse energy) of $[Cr(bpmp)_2][PF_6]_3$ in Ar-saturated acidified DMF monitored at 445 nm. Shown are comparative traces without (red) and with 1 mM DPA (blue). The transient absorption amplitudes directly after the laser pulse are highlighted in the inset, which displays the post-pulse region on enlarged scale. The seemingly static signal increase in the blue curve is due to (weak) $[Cr(bpmp)_2][PF_6]_3$-derived signals and not a result of static ^{3}DPA formation.

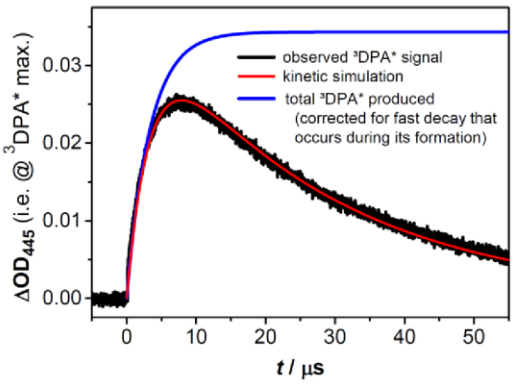

Figure S6: Transient absorption trace from Figure 6a) of the main paper (excitation of $[Cr(bpmp)_2][PF_6]_3$ in the presence of 1 mM DPA with ~40 mJ laser pulses at 532 nm), together with a kinetic simulation allowing the quantification of the ^{3}DPA formation. The experimental trace (black) was simulated with conventional A $\overset{k1}{\rightarrow}$ B $\overset{k2}{\rightarrow}$ C kinetics with k_1 being dynamic DTET to give ^{3}DPA (1/~5 μs) and k_2 being the ^{3}DPA decay (1/~27 μs) under our conditions. The latter rate constant was obtained by fitting the long-term kinetics (t > 20 μs) individually. This procedure directly yields the maximum ΔOD value of intermediate B in this kinetic model (i.e. ^{3}DPA, see blue curve), as previously described by one of us for a related reaction sequence.[13] Two independent measurements on the maximum ^{3}DPA formation were carried out for both $[Cr(bpmp)_2][PF_6]_3$ and $[Ru(bpy)_3][PF_6]_2$, and they gave practically identical results for the DTET quantum yield (0.92 (92%) ± 0.05, see main paper for details). A systematic error that could potentially arise from very weak contributions of excited $[Cr(bpmp)_2][PF_6]_3$ to the transient absorption signal at 445 nm is expected to be smaller than 5%.

6. Delayed sensitizer phosphorescence measurements

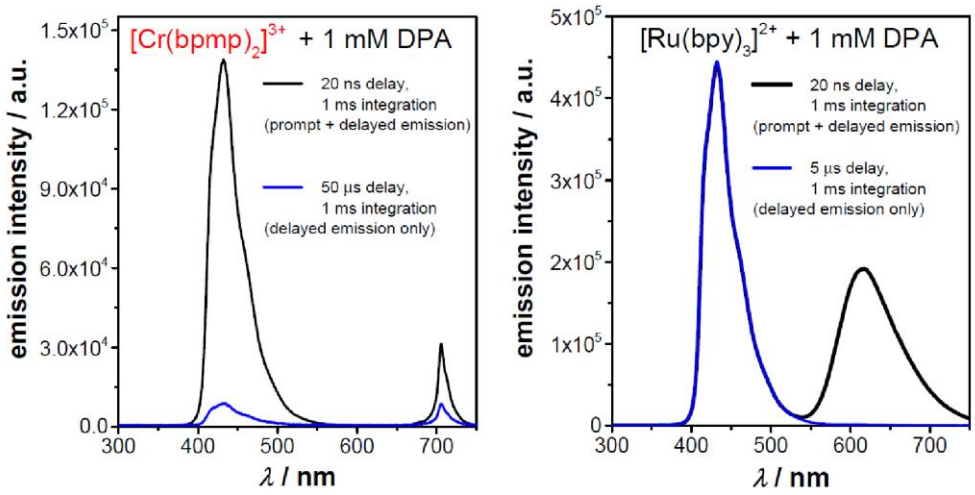

Figure S7: Time-gated emission spectra upon pulsed laser excitation (532 nm, ~5 ns pulse duration, ~40 mJ pulse energy) of Ar-saturated acidified DMF solutions containing DPA (1 mM) and either $[Cr(bpmp)_2][PF_6]_3$ (left) or $[Ru(bpy)_3][PF_6]_2$ (right) as sensitizer under the integration conditions (relative to the laser pulse) as displayed in the respective subfigure. The delayed emission spectra (blue) have been measured with a sufficiently long-time delay that ensures complete decay of the initial (prompt) sensitizer emission.

In contrast to the $[Cr(bpmp)_2]^{3+}$/DPA pair (Figure S7, left), time-gated emission measurements with the $[Ru(bpy)_3]^{2+}$/DPA pair (Figure S7, right) did not yield a detectable delayed phosphorescence of the sensitizer. This is assigned to the large energy difference of the corresponding excited states of the $[Ru(bpy)_3]^{2+}$/DPA couple of about 0.3 eV, which prohibits significant back-EnT.

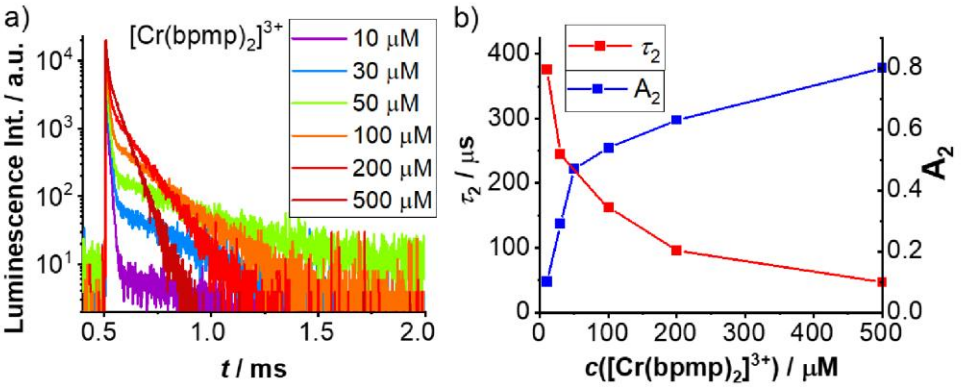

Figure S8: a) Phosphorescence decay kinetics of the sensitizer $[Cr(bpmp)_2][PF_6]_3$ obtained for varying concentrations of the Cr^{III} complex in the presence of 1 mM DPA in deaerated acidified DMF solution. Excitation was at 462 nm using a pulsed xenon lamp (frequency of 100 Hz) and detection at 709 nm, respectively. b) Phosphorescence lifetime τ_2 (delayed phosphorescence emission from TDET) and its relative amplitude obtained from the bi-exponentially fitted decay curves recorded for different $[Cr(bpmp)_2][PF_6]_3$ concentrations.

Table S1: Summary of the phosphorescence decay kinetics fitted bi-exponentially and the corresponding phosphorescence lifetimes τ_{709} and the relative amplitudes of $[Cr(bpmp)_2][PF_6]_3$ at different concentrations in the presence of 1 mM DPA. Excitation was at 462 nm with a flash xenon lamp. Estimated uncertainty of the lifetime is ±5%.

$[Cr(bpmp)_2]^{3+}$ [µM]	τ_1 [µs]	A_1	τ_2 [µs]	A_2
10	8.9	0.90	375	0.10
30	8.8	0.71	245	0.29
50	8.7	0.52	307	0.48
100	8.5	0.46	163	0.54
200	8.4	0.37	96	0.63
500	7.0	0.2	47	0.80

At high $[Cr(bpmp)_2][PF_6]_3$ concentrations (Figure S8, Table S1), τ_2 is shortened while its amplitude A_2 increases. An increasing sensitizer concentration leads to an increasing number of DPA molecules in the triplet state via DTET. This subsequently feeds the TDET process, which accounts for the increase of A_2. The shortened τ_2 of the delayed sensitizer phosphorescence is assigned to the deactivation via DTET, providing a clear hint for the excited state equilibrium[14] between the $^2E/^2T_2$ states of $[Cr(bpmp)_2][PF_6]_3$ and the T_1 state of DPA.

7. Photon upconversion studies of $[Cr(bpmp)_2][PF_6]_3$/DPA pair

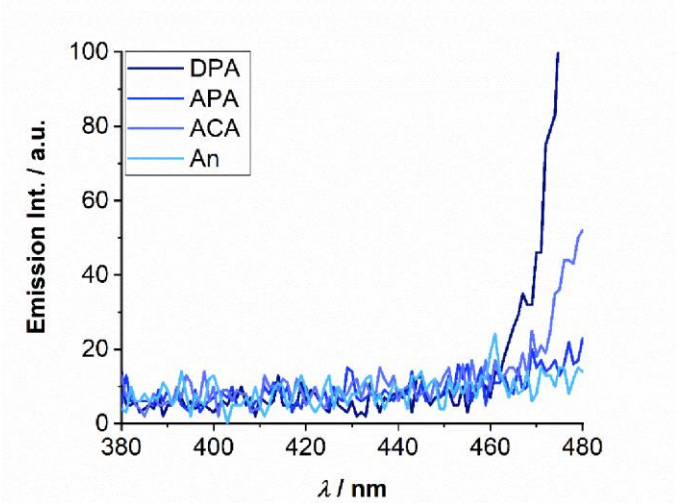

Figure S9: Emission spectra of the anthracene annihilator solutions (1 mM) in acidified DMF under 532 nm (cw, 62 mW) laser excitation in the absence of a sensitizer.

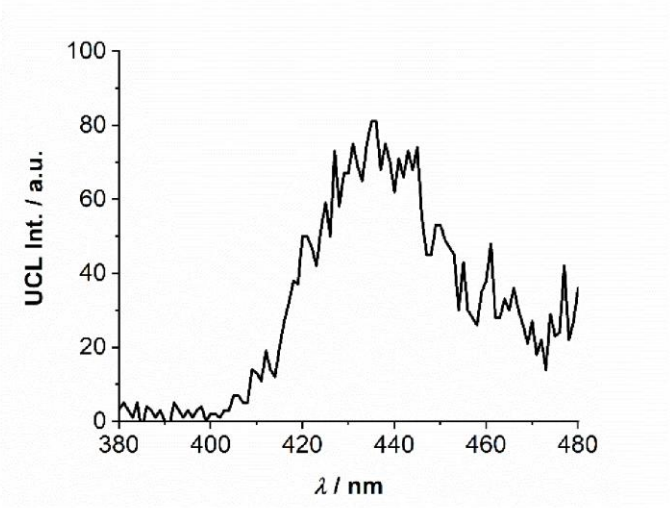

Figure S10: sTTA-UC emission spectrum of $[Cr(bpmp)_2][PF_6]_3$ (50 µM)/DPA (1 mM) in deoxygenated acidified DMF under xenon lamp excitation at 532 nm (excitation power density of ca. 1 $mW \cdot cm^{-2}$, excitation and emission slits: 12 nm, a 532 nm notch filter was placed between the sample and the detector).

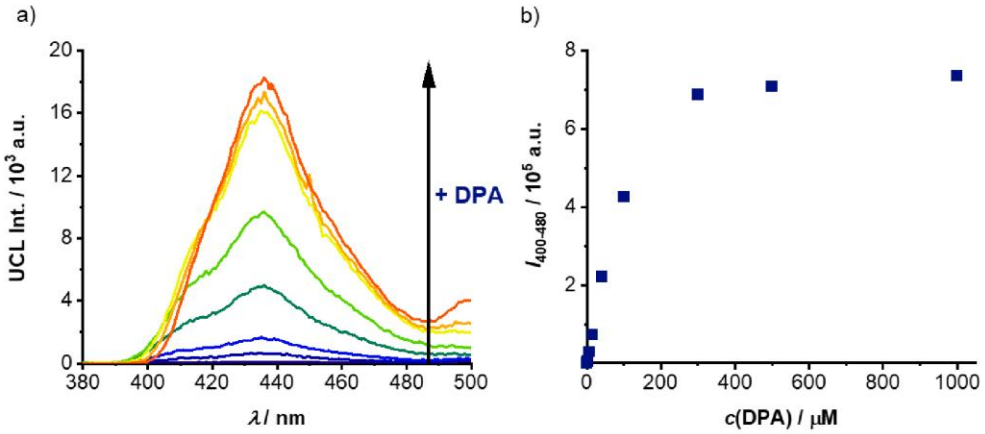

Figure S11: a) sTTA-UC emission spectra of $[Cr(bpmp)_2][PF_6]_3$ (500 µM) obtained with increasing DPA concentration up to 1 mM; b) Plot of the integrated UCL emission intensity as a function of DPA concentration. Excitation with a 532 nm laser (cw, 7 mW).

Power density dependence and Φ_{UC} determination

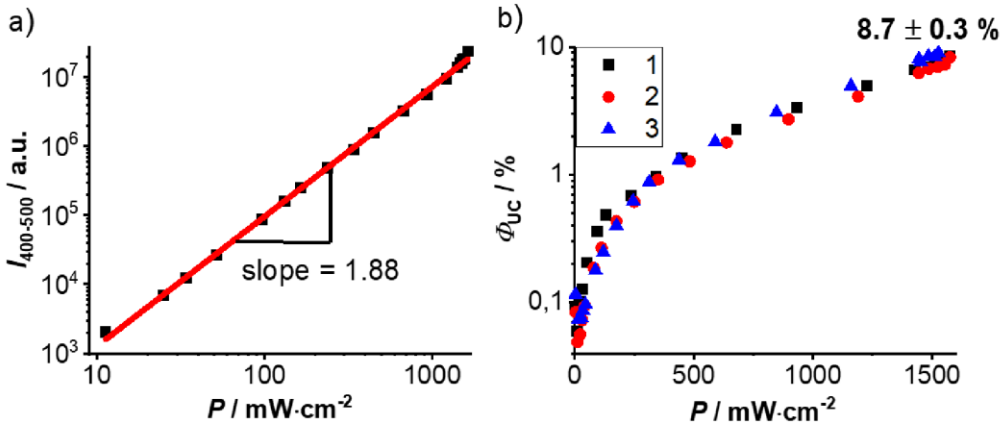

Figure S12: a) Excitation power density dependence of the integrated UCL ($I_{400-500}$) of DPA from the $[Cr(bpmp)_2][PF_6]_3$/DPA pair with a 532 nm laser with increasing power density up to ca. 1.5 W·cm^{-2}, linear fit gives a slope of 1.88; b) relatively determined Φ_{UC} of the $[Cr(bpmp)_2][PF_6]_3$/DPA pair as function of excitation power density of the 532 nm laser according to three independent sets of measurements.

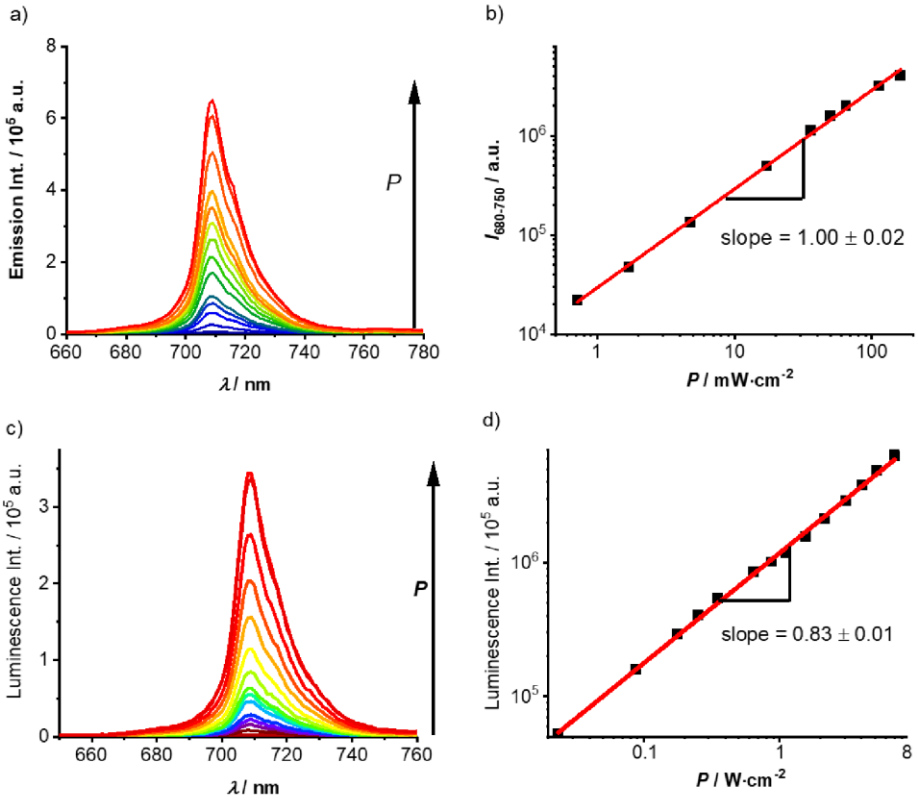

Figure S13*:* a) Phosphorescence spectra of the reference solution $[Cr(bpmp)_2][PF_6]_3$ (50 µM) in acidified DMF with increasing excitation power density of a 532 nm laser (cw, 1.5 W·cm^{-2}), b) excitation power density dependence of integrated the phosphorescence intensity ($I_{680-750}$) of $[Cr(bpmp)_2][PF_6]_3$; linear fit gives a slope of ca. 1. c) Phosphorescence spectra of the reference solution $[Cr(bpmp)_2][PF_6]_3$ (50 µM) in deoxygenated acidified DMF measured with increasing excitation power density of a 520 nm laser (cw, 8 W·cm^{-2}), d) excitation power density dependence of the integrated phosphorescence intensity ($I_{680-750}$) of $[Cr(bpmp)_2][PF_6]_3$; the linear fit gives a slope of ca. 0.83.

Photostability

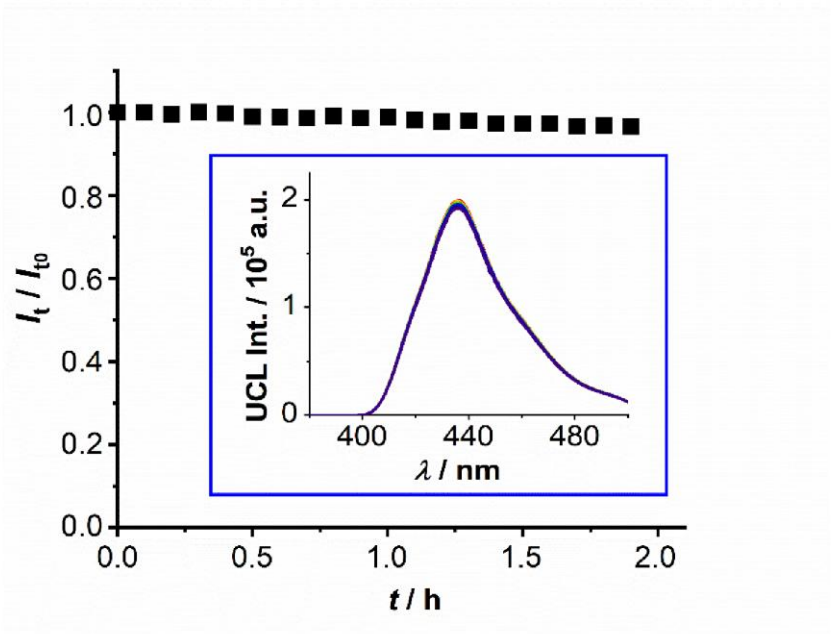

Figure S14: Photostability study of $[Cr(bpmp)_2][PF_6]_3$ (50 µM)/DPA (1 mM) in deaerated acidified DMF under laser (532 nm, cw, 1.5 $W \cdot cm^{-2}$) illumination for 2 hours, inset: UCL emission spectra were taken every 2 min.

8. Photon upconversion and photodimerization with other anthracenes

Triplet energies of annihilators

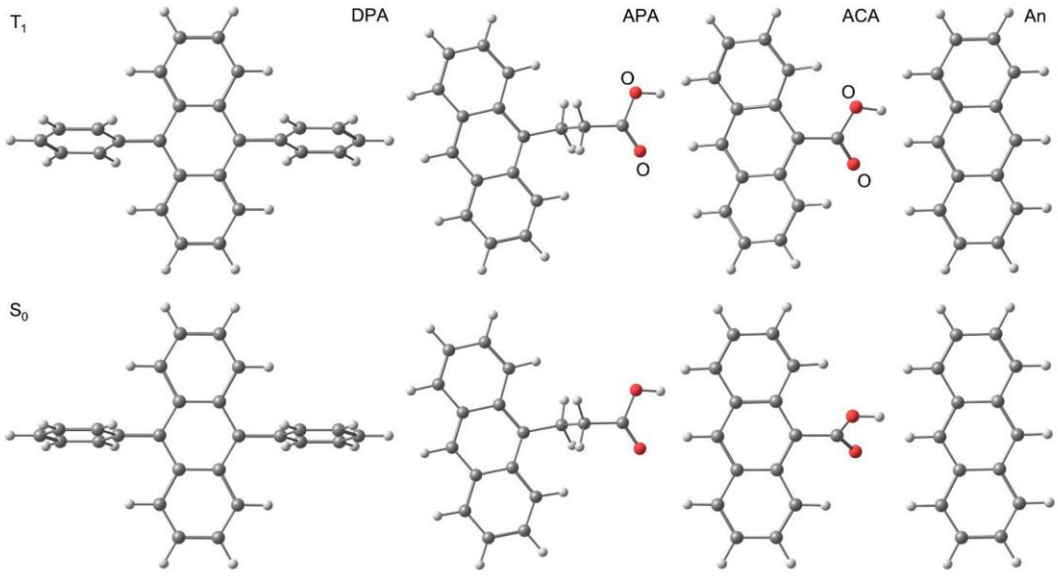

Figure S15: Geometries of the anthracene annihilators (DPA, APA, ACA, and An) in the first triplet state (T_1) and ground state (S_0) optimized at the CPCM(DMF)-RI-B3LYP-D3BJ-ZORA/def2-TZVPP basis of theory.

DPA, S_0; CPCM(DMF)-RI-B3LYP-D3BJ-ZORA/def2-TZVPP

−27261.3900 eV

6	1.398963000	3.060850000	12.714689000
6	0.146327000	2.792054000	13.345514000
1	0.057996000	1.914961000	13.968623000
6	-0.926958000	3.614291000	13.171706000
1	-1.866452000	3.385829000	13.657187000
6	-0.817851000	4.771778000	12.357060000
1	-1.676318000	5.417343000	12.227551000
6	0.361578000	5.070612000	11.739236000
1	0.440483000	5.955748000	11.125667000
6	1.510115000	4.234769000	11.886291000
6	2.729572000	4.533784000	11.257382000
6	2.860742000	5.761922000	10.425214000
6	2.424835000	5.788242000	9.100042000
1	1.982371000	4.900526000	8.666918000
6	2.555786000	6.943684000	8.336099000
1	2.211176000	6.950613000	7.310466000
6	3.124892000	8.086797000	8.888293000
1	3.227281000	8.984432000	8.292979000
6	3.564279000	8.068194000	10.208256000
1	4.009589000	8.951523000	10.646816000
6	3.433282000	6.912568000	10.969408000
1	3.779159000	6.898097000	11.994507000
6	3.838455000	3.692025000	11.436848000
6	5.090957000	3.960540000	10.805644000
1	5.179231000	4.837454000	10.182279000
6	6.164220000	3.138264000	10.979399000
1	7.103609000	3.366518000	10.493618000
6	6.055227000	1.981016000	11.794396000
1	6.913686000	1.335449000	11.923939000
6	4.875876000	1.682387000	12.412464000
1	4.797011000	0.797387000	13.026237000
6	3.727317000	2.518192000	12.265323000
6	2.507876000	2.219137000	12.894222000
6	2.377029000	0.991306000	13.726897000
6	2.811188000	0.966548000	15.052675000
1	3.251917000	1.855173000	15.485717000
6	2.680716000	-0.188489000	15.817302000
1	3.023957000	-0.194228000	16.843404000
6	2.113797000	-1.332719000	15.265175000
1	2.011790000	-2.230060000	15.860996000
6	1.676100000	-1.315645000	13.944625000
1	1.232456000	-2.199853000	13.506148000
6	1.806632000	-0.160416000	13.182787000
1	1.462053000	-0.147101000	12.157237000

DPA, T_1; CPCM(DMF)-RI-B3LYP-D3BJ-ZORA/def2-TZVPP

−27259.7599 eV

6	1.346732000	3.044691000	12.664491000
6	0.113976000	2.774721000	13.263780000
1	0.022703000	1.919304000	13.914826000
6	-1.007717000	3.588885000	13.045230000
1	-1.948639000	3.343471000	13.518876000
6	-0.897255000	4.701315000	12.238953000
1	-1.751670000	5.342184000	12.068189000
6	0.336538000	5.009128000	11.642599000
1	0.418970000	5.895677000	11.032965000
6	1.462720000	4.202301000	11.825519000
6	2.736082000	4.529877000	11.239989000
6	2.871589000	5.749598000	10.416340000
6	2.264526000	5.850719000	9.160273000
1	1.704592000	5.011337000	8.770080000
6	2.382072000	7.013648000	8.407286000
1	1.910189000	7.073761000	7.435457000
6	3.098811000	8.099412000	8.901854000
1	3.187919000	9.004637000	8.316170000
6	3.710110000	8.008688000	10.149165000
1	4.270505000	8.846371000	10.542751000
6	3.601273000	6.842381000	10.895902000
1	4.075395000	6.778289000	11.866039000
6	3.891173000	3.708462000	11.487503000
6	5.123955000	3.978485000	10.888300000
1	5.215218000	4.833882000	10.237229000
6	6.245684000	3.164409000	11.106985000
1	7.186628000	3.409867000	10.633404000
6	6.135244000	2.052021000	11.913325000
1	6.989697000	1.411233000	12.084204000
6	4.901428000	1.744148000	12.509594000
1	4.819000000	0.857631000	13.119276000
6	3.775201000	2.550871000	12.326489000
6	2.501802000	2.223209000	12.911907000
6	2.366262000	1.003533000	13.735617000
6	2.973045000	0.902611000	14.991834000
1	3.532830000	1.742085000	15.382042000
6	2.855347000	-0.260195000	15.744983000
1	3.326990000	-0.320130000	16.716938000
6	2.138746000	-1.346053000	15.250425000
1	2.049514000	-2.251182000	15.836237000
6	1.527741000	-1.255555000	14.002958000
1	0.967451000	-2.093308000	13.609377000
6	1.636756000	-0.089373000	13.256061000
1	1.162819000	-0.025542000	12.285812000

APA, S_0; CPCM(DMF)-RI-B3LYP-D3BJ-ZORA/def2-TZVPP

−21960.3503 eV

6	3.648319000	0.459001000	0.059291000
6	3.598951000	-0.959204000	0.108513000
6	2.395098000	-1.598211000	0.076560000
6	1.174232000	-0.864917000	-0.006952000
6	2.501931000	1.195298000	-0.030196000
6	1.216914000	0.573086000	-0.072464000
6	-0.056714000	-1.515616000	-0.021068000
6	-1.251224000	-0.802408000	-0.082802000
6	0.017958000	1.309355000	-0.161821000
6	-1.219745000	0.637608000	-0.146343000
6	-2.509202000	-1.474316000	-0.075119000
6	-3.680183000	-0.777173000	-0.112008000
6	-3.657900000	0.642459000	-0.157766000
6	-2.473948000	1.321958000	-0.177573000
1	4.606246000	0.960988000	0.094842000
1	4.517842000	-1.525831000	0.177331000
1	2.341197000	-2.678970000	0.120883000
1	2.577639000	2.271817000	-0.060492000
1	-0.086671000	-2.597665000	0.028551000
1	-2.511238000	-2.556541000	-0.032573000
1	-4.628034000	-1.298666000	-0.102074000
1	-4.590993000	1.189914000	-0.178730000
1	-2.492159000	2.401030000	-0.210442000
6	0.077733000	2.813538000	-0.238327000
1	0.941340000	3.117274000	-0.826506000
6	0.175990000	3.458479000	1.162623000
1	-0.791381000	3.210503000	-0.756185000
1	0.985248000	2.993630000	1.721886000
1	-0.754097000	3.312285000	1.707617000
6	0.490642000	4.922577000	1.043131000
8	1.603672000	5.371396000	0.871659000
8	-0.603548000	5.700159000	1.100087000
1	-0.336879000	6.624591000	0.971484000

APA, T_1; CPCM(DMF)-RI-B3LYP-D3BJ-ZORA/def2-TZVPP
−21958.7113 eV

6	3.719021000	0.374202000	0.060363000
6	3.644914000	-1.001618000	0.098251000
6	2.387634000	-1.627841000	0.062524000
6	1.209025000	-0.882010000	-0.014554000
6	2.541801000	1.144511000	-0.023484000
6	1.279739000	0.551772000	-0.068327000
6	-0.062449000	-1.512188000	-0.038164000
6	-1.275299000	-0.773315000	-0.082255000
6	0.060781000	1.319435000	-0.163924000
6	-1.222900000	0.662247000	-0.132724000
6	-2.513561000	-1.417258000	-0.070759000
6	-3.715152000	-0.687957000	-0.095911000
6	-3.672709000	0.689382000	-0.126373000
6	-2.432598000	1.358985000	-0.145591000
1	4.677502000	0.874307000	0.094233000
1	4.543435000	-1.600292000	0.161442000
1	2.319561000	-2.707914000	0.101080000
1	2.638242000	2.219418000	-0.052701000
1	-0.111611000	-2.593287000	0.003410000
1	-2.538759000	-2.499297000	-0.035974000
1	-4.662607000	-1.209860000	-0.086359000
1	-4.586771000	1.267480000	-0.140169000
1	-2.435658000	2.438330000	-0.171675000
6	0.139208000	2.813317000	-0.239433000
1	1.006327000	3.112981000	-0.827210000
6	0.246920000	3.455133000	1.168341000
1	-0.729535000	3.220402000	-0.750589000
1	1.128144000	3.075715000	1.679123000
1	-0.636039000	3.201582000	1.752843000
6	0.370957000	4.948809000	1.067295000
8	1.414969000	5.564587000	1.061569000
8	-0.822517000	5.552072000	0.931658000
1	-0.682978000	6.505595000	0.819067000

ACA, S_0; CPCM(DMF)-RI-B3LYP-D3BJ-ZORA/def2-TZVPP

−19821.1873 eV

6	-1.170130000	-0.706193000	5.552378000
1	-1.407237000	-0.136694000	6.437929000
6	-1.466049000	-2.038941000	5.517240000
1	-1.934744000	-2.506299000	6.373286000
6	-1.171829000	-2.824845000	4.372407000
1	-1.415942000	-3.878825000	4.368460000
6	-0.596172000	-2.245234000	3.281732000
1	-0.372915000	-2.827931000	2.396769000
6	-0.278388000	-0.855451000	3.272707000
6	1.157794000	1.699085000	0.952261000
1	1.347046000	1.070850000	0.091327000
6	1.463190000	3.027204000	0.925321000
1	1.893283000	3.473795000	0.038828000
6	1.226645000	3.831308000	2.070574000
1	1.488305000	4.880971000	2.046513000
6	0.681357000	3.298338000	3.201929000
1	0.513409000	3.932091000	4.058836000
6	0.322478000	1.917830000	3.268336000
6	-0.240893000	1.316478000	4.411187000
6	-0.554267000	-0.057551000	4.439129000
6	0.285418000	-0.257283000	2.148761000
1	0.493572000	-0.863712000	1.275497000
6	0.587322000	1.101524000	2.114062000
6	-0.530153000	2.181461000	5.591109000
8	0.062752000	1.751627000	6.715245000
1	-0.194764000	2.339019000	7.444284000
8	-1.206912000	3.186763000	5.560601000

ACA, T_1; CPCM(DMF)-RI-B3LYP-D3BJ-ZORA/def2-TZVPP

−19819.5630 eV

6	-1.162514000	-0.711037000	5.542608000
1	-1.398969000	-0.142316000	6.428889000
6	-1.477102000	-2.082337000	5.524569000
1	-1.947611000	-2.531140000	6.389271000
6	-1.187071000	-2.843564000	4.412656000
1	-1.425884000	-3.898890000	4.390508000
6	-0.589844000	-2.238692000	3.296932000
1	-0.365337000	-2.829183000	2.417083000
6	-0.278533000	-0.876971000	3.288704000
6	1.139715000	1.709960000	0.954472000
1	1.323698000	1.087761000	0.087506000
6	1.466752000	3.073947000	0.916845000
1	1.893274000	3.501949000	0.019089000
6	1.250800000	3.857122000	2.030363000
1	1.512487000	4.906890000	2.024839000
6	0.691273000	3.291982000	3.189153000
1	0.532816000	3.925603000	4.048140000
6	0.332841000	1.944308000	3.245069000
6	-0.231086000	1.323929000	4.422563000
6	-0.552874000	-0.086453000	4.453633000
6	0.287815000	-0.261463000	2.141324000
1	0.495596000	-0.868076000	1.268884000
6	0.587107000	1.126379000	2.096507000
6	-0.518464000	2.181711000	5.591665000
8	0.005178000	1.714754000	6.738531000
1	-0.257328000	2.310210000	7.458943000
8	-1.144560000	3.223000000	5.547962000

An, S_0; CPCM(DMF)-RI-B3LYP-D3BJ-ZORA/def2-TZVPP

−14684.4691 eV

6	3.667604000	0.583209000	-0.000121000
6	3.618735000	-0.838964000	-0.000129000
6	2.419522000	-1.490067000	-0.000131000
6	1.192484000	-0.762629000	-0.000167000
6	2.516149000	1.316036000	-0.000104000
6	1.242070000	0.676583000	-0.000134000
6	-0.048408000	-1.400428000	-0.000067000
6	-1.242068000	-0.676563000	0.000071000
6	0.048403000	1.400452000	-0.000002000
6	-1.192485000	0.762645000	0.000102000
6	-2.516136000	-1.316038000	0.000100000
6	-3.667595000	-0.583223000	0.000171000
6	-3.618741000	0.838953000	0.000163000
6	-2.419537000	1.490071000	0.000115000
1	4.628264000	1.081079000	0.000163000
1	4.542234000	-1.402656000	0.000310000
1	2.378464000	-2.572409000	0.000030000
1	2.551590000	2.398526000	0.000028000
1	-0.087217000	-2.483577000	-0.000076000
1	0.087199000	2.483598000	0.000033000
1	-2.551545000	-2.398529000	-0.000014000
1	-4.628250000	-1.081104000	-0.000064000
1	-4.542254000	1.402623000	-0.000227000
1	-2.378491000	2.572413000	-0.000049000

An, T_1; CPCM(DMF)-RI-B3LYP-D3BJ-ZORA/def2-TZVPP

−14682.7957 eV

6	3.711380000	0.559528000	-0.000134000
6	3.663981000	-0.818497000	-0.000118000
6	2.419496000	-1.478945000	-0.000178000
6	1.222590000	-0.761925000	-0.000180000
6	2.515132000	1.304978000	-0.000207000
6	1.272197000	0.673469000	-0.000175000
6	-0.048361000	-1.403363000	-0.000053000
6	-1.272194000	-0.673458000	0.000119000
6	0.048361000	1.403369000	-0.000009000
6	-1.222597000	0.761932000	0.000146000
6	-2.515124000	-1.304973000	0.000163000
6	-3.711368000	-0.559532000	0.000150000
6	-3.663996000	0.818493000	0.000173000
6	-2.419509000	1.478949000	0.000206000
1	4.661937000	1.075713000	0.000274000
1	4.576131000	-1.399744000	0.000413000
1	2.384754000	-2.561405000	-0.000055000
1	2.556797000	2.387113000	-0.000131000
1	-0.087254000	-2.485801000	-0.000072000
1	0.087253000	2.485806000	0.000017000
1	-2.556780000	-2.387109000	0.000071000
1	-4.661919000	-1.075731000	-0.000232000
1	-4.576154000	1.399727000	-0.000299000
1	-2.384762000	2.561407000	0.00011300

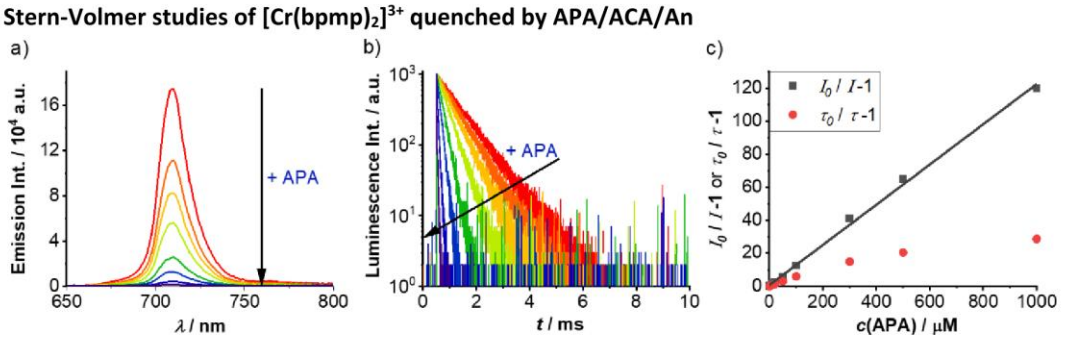

Figure S16: Stern-Volmer study based on a) phosphorescence intensity and b) decay of $[Cr(bpmp)_2][PF_6]_3$ (0.5 mM, in $DMF/HClO_4$) in the presence of APA with different concentrations up to 1 mM (exc. 532 nm, em. 709 nm), and their respective Stern-Volmer plots based on phosphorescence intensity (black) and lifetime (red) with APA concentrations up to 1 mM.

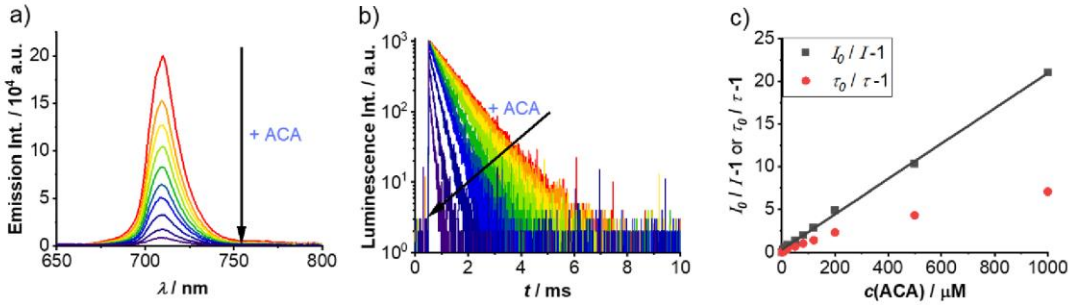

Figure S17: Stern-Volmer study based on a) phosphorescence intensity and b) decay of $[Cr(bpmp)_2][PF_6]_3$ (0.5 mM, in $DMF/HClO_4$) in the presence of ACA with different concentrations (exc. 532 nm, em. 709 nm), and their respective Stern-Volmer plots based on phosphorescence intensity (black) and lifetime (red) with ACA concentrations up to 1 mM.

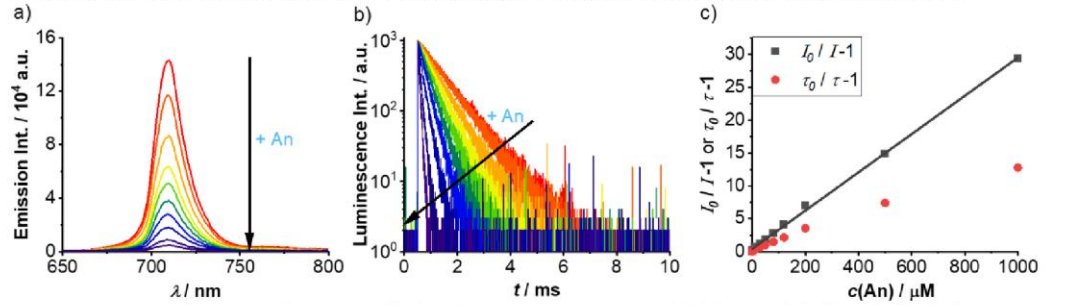

Figure S18: Stern-Volmer study based on a) phosphorescence intensity and b) decay of $[Cr(bpmp)_2][PF_6]_3$ (0.5 mM, in $DMF/HClO_4$) in the presence of An with different concentrations (exc. 532 nm, em. 709 nm), and their respective Stern-Volmer plots based on phosphorescence intensity (black) and lifetime (red) with An concentrations up to 1 mM.

Similar to the $[Cr(bpmp)_2][PF_6]_3$/DPA pair, the non-linear lifetime-based Stern-Volmer plots observed with APA/APA/An annihilators are most likely due to the back-energy transfer from the T_1 state of these anthracenes to the doublet states of the sensitizer.

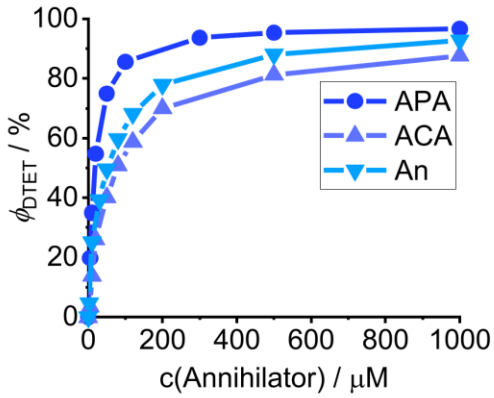

Figure S19: Φ_{DTET} derived from the $[Cr(bpmp)_2][PF_6]_3$ lifetimes plotted as a function of the annihilators (APA/ACA/An) concentration up to 1 mM (exc. 532 nm, em. 709 nm).

Photon upconversion

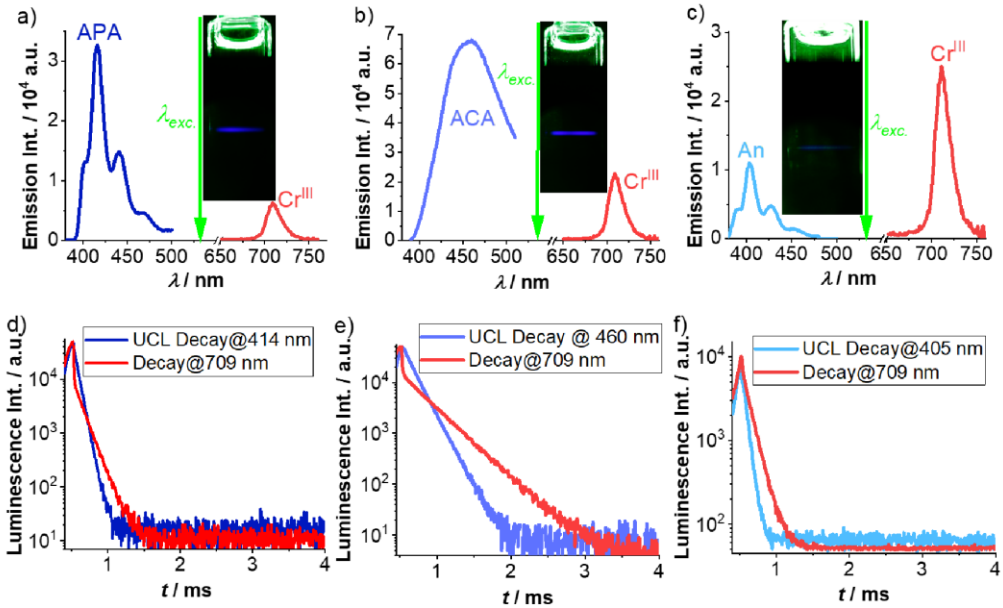

Figure S20: a) UCL spectra and d) UCL decays of $[Cr(bpmp)_2][PF_6]_3$/APA, b) UCL spectra and e) UCL decays of $[Cr(bpmp)_2][PF_6]_3$/ACA, c) UCL spectra and f) UCL decays of $[Cr(bpmp)_2][PF_6]_3$/An, respectively. The red emission traces in d)-f) correspond to the concomitant sensitizer phosphorescence decays. Insets: Photographs of the samples under 532 nm laser excitation (laser power of about 40 mW). The UCL spectra were obtained under 532 nm laser excitation (cw, 1.5 W/cm^2), while the UCL decays were measured with the same laser operated in the pulsed mode (250 Hz, pulse width 500 μs). All samples contain the sensitizer and acceptor concentrations of 50 μM and 1 mM, respectively, in deaerated acidified DMF.

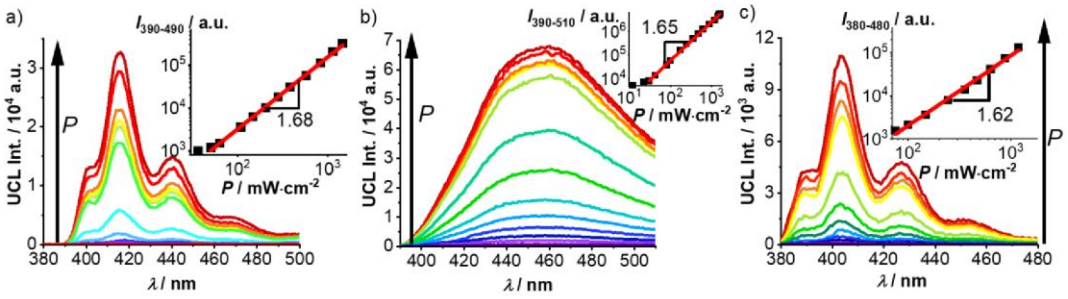

Figure S21: UCL spectra of a) $[Cr(bpmp)_2][PF_6]_3$/APA, b) $[Cr(bpmp)_2][PF_6]_3$/ACA, and c) $[Cr(bpmp)_2][PF_6]_3$/An and integrated UCL as a function of excitation power density (insets) of a 532 nm laser (cw, ca. 1.5 W·cm^{-2}). All UC studies were done with samples containing a sensitizer concentration of 50 µM and an annihilator concentration of 1 mM in deaerated acidified DMF at room temperature.

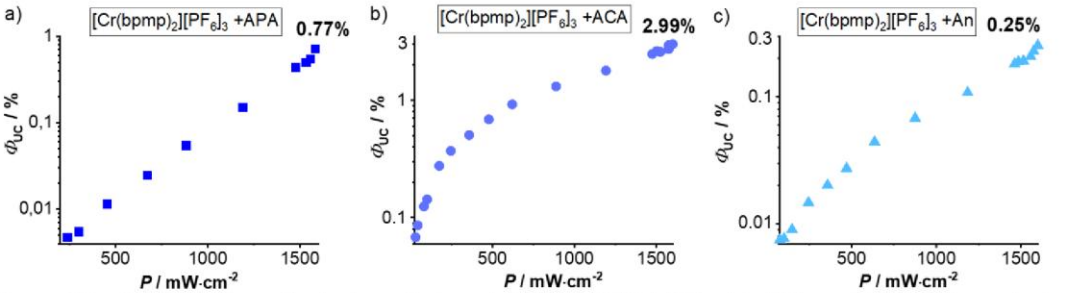

Figure S22: Relatively determined Φ_{UC} of the a) $[Cr(bpmp)_2][PF_6]_3$/APA, b) $[Cr(bpmp)_2][PF_6]_3$/ACA, and c) $[Cr(bpmp)_2][PF_6]_3$/An pairs with increasing power density of the 532 nm-laser up to ca. 1.5 W·cm^{-2}.

Table S2: Summary of the data derived from the SV and UC studies.

Quencher	K_{SV}[a] / 10^4 M^{-1}		k_{DTET}[a] / 10^7 M^{-1}s^{-1}	τ_{UC}[b,d] / µs	τ_{709}[b,d] / µs	Φ_{DTET}[b] / %	Φ_{UC}[b] / %
	based on I_{709}	based on τ_{709}	based on τ_{709}				
DPA	5.7	5.0	5.6	162	7 (15%), 303 (85%)	99.2	8.7; 12.0[c]
APA	12	5.9	6.7	62	6 (20%), 119 (80%)	99.3	0.77
ACA	2.2	1.2	1.4	153	13 (5%), 316 (95%)	98.5	2.99
An	3.3	1.8	2.0	57	15 (6%), 113 (94%)	98.3	0.25

[a]: SV studies of $[Cr(bpmp)_2][PF_6]_3$ (0.5 mM) in deaerated acidified DMF done with increasing concentrations of the four anthracene annihilators. [b]: UC studies of $[Cr(bpmp)_2][PF_6]_3$ (50 µM) in deaerated acidified DMF in the presence of 1 mM anthracene annihilator. The luminescence decays were obtained with a pulsed 532 nm-laser (250 Hz, pulse width 500 µs). A 532 nm-laser (cw, ca. 1.5 W·cm^{-2}) was used to determine the Φ_{UC} values of all sTTA-UC pairs. [c]: For the $[Cr(bpmp)_2][PF_6]_3$/DPA pair, a maximum Φ_{UC} value of 12% was obtained with a more intense 520 nm-laser (cw, ca. 8 W·cm^{-2}) enabling to reach saturation. [d]: The delayed fluorescence lifetimes τ_{UC} from the anthracenes were fitted mono-exponentially, while the sensitizer lifetimes τ_{709} were fitted bi-exponentially; the respective relative amplitudes are given in brackets. The estimated uncertainty of the lifetimes amounts to ±5%.

The integrated UCL intensities of APA, ACA, and An showed an excitation power density dependence (532 nm laser, cw, 1.5 W·cm^{-2}) with slopes of about 1.65 (Figure S21), probably due to the involved photodimerization. In addition, the Φ_{UC} values obtained with these annihilators are considerably lower than the $[Cr(bpmp)_2][PF_6]_3$/DPA pair. The lower Φ_{UC} values are ascribed to the lower Φ_F of the anthracene annihilators (Figure S1), the more efficient TDET due to their higher triplet energies (Figure S15), the inherently less efficient TTA compared to DPA,[15] and the additional deactivation pathway of the UC-activated singlet state of the APA, ACA, and An annihilators via photodimerization (see below).

Photodimerization

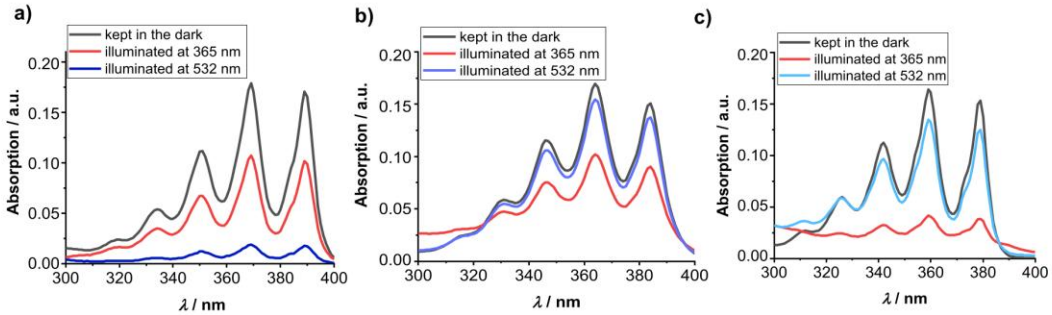

Figure S23: Absorption spectra of a) $[Cr(bpmp)_2][PF_6]_3$/APA, b) $[Cr(bpmp)_2][PF_6]_3$/ACA, and c) $[Cr(bpmp)_2][PF_6]_3$/An kept in the dark under air (black), illuminated with 532 nm laser light without oxygen for 2 hours (blue), and illuminated at 365 nm under air for 10-30 min (red), respectively. All samples were diluted by a factor of 10 for the absorption measurements using an optical cell with a path length of 2 mm.

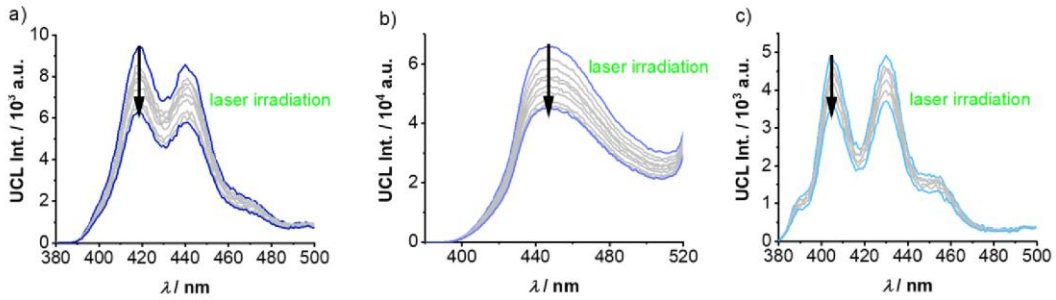

Figure S24: UCL emission spectra of a) $[Cr(bpmp)_2][PF_6]_3$/APA, b) $[Cr(bpmp)_2][PF_6]_3$/ACA, and c) $[Cr(bpmp)_2][PF_6]_3$/An in acidified DMF under laser (532 nm, cw, 1.5 $W \cdot cm^{-2}$) irradiation up to ca. 1 hour.

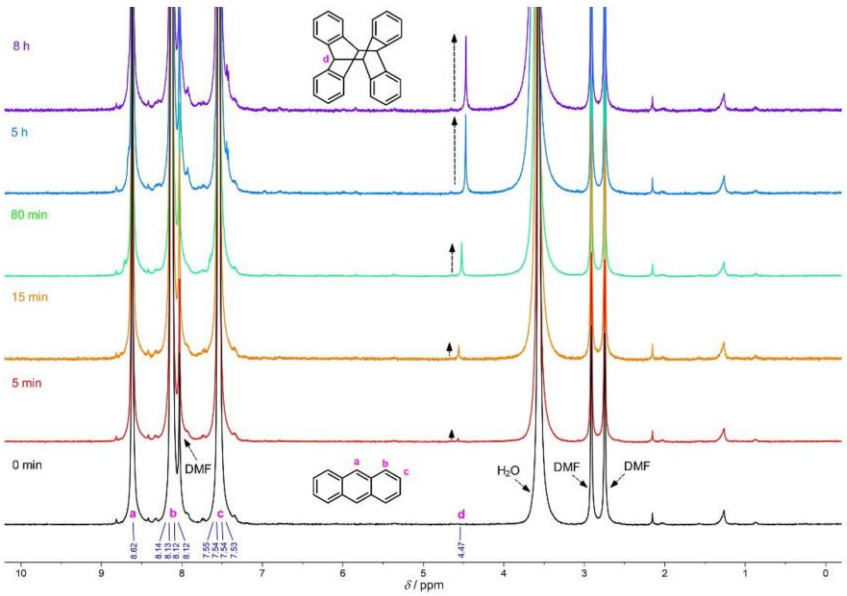

Figure S25: ^1H NMR spectra of the solution of the photolysis experiment in d_7-DMF showing the increase of the resonance of the bridgehead protons at 4.47 ppm characteristic for the anthracene dimer.[16]

9. References

[1] F. Reichenauer, C. Wang, C. Förster, P. Boden, N. Ugur, R. Báez-Cruz, J. Kalmbach, L. M. Carrella, E. Rentschler, C. Ramanan, G. Niedner-Schatteburg, M. Gerhards, M. Seitz, U. Resch-Genger,K. Heinze, *J. Am. Chem. Soc.* **2021**, *143*, 11843–11855.
[2] C. Würth, J. Pauli, C. Lochmann, M. Spieles,U. Resch-Genger, *Anal. Chem.* **2012**, *84*, 1345–1352.
[3] a) T. N. Singh-Rachford,F. N. Castellano, *Coord. Chem. Rev.* **2010**, *254*, 2560-2573; b) J. B. Bilger, C. Kerzig, C. B. Larsen,O. S. Wenger, *J. Am. Chem. Soc.* **2021**, *143*, 1651-1663.
[4] Y. Zhou, F. N. Castellano, T. W. Schmidt,K. Hanson, *ACS Energy Lett.* **2020**, *5*, 2322-2326.
[5] a) I. Momiji, C. Yoza,K. Matsui, *J. Phys. Chem. B* **2000**, *104*, 1552-1555

; b) H. Saigusa,E. C. Lim, *Acc. Chem. Res.* **1996**, *29*, 171–178; c) N. S. Bazilevskaya,A. S. Cherkasov, *Opt. Spectrosc.* **1965**, *18*, 30.
[6] F. Neese, *WIREs Comput. Mol. Sci.* **2011**, *2*, 73-78.
[7] a) A. D. Becke, *J. Chem. Phys.* **1993**, *98*, 5648–5652; b) C. Lee, W. Yang,R. G. Parr, *Phys. Rev. B* **1988**, *37*, 785–789; c) B. Miehlich, A. Savin, H. Stoll,H. Preuss, *Chem. Phys. Lett.* **1989**, *157*, 200–206.
[8] a) F. Weigend,R. Ahlrichs, *Phys. Chem. Chem. Phys.* **2005**, *7*, 3297–3305; b) F. Weigend, *Phys. Chem. Chem. Phys.* **2006**, *8*, 1057–1065.
[9] a) F. Neese, F. Wennmohs, A. Hansen,U. Becker, *Chem. Phys.* **2009**, *356*, 98–109; b) R. Izsák,F. Neese, *J. Chem. Phys.* **2011**, *135*, 144105.
[10] a) D. A. Pantazis, X.-Y. Chen, C. R. Landis,F. Neese, *J. Chem. Theory Comput.* **2008**, *4*, 908–919; b) E. van Lenthe, E. J. Baerends,J. G. Snijders, *J. Chem. Phys.* **1993**, *99*, 4597–4610; c) C. van Wüllen, *J. Chem. Phys.* **1998**, *109*, 392–399.
[11] a) S. Grimme, J. Antony, S. Ehrlich,H. Krieg, *J. Chem. Phys.* **2010**, *132*, 154104; b) S. Grimme, S. Ehrlich,L. Goerigk, *J. Comput. Chem.* **2011**, *32*, 1456–1465.
[12] V. Barone,M. Cossi, *J. Phys. Chem. A* **1998**, *102*, 1995–2001.
[13] C. Kerzig,M. Goez, *Phys. Chem. Chem. Phys.* **2014**, *16*, 25342-25349.
[14] D. Meroni, A. Monguzzi,F. Meinardi, *J. Chem. Phys.* **2020**, *153*, 114302.
[15] R. R. Islangulov, D. V. Kozlov,F. N. Castellano, *Chem. Commun.* **2005**, 3776-3778.
[16] S. Baluschev, F. Yu, T. Miteva, S. Ahl, A. Yasuda, G. Nelles, W. Knoll,G. Wegner, *Nano Lett.* **2005**, *5*, 2482-2484.

6.3 Supporting Information: Decoupled Enhancement of Electrochemical Properties in Molecular Rubies

Decoupled Enhancement of Electrochemical Properties in Molecular Rubies

Florian Reichenauer,[a] Anika P. Busch,[a] Robert Naumann,[a] Christoph Förster[a] and Katja Heinze[a]

[a] Department of Chemistry, Johannes Gutenberg University of Mainz, Duesbergweg 10-14, 55128 Mainz, Germany

Supporting Information

Authors Contributions

A. P. Busch and F. Reichenauer conducted the synthesis, ground-state characterization, and steady-state spectroscopic measurements, with F. Reichenauer performing quantum chemical calculations and preparing the original manuscript draft. A. P. Busch, R. Naumann, and F. Reichenauer collected and interpreted emission data for Stern-Volmer analysis and measured quantum yields. C. Förster solved and refined the single crystal structures. K. Heinze designed and supervised the project.

Table of Contents

General Methods

All reactions and measurements were performed under argon atmosphere unless otherwise noted. Gloveboxes (UniLab/MBraun − Ar 5.0, O_2 < 1 ppm, H_2O < 0.1 ppm) were used to store and weight sensitive compounds for synthesis as well as to prepare samples that require the absence of oxygen and/or water. The reagents were purchased from commercial suppliers (Acros Organics, Fischer Scientific and Sigma Aldrich) and used without further purification. Anhydrous $Cr(OTf)_3$ was prepared according to the synthetic procedure described in Section 6.4. Acetonitrile, 1,4-dioxane and tetrahydrofuran were dried and distilled from CaH_2, sodium and potassium, respectively. Column chromatography was performed using aluminium oxide (neutral, Brockmann I). Analytical thin layer chromatography (TLC) was done on aluminium oxide F254 (Macherey-Nagel, coated on polyester sheets) and the spots were visualized by ultraviolet light.

NMR Spectra were recorded on a *Bruker Avance II 400* spectrometer at 400.42 MHz (^{1}H) and 100.70 MHz (^{13}C{^{1}H}) in deuterated acetonitrile (Deutero GmbH). All data were evaluated with the software *MestReNova 12.0.4-22023*. The resonances are reported in ppm versus the solvent signal as internal standard (^{1}H; (^{13}C) NMR: actonitrile-d_3: δ = 1.94, 2.13; (1.32, 118.26) ppm)[1] and *J* values are given in Hz. (s) = singlet, (d) = doublet, (t) = triplet, (q) = quartet.

IR spectra were recorded with a *Bruker Alpha FTIR* spectrometer with an ATR unit containing a diamond crystal.

ESI$^+$ mass spectra were measured on an *Agilent 6545 HPLC-ESI-QTOF-MS* spectrometer at a temperature of 275 °C for the ligands and 150 °C for the bis(tridentate) complexes. The bis(tridentate) complexes were directly injected into the ion source (without HPLC) and the spectra were corrected using a background measurement of the pure solvent.

Elemental analyses was performed by the central analytic service of the Department of Chemistry of the Johannes Gutenberg University Mainz using an *Elementar vario EL Cube* (precursor) or by the Mikroanalytisches Labor Kolbe, c/o Fraunhofer Institut UMSICHT, Oberhausen, Germany (bis(tridentate) complexes).

Electrochemical experiments were carried out on a *BioLogic SP-200* voltammetric analyzer using platinum wires as *counter* and working electrodes and a 0.01 M Ag/Ag(NO_3) electrode as reference electrode. Cyclic voltammetry and square wave measurements were carried out at scan rates of 100 mV s^{-1} using 0.1 M [^{n}Bu$_4$N](PF$_6$) in CH_3CN as supporting electrolyte. Potentials are referenced against the ferrocene/ferrocenium (FcH/FcH^+) couple.

UV/Vis/NIR spectra were recorded on an *Agilent Cary 5000* spectrometer in acetonitrile (Optima® LC/MS grade, Fisher Scientific) at room temperature. Measurements from 1000-200 nm were conducted using 1.00 cm path length cuvettes, while measurements of the NIR bands within 900-600 nm were performed using a 10.0 cm path length cuvette. Molar extinction coefficients are given at maximum absorption and for shoulders (highlighted as sh).

Steady-state emission spectra and photoluminescent decay curves of the complexes were measured with an *FLS1000 spectrometer* from *Edinburgh Instruments* equipped with a cooled photomultiplier detector PMT-980. A xenon arc lamp Xe2 (450 W) was used for excitation in steady-state measurements. Time-resolved luminescence experiments were conducted using a pulsed diode laser VPL-450 as excitation source. Absolute luminescence quantum yields Φ were determined using an integrating sphere from *Edinburgh Instruments* with a relative uncertainty estimated as ±10%. Steady-state measurements were additionally performed with a *spectrofluorometer FS5* from *Edinburgh Instruments*. All measurements were carried out in degassed acetonitrile (Optima® LC/MS grade, Fisher Scientific).

Stern-Volmer measurements were conducted by titration of deaerated solutions of *trans*-anethol in acetonitrile to deaerated solutions of the corresponding complex in the same solvent in inert gas cuvettes. The titration steps were done in the glovebox. The Stern-Volmer analyses were performed on the basis of eq. S1 and S2.[2]

$$\frac{\tau_0}{\tau} - 1 = K_{\mathrm{SV}}[\mathrm{Q}] \qquad \text{(eq. S1)}$$

$$k_{\mathrm{q}} = \frac{K_{SV}}{\tau_0} \qquad \text{(eq. S2)}$$

DFT calculations were performed using the quantum computing suite ORCA 5.0.4.[3,4] Geometry optimization was done using unrestricted Kohn-Sham orbitals DFT (UKS) and the B3LYP functional[5–7] in combination with Ahlrich's split valance triple-zeta basis set ZORA-def2-TZVPP[8] and the Def2/J auxiliary basis set for all atoms. Tight convergence criteria were chosen for DFT calculations (keywords *tightscf* and *tightopt*). All DFT calculations make use of the resolution of identity (Split-RI-J) approach for the Coulomb term in combination with the chain-of-spheres approximation for the exchange term (keyword *RIJCOSX*).[9,10] The zeroth order regular approximation was used to describe relativistic effects in all calculations (keyword *ZORA*).[11–13] To account for solvent effects, a conductor-like screening model (keyword *CPCM*(acetonitrile)) modelling acetonitrile was used in all calculations.[14,15] Atom-pairwise dispersion correction was performed with the Becke-Johnson damping scheme (keyword *D3BJ*).[16,17] A numerical frequency calculation confirmed that the optimised geometry corresponds to a minimum structure or a transition state structure, respectively. Explicit counter ions and/or solvent

molecules were neglected. Fifty vertical spin-allowed transitions were calculated by TD-DFT. The charge transfer number analyses of the TD-DFT calculated transitions were done using TheoDORE 2.4.[18,19] All calculations were computed on the Elwetritsch supercomputer at RPTU Kaiserslautern-Landau (hpc.rz.rptu.de). This is a member of the AHRP (Alliance for High Performance Computing Rhineland-Palatinate).

CASSCF(x,y)-SC-NEVPT2 calculations of ground and excited state properties with respect to pure metal-centered (MC) states were performed using the complete-active-space self-consistent field (CASSCF) method[20,21] in conjunction with the strongly contracted N-electron valence perturbation theory to second order (SC-NEVPT2)[22–24] in order to recover missing dynamic electron correlation. All electronic states are classified by irreducible representations of the O point group, in spite of the lower actual symmetry of the considered complexes. The active space (7,12) comprising of five d-orbitals, two occupied σ bonding orbitals and five unoccupied d orbitals of second d-shell[25] was considered for all CASSCF-calculations including 10 quartet and 10 doublet roots. The geometries of the DFT optimized $^4A_2$ states were used for the calculations.

Crystal structure determination. Intensity data were collected with a *STOE IPDS-2T* diffractometer and a *STOE STADIVARI* diffractometer from STOE & Cie GmbH with an Oxford cooling using Mo-Kα radiation (λ = 0.71073 Å). The diffraction frames were integrated using the STOE X-Area software package and were corrected for absorption with MULABS34[26] of the PLATON[27] software package. The structures were solved with SHELXT[28] and refined by the full-matrix method based on F^2 using SHELXL[29] of the SHELX[30] software package and the ShelXle[31] graphical interface. All non-hydrogen atoms were refined anisotropically while the positions of all hydrogen atoms were generated with appropriate geometric constraints and allowed to ride on their respective parent atoms with fixed isotropic thermal parameters.

Crystallographic Data of [Cr(ddpd^{CF3})$_2$](OTf)$_3$
$C_{41}H_{35}CrF_{15}N_{11}O_9S_3$ (1258.98); orthorhombic; $P2_12_12_1$; a = 9.3452(19) Å, b = 14.503(3) Å, c = 36.698(7) Å; α = 90°; β = 90°; γ = 90°; V = 4973.8(17) Å^3; Z = 4; density, calcd. = 1.681 g cm^{-3}, T = 120(2) K, μ = 0.479 mm^{-1}; F(000) = 2548; crystal size 0.710 × 0.300 × 0.060 mm^3; θ = 2.627 to 28.044°; −10 ≤ h ≤ 12, −16 ≤ k ≤ 19, −35 ≤ l ≤ 48; reflections collected = 15287; reflections unique = 10839 [R(int) = 0.0428]; completeness to θ = 25.242°: 97.6%; absorption correction: integration; max. and min. transmission 0.9671 and 0.8367; data 10839; restraints 1263, parameters 976; goodness-of-fit on F^2 = 1.047; final indices [$I > 2\sigma(I)$] R_1 = 0.0936, wR_2 = 0.2278; R indices (all data) R_1 = 0.1392, wR_2 = 0.2681; largest diff. peak and hole 1.486 and −0.697 e Å^{-3}.

Crystallographic Data of [Cr(ddpd^{OMe})$_2$](OTf)$_3$
$C_{43}H_{44}CrF_9N_{12}O_{11}S_3$ (1224.08); monoclinic; Cc; a = 12.086(2) Å, b = 25.331(5) Å, c = 17.347(4) Å; α = 90°; β = 109.28(3)°; γ = 90°; V = 5013.0(19) Å^3; Z = 4; density, calcd. = 1.622 g cm^{-3}, T = 120(2) K, μ = 0.459 mm^{-1}; F(000) = 2508; crystal size 0.360 × 0.213 × 0.060 mm^3; θ = 2.617 to 28.021°; −15 ≤ h ≤ 15, −33 ≤ k ≤ 33, −22 ≤ l ≤ 22; reflections collected = 28136; reflections unique = 10796 [R(int) = 0.0854]; completeness to θ = 25.242°: 99.9%; absorption correction: semi-empirical from equivalents; max. and min. transmission 1.14480 and 0.84904; data 10796; restraints 349, parameters 794; goodness-of-fit on F^2 = 1.055; final indices [$I > 2\sigma(I)$] R_1 = 0.0536, wR_2 = 0.1163; R indices (all data) R_1 = 0.0749, wR_2 = 0.1305; largest diff. peak and hole 0.454 and −0.551 e Å^{-3}.

Synthetic Procedures

Synthesis of ddpd^{CF3} (L^{CF3})

A grey suspension of sodium hydride (2.54 g, 63.5 mmol, 2.0 eq.) and 2-(methylamino)pyridine (6.7 mL, 63.5 mmol, 2.0 eq.) in dry THF (250 mL) was stirred for 60 minutes at room temperature, forming a yellow suspension. A solution of 2,6-dichloro-4-(trifluoromethyl)pyridine (4.7 mL, 31.8 mmol, 1.0 eq.) in dry THF (50 mL) was added dropwise over 30 minutes. The orange-coloured mixture was then heated at 64 °C for 72 hours, resulting in a brown solution. After cooling to room temperature, the reaction was quenched by the slow addition of water (300 mL), with gas evolution observed. The organic layer was separated, and the aqueous layer (pH = 7) was extracted with ethyl acetate (3 x 150 mL). The combined organic extracts were dried over sodium sulfate, filtered, and concentrated under reduced pressure (200 mbar, 40 °C). The resulting brown crude product was purified by column chromatography (Alox II, 9:1:0.05, cyclohexane/ethyl acetate/triethylamine, R_f = 0.53) to afford **L^{CF3}** as a yellow oil (10.52 g, 29.3 mmol, 92%).

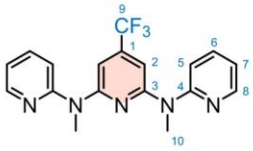

^{1}H NMR (CD_3CN): δ = 8.33 (2 H, ddd, $^3J_{HH}$ = 4.9, $^4J_{HH}$ = 2.0, $^5J_{HH}$ = 0.9, H^8), 7.61 (2 H, ddd, $^3J_{HH}$ = 8.4, $^3J_{HH}$ = 7.3, $^4J_{HH}$ = 2.0, H^6), 7.29 (2 H, dt, $^3J_{HH}$ = 8.3, $^{4/5}J_{HH}$ = 1.0, H^5), 6.97 (2 H, ddd, $^3J_{HH}$ = 7.3, $^3J_{HH}$ = 4.9, $^4J_{HH}$ = 1.0, H^7), 6.83 (2 H, s, H^2), 3.50 (6 H, s, H^{10}) ppm.
^{13}C{^{1}H} NMR (CD_3CN): δ = 158.2 (s, C^4), 157.6 (s, C^3), 149.0 (s, C^8), 141.0 (q, C^1), 138.3 (s, C^6), 124.6 (q, C^9), 119.5 (s, C^7), 117.9 (s, C^5), 99.4 (s, C^2), 33.6 (s, C^{10}) ppm.
^{19}F NMR (CD_3CN): δ = –66.5 (3 F, s, CF_3) ppm.
MS (ESI^+, CH_3CN): *m/z* (%) = 360.14 (100) [ddpd^{CF3}+H]$^+$.
IR (ATR): $\tilde{\nu}_{max}$ = 3008 (w), 2252 (w), 1562 (vs), 1471 (s), 1415 (vs), 1391 (vs), 1337 (s), 1305 (s), 1264 (m), 1239 (m), 1172 (vs), 1125 (vs), 1079 (s), 1048 (m), 989 (s), 908 (m), 834 (m), 778 (s), 740 (m), 705 (m), 675 (m), 653 (w), 637 (w), 624 (w), 562 (w), 507 (w), 448 (w), 411 (w) cm^{-1}.
Elemental analysis calcd. for $C_{18}H_{16}F_3N_5$: C, 60.16; H, 4.49; N, 19.49. Found: C, 60.28; H, 4.57; N, 19.59.

Synthesis of ddpd^{OMe} (L^{OMe})

A grey suspension of sodium hydride (2.93 g, 73.2 mmol, 2.0 eq.) and 2-(methylamino)pyridine (7.7 mL, 73.2 mmol, 2.0 eq.) in dry THF (300 mL) was stirred for 60 minutes at room temperature, forming a yellow suspension. A solution of 2,6-dibromo-4-(methoxy)pyridine (10.29 g, 36.6 mmol, 1.0 eq.) in dry THF (100 mL) was added dropwise over 30 minutes. The orange-coloured mixture was then heated at 64 °C for 72 hours, resulting in a brown solution. After cooling to room temperature, the reaction was quenched by the slow addition of water (300 mL), with gas evolution observed. The organic layer was separated, and the aqueous layer (pH = 7) was extracted with ethyl acetate (3 x 150 mL). The combined organic extracts were dried over sodium sulfate, filtered, and concentrated under reduced pressure (200 mbar, 40 °C). The resulting brown crude product was purified by column chromatography (Alox II, 9.5:0.5:0.05, cyclohexane/ethyl acetate/triethylamine, R_f = 0.23) to afford **L^{OMe}** as a yellow oil (4.50 g, 14.0 mmol, 38%).

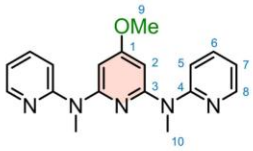

^{1}H NMR (CD_3CN): δ = 8.28 (2 H, ddd, $^3J_{HH}$ = 4.9, $^4J_{HH}$ = 2.0, $^5J_{HH}$ = 0.9, H^8), 7.53 (2 H, ddd, $^3J_{HH}$ = 8.5, $^3J_{HH}$ = 7.2, $^4J_{HH}$ = 2.0, H^6), 7.25 (2 H, dt, $^3J_{HH}$ = 8.4, $^{4/5}J_{HH}$ = 1.0, H^5), 6.86 (2 H, ddd, $^3J_{HH}$ = 7.2, $^3J_{HH}$ = 4.9, $^4J_{HH}$ = 1.0, H^7), 6.28 (2 H, s, H^2), 3.74 (3 H, s, H^9), 3.47 (6 H, s, H^{10}) ppm.
^{13}C{^{1}H} NMR (CD_3CN): δ = 169.4 (s, C^1), 158.7 (s, C^4), 158.4 (s, C^3), 148.7 (q, C^8), 137.7 (s, C^6), 117.9 (q, C^7), 116.8 (s, C^5), 93.1 (s, C^2), 55.9 (s, C^9), 36.4 (s, C^{10}) ppm.
MS (ESI^+, CH_3CN): *m/z* (%) = 322.17 (100) [ddpd^{OMe}+H]$^+$.
IR (ATR): $\tilde{\nu}_{max}$ = 3005 (w), 2291 (w), 2251 (w), 1581 (vs), 1561 (vs), 1468 (vs), 1413 (vs), 1330 (m), 1296 (s), 1234 (m), 1210 (s), 1179 (w), 1153 (m), 1110 (s), 1051 (m), 987 (s), 943 (w), 918 (w), 818 (w), 779 (s), 741 (m), 669 (w), 643 (w), 623 (w), 554 (w), 515 (w), 411 (w) cm^{-1}.
Elemental analysis calcd. for $C_{18}H_{19}N_5O$: C, 67.27; H, 5.96; N, 21.79. Found: C, 66.56; H, 5.80; N, 21.63.

Synthesis of ddpd^{NMe2} (L^{NMe2})

A grey suspension of sodium hydride (6.06 g, 152 mmol, 6.0 eq.) and 2-(methylamino)pyridine (15.9 mL, 152 mmol, 6.0 eq.) in dry 1,4-dioxane (200 mL) was stirred for 60 minutes at room temperature, forming a yellow suspension. A solution of 2,6-dichloro-4-(dimethylamino)pyridine (5.08 g, 25.3 mmol, 1.0 eq.) in dry 1,4-dioxane (100 mL) was added dropwise over 30 minutes. The orange-coloured mixture was then heated at 101 °C for 72 hours, resulting in a brown solution. After cooling to room temperature, the reaction was quenched by the slow addition of water (300 mL), with gas evolution observed. The organic layer was separated, and the aqueous layer (pH = 7) was extracted with ethyl acetate (3 x 150 mL). The combined organic extracts were dried over sodium sulfate, filtered, and concentrated under reduced pressure (80 mbar, 40 °C). The resulting brown crude product was purified by column chromatography (Alox II, 8:2:0.05, cyclohexane/ethyl acetate/triethylamine, R_f = 0.36) to afford impure **L^{NMe2}** as a yellow oil (0.86 g).

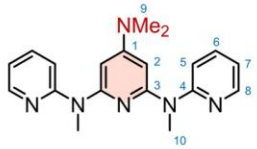

^{1}H NMR (CD_3CN): δ = 8.22 (2 H, ddd, $^3J_{HH}$ = 5.0, $^4J_{HH}$ = 2.1, $^5J_{HH}$ = 1.0, H^8), 7.47 (2 H, ddd, $^3J_{HH}$ = 8.6, $^3J_{HH}$ = 7.1, $^4J_{HH}$ = 2.0, H^6), 7.14 (2 H, dt, $^3J_{HH}$ = 8.6, $^{4/5}J_{HH}$ = 0.9, H^5), 6.77 (2 H, ddd, $^3J_{HH}$ = 7.2, $^3J_{HH}$ = 5.0, $^4J_{HH}$ = 1.0, H^7), 6.14 (2 H, s, H^2), 3.45 (6 H, s, H^{10}), 2.92 (6 H, s, H^9) ppm.
MS (ESI$^+$, CH_3CN): *m/z* (%) = 335.20 (100) [ddpd^{NMe2}+H]$^+$.
IR (ATR): $\tilde{\nu}_{max}$ = 2891 (w), 2805 (w), 1585 (vs), 1530 (s), 1469 (s), 1421 (vs), 1410 (vs), 1330 (s), 1288 (m), 1247 (m), 1170 (m), 1152 (m), 1107 (m), 1047 (w), 983 (m), 928 (w), 825 (w), 775 (s), 736 (m), 645 (w), 622 (w), 523 (w), 449 (w), 409 (w) cm^{-1}.

Synthesis of [Cr(ddpd^{CF3})](OTf)$_3$ ([1^{CF3}](OTf)$_3$)

A pale yellow solution of the ligand ddpd^{CF3} (1.60 g, 4.45 mmol, 2.0 eq.) in dry acetonitrile (30 mL) was added dropwise to a green-blue solution of chromium(III) triflate (1.13 g, 2.26 mmol, 1.0 eq.) in dry acetonitrile (70 mL) without any observed colour change. The mixture was then heated at 70 °C for 12 hours, yielding a red solution. After cooling to room temperature, the solvent was removed under reduced pressure (180 mbar, 40 °C), and the red residue was dried under reduced pressure (8 x 10^{-3} mbar) for 24 hours. The residue was washed with THF (4 x 150 mL), each time stirring for 60 minutes, followed by decanting to separate the yellow solid product from impurities in the red solution. The yellow powder was subsequently washed with diethyl ether (2 x 150 mL) and dried under reduced pressure (8 x 10^{-3} mbar). Slow diffusion of cold diethyl ether into a concentrated acetonitrile solution resulted in orange crystals of **[1^{CF3}](OTf)$_3$** (1.98 g, 1.62 mmol, 71%) suitable for X-ray diffraction. (Procedure adapted from Section 6.4)

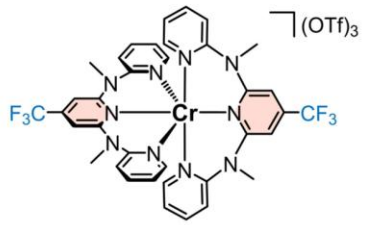

MS (ESI$^+$, CH_3CN): *m/z* (%) = 256.74 (7) [**1^{CF3}**]$^{3+}$, 459.59 (41) [**1^{CF3}**+OTf]$^{2+}$, 1068.12 (100) [**1^{CF3}**+2 OTf]$^+$.
IR (ATR): $\tilde{\nu}_{max}$ = 3097 (w), 1634 (w), 1612 (w), 1584 (s), 1498 (s), 1477 (m), 1433 (s), 1381 (s), 1333 (w), 1255 (vs), 1226 (s), 1203 (w), 1141 (vs), 1097 (m), 1071 (w), 1030 (vs), 971 (m), 921 (m), 863 (w), 781 (s), 755 (w), 713 (m), 675 (w), 637 (s), 573 (w), 518 (m), 444 (w), 411 (w) cm^{-1}.
Elemental analysis calcd. for $C_{42}H_{40}CrF_{15}N_{10}O_9S_3$: C, 38.46; H, 2.65; N, 11.50; S, 7.90. Found: C, 38.43; H, 2.63; N, 11.53; S, 7.88.
UV/Vis (CH_3CN): λ_{max} (ε) = 770 (0.16), 737 (0.36), 698 (0.23), 450 (2950), 367 (10090, sh), 324 (17880), 300 (21900) nm (M^{-1} cm^{-1}).
Emission (CH_3CN, room temperature): λ_{max} = 777, 738 nm (λ_{exc} = 450 nm).

Synthesis of [Cr(ddpd^{OMe})](OTf)$_3$ ([1^{OMe}](OTf)$_3$)

A pale yellow solution of the ligand ddpd^{OMe} (1.41 g, 4.39 mmol, 2.0 eq.) in dry acetonitrile (30 mL) was added dropwise to a green-blue solution of chromium(III) triflate (1.10 g, 2.20 mmol, 1.0 eq.) in dry acetonitrile (70 mL) without any observed colour change. The mixture was then heated at 70 °C for 12 hours, yielding a red solution. After cooling to room temperature, the solvent was removed under reduced pressure (180 mbar, 40 °C), and the red residue was dried under reduced pressure (8 x 10^{-3} mbar) for 24 hours. The residue was washed with THF (4 x 150 mL), each time stirring for 60 minutes, followed by decanting to separate the yellow solid product from impurities in the red solution. The yellow powder was subsequently washed with diethyl ether (2 x 70 mL) and dried under reduced pressure (8 x 10^{-3} mbar). Slow diffusion of cold diethyl ether into a concentrated acetonitrile solution resulted in orange crystals of **[1^{OMe}](OTf)$_3$** (1.17 g, 1.02 mmol, 51%) suitable for X-ray diffraction. (Procedure adapted from Section 6.4)

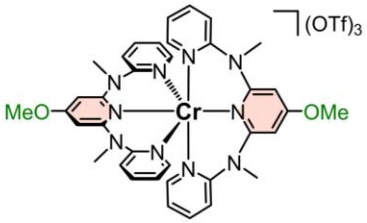

MS (ESI$^+$, CH_3CN): *m/z* (%) = 231.42 (12) [**1^{OMe}**]$^{3+}$, 421.61 (49) [**1^{OMe}**+OTf]$^{2+}$, 992.16 (100) [**1^{OMe}**+2 OTf]$^+$.
IR (ATR): $\tilde{\nu}_{max}$ = 3097 (w), 1610 (vs), 1578 (m), 1474 (m), 1437 (s), 1329 (m), 1260 (vs), 1224 (m), 1146 (s), 1133 (m), 1098 (w), 1069 (m), 1030 (s), 979 (w), 952 (w), 844 (w), 781 (m), 755 (w), 660 (w), 637 (s), 573 (w), 517 (w), 448 (w) cm^{-1}.
Elemental analysis calcd. for $C_{39}H_{38}CrF_9N_{10}O_{11}S_3$: C, 41.02; H, 3.35; N, 12.27; S, 8.42. Found: C, 41.29; H, 3.39; N, 13.32; S, 8.31.
UV/Vis (CH_3CN): λ_{max} (ε) = 778 (0.13), 734 (0.26), 695 (0.18), 411 (2990), 330 (10270, sh), 299 (27590), 223 (73270) nm (M^{-1} cm^{-1}).
Emission (CH_3CN, room temperature): λ_{max} = 786, 736 nm (λ_{exc} = 411 nm).

Synthesis of [Cr(ddpd^{NMe2})](OTf)$_3$ ([1^{NMe2}](OTf)$_3$)

A pale yellow solution of the ligand ddpd^{NMe2} (0.80 g, 2.39 mmol, 2.0 eq.) in dry acetonitrile (25 mL) was added dropwise to a green-blue solution of chromium(III) triflate (0.60 g, 1.20 mmol, 1.0 eq.) in dry acetonitrile (45 mL) without any observed colour change. The mixture was then heated at 70 °C for 12 hours, yielding a red solution. After cooling to room temperature, the solvent was removed under reduced pressure (180 mbar, 40 °C), and the red residue was dried under reduced pressure (8 x 10^{-3} mbar) for 24 hours. The residue was washed with THF (6 x 60 mL), each time stirring for 60 minutes, followed by decanting to separate the yellow solid product from impurities in the red solution. The yellow powder (0.44 g, 0.38 mmol, 32%) consisting of **[1^{NMe2}](OTf)$_3$** was subsequently washed with diethyl ether (2 x 50 mL) and dried under reduced pressure (8 x 10^{-3} mbar). (Procedure adapted from Section 6.4)

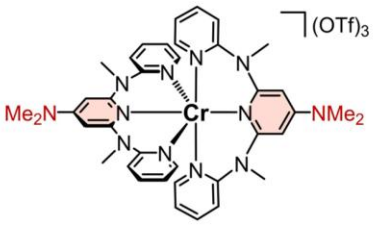

MS (ESI$^+$, CH_3CN): *m/z* (%) = 240.11 (54) [**1^{NMe2}**]$^{3+}$, 434.64 (100) [**1^{NMe2}**+OTf]$^{2+}$, 1018.23 (80) [**1^{NMe2}**+2 OTf]$^+$.
IR (ATR): $\tilde{\nu}_{max}$ = 3095 (w), 1621 (vs), 1608 (vs), 1569 (s), 1532 (w), 1495 (s), 1467 (s), 1434 (s), 1386 (w), 1347 (m), 1328 (w), 1258 (vs), 1224 (m), 1150 (s), 1055 (m), 1029 (vs), 972 (w), 822 (w), 781 (m), 754 (w), 636 (vs), 573 (w), 517 (m), 447 (m) cm^{-1}.
UV/Vis (CH_3CN): λ_{max} (ε) = 798 (0.04), 738 (0.20), 698 (0.27), 392 (5420), 315 (24540, sh), 296 (28920), 262 (43580), 224 (34000) nm (M^{-1} cm^{-1}).
Emission (CH_3CN, room temperature): λ_{max} = 809, 739 nm (λ_{exc} = 392 nm).

Analytical Data of the Ligands

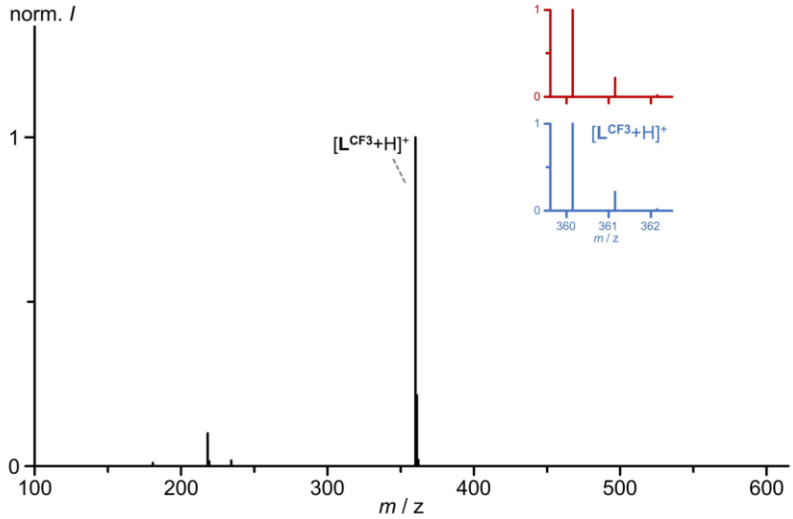

Fig. S1 ESI$^+$ mass spectrum of $\mathbf{L^{CF3}}$ in CH_3CN with insets of the experimentally found (red) and calculated (blue, normalized) isotope pattern for $[\mathbf{L^{CF3}}+H]^+$ ($C_{18}H_{17}F_3N_5$).

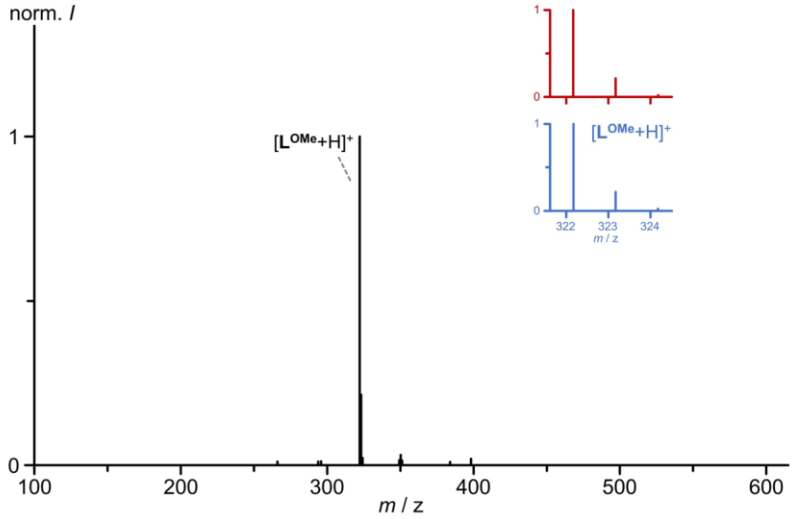

Fig. S2 ESI$^+$ mass spectrum of $\mathbf{L^{OMe}}$ in CH_3CN with insets of the experimentally found (red) and calculated (blue, normalized) isotope pattern for $[\mathbf{L^{OMe}}+H]^+$ ($C_{18}H_{19}N_5O$).

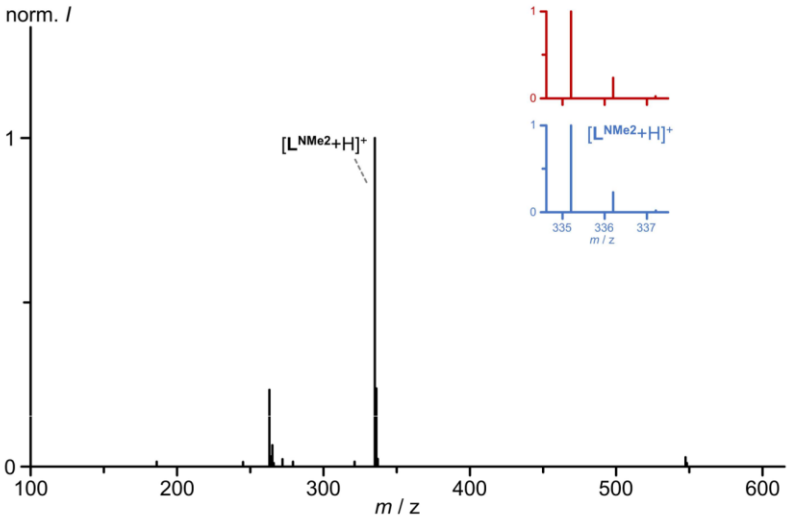

Fig. S3 ESI⁺ mass spectrum of $\mathbf{L^{NMe2}}$ in CH_3CN with insets of the experimentally found (red) and calculated (blue, normalized) isotope pattern for $[\mathbf{L^{NMe2}}+H]^+$ ($C_{19}H_{23}N_6$).

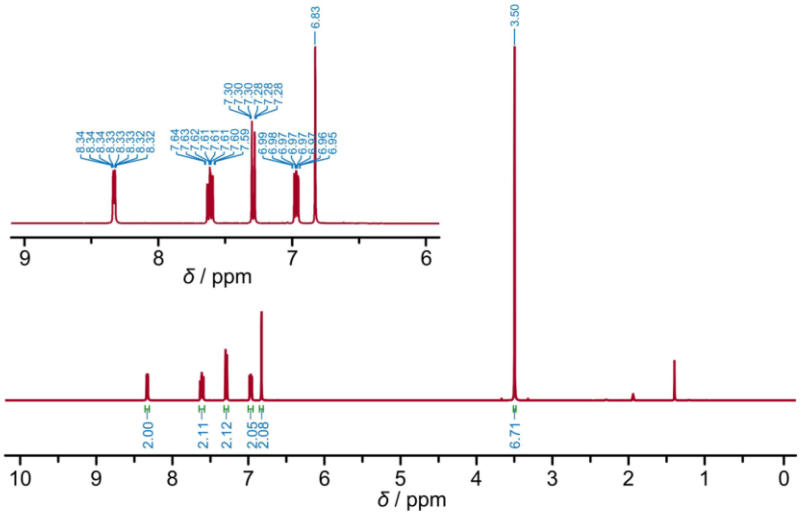

Fig. S4 ^1H NMR spectrum of $\mathbf{L^{CF3}}$ in CD_3CN with inset of the aromatic region.

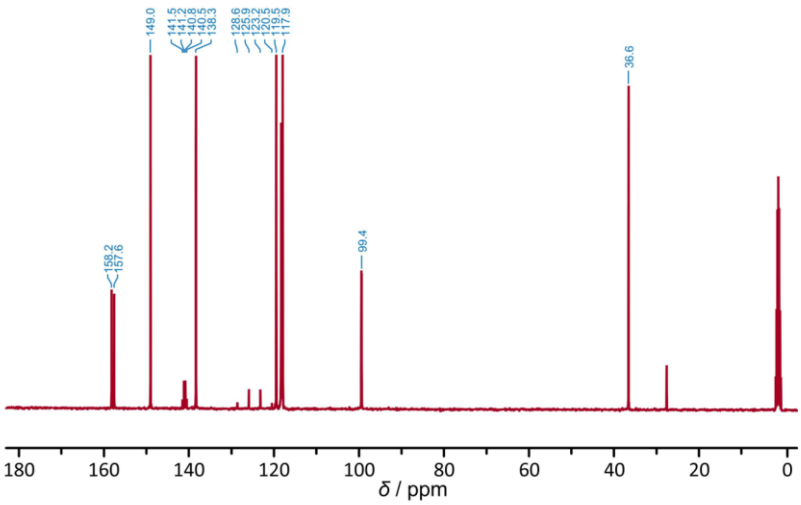

Fig. S5 $^{13}C\{^{1}H\}$ NMR spectrum of $\mathbf{L^{CF3}}$ in CD_3CN.

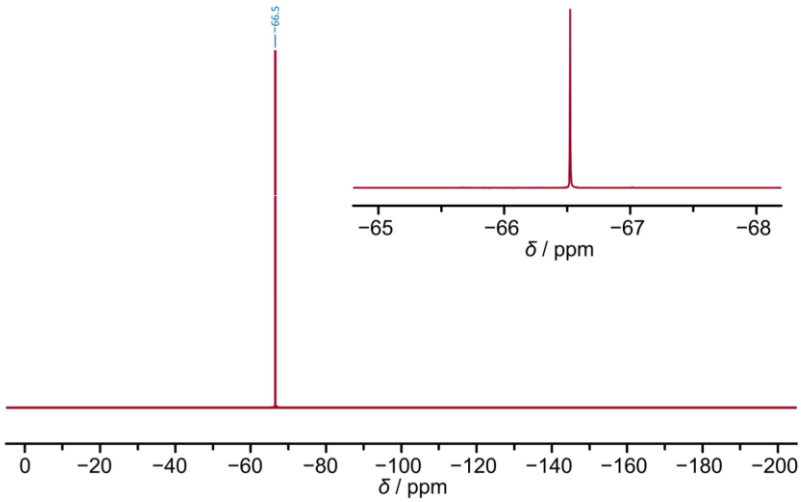

Fig. S6 ^{19}F NMR spectrum of $\mathbf{L^{CF3}}$ in CD_3CN.

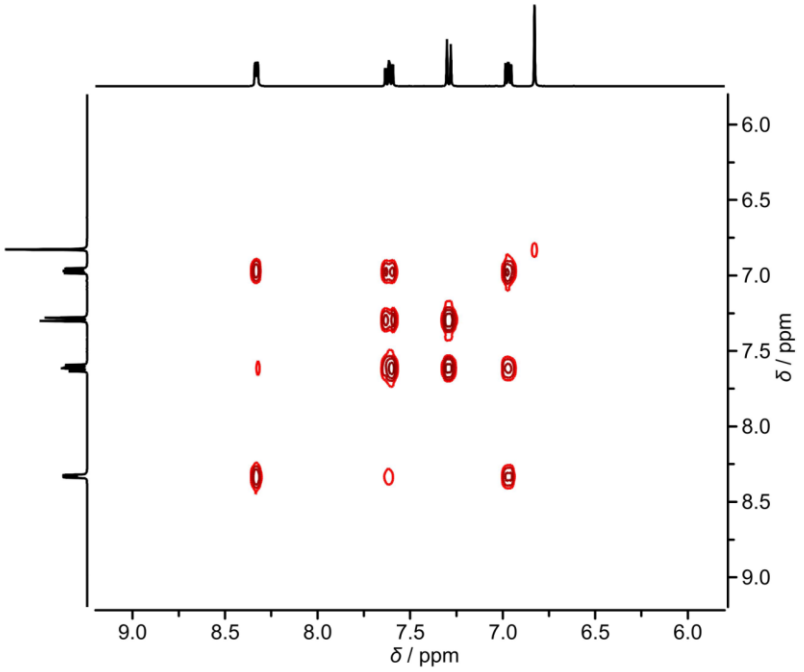

Fig. S7 $^{1}H,^{1}H$ COSY of $\mathbf{L^{CF3}}$ in CD_3CN.

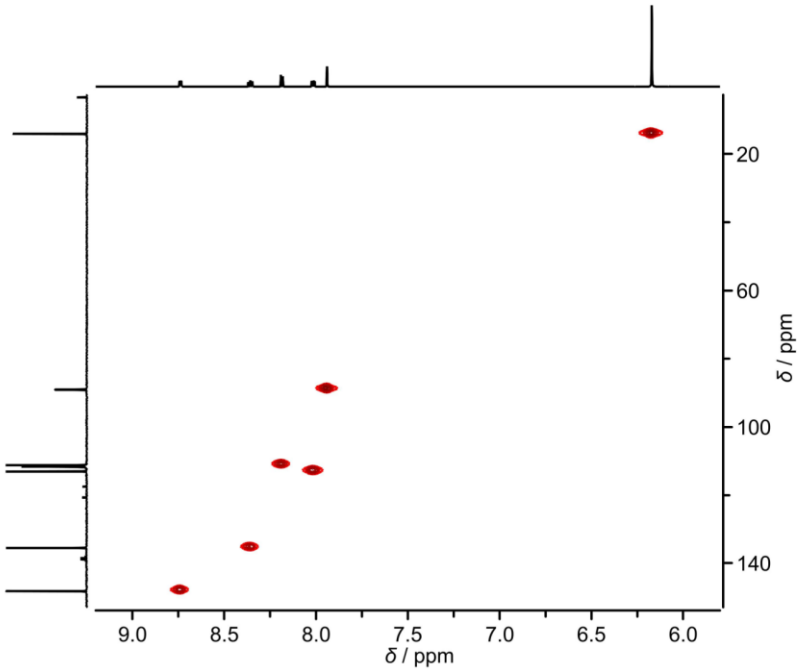

Fig. S8 $^{13}C,^{1}H$ HSQC of $\mathbf{L^{CF3}}$ in CD_3CN.

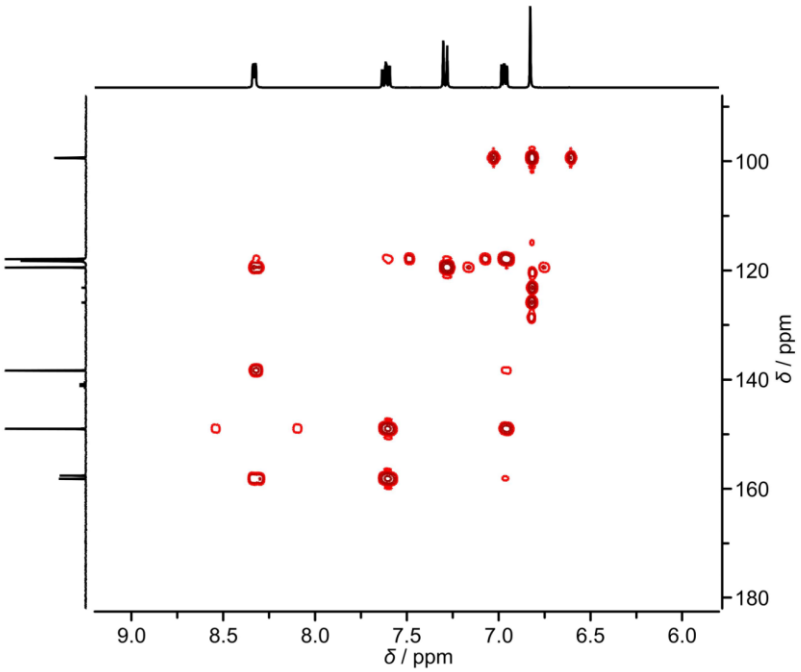

Fig. S9 $^{13}C,^{1}H$ HMBC of $\mathbf{L^{CF3}}$ in CD_3CN.

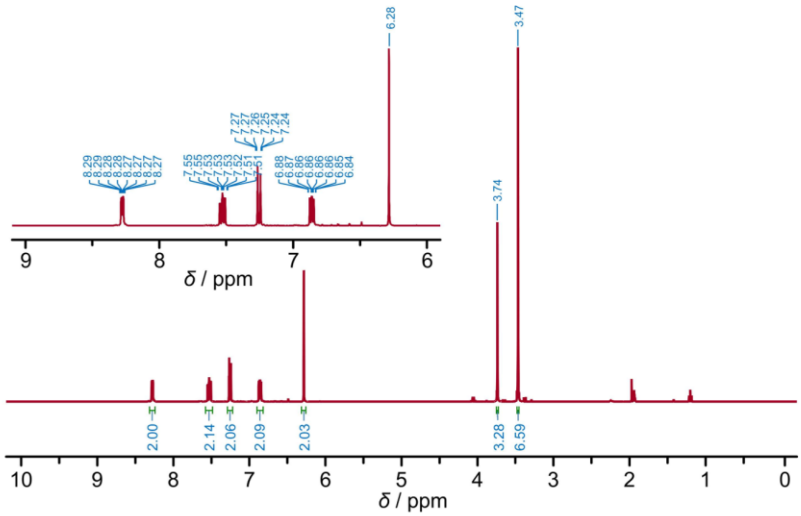

Fig. S10 ^{1}H NMR spectrum of $\mathbf{L^{OMe}}$ in CD_3CN with inset of the aromatic region.

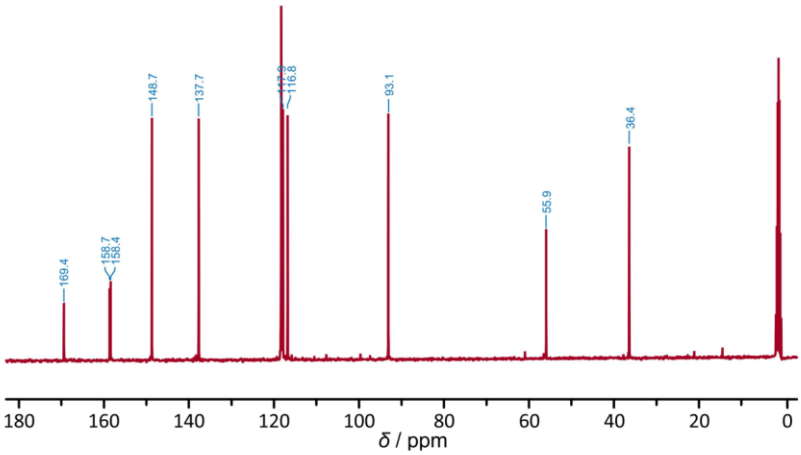

Fig. S11 $^{13}C\{^{1}H\}$ NMR spectrum of $\mathbf{L^{OMe}}$ in CD_3CN.

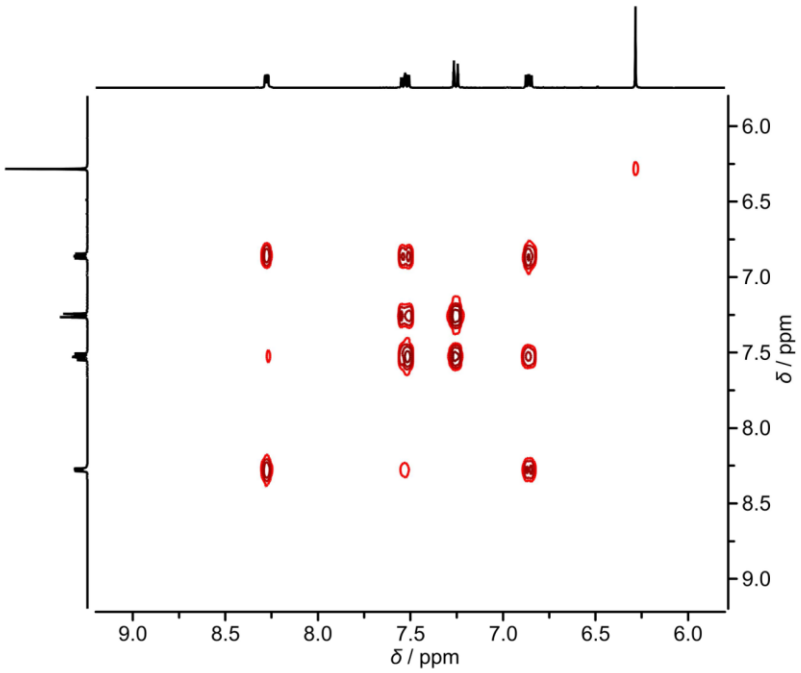

Fig. S12 $^{1}H,^{1}H$ COSY of $\mathbf{L^{OMe}}$ in CD_3CN.

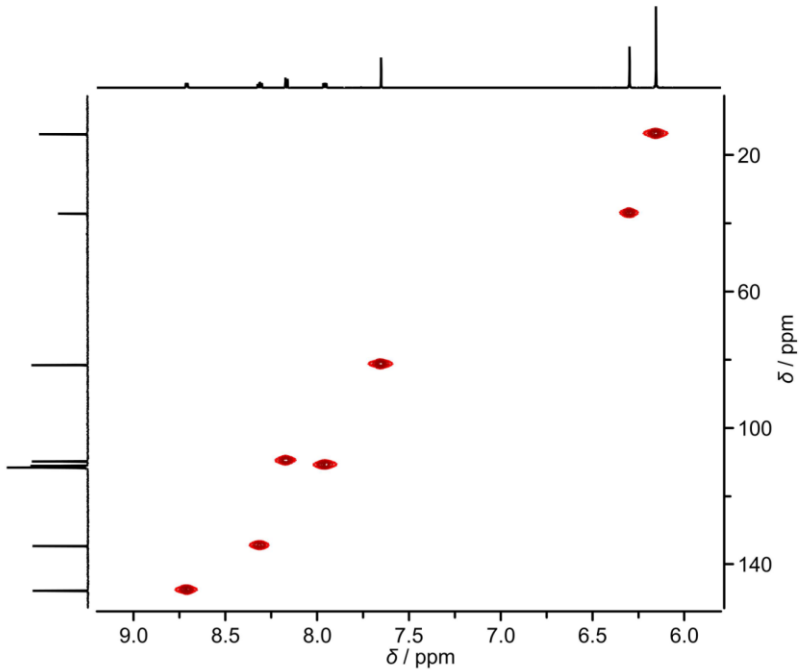

Fig. S13 $^{13}C,^{1}H$ HSQC of $\mathbf{L^{OMe}}$ in CD_3CN.

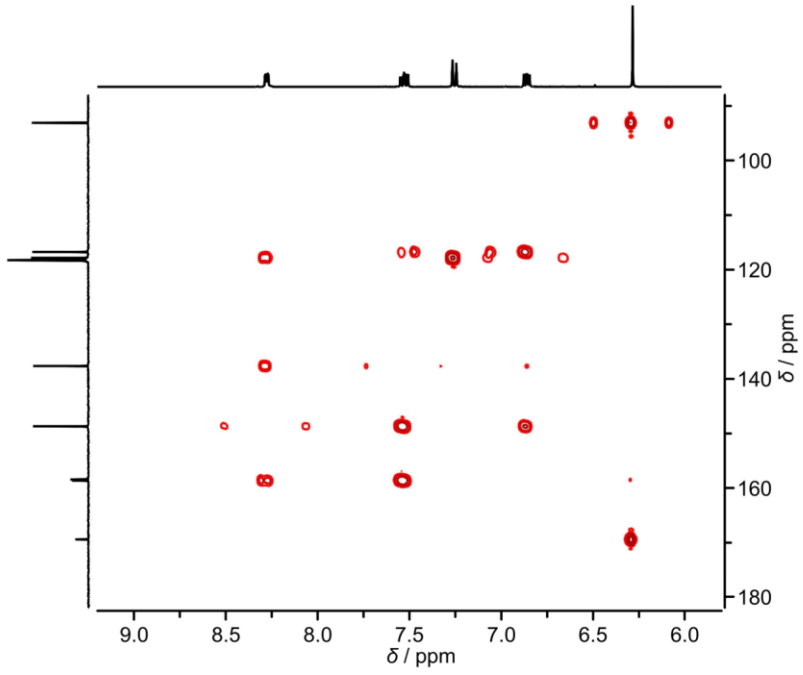

Fig. S14 $^{13}C,^{1}H$ HMBC of $\mathbf{L^{OMe}}$ in CD_3CN.

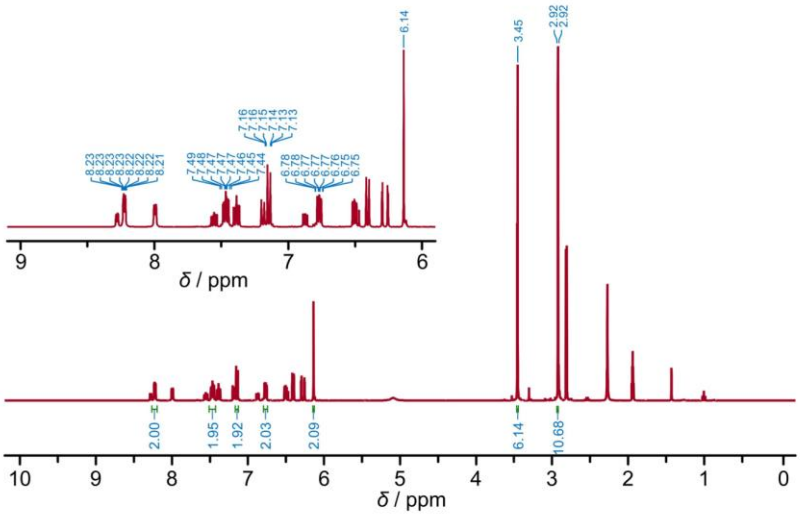

Fig. S15 ^{1}H NMR spectrum of $\mathbf{L^{NMe2}}$ in CD_3CN with inset of the aromatic region.

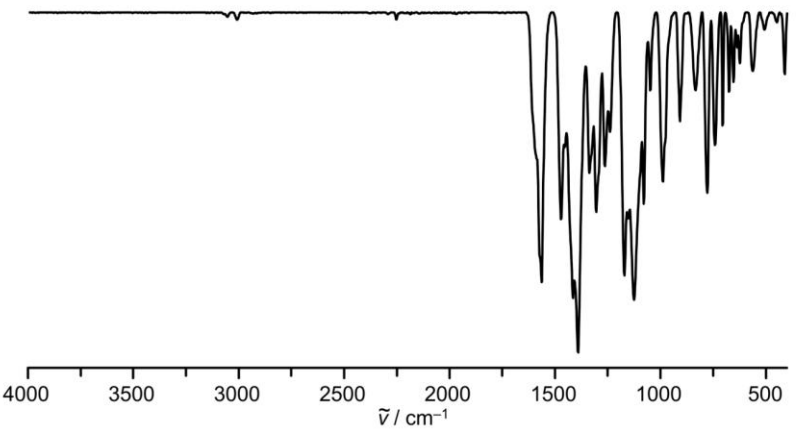

Fig. S16 ATR-IR spectrum of $\mathbf{L^{CF3}}$.

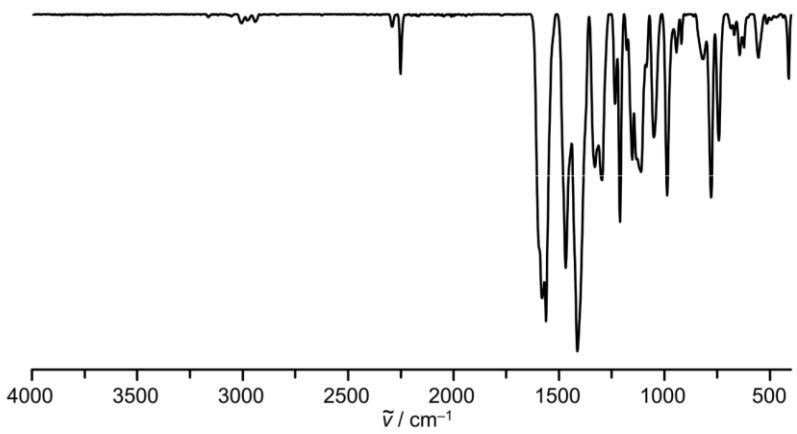

Fig. S17 ATR-IR spectrum of $\mathbf{L^{OMe}}$.

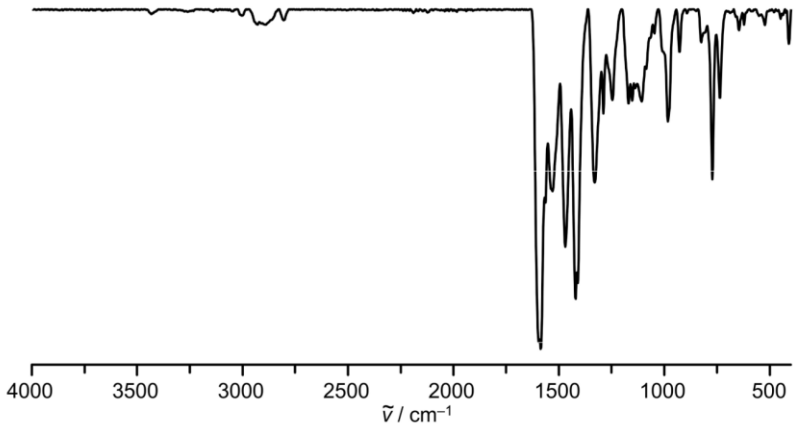

Fig. S18 ATR-IR spectrum of $\mathbf{L^{NMe}}$.

Analytical and DFT/TDDFT Data of the Complexes

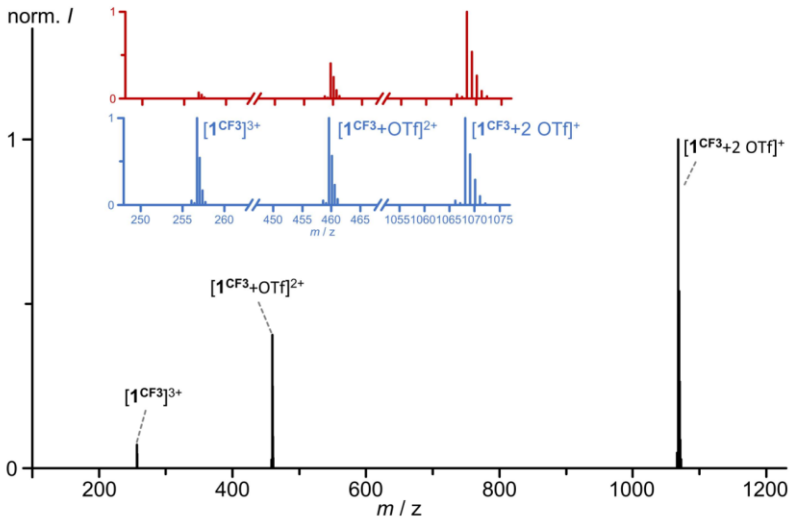

Fig. S19 ESI$^+$ mass spectrum of **[1^{CF3}](OTf)$_3$** in CH_3CN with insets of the experimentally found (red) and calculated (blue, normalized) isotope pattern for [1^{CF3}]$^{3+}$ ($C_{36}H_{32}CrF_6N_{10}$), [1^{CF3}+OTf]$^{2+}$ ($C_{37}H_{32}CrF_9N_{10}O_3S$) and [1^{CF3}+2 OTf]$^+$ ($C_{38}H_{32}CrF_{12}N_{10}O_6S_2$).

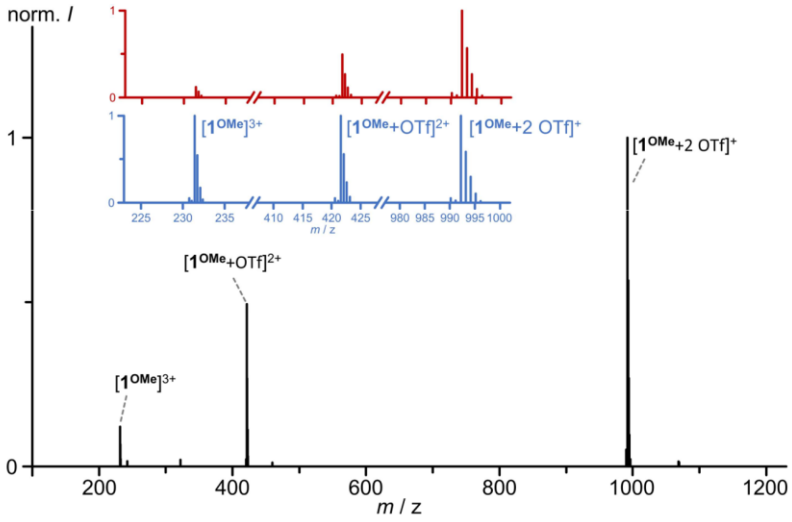

Fig. S20 ESI$^+$ mass spectrum of **[1^{OMe}](OTf)$_3$** in CH_3CN with insets of the experimentally found (red) and calculated (blue, normalized) isotope pattern for [1^{OMe}]$^{3+}$ ($C_{36}H_{38}CrN_{10}O_2$), [1^{OMe}+OTf]$^{2+}$ ($C_{37}H_{38}CrF_3N_{10}O_5S$) and [1^{OMe}+2 OTf]$^+$ ($C_{38}H_{38}CrF_6N_{10}O_8S_2$).

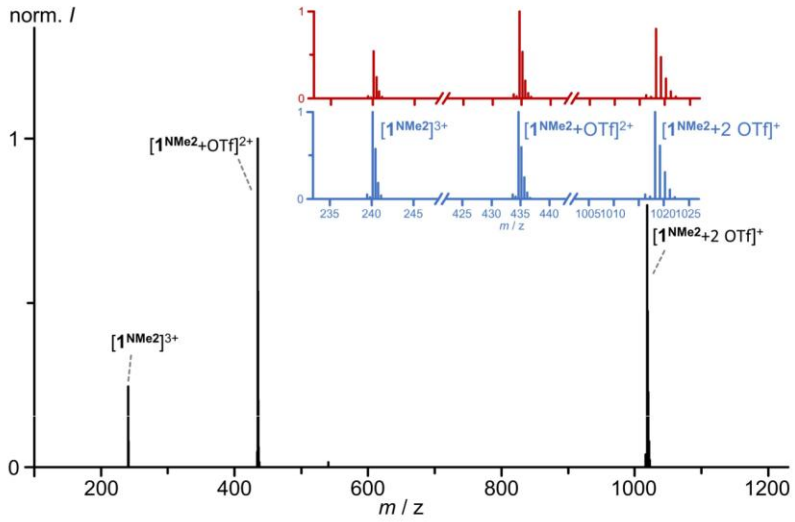

Fig. S21 ESI$^+$ mass spectrum of **[1^{NMe2}](OTf)$_3$** in CH_3CN with insets of the experimentally found (red) and calculated (blue, normalized) isotope pattern for [1^{NMe2}]$^{3+}$ ($C_{38}H_{44}CrN_{12}$), [1^{NMe2}+OTf]$^{2+}$ ($C_{39}H_{44}CrF_3N_{12}O_3S$) and [1^{NMe2}+2 OTf]$^+$ ($C_{40}H_{44}CrF_6N_{12}O_6S_2$).

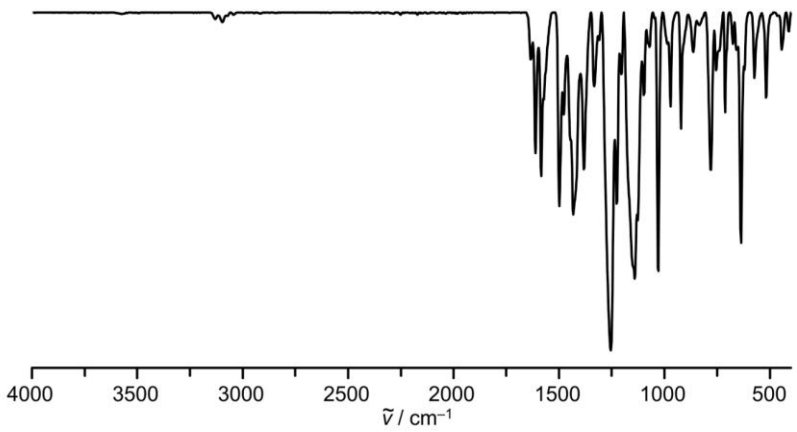

Fig. S22 ATR-IR spectrum of **[1^{CF3}](OTf)$_3$**.

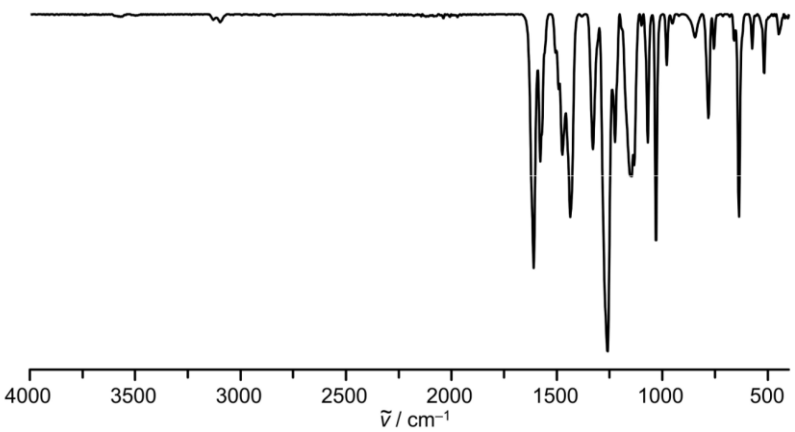

Fig. S23 ATR-IR spectrum of **[1^{OMe}](OTf)$_3$**.

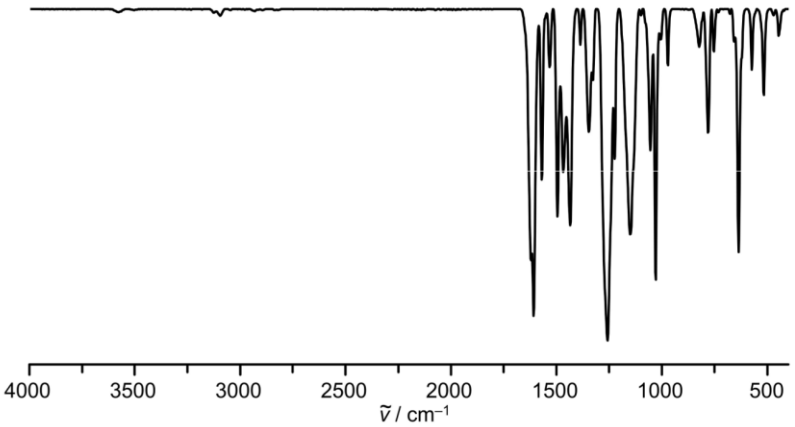

Fig. S24 ATR-IR spectrum of **[1^{NMe2}](OTf)$_3$**.

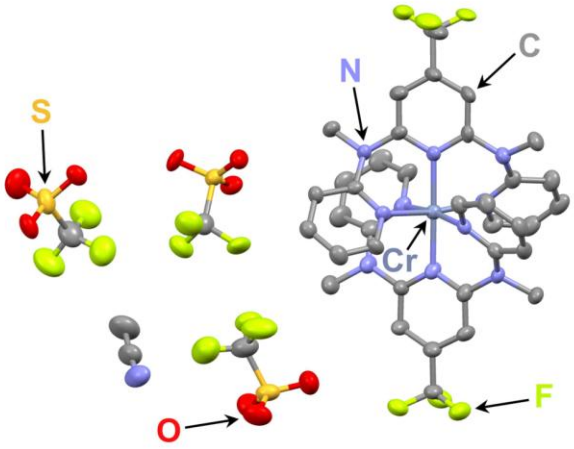

Fig. S25 Molecular structure of **[1^{CF3}](OTf)$_3$ x CH$_3$CN** in the solid state (orthorhombic space group $P2_12_12_1$). H atoms omitted, thermal ellipsoids at 50% probability level.

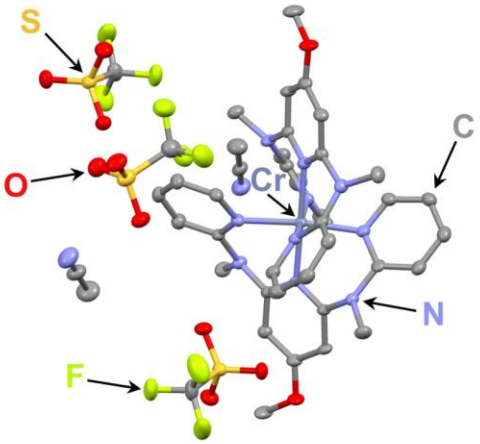

Fig. S26 Molecular structure of **[1^{OMe}](OTf)$_3$ x CH$_3$CN** in the solid state (monoclinic space group *Cc*). H atoms omitted, thermal ellipsoids at 50% probability level.

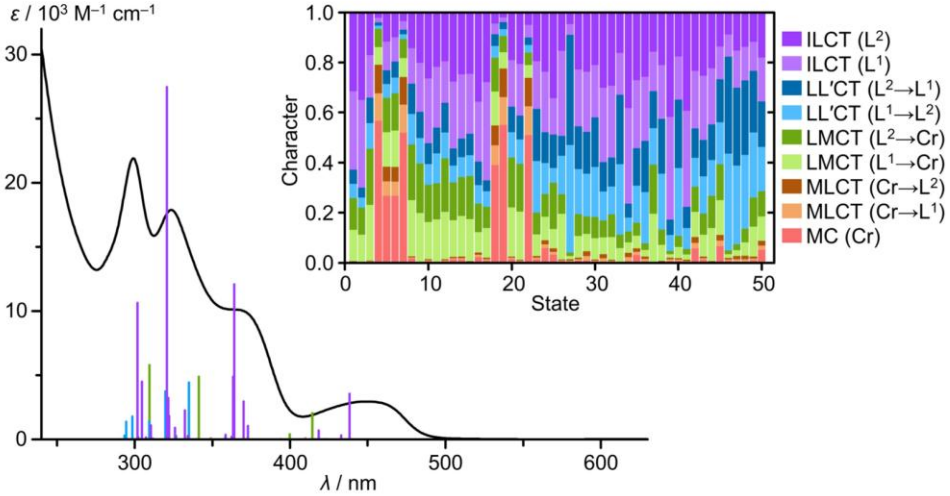

Fig. S27 UV/VIS absorption spectrum of **[1^{CF3}](OTf)$_3$** in CH_3CN (black) with TD-DFT calculated oscillator strengths coloured according to the most dominant character of the corresponding transition (red: MC, orange: MLCT, green: LMCT, purple: LC). Inset: Charge transfer number analysis of the 50 lowest energy spin-allowed transitions calculated by Loewdin population analysis with the complex cation fragmented into chromium (Cr), **L^{CF3}** ligand 1 (L^1) and **L^{CF3}** ligand 2 (L^2).

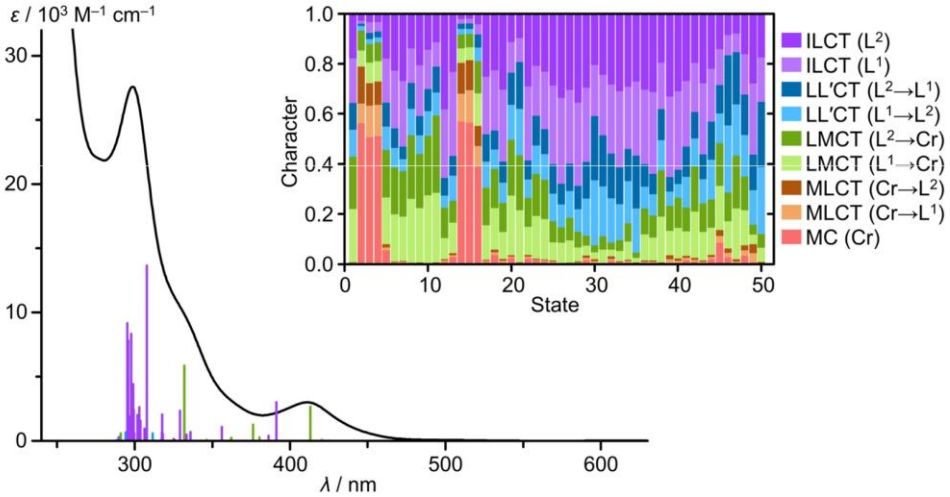

Fig. S28 UV/VIS absorption spectrum of **[1^{OMe}](OTf)$_3$** in CH_3CN (black) with TD-DFT calculated oscillator strengths coloured according to the most dominant character of the corresponding transition (red: MC, orange: MLCT, green: LMCT, purple: LC). Inset: Charge transfer number analysis of the 50 lowest energy spin-allowed transitions calculated by Loewdin population analysis with the complex cation fragmented into chromium (Cr), **L^{OMe}** ligand 1 (L^1) and **L^{OMe}** ligand 2 (L^2).

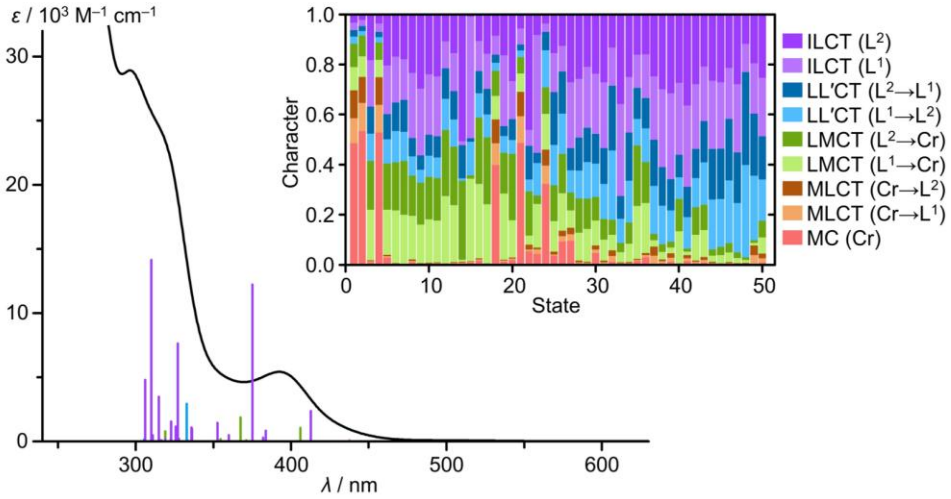

Fig. S29 UV/VIS absorption spectrum of **[1^{NMe2}](OTf)$_3$** in CH_3CN (black) with TD-DFT calculated oscillator strengths coloured according to the most dominant character of the corresponding transition (red: MC, orange: MLCT, green: LMCT, purple: LC). Inset: Charge transfer number analysis of the 50 lowest energy spin-allowed transitions calculated by Loewdin population analysis with the complex cation fragmented into chromium (Cr), **L^{NMe2}** ligand 1 (L^1) and **L^{NMe2}** ligand 2 (L^2).

Table S1 TD-DFT calculated oscillator strengths and difference electron densities of the ten lowest energy spin-allowed transitions of **[1^{CF3}]$^{3+}$** (Py^{c}: pyridine central, Py^{t}: pyridine terminal).

#	λ / nm	oscillator strength	character	from	to	**difference electron density** (purple: density loss, orange: density gain)
1	438.3	0.0237811	ILCT (63%) + LMCT (25%)	p (NMe) + π (Py^{c})	t_{2g} (d_{xz}+d_{yz}) + π* (Py^{c})	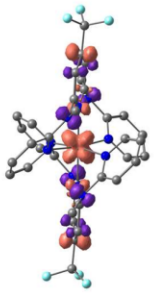
2	432.9	0.0021817	ILCT (70%) + LMCT (22%)	p (NMe) + π (Py^{c})	t_{2g} (d_{xz}+d_{yz}) and t_{2g} (d_{xz}–d_{yz}) + π* (Py^{c})	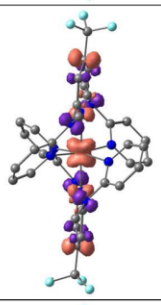
3	424.8	0.0000609	LMCT (45%) + ILCT (34%) + LL'CT (20%)	p (NMe) + π (Py^{c})	t_{2g} (d_{xy}) + π* (Py^{t})	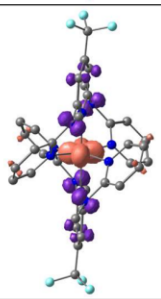
4	422.5	0.0001486	MC (57%) + MLCT (22%)	t_{2g} (d_{xz}+d_{yz})	e_g (d_{z^2}) + p (N)	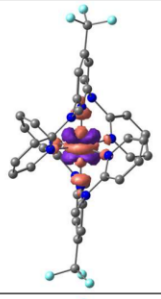
5	418.5	0.0046873	LMCT (28%) + MC (27%) + ILCT (23%)	t_{2g} (d_{xy}) + p (NMe)	e_g ($d_{x^2-y^2}$) + p (N)	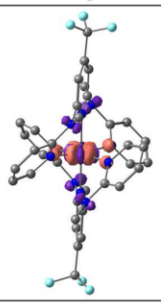

6	414.3	0.0137091	LMCT (30%) + MC (27%)	t_{2g} (d_{xy}) + p (NMe)	e_g ($d_{x^2-y^2}$)	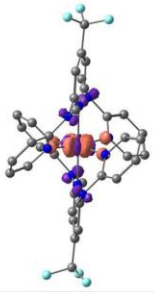
7	409.9	0.0006938	MC (52%) + MLCT (22%)	t_{2g} ($d_{xz}+d_{yz}$) and t_{2g} ($d_{xz}-d_{yz}$)	e_g ($d_{x^2-y^2}$) + p (N)	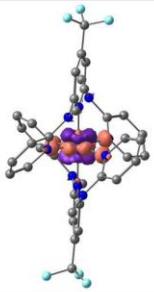
8	399.7	0.0028341	LMCT (45%) + ILCT (28%) + LL'CT (24%)	p (NMe) + π (Py^c)	t_{2g} ($d_{xz}-d_{yz}$) + π* (Py^c)	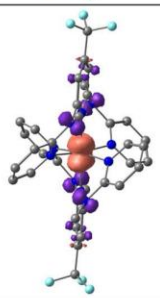
9	394.0	0.0002963	ILCT (40%) + LMCT (39%) + LL'CT (21%)	p (NMe) + π (Py^c)	t_{2g} ($d_{xz}-d_{yz}$) + π* (Py^c)	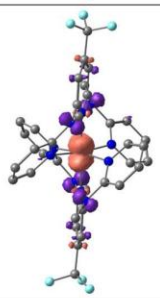
10	373.0	0.0070386	ILCT (52%) + LMCT (30%)	p (NMe)	t_{2g} ($d_{xz}-d_{yz}$) and t_{2g} (d_{xy}) + π* (Py^c)	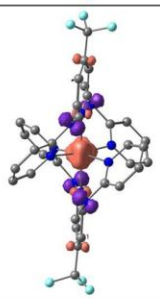

Table S2 TD-DFT calculated oscillator strengths and difference electron densities of the ten lowest energy spin-allowed transitions of **[1^{OMe}]$^{3+}$** (Py^{c}: pyridine central, Py^{t}: pyridine terminal).

#	λ / nm	oscillator strength	character	from	to	**difference electron density** (purple: density loss, orange: density gain)
1	424.6	0.0000882	LMCT (42%) + ILCT (36%) + LL'CT (21%)	p (NMe) + π (Py^{c})	t_{2g} (d_{xy}) + π* (Py^{t})	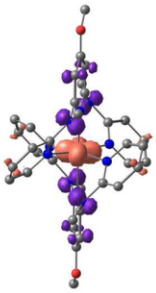
2	421.8	0.0001026	MC (56%) + MLCT (23%)	t_{2g} (d_{xz}+d_{yz})	e_g (d_{z^2}) + p (N)	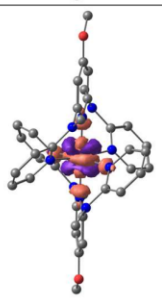
3	421.1	0.0003148	MC (51%) + MLCT (22%)	t_{2g} (d_{xy})	e_g ($d_{x^2-y^2}$) + p (N)	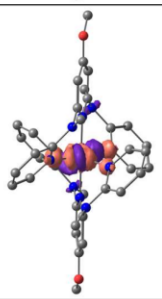
4	420.3	0.0006025	MC (51%) + MLCT (22%)	t_{2g} (d_{xy})	e_g ($d_{x^2-y^2}$) + p (N)	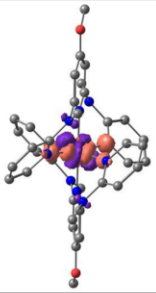
5	413.1	0.0178747	LMCT (38%) + ILCT (35%)	p (NMe) + π (Py^{c})	t_{2g} (d_{xy}) + π* (Py^{t})	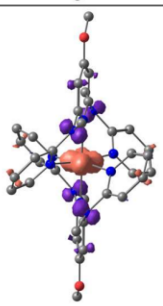

6	391.1	0.0200953	ILCT (46%) + LMCT (37%)	p (NMe) + π (Py^{c})	t_{2g} (d_{xz}+d_{yz}) and t_{2g} (d_{xy}) + π* (Py^{t})	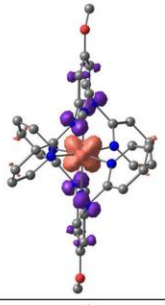
7	386.1	0.0028314	ILCT (53%) + LMCT (36%)	p (NMe)	t_{2g} (d_{xz}–d_{yz}) and t_{2g} (d_{xy}) + π* (Py^{t})	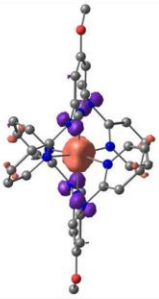
8	380.4	0.0018292	LMCT (51%) + ILCT (27%) + LL'CT (21%)	p (NMe) + π (Py^{c})	t_{2g} (d_{xz}–d_{yz}) + π* (Py^{c})	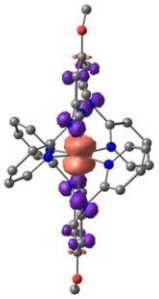
9	376.3	0.0085714	LMCT (43%) + ILCT (41%)	p (NMe) + π (Py^{c})	t_{2g} (d_{xz}–d_{yz}) and t_{2g} (d_{xy})	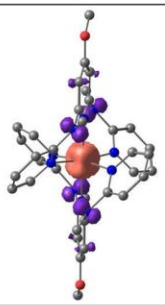
10	362.1	0.0016938	LMCT (51%) + ILCT (30%)	p (NMe)	t_{2g} (d_{xz}+d_{yz}) and t_{2g} (d_{xy})	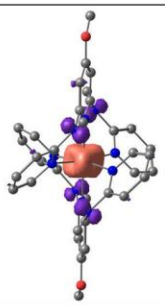

Table S3 TD-DFT calculated oscillator strengths and difference electron densities of the ten lowest energy spin-allowed transitions of **[1^{NMe2}]$^{3+}$** (Py^{c}: pyridine central, Py^{t}: pyridine terminal).

#	λ / nm	oscillator strength	character	from	to	**difference electron density** (purple: density loss, orange: density gain)
1	437.5	0.0006841	MC (49%) + MLCT (21%)	t_{2g} (d_{xz}+d_{yz})	e_g ($d_{x^2-y^2}$) + p (N)	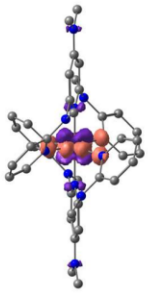
2	425.8	0.0001244	MC (54%) + MLCT (22%)	t_{2g} (d_{xz}+d_{yz})	e_g (d_{z^2}) + p (N)	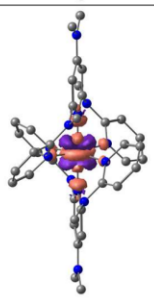
3	425.5	0.0000071	LMCT (40%) + ILCT (37%)	p (NMe) + π (Py^{c})	t_{2g} (d_{xy}) + π* (Py^{t})	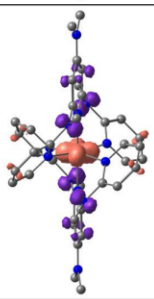
4	423.9	0.0000191	MC (53%) + MLCT (22%)	t_{2g} (d_{xy})	e_g ($d_{x^2-y^2}$) + p (N)	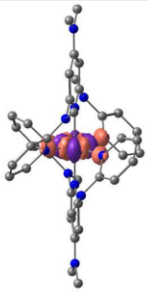
5	412.6	0.0158841	ILCT (40%) + LMCT (36%) + LL'CT (20%)	p (NMe) + π (Py^{c})	t_{2g} (d_{xy}) + π* (Py^{t})	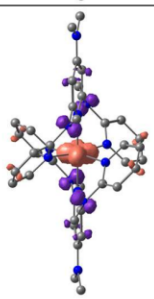

6	406.0	0.0070948	LMCT (40%) + ILCT (35%) + LL'CT (24%)	p (NMe_2) + p (NMe) + π (Py^c)	t_{2g} (d_{xy}) + π* (Py^t)	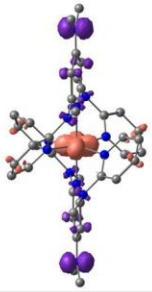
7	403.9	0.0003071	LMCT (41%) + ILCT (34%) + LL'CT (24%)	p (NMe_2) + π (Py^c)	t_{2g} (d_{xy}) + π* (Py^t)	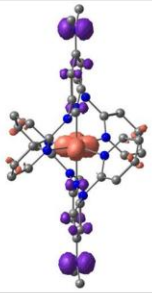
8	383.7	0.0056665	ILCT (49%) + LMCT (33%)	p (NMe) + π (Py^c)	t_{2g} (d_{xz}+d_{yz}) and t_{2g} (d_{xy}) + π* (Py^t)	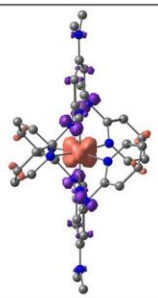
9	382.1	0.0019387	ILCT (56%) + LMCT (32%)	p (NMe)	t_{2g} (d_{xz}–d_{yz}) and t_{2g} (d_{xy}) + π* (Py^t)	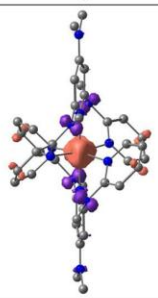
10	375.0	0.0814432	ILCT (48%) + LMCT (34%)	p (NMe_2) + π (Py^c)	t_{2g} (d_{xz}+d_{yz}) and t_{2g} (d_{xz}–d_{yz}) + π* (Py^c)	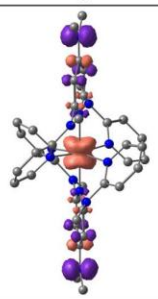

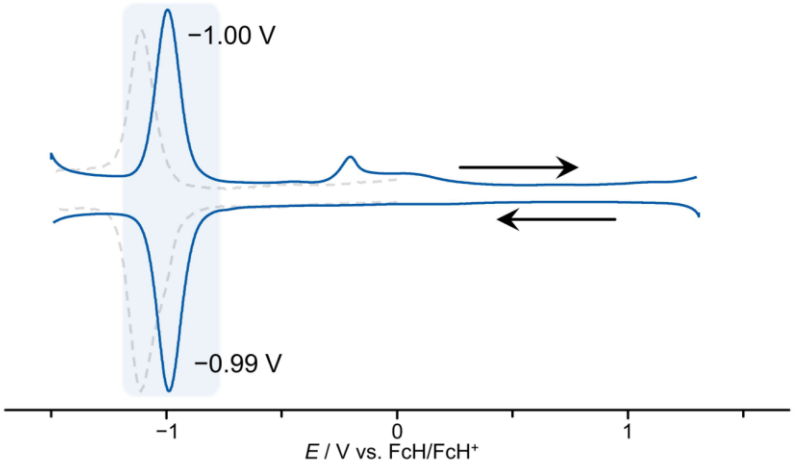

Fig. S30 Square wave voltamogramms of 3 mM **[1^{CF3}](OTf)$_3$** (blue, solid line) and **[1^{H}](PF$_6$)$_3$** (grey, dashed line)[32] in a 100 mM solution of [^{n}Bu$_4$N][PF$_6$] in CH$_3$CN (peak potentials E_p against FcH$^+$/FcH).

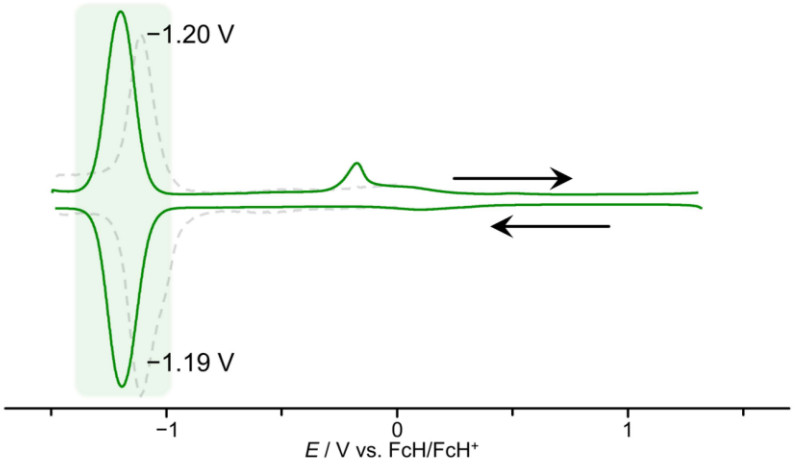

Fig. S31 Square wave voltamogramms of 3 mM **[1^{OMe}](OTf)$_3$** (green, solid line) and **[1^{H}](PF$_6$)$_3$** (grey, dashed line)[32] in a 100 mM solution of [^{n}Bu$_4$N][PF$_6$] in CH$_3$CN (peak potentials E_p against FcH$^+$/FcH).

Table S4 CASSCF(7,12)-SC/NEVPT2 calculated transition energies (in cm^{-1}) of $[1^{X}]^{3+}$ (X = H[32], CF_3, OMe, NMe_2) at DFT optimized geometries, with assignments to the lowest ^2E, $^2T_1$ and $^4T_2$ states (bold values indicate the lowest state of each multiplicity.

	$^2E(2)$	$^2E(1)$	$^2T_1(3)$	$^2T_1(2)$	$^2T_1(1)$	$^2T_2(3)$	$^2T_2(2)$	$^2T_2(1)$	$^4T_2(3)$	$^4T_2(2)$	$^4T_2(1)$
$[1^{H}]^{3+}$	16180	15597	16011	15928	**15051**	24361	23984	23823	24310	23262	**23216**
$[1^{CF3}]^{3+}$	16175	15605	16078	15882	**15078**	24308	23927	23893	24334	23381	**23140**
$[1^{OMe}]^{3+}$	16195	15580	15952	15926	**14963**	24498	24069	23770	24174	23243	**23000**
$[1^{NMe2}]^{3+}$	16170	15553	15977	15724	**14827**	24586	24182	23672	23937	23265	**22740**

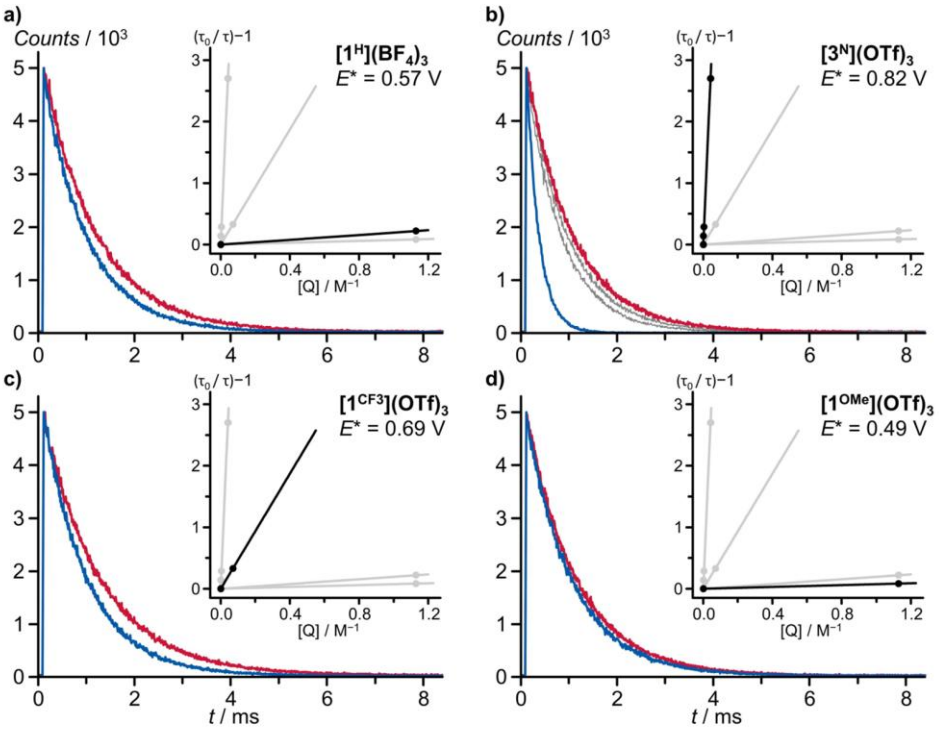

Fig. S32 Quencher concentration dependent emission decay traces recorded at 778 nm following excitation (λ_{exc} = 450 nm) of solutions of $[1^{H}](BF_4)_3$, $[3^{N}](OTf)_3$ (Section 3.7 and 6.6), $[1^{CF3}](OTf)_3$ and $[1^{OMe}](OTf)_3$ in deaerated CH_3CN for Stern-Volmer analysis with *trans*-anethol, corresponding Stern-Volmer plot (each black) and excited state potential vs. FcH/FcH^+.

References

[1] H. E. Gottlieb, V. Kotlyar, A. Nudelman, *J. Org. Chem.* **1997**, *62*, 7512–7515.
[2] J. R. Lakowicz, *Principles of Fluorescence Spectroscopy*, Springer, New York, **2010**.
[3] F. Neese, *WIREs Comput. Mol. Sci.* **2012**, *2*, 73–78.
[4] F. Neese, *WIREs Comput. Mol. Sci.* **2022**, *12*, 12753.
[5] C. Lee, W. Yang, R. G. Parr, *Phys. Rev. B: Condens. Matter Mater. Phys.* **1988**, *37*, 785–789.
[6] B. Miehlich, A. Savin, H. Stoll, H. Preuss, *Chem. Phys. Lett.* **1989**, *157*, 200–206.
[7] A. D. Becke, *J. Chem. Phys.* **1993**, *98*, 5648–5652.
[8] F. Weigend, R. Ahlrichs, *Phys. Chem. Chem. Phys.* **2005**, *7*, 3297–3305.
[9] F. Neese, F. Wennmohs, A. Hansen, U. Becker, *Chem. Phys.* **2009**, *356*, 98–109.
[10] R. Izsák, F. Neese, *J. Chem. Phys.* **2011**, *135*, 144105.
[11] E. van Lenthe, E. J. Baerends, J. G. Snijders, *J. Chem. Phys.* **1993**, *99*, 4597–4610.
[12] C. van Wüllen, *J. Chem. Phys.* **1998**, *109*, 392–399.
[13] F. Weigend, *Phys. Chem. Chem. Phys.* **2006**, *8*, 1057–1065.
[14] S. Miertuš, E. Scrocco, J. Tomasi, *Chem. Phys.* **1981**, *55*, 117–129.
[15] V. Barone, M. Cossi, *J. Phys. Chem. A* **1998**, *102*, 1995–2001.
[16] S. Grimme, J. Antony, S. Ehrlich, H. Krieg, *J. Chem. Phys.* **2010**, *132*, 154104.
[17] S. Grimme, S. Ehrlich, L. Goerigk, *J. Comput. Chem.* **2011**, *32*, 1456–1465.
[18] F. Plasser, *J. Chem. Phys.* **2020**, *152*, 84108.
[19] S. Mai, F. Plasser, J. Dorn, M. Fumanal, C. Daniel, L. González, *Coord. Chem. Rev.* **2018**, *361*, 74–97.
[20] B. O. Roos, P. R. Taylor, P. E.M. Sigbahn, *Chem. Phys.* **1980**, *48*, 157–173.
[21] P. E. M. Siegbahn, J. Almlöf, A. Heiberg, B. O. Roos, *J. Chem. Phys.* **1981**, *74*, 2384–2396.
[22] C. Angeli, R. Cimiraglia, S. Evangelisti, T. Leininger, J.-P. Malrieu, *J. Chem. Phys.* **2001**, *114*, 10252–10264.
[23] C. Angeli, R. Cimiraglia, J.-P. Malrieu, *Chem. Phys. Lett.* **2001**, *350*, 297–305.
[24] C. Angeli, R. Cimiraglia, J.-P. Malrieu, *J. Chem. Phys.* **2002**, *117*, 9138–9153.
[25] K. Pierloot, *Int. J. Quantum Chem.* **2011**, *111*, 3291–3301.
[26] R. H. Blessing, *Acta Crystallogr. Sect. A: Found. Crystallogr.* **1995**, *51 (Pt 1)*, 33–38.
[27] A. L. Spek, *Acta Crystallogr. Sect. D: Biol. Crystallogr.* **2009**, *65*, 148–155.
[28] G. M. Sheldrick, *Acta Crystallogr. Sect. A: Found. Adv.* **2015**, *71*, 3–8.
[29] G. M. Sheldrick, *Acta Crystallogr. Sect. C. Struct. Chem.* **2015**, *71*, 3–8.
[30] G. M. Sheldrick, *Acta Crystallogr. Sect. A: Found. Crystallogr.* **2008**, *64*, 112–122.
[31] C. B. Hübschle, G. M. Sheldrick, B. Dittrich, *J. Appl. Crystallogr.* **2011**, *44*, 1281–1284.
[32] S. Otto, M. Grabolle, C. Förster, C. Kreitner, U. Resch-Genger, K. Heinze, *Angew. Chem., Int. Ed.* **2015**, *54*, 11572–11576.

6.4 Supporting Information: Bridge Editing of Spin-Flip Emitters gives Insight into Excited State Energies and Dynamics

Supplementary Information

Bridge Editing of Spin-Flip Emitters gives Insight into Excited State Energies and Dynamics

Florian Reichenauer,[a] Robert Naumann,[a] Christoph Förster,[a] Winald R. Kitzmann,[a] Antti-Pekka M. Reponen,[b] Sascha Feldmann[b] and Katja Heinze*[a]

[a] Department of Chemistry, Johannes Gutenberg University Mainz, Duesbergweg 10-14, 55128 Mainz, Germany

[b] Rowland Institute, Harvard University, 100 Edwin H. Land Boulevard, Cambridge, MA 02142

General Methods

All reactions and measurements were performed under argon atmosphere unless otherwise noted. Gloveboxes (UniLab/MBraun − Ar 5.0, O_2 < 1 ppm, H_2O < 0.1 ppm) were used to store and weight sensitive compounds for synthesis as well as to prepare samples that require the absence of oxygen and/or water. The reagents were purchased from commercial suppliers (Acros Organics, Alfa Aesar, Fischer Scientific and Sigma Aldrich) and used without further purification. Acetonitrile and petroleum ether were dried and distilled from CaH_2. Anhydrous DMF (Sigma Aldrich) was used without further purification. Column chromatography was performed using aluminum oxide (neutral, Brockmann I). Analytical thin layer chromatography (TLC) was done on aluminum oxide F254 (Macherey-Nagel, coated on polyester sheets) and the spots were visualised by ultraviolet light.

NMR Spectra were recorded on a *Bruker Avance II 400* spectrometer at 400.42 MHz (^{1}H) and 100.70 MHz (^{13}C{^{1}H}) in deuterated acetonitrile (Deutero GmbH). All data were evaluated with the software *MestReNova 12.0.4-22023*. The resonances are reported in ppm versus the solvent signal as internal standard (^{1}H; (^{13}C) NMR: actonitrile-d_3: δ = 1.94, 2.13; (1.32, 118.26) ppm)[1] and *J* values are given in Hz. (s) = singlet, (d) = doublet, (t) = triplet, (q) = quartet.

IR spectra were recorded with a *Bruker Alpha FTIR* spectrometer with an ATR unit containing a diamond crystal.

ESI$^+$ mass spectra were recorded on an *Agilent 6545 HPLC-ESI-QTOF-MS* spectrometer.

Elemental analyses were performed by the central analytic service of the Department of Chemistry of the Johannes Gutenberg University Mainz using an *Elementar vario EL Cube* or by the Mikroanalytisches Labor Kolbe, c/o Fraunhofer Institut UMSICHT, Oberhausen, Germany.

Electrochemical experiments were carried out on a *BioLogic SP-200* voltammetric analyser using platinum wires as *counter* and working electrodes and a 0.01 M Ag/Ag(NO_3) electrode as reference electrode. Cyclic voltammetry and square wave measurements were carried out at scan rates of 100 mV s^{-1} using 0.1 M [^{n}Bu$_4$N][PF_6] in CH_3CN as supporting electrolyte. Potentials are referenced against the ferrocenium/ferrocene couple.

UV/VIS/NIR spectra were recorded on an *Agilent Cary 5000* spectrometer using gastight 1.00 cm quartz cuvettes with a Schott valve. Measurements were carried out in acetonitrile (Optima® LC/MS grade, Fisher Scientific). Molar absorption coefficients are given at maximum absorption and for shoulders (highlighted as sh). For deconvolution of NIR absorption band patterns, the spectra were baseline corrected using a biexponential function (eq. S1) to model the tailing of higher energy bands. Deconvolution of the baseline corrected spectra was achieved with five Voigt functions using the *Origin94* software package.

$$\varepsilon(\tilde{\nu}) = \varepsilon_0 + A_1 e^{\frac{\tilde{\nu}-\tilde{\nu}_0}{t_1}} + A_2 e^{\frac{\tilde{\nu}-\tilde{\nu}_0}{t_2}} \qquad \text{(eq. S1)}$$

Steady-state emission spectra and photoluminescent decay curves of the complexes were measured with a *FLS1000 spectrometer* from *Edinburgh Instruments* equipped with a cooled photomultiplier detector PMT-980. A xenon arc lamp Xe2 (450 W) was used for excitation in steady-state measurements. Time-resolved luminescence experiments were conducted using a pulsed diode laser VPL-450 as excitation source. Absolute luminescence quantum yields Φ were determined using an integrating sphere from *Edinburgh Instruments* with a relative uncertainty estimated as ±10%. Room temperature measurements were done in acetonitrile (Optima® LC/MS grade, Fisher Scientific). Measurements at low temperature were carried out using a liquid nitrogen cooled cryostat *Optistat DN* from *Oxford Instruments* in a 2:3 mixture of methanol (Optima® LC/MS grade) and ethanol (Fisher Scientific). Biexponential Arrhenius fits were performed for the entire measured temperature range on basis of eq. 1 (see main text) justified by the absent phase transition of the solvent mixture.[2] Emission spectra of the ligands were measured with a *spectrofluorometer FS5* from *Edinburgh Instruments*.

fs-Transient absorption spectra were recorded using a setup based on modules supplied by *Light Conversion*. The seed laser of the setup (*Light Conversion* PHAROS, Yb:KGW lasing medium) generates 1030 nm pulses with energy 400 µJ and duration 200 fs at a repetition rate of 50 kHz. The pump beam was generated from the seed in a harmonic generation unit (*Light Conversion* HIRO) *via* nonlinear crystals (beta-barium borate, lithium triborate) with residual fundamental removed by dichroic mirrors within the unit. The pump was passed through an optical chopper (operating at 100 Hz) and a beamsplitter/photodiode combination was used to divide and sort the measurements into pumped and unpumped. The pump was focused onto the sample with an effective beam diameter of roughly 900 µm. The probe beam was generated from the seed laser using supercontinuum generation in a sapphire crystal. The pump-probe delay was controlled over a range of 8 ns by changing probe path length *via* a multipass delay stage. For changing the wavelength region of the generated probe, the seed can be passed through a second harmonic generating medium prior to focusing onto the sapphire. Residual fundamental was filtered out and the white light probe was then focused onto the sample with an effective beam diameter of roughly 400 µm. The probe beam was passed into a grating spectrograph (*Andor Kymera 193i*, grating blaze wavelength 800 nm, 150 lines/mm for VIS-NIR probe and 300 nm, 300 lines/mm for UV-VIS probe) and recorded using a Si NMOS photodiode array detector (256 pixels). A 343 nm pump and 515 nm pump with fluences of 70 µJ cm^{-2} and 3 mJ cm^{-2} were used for **[1^O][OTf]$_3$** and **[1^S][OTf]$_3$**, respectively, with a repetition rate of 1 kHz. Experiments were carried out using a probe generated with 1030 nm fundamental, spanning 500 to 920 nm. The probe pulse arrival time has slight wavelength dependence (roughly 0.5 ps from lowest to highest wavelength), which is

corrected for by applying a wavelength-dependent time offset determined by a polynomial fit to selected points in the coherent artifact at time zero. Samples were measured in 1 mm path length cuvettes, with an OD of OD of 1.29 at 343 nm for **[1^{O}][OTf]$_3$** and an OD of 0.07 at 515 nm for **[1^{S}][OTf]$_3$**. No decomposition of the samples due to the TA experiments could be observed via UV/Vis absorption spectroscopy. Chirp correction and global analysis of the TA data using a consecutive kinetic model was performed using the KiMoPack python package.[3] For **[1^{S}][OTf]$_3$**, the data at time delays <0.5 ps was not included in the global analysis because of the strong artifacts around time zero. For **[1^{O}][OTf]$_3$**, the ultrafast component with a time constant of 0.03 ps does not carry any physical meaning as it is faster than the excitation pulse width of ca. 200 fs.

Photolysis experiments were conducted by irradiating deaerated stirred solutions of the complexes in inert gas cuvettes. An *Ultra-High Power* collimated LED from *Prizmatix* (UHP-T-460-DI; output power (free): 5.5 W) with a maximum at 456 nm and the centroid at 460 nm was used. The output power was adjusted constant with 1.1 W (20% setting) for all experiments using a *UHPTLCC-02-USB Controller*. The beam of light was focused onto the cuvette with a plano convex lens. At the cuvette, the beam diameter was roughly 1 cm. The temperature of the irradiated solution was kept at 20 °C with a Peltier module. Due to the excitation source being non-monochromatic, the complexes exhibiting a different spectral absorption within the excitation range and the absorbance changing over time upon irradiation, the irradiation and decomposition times of the different complexes are not comparable and only a qualitative comparison can be made.

Stern-Volmer measurements were conducted by titration of deaerated solutions of *trans*-stilbene or anthracene in acetonitrile to deaerated solutions of the corresponding complex in the same solvent in inert gas cuvettes. The titration steps were done in the glovebox. The Stern-Volmer analyses were performed on the basis of eq. S2 and S3.[4]

$$\frac{\tau_0}{\tau} - 1 = K_{SV}[Q] \qquad \text{(eq. S2)}$$

$$k_q = \frac{K_{SV}}{\tau_0} \qquad \text{(eq. S3)}$$

DFT calculations were performed using the quantum computing suite ORCA 5.0.4.[5,6] Geometry optimisation was performed using (un-)restricted Kohn-Sham orbitals DFT (UKS/RKS) and the B3LYP functional[7-9] in combination with Ahlrich's split valance triple-zeta basis set ZORA-def2-TZVPP[10] for all atoms. Tight convergence criteria were chosen for DFT calculations (keywords *tightscf* and *tightopt*). All DFT calculations make use of the resolution of identity (Split-RI-J) approach for the Coulomb term in combination with the chain-of-spheres approximation for the exchange term (keyword *RIJCOSX*).[11,12] The zeroth order regular approximation was used to describe relativistic effects in all calculations (keyword *ZORA*).[13-19] To account for solvent effects, a conductor-like screening model (keyword *CPCM*(acetonitrile)) modeling acetonitrile was used in all calculations.[20,21] Atom-pairwise dispersion correction was performed with the Becke-Johnson damping scheme (keyword *D3BJ*).[22,23] A numerical frequency calculation confirmed that the optimised geometry corresponds to a minimum structure. Explicit counter ions and/or solvent molecules were neglected. Fifty vertical spin-allowed transitions were calculated by TD-DFT. The charge transfer number analyses of the TD-DFT calculated transitions were done using TheoDORE 2.4.[24] Exited state geometry optimisations were done using TD-DFT and the given state was selected according to the TD-DFT calculation at the initial geometry (keyword *iroot*). To prevent root flipping after a step during the optimization the total overlap between the excited state wavefunctions was calculated and compared with the previous one (keyword *followiroot*). The characters of the optimised geometries were assigned to $^4T_2$, ^{4}LMCT, $^2T_1$ and ^{2}E states according to the spin densities of the relaxed geometries. Starting from the optimised ground state geometries, distorted $^4T_2$ and ^{4}LMCT states (see main text) could be localised. All calculations were computed on the Elwetritsch supercomputer at RPTU Kaiserslautern-Landau (hpc.rz.rptu.de). This is a member of the AHRP (Alliance for High Performance Computing Rhineland-Palatinate).

CASSCF(x,y)-SC-NEVPT2 calculations of ground and excited state properties with respect to pure metal-centered (MC) states were performed using the complete-active-space self-consistent field (CASSCF) method[25,26] in conjunction with the strongly contracted N-electron valence perturbation theory to second order (SC-NEVPT2)[27-29] in order to recover missing dynamic electron correlation. All electronic states are classified by irreducible representations of the O point group, in spite of the lower actual symmetry of the considered complexes. To figure out the dominant bonding/antibonding orbitals describing the interaction between chromium and the ligand, an active space screening procedure was performed by comparing the results of four different active spaces with the experimental values. The active space (7,12) comprising of five d-orbitals, two occupied σ bonding orbitals and five unoccupied d orbitals of second d-shell[30] give results closest to the experimental values and was considered for all other CASSCF-calculations. 10 quartet and 10 doublet roots were calculated for all CAS calculations.

Active spaces for the active space screening procedure of the CASSCF calculations:

CAS(3,5)	five d orbitals
CAS(3,10)	five d orbitals + five unoccupied d orbitals of second d-shell
CAS(13,10)	five d orbitals + five occupied σ and π bonding orbitals
CAS(7,12)	five d orbitals + two occupied σ bonding orbitals + five unoccupied d orbitals of second d-shell

Crystal structure determinations. Intensity data were collected with a *STOE IPDS-2T* diffractometer and a *STOE STADIVARI* diffractometer from STOE & CIE GmbH with an Oxford cooling using Mo-K_α radiation (λ = 0.71073 Å). The diffraction frames were integrated using the STOE X-Area software package[31] and were corrected for absorption with MULABS[32] of the PLATON[33] software package or with the X-Area software package[31,34,35] (integration or semi-empirical from equivalents. The structures were solved with SHELXT[36] and refined by the full-matrix method based on F^2 using SHELXL[37] of the SHELX[38] software package and the ShelXle[39] graphical interface. All non-hydrogen atoms were refined anisotropically while the positions of all hydrogen atoms were generated with appropriate geometric constraints and allowed to ride on their respective parent atoms with fixed isotropic thermal parameters. Crystallographic data for the structures reported in this paper have been deposited with the Cambridge Crystallographic Data Centre as supplementary publication no. CCDC-2380708 for bptp, CCDC-2380706 for **[1^{O}][OTf]$_3$** and CCDC-2380707 for **[1^{S}][OTf]$_3$**.

Crystallographic Data of bptp: $C_{15}H_{11}N_3S_2$ (297.39); monoclinic; *C*2/c; a = 12.378(3) Å, b = 9.0617(18) Å, c = 12.393(3) Å; α = 90°; β = 99.98(3)°; γ = 90°; V = 1369.0(5) Å^3; Z = 4; density, calcd. = 1.443 g cm^{-3}, T = 120(2) K, μ = 0.380 mm^{-1}; F(000) = 616; crystal size 0.820 × 0.600 × 0.480 mm^3; θ = 3.338 to 27.841°; −16≤h≤14, −11≤k≤11, −16≤l≤16; reflections collected = 3504; reflections unique = 1621 [R(int) = 0.0181]; completeness to θ = 25.242°: 99.6%; absorption correction: integration; max. and min. transmission 0.8808 and 0.7687; data 1621; restraints 0, parameters 92; goodness-of-fit on F^2 = 1.055; final indices [$I > 2\sigma(I)$] R_1 = 0.0348, wR_2 = 0.0905; R indices (all data) R_1 = 0.0409, wR_2 = 0.0948; largest diff. peak and hole 0.419 and −0.284 e Å^{-3}.

Crystallographic Data of [1^{O}][OTf]$_3$: $C_{33}H_{24}CrF_9N_6O_{14}S_3$ (1047.76); monoclinic; $P2_1/n$; a = 15.110(3) Å, b = 13.307(3) Å, c = 19.705(4) Å; α = 90°; β = 98.83(3)°; γ = 90°; V = 3915.1(1) Å^3; Z = 4; density, calcd. = 1.778 g cm^{-3}, T = 120(2) K, μ = 0.573 mm^{-1}; F(000) = 2116; crystal size 0.260 × 0.133 × 0.070 mm^3; θ = 2.395 to 28.175°; −19≤h≤19, −17≤k≤17, −18≤l≤26; reflections collected = 31536; reflections unique = 9445 [R(int) = 0.0948]; completeness to θ = 25.242°: 99.5%; absorption correction: semi-empirical from equivalents; max. and min. transmission 1.0905 and 0.8732; data 9445; restraints 1, parameters 601; goodness-of-fit on F^2 = 1.112; final indices [$I > 2\sigma(I)$] R_1 = 0.0570, wR_2 = 0.1002; R indices (all data) R_1 = 0.1019, wR_2 = 0.1174; largest diff. peak and hole 0.888 and −0.475 e Å^{-3}.

Crystallographic Data of [1^{S}][OTf]$_3$: $C_{35.5}H_{27}CrF_9N_7O_{9.5}S_7$ (1151.06); monoclinic; $P2_1/n$; a = 14.7224(3) Å, b = 13.3391(3) Å, c = 22.8690(5) Å; α = 90°; β = 93.810(2)°; γ = 90°; V = 4481.17(17) Å^3; Z = 4; density, calcd. = 1.706 g cm^{-3}, T = 120(2) K, μ = 0.682 mm^{-1}; F(000) = 2328; crystal size 0.380 × 0.293 × 0.160 mm^3; θ = 2.062 to 31.145°; −19≤h≤20, −18≤k≤19, −30≤l≤32; reflections collected = 84775; reflections unique = 13233 [R(int) = 0.0475]; completeness to θ = 25.242°: 99.9%; absorption correction: semi-empirical from equivalents; max. and min. transmission 0.9168 and 0.0644; data 13233; restraints 139, parameters 793; goodness-of-fit on F^2 = 1.041; final indices [$I > 2\sigma(I)$] R_1 = 0.0420, wR_2 = 0.1142; R indices (all data) R_1 = 0.0618, wR_2 = 0.1213; largest diff. peak and hole 1.568 and −0.675 e Å^{-3}.

Synthetic Procedures

Synthesis of 2,6-bis(2-oxopyridin-1(2*H*)-yl)pyridine[40]

Potassium *tert*-butoxide (4.85 g, 43.2 mmol) was combined with an orange solution of 2-hydroxypyridine (4.11 g, 43.2 mmol) in anhydrous DMF (100 mL). The resulting brown solution was stirred for one hour at room temperature. 2,6-Dibromopyridine (5.12 g, 21.6 mmol) was added in portions and the mixture was heated at 145 °C for 24 hours. After cooling to room temperature, the solvent of the dark brown solution was removed under reduced pressure (5 mbar, 80 °C). The crude residue was suspended in water (100 mL) and the product was extracted with ethyl acetate (3 x 100 mL). The combined organic phases were washed with a saturated aqueous solution of sodium chloride (100 mL), dried with sodium sulfate and filtered. After removing the solvent under reduced pressure (200 mbar, 40 °C), the product was purified by column chromatography on alumina (3:1:0.05 ethyl acetate/methanol/triethylamine, R_f = 0.31) yielding the pale brown solid compound 2,6-bis(2-oxopyridin-1(2*H*)-yl)pyridine (4.19 g, 73%).

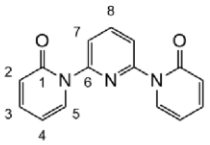

^{1}H NMR (CD_3CN): δ = 8.05 (1 H, dd, $^3J_{HH}$ = 8.4, $^3J_{HH}$ = 7.5, H^8), 7.86 (2 H, d, $^3J_{HH}$ = 7.9, H^7), 7.84 (2 H, ddd, $^3J_{HH}$ = 7.1, $^4J_{HH}$ = 2.1, $^5J_{HH}$ = 0.8, H^5), 7.47 (2 H, ddd, $^3J_{HH}$ = 9.4, $^3J_{HH}$ = 6.5, $^4J_{HH}$ = 2.1, H^3), 6.52 (2 H, ddd, $^3J_{HH}$ = 9.3, $^4J_{HH}$ = 1.3, $^5J_{HH}$ = 0.7, H^2), 6.32 (2 H, ddd, $^3J_{HH}$ = 7.1, $^3J_{HH}$ = 6.5, $^4J_{HH}$ = 1.3, H^4) ppm.

MS (ESI^+, CH_3CN): *m*/*z* (%) = 266.09 (53) $[M+H]^+$, 288.07 (100) $[M+Na]^+$, 553.16 (59) $[2\ M+Na]^+$.

IR (ATR): $\tilde{\nu}_{max}$ = 3119 (w), 3089 (w), 1659 (vs, C=O), 1598 (vs), 1576 (vs), 1537 (vs), 1443 (s), 1384 (s), 1289 (s), 1257 (s), 1243 (s), 1145 (s), 1127 (s), 1088 (w), 1007 (w), 991(w), 880 (s), 854 (s), 815 (w), 779 (s), 763 (vs), 746 (s), 730 (w), 686 (w), 616 (w), 575 (s), 537 (w), 522 (s), 474 (w), 464 (w), 429 (w), 409 (w) cm^{-1}.

Synthesis of 2,6-bis(pyridin-2-yloxy)pyridine (bpop)

A solution of 2-bromopyridine (16.7 mL, 171 mmol) in anhydrous DMF (400 mL) was deaerated by purging with argon for half an hour and combined with 2,6-dihydroxypyridine hydrochloride (12.6 g, 85.4 mmol). Addition of potassium carbonate (35.4 g, 256 mmol) to the colourless solution yielded a deep blue suspension. The reaction mixture was heated at 145 °C for 24 hours. After cooling to room temperature, the blue suspension was filtered and the solvent was removed under reduced pressure (5 mbar, 80 °C). The crude residue was suspended in water (400 mL) and the product was extracted with ethyl acetate (3 x 200 mL). The combined organic phases were washed with a saturated aqueous solution of sodium chloride (200 mL), dried with sodium sulfate and filtered. After removing the solvent under reduced pressure (200 mbar, 40 °C), the product was purified by column chromatography on alumina (7:3:0.05 cyclohexane/ethyl acetate/triethylamine, R_f = 0.38) yielding the colourless solid ligand bpop (273 mg, 1.2%).

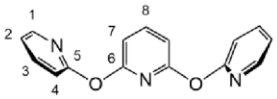

Elemental analysis calcd. for $C_{15}H_{11}N_3O_2$: C, 67.92; H, 4.18; N, 15.84. Found: C, 67.77; H, 4.42; N, 15.80.

^{1}H NMR (CD_3CN): δ = 8.20 (2 H, ddd, $^3J_{HH}$ = 5.0, $^4J_{HH}$ = 2.0, $^5J_{HH}$ = 0.8, H^1), 7.89 (1 H, t, $^3J_{HH}$ = 7.9, H^8), 7.77 (2 H, ddd, $^3J_{HH}$ = 8.2, $^3J_{HH}$ = 7.3, $^4J_{HH}$ = 2.0, H^3), 7.13 (2 H, ddd, $^3J_{HH}$ = 7.3, $^3J_{HH}$ = 4.9, $^4J_{HH}$ = 0.9, H^2), 7.01 (2 H, dt, $^3J_{HH}$ = 8.2, $^4J_{HH}$ = 0.9, H^4), 6.86 (2 H, d, $^3J_{HH}$ = 7.9, H^7) ppm.

^{13}C{^{1}H} NMR (CD_3CN): δ = 162.6 (s, C^5), 161.5 (s, C^6), 148.8 (s, C^1), 143.9 (s, C^8), 140.8 (s, C^3), 121.2 (s, C^2), 114.6 (s, C^4), 109.9 (s, C^7) ppm.

MS (ESI^+, CH_3CN): *m*/*z* (%) = 266.09 (100) $[M+H]^+$, 288.07 (6) $[M+Na]^+$, 553.16 (2) $[2\ M+Na]^+$.

IR (ATR): $\tilde{\nu}_{max}$ = 3057 (w), 3009 (w), 1585 (vs), 1567 (vs), 1468 (s), 1441 (s), 1414 (vs), 1286 (s), 1260 (s), 1206 (vs), 1142 (s), 1097 (w), 1075 (w), 1044 (w), 1006 (vs), 991 (vs), 870 (s), 847 (w), 776 (vs), 740 (s), 627 (w), 589 (w), 506 (w), 454 (w), 412 (s) cm^{-1}.

UV/Vis (CH_3CN): λ_{max} (ε) = 267 (11430), 215 (18070) nm (M^{-1} cm^{-1}).

Emission (CH_3CN, room temperature): λ_{max} = 307 nm (λ_{exc} = 267 nm).

Synthesis of 2,6-bis(pyridin-2-ylthio)pyridine[41] (bptp)

Potassium *tert*-butoxide (5.23 g, 46.6 mmol) was combined with a yellow solution of 2-mercaptopyridine (5.18 g, 46.6 mmol) in anhydrous DMF (100 mL). The resulting red solution was stirred for one hour at room temperature. 2,6-Dibromopyridine (5.52 g, 23.3 mmol) was added in portions and the mixture was heated at 145 °C for 24 hours. After cooling to room temperature, the solvent of the dark red solution was removed under reduced pressure (5 mbar, 80 °C). The crude residue was suspended in water (100 mL) and the product was extracted with ethyl acetate (3 x 100 mL). The combined organic phases were washed with a saturated aqueous solution of sodium chloride (100 mL), dried with sodium sulfate and filtered. After removing the solvent under reduced pressure (200 mbar, 40 °C), the product was purified by column chromatography on alumina (7:3:0.05 cyclohexane/ethyl acetate/triethylamine, R_f = 0.28) yielding the pale yellow solid ligand bptp (5.49 g, 79%).

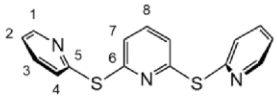

Elemental analysis calcd. for $C_{15}H_{11}N_3S_2$: C, 60.58; H, 3.73; N, 14.13. Found: C, 60.53; H, 3.95; N, 14.12.

^{1}H NMR (CD_3CN): δ = 8.46 (2 H, ddd, $^3J_{HH}$ = 4.8, $^4J_{HH}$ = 1.9, $^5J_{HH}$ = 0.9, H^1), 7.62 (2 H, td, $^3J_{HH}$ = 7.8, $^4J_{HH}$ = 1.9, H^3), 7.59 (1 H, t, $^3J_{HH}$ = 7.8, H^8), 7.40 (2 H, dt, $^3J_{HH}$ = 8.0, $^4J_{HH}$ = 1.0, H^4), 7.27 (2 H, d, $^3J_{HH}$ = 7.8, H^7), 7.21 (2 H, ddd, $^3J_{HH}$ = 7.5, $^3J_{HH}$ = 4.8, $^4J_{HH}$ = 1.1, H^2) ppm.

^{13}C{^{1}H} NMR (CD_3CN): δ = 158.2 (s, C^6), 156.7 (s, C^5), 151.1 (s, C^1), 139.2 (s, C^8), 138.3 (s, C^3), 127.2 (s, C^4), 124.2 (s, C^7), 123.2 (s, C^2) ppm.

MS (ESI$^+$, CH_3CN): *m*/*z* (%) = 298.05 (100) $[M+H]^+$, 320.03 (25) $[M+Na]^+$, 617.07 (12) $[2\ M+Na]^+$.

IR (ATR): $\tilde{\nu}_{max}$ = 3042 (w), 2987 (w), 1708 (w), 1571 (s), 1544 (vs), 1448 (s), 1409 (vs), 1279 (w), 1236 (w), 1162 (s), 1141 (s), 1113 (vs), 1083 (s), 1044 (s), 985 (s), 885 (w), 787 (s), 756 (vs), 736 (s), 719 (vs), 655 (w), 618 (w), 593 (w), 514 (w), 461 (w), 420 (w) cm^{-1}.

UV/Vis (CH_3CN): λ_{max} (ε) = 308 (10190), 285 (12600), 244 (16850) nm ($M^{-1}\ cm^{-1}$).

Emission (CH_3CN, room temperature): λ_{max} = 349 nm (λ_{exc} = 308 nm).

Synthesis of chromium(III) triflate[42]

Trimethylsilyl trifluormethansulfonate (50.0 g, 225 mmol) was poured into a suspension of purple chromium(III) chloride (3.56 g, 22.5 mmol) in dried acetonitrile (150 mL) and the heterogeneous mixture was heated to 82 °C. To start the reaction, chromium(II) chloride (50.0 mg, 0.407 mmol) was added, changing the colour of the solution to green. Heating the reaction mixture at 82 °C for 24 hours yielded a green-blue solution. After cooling to room temperature, the solvent was removed under reduced pressure (180 mbar, 40 °C). The residue was washed with dry petroleum ether (3 x 50 mL) and dried under reduced pressure (8 x 10^{-3} mbar) for three days. The absence of chloride ions in the green-blue chromium(III) triflate (11.1 g, 99%) was verified by a negative silver(I) salt precipitation with silver(I) triflate in dry acetonitrile.

MS (ESI$^+$, CH_3CN): *m*/*z* (%) = 431.90 (17) $[M–OTf+2\ CH_3CN]^+$, 472.92 (5) $[M–OTf+3\ CH_3CN]^+$, 513.95 (11) $[M–OTf+4\ CH_3CN]^+$, 598.88 (16) $[M+H_2O+2\ CH_3CN]^+$, 639.91 (100) $[M+H_2O+3\ CH_3CN]^+$.

IR (ATR): $\tilde{\nu}_{max}$ = 1344 (vs), 1247 (w), 1234 (s), 1178 (vs), 987 (vs), 955 (vs), 824 (w), 767 (w), 624 (vs), 605 (vs), 571 (w), 534 (s), 515 (s), 423 (vs) cm^{-1}.

UV/Vis (CH_3CN): λ_{max} (ε) = 706 (7.3), 592 (51), 430 (35), 311 (17), 222 (4920) nm ($M^{-1}\ cm^{-1}$).

Synthesis of [Cr(bpop$_2$)][OTf]$_3$ ([1^O][OTf]$_3$)

A pale yellow solution of bpop (240 mg, 0.905 mmol) in dry acetonitrile (10 mL) was added dropwise to a green-blue solution of chromium(III) triflate (226 mg, 0.453 mmol) in dry acetonitrile (15 mL) without a colour change. Heating the reaction mixture at 82 °C for 2 hours yielded a red solution. After cooling to room temperature, the solvent was removed under reduced pressure (180 mbar, 40 °C) and the red residue was dried under reduced pressure (8 x 10^{-3} mbar) for 24 hours. Washing the residue with THF (4 x 25 mL) by stirring for half an hour each time followed by decanting the solution, separated the yellow solid product from impurities in the red solution. The yellow powder was dried under reduced pressure (8 x 10^{-3} mbar) and dissolved in acetonitrile (2.5 mL). Slow diffusion of cooled diethyl ether (fridge) into the concentrated acetonitrile solution resulted in yellow crystals of **[1^O][OTf]$_3$** (113 mg, 24%) with diffraction quality.

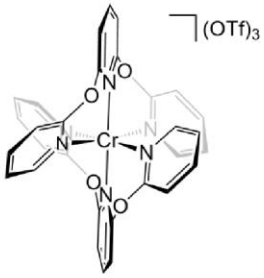

Elemental analysis calcd. for $C_{33}H_{22}CrF_9N_6O_{13}S_3$ x 2 H_2O: C, 37.19; H, 2.46; N, 7.89; S, 9.02. Found: C, 37.18; H, 2.31; N, 7.90; S, 9.03.

MS (ESI$^+$, CH_3CN): *m*/*z* (%) = 194.04 (21) [**1^O**]$^{3+}$, 365.53 (67) [**1^O**+OTf]$^{2+}$, 880.01 (100) [**1^O**+2 OTf]$^+$.

IR (ATR): $\tilde{\nu}_{max}$ = 3119 (w), 3072 (w), 3034 (w), 1612 (vs), 1569 (s), 1483 (s), 1455 (s), 1441 (s), 1425 (vs), 1309 (s), 1240 (vs), 1224 (vs), 1154 (vs), 1108 (s), 1084 (w), 1064 (s), 1028 (vs), 1007 (vs) 871 (s), 846 (s), 789 (s), 755 (w), 729 (w), 677 (w), 658 (w), 636 (vs), 573 (s), 517 (s), 464 (w), 447 (w), 423 (w), 406 (w) cm^{-1}.

UV/Vis (CH_3CN): λ_{max} (ε) = 737 (0.22), 716 (0.35), 689 (0.20), 463 (100), 369 (1640), 268 (17670, sh), 257 (19060), 238 (23480, sh) nm (M^{-1} cm^{-1}).

Emission (CH_3CN, room temperature): λ_{max} = 741, 716 nm (λ_{exc} = 450 nm).

Synthesis of [Cr(bptp$_2$)][OTf]$_3$ ([1^S][OTf]$_3$)

A pale yellow solution of bptp (530 mg, 1.78 mmol) in dry acetonitrile (20 mL) was added dropwise to a green-blue solution of chromium(III) triflate (445 mg, 0.891 mmol) in dry acetonitrile (30 mL) without a colour change. Heating the reaction mixture at 82 °C for 2 hours yielded a red solution. After cooling to room temperature, the solvent was removed under reduced pressure (180 mbar, 40 °C) and the red residue was dried under reduced pressure (8 x 10^{-3} mbar) for 24 hours. Washing the residue with THF (4 x 50 mL) by stirring for half an hour each time followed by decanting the solution separated the yellow solid product from impurities in the red solution. The yellow powder was dried under reduced pressure (8 x 10^{-3} mbar) and dissolved in acetonitrile (5.0 mL). Slow diffusion of cooled diethyl ether (fridge) into the concentrated acetonitrile solution resulted in yellow crystals of **[1^S][OTf]$_3$** (304 mg, 31%) with diffraction quality.

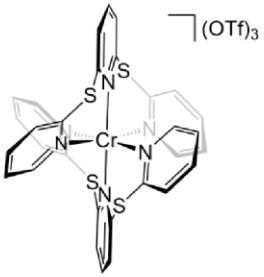

Elemental analysis calcd. for $C_{33}H_{22}CrF_9N_6O_9S_7$: C, 36.23; H, 2.03; N, 7.68; S, 20.51. Found: C, 36.13; H, 2.06; N, 7.66; S, 20.43.

MS (ESI$^+$, CH_3CN): *m*/*z* (%) = 215.34 (37) [**1^S**]$^{3+}$, 397.49 (96) [**1^S**+OTf]$^{2+}$, 943.92 (100) [**1^S**+2 OTf]$^+$.

IR (ATR): $\tilde{\nu}_{max}$ = 3107 (w), 3081 (w), 1593 (s), 1570 (s), 1560 (s), 1544 (w), 1469 (s), 1419 (s), 1378 (w), 1253 (vs), 1224 (vs), 1153 (vs), 1108 (w), 1092 (w), 1067 (w), 1028 (vs), 1009 (s), 808 (w), 776 (s), 756 (w), 739 (w), 725 (s), 690 (w), 636 (vs), 573 (s), 517 (s), 474 (w), 447 (w), 432 (w), 406 (w) cm^{-1}.

UV/Vis (CH_3CN): λ_{max} (ε) = 724 (0.14, sh), 713 (0.43), 683 (0.22), 452 (1880), 426 (1560, sh), 353 (7000, sh), 321 (16290), 299 (18920, sh), 290 (20200), 225 (44560, sh) nm (M^{-1} cm^{-1}).

Emission (CH_3CN, room temperature): λ_{max} = 727, 713 nm (λ_{exc} = 450 nm).

Analytical data of the ligands and precursor

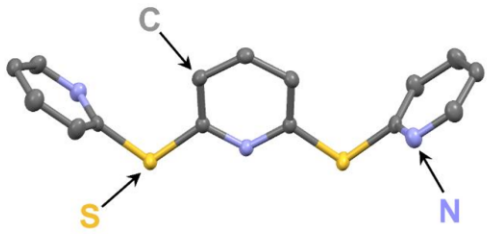

Fig. S1 Molecular structure of bptp in the solid state. Hydrogen atoms omitted, thermal ellipsoids at 50% probability level.

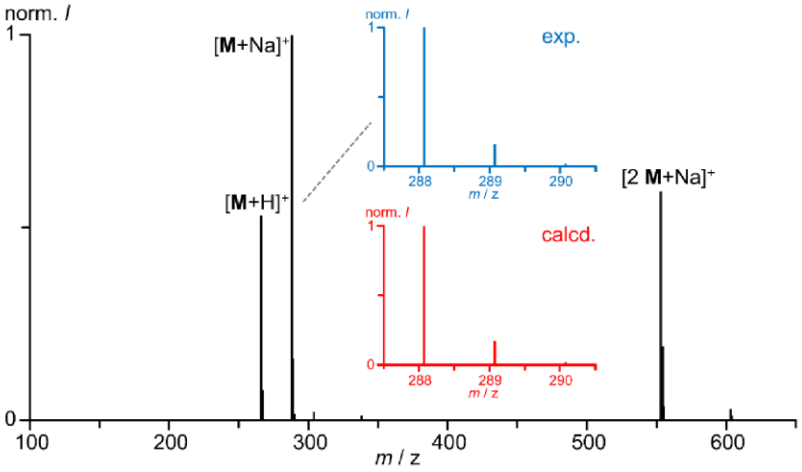

Fig. S2 ESI+ mass spectrum of 2,6-bis(2-oxopyridin-1(2H)-yl)pyridine in CH_3CN with insets of the experimentally found (blue) and calculated (red) isotope pattern for $[M+Na]^+$ ($C_{15}H_{11}N_3NaO_2$).

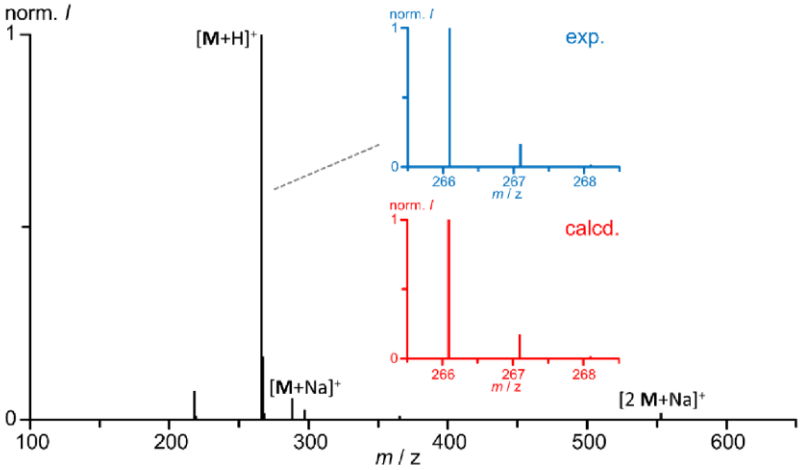

Fig. S3 ESI+ mass spectrum of bpop in CH_3CN with insets of the experimentally found (blue) and calculated (red) isotope pattern for $[M+H]^+$ ($C_{15}H_{12}N_3O_2$).

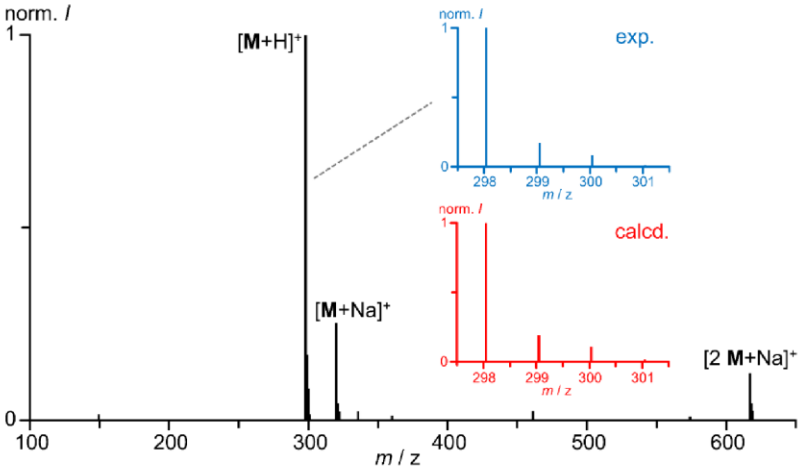

Fig. S4 ESI+ mass spectrum of bptp in CH_3CN with insets of the experimentally found (blue) and calculated (red) isotope pattern for $[M+H]^+$ ($C_{15}H_{12}N_3S_2$).

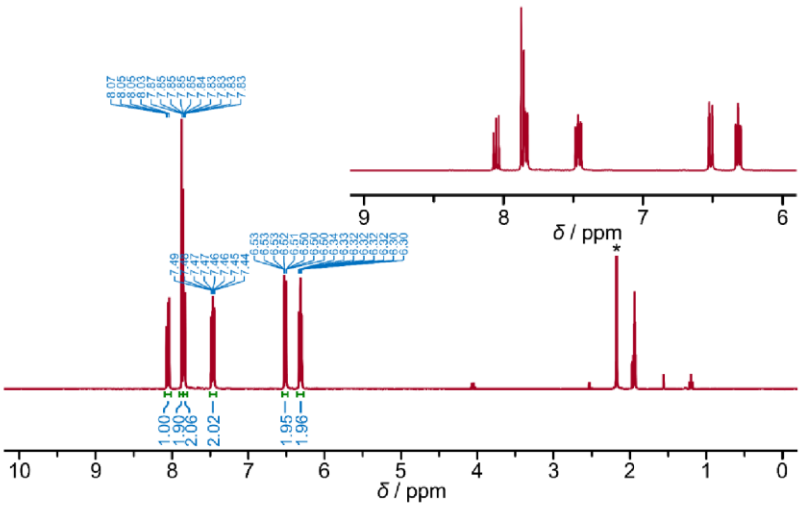

Fig. S5 ^1H NMR spectrum of 2,6-bis(2-oxopyridin-1(2H)-yl)pyridine in CD_3CN with inset of the aromatic region. The asterisk denotes the water peak.

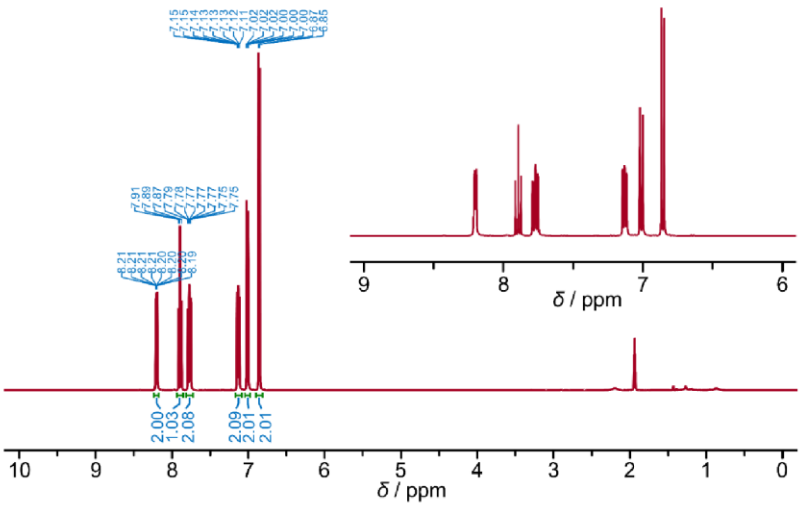

Fig. S6 ^{1}H NMR spectrum of bpop in CD_3CN with inset of the aromatic region.

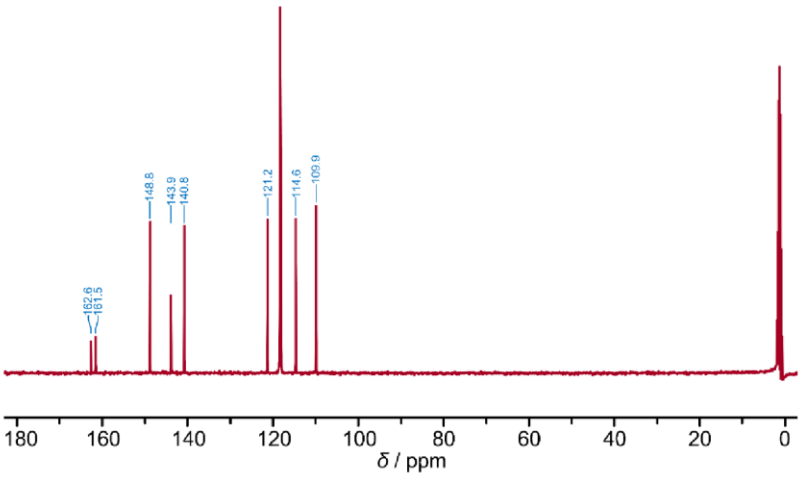

Fig. S7 $^{13}C\{^{1}H\}$ NMR spectrum of bpop in CD_3CN.

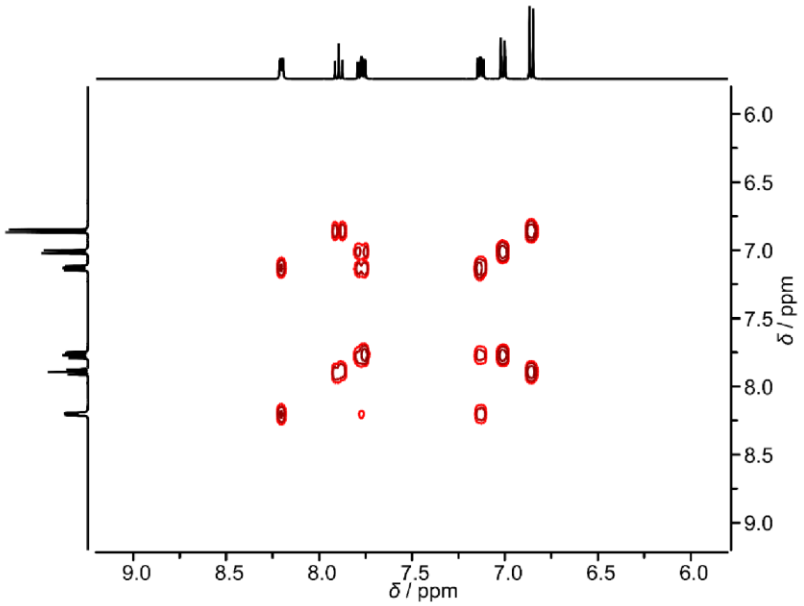

Fig. S8 $^{1}H,^{1}H$ COSY of bpop in CD_3CN.

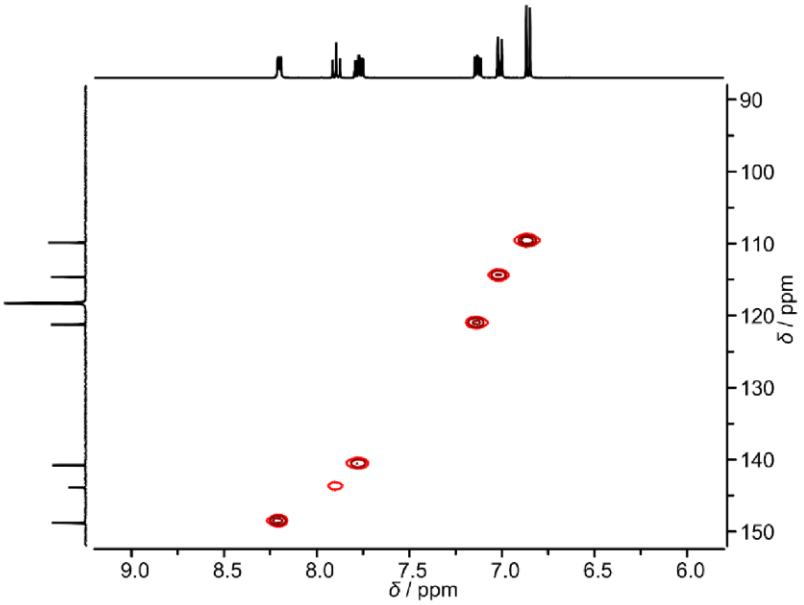

Fig. S9 $^{13}C,^{1}H$ HSQC of bpop in CD_3CN.

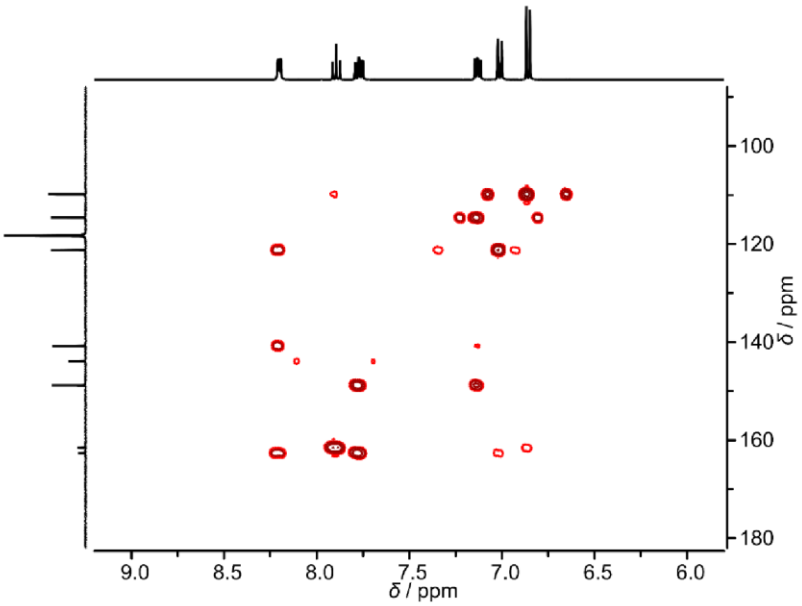

Fig. S10 $^{13}C,^{1}H$ HMBC of bpop in CD_3CN.

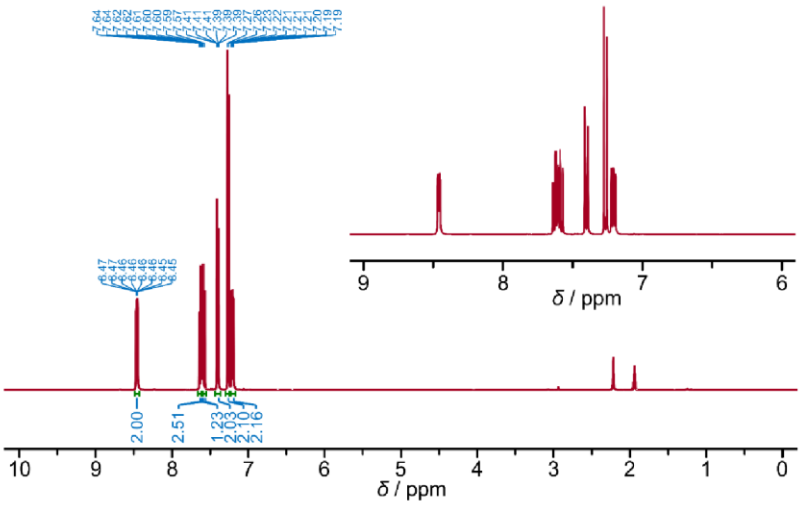

Fig. S11 ^{1}H NMR spectrum of bptp in CD_3CN with inset of the aromatic region.

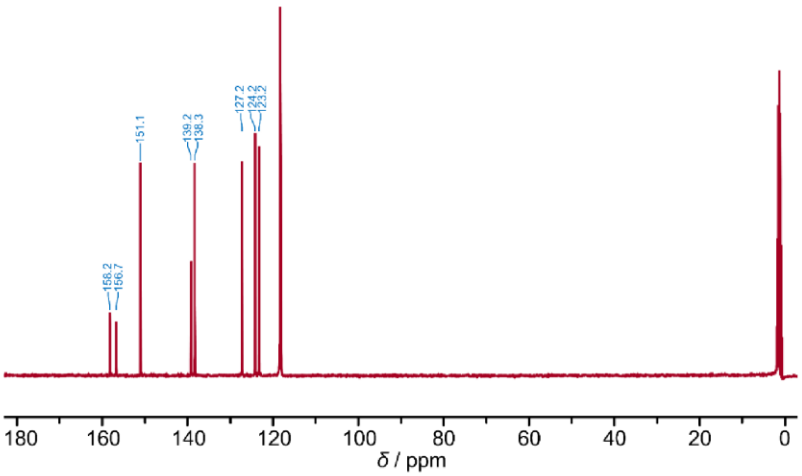

Fig. S12 $^{13}C\{^{1}H\}$ NMR spectrum of bptp in CD_3CN.

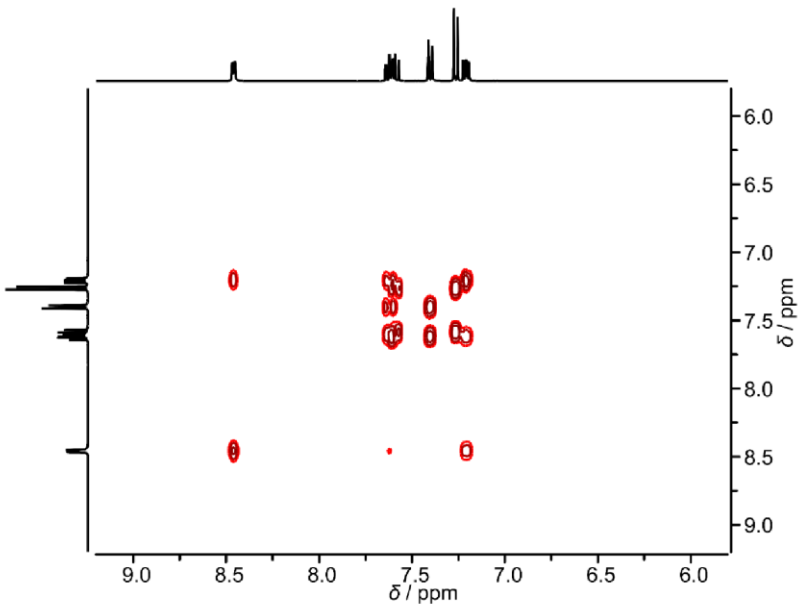

Fig. S13 $^{1}H,^{1}H$ COSY of bptp in CD_3CN.

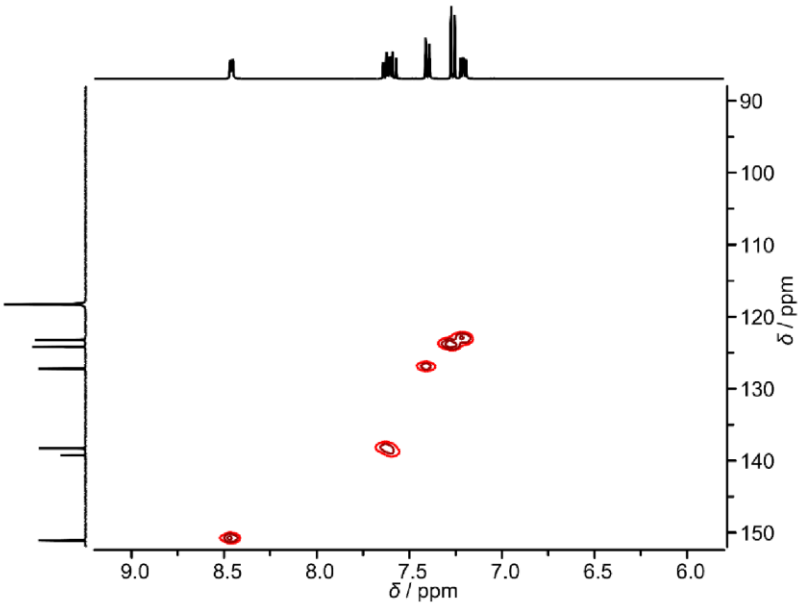

Fig. S14 $^{13}C,^{1}H$ HSQC of bptp in CD_3CN.

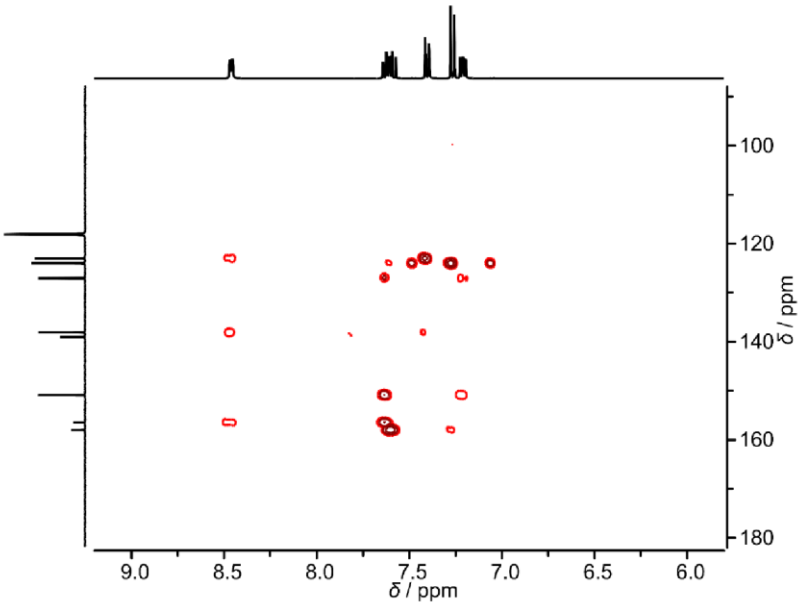

Fig. S15 $^{13}C,^{1}H$ HMBC of bptp in CD_3CN.

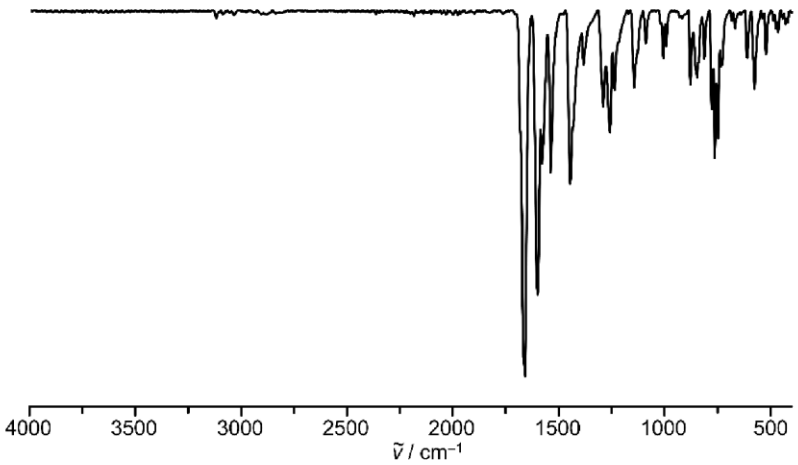

Fig. S16 ATR-IR spectrum of 2,6-bis(2-oxopyridin-1(2H)-yl)pyridine.

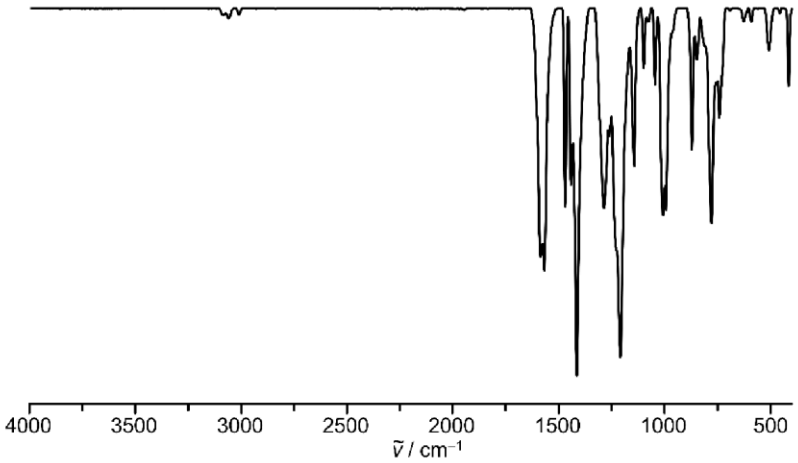

Fig. S17 ATR-IR spectrum of bpop.

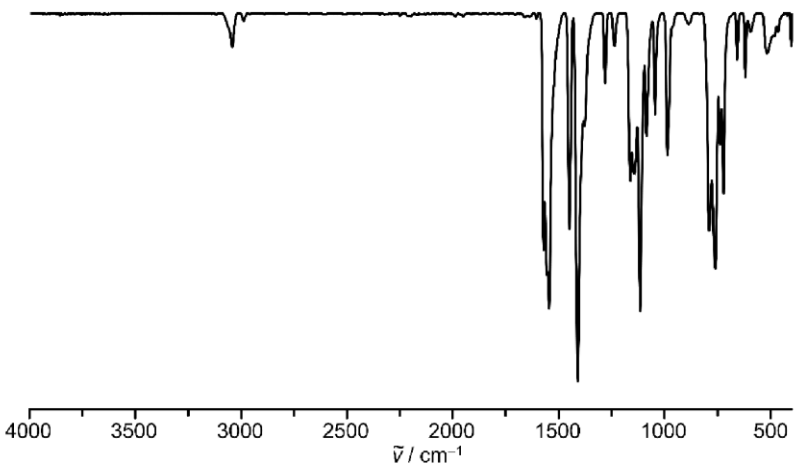

Fig. S18 ATR-IR spectrum of bptp.

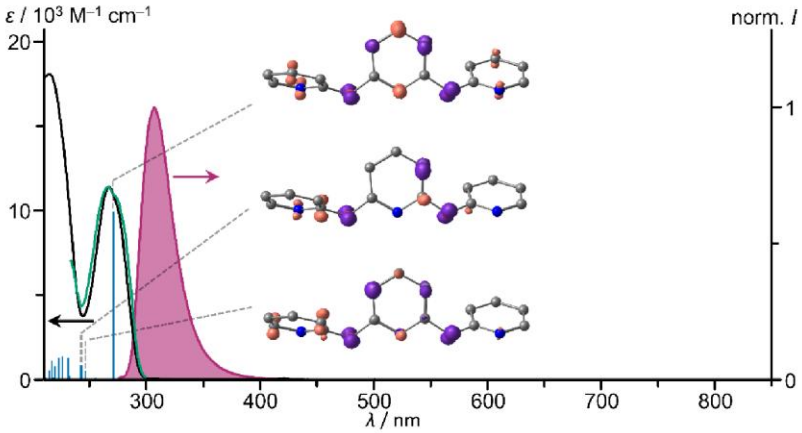

Fig. S19 UV/VIS/NIR absorption spectrum (black), excitation spectrum (λ_{em} = 307 nm, green) and emission spectrum (λ_{exc} = 267 nm, purple) of bpop in deaerated acetonitrile at room temperature, TD-DFT calculated oscillator strengths (blue) and difference electron densities (isosurface value 0.01 a.u.) of three low energy transitions.

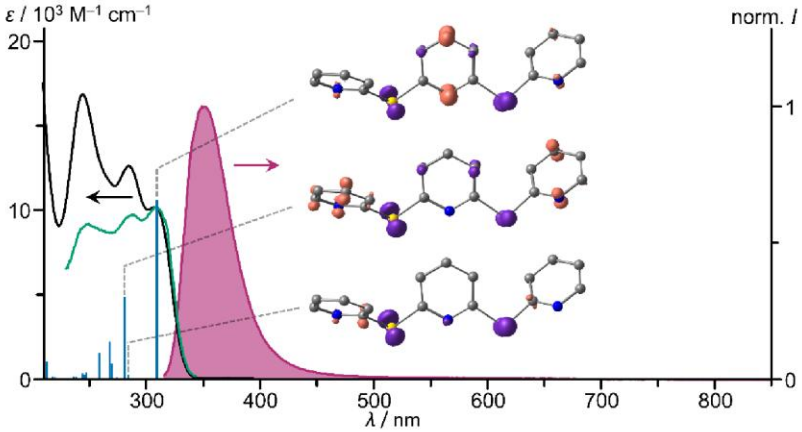

Fig. S20 UV/VIS/NIR absorption spectrum (black), excitation spectrum (λ_{em} = 351 nm, green) and emission spectrum (λ_{exc} = 308 nm, purple) of bptp in deaerated acetonitrile at room temperature, TD-DFT calculated oscillator strengths (blue) and difference electron densities (isosurface value 0.01 a.u.) of three low energy transitions.

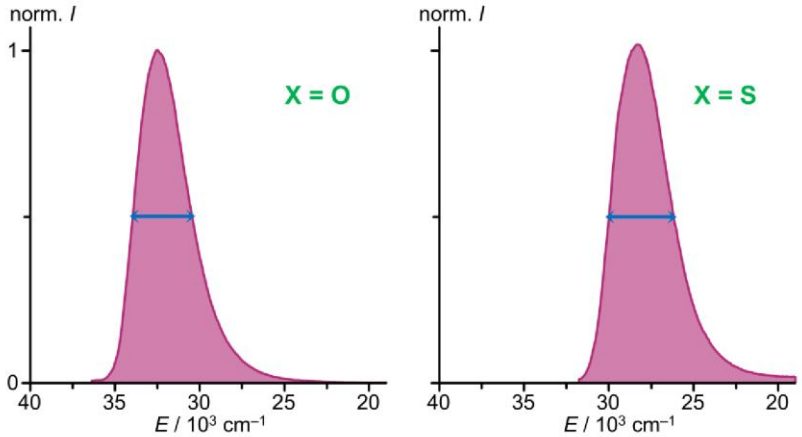

Fig. S21 Normalised emission spectra (purple) of the ligands bpop (λ_{exc} = 267 nm) and bptp (λ_{exc} = 308 nm) in acetonitrile and illustration of the full width at half maximum (FWHM).

Analytical data of Cr compounds

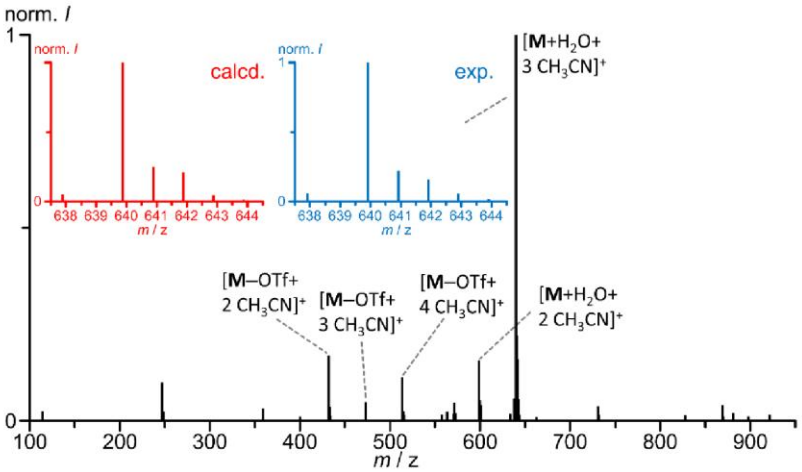

Fig. S22 ESI$^+$ mass spectrum of $Cr(OTf)_3$ in CH_3CN with insets of the experimentally found (blue) and calculated (red) isotope pattern for $[M+H_2O+3\ CH_3CN]^+$ ($C_9H_{11}CrF_9N_3O_{10}S_3$).

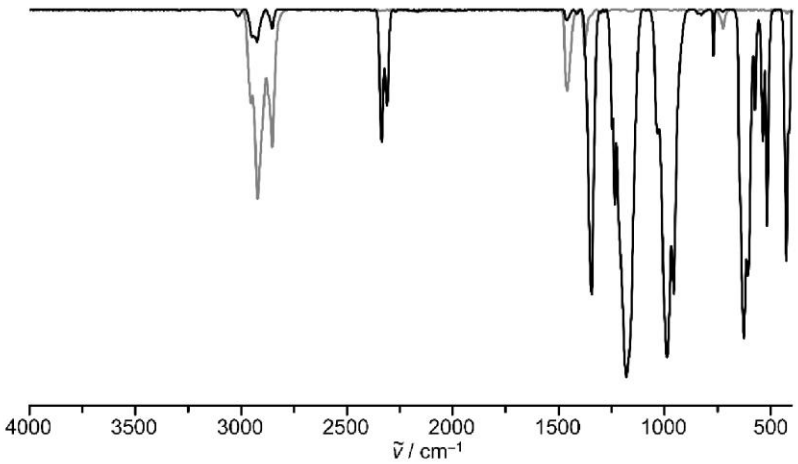

Fig. S23 ATR-IR spectrum of $Cr(OTf)_3$ as suspension in nujol (black) and ATR-IR spectrum of nujol (grey).

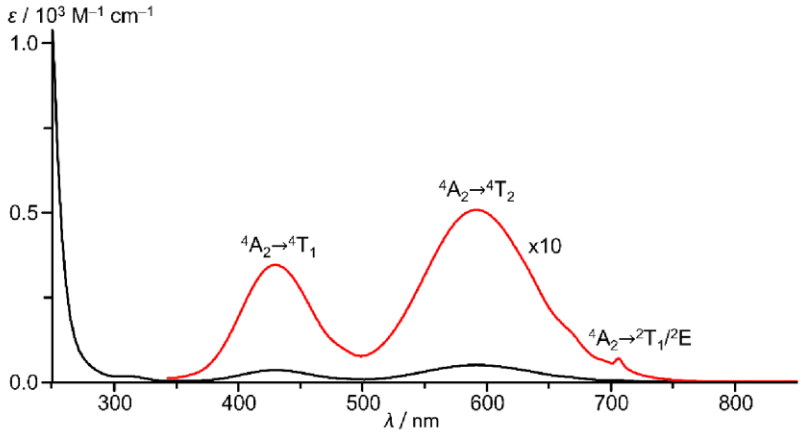

Fig. S24 UV/VIS/NIR absorption spectrum (black) of $Cr(OTf)_3$ in dry acetonitrile at room temperature and zoomed region of the ligand field bands (red).

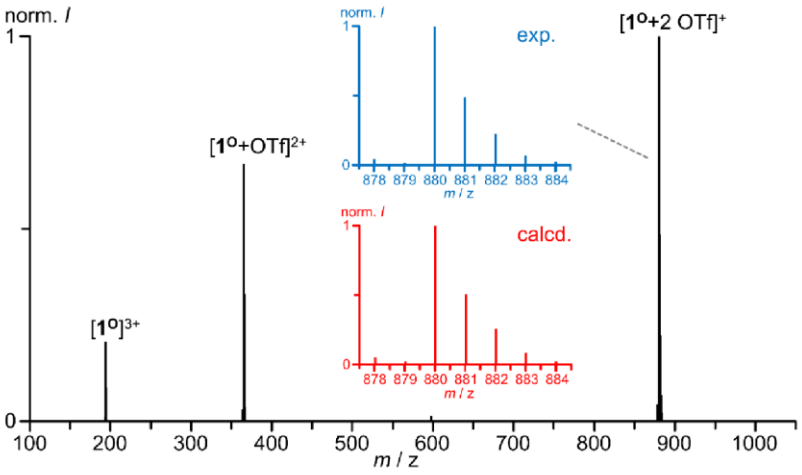

Fig. S25 ESI⁺ mass spectrum of **[1^{O}][OTf]$_3$** in CH_3CN with insets of the experimentally found (blue) and calculated (red) isotope pattern for [**1^{O}**+2 OTf]⁺ ($C_{32}H_{22}CrF_6N_6O_{10}S_2$).

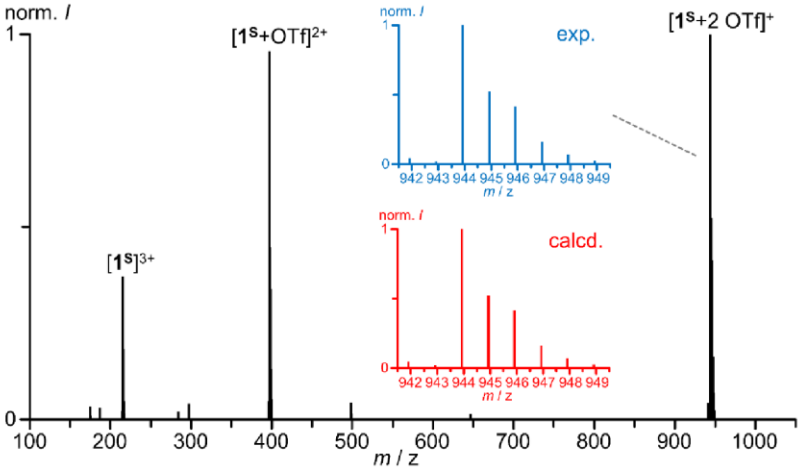

Fig. S26 ESI⁺ mass spectrum of **[1^{S}][OTf]$_3$** in CH_3CN with insets of the experimentally found (blue) and calculated (red) isotope pattern for [**1^{S}**+2 OTf]⁺ ($C_{32}H_{22}CrF_6N_6O_6S_6$).

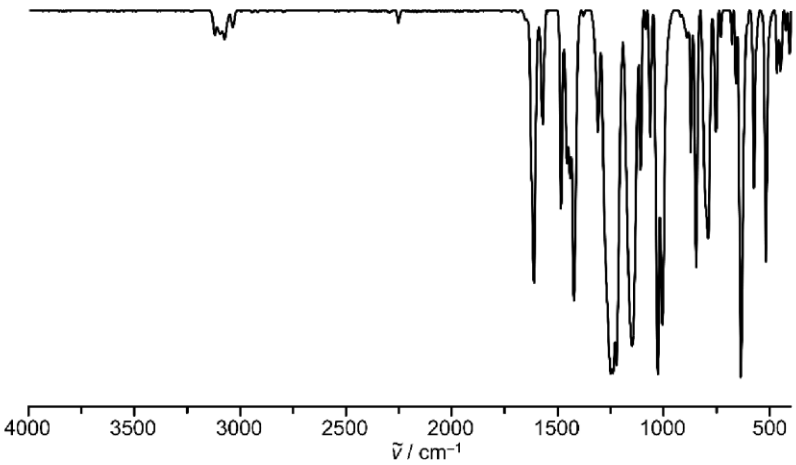

Fig. S27 ATR-IR spectrum of **[1^{O}][OTf]$_3$**.

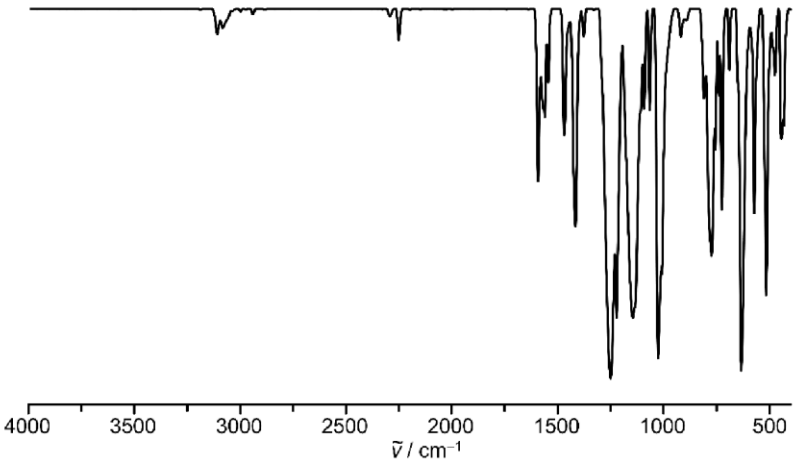

Fig. S28 ATR-IR spectrum of **[1^{S}][OTf]$_3$**.

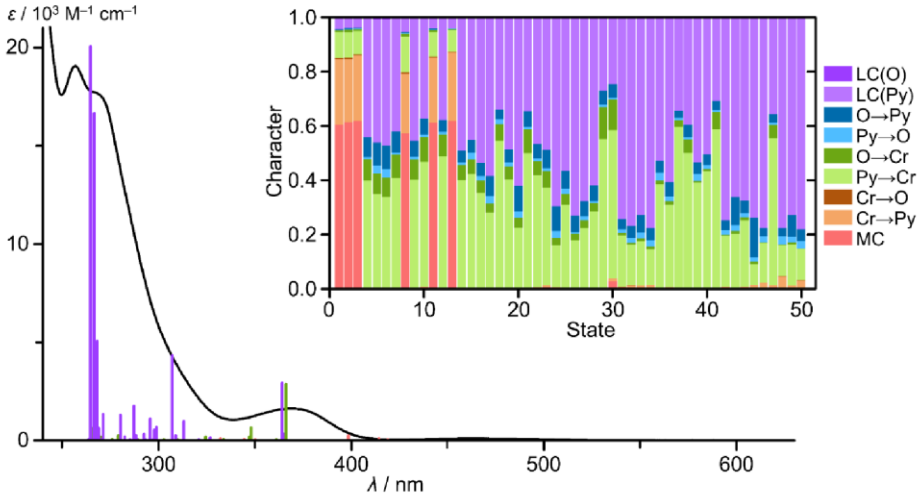

Fig. S29 UV/VIS absorption spectrum of **[1^{O}][OTf]$_3$** in CH_3CN (black) with TD-DFT calculated oscillator strengths of **[1^{O}]$^{3+}$** coloured according to the most dominant character of the corresponding transition (red: MC, green: LMCT, purple: LC). Inset: Charge transfer number analysis of the 50 lowest energy spin-allowed transitions calculated by Loewdin population analysis with the complex cation **[1^{O}]$^{3+}$** fragmented into chromium (Cr), the pyridine system (Py) and the oxygen atoms (O).

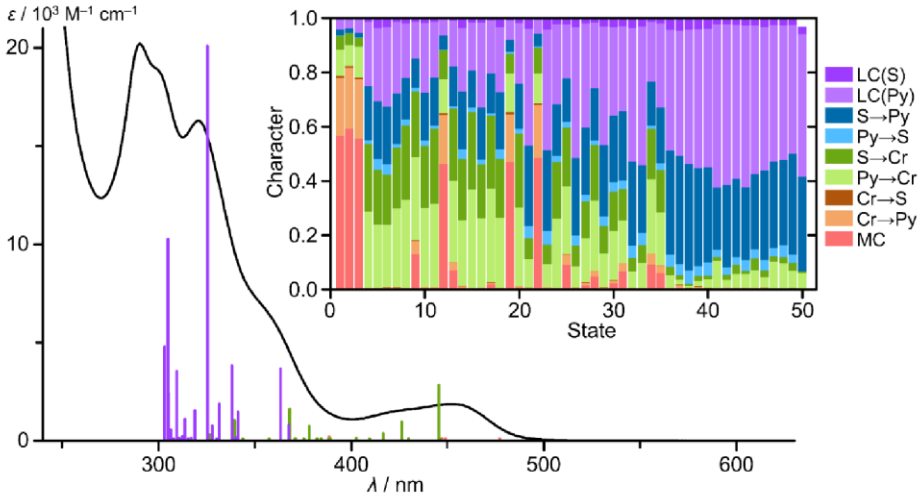

Fig. S30 UV/VIS absorption spectrum of **[1^{S}][OTf]$_3$** in CH_3CN (black) with TD-DFT calculated oscillator strengths of **[1^{S}]$^{3+}$** coloured according to the most dominant character of the corresponding transition (red: MC, green: LMCT, purple: LC). Inset: Charge transfer number analysis of the 50 lowest energy spin-allowed transitions calculated by Loewdin population analysis with the complex cation **[1^{S}]$^{3+}$** fragmented into chromium (Cr), the pyridine system (Py) and the sulphur atoms (S).

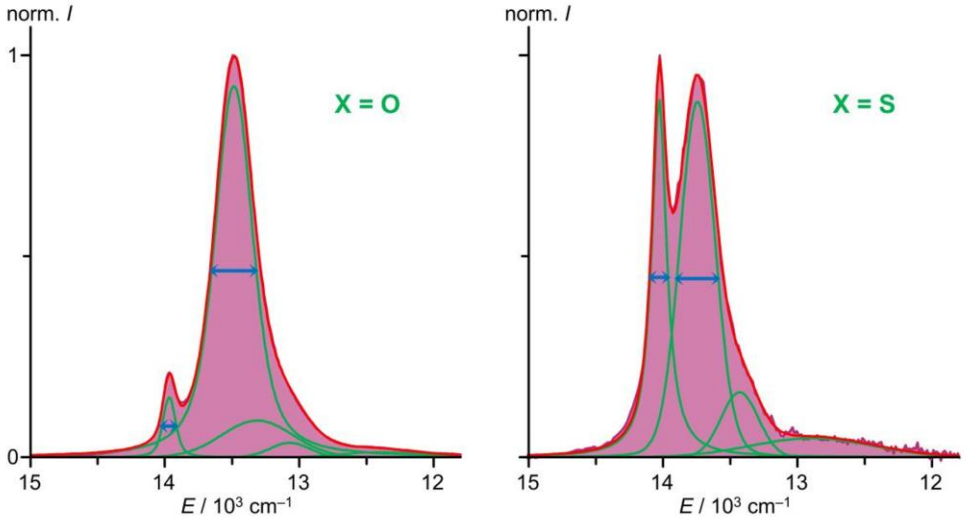

Fig. S31 Normalised emission spectra (purple) of the complexes $[\mathbf{1}^{O}]^{3+}$ (λ_{exc} = 450 nm) and $[\mathbf{1}^{S}]^{3+}$ (λ_{exc} = 450 nm) in acetonitrile at 293 K fitted with Voigt functions (green) in a sum fit (red) used for determining the full width at half maximum (FWHM).

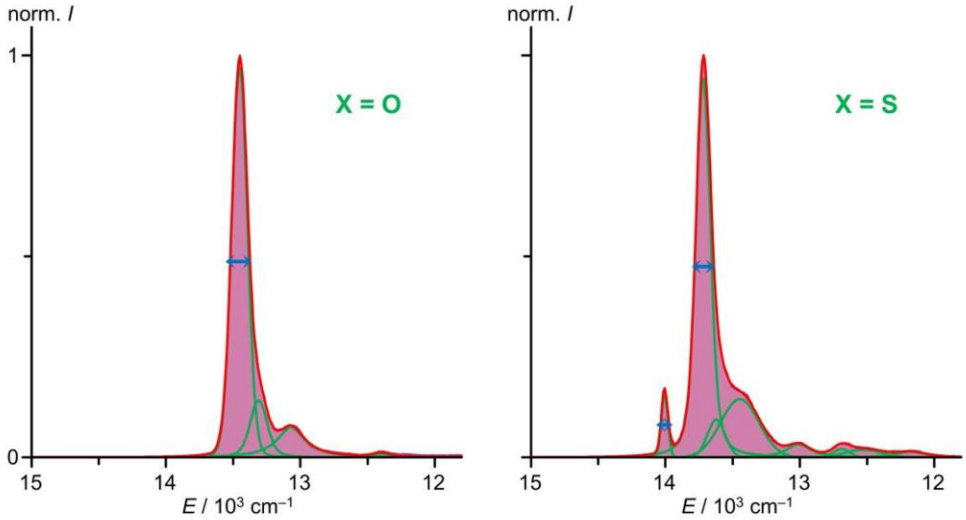

Fig. S32 Normalised emission spectra (purple) of the complexes $[\mathbf{1}^{O}]^{3+}$ (λ_{exc} = 450 nm) and $[\mathbf{1}^{S}]^{3+}$ (λ_{exc} = 450 nm) in ethanol/methanol (3:2) at 77 K fitted with Voigt functions (green) in a sum fit (red) used for determining the full width at half maximum (FWHM).

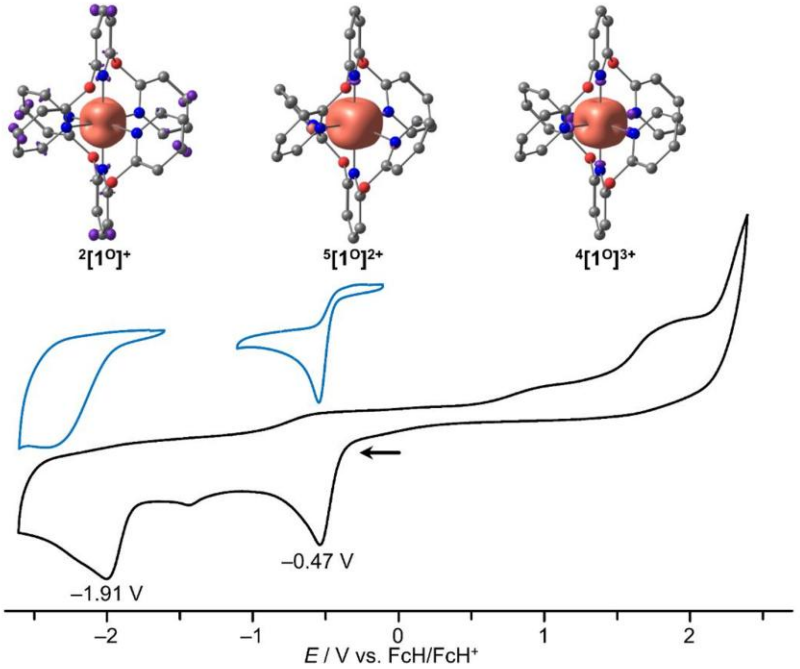

Fig. S33 Cyclic voltammograms of 3 mM **[1^{O}][OTf]$_3$** in a 100 mM solution of [^{n}Bu$_4$N][PF$_6$] in CH$_3$CN over the full range (peak potentials E_p against FcH$^+$/FcH) and in the range of the reduction waves and calculated spin densities (contour value: 0.01 a.u.) of the thermodynamically most stable reduced species.

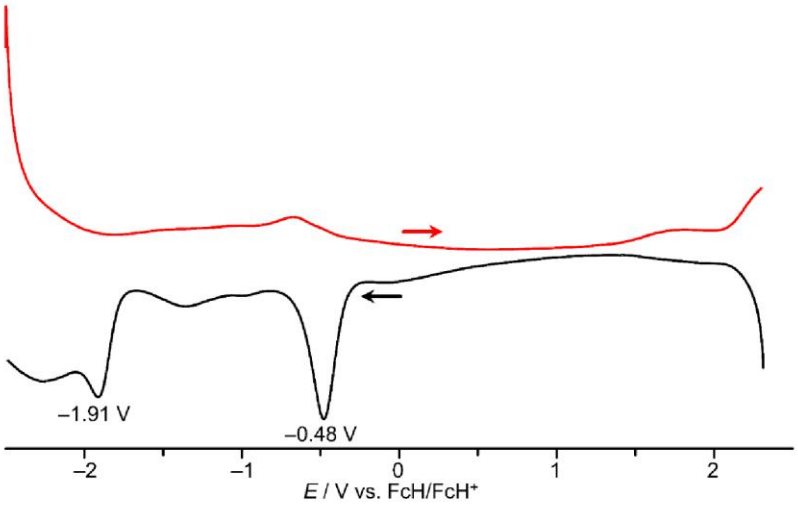

Fig. S34 Square wave voltamogramms of 3 mM **[1^{O}][OTf]$_3$** in a 100 mM solution of [^{n}Bu$_4$N][PF$_6$] in CH$_3$CN (peak potentials E_p against FcH$^+$/FcH).

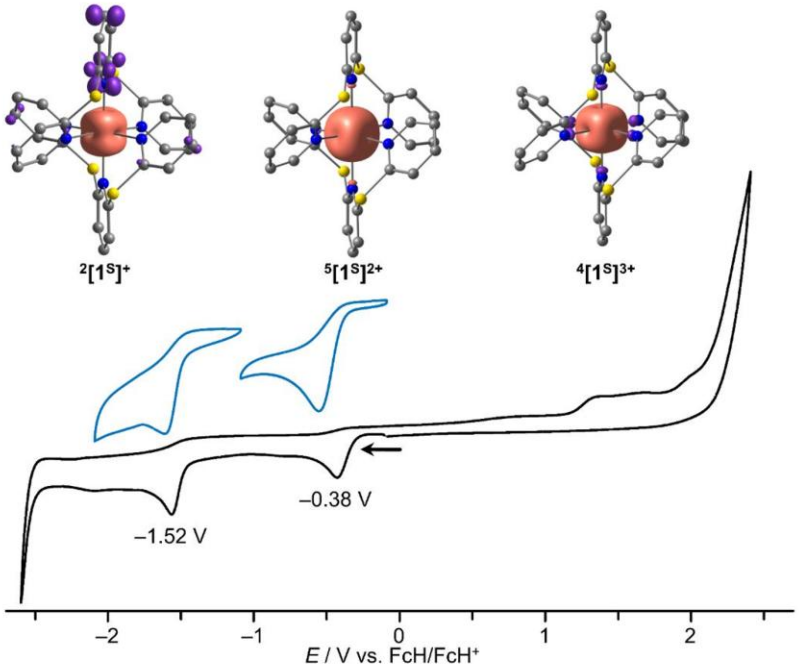

Fig. S35 Cyclic voltammograms of 3 mM **[1^{S}][OTf]$_3$** in a 100 mM solution of [^{n}Bu$_4$N][PF$_6$] in CH$_3$CN over the full range (peak potentials E_p against FcH$^+$/FcH) and in the range of the reduction waves and calculated spin densities (contour value: 0.01 a.u.) of the thermodynamically most stable reduced species.

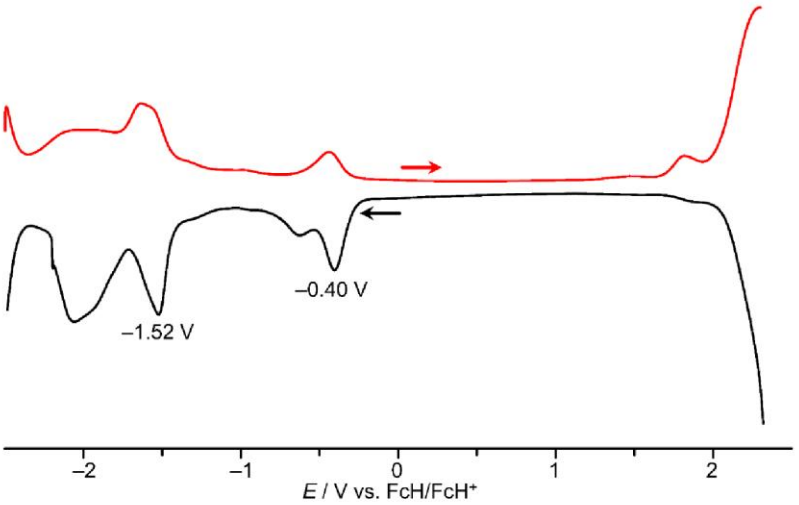

Fig. S36 Square wave voltamogramms of 3 mM **[1^{S}][OTf]$_3$** in a 100 mM solution of [^{n}Bu$_4$N][PF$_6$] in CH$_3$CN (peak potentials E_p against FcH$^+$/FcH).

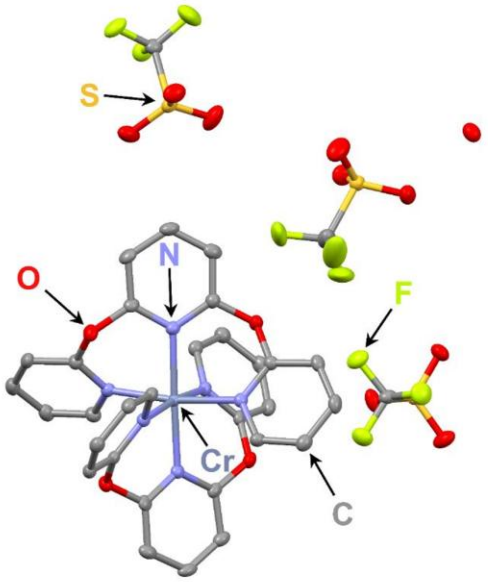

Fig. S37 Molecular structure of **[1^{O}][OTf]$_3$xH$_2$O** in the solid state. Hydrogen atoms omitted, thermal ellipsoids at 50% probability level.

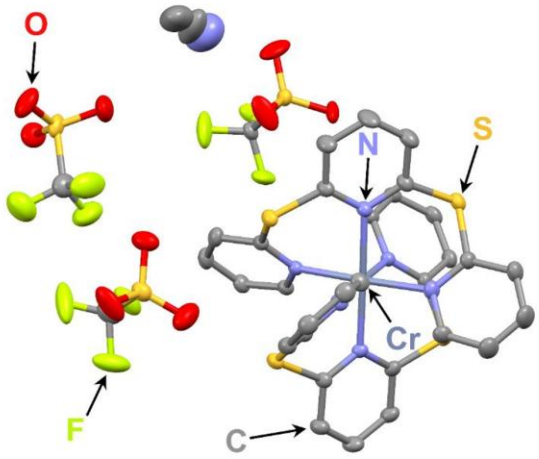

Fig. S38 Molecular structure of **[1^{S}][OTf]$_3$xCH$_3$CN** in the solid state. Hydrogen atoms omitted, thermal ellipsoids at 50% probability level.

Table S1 Structure parameters of the complex series $[1^{X}]^{3+}$ from crystal structure determination (XRD) and DFT geometry optimisation with an exemplary structure illustration.[43,44] Bond lengths are given in Å and angles in °.

Complex	Method	Parameter				Graphical illustration
		d (Cr–N_c^1)	*d* (Cr–N_c^2)			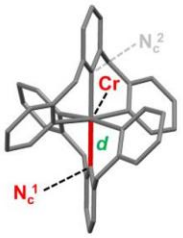
$[1^{S}]^{3+}$	XRD	2.1006(16)	2.0868(16)			
	DFT	*2.1400*	*2.1399*			
$[1^{O}]^{3+}$	XRD	2.0391(28)	2.0377(28)			
	DFT	*2.0510*	*2.0507*			
$[1^{NMe}]^{3+}$	XRD	2.0405(18)	2.0358(18)			
	DFT	*2.0463*	*2.0460*			
$[1^{CH2}]^{3+}$	XRD	2.0771(13)	2.0599(13)			
	DFT	*2.1127*	*2.1119*			
		d (Cr–N_t^1)	*d* (Cr–N_t^2)	*d* (Cr–N_t^3)	*d* (Cr–N_t^4)	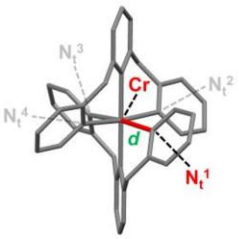
$[1^{S}]^{3+}$	XRD	2.0852(17)	2.0785(16)	2.0723(16)	2.0639(16)	
	DFT	*2.1178*	*2.1180*	*2.1178*	*2.1180*	
$[1^{O}]^{3+}$	XRD	2.0601(26)	2.0479(31)	2.0380(27)	2.0419(31)	
	DFT	*2.0707*	*2.0705*	*2.0707*	*2.0705*	
$[1^{NMe}]^{3+}$	XRD	2.0530(18)	2.0418(19)	2.0414(18)	2.0309(18)	
	DFT	*2.0580*	*2.0576*	*2.0578*	*2.0575*	
$[1^{CH2}]^{3+}$	XRD	2.0886(13)	2.0755(13)	2.0703(13)	2.0691(13)	
	DFT	*2.1128*	*2.1112*	*2.1100*	*2.1128*	
		∡ (N_c^1CrN_c^2)	α (N_t^1CrN_t^3)	α (N_t^2CrN_t^4)		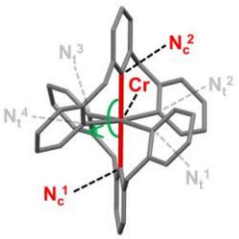
$[1^{S}]^{3+}$	XRD	178.83(7)	177.38(7)	178.15(7)		
	DFT	*179.99*	*178.65*	*178.69*		
$[1^{O}]^{3+}$	XRD	178.24(12)	172.30(12)	172.82(12)		
	DFT	*180.00*	*173.99*	*173.94*		
$[1^{NMe}]^{3+}$	XRD	179.90(9)	171.98(7)	171.78(7)		
	DFT	*179.88*	*172.97*	*173.06*		
$[1^{CH2}]^{3+}$	XRD	178.58(4)	177.47(4)	177.65(4)		
	DFT	*179.72*	*176.56*	*176.74*		
		β (N_t^1CrN_t^2)	∡ (N_t^2CrN_t^3)	β (N_t^3CrN_t^4)	∡ (N_t^4CrN_t^1)	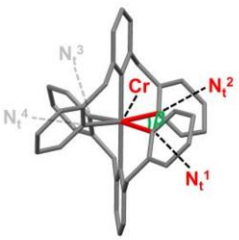
$[1^{S}]^{3+}$	XRD	85.70(7)	96.75(7)	84.97(6)	92.59(7)	
	DFT	*85.58*	*94.44*	*85.58*	*94.43*	
$[1^{O}]^{3+}$	XRD	89.63(11)	90.65(11)	89.79(11)	90.90(11)	
	DFT	*90.06*	*90.27*	*90.06*	*90.25*	
$[1^{NMe}]^{3+}$	XRD	90.44(7)	91.27(7)	89.08(7)	90.35(7)	
	DFT	*88.99*	*91.53*	*88.93*	*91.40*	
$[1^{CH2}]^{3+}$	XRD	85.08(5)	93.04(5)	84.63(5)	97.25(5)	
	DFT	*84.82*	*95.02*	*84.86*	*95.49*	

Complex	Method	Parameter				Graphical illustration
		∡ ($N_c^1CrN_t^1$)	∡ ($N_c^1CrN_t^2$)	∡ ($N_c^1CrN_t^3$)	∡ ($N_c^1CrN_t^4$)	
$[1^S]^{3+}$	XRD	89.30(7)	89.42(6)	89.81(6)	91.26(6)	
	DFT	*89.33*	*90.65*	*89.33*	*90.66*	
$[1^O]^{3+}$	XRD	86.00(11)	94.62(12)	86.31(11)	92.56(12)	
	DFT	*86.99*	*93.03*	*87.00*	*93.03*	
$[1^{NMe}]^{3+}$	XRD	86.00(7)	93.90(7)	86.07(7)	94.32(8)	
	DFT	*86.50*	*93.39*	*86.47*	*93.56*	
$[1^{CH2}]^{3+}$	XRD	89.69(5)	89.11(5)	88.59(5)	91.20(5)	
	DFT	*88.26*	*91.65*	*88.31*	*91.60*	
		∡ ($N_c^2CrN_t^1$)	∡ ($N_c^2CrN_t^2$)	∡ ($N_c^2CrN_t^3$)	∡ ($N_c^2CrN_t^4$)	
$[1^S]^{3+}$	XRD	91.44(7)	89.73(6)	89.50(6)	89.61(6)	
	DFT	*90.68*	*89.35*	*90.67*	*89.35*	
$[1^O]^{3+}$	XRD	92.78(11)	86.63(11)	94.92(11)	86.19(12)	
	DFT	*93.01*	*86.97*	*93.00*	*86.97*	
$[1^{NMe}]^{3+}$	XRD	94.08(7)	86.04(7)	93.85(7)	85.74(8)	
	DFT	*93.56*	*86.52*	*93.46*	*86.54*	
$[1^{CH2}]^{3+}$	XRD	90.68(5)	89.55(5)	91.00(5)	90.11(5)	
	DFT	*92.02*	*88.34*	*91.41*	*88.41*	
		a (C^1–X^1)	*a* (C^2–X^1)	*a* (C^3–X^2)	*a* (C^4–X^2)	
$[1^S]^{3+}$	XRD	1.7916(27)	1.7686(21)	1.7637(19)	1.7661(20)	
	DFT	*1.7642*	*1.7697*	*1.7642*	*1.7695*	
$[1^O]^{3+}$	XRD	1.3702(41)	1.3777(40)	1.3841(36)	1.3787(42)	
	DFT	*1.3677*	*1.3617*	*1.3677*	*1.3618*	
$[1^{NMe}]^{3+}$	XRD	1.3971(28)	1.4022(29)	1.3866(28)	1.4114(29)	
	DFT	*1.3901*	*1.4009*	*1.3904*	*1.4007*	
$[1^{CH2}]^{3+}$	XRD	1.5014(21)	1.5074(19)	1.5015(19)	1.5092(19)	
	DFT	*1.4999*	*1.5045*	*1.4998*	*1.5044*	
		a (C^5–X^3)	*a* (C^6–X^3)	*a* (C^7–X^4)	*a* (C^8–X^4)	
$[1^S]^{3+}$	XRD	1.7634(19)	1.7688(21)	1.7573(19)	1.7589(21)	
	DFT	*1.7642*	*1.7697*	*1.7643*	*1.7695*	
$[1^O]^{3+}$	XRD	1.3736(45)	1.3815(43)	1.3746(44)	1.3687(44)	
	DFT	*1.3677*	*1.3617*	*1.3678*	*1.3618*	
$[1^{NMe}]^{3+}$	XRD	1.3917(28)	1.3961(29)	1.3914(28)	1.4070(29)	
	DFT	*1.3910*	*1.4006*	*1.3906*	*1.4009*	
$[1^{CH2}]^{3+}$	XRD	1.5041(19)	1.5147(18)	1.5051(21)	1.5145(18)	
	DFT	*1.5003*	*1.5049*	*1.4997*	*1.5044*	
		∡ ($C^1X^1C^2$)	∡ ($C^3X^2C^4$)	∡ ($C^5X^3C^6$)	∡ ($C^7X^4C^8$)	
$[1^S]^{3+}$	XRD	103.29(12)	102.83(9)	104.08(9)	104.58(9)	
	DFT	*104.44*	*104.45*	*104.44*	*104.45*	
$[1^O]^{3+}$	XRD	122.10(26)	118.16(26)	119.36(27)	123.34(28)	
	DFT	*122.47*	*122.45*	*122.48*	*122.44*	
$[1^{NMe}]^{3+}$	XRD	122.03(19)	121.39(19)	122.13(19)	122.79(18)	
	DFT	*122.30*	*122.34*	*122.25*	*122.25*	
$[1^{CH2}]^{3+}$	XRD	112.04(11)	117.90(11)	118.65(12)	117.20(11)	
	DFT	*115.14*	*115.33*	*115.13*	*115.00*	

Table S2 Structure parameters of the complex series $[1^{X}]^{3+}$ from crystal structure determination (XRD) and DFT geometry optimisation each with an exemplary structure illustration.[43,44] The planes Py^{n} (n = 1–6) or CrN_4 were calculated by a least-square fit and contain the corresponding pyridine ring or the meridional coordinating nitrogen atoms and the chromium centre. Angles are given in °.

Complex	Method	Parameter		Graphical illustration
		ϕ (Py^1, Py^2)		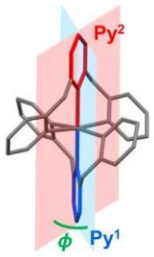
$[1^{S}]^{3+}$	XRD	18.47(22)		
	DFT	*17.09*		
$[1^{O}]^{3+}$	XRD	21.84(186)		
	DFT	*25.17*		
$[1^{NMe}]^{3+}$	XRD	18.31(210)		
	DFT	*18.79*		
$[1^{CH2}]^{3+}$	XRD	29.54(20)		
	DFT	*26.07*		
		δ^1 (Py^3, Py^5)	δ^2 (Py^4, Py^6)	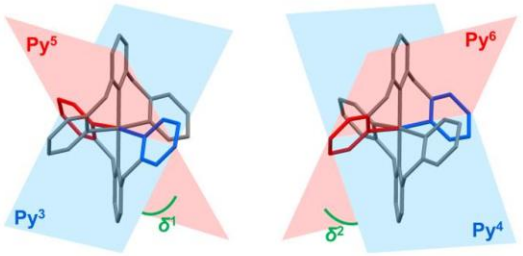
$[1^{S}]^{3+}$	XRD	81.68(18)	86.26(17)	
	DFT	*82.03*	*81.85*	
$[1^{O}]^{3+}$	XRD	73.51(122)	69.75(235)	
	DFT	*68.41*	*68.56*	
$[1^{NMe}]^{3+}$	XRD	79.06(75)	80.63(91)	
	DFT	*78.79*	*78.68*	
$[1^{CH2}]^{3+}$	XRD	72.28(32)	71.23(21)	
	DFT	*70.38*	*69.89*	
		∡(Py^3, CrN_4)	∡(Py^4, CrN_4)	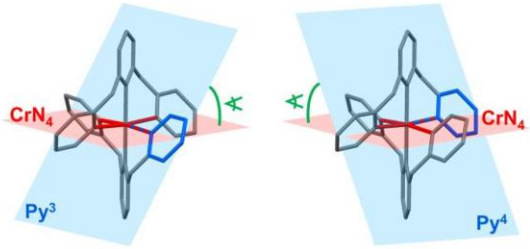
$[1^{S}]^{3+}$	XRD	49.48(18)	47.39(21)	
	DFT	*48.99*	*49.07*	
$[1^{O}]^{3+}$	XRD	55.42(82)	56.31(180)	
	DFT	*55.79*	*55.73*	
$[1^{NMe}]^{3+}$	XRD	49.73(115)	46.82(73)	
	DFT	*50.69*	*50.60*	
$[1^{CH2}]^{3+}$	XRD	56.64(16)	53.96(14)	
	DFT	*55.16*	*54.87*	
		∡(Py^5, CrN_4)	∡(Py^6, CrN_4)	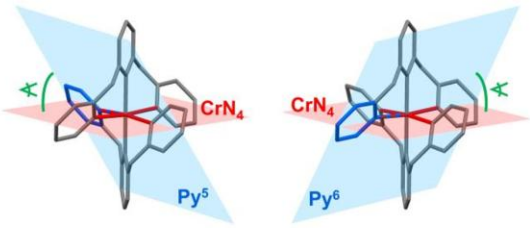
$[1^{S}]^{3+}$	XRD	49.13(16)	46.60(17)	
	DFT	*48.98*	*49.07*	
$[1^{O}]^{3+}$	XRD	51.07(126)	54.03(218)	
	DFT	*55.80*	*55.72*	
$[1^{NMe}]^{3+}$	XRD	51.27(104)	52.58(85)	
	DFT	*50.53*	*50.72*	
$[1^{CH2}]^{3+}$	XRD	52.28(29)	55.39(20)	
	DFT	*54.47*	*55.24*	

Table S3 TD-DFT calculated oscillator strengths and difference electron densities of the ten lowest energy spin-allowed transitions of $[1^{O}]^{3+}$.

#	λ / nm	oscillator strength	character	from	to	difference electron density (purple: density loss, orange: density gain)
1	419.0	0.0000032	MC (61%) + MLCT (24%)	t_{2g} (d_{xy})	e_g ($d_{x^2-y^2}$)	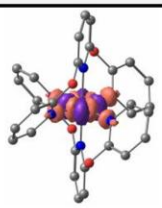
2	414.3	0.0002689	MC (62%) + MLCT (24%)	t_{2g} ($d_{xz}+d_{yz}$)'	e_g (d_{z^2})	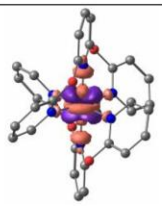
3	398.4	0.0009169	MC (62%) + MLCT (25%)	t_{2g} ($d_{xz}+d_{yz}$)' + t_{2g} ($d_{xz}+d_{yz}$)''	e_g (d_{z^2})	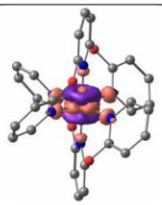
4	366.2	0.0131411	LMCT (48%) + LC (32%)	p (O) and π (Py_t)	t_{2g} (d_{xy}) and π (Py_t)	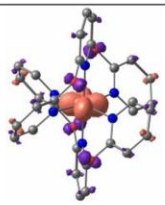
5	364.7	0.0013474	LMCT (42%) + LC (32%)	p (O) and π (Py_c)	t_{2g} ($d_{xz}+d_{yz}$)' and π (Py_c)	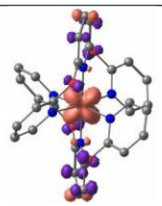
6	364.1	0.0134968	LMCT (41%) + LC (34%)	p (O) and π (Py_c)	t_{2g} ($d_{xz}+d_{yz}$)' and π (Py_c)	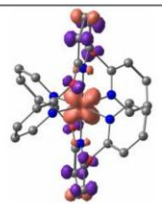
7	361.2	0.0000006	LMCT (49%) + ILCT (26%)	p (O) and π (Py_c)	t_{2g} (d_{xy}) and π (Py_t)	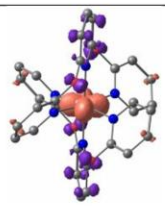

#	λ / nm	oscillator strength	character	from	to	difference electron density (purple: density loss, orange: density gain)
8	350.2	0.0000000	MC (57%) + MLCT (23%)	t_{2g} (d_{xy})	e_g (d_{z^2})	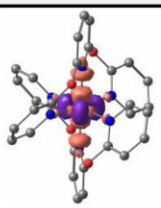
9	348.0	0.0028086	LMCT (47%) + LC (36%)	p (O)	t_{2g} (d_{xz}+d_{yz})''	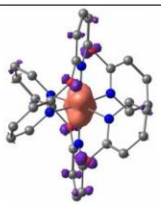
10	347.2	0.0006875	LMCT (55%) + LC (27%)	p (O)	t_{2g} (d_{xz}+d_{yz})''	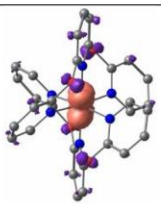

Table S4 TD-DFT calculated oscillator strengths and difference electron densities of the ten lowest energy spin-allowed transitions of **[1^S]$^{3+}$**.

#	λ / nm	oscillator strength	character	from	to	difference electron density (purple: density loss, orange: density gain)
1	477.0	0.0000202	MC (57%) + MLCT (22%)	t_{2g} (d_{xz}+d_{yz})'	e_g (d_{z^2})	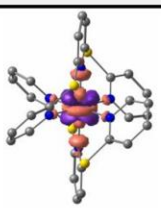
2	448.9	0.0001916	MC (59%) + MLCT (23%)	t_{2g} (d_{xz}+d_{yz})' + t_{2g} (d_{xz}+d_{yz})''	e_g (d_{z^2})	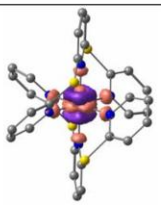
3	447.0	0.0000868	MC (56%) + MLCT (23%)	t_{2g} (d_{xy})	e_g ($d_{x^2-y^2}$)	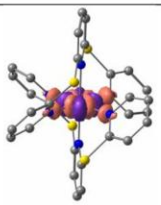

#	λ / nm	oscillator strength	character	from	to	difference electron density (purple: density loss, orange: density gain)
4	446.2	0.0000026	LMCT (53%) + ILCT (32%)	p (S) and π (Py_c)	t_{2g} (d_{xy})	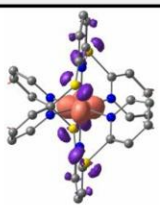
5	445.6	0.0228827	LMCT (44%) + ILCT (36%)	p (S) and π (Py_c)	t_{2g} ($d_{xz}+d_{yz}$)' and π (Py_c)	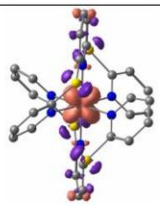
6	429.8	0.0001514	LMCT (41%) + ILCT (37%)	p (S) and π (Py_c)	t_{2g} ($d_{xz}+d_{yz}$)' + t_{2g} ($d_{xz}+d_{yz}$)'' and π (Py_c)	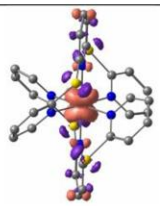
7	426.1	0.0072654	LMCT (51%) + ILCT (29%)	p (S)	t_{2g} (d_{xy})	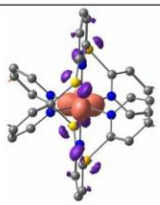
8	416.6	0.0023140	LMCT (60%) + ILCT (26%)	p (S) and π (Py_c)	t_{2g} ($d_{xz}+d_{yz}$)''	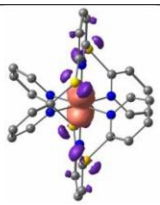
9	409.4	0.0000000	LMCT (55%) + ILCT (19%)	p (S)	e_g (d_{z^2}) and e_g ($d_{x^2-y^2}$)	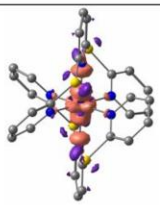
10	402.6	0.0004712	LMCT (52%) + ILCT (28%)	p (S)	t_{2g} ($d_{xz}+d_{yz}$)''	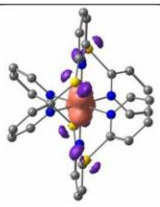

S32

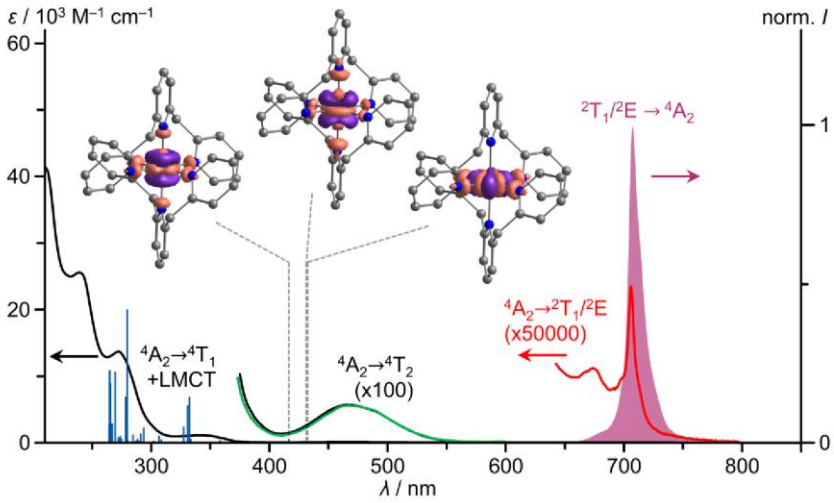

Fig. S39 UV/VIS/NIR absorption spectrum (black, red), excitation spectrum (λ_{em} = 708 nm, green) and emission spectrum (λ_{exc} = 462 nm, purple) of **[1^{CH2}][OTf]$_3$** in deaerated acetonitrile at room temperature, TD-DFT calculated oscillator strengths (blue) and difference electron densities of three low energy transitions of ^{4}MC character of **[1^{CH2}]$^{3+}$**.[43] The regions of the spin forbidden absorption bands, the lowest energy spin allowed absorption band and the excitation spectrum are zoomed.

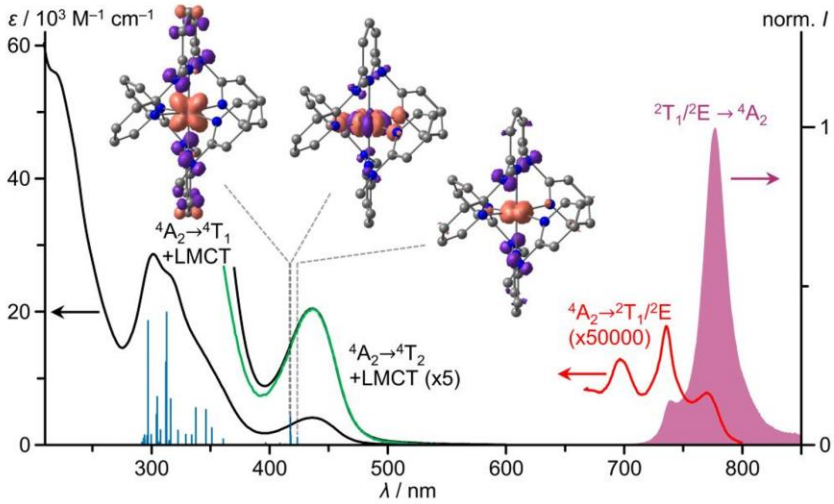

Fig. S40 UV/VIS/NIR absorption spectrum (black, red), excitation spectrum (λ_{em} = 775 nm, green) and emission spectrum (λ_{exc} = 435 nm, purple) of **[1^{NMe}][BF$_4$]$_3$** in deaerated acetonitrile at room temperature, TD-DFT calculated oscillator strengths (blue) and difference electron densities of three low energy transitions of ^{4}LMCT and ^{4}MC character of **[1^{NMe}]$^{3+}$**.[44] The regions of the spin forbidden absorption bands, the lowest energy spin allowed/LMCT absorption band and the excitation spectrum are zoomed.

Table S5 CASSCF(x,y)-SC/NEVPT2 results of the complex series $[1^{X}]^{3+}$ depending on the active space with energies in cm^{-1} (bold values indicate the lowest state of each multiplicity).

Complex	(x,y)	$^2E(1)$	$^2E(2)$	$^2T_1(1)$	$^2T_1(2)$	$^2T_1(3)$	$^2T_2(1)$	$^2T_2(2)$	$^2T_2(3)$	$^4T_2(1)$	$^4T_2(2)$	$^4T_2(3)$
$[1^{O}]^{3+}$	(3,5)	16440	17239	**15924**	16849	17181	25217	25641	25674	**22000**	22486	23571
	(3,10)	16196	16991	**15659**	16580	16936	24926	25372	25376	**21614**	22068	23168
	(13,10)	16271	16912	**15760**	16515	16792	24507	25053	25094	**22267**	22638	23787
	(7,12)	15726	16299	**15265**	15915	16206	23861	24310	24334	**22664**	23047	24073
$[1^{S}]^{3+}$	(3,5)	16610	17470	**16325**	17228	17501	25045	25415	25489	**19511**	20638	20667
	(3,10)	16369	17224	**16067**	16950	17266	24786	25110	25185	**19144**	20294	20304
	(13,10)	16536	17154	**16226**	16938	17159	24564	24835	24878	**19762**	20974	21040
	(7,12)	15958	16544	**15725**	16292	16568	23835	24178	24186	**20293**	21372	21393
$[1^{NMe}]^{3+}$	(3,5)	16345	17155	**15712**	16897	17002	25205	25414	25779	**22626**	22648	23846
	(3,10)	16091	16902	**15454**	16625	16758	24940	25101	25479	**22233**	22243	23432
	(13,10)	16140	16749	**15460**	16519	16545	24551	24588	25074	**22700**	22818	23928
	(7,12)	15597	16180	**15051**	15928	16011	23823	23984	24361	**23216**	23262	24310
$[1^{CH2}]^{3+}$	(3,5)	16562	17407	**16331**	17135	17440	25270	25462	25502	**20914**	21103	22027
	(3,10)	16322	17165	**16069**	16858	17206	25007	25173	25200	**20571**	20692	21636
	(13,10)	16503	17144	**16286**	16894	17125	24814	24899	25014	**21276**	21415	22374
	(7,12)	15882	16454	**15691**	16208	16467	24006	24085	24208	**21727**	21840	22679

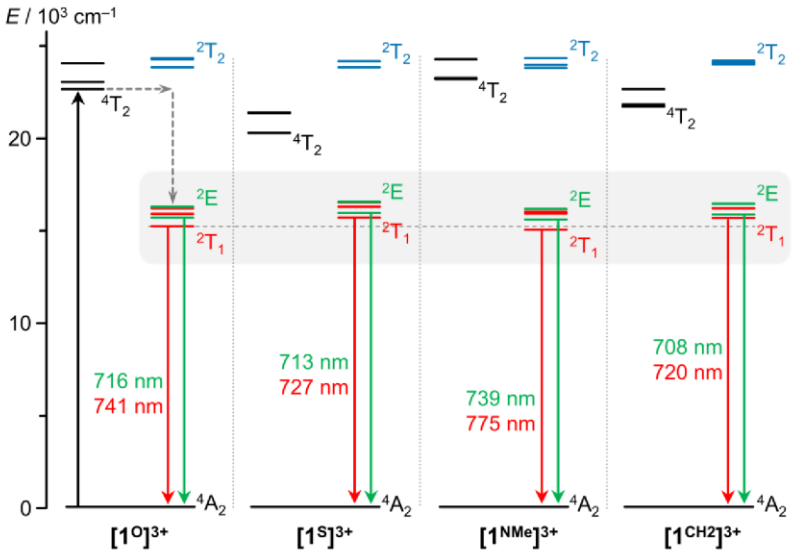

Fig. S41 CASSCF(7,12)-SC-NEVPT2 calculated energy diagram of the metal centred excited states of the $[1^{X}]^{3+}$ complex series with experimental observed maxima of the main room temperature emission bands and arrows indicating excitation (black) inter-system-crossing/internal conversion/vibrational cooling (dotted) and emission (red from $^2T_1$, green from ^2E).

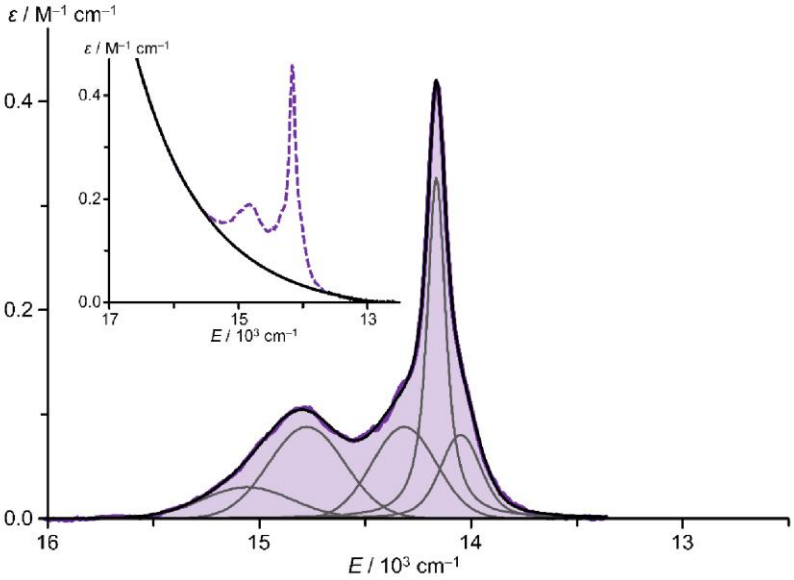

Fig. S42 Baseline corrected NIR absorption spectra of **[1^{CH2}][OTf]$_3$** (purple) in acetonitrile with sum fit (black) consisting of five Voigt functions (grey). Inset: NIR absorption spectra of **[1^{CH2}](OTf)$_3$** (purple, dotted) with exponential fit (black) describing the tail of the spin-allowed transitions used for the baseline correction.

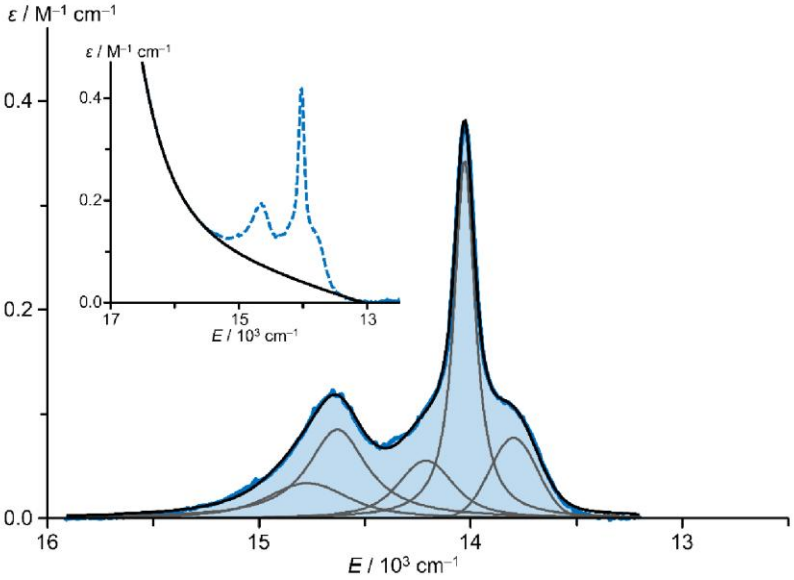

Fig. S43 Baseline corrected NIR absorption spectra of **[1^{S}][OTf]$_3$** (blue) in acetonitrile with sum fit (black) consisting of five Voigt functions (grey). Inset: NIR absorption spectra of **[1^{S}][OTf]$_3$** (blue, dotted) with exponential fit (black) describing the tail of the spin-allowed transitions used for the baseline correction.

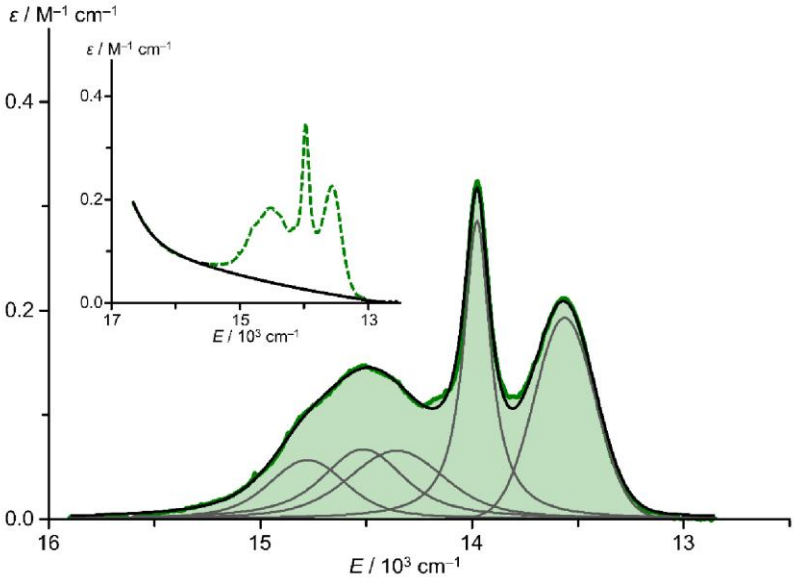

Fig. S44 Baseline corrected NIR absorption spectra of **[1^{O}][OTf]$_3$** (green) in acetonitrile with sum fit (black) consisting of five Voigt functions (grey). Inset: NIR absorption spectra of **[1^{O}][OTf]$_3$** (green, dotted) with exponential fit (black) describing the tail of the spin-allowed transitions used for the baseline correction.

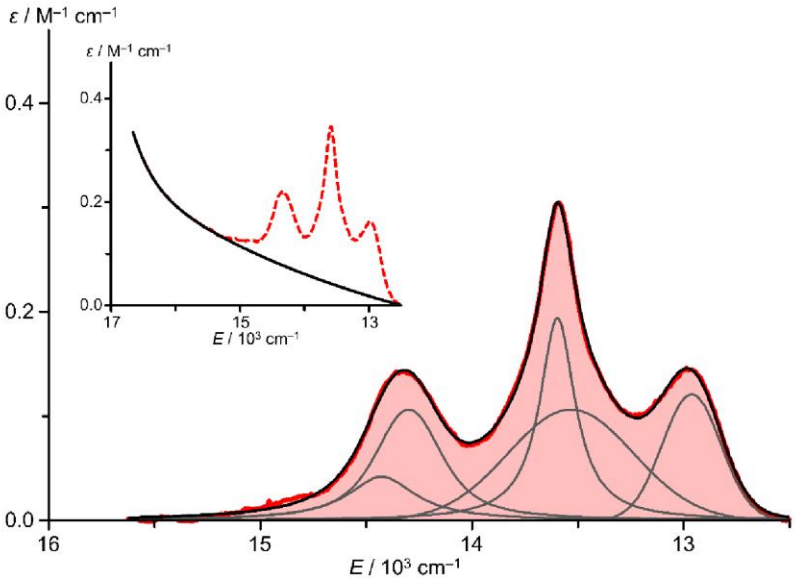

Fig. S45 Baseline corrected NIR absorption spectra of **[1^{NMe}][BF$_4$]$_3$** (red) in acetonitrile with sum fit (black) consisting of five Voigt functions (grey). Inset: NIR absorption spectra of **[1^{NMe}][BF$_4$]$_3$** (red, dotted) with exponential fit (black) describing the tail of the spin-allowed transitions used for the baseline correction.

Computational studies on the doublet energies

Table S6 CASSCF(7,12)-SC/NEVPT2 results of the complex series $[1^{X}]^{3+}$ at DFT optimised geometries of the four Molecular Rubies with energies in cm^{-1} (bold values indicate the lowest state of each multiplicity).

$[1^{X}]^{3+}$	Geo.	$^{2}E(1)$	$^{2}E(2)$	$^{2}T_1(1)$	$^{2}T_1(2)$	$^{2}T_1(3)$	$^{2}T_2(1)$	$^{2}T_2(2)$	$^{2}T_2(3)$	$^{4}T_2(1)$	$^{4}T_2(2)$	$^{4}T_2(3)$
$[1^{O}]^{3+}$	$[1^{O}]^{3+}$	15726	16299	**15265**	15915	16206	23861	24310	24334	**22664**	23047	24073
	$[1^{S}]^{3+}$	16089	16678	**15944**	16396	16735	23926	24100	24290	**19584**	20500	20824
	$[1^{NMe}]^{3+}$	15650	16215	**15131**	15892	16170	23923	24004	24336	**23139**	23235	24299
	$[1^{CH2}]^{3+}$	16000	16574	**15838**	16258	16593	24129	24136	24196	**20907**	21266	21770
$[1^{S}]^{3+}$	$[1^{O}]^{3+}$	15378	15920	**14183**	15436	15580	23569	23951	24622	**23222**	23249	24567
	$[1^{S}]^{3+}$	15958	16544	**15725**	16292	16568	23835	24178	24186	**20293**	21372	21393
	$[1^{NMe}]^{3+}$	15313	15868	**14050**	15392	15467	23558	23841	24666	**23312**	23748	24691
	$[1^{CH2}]^{3+}$	15759	16325	**15433**	16064	16290	23834	23988	24064	**21506**	22016	22594
$[1^{NMe}]^{3+}$	$[1^{O}]^{3+}$	15669	16257	**15224**	15983	16115	23796	24172	24324	**22674**	23213	24130
	$[1^{S}]^{3+}$	16040	16622	**15882**	16374	16677	23892	24149	24253	**20119**	20981	21047
	$[1^{NMe}]^{3+}$	15597	16180	**15051**	15928	16011	23823	23984	24361	**23216**	23262	24310
	$[1^{CH2}]^{3+}$	15958	16535	**15796**	16293	16555	24041	24132	24145	**21141**	21344	21982
$[1^{CH2}]^{3+}$	$[1^{O}]^{3+}$	15599	16159	**15078**	15832	16035	23746	24159	24327	**23045**	23916	24780
	$[1^{S}]^{3+}$	16006	16585	**15868**	16376	16633	23868	24185	24256	**20689**	21169	21534
	$[1^{NMe}]^{3+}$	15522	16088	**14933**	15799	15936	23780	23927	24342	**23529**	24048	24975
	$[1^{CH2}]^{3+}$	15882	16454	**15691**	16208	16467	24006	24085	24208	**21727**	21840	22679

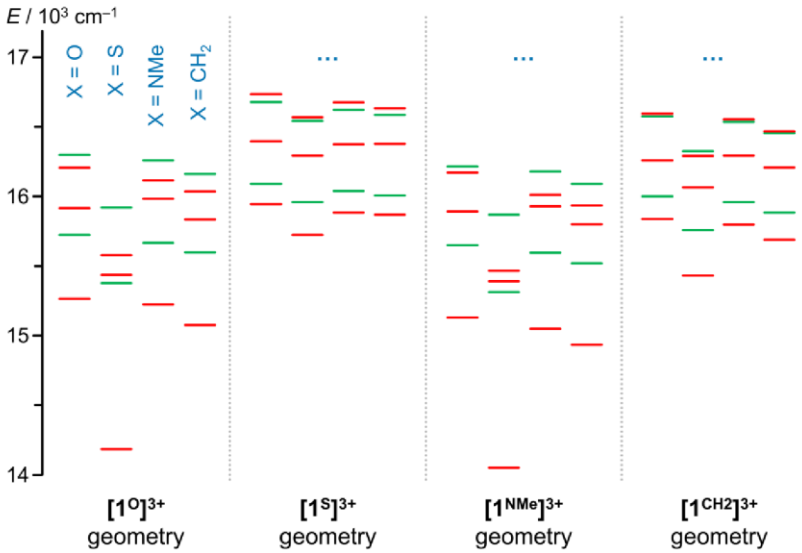

Fig. S46 CASSCF(7,12)-SC-NEVPT2 calculated $^{2}T_1$ (red) and ^{2}E energies (green) of $[1^{X}]^{3+}$ (X = O, S, NMe, CH_2) at DFT-optimised geometries of $[1^{X}]^{3+}$ (X = O, S, NMe, CH_2) – X substitution at fixed geometry.

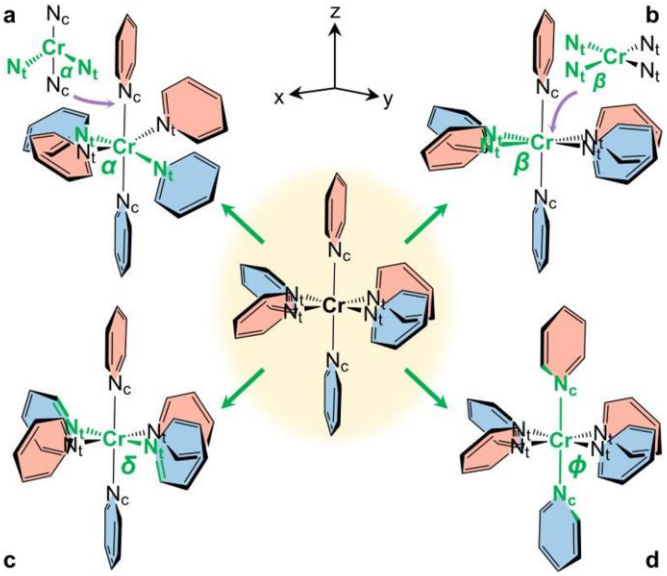

Fig. S47 Parameters α, β, δ and ϕ used for characterising the structure of the Molecular Rubies $[\mathbf{1^X}]^{3+}$ (X = S, O, NMe, CH_2) illustrated on the reference $[Cr(py)_6]^{3+}$. The structures demonstrate, which structural modifications were performed on the reference system $[Cr(py)_6]^{3+}$ to investigate their influence on the doublet energies: Compression of the angle α to yield N_t distortion within the xz/yz plane (a); compression of the angle β to yield N_t distortion within the xy plane (b); torsion δ of the terminal pyridine (c); torsion ϕ of the central pyridines (d).

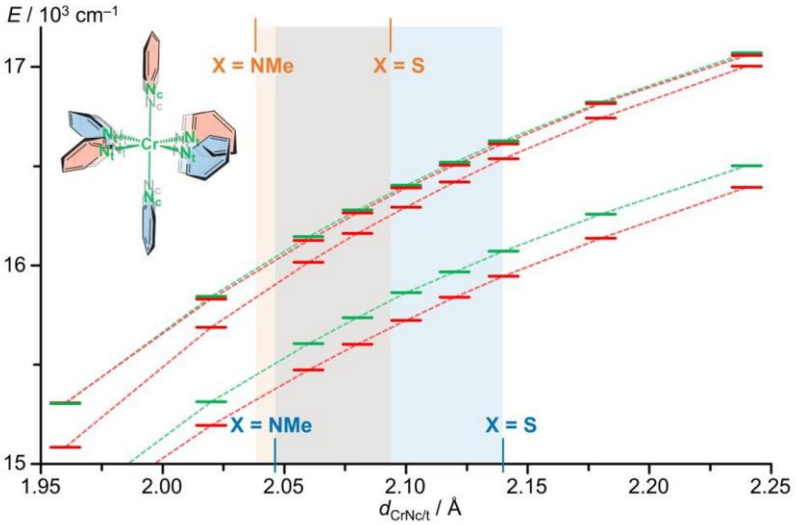

Fig. S48 CASSCF(7,12)-SC-NEVPT2 results of the model $[Cr(py)_6]^{3+}$ showing the dependence of the $^2T_1$ (red) and ^2E energies (green) on the Cr–$N_{c/t}$ elongation in local O_h symmetry including structures illustrating the geometry modification. The corresponding parameter for $\mathbf{[1^X]^{3+}}$ falls within the blue and orange shaded regions according to CASSCF(7,12)-SC-NEVPT2 calculations and the crystal structures.

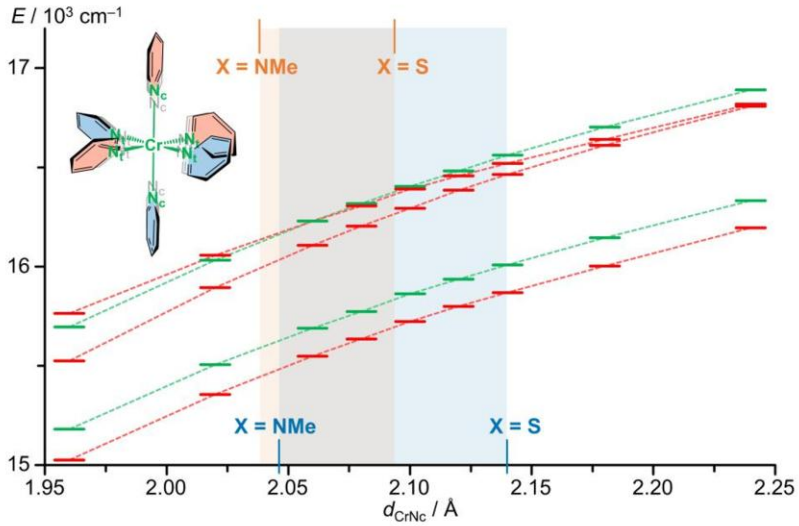

Fig. S49 CASSCF(7,12)-SC-NEVPT2 results of the model $[Cr(py)_6]^{3+}$ showing the dependence of the $^2T_1$ (red) and ^2E energies (green) on the Cr–$N_{c/t}$ elongation in local D_{4h} symmetry including structures illustrating the geometry modification. The corresponding parameter for $\mathbf{[1^X]^{3+}}$ falls within the blue and orange shaded regions according to CASSCF(7,12)-SC-NEVPT2 calculations and the crystal structures.

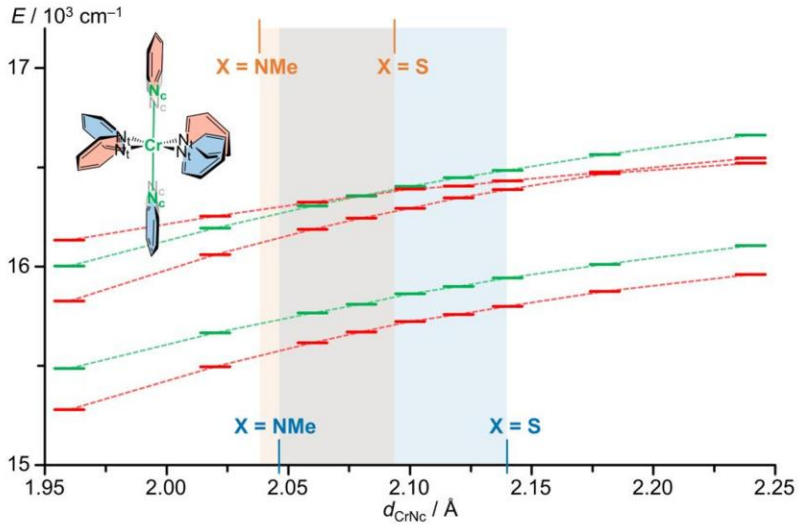

Fig. S50 CASSCF(7,12)-SC-NEVPT2 results of the model $[Cr(py)_6]^{3+}$ showing the dependence of the $^2T_1$ (red) and ^2E energies (green) on the Cr–N_c elongation including structures illustrating the geometry modification. The corresponding parameter for $\mathbf{[1^X]^{3+}}$ falls within the blue and orange shaded regions according to CASSCF(7,12)-SC-NEVPT2 calculations and the crystal structures.

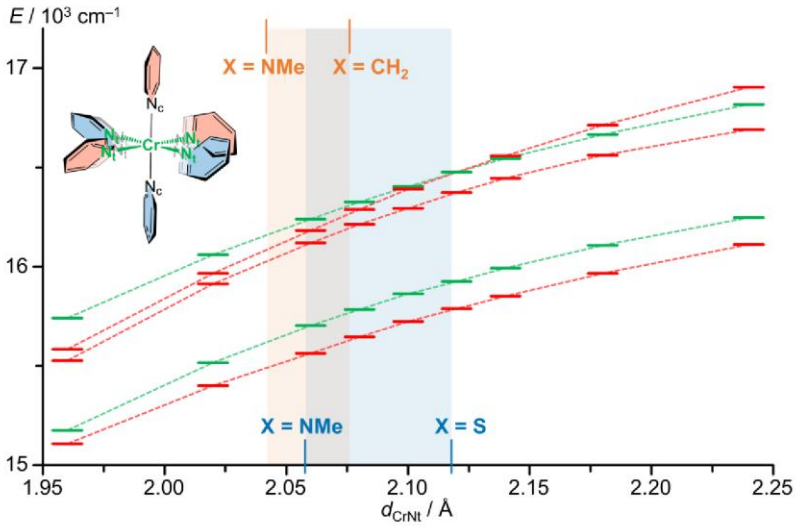

Fig. S51 CASSCF(7,12)-SC-NEVPT2 results of the model $[Cr(py)_6]^{3+}$ showing the dependence of the $^2T_1$ (red) and ^2E energies (green) on the Cr–N_t elongation including structures illustrating the geometry modification. The corresponding parameter for $[\mathbf{1^X}]^{3+}$ falls within the blue and orange shaded regions according to CASSCF(7,12)-SC-NEVPT2 calculations and the crystal structures.

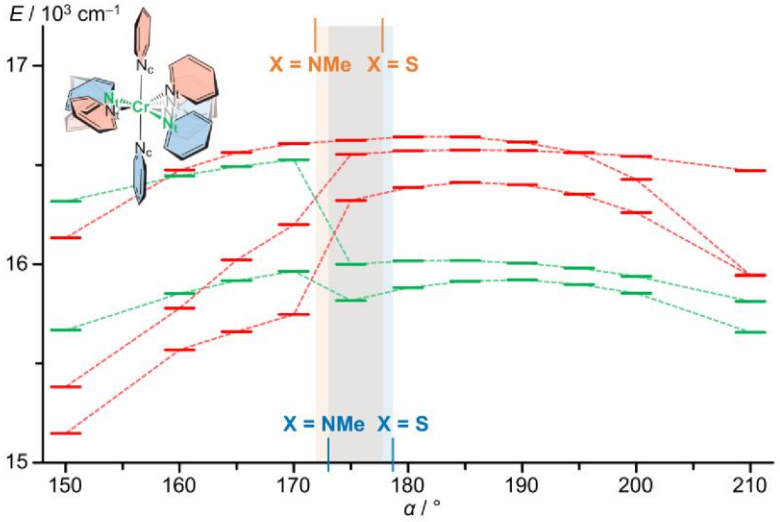

Fig. S52 CASSCF(7,12)-SC-NEVPT2 results of the model $[Cr(py)_6]^{3+}$ showing the dependence of the $^2T_1$ (red) and ^2E energies (green) on the N_t distortion within the xz/yz plane including structures illustrating the geometry modification. The corresponding parameter for $[\mathbf{1^X}]^{3+}$ falls within the blue and orange shaded regions according to CASSCF(7,12)-SC-NEVPT2 calculations and the crystal structures.

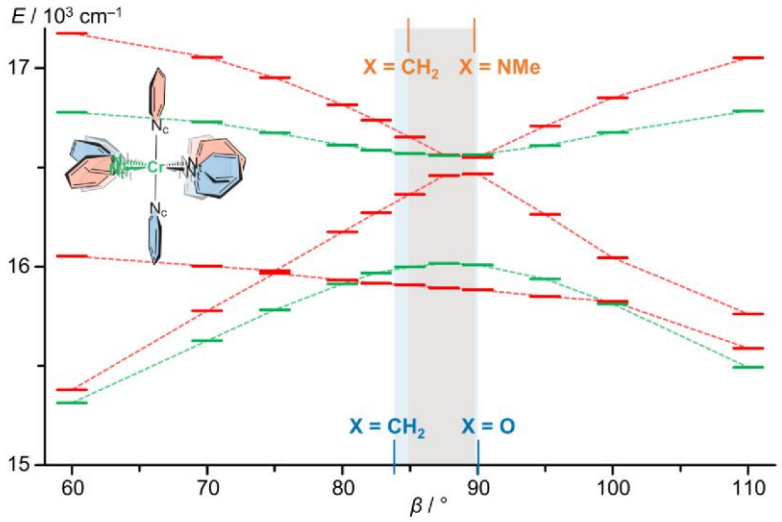

Fig. S53 CASSCF(7,12)-SC-NEVPT2 results of the model $[Cr(py)_6]^{3+}$ showing the dependence of the $^2T_1$ (red) and ^2E energies (green) on the N_t distortion within the xy plane including structures illustrating the geometry modification. The corresponding parameter for $\mathbf{[1^X]^{3+}}$ falls within the blue and orange shaded regions according to CASSCF(7,12)-SC-NEVPT2 calculations and the crystal structures.

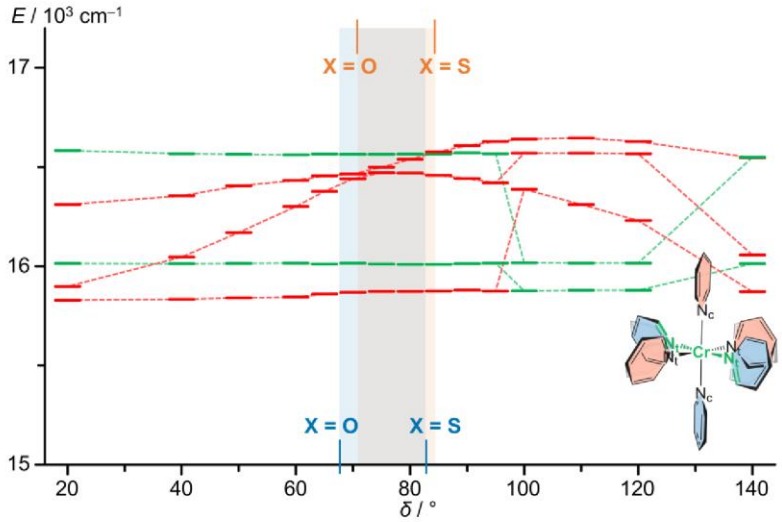

Fig. S54 CASSCF(7,12)-SC-NEVPT2 results of the model $[Cr(py)_6]^{3+}$ showing the dependence of the $^2T_1$ (red) and ^2E energies (green) on the torsion of the terminal pyridines ($\phi = 19°$) including structures illustrating the geometry modification. The corresponding parameter for $\mathbf{[1^X]^{3+}}$ falls within the blue and orange shaded regions according to CASSCF(7,12)-SC-NEVPT2 calculations and the crystal structures.

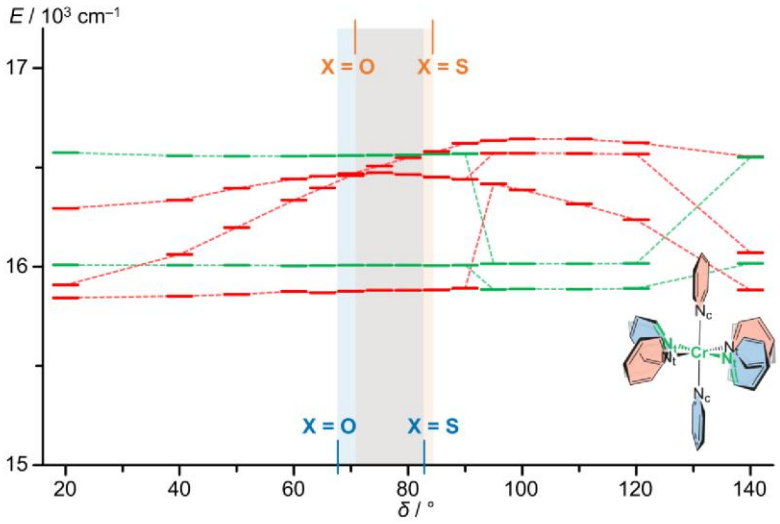

Fig. S55 CASSCF(7,12)-SC-NEVPT2 results of the model $[Cr(py)_6]^{3+}$ showing the dependence of the $^2T_1$ (red) and ^2E energies (green) on the torsion of the terminal pyridines ($\phi = 26°$) including structures illustrating the geometry modification. The corresponding parameter for $\mathbf{[1^X]^{3+}}$ falls within the blue and orange shaded regions according to CASSCF(7,12)-SC-NEVPT2 calculations and the crystal structures.

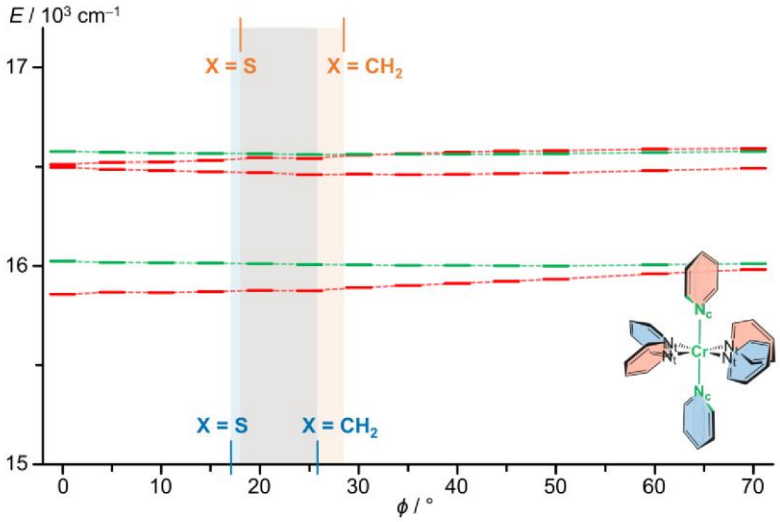

Fig. S56 CASSCF(7,12)-SC-NEVPT2 results of the model $[Cr(py)_6]^{3+}$ showing the dependence of the $^2T_1$ (red) and ^2E energies (green) on the torsion of the central pyridines ($\delta = 80°$) including structures illustrating the geometry modification. The corresponding parameter for $\mathbf{[1^X]^{3+}}$ falls within the blue and orange shaded regions according to CASSCF(7,12)-SC-NEVPT2 calculations and the crystal structures.

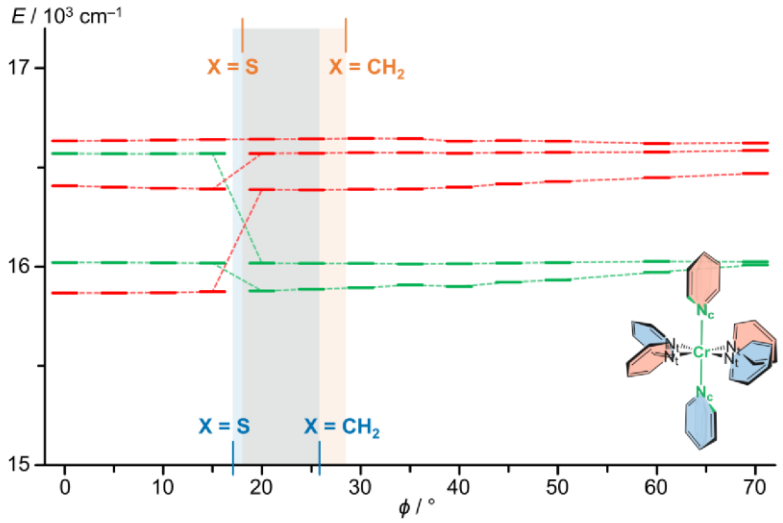

Fig. S57 CASSCF(7,12)-SC-NEVPT2 results of the model $[Cr(py)_6]^{3+}$ showing the dependence of the $^2T_1$ (red) and ^2E energies (green) on the torsion of the central pyridines (δ = 100°) including structure illustrating the geometry modification. The corresponding parameter for $\mathbf{[1^X]^{3+}}$ falls within the blue and orange shaded regions according to CASSCF(7,12)-SC-NEVPT2 calculations and the crystal structures.

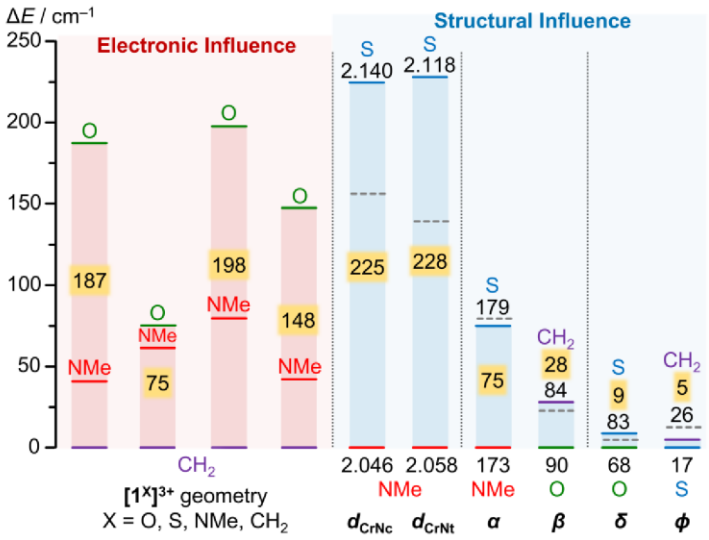

Fig. S58 Electronic and structural impact on the relative CASSCF(7,12)-SC-NEVPT2 energies of the lowest doublet states. The bridging groups X are indicated at the top and bottom of each column define the constitution at minimal and maximal energy and are described by bond lengths (in Å) and angles (in °). The maximum energy shifts ΔE highlighted in yellow are given in cm^{-1}. Left: $\mathbf{[1^X]^{3+}}$ (X = O: green; X = NMe: red; X = CH_2: purple). Right: $[Cr(py)_6]^{3+}$ with structural parameters taken from of the geometries of $\mathbf{[1^X]^{3+}}$ with X = O, S, NMe, CH_2 (green, blue, red, purple).

Computational studies on the quartet states

Table S7 Bond lengths of TD-DFT optimised geometries of quartet states of the complex series $[1^{X}]^{3+}$ (bold values indicate largest bond elongations) with single point energy differences between the excited quartet states ^{4}ES and the lowest optimised doublet state ^{2}E. Distances are given in Å and energies in eV. The colour code corresponds to the different tridentate ligands.

character	Cr–N5 (N_t)	Cr–N2 (N_c)	Cr–N4 (N_t)	Cr–N7 (N_t)	Cr–N3 (N_c)	Cr–N6 (N_t)	ΔE (^{4}ES–^{2}E)
$[1^{O}]^{3+}$							
$^4A_2$	2.071	2.051	2.071	2.071	2.051	2.071	
$^4T_2(1)$	2.049	**2.107**	2.049	2.095	**2.493**	2.094	1.28
$^4T_2(2)$	2.076	**2.239**	2.076	2.077	**2.241**	2.077	1.39
$[1^{S}]^{3+}$							
$^4A_2$	2.118	2.140	2.118	2.118	2.140	2.118	
$^4T_2(1)$	2.106	**2.421**	2.109	2.073	**2.214**	2.075	1.17
$^4T_2(2)$	2.106	**2.364**	2.105	2.078	**2.238**	2.080	1.17
$^4T_2(3)$	2.086	**2.265**	2.086	2.100	**2.311**	2.100	1.17
$^4T_2(4)$	2.095	**2.290**	2.095	2.091	**2.289**	2.091	1.17
^{4}LMCT(1)	2.123	**2.356**	2.123	2.149	**2.462**	2.149	1.20
^{4}LMCT(2)	**2.405**	2.200	**2.403**	2.132	2.115	2.134	1.16
$[1^{NMe}]^{3+}$							
$^4A_2$	2.058	2.046	2.058	2.058	2.046	2.058	
$^4T_2$	2.036	2.061	2.036	2.138	**2.316**	2.138	1.30
^{4}LMCT(1)	2.043	2.059	2.044	2.052	2.045	2.052	1.76
^{4}LMCT(2)	**2.310**	2.087	**2.301**	2.152	2.046	2.112	1.76
$[1^{CH2}]^{3+}$							
$^4A_2$	2.113	2.112	2.111	2.110	2.113	2.113	
$^4T_2$	2.068	**2.161**	2.068	2.121	**2.546**	2.121	1.54

fs-Transient absorption spectroscopy

In order to obtain information on the ultrafast processes after light excitation, we measured femtosecond TA spectra of $[1^{O}]^{3+}$ and $[1^{S}]^{3+}$. As the dd absorptions of $[1^{O}]^{3+}$ are too weak for obtaining meaningful TA data, TA spectra of $[1^{O}]^{3+}$ were recorded in CH_3CN with ^{4}LMCT excitation at 343 nm (Fig. S59–S61). Global analysis with a consecutive kinetic model yields two time constants. The initially observed broad excited state absorption (ESA) in the red to NIR spectral region decays with a time constant of τ_1 = 1.0 ps to a spectrally similar component with a lifetime of τ_2 = 47 ps. The spectral similarity of the two components decaying with τ_1 and τ_2 to the final long-lived state indicates that they belong to similar electronic states, possibly LMCT states. The ultrafast process with the time constant τ_1 likely corresponds to internal conversion (IC) and vibrational cooling (VC) on the ^{2}LMCT manifold. Finally, a blue-shifted signal that does not decay on the timescale of the experiment (8 ns) is obtained. ISC appears to be faster the time resolution of our experiment (200 fs). Due to the higher absorption coefficient of the dd/LMCT band of $[1^{S}]^{3+}$, TA spectra of $[1^{S}]^{3+}$ in water were obtained with excitation at 515 nm. The initial TA spectrum features a broad ESA in the green to red spectral region that decays to a long-lived component within τ_1 = 1.2 ps (Fig. S62–S64). A small spectral shift is associated with a time constant of τ_2 = 90 ps yielding the non-decaying component, i.e. the characteristics of the long-lived SF states. The TA spectra are qualitatively similar to those of $[1^{NMe}]^{3+}$. Hence, we assign the ultrafast component τ_1 to ISC from the quartet to the doublet states, which is convoluted with IC/VC within the doublet manifold. The longer component τ_2 is assigned to reorganization of the solvent cage around the doublet states. The final spectrum that does not decay on the time scale of the experiment corresponds to the emissive SF states.

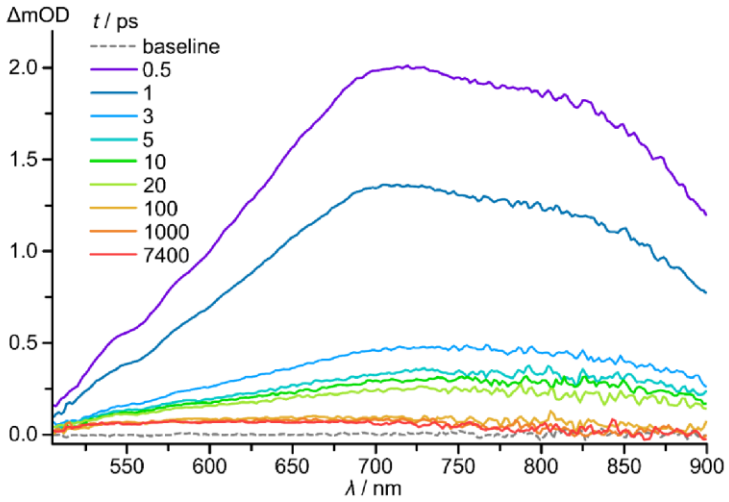

Fig. S59 Transient absorption spectra of $[1^{O}][OTf]_3$ in acetonitrile after pulsed excitation at 343 nm at various time delays (fluence: 70 µJ cm^{-2}, repetition rate: 1 kHz).

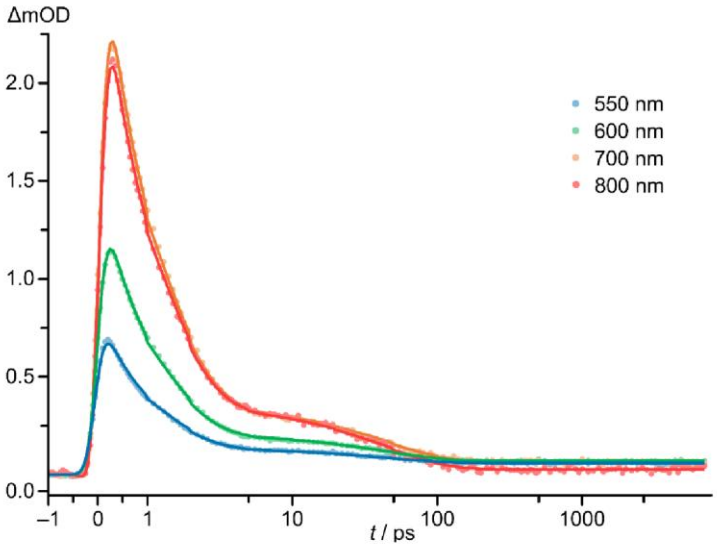

Fig. S60 Decay traces of excited state absorptions of **[1^{O}][OTf]$_3$** in acetonitrile (coloured symbols) at different wavelengths with global fit (solid lines).

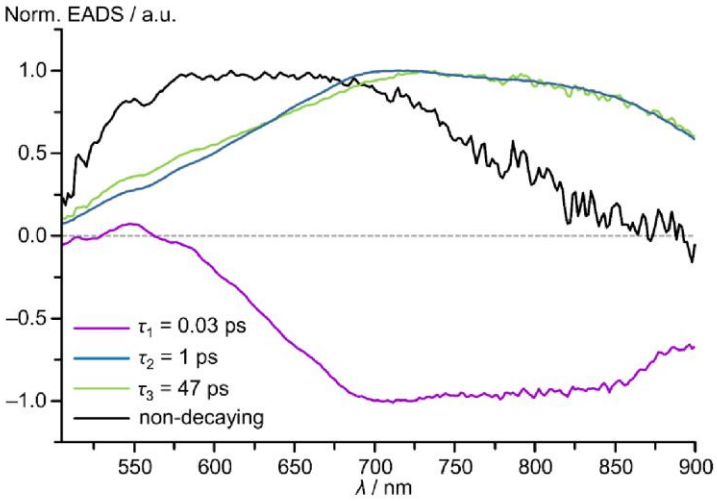

Fig. S61 Normalised evolution associated difference spectra obtained from a global analysis of transient absorption data of **[1^{O}][OTf]$_3$** (acetonitrile, λ_{exc} = 343 nm, fluence: 70 µJ cm^{-2}, repetition rate: 1 kHz).

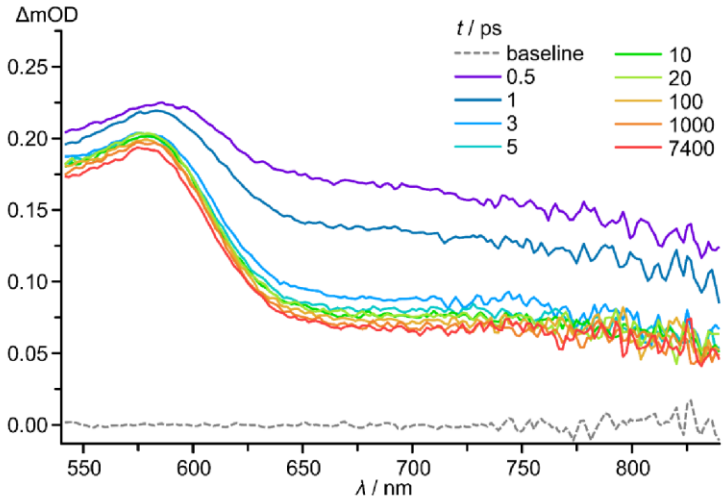

Fig. S62 Transient absorption spectra of **[1^S][OTf]$_3$** in water after pulsed excitation at 515 nm at various time delays (fluence: 3 mJ cm^{-2}, repetition rate: 1 kHz).

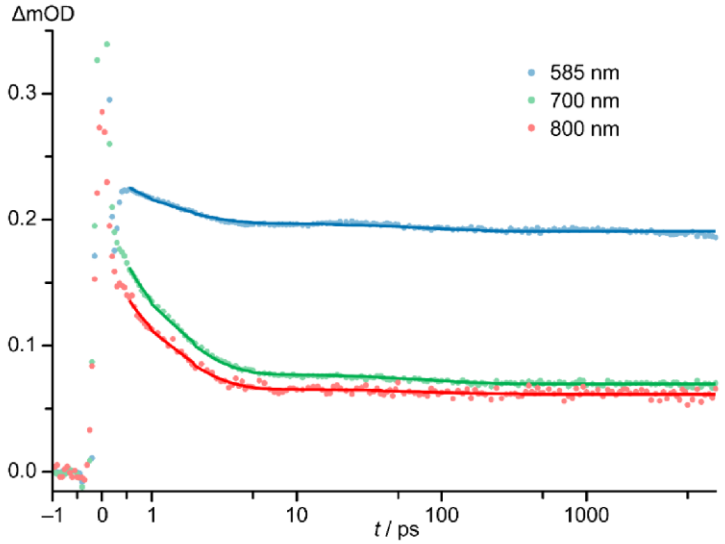

Fig. S63 Decay traces of excited state absorptions of **[1^S][OTf]$_3$** in water (coloured symbols) at different wavelengths with global fit (solid lines).

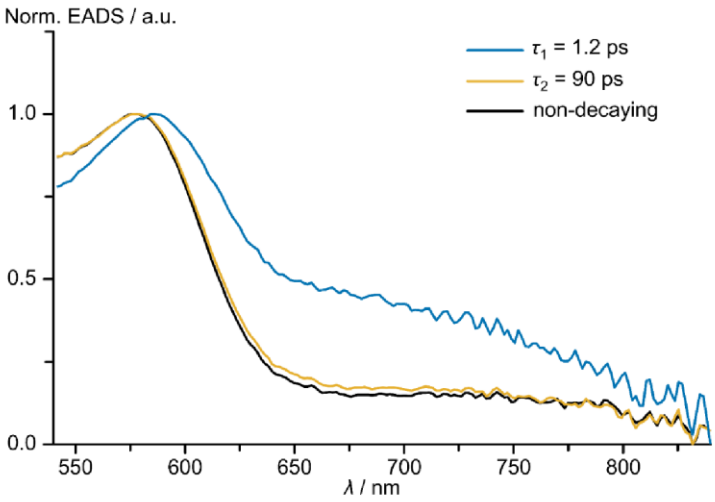

Fig. S64 Normalised evolution associated difference spectra obtained from a global analysis of transient absorption data of **[1^S][OTf]$_3$** (water, λ_{exc} = 515 nm, fluence: 3 mJ cm^{-2}, repetition rate: 1 kHz).

Variable-temperature emission spectroscopy

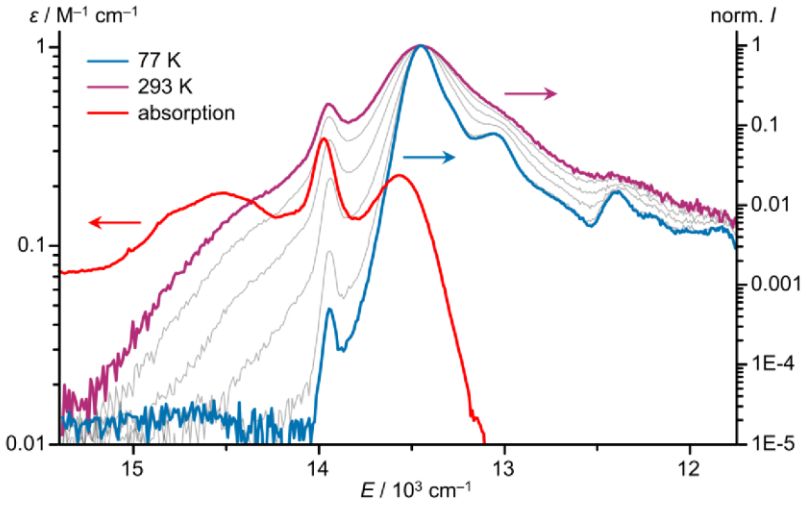

Fig. S65 Spin- and symmetry forbidden absorption band (logarithmic scale) of an acetonitrile solution (red) and temperature dependent emission spectra (λ_{exc} = 450 nm, logarithmic scale) of a (frozen) solution of **[1^{O}][OTf]$_3$** in deaerated ethanol/methanol (3:2) at 77 K (blue), 293 K (purple) and temperatures between 77 und 293 K (grey).

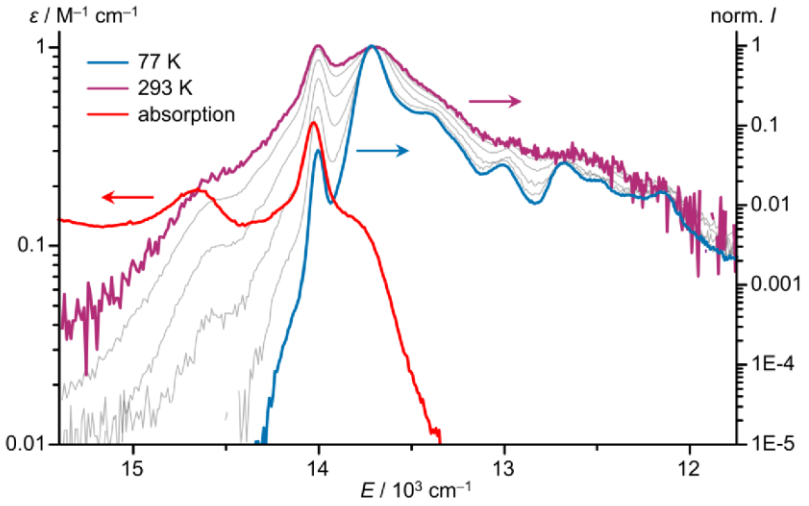

Fig. S66 Spin- and symmetry forbidden absorption band (logarithmic scale) of an acetonitrile solution (red) and temperature dependent emission spectra (λ_{exc} = 450 nm, logarithmic scale) of a (frozen) solution of **[1^{S}][OTf]$_3$** in deaerated ethanol/methanol (3:2) at 77 K (blue), 293 K (purple) and temperatures between 77 and 293 K (grey).

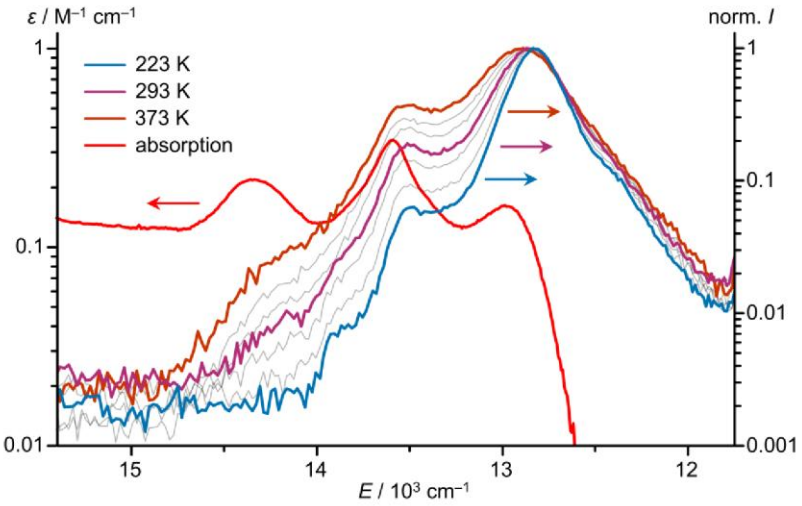

Fig. S67 Spin- and symmetry forbidden absorption band (logarithmic scale) of an acetonitrile solution (red) and temperature dependent emission spectra (λ_{exc} = 436 nm, logarithmic scale) of a solution of **[1^{NMe}][BF$_4$]$_3$** in deaerated ethylene glycol/water (2:1) at 223 K (blue), 293 K (purple), 373 K (brown) and temperatures between 223 and 373 K (grey).[44]

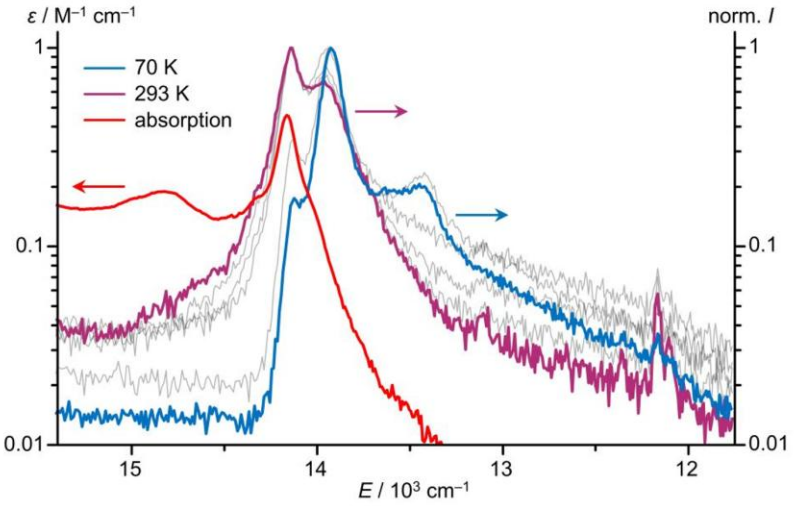

Fig. S68 Spin- and symmetry forbidden absorption band (logarithmic scale) of an acetonitrile solution (red) and temperature dependent emission spectra (λ_{exc} = 355 nm, logarithmic scale) of **[1^{CH2}][OTf]$_3$** in KBr at 70 K (blue), 293 K (purple) and temperatures between 70 and 293 K (grey).[43]

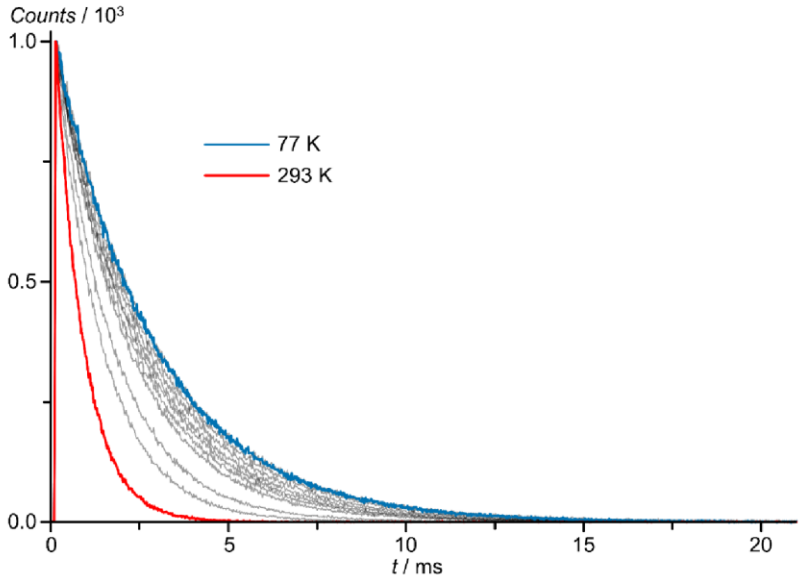

Fig. S69 Normalised temperature dependent emission decay traces recorded at 742 nm following excitation (λ_{exc} = 450 nm) of a 0.33 mM solution of **[1^{O}][OTf]$_3$** in deaerated ethanol/methanol (3:2).

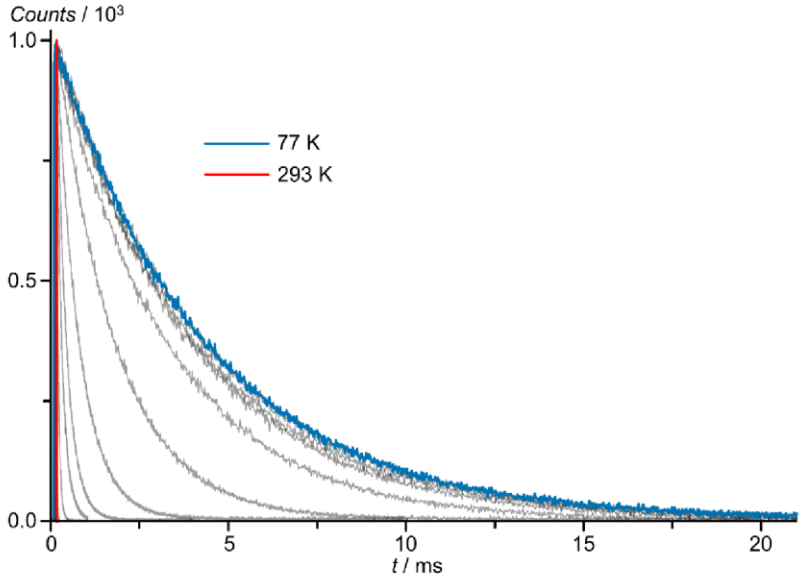

Fig. S70 Normalised temperature dependent emission decay traces recorded at 729 nm following excitation (λ_{exc} = 450 nm) of a 0.13 mM solution of **[1^{S}][OTf]$_3$** in deaerated ethanol/methanol (3:2).

Photolysis experiments

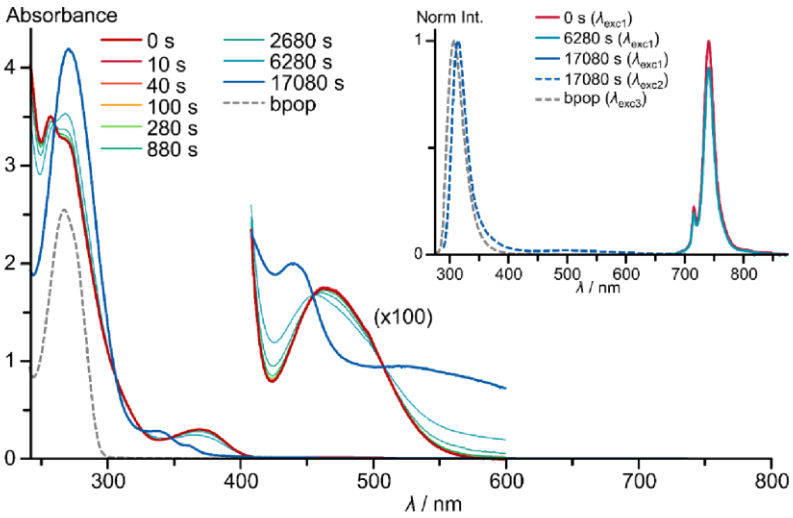

Fig. S71 UV/VIS/NIR absorption (with zoom) and normalised emission spectra of 0.205 mM **[1^{O}][OTf]$_3$** in deaerated acetonitrile after different UHP-LED irradiation time periods (λ_{exc} = 460 nm) with an output power of 1.1 W and UV/VIS/NIR absorption and normalised emission spectra of bpop in acetonitrile (λ_{exc1} = 462 nm, λ_{exc2} = 270 nm, λ_{exc3} = 267 nm).

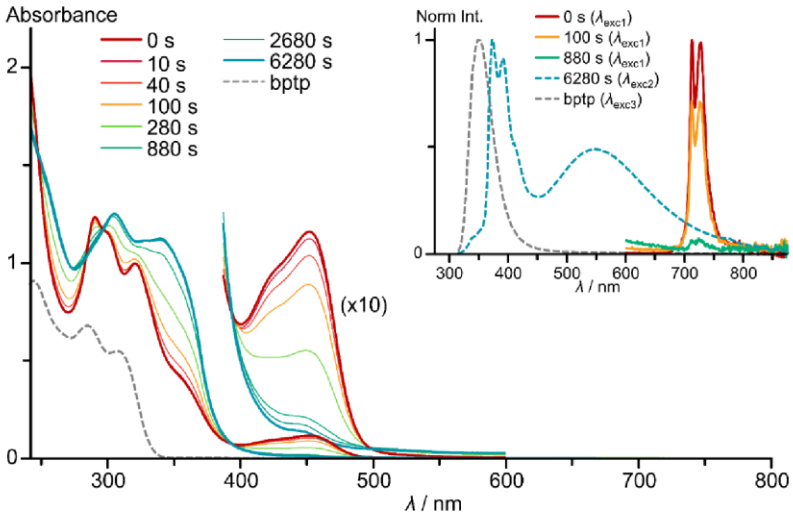

Fig. S72 UV/VIS/NIR absorption (with zoom) and normalised emission spectra of 0.061 mM **[1^{S}][OTf]$_3$** in deaerated acetonitrile after different UHP-LED irradiation time periods (λ_{exc} = 460 nm) with an output power of 1.1 W and UV/VIS/NIR absorption and normalised emission spectra of bptp in acetonitrile (λ_{exc1} = 452 nm, λ_{exc2} = 308 nm, λ_{exc3} = 308 nm).

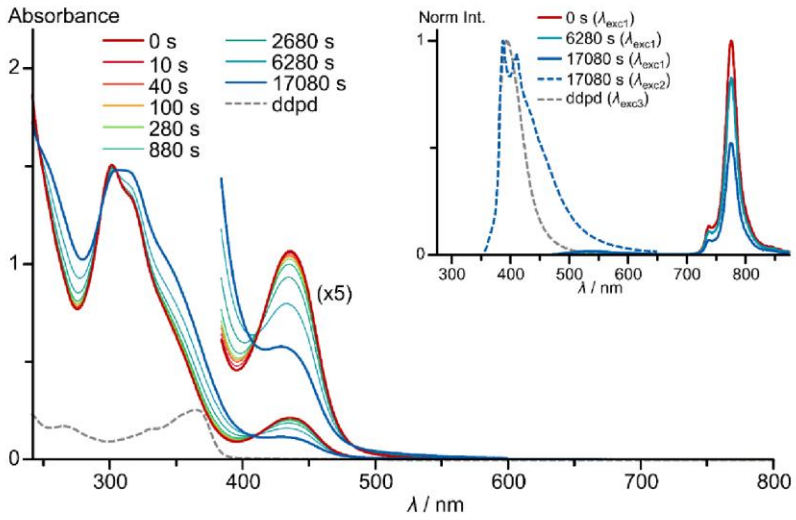

Fig. S73 UV/VIS/NIR absorption (with zoom) and normalised emission spectra of 0.066 mM **[1^{NMe}][OTf]$_3$** in deaerated acetonitrile after different UHP-LED irradiation time periods (λ_{exc} = 460 nm) with an output power of 1.1 W and UV/VIS/NIR absorption and normalised emission spectra of ddpd in dichloromethane (λ_{exc1} = 436 nm, λ_{exc2} = 345 nm, λ_{exc3} = 369 nm).[44]

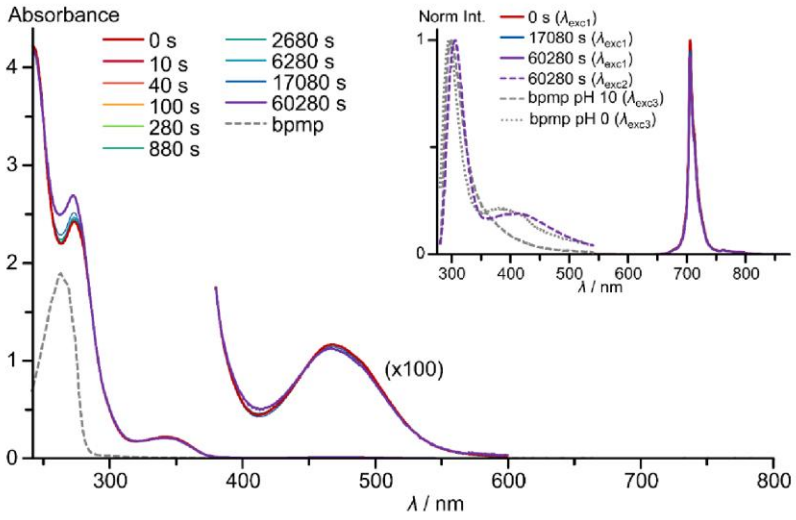

Fig. S74 UV/VIS/NIR absorption (with zoom) and normalised emission spectra of 0.177 mM **[1^{CH2}][OTf]$_3$** in deaerated acetonitrile after different UHP-LED irradiation time periods (λ_{exc} = 460 nm) with an output power of 1.1 W and UV/VIS/NIR absorption and normalised emission spectra of bpmp in water at pH = 0 and pH = 10 (λ_{exc1} = 467 nm, λ_{exc2} = 270 nm, λ_{exc3} = 266 nm).[43]

Quenching Experiments

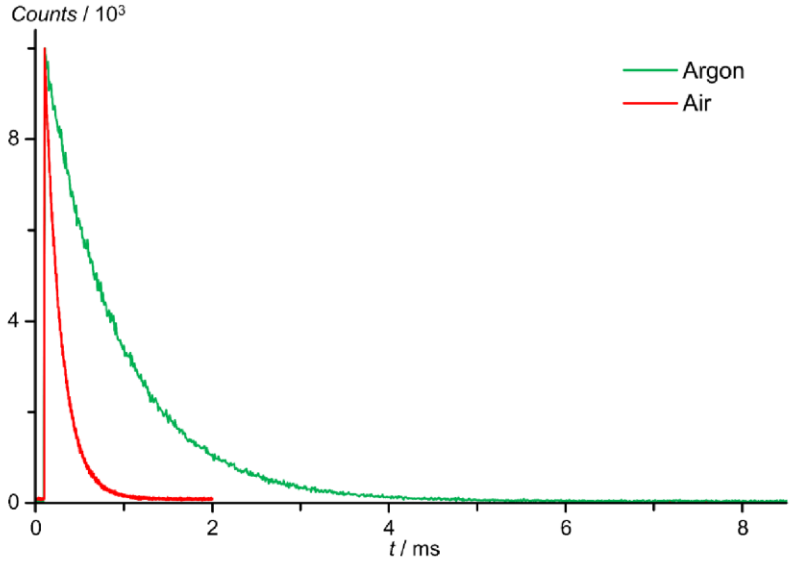

Fig. S75 Emission decay traces recorded at 742 nm following excitation (λ_{exc} = 450 nm) of a solution of **[1^{O}][OTf]$_3$** in deaerated acetonitrile (green) and air saturated acetonitrile (red).

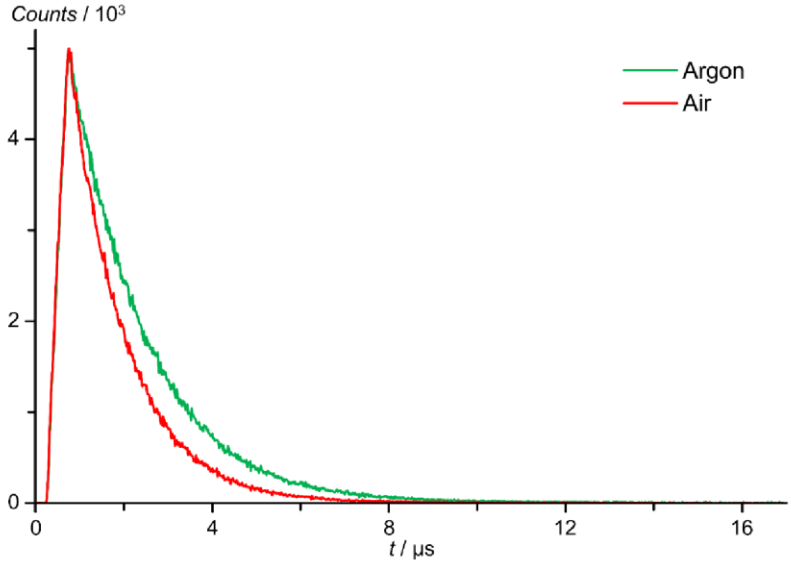

Fig. S76 Emission decay traces recorded at 729 nm following excitation (λ_{exc} = 450 nm) of a solution of **[1^{S}][OTf]$_3$** in deaerated acetonitrile (green) and air saturated acetonitrile (red).

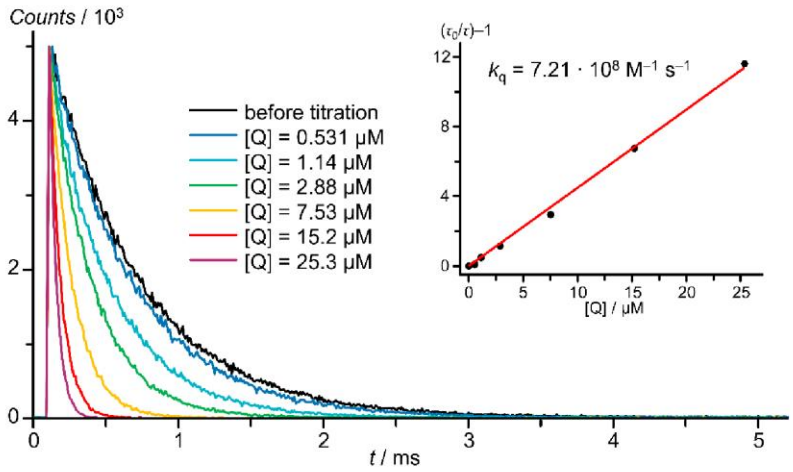

Fig. S77 Quencher concentration dependent emission decay traces recorded at 742 nm following excitation (λ_{exc} = 450 nm) of a solution of **[1^{O}][OTf]$_3$** in deaerated acetonitrile for Stern-Volmer analysis with anthracene and the corresponding Stern-Volmer plot with linear fit (red line).

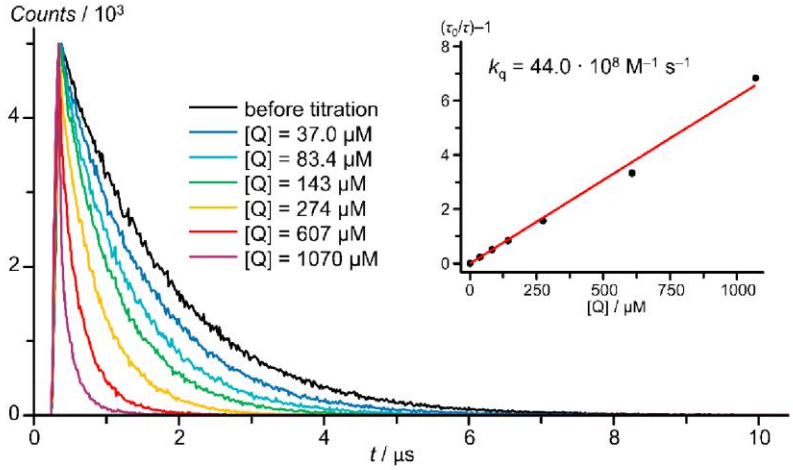

Fig. S78 Quencher concentration dependent emission decay traces recorded at 729 nm following excitation (λ_{exc} = 450 nm) of a solution of **[1^{S}][OTf]$_3$** in deaerated acetonitrile for Stern-Volmer analysis with anthracene and the corresponding Stern-Volmer plot with linear fit (red line).

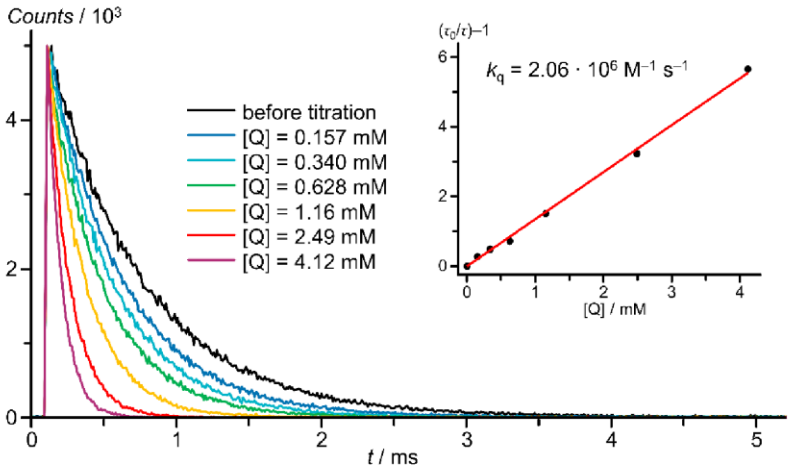

Fig. S79 Quencher concentration dependent emission decay traces recorded at 742 nm following excitation (λ_{exc} = 450 nm) of a solution of **[1^{O}][OTf]$_3$** in deaerated acetonitrile for Stern-Volmer analysis with trans-stilbene and the corresponding Stern-Volmer plot with linear fit (red line).

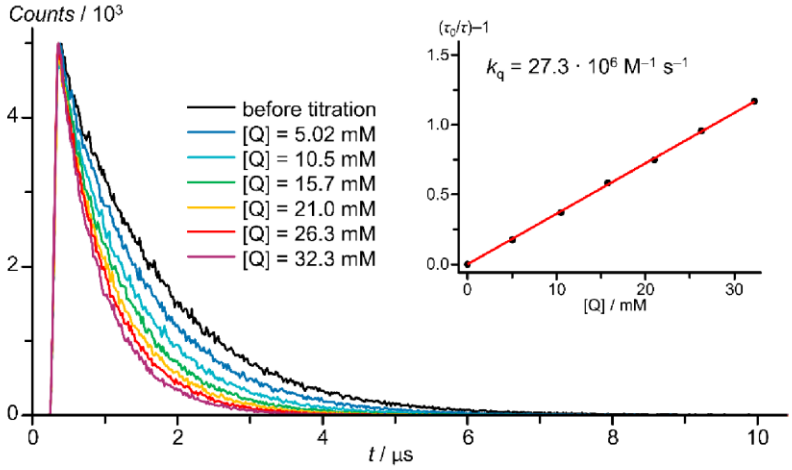

Fig. S80 Quencher concentration dependent emission decay traces recorded at 729 nm following excitation (λ_{exc} = 450 nm) of a solution of **[1^{S}][OTf]$_3$** in deaerated acetonitrile for Stern-Volmer analysis with trans-stilbene and the corresponding Stern-Volmer plot with linear fit (red line).

References

[1] H. E. Gottlieb, V. Kotlyar and A. Nudelman, *J. Org. Chem.*, 1997, **62**, 7512–7515.

[2] F. Barigelletti, D. Sandrini, M. Maestri, V. Balzani, A. von Zelewsky, L. Chassot, P. Jolliet and U. Maeder, *Inorg. Chem.*, 1988, **27**, 3644–3647.

[3] C. Müller, T. Pascher, A. Eriksson, P. Chabera and J. Uhlig, *J. Phys. Chem. A.*, 2022, **126**, 4087–4099.

[4] J. R. Lakowicz, *Principles of Fluorescence Spectroscopy,* Springer, New York, 2010.

[5] F. Neese, *WIREs Comp. Mol. Sci.*, 2012, **2**, 73–78.

[6] F. Neese, *WIREs Comp. Mol. Sci.*, 2022, **12**, 12753.

[7] C. Lee, W. Yang and R. G. Parr, *Phys. Rev. B: Condens. Matter Mater. Phys.*, 1988, **37**, 785–789.

[8] B. Miehlich, A. Savin, H. Stoll and H. Preuss, *Chem. Phys. Lett.*, 1989, **157**, 200–206.

[9] A. D. Becke, *J. Chem. Phys.*, 1993, **98**, 5648–5652.

[10] F. Weigend and R. Ahlrichs, *Phys. Chem. Chem. Phys.*, 2005, **7**, 3297–3305.

[11] F. Neese, F. Wennmohs, A. Hansen and U. Becker, *Chem. Phys.*, 2009, **356**, 98–109.

[12] R. Izsák and F. Neese, *J. Chem. Phys.*, 2011, **135**, 144105.

[13] F. Weigend, *Phys. Chem. Chem. Phys.*, 2006, **8**, 1057–1065.

[14] D. A. Pantazis and F. Neese, *J. Chem. Theory Comput.*, 2009, **5**, 2229–2238.

[15] D. A. Pantazis, X.-Y. Chen, C. R. Landis and F. Neese, *J. Chem. Theory Comput.*, 2008, **4**, 908–919.

[16] D. A. Pantazis and F. Neese, *Theor. Chem. Acc.*, 2012, **131**, 89.

[17] D. A. Pantazis and F. Neese, *J. Chem. Theory Comput.*, 2011, **7**, 677–684.

[18] C. van Wüllen, *J. Chem. Phys.*, 1998, **109**, 392–399.

[19] E. van Lenthe, E. J. Baerends and J. G. Snijders, *J. Chem. Phys.*, 1993, **99**, 4597–4610.

[20] S. Miertuš, E. Scrocco and J. Tomasi, *Chem. Phys.*, 1981, **55**, 117–129.

[21] V. Barone and M. Cossi, *J. Phys. Chem. A*, 1998, **102**, 1995–2001.

[22] S. Grimme, J. Antony, S. Ehrlich and H. Krieg, *J. Chem. Phys.*, 2010, **132**, 154104.

[23] S. Grimme, S. Ehrlich and L. Goerigk, *J. Comput. Chem.*, 2011, **32**, 1456–1465.

[24] F. Plasser, *J. Chem. Phys.*, 2020, **152**, 84108.

[25] B. O. Roos, P. R. Taylor and P. E. M. Sigbahn, *Chem. Phys.*, 1980, **48**, 157–173.

[26] P. E. M. Siegbahn, J. Almlöf, A. Heiberg and B. O. Roos, *J. Chem. Phys.*, 1981, **74**, 2384–2396.

[27] C. Angeli, R. Cimiraglia, S. Evangelisti, T. Leininger and J.-P. Malrieu, *J. Chem. Phys.*, 2001, **114**, 10252–10264.

[28] C. Angeli, R. Cimiraglia and J.-P. Malrieu, *Chem. Phys. Lett.*, 2001, **350**, 297–305.

[29] C. Angeli, R. Cimiraglia and J.-P. Malrieu, *J. Chem. Phys.*, 2002, **117**, 9138–9153.

[30] K. Pierloot, *Int. J. Quantum Chem.*, 2011, **111**, 3291–3301.

[31] STOE & Cie, X-Area, STOE & Cie GmbH, Darmstadt, Germany.

[32] R. H. Blessing, *Acta Crystallogr. A* 1995, **51**, 33–38.

[33] A. L. Spek, *Acta Crystallogr. D* 2009, **65**, 148–155.

[34] J. Koziskova, F. Hahn, J. Richter and J. Kožíšek, *Acta Chim. Slovaca* 2016, **9**, 136–140.

[35] STOE & Cie, X-Area LANA, STOE & Cie GmbH, Darmstadt, Germany.

[36] G. M. Sheldrick, *Acta Crystallogr., Sect. A: Found. Adv.*, 2015, **71**, 3–8.

[37] G. M. Sheldrick, *Acta Crystallogr., Sect. C: Struct. Chem.*, 2015, **71**, 3–8.

[38] G. M. Sheldrick, *Acta Crystallogr., Sect. A: Found. Crystallogr.*, 2008, **64**, 112–122.

[39] C. B. Hübschle, G. M. Sheldrick and B. Dittrich, *J. Appl. Crystallogr.*, 2011, **44**, 1281–1284.

[40] P.-S. Wang, C.-K. Liang and M.-k. Leung, *Tetrahedron*, 2005, **61**, 2931–2939.

[41] S. Balamurugan, S. Ganesan, S. Kamaraj, V. Mathew, J. Kim, N. Arumugam and A. I. Almansour, *Optical Materials*, 2022, **125**, 112082.

[42] R. D. Köhn, A. G. N. Coxon, S. Chunawat, C. Heron, S. Mihan, C. L. Lyall, S. B. Reeksting and G. Kociok-Köhn, *Polyhedron*, 2020, **185**, 114572.

[43] F. Reichenauer, C. Wang, C. Förster, P. Boden, N. Ugur, R. Báez-Cruz, J. Kalmbach, L. M. Carrella, E. Rentschler, C. Ramanan, G. Niedner-Schatteburg, M. Gerhards, M. Seitz, U. Resch-Genger and K. Heinze, *J. Am. Chem. Soc.*, 2021, **143**, 11843–11855.

[44] S. Otto, M. Grabolle, C. Förster, C. Kreitner, U. Resch-Genger, K. Heinze, *Angew. Chem. Int. Ed. Engl.*, 2015, **54**, 11572–11576.

6.5 Supporting Information: Factorizing the Nephelauxetic Effect in Heteroleptic Molecular Rubies

Factorizing the Nephelauxetic Effect in Heteroleptic Molecular Rubies

Florian Reichenauer, Dimitri Zorn, Robert Naumann, Christoph Förster and Katja Heinze*

Department of Chemistry, Johannes Gutenberg University Mainz, Duesbergweg 10-14, 55128 Mainz (Germany); katja.heinze@uni-mainz.de

Supporting Information

Crystallographic Data of 2^{NMe} and $[3^{CH2,NMe}](OTf)_3$

Crystallographic Data of 2^{NMe}

$C_{20}H_{17}CrF_9N_5O_9S_3$ (790.57); triclinic; $P\bar{1}$; a = 10.800(2) Å, b = 11.174(2) Å, c = 14.057(3) Å; α = 72.70(3)°; β = 70.14(3)°; γ = 63.42(3)°; V = 1405.4(7) Å^3; Z = 2; density, calcd. = 1.868 g cm^{-3}, T = 120(2) K, μ = 0.750 mm^{-1}; F(000) = 794; crystal size 0.340 × 0.290 × 0.240 mm^3; θ = 2.368 to 27.925°; −14≤h≤12, −14≤k≤13, −18≤l≤18; reflections collected = 13808; reflections unique = 6665 [R(int) = 0.0255]; completeness to θ = 25.242°: 99.7%; absorption correction: semi-empirical from equivalents; max. and min. transmission 1.14010 and 0.89722; data 6665; restraints 0, parameters 426; goodness-of-fit on F^2 = 1.059; final indices [$I > 2\sigma(I)$] R_1 = 0.0310, wR_2 = 0.0767; R indices (all data) R_1 = 0.0353, wR_2 = 0.0793; largest diff. peak and hole 0.497 and −0.544 e Å^{-3}.

Crystallographic Data of $[3^{CH2,NMe}](OTf)_3$

$C_{39}H_{38}CrF_9N_8O_{10}S_3$ (1097.95); triclinic; $P\bar{1}$; a = 10.529(2) Å, b = 12.643(3) Å, c = 17.732(4) Å; α = 89.56(3)°; β = 82.52(3)°; γ = 75.73(3)°; V = 2267.4(9) Å^3; Z = 2; density, calcd. = 1.608 g cm^{-3}, T = 120(2) K, μ = 0.493 mm^{-1}; F(000) = 1122; crystal size 0.190 × 0.133 × 0.100 mm^3; θ = 2.651 to 27.955°; −13≤h≤13, −16≤k≤16, −23≤l≤23; reflections collected = 21979; reflections unique = 10750 [R(int) = 0.0555]; completeness to θ = 25.242°: 99.6%; absorption correction: semi-empirical from equivalents; max. and min. transmission 1.14673 and 0.85999; data 10750; restraints 348, parameters 709; goodness-of-fit on F^2 = 1.075; final indices [$I > 2\sigma(I)$] R_1 = 0.0513, wR_2 = 0.1167; R indices (all data) R_1 = 0.0719, wR_2 = 0.1317; largest diff. peak and hole 0.569 and −0.678 e Å^{-3}.

Analytical Data of the Chlorido and Triflato Chromium(III) Precursor Complexes

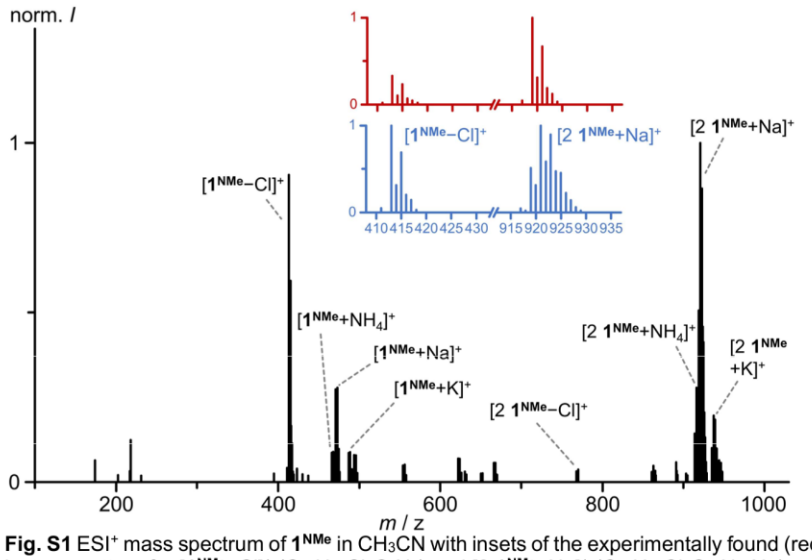

Fig. S1 ESI$^+$ mass spectrum of $\mathbf{1}^{\mathbf{NMe}}$ in CH_3CN with insets of the experimentally found (red) and calculated (blue, normalized) isotope pattern for $[\mathbf{1}^{\mathbf{NMe}}–Cl]^+$ ($C_{17}H_{17}Cl_2CrN_5$) and $[2\ \mathbf{1}^{\mathbf{NMe}}+Na]^+$ ($C_{34}H_{34}Cl_6Cr_2N_{10}Na$).

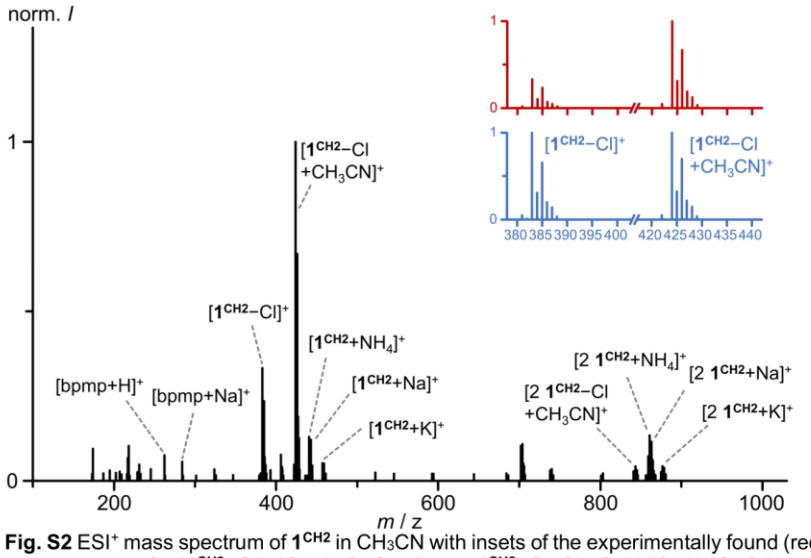

Fig. S2 ESI$^+$ mass spectrum of $\mathbf{1}^{\mathbf{CH2}}$ in CH_3CN with insets of the experimentally found (red) and calculated (blue, normalized) isotope pattern for $[\mathbf{1}^{\mathbf{CH2}}–Cl]^+$ ($C_{17}H_{15}Cl_2CrN_3$) and $[\mathbf{1}^{\mathbf{CH2}}–Cl+CH_3CN]^+$ ($C_{19}H_{18}Cl_2CrN_4$).

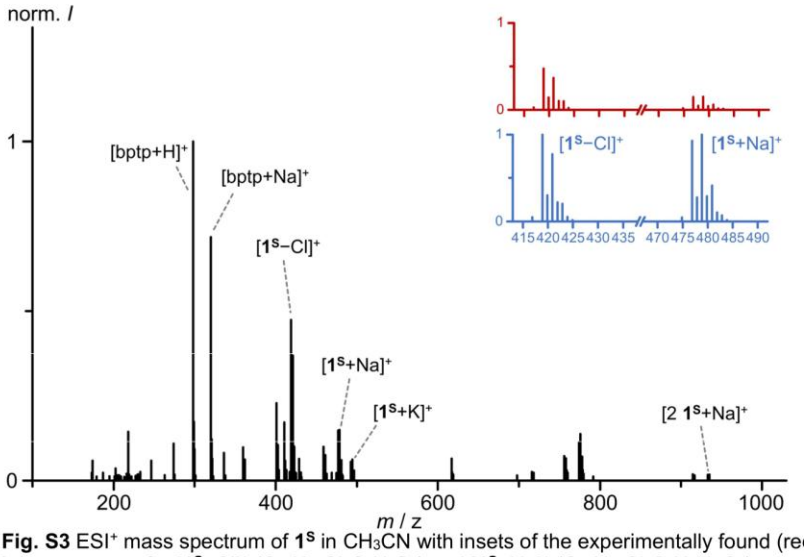

Fig. S3 ESI$^+$ mass spectrum of $\mathbf{1^S}$ in CH_3CN with insets of the experimentally found (red) and calculated (blue, normalized) isotope pattern for $[\mathbf{1^S}–Cl]^+$ ($C_{15}H_{11}Cl_2CrN_3S_2$) and $[\mathbf{1^S}+Na]^+$ ($C_{15}H_{11}Cl_3CrN_3NaS_2$).

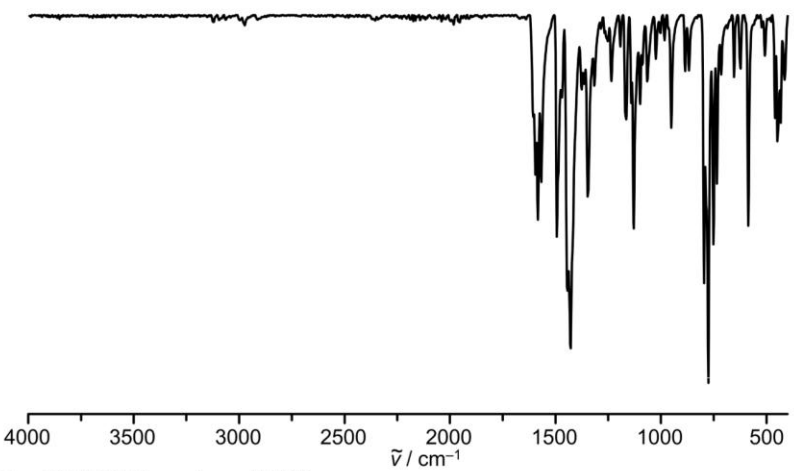

Fig. S4 ATR-IR spectrum of $\mathbf{1^{NMe}}$.

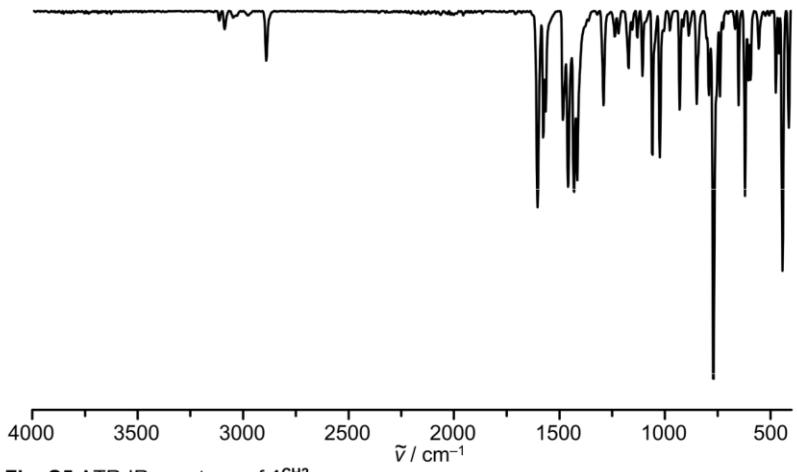

Fig. S5 ATR-IR spectrum of $\mathbf{1}^{CH2}$.

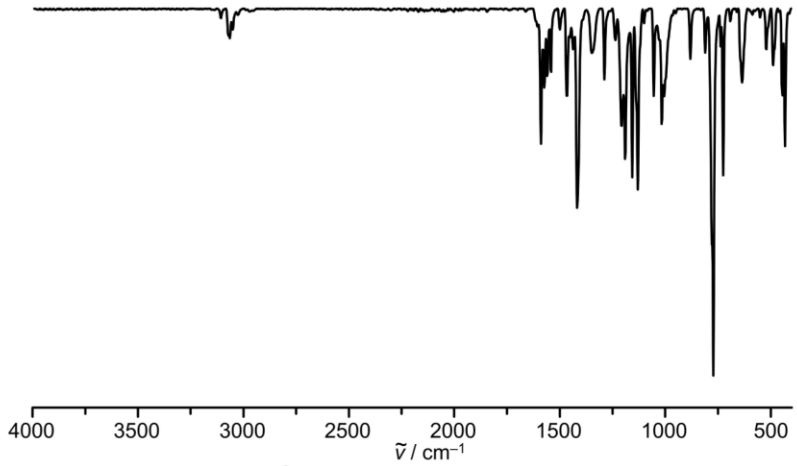

Fig. S6 ATR-IR spectrum of $\mathbf{1}^{S}$.

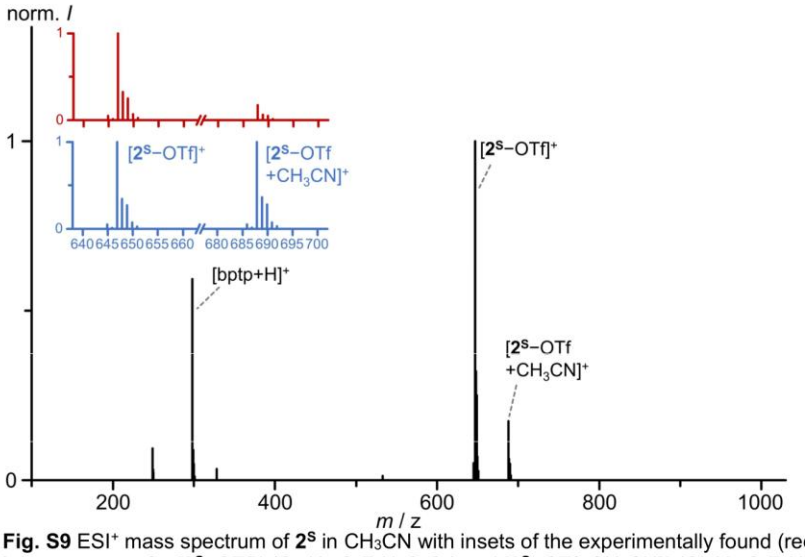

Fig. S9 ESI$^+$ mass spectrum of $\mathbf{2^S}$ in CH_3CN with insets of the experimentally found (red) and calculated (blue, normalized) isotope pattern for $[\mathbf{2^S}–OTf]^+$ ($C_{17}H_{11}CrF_6N_3O_6S_4$) and $[\mathbf{2^S}–OTf+CH_3CN]^+$ ($C_{19}H_{14}CrF_6N_4O_6S_4$).

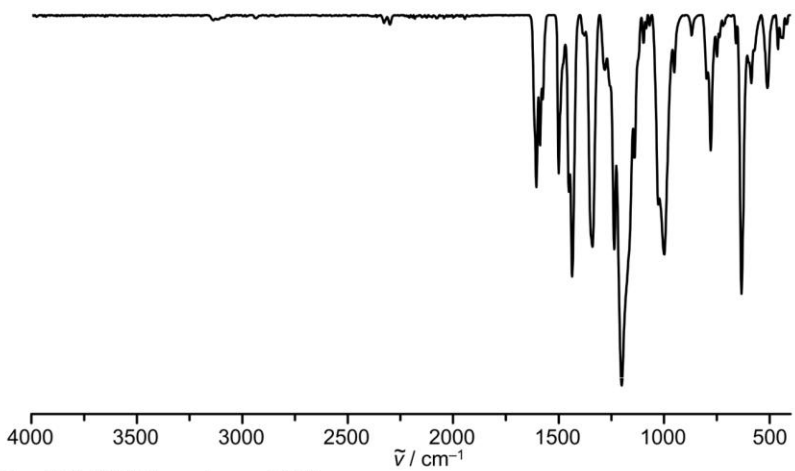

Fig. S10 ATR-IR spectrum of $\mathbf{2^{NMe}}$.

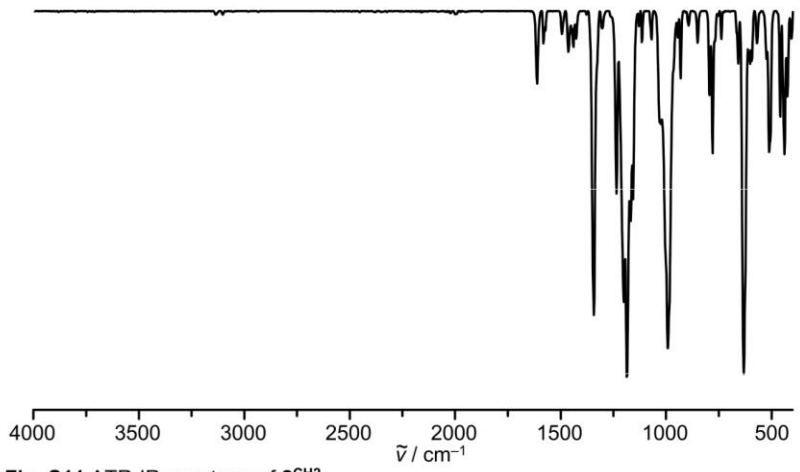

Fig. S11 ATR-IR spectrum of $\mathbf{2}^{\mathbf{CH2}}$.

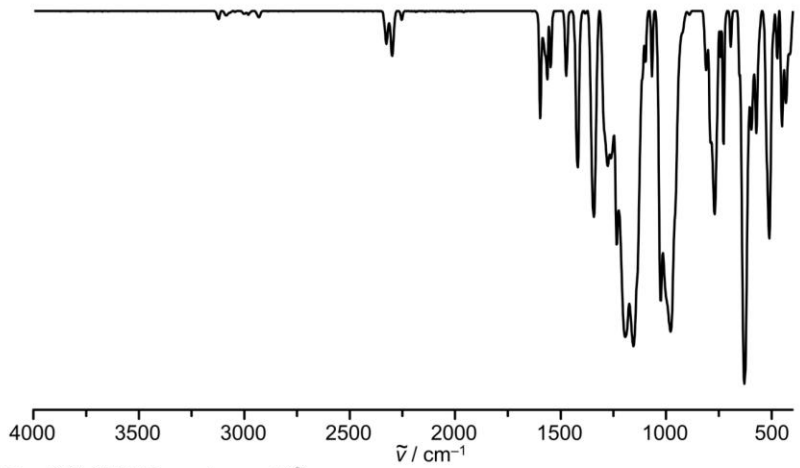

Fig. S12 ATR-IR spectrum of $\mathbf{2}^{\mathbf{S}}$.

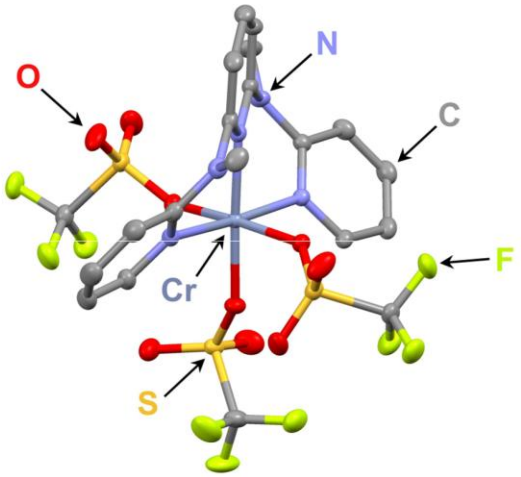

Fig. S13 Molecular structure of $\mathbf{2}^{\mathbf{NMe}}$ in the solid state (monoclinic space group $P\bar{1}$). H atoms omitted, thermal ellipsoids at 50% probability level.

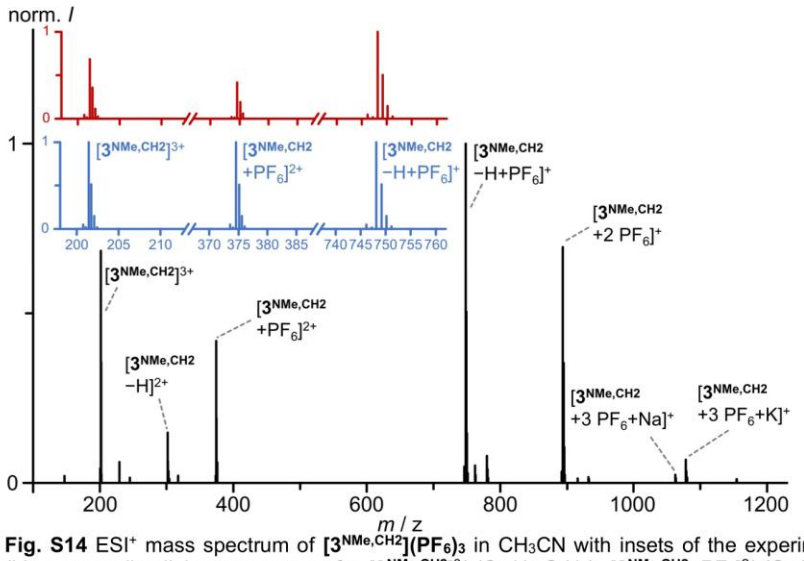

Fig. S14 ESI$^+$ mass spectrum of $[\mathbf{3}^{\mathbf{NMe,CH2}}](\mathbf{PF_6})_3$ in CH_3CN with insets of the experimentally found (red) and calculated (blue, normalized) isotope pattern for $[\mathbf{3}^{\mathbf{NMe,CH2}}]^{3+}$ ($C_{34}H_{32}CrN_8$), $[\mathbf{2}^{\mathbf{NMe,CH2}}+PF_6]^{2+}$ ($C_{34}H_{32}CrF_6N_8P$) and $[\mathbf{2}^{\mathbf{NMe,CH2}}-H+PF_6]^+$ ($C_{34}H_{31}CrF_6N_8P$).

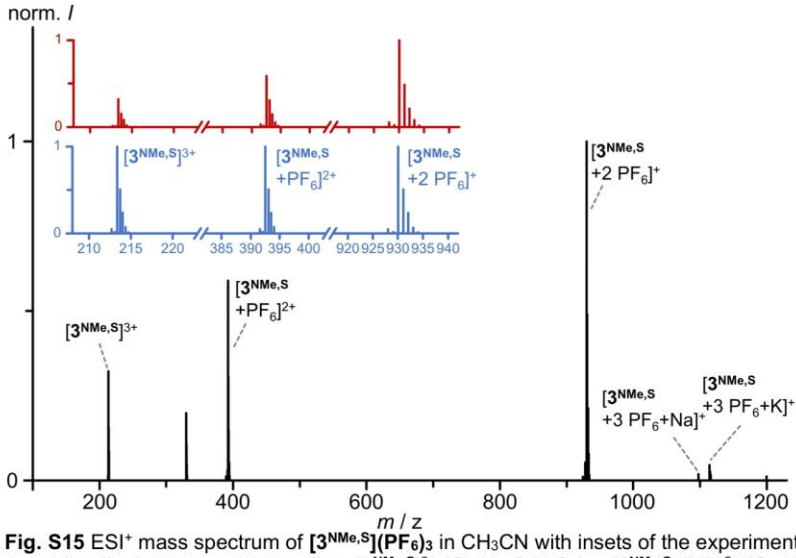

Fig. S15 ESI$^+$ mass spectrum of $[\mathbf{3}^{\mathbf{NMe,S}}](\mathbf{PF_6})_3$ in CH_3CN with insets of the experimentally found (red) and calculated (blue, normalized) isotope pattern for $[\mathbf{3}^{\mathbf{NMe,S}}]^{3+}$ ($C_{32}H_{28}CrN_8S_2$), $[\mathbf{2}^{\mathbf{NMe,S}}+PF_6]^{2+}$ ($C_{32}H_{28}CrF_6N_8S_2P$) and $[\mathbf{2}^{\mathbf{NMe,S}}+2\ PF_6]^+$ ($C_{32}H_{28}CrF_{12}N_8S_2P_2$).

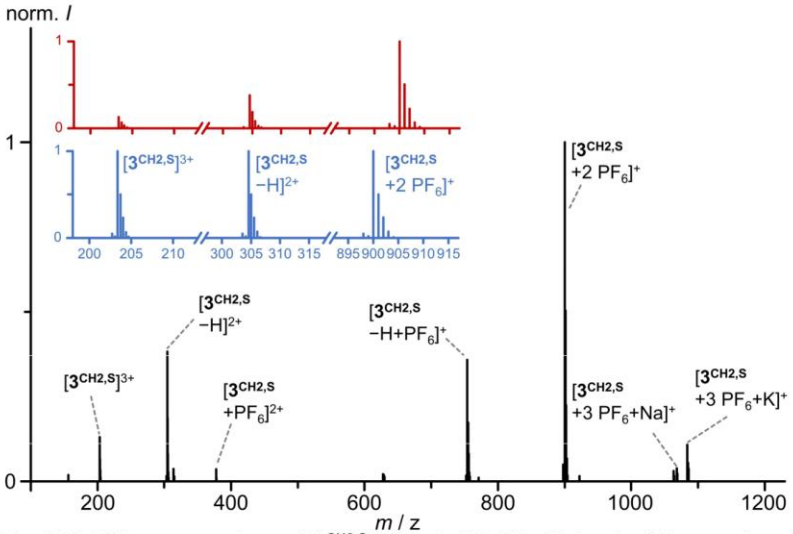

Fig. S16 ESI$^+$ mass spectrum of $[\mathbf{3}^{\mathbf{CH2,S}}](\mathbf{PF_6})_3$ in CH_3CN with insets of the experimentally found (red) and calculated (blue, normalized) isotope pattern for $[\mathbf{3}^{\mathbf{CH2,S}}]^{3+}$ ($C_{32}H_{26}CrN_6S_2$), $[\mathbf{2}^{\mathbf{CH2,S}}-H]^{2+}$ ($C_{32}H_{25}CrN_6S_2$) and $[\mathbf{2}^{\mathbf{CH2,S}}+2\ PF_6]^+$ ($C_{32}H_{26}CrF_{12}N_6S_2P_2$).

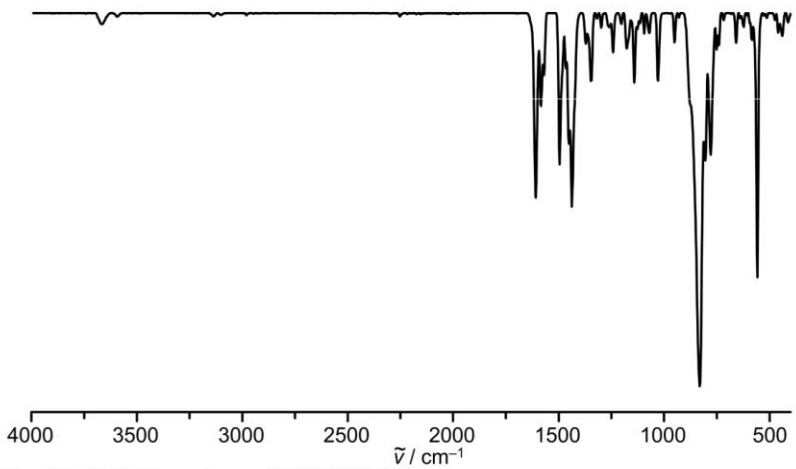

Fig. S17 ATR-IR spectrum of $[\mathbf{3}^{\mathbf{NMe,CH2}}](\mathbf{PF_6})_3$.

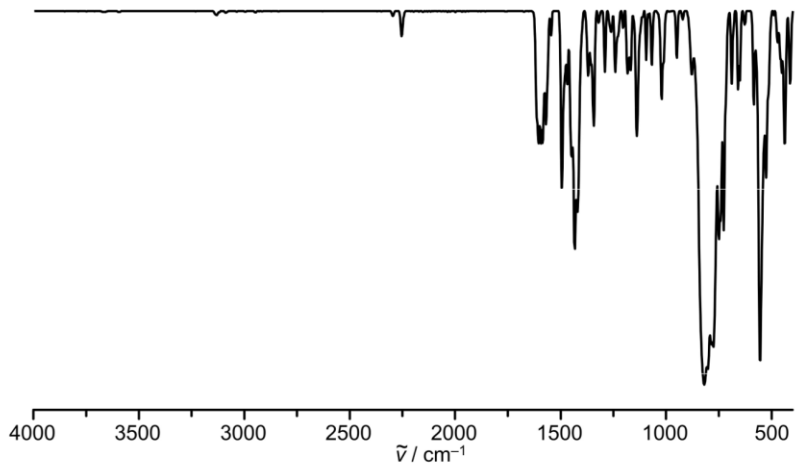

Fig. S18 ATR-IR spectrum of **[3^{NMe,S}](PF$_6$)$_3$**.

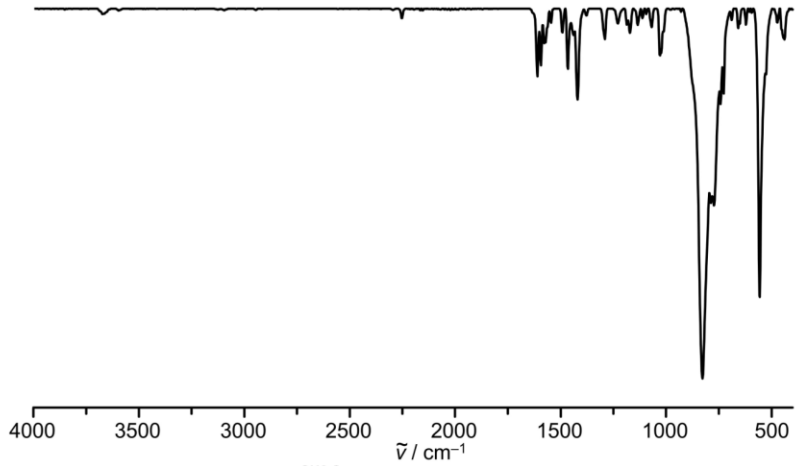

Fig. S19 ATR-IR spectrum of **[3^{CH2,S}](PF$_6$)$_3$**.

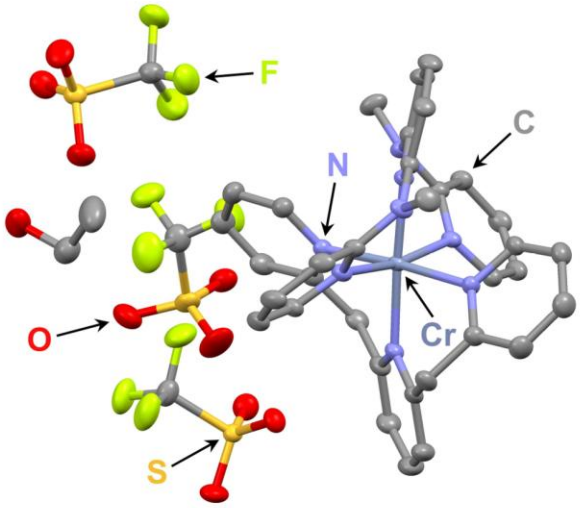

Fig. S20 Molecular structure of **[3^{NMe,CH2}](OTf)$_3$ × EtOH** in the solid state (monoclinic space group $P\bar{1}$). H atoms omitted, thermal ellipsoids at 50% probability level.

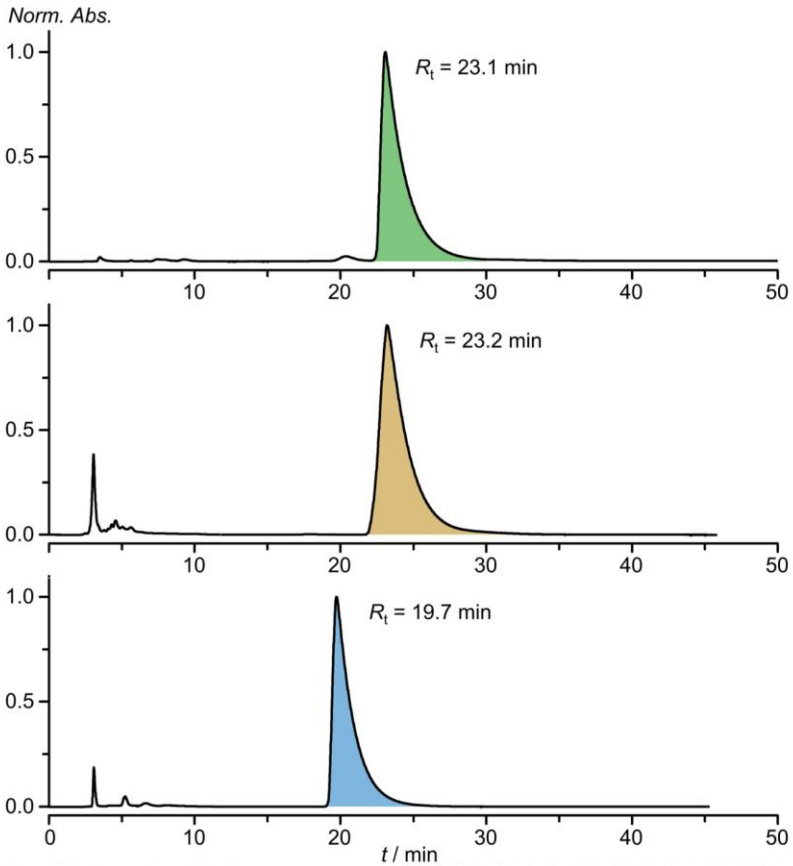

Fig. S21 Analytical HPLC chromatograms (H_2O/CH_3CN (50:50), 0.3 M $[NH_4][HCO_2]$, 0.1% HCO_2H) of purified samples of **[3^{NMe,CH2}](PF$_6$)$_3$** (top), **[3^{NMe,S}](PF$_6$)$_3$** (middle) and **[3^{CH2,S}](PF$_6$)$_3$** (bottom).

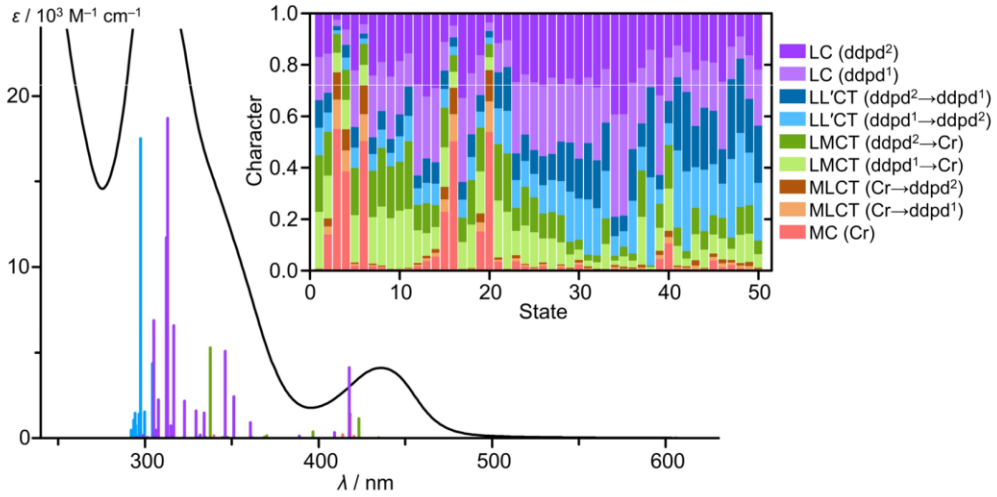

Fig. S22 UV/VIS absorption spectrum of **[3^{NMe,NMe}](BF$_4$)$_3$** in CH_3CN (black) with TD-DFT calculated oscillator strengths colored according to the most dominant character of the corresponding transition (red: MC, orange: MLCT, green: LMCT, purple: LC). Inset: Charge transfer number analysis of the 50 lowest energy spin-allowed transitions calculated by Loewdin population analysis with the complex cation fragmented into chromium (Cr), ddpd ligand 1 (ddpd^1) and ddpd ligand 2 (ddpd^2).[35]

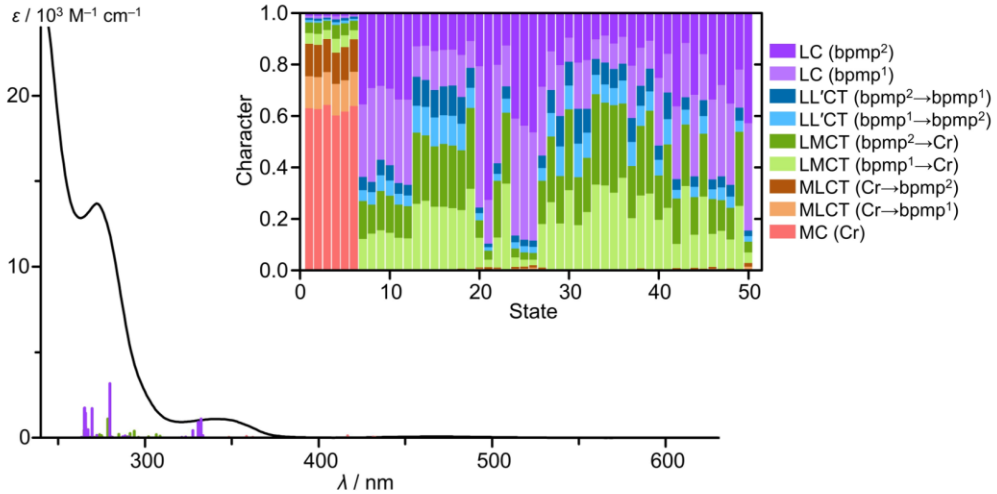

Fig. S23 UV/VIS absorption spectrum of **[3^{CH2,CH2}](OTf)$_3$** in CH_3CN (0.01 M $HClO_4$) (black) with TD-DFT calculated oscillator strengths colored according to the most dominant character of the corresponding transition (red: MC, orange: MLCT, green: LMCT, purple: LC). Inset: Charge transfer number analysis of the 50 lowest energy spin-allowed transitions calculated by Loewdin population analysis with the complex cation fragmented into chromium (Cr), bpmp ligand 1 (bpmp^1) and bpmp ligand 2 (bpmp^2).[36]

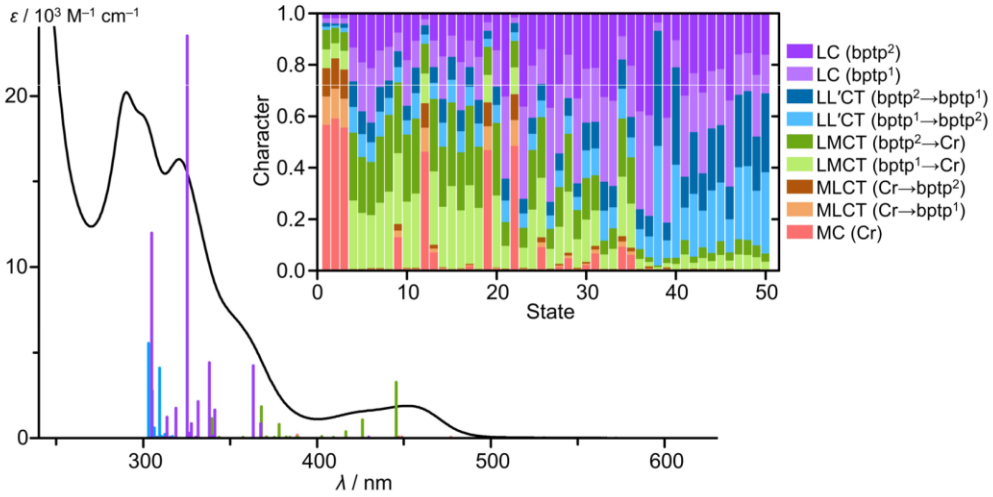

Fig. S24 UV/VIS absorption spectrum of **[3^{S,S}](OTf)$_3$** in CH_3CN (black) with TD-DFT calculated oscillator strengths colored according to the most dominant character of the corresponding transition (red: MC, orange: MLCT, green: LMCT, purple: LC). Inset: Charge transfer number analysis of the 50 lowest energy spin-allowed transitions calculated by Loewdin population analysis with the complex cation fragmented into chromium (Cr), bptp ligand 1 (bptp^1) and bptp ligand 2 (bptp^2).[3]

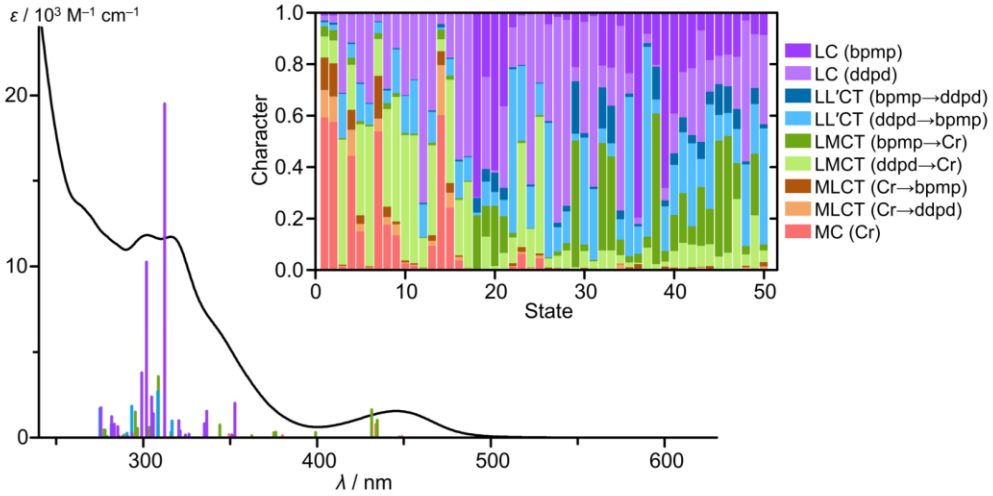

Fig. S25 UV/VIS absorption spectrum of **[3^{NMe,CH2}](PF$_6$)$_3$** in CH_3CN (0.01 M $HClO_4$) (black) with TD-DFT calculated oscillator strengths colored according to the most dominant character of the corresponding transition (red: MC, orange: MLCT, green: LMCT, purple: LC). Inset: Charge transfer number analysis of the 50 lowest energy spin-allowed transitions calculated by Loewdin population analysis with the complex cation fragmented into chromium (Cr), ddpd ligand (ddpd) and bpmp ligand (bpmp).

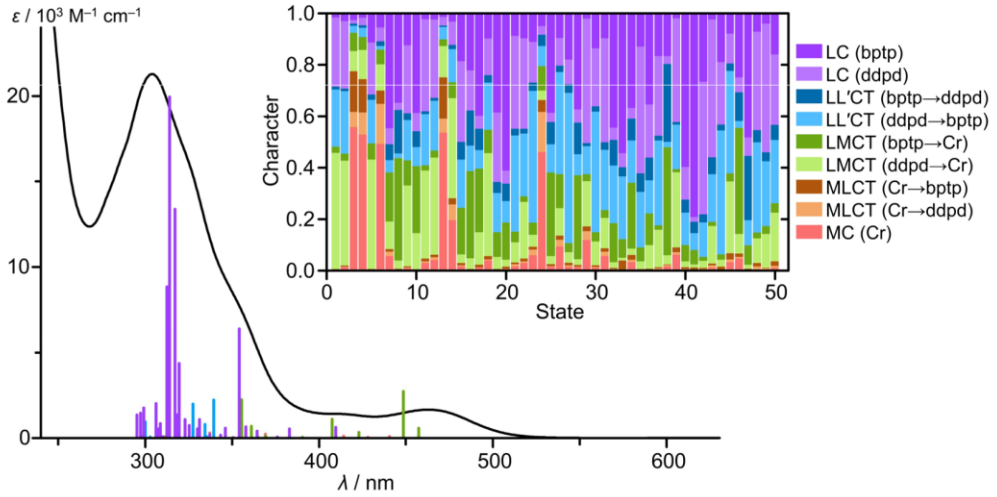

Fig. S26 UV/VIS absorption spectrum of **[3^{NMe,S}](PF$_6$)$_3$** in CH_3CN (black) with TD-DFT calculated oscillator strengths colored according to the most dominant character of the corresponding transition (red: MC, orange: MLCT, green: LMCT, purple: LC). Inset: Charge transfer number analysis of the 50 lowest energy spin-allowed transitions calculated by Loewdin population analysis with the complex cation fragmented into chromium (Cr), ddpd ligand (ddpd) and bptp ligand (bptp).

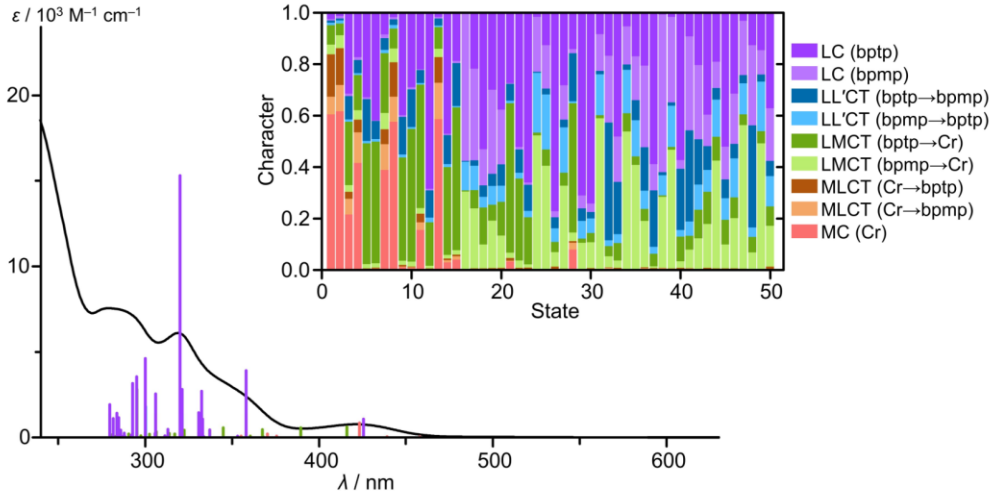

Fig. S27 UV/VIS absorption spectrum of **[3^{CH2,S}](PF$_6$)$_3$** in CH_3CN (0.01 M $HClO_4$) (black) with TD-DFT calculated oscillator strengths colored according to the most dominant character of the corresponding transition (red: MC, orange: MLCT, green: LMCT, purple: LC). Inset: Charge transfer number analysis of the 50 lowest energy spin-allowed transitions calculated by Loewdin population analysis with the complex cation fragmented into chromium (Cr), bpmp ligand (bpmp) and bptp ligand (bptp).

Table S1 TD-DFT calculated oscillator strengths and difference electron densities of the ten lowest energy spin-allowed transitions of $[3^{NMe,CH2}]^{3+}$.

#	λ / nm	oscillator strength	character	from	to	**difference electron density** (purple: density loss, orange: density gain)
1	448.8	0.0000739	MC (59%) + MLCT (23%)	t_{2g} (d_{xz}+d_{yz})	e_g (d_{z^2})	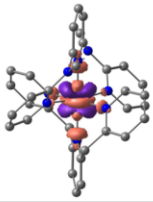
2	447.3	0.0000106	MC (58%) + MLCT (23%)	t_{2g} (d_{xy})	e_g ($d_{x^2-y^2}$)	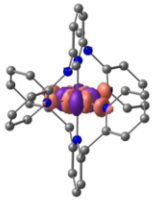
3	434.6	0.0069236	LMCT (49%) + ILCT (31%)	p (NMe) + π (Py^{NMe})	t_{2g} (d_{xy}) + π^* (Py^{NMe})	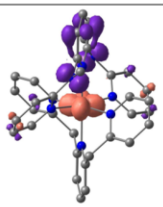
4	433.9	0.0051016	MC (45%) + LMCT (20%)	t_{2g} (d_{xz}+d_{yz}) and p (NMe)	t_{2g} (d_{xz}+d_{yz}) and e_g ($d_{x^2-y^2}$)	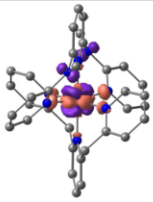
5	431.5	0.0113046	LMCT (37%) + ILCT (27%)	p (NMe) + π (Py^{NMe})	t_{2g} (d_{xz}+d_{yz}) + π^* (Py^{NMe})	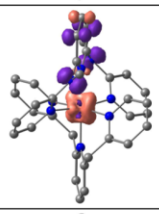
6	399.2	0.0018560	LMCT (55%) + ILCT (35%)	p (NMe) + π (Py^{NMe})	t_{2g} (d_{xz}+d_{yz})' + π^* (Py^{NMe})	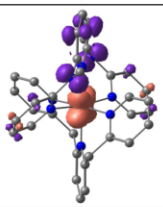
7	380.0	0.0005535	MC (54%) + MLCT (22%)	t_{2g} (d_{xz}+d_{yz})'	e_g ($d_{x^2-y^2}$)	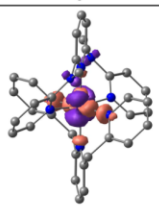

8	376.2	0.0020706	LMCT (40%) + ILCT (29%)	p (NMe) + π (Py^{NMe})	e_g (d_{z^2}) and e_g ($d_{x^2-y^2}$)	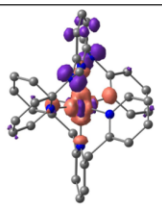
9	375.3	0.0008245	LMCT (50%)	p (NMe) + π (Py^{NMe})	e_g ($d_{x^2-y^2}$)	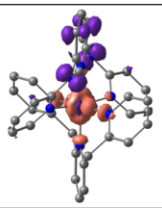
10	375.0	0.0017215	LMCT (49%) + ILCT (32%)	p (NMe) + π (Py^{NMe})	t_{2g} (d_{xy}) + π* (Py^{NMe})	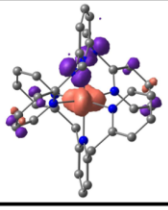

Table S2 TD-DFT calculated oscillator strengths and difference electron densities of the ten lowest energy spin-allowed transitions of $[3^{NMe,S}]^{3+}$.

#	λ / nm	oscillator strength	character	from	to	**difference electron density** (purple: density loss, orange: density gain)
1	457.4	0.0038301	LMCT (48%) + ILCT (28%) + LL'CT (23%)	p (NMe) + π (Py^{NMe})	t_{2g} (d_{xy}) + π^* (Py^{NMe}) + π^* (Py^{S})	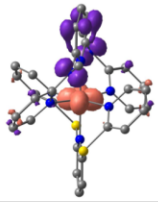
2	448.5	0.0193224	LMCT (43%) + ILCT (29%) + LL'CT (25%)	p (NMe) + π (Py^{NMe})	t_{2g} (d_{xz}+d_{yz}) + π^* (Py^{NMe}) + π^* (Py^{S})	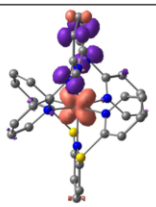
3	440.5	0.0004832	MC (56%) + MLCT (22%)	t_{2g} (d_{xz}+d_{yz})	e_g (d_{z^2}) and e_g ($d_{x^2-y^2}$)	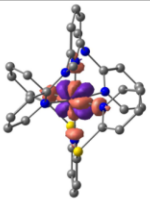
4	428.1	0.0002021	MC (53%) + MLCT (22%)	t_{2g} (d_{xy})	e_g ($d_{x^2-y^2}$)	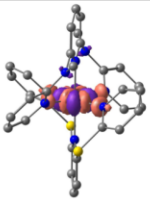
5	422.9	0.0022839	LMCT (49%) + ILCT (31%)	p (NMe) + π (Py^{NMe})	t_{2g} (d_{xz}+d_{yz})'	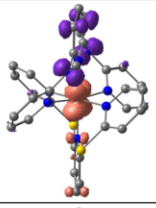
6	414.2	0.0006301	MC (49%) + MLCT (21%)	t_{2g} (d_{xz}+d_{yz}) and t_{2g} (d_{xz}+d_{yz})'	e_g (d_{z^2}) and e_g ($d_{x^2-y^2}$)	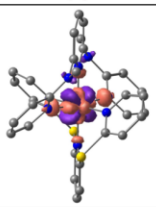
7	409.6	0.0042597	ILCT (51%) + LMCT (30%)	p (S) + π (Py^{S})	t_{2g} (d_{xz}+d_{yz}) + π^* (Py^{S})	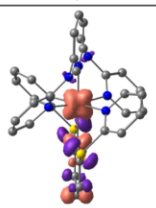

8	407.5	0.0077043	LMCT (43%) + ILCT (37%)	p (S) + π (Py^S)	t_{2g} (d_{xy}) + π* (Py^S)	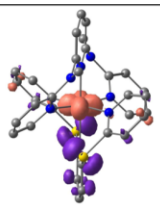
9	390.3	0.0000730	LMCT (41%) + ILCT (39%)	p (NMe) + π (Py^{NMe})	t_{2g} (d_{xy}) + π* (Py^{NMe})	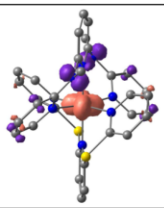
10	383.0	0.0036529	ILCT (46%) + LMCT (40%)	p (S) + π (Py^S)	t_{2g} (d_{xz}+d_{yz})' + π* (Py^S)	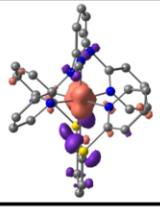

Table S3 TD-DFT calculated oscillator strengths and difference electron densities of the ten lowest energy spin-allowed transitions of $[3^{CH2,S}]^{3+}$.

#	λ / nm	oscillator strength	character	from	to	**difference electron density** (purple: density loss, orange: density gain)
1	458.1	0.0000364	MC (61%) + MLCT (23%)	t_{2g} (d_{xz}+d_{yz}) and t_{2g} (d_{xz}+d_{yz})'	e_g ($d_{x^2-z^2}$)	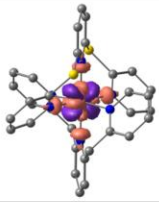
2	439.1	0.0000329	MC (62%) + MLCT (25%)	t_{2g} (d_{xy})	e_g (d_{y^2}) and e_g ($d_{x^2-z^2}$)	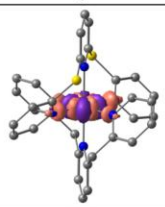
3	425.6	0.0073083	ILCT (32%) + LMCT (27%) + MC (22%)	p (S) + π (Py^S)	t_{2g} (d_{xz}+d_{yz}) + π* (Py^S)	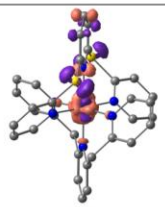
4	423.2	0.0056992	MC (42%)	t_{2g} (d_{xz}+d_{yz}) and t_{2g} (d_{xz}+d_{yz})'	t_{2g} (d_{xz}+d_{yz}) and e_g (d_{y^2})	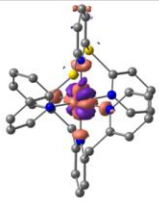
5	416.0	0.0040292	LMCT (49%) + ILCT (33%)	p (S) + π (Py^S)	t_{2g} (d_{xy}) + π* (Py^S)	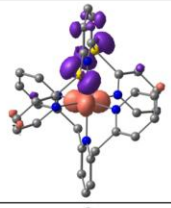
6	389.5	0.0036051	LMCT (49%) + ILCT (42%)	p (S) + π (Py^S)	t_{2g} (d_{xz}+d_{yz})' + π* (Py^S)	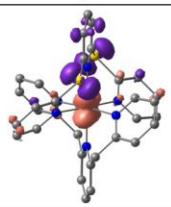
7	375.5	0.0002897	MC (39%) + LMCT (30%)	t_{2g} (d_{xy}) and p (S)	e_g (d_{y^2}) and e_g ($d_{x^2-z^2}$)	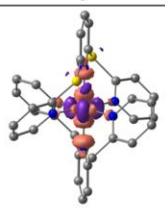

8	370.4	0.0010287	MC (58%) + MLCT (23%)	t_{2g} (d_{xz}+d_{yz}) and t_{2g} (d_{xz}+d_{yz})'	e_g (d_{y^2}) and e_g ($d_{x^2-z^2}$)	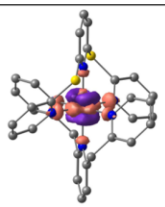
9	367.9	0.0000522	LMCT (42%) + ILCT (40%)	p (S) + π (Py^S)	t_{2g} (d_{xz}+d_{yz}) + π* (Py^S)	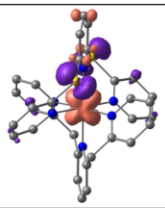
10	367.5	0.0029098	LMCT (53%) + ILCT (30%)	p (S) + π (Py^S)	t_{2g} (d_{xy}) + π* (Py^S)	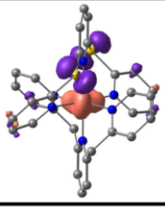

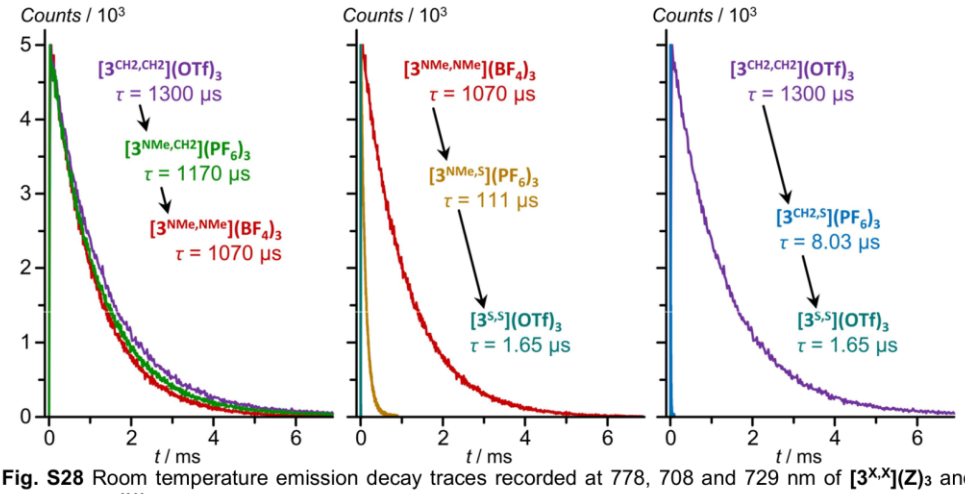

Fig. S28 Room temperature emission decay traces recorded at 778, 708 and 729 nm of $[3^{X,X}](Z)_3$ and at 743, 755 and 717 nm of $[3^{X,Y}](Z)_3$ (X, Y = NMe, CH_2, S; Z = BF_4, OTf, PF_6) following excitation (λ_{exc} = 450 nm) of solutions in deaerated CH_3CN.

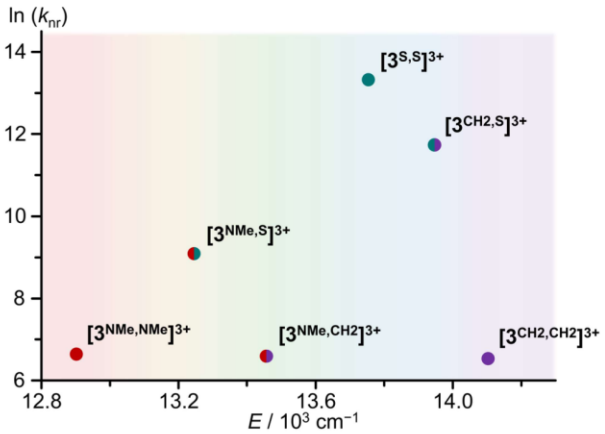

Fig. S29 Natural logarithmic non-radiative rate of the homoleptic and heteroleptic complexes $[3^{X,X}]^{3+}$ and $[3^{X,Y}]^{3+}$ (X, Y = NMe, CH_2, S, colour-coded) plotted against the maxima of the lowest-energy spin-flip emission band.

Experimental and Computational Studies on the Doublet Energies

Table S4 CASSCF(7,12)-SC/NEVPT2 calculated transition energies (in cm^{-1}) of $[3^{X,X}]^{3+}$ and $[3^{X,Y}]^{3+}$ (X, Y = NMe, CH_2, S) at DFT optimized geometries with assignments to the lowest ^2E, $^2T_1$ and $^4T_2$ state (values in bold indicate the lowest state of each multiplicity).

	$^2E(2)$	$^2E(1)$	$^2T_1(3)$	$^2T_1(2)$	$^2T_1(1)$	$^2T_2(3)$	$^2T_2(2)$	$^2T_2(1)$	$^4T_2(3)$	$^4T_2(2)$	$^4T_2(1)$
$[3^{NMe,NMe}]^{3+}$	16161	15576	15992	15908	**15029**	24326	23949	23789	24315	23265	**23219**
$[3^{CH2,CH2}]^{3+}$	16433	15858	16443	16181	**15670**	24154	24036	23958	22672	21840	**21665**
$[3^{S,S}]^{3+}$	16530	15941	16560	16279	**15713**	24163	24144	23800	21372	21371	**20296**
$[3^{NMe,CH2}]^{3+}$	16434	15868	16399	16224	**15558**	24287	24047	23946	22275	21305	**21193**
$[3^{NMe,S}]^{3+}$	15677	**15308**	16239	16194	16003	24242	24050	23746	23859	22663	**22139**
$[3^{CH2,S}]^{3+}$	16477	15903	16504	16232	**15707**	24152	24107	23884	22370	21528	**20803**

Table S5 Five band maxima from deconvoluted SF absorption bands of $[3^{X,X}]^{3+}$ and $[3^{X,Y}]^{3+}$ (X, Y = NMe, CH_2, S), CASSCF(7,12)-SC/NEVPT2 calculated transition energies (in italics; scaled by 0.884), assignments and selected energy differences (in cm^{-1}).

	No.	#5	#4	#3	#2	#1	Δ*E* (#5–#1)	Δ*E* (#2–#1)
$[3^{NMe,NMe}]^{3+}$	*exp.*	14430	14300	13530*	13600*	12960	1470	640
	calcd.	*14290*	*14140*	*14070*	*13780*	*13290*	*1000*	*490*
	term	$^2E(2)$	$^2T_1(3)$	$^2T_1(2)$	$^2E(1)$	$^2T_1(1)$		
$[3^{CH2,CH2}]^{3+}$	*exp.*	15060	14780	14320	14160	14050	1010	110
	calcd.	*14540*	*14530*	*14310*	*14030*	*13860*	*680*	*170*
	term	$^2T_1(3)$	$^2E(2)$	$^2T_1(2)$	$^2E(1)$	$^2T_1(1)$		
$[3^{S,S}]^{3+}$	*exp.*	14770	14630	14210	14030	13800	970	230
	calcd.	*14650*	*14620*	*14400*	*14100*	*13900*	*750*	*200*
	term	$^2T_1(3)$	$^2E(2)$	$^2T_1(2)$	$^2E(1)$	$^2T_1(1)$		
$[3^{NMe,CH2}]^{3+}$	*exp.*	14500*	14670*	13970	13860	13530	1140	330
	calcd.	*14530*	*14500*	*14350*	*14030*	*13760*	*770*	*270*
	term	$^2E(2)$	$^2T_1(3)$	$^2T_1(2)$	$^2E(1)$	$^2T_1(1)$		
$[3^{NMe,S}]^{3+}$	*exp.*	14580	14430	13910	13760	13360	1220	400
	calcd.	*14360*	*14320*	*14150*	*13870*	*13540*	*820*	*330*
	term	$^2T_1(3)$	$^2T_1(2)$	$^2T_1(1)$	$^2E(2)$	$^2E(1)$		
$[3^{CH2,S}]^{3+}$	*exp.*	14980	14770	14340	14160	14050	930	110
	calcd.	*14600*	*14570*	*14360*	*14070*	*13890*	*710*	*180*
	term	$^2T_1(3)$	$^2E(2)$	$^2T_1(2)$	$^2E(1)$	$^2T_1(1)$		

* Reverse order of experimentally and computationally determined microstate energies.

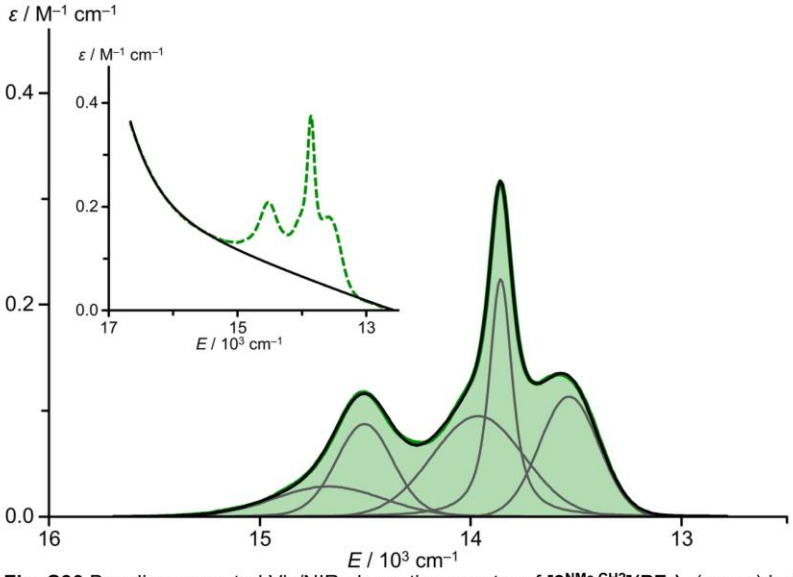

Fig. S30 Baseline corrected Vis/NIR absorption spectra of **[3^{NMe,CH2}](PF$_6$)$_3$** (green) in CH_3CN with sum fit (black) consisting of five Voigt functions (grey). Inset: Vis/NIR absorption spectra of **[3^{NMe,CH2}](PF$_6$)$_3$** (green, dotted) with exponential fit (black) describing the tail of the spin-allowed transitions used for the baseline correction.

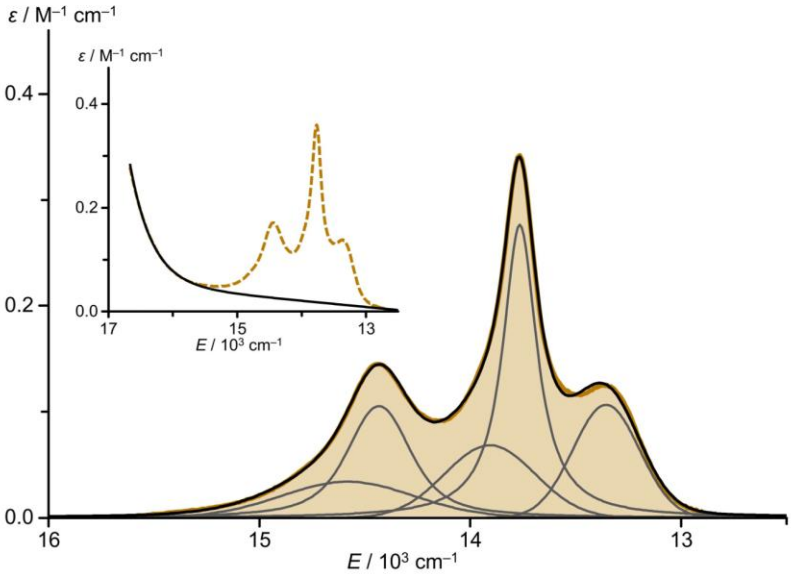

Fig. S31 Baseline corrected Vis/NIR absorption spectra of **[3^{NMe,S}](PF$_6$)$_3$** (orange) in CH_3CN with sum fit (black) consisting of five Voigt functions (grey). Inset: Vis/NIR absorption spectra of **[3^{NMe,S}](PF$_6$)$_3$** (orange, dotted) with exponential fit (black) describing the tail of the spin-allowed transitions used for the baseline correction.

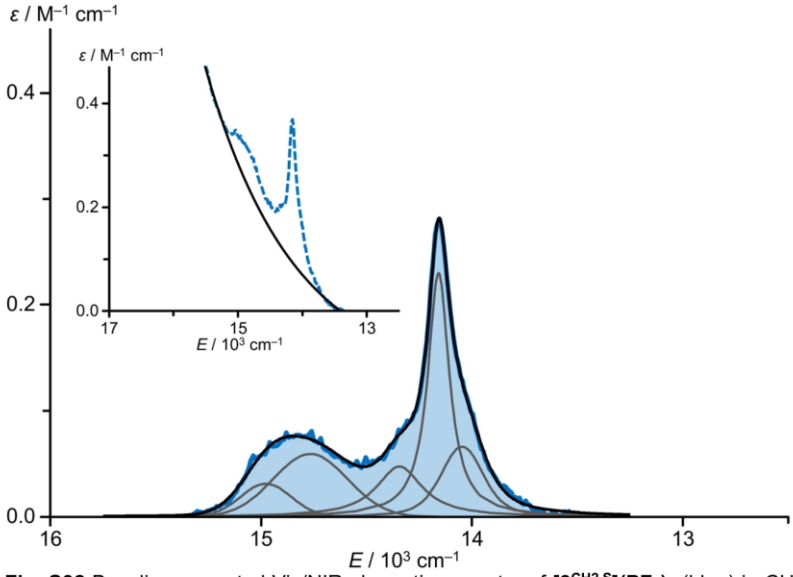

Fig. S32 Baseline corrected Vis/NIR absorption spectra of **[3^{CH2,S}](PF$_6$)$_3$** (blue) in CH_3CN with sum fit (black) consisting of five Voigt functions (grey). Inset: Vis/NIR absorption spectra of **[3^{CH2,S}](PF$_6$)$_3$** (blue, dotted) with exponential fit (black) describing the tail of the spin-allowed transitions used for the baseline correction.

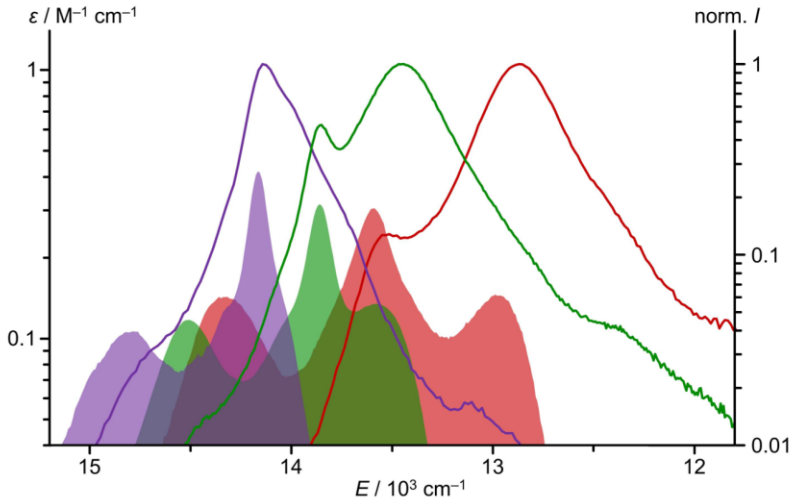

Fig. S33 Corrected spin- and symmetry forbidden absorption bands (filled areas, logarithmic scale) and normalized emission spectra (solid lines, logarithmic scale) of **[3^{NMe,NMe}](BF$_4$)$_3$** (red, λ_{exc} = 435 nm), **[3^{CH2,CH2}](OTf)$_3$** (purple, λ_{exc} = 465 nm) and **[3^{NMe,CH2}](PF$_6$)$_3$** (green, λ_{exc} = 446 nm) in CH_3CN at room temperature.[2,3]

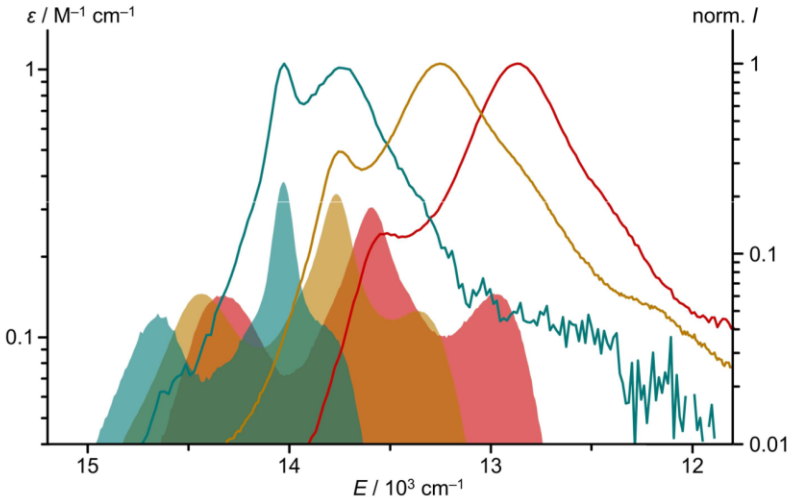

Fig. S34 Corrected spin- and symmetry forbidden absorption bands (filled areas, logarithmic scale) and morlamized emission spectra (solid lines, logarithmic scale) of $[3^{NMe,NMe}](BF_4)_3$ (red, λ_{exc} = 435 nm), $[3^{S,S}](OTf)_3$ (green-blue, λ_{exc} = 452 nm) and $[3^{NMe,S}](PF_6)_3$ (orange, λ_{exc} = 463 nm) in CH_3CN at room temperature.[1,2]

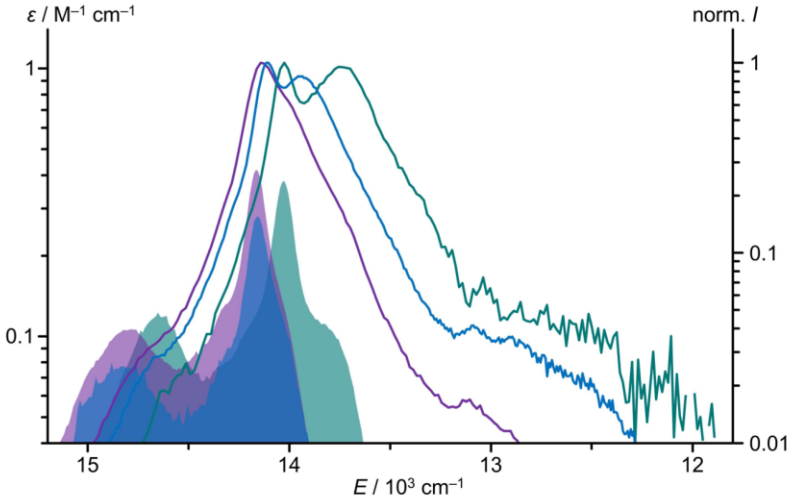

Fig. S35 Corrected spin- and symmetry forbidden absorption bands (filled areas, logarithmic scale) and emission spectra (solid lines, logarithmic scale) of $[3^{CH2,CH2}](OTf)_3$ (purple, λ_{exc} = 465 nm), $[3^{S,S}](OTf)_3$ (green-blue, λ_{exc} = 452 nm) and $[3^{CH2,S}](PF_6)_3$ (blue, λ_{exc} = 422 nm) in CH_3CN at room temperature.[1,3]

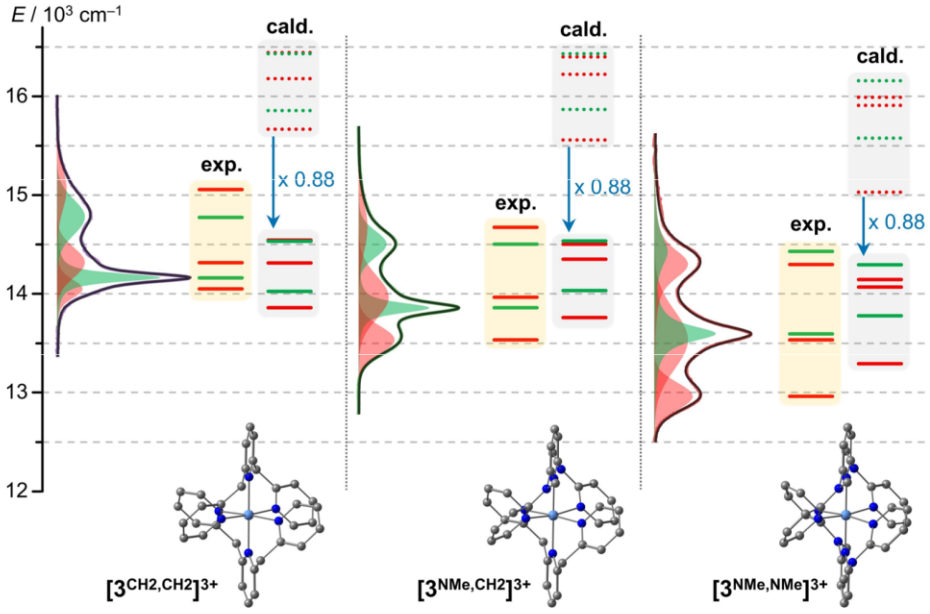

Fig. S36 Comparison of experimental (from deconvoluted SF absorption bands, yellow background) and CASSCF(7,12)-SC/NEVPT2 calculated $^2T_1$ (red) and ^2E (green) energies of $[3^{CH2,CH2}]^{3+}$, $[3^{NMe,CH2}]^{3+}$ and $[3^{NMe,NMe}]^{3+}$. The calculated values (dotted, grey background) were corrected with the common scaling factor 0.884 (see main article) to yield the corrected calculated energies (solid, grey background).[1]

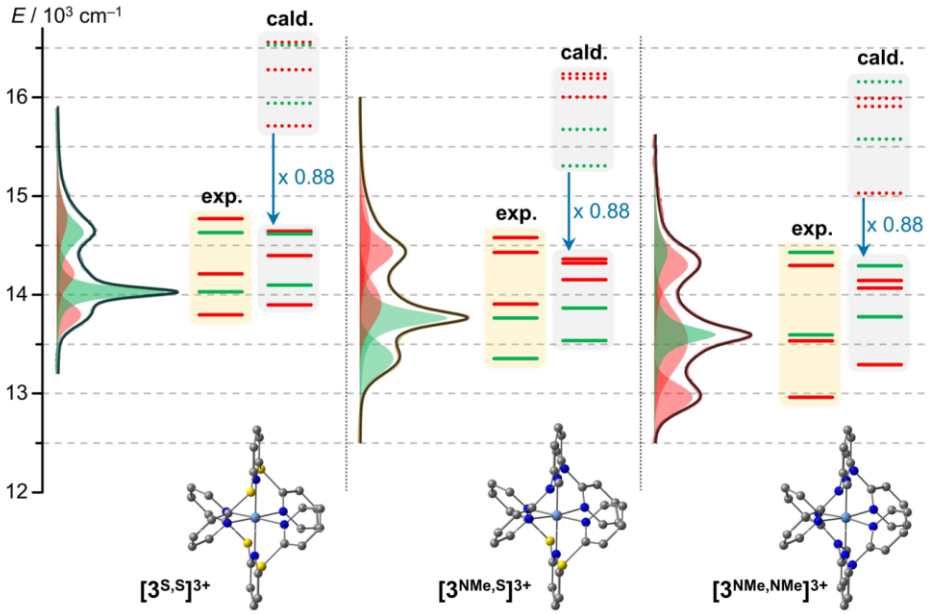

Fig. S37 Comparison of experimental (from deconvoluted SF absorption bands, yellow background) and CASSCF(7,12)-SC/NEVPT2 calculated $^2T_1$ (red) and ^2E (green) energies of $[3^{S,S}]^{3+}$, $[3^{NMe,S}]^{3+}$ and $[3^{NMe,NMe}]^{3+}$. The calculated values (dotted, grey background) were corrected with the common scaling factor 0.884 (see main article) to yield the corrected calculated energies (solid, grey background).[1]

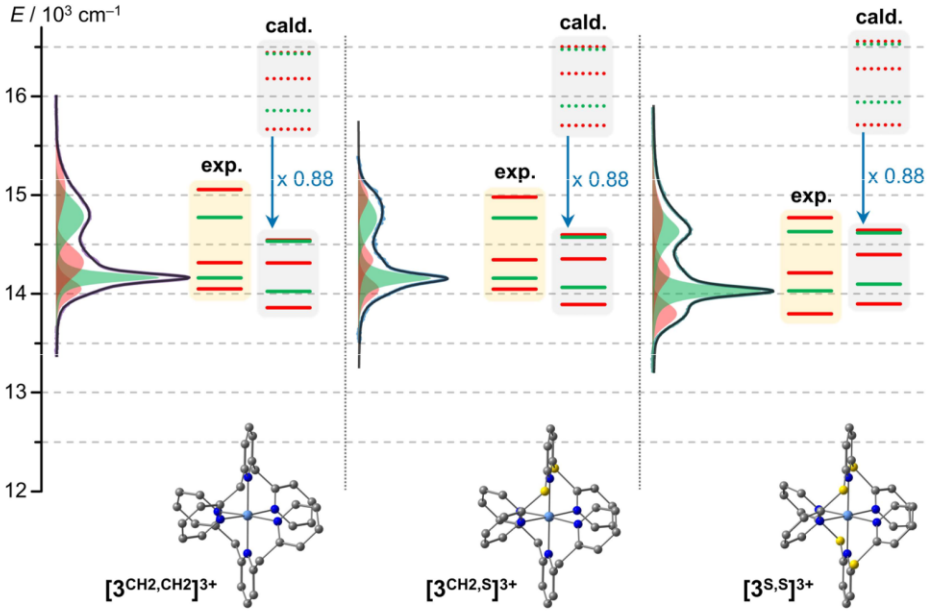

Fig. S38 Comparison of experimental (from deconvoluted SF absorption bands, yellow background) and CASSCF(7,12)-SC/NEVPT2 calculated $^2T_1$ (red) and ^2E (green) energies of $[3^{CH2,CH2}]^{3+}$, $[3^{CH2,S}]^{3+}$ and $[3^{S,S}]^{3+}$. The calculated values (dotted, grey background) were corrected with the common scaling factor 0.884 (see main article) to yield the corrected calculated energies (solid, grey background).[1]

References

(1) Reichenauer, F.; Naumann, R.; Förster, C.; Kitzmann, W. R.; Reponen, A.-P. M.; Feldmann, S.; Heinze, K. Bridge Editing of Spin-Flip Emitters gives Insight into Excited State Energies and Dynamics, submitted.

(2) Otto, S.; Grabolle, M.; Förster, C.; Kreitner, C.; Resch-Genger, U.; Heinze, K. $[Cr(ddpd)_2]^{3+}$: a molecular, water-soluble, highly NIR-emissive ruby analogue, *Angew. Chem. Int. Ed.* **2015**, *54*, 11572–11576. DOI: 10.1002/anie.201504894.

(3) Reichenauer, F.; Wang, C.; Förster, C.; Boden, P.; Ugur, N.; Báez-Cruz, R.; Kalmbach, J.; Carrella, L. M.; Rentschler, E.; Ramanan, C.; Niedner-Schatteburg, G.; Gerhards, M.; Seitz, M.; Resch-Genger, U.; Heinze, K. Strongly Red-Emissive Molecular Ruby $[Cr(bpmp)_2]^{3+}$ surpasses $[Ru(bpy)_3]^{2+}$, *J. Am. Chem. Soc.* **2021**, *143*, 11843–11855. DOI: 10.1021/jacs.9b06524.

6.6 Supporting Information: Post-Synthetic Excited State Manipulation in Molecular Rubies

Post-Synthetic Excited State Manipulation in Molecular Rubies

Florian Reichenauer,[a] Lucas Leuschner,[a] Robert Naumann,[a] Christoph Förster[a] and Katja Heinze[a]

[a] Department of Chemistry, Johannes Gutenberg University of Mainz, Duesbergweg 10-14, 55128 Mainz, Germany

Supporting Information

Authors Contributions

L. Leuschner and F. Reichenauer performed the synthesis, ground-state characterization, and steady-state spectroscopic measurements. F. Reichenauer investigated excited-state energy tuning, conducted quantum chemical calculations, drafted the original manuscript, and, together with R. Naumann, measured photoluminescence efficiency. C. Förster solved and refined the single crystal structures. K. Heinze conceived and supervised the project.

Table of Contents

General Methods

All reactions and measurements were performed under argon atmosphere unless otherwise noted. Gloveboxes (UniLab/MBraun − Ar 5.0, O_2 < 1 ppm, H_2O < 0.1 ppm) were used to store and weight sensitive compounds for synthesis as well as to prepare samples that require the absence of oxygen and/or water. The reagents were purchased from commercial suppliers (Acros Organics, Fischer Scientific and Sigma Aldrich) and used without further purification. The ligand bptp[1] and anhydrous $Cr(OTf)_3$ were prepared according to synthetic procedures described in Section 6.4. Acetonitrile and petroleum ether were dried and distilled from CaH_2, and 1,4-dioxane from sodium, respectively. Column chromatography was performed using aluminium oxide (neutral, Brockmann I). Analytical thin layer chromatography (TLC) was done on aluminium oxide F254 (Macherey-Nagel, coated on polyester sheets) and the spots were visualized by ultraviolet light.

NMR Spectra were recorded on a *Bruker Avance II 400* spectrometer at 400.42 MHz (^{1}H) and 100.70 MHz (^{13}C{^{1}H}) in deuterated acetonitrile (Deutero GmbH). All data were evaluated with the software *MestReNova 12.0.4-22023*. The resonances are reported in ppm versus the solvent signal as internal standard (^{1}H; (^{13}C) NMR: actonitrile-d_3: δ = 1.94, 2.13; (1.32, 118.26) ppm)[2] and *J* values are given in Hz. (s) = singlet, (d) = doublet, (t) = triplet, (q) = quartet.

IR spectra were recorded with a *Bruker Alpha FTIR* spectrometer with an ATR unit containing a diamond crystal.

ESI$^+$ mass spectra were measured on an *Agilent 6545 HPLC-ESI-QTOF-MS* spectrometer at a temperature of 275 °C for the ligands and 150 °C for the bis(tridentate) complexes. The bis(tridentate) complexes were directly injected into the ion source (without HPLC) and the spectra were corrected using a background measurement of the pure solvent.

Elemental analyses was performed by the central analytic service of the Department of Chemistry of the Johannes Gutenberg University Mainz using an *Elementar vario EL Cube* (precursor) or by the Mikroanalytisches Labor Kolbe, c/o Fraunhofer Institut UMSICHT, Oberhausen, Germany (bis(tridentate) complexes).

Electrochemical experiments were carried out on a *BioLogic SP-200* voltammetric analyzer using platinum wires as *counter* and working electrodes and a 0.01 M Ag/Ag(NO_3) electrode as reference electrode. Cyclic voltammetry and square wave measurements were conducted at scan rates of 100 mV s^{-1} using 0.1 M [^{n}Bu$_4$N](PF$_6$) in CH_3CN as supporting electrolyte. Potentials are referenced against the ferrocene/ferrocenium (FcH/FcH^+) couple.

Spectroelectrochemical experiments were performed using a TSC 1600 closed measuring cell from *RHD Instruments*. Glassy Carbon was used as counter electrode, a silver wire as pseudo reference electrode and a platinum mesh as working electrode. *A J&M TIDAS S MMS* was used as UV/Vis/NIR detector, a *Hamamatsu L10290* as excitation source.

UV/Vis/NIR spectra were recorded on an *Agilent Cary 5000* spectrometer in acetonitrile (Optima® LC/MS grade, Fisher Scientific) at room temperature. Measurements from 1000-200 nm were conducted using 1.00 cm path length cuvettes, while measurements of the NIR bands within 900-600 nm were performed using a 10.0 cm path length cuvette. Molar extinction coefficients are given at maximum absorption and for shoulders (highlighted as sh). For deconvolution of NIR absorption band patterns, the spectra were baseline corrected using a biexponential function (eq. S1) to model the tailing of higher energy bands. Deconvolution of the baseline corrected spectra was achieved with five Voigt functions using the *Origin94* software package.

$$\varepsilon(\tilde{\nu}) = \varepsilon_0 + A_1 e^{\frac{\tilde{\nu}-\tilde{\nu}_0}{t_1}} + A_2 e^{\frac{\tilde{\nu}-\tilde{\nu}_0}{t_2}} \qquad \text{(eq. S1)}$$

Steady-state emission spectra and photoluminescent decay curves of the complexes were measured with an *FLS1000 spectrometer* from *Edinburgh Instruments* equipped with a cooled photomultiplier detector PMT-980. A xenon arc lamp Xe2 (450 W) was used for excitation in steady-state measurements. Time-resolved luminescence experiments were conducted using a pulsed diode laser VPL-450 as excitation source. Absolute luminescence quantum yields Φ were determined using an integrating sphere from *Edinburgh Instruments* with a relative uncertainty estimated as ±10%. Steady-state measurements were additionally performed with a *spectrofluorometer FS5* from *Edinburgh Instruments*. All measurements were carried out in degassed acetonitrile (Optima® LC/MS grade, Fisher Scientific).

Lewis-acid impact was examined by titration of deaerated solutions of boron trifluoride and tris(pentafluorophenyl)borane in acetonitrile to deaerated solutions of the complex in the same solvent in inert gas cuvettes. The titration steps were done in the glovebox and the optical property modification was monitored by UV/Vis/NIR and emission spectroscopy.

Photolysis experiments were conducted by irradiating deaerated stirred solutions of the complexes in inert gas cuvettes. An *Ultra-High Power* collimated LED from *Prizmatix* (UHP-T-460-DI; output power (free): 5.5 W) with a maximum at 456 nm and the centroid at 460 nm was used. The output power was adjusted constant with 1.1 W (20% setting) for all experiments using a *UHPTLCC-02-USB Controller*. The beam of light was focused onto the cuvette with a plano convex lens. At the cuvette, the beam diameter was roughly 1 cm. The temperature of the irradiated solution was kept at 20 °C with a Peltier

module. Due to the excitation source being non-monochromatic, the complexes exhibiting a different spectral absorption within the excitation range and the absorbance changing over time upon irradiation, the irradiation and decomposition times of the different complexes are not comparable and only a qualitative comparison can be made.

DFT calculations were performed using the quantum computing suite ORCA 5.0.4.[3,4] Geometry optimization was done using unrestricted Kohn-Sham orbitals DFT (UKS) and the B3LYP functional[5–7] in combination with Ahlrich's split valance triple-zeta basis set ZORA-def2-TZVPP[8] and the SARC/J auxiliary basis set for all atoms. Tight convergence criteria were chosen for DFT calculations (keywords *tightscf* and *tightopt*). All DFT calculations make use of the resolution of identity (Split-RI-J) approach for the Coulomb term in combination with the chain-of-spheres approximation for the exchange term (keyword *RIJCOSX*).[9,10] The zeroth order regular approximation was used to describe relativistic effects in all calculations (keyword *ZORA*).[11–13] To account for solvent effects, a conductor-like screening model (keyword *CPCM*(acetonitrile)) modelling acetonitrile was used in all calculations.[14,15] Atom-pairwise dispersion correction was performed with the Becke-Johnson damping scheme (keyword *D3BJ*).[16,17] A numerical frequency calculation confirmed that the optimised geometry corresponds to a minimum structure or a transition state structure, respectively. Explicit counter ions and/or solvent molecules were neglected. Fifty vertical spin-allowed transitions were calculated by TD-DFT. The charge transfer number analyses of the TD-DFT calculated transitions were done using TheoDORE 2.4.[18,19] All calculations were computed on the Elwetritsch supercomputer at RPTU Kaiserslautern-Landau (hpc.rz.rptu.de). This is a member of the AHRP (Alliance for High Performance Computing Rhineland-Palatinate).

CASSCF(x,y)-SC-NEVPT2 calculations of ground and excited state properties with respect to pure metal-centered (MC) states were performed using the complete-active-space self-consistent field (CASSCF) method[20,21] in conjunction with the strongly contracted N-electron valence perturbation theory to second order (SC-NEVPT2)[22–24] in order to recover missing dynamic electron correlation. All electronic states are classified by irreducible representations of the O point group, in spite of the lower actual symmetry of the considered complexes. The active space (7,12) comprising of five d-orbitals, two occupied σ bonding orbitals and five unoccupied d orbitals of second d-shell[25] was considered for all CASSCF-calculations including 10 quartet and 10 doublet roots. The geometries of the DFT optimized $^4A_2$ states were used for the calculations. For quantitative comparison with the experimental doublet energies derived from the deconvoluted NIR absorption bands, the calculated energies were scaled using a common empirical scaling factor of 0.876, which was obtained by averaging the ratios of the maxima of the Voigt functions to the calculated SF state energies.

Crystal structure determination. Intensity data were collected with a *STOE IPDS-2T* diffractometer and a *STOE STADIVARI* diffractometer from STOE & Cie GmbH with an Oxford cooling using Mo-Kα radiation (λ = 0.71073 Å). The diffraction frames were integrated using the STOE X-Area software package and were corrected for absorption with MULABS34[26] of the PLATON[27] software package. The structures were solved with SHELXT[28] and refined by the full-matrix method based on F^2 using SHELXL[29] of the SHELX[30] software package and the ShelXle[31] graphical interface. All non-hydrogen atoms were refined anisotropically while the positions of all hydrogen atoms were generated with appropriate geometric constraints and allowed to ride on their respective parent atoms with fixed isotropic thermal parameters.

Crystallographic Data of L^N
$C_{16}H_{16}N_6$ (292.35); triclinic; $P\bar{1}$; a = 9.2758(5) Å, b = 9.6463(5) Å, c = 9.7887(5) Å; α = 100.322(4)°; β = 106.679(4)°; γ = 116.515(4)°; V = 700.86(7) Å^3; Z = 1; density, calcd. = 0.693 g cm^{-3}, T = 120(2) K, μ = 0.044 mm^{-1}; F(000) = 154; crystal size 1.18 × 0.813 × 0.59 mm^3; θ = 2.327 to 30.777°; −12 ≤ h ≤ 13, −13 ≤ k ≤ 13, −13 ≤ l ≤ 14; reflections collected = 11986; reflections unique = 11986 [R(int) = 0.0289]; completeness to θ = 25.242°: 100.0%; absorption correction: multi-scan; max. and min. transmission 0.9708 and 0.3016; data 3912; restraints 0, parameters 91; goodness-of-fit on F^2 = 1.101; final indices [$I > 2\sigma(I)$] R_1 = 0.0675, wR_2 = 0.1803; R indices (all data) R_1 = 0.0835, wR_2 = 0.1911; largest diff. peak and hole 0.513 and −0.584 e Å^{-3}.

Crystallographic Data of 1^N
$C_{22}H_{30}Cl_3CrN_8O_2$ (596.89); triclinic; $P\bar{1}$; a = 9.0988(4) Å, b = 12.1018(5) Å, c = 12.4738(5) Å; α = 79.220(3)°; β = 86.730(3)°; γ = 89.812(3)°; V = 1347.04(10) Å^3; Z = 2; density, calcd. = 1.472 g cm^{-3}, T = 120(2) K, μ = 0.758 mm^{-1}; F(000) = 618; crystal size 0.360 × 0.287 × 0.230 mm^3; θ = 2.154 to 30.832°; −12 ≤ h ≤ 13, −17 ≤ k ≤ 14, −17 ≤ l ≤ 18; reflections collected = 23127; reflections unique = 7476 [R(int) = 0.0176]; completeness to θ = 25.242°: 100.0%; semi-empirical from equivalents: integration; max. and min. transmission 0.9070 and 0.4586; data 7476; restraints 48, parameters 427; goodness-of-fit on F^2 = 1.073; final indices [$I > 2\sigma(I)$] R_1 = 0.0312, wR_2 = 0.0869; R indices (all data) R_1 = 0.0385, wR_2 = 0.0900; largest diff. peak and hole 0.296 and −0.755 e Å^{-3}.

Crystallographic Data of 2^N
$C_{21}H_{19}CrF_9N_7O_9S_3$ (832.61); triclinic; $P\bar{1}$; a = 9.2185(18) Å, b = 11.064(2) Å, c = 16.380(3) Å; α = 88.19(3)°, β = 78.01(3)°, γ = 70.57(3)°; V = 1539.9(6) Å^3; Z = 2; density, calcd. = 1.796 g cm^{-3}, T = 120(2) K, μ = 0.691 mm^{-1}; F(000) = 838; crystal size 0.210 × 0.120 × 0.050 mm^3; θ = 1.272 to 32.901°; −12 ≤ h ≤ 12, −16 ≤ k ≤ 16, −24 ≤ l ≤ 23; reflections collected = 36650; reflections unique = 9904 [R(int) = 0.0256]; completeness to θ = 25.242°: 99.9%; absorption correction: integration; max. and min. transmission 0.9704 and 0.8703; data 9904; restraints 437, parameters 556; goodness-of-fit on F^2 = 1.119; final indices [$I > 2\sigma$(I)] R_1 = 0.0371, wR_2 = 0.1084; R indices (all data) R_1 = 0.0465, wR_2 = 0.1111; largest diff. peak and hole 0.720 and −0.698 e Å^{-3}.

Crystallographic Data of $[3^{N}](OTf)_3$

$C_{36}H_{36}CrF_9N_{12}O_{10}S_3$ (1115.95); monoclinic; $P2_1/n$; a = 9.3871(19) Å, b = 33.910(7) Å, c = 13.518(3) Å; α = 90°; β = 90.29(3)°; γ = 90°; V = 4302.9(15) Å^3; Z = 4; density, calcd. = 1.723 g cm^{-3}, T = 120(2) K, μ = 0.524 mm^{-1}; F(000) = 2276; crystal size 0.270 × 0.217 × 0.190 mm^3; θ = 2.349 to 27.905°; −12 ≤ h ≤ 12, −39 ≤ k ≤ 44, −17 ≤ l ≤ 17; reflections collected = 50156; reflections unique = 10244 [R(int) = 0.0614]; completeness to θ = 25.242°: 99.9%; absorption correction: semi-empirical from equivalents; max. and min. transmission 1.16290 and 0.89414; data 10244; restraints 114, parameters 720; goodness-of-fit on F^2 = 1.031; final indices [$I > 2\sigma(I)$] R_1 = 0.0390, wR_2 = 0.0897; R indices (all data) R_1 = 0.0507, wR_2 = 0.0959; largest diff. peak and hole 0.471 and −0.545 e Å^{-3}.

Crystallographic Data of $[3^{N,S}](OTf)_3$

$C_{36}H_{30}CrF_9N_{10}O_9S_5$ (1130.0); monoclinic; $P2_1$; a = 13.082(3) Å, b = 13.292(3) Å, c = 13.437(3) Å; α = 90°; β = 102.97(3)°; γ = 90°; V = 2276.9(8) Å^3; Z = 2; density, calcd. = 1.648 g cm^{-3}, T = 120(2) K, μ = 0.582 mm^{-1}; F(000) = 1146; crystal size 0.820 × 0.463 × 0.120 mm^3; θ = 2.491 to 28.000°; −17 ≤ h ≤ 16, −17 ≤ k ≤ 17, −17 ≤ l ≤ 17; reflections collected = 19209; reflections unique = 10818 [R(int) = 0.0292]; completeness to θ = 25.242°: 99.8%; absorption correction: integration; max. and min. transmission 0.9267 and 0.7187; data 10818; restraints 453, parameters 736; goodness-of-fit on F^2 = 1.072; final indices [$I > 2\sigma(I)$] R_1 = 0.0396, wR_2 = 0.0911; R indices (all data) R_1 = 0.0471, wR_2 = 0.0960; largest diff. peak and hole 0.634 and −0.257 e Å^{-3}.

Synthetic Procedures

Synthesis of ddad (L^N)

A suspension of KHMDS (5.03 g, 25.2 mmol, 3.0 eq.) in dry 1,4-dioxane (150 mL) was combined with 2-(methylamino)pyridine (2.60 mL, 25.2 mmol, 3.0 eq.), turning the mixture yellow. 2,6-Dibromopyrazine was carefully added in portions, and the resulting brown reaction mixture was heated at 101 °C for 64 h. After cooling to room temperature, the reaction was quenched by slow addition of water (300 mL) and the brown solution was extracted with a diethyl ether/THF mixture (1:1, 3 x 70 mL). The combined organic layers were washed with sodium carbonate solution (1 M, 100 mL), dried over sodium sulfate, and filtered. The solvent was removed under reduced pressure (300 mbar, 40 °C) and the crude product was purified by column chromatography (Alox II, 2:1:0.02, cyclohexane/ethyl acetate/triethylamine, R_f = 0.42). The yellow oil, consisting of **L^N** (6.16 g, 21.1 mmol, 64%), crystallized after prolonged cooling. (Procedure adapted from literature)[32]

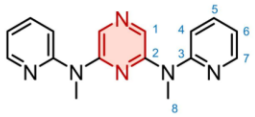

^{1}H NMR (CD_3CN): δ = 8.31 (2 H, ddd, $^3J_{HH}$ = 4.9, $^4J_{HH}$ = 2.0, $^5J_{HH}$ = 0.9, H^7), 8.02 (2 H, s, H^1), 7.63 (2 H, ddd, $^3J_{HH}$ = 8.4, $^3J_{HH}$ = 7.3, $^4J_{HH}$ = 2.0, H^5), 7.28 (2 H, dt, $^3J_{HH}$ = 8.3, $^{4/5}J_{HH}$ = 0.9, H^4), 6.96 (2 H, ddd, $^3J_{HH}$ = 7.2, $^3J_{HH}$ = 4.9, $^4J_{HH}$ = 0.9, H^6), 3.50 (6 H, s, H^8) ppm.
^{13}C{^{1}H} NMR (CD_3CN): δ = 157.9 (s, C^3), 152.4 (q, C^2), 148.9 (s, C^7), 138.4 (q, C^5), 127.3 (s, C^1), 119.0 (s, C^6), 116.4 (s, C^4), 35.9 (s, C^8) ppm.
MS (ESI^+, CH_3CN): *m/z* (%) = 293.15 (100) $[ddad+H]^+$, 315.13 (3) $[ddad+Na]^+$.
IR (ATR): $\tilde{\nu}_{max}$ = 3053 (w), 3008 (w), 1587 (s), 1573 (s), 1526 (vs), 1467 (vs), 1416 (vs), 1375 (s), 1333 (vs), 1293 (s), 1268 (s), 1209 (s), 1154 (vs), 1110 (vs), 1075 (m), 1048 (w), 987 (s), 868 (w), 832 (w), 776 (s), 740 (s), 695 (w), 678 (w), 647 (w), 622 (w), 557 (w), 474 (m), 411 (m) cm^{-1}.
Elemental analysis calcd. for $C_{16}H_{16}N_6$: C, 65.74; H, 5.52; N, 28.75. Found: C, 65.91; H, 5.43; N, 28.57.
UV/Vis (CH_3CN): λ_{max} (ε) = 442 (10), 357 (21100), 294 (15560, sh), 272 (21980), 233 (15960) nm (M^{-1} cm^{-1}).
Emission (CH_3CN, room temperature): λ_{max} = 535 nm (λ_{exc} = 455 nm).

Synthesis of $Cr(ddad)Cl_3$ (1^N)

Under ambient conditions, a pale yellow solution of the ligand ddad (5.49 g, 18.8 mmol, 1.0 eq.) in isopropanol (100 mL) was combined with a deep green solution of chromium(III) chloride hexahydrate (5.00 g, 18.8 mmol, 1.0 eq.) in isopropanol (200 mL). Upon heating the mixture to 60–70 °C, a green solid precipitated within 15 minutes. The green suspension was then heated at 82 °C for 16 hours. After cooling to room temperature, the suspension was filtered and washed sequentially with isopropanol (3 x 50 mL), methanol (3 x 50 mL) and diethyl ether (2 x 50 mL). The resulting green product powder (6.86 g, 15.2 mmol, 81%) was dried under reduced pressure. Slow diffusion of diethyl ether into a concentrated acetonitrile solution of the complex yielded green crystals of **1^N** suitable for X-ray diffraction analysis. (Procedure adapted from Section 6.5)[33]

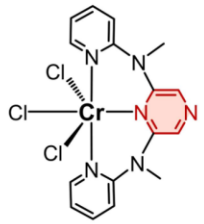

MS (ESI^+, CH_3CN): *m/z* (%) = 414.02 (82) $[\mathbf{1^N}–Cl]^+$, 467.02 (46) $[\mathbf{1^N}+NH_4]^+$, 471.98 (79) $[\mathbf{1^N}+Na]^+$, 487.95 (29) $[\mathbf{1^N}+K]^+$, 918.01 (14) $[2\ \mathbf{1^N}+NH_4]^+$, 922.97 (100) $[2\ \mathbf{1^N}+Na]^+$, 938.94 (13) $[2\ \mathbf{1^N}+K]^+$.
IR (ATR): $\tilde{\nu}_{max}$ = 2144 (w), 1605 (m), 1569 (m), 1520 (w), 1494 (m), 1464 (m), 1436 (vs), 1389 (w), 1346 (s), 1318 (w), 1272 (w), 1254 (w), 1296 (m), 1170 (w), 1146 (w), 1125 (s), 1095 (s), 1063 (w), 1032 (w), 970 (w), 859 (m), 791 (m), 780 (s), 769 (vs), 757 (s), 741 (w), 677 (w), 651 (w), 637 (w), 592 (w), 510 (w), 488 (vs), 442 (s), 415 (w), 403 (w) cm^{-1}.

Synthesis of Cr(ddad)(OTf)$_3$ (2^N)

Trimethylsilyl trifluoromethanesulfonate (10 mL, 55.3 mmol, 20 eq.) was added to a green suspension of $\mathbf{1^N}$ (1.25 g, 2.76 mmol, 1.0 eq.) in dry acetonitrile (100 mL), immediately forming a red-brown solution. The mixture was heated at 82 °C for 3 days, then allowed to cool to room temperature. The solvent was removed using a water bath under reduced pressure (0.3 mbar, 30 °C). The crude residue was dried under reduced pressure (0.02 mbar) for 16 hours and washed with dry ethanol (2 x 60 mL), stirring for one hour each time, followed by decantation. The product was suspended in dry ethanol (60 mL), filtered, and the solid was washed with dry petroleum ether (2 x 40 mL). Further drying under reduced pressure (0.02 mbar) for 24 hours yielded $\mathbf{2^N}$ (1.95 g, 2.46 mmol, 89%) as a powder. By cooling a concentrated acetonitrile solution of the product, diluted with an equal volume of diethyl ether, at −18 °C, red-brown crystals with X-ray diffraction quality were obtained. (Procedure adapted from Section 6.5)

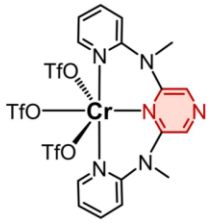

MS (ESI$^+$, CH_3CN): *m/z* (%) = 641.99 (44) [$\mathbf{2^N}$–OTf]$^+$, 683.01 (12) [$\mathbf{2^N}$–OTf+CH_3CN]$^+$, 808.97 (7) [$\mathbf{2^N}$+NH_4]$^+$, 813.93 (27) [$\mathbf{2^N}$+Na]$^+$, 829.90 (6) [$\mathbf{2^N}$+K]$^+$.
IR (ATR): $\tilde{\nu}_{max}$ = 1612 (m), 1576 (m), 1524 (w), 1499 (m), 1469 (w), 1438 (s), 1389 (w), 1344 (s), 1287 (w), 1234 (s), 1190 (vs), 1174 (vs), 1126 (vs), 1092 (s), 1071 (w), 1024 (vs), 986 (vs), 863 (w), 776 (s), 697 (w), 659 (w), 628 (vs), 593 (s), 571 (m), 545 (w), 509 (s), 486 (s), 444 (m), 418 (w) cm^{-1}.

Synthesis of [Cr(ddad)](OTf)$_3$ ([3^N](OTf)$_3$)

A pale yellow solution of the ligand ddad (1.17 g, 4.00 mmol, 2.0 eq.) in dry acetonitrile (30 mL) was added dropwise to a green-blue solution of chromium(III) triflate (1.00 g, 2.00 mmol, 1.0 eq.) in dry acetonitrile (70 mL) without any observed colour change. The reaction mixture was then heated at 70 °C for 12 hours, yielding a red solution. After cooling to room temperature, the solvent was removed under reduced pressure (180 mbar, 40 °C), and the red residue was dried under reduced pressure (8 x 10^{-3} mbar) for 24 hours. The residue was washed with THF (4 x 150 mL), stirring for 60 minutes each time, followed by decanting to separate the yellow solid product from impurities in the red solution. The yellow powder was subsequently washed with diethyl ether (2 x 150 mL) and dried under reduced pressure (8 x 10^{-3} mbar). Slow diffusion of cold diethyl ether into a concentrated acetonitrile solution resulted in orange crystals of $\mathbf{[3^N](OTf)_3}$ (1.43 g, 1.27 mmol, 63%) suitable for X-ray diffraction. (Procedure adapted from Section 6.4)

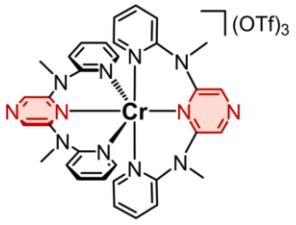

MS (ESI$^+$, CH_3CN): *m/z* (%) = 212.08 (8) [$\mathbf{3^N}$]$^{3+}$, 392.59 (41) [$\mathbf{3^N}$+OTf]$^{2+}$, 934.13 (100) [$\mathbf{3^N}$+2 OTf]$^+$.
IR (ATR): $\tilde{\nu}_{max}$ = 3094 (w), 1610 (s), 1570 (s), 1525 (w), 1497 (s), 1469 (m), 1435 (vs), 1374 (w), 1344 (s), 1311 (w), 1253 (vs), 1224 (s), 1150 (s), 1127 (vs), 1091 (s), 1070 (w), 1029 (vs), 965 (m), 862 (w), 780 (s), 756 (m), 660 (w), 636 (vs), 593 (w), 574 (m), 517 (m), 491 (m), 443 (w), 410 (w) cm^{-1}.
Elemental analysis calcd. for $C_{35}H_{32}CrF_9N_{12}O_9S_3$: C, 38.79; H, 2.98; N, 15.51; S, 8.87. Found: C, 39.15; H, 3.14; N, 15.68; S, 8.94.
UV/Vis (CH_3CN): λ_{max} (ε) = 773 (0.23), 742 (0.50), 703 (0.32), 491 (2050), 393 (11890), 350 (14960, sh), 333 (16560), 301 (23500) nm (M^{-1} cm^{-1}).
Emission (CH_3CN, room temperature): λ_{max} = 779, 743 nm (λ_{exc} = 493 nm).

Synthesis of [Cr(bptp)(ddad)](OTf)$_3$ ([3^{N,S}](OTf)$_3$)

A solution of the ligand bptp (0.30 g, 1.00 mmol, 1.0 eq.) in dry acetonitrile (20 mL) was added dropwise to a solution of the triflato complex **2^N** (0.79 g, 1.00 mmol, 1.0 eq.) in dry acetonitrile (100 mL). The reaction mixture was heated at 60 °C for 16 hours, turning the solution into red-orange. After cooling to room temperature, the solvent was removed under reduced pressure (180 mbar, 40 °C), and the residue was dried under reduced pressure (0.02 mbar) for five hours. The red-brown crude product was stirred as suspension in THF (100 mL) for ten hours, yielding a yellow solid and a red solution. The solvent was decanted and the solid residue was washed with THF (2 x 100 mL), each time stirring for one hour, followed by decantation. Finally, the yellow powder was filtered as a suspension in THF (50 mL), washed with diethyl ether (2 x 50 mL), and dried under reduced pressure (0.02 mbar) for three hours. Slow diffusion of cold diethyl ether into a concentrated acetonitrile solution yielded red crystals of **[3^{N,S}](OTf)$_3$** (0.34 g, 0.297 mmol, 30%), suitable for X-ray diffraction. (Procedure adapted from Section 6.5)

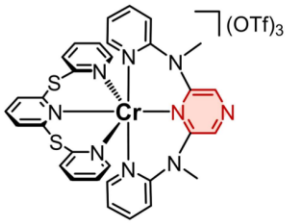

MS (ESI$^+$, CH_3CN): *m*/*z* (%) = 213.71 (27) [**3^{N,S}**]$^{3+}$, 395.04 (100) [**3^{N,S}**+OTf]$^{2+}$, 939.03 (83) [**3^{N,S}**+2 OTf]$^+$.
IR (ATR): $\tilde{\nu}_{max}$ = 3090 (w), 2252 (w), 1611 (m), 1594 (m), 1570 (m), 1545 (w), 1524 (w), 1496 (m), 1469 (m), 1434 (vs), 1370 (w), 1344 (m), 1250 (vs), 1223 (vs), 1146 (vs), 1125 (vs), 1088 (s), 1068 (m), 1026 (vs), 965 (m), 919 (w), 962 (w), 777 (vs), 756 (m), 741 (w), 726 (m), 690 (w), 658 (w), 633 (vs), 593 (w), 573 (s), 516 (vs), 490 (s), 439 (m), 411 (w) cm^{-1}.
UV/Vis (CH_3CN): λ_{max} (ε) = 749 (0.25, sh), 729 (0.55), 691 (0.56), 502 (1250), 411 (4980), 346 (11100), 300 (19920), 224 (40940) nm (M^{-1} cm^{-1}).
Emission (CH_3CN, room temperature): λ_{max} = 756, 730 nm (λ_{exc} = 503 nm).

Analytical Data of the Ligand

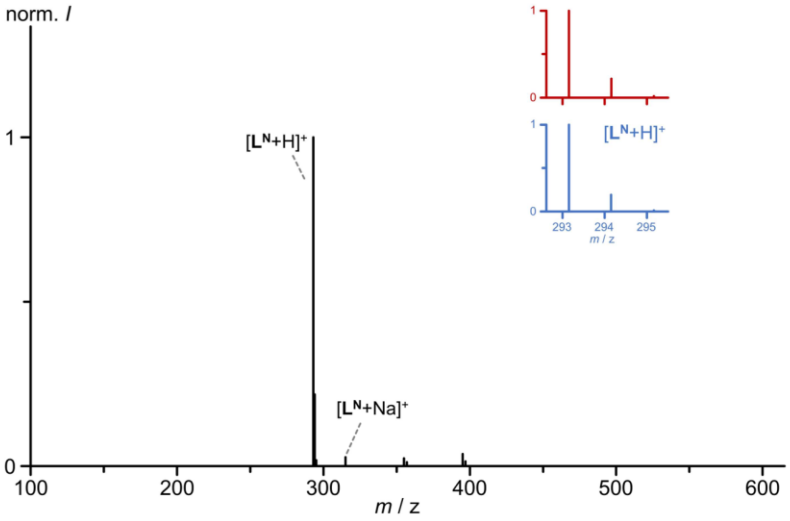

Fig. S1 ESI$^+$ mass spectrum of $\mathbf{L^N}$ in CH_3CN with insets of the experimentally found (red) and calculated (blue, normalized) isotope pattern for $[\mathbf{L^N}+H]^+$ ($C_{16}H_{17}N_6$).

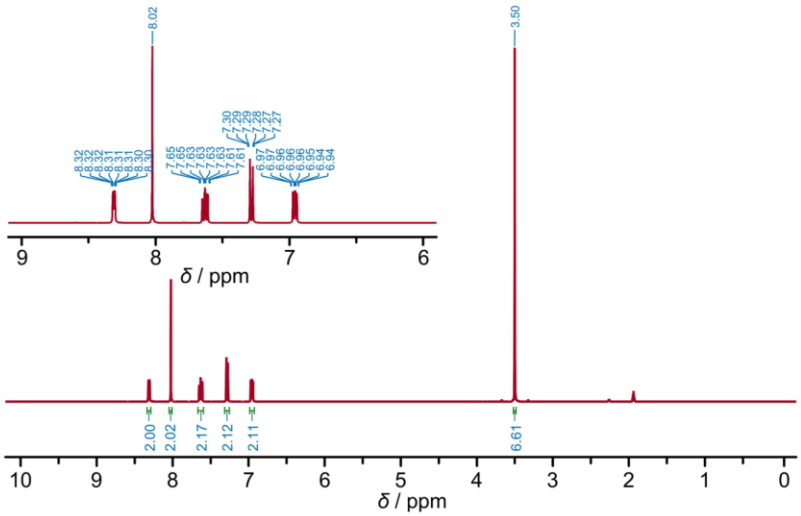

Fig. S2 ^{1}H NMR spectrum of $\mathbf{L^N}$ in CD_3CN with inset of the aromatic region.

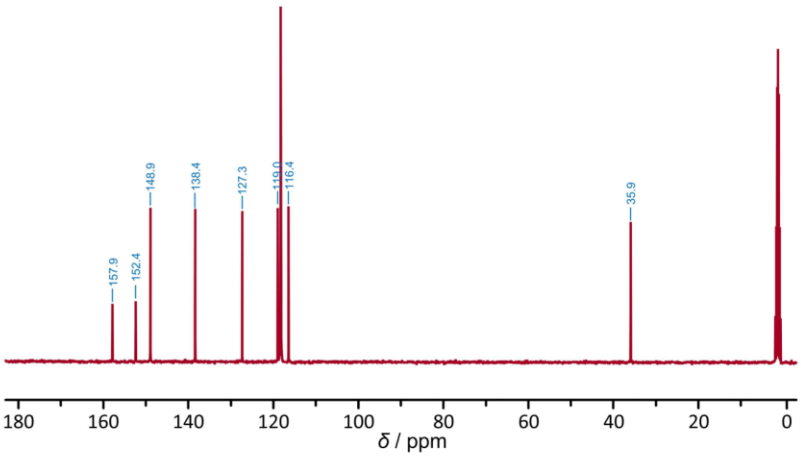

Fig. S3 $^{13}C\{^{1}H\}$ NMR spectrum of $\mathbf{L^N}$ in CD_3CN.

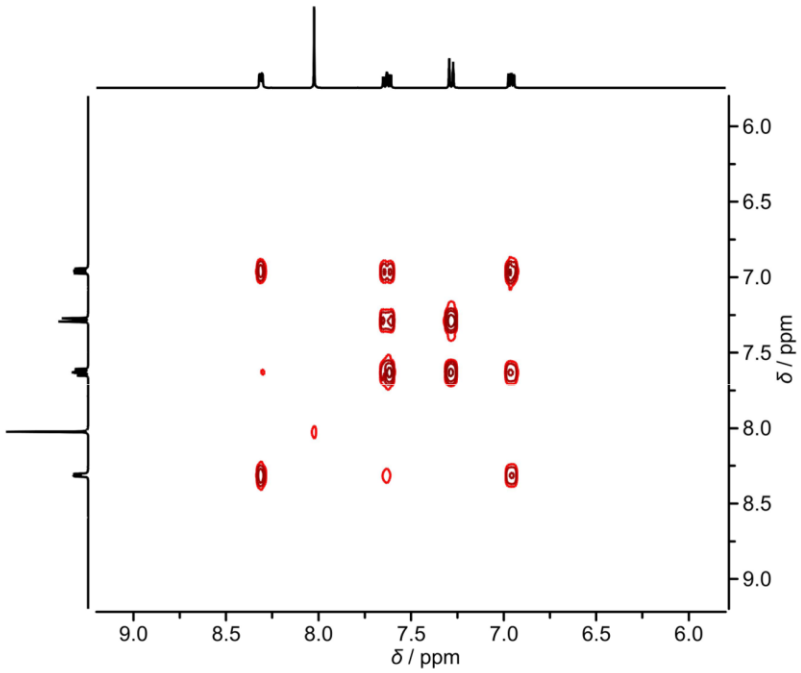

Fig. S4 $^{1}H,^{1}H$ COSY of $\mathbf{L^N}$ in CD_3CN.

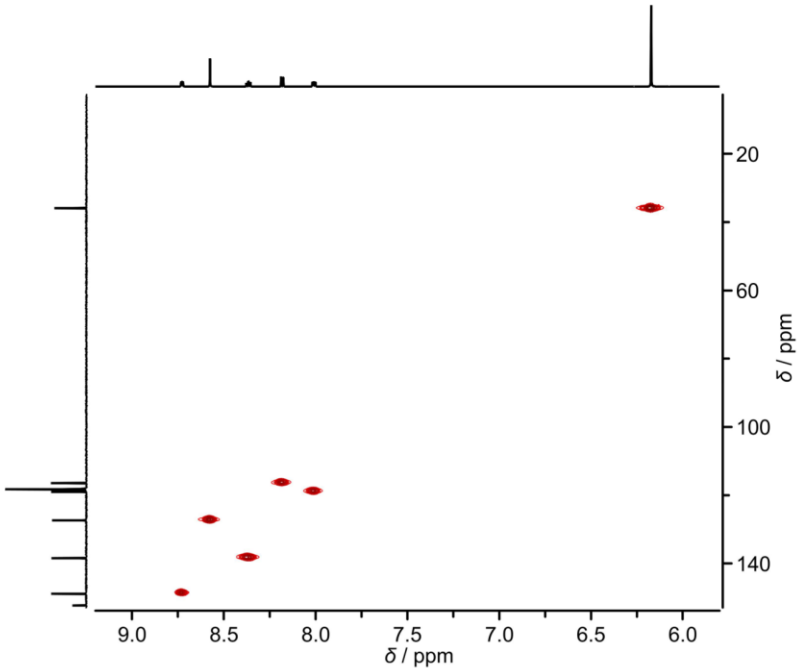

Fig. S5 $^{13}C,^{1}H$ HSQC of $\mathbf{L^N}$ in CD_3CN.

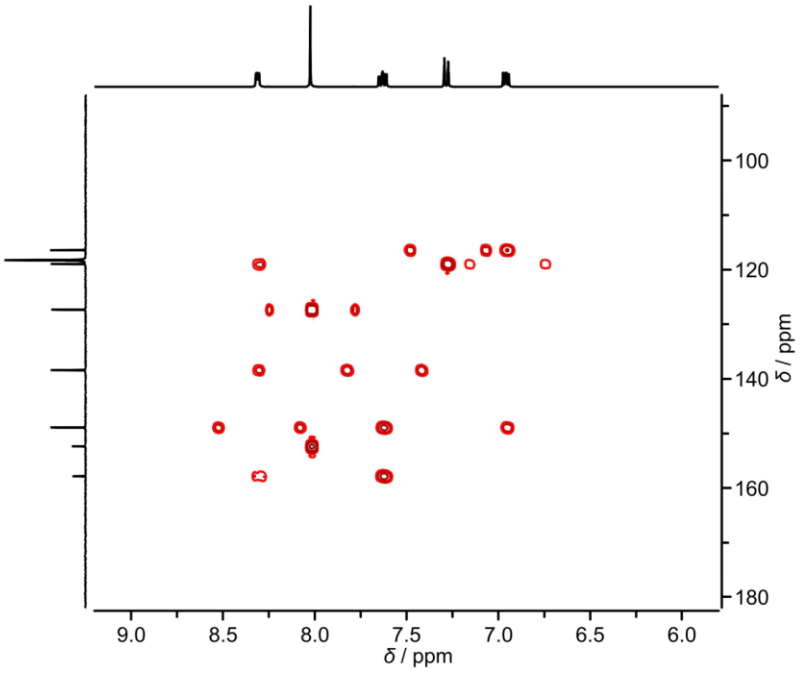

Fig. S6 $^{13}C,^{1}H$ HMBC of $\mathbf{L^N}$ in CD_3CN.

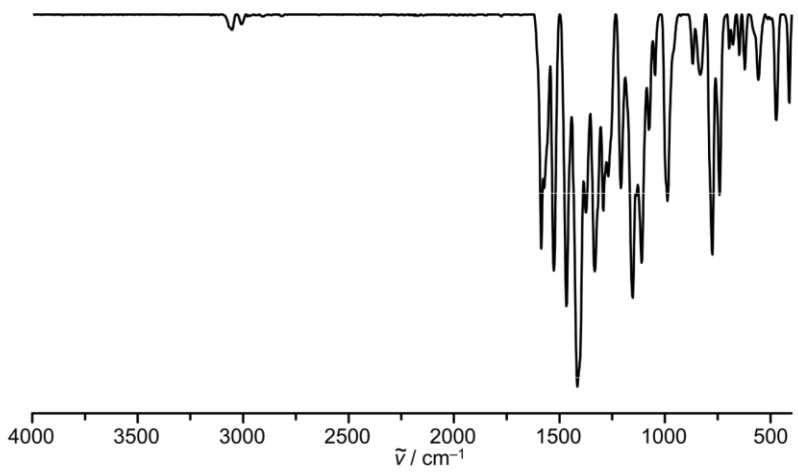

Fig. S7 ATR-IR spectrum of $\mathbf{L^N}$.

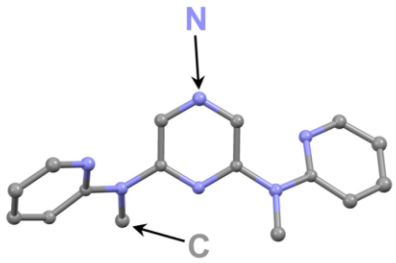

Fig. S8 Molecular structure of $\mathbf{L^N}$ in the solid state (triclinic space group $P\bar{1}$). H atoms omitted, thermal ellipsoids at 50% probability level.

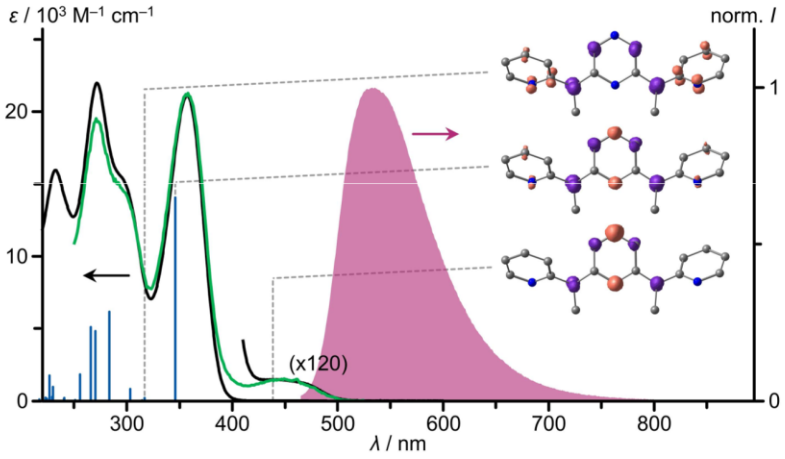

Fig. S9 UV/Vis/NIR absorption spectrum (black), excitation spectrum (λ_{em} = 535 nm, green) and emission spectrum (λ_{exc} = 455 nm, purple) of $\mathbf{L^N}$ in deaerated CH_3CN at room temperature, TD-DFT calculated oscillator strengths (blue) and difference electron densities (isosurface value 0.01 a.u.) of three low energy transitions. The region of the lowest absorption band is scaled with the indicated factor.

Analytical Data of the Precursor Complexes

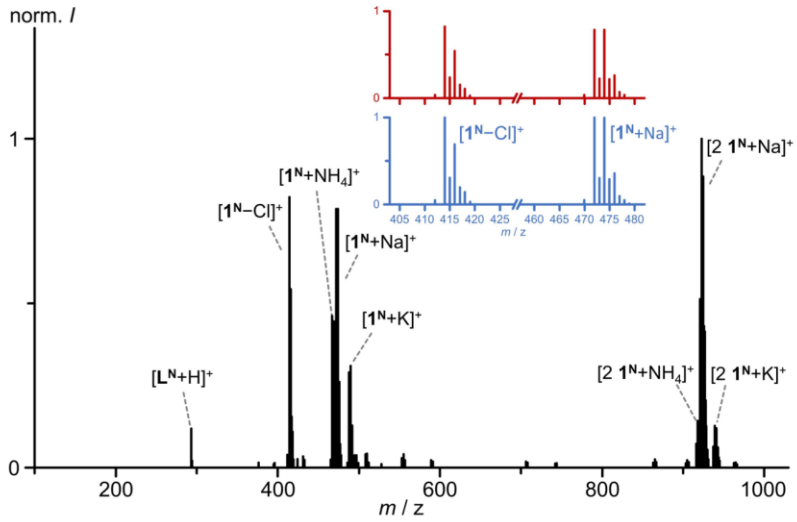

Fig. S10 ESI$^+$ mass spectrum of **1^N** in CH_3CN with insets of the experimentally found (red) and calculated (blue, normalized) isotope pattern for [**1**–Cl]$^+$ ($C_{16}H_{16}Cl_2CrN_6$) and [**1^N**+Na]$^+$ ($C_{16}H_{16}Cl_3CrN_6Na$).

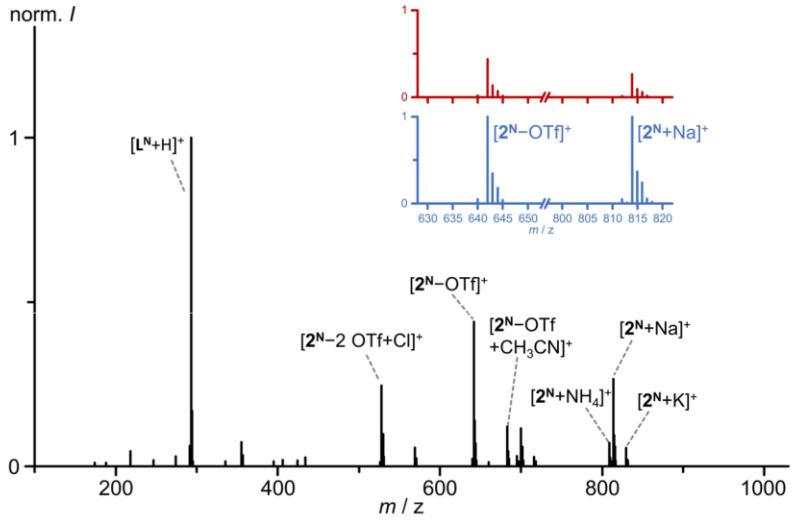

Fig. S11 ESI$^+$ mass spectrum of **2^N** in CH_3CN with insets of the experimentally found (red) and calculated (blue, normalized) isotope pattern for [**2^N**–OTf]$^+$ ($C_{18}H_{16}CrF_6N_6O_6S_2$) and [**2^N**+Na]$^+$ ($C_{19}H_{16}CrF_9N_6NaO_9S_3$).

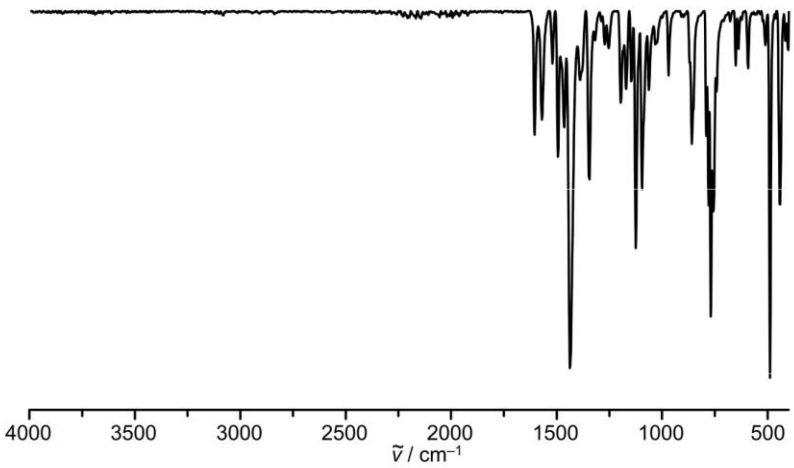

Fig. S12 ATR-IR spectrum of $\mathbf{1^N}$.

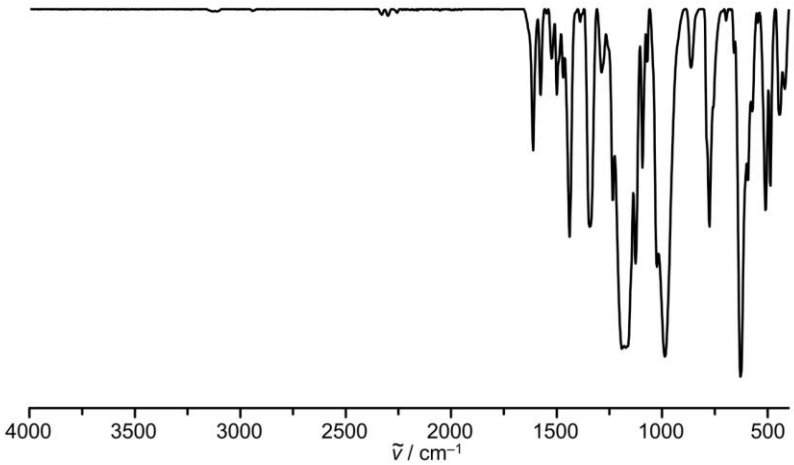

Fig. S13 ATR-IR spectrum of $\mathbf{2^N}$.

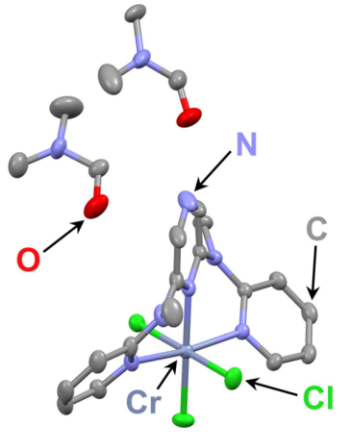

Fig. S14 Molecular structure of **1^N x 2 DMF** in the solid state (triclinic space group $P\bar{1}$). H atoms omitted, thermal ellipsoids at 50% probability level.

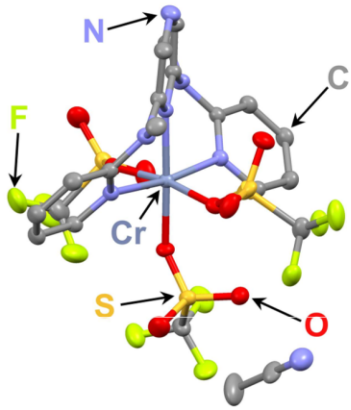

Fig. S15 Molecular structure of **2^N x CH_3CN** in the solid state (triclinic space group $P\bar{1}$). H atoms omitted, thermal ellipsoids at 50% probability level.

Analytical and DFT/TDDFT Data of the Target Complexes

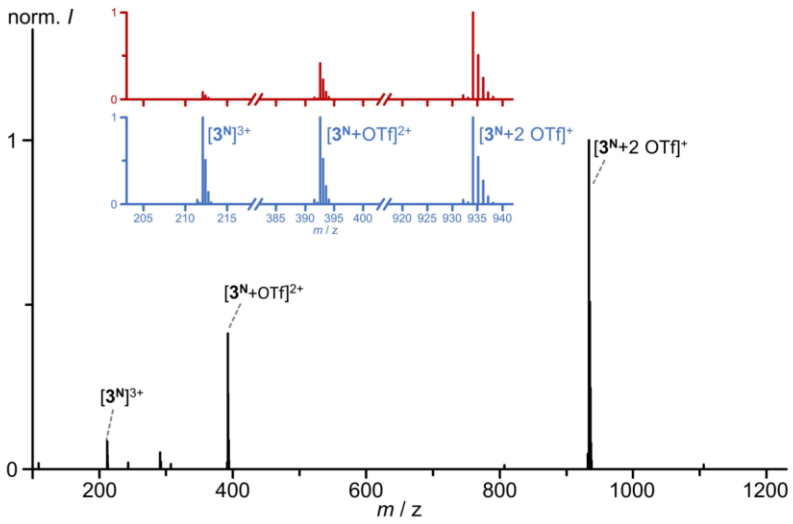

Fig. S16 ESI$^+$ mass spectrum of **[3^N](OTf)$_3$** in CH_3CN with insets of the experimentally found (red) and calculated (blue, normalized) isotope pattern for **[3^N]**$^{3+}$ ($C_{35}H_{40}CrN_{12}$), **[3^N+OTf]**$^{2+}$ ($C_{36}H_{40}CrF_3N_{12}O_3S$) and **[3^N+2 OTf]**$^+$ ($C_{37}H_{40}CrF_6N_{12}O_6S_2$).

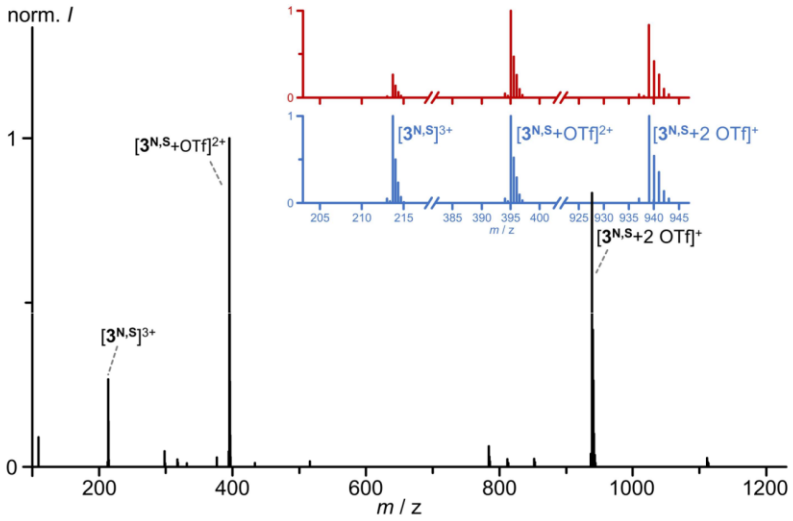

Fig. S17 ESI$^+$ mass spectrum of **[3^{N,S}](OTf)$_3$** in CH_3CN with insets of the experimentally found (red) and calculated (blue, normalized) isotope pattern for **[3^{N,S}]**$^{3+}$ ($C_{31}H_{27}CrN_9S_2$), **[3^{N,S}+OTf]**$^{2+}$ ($C_{32}H_{27}CrF_3N_9O_3S_3$) and **[3^{N,S}+2 OTf]**$^+$ ($C_{33}H_{27}CrF_6N_9O_6S_4$).

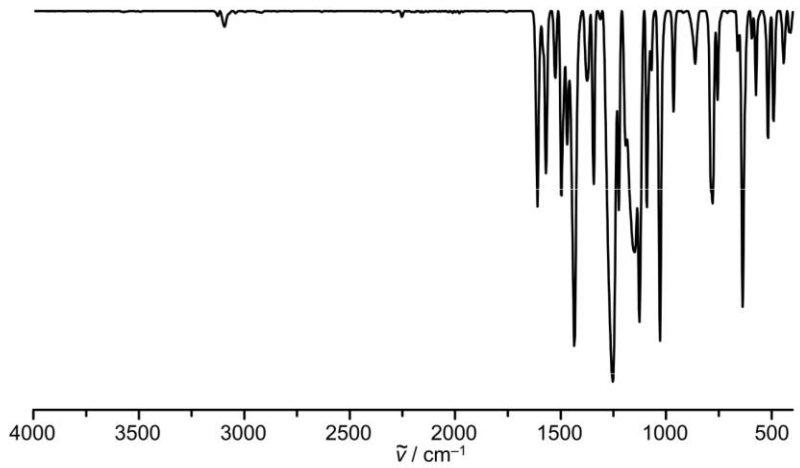

Fig. S18 ATR-IR spectrum of **[3^{N}](OTf)$_3$**.

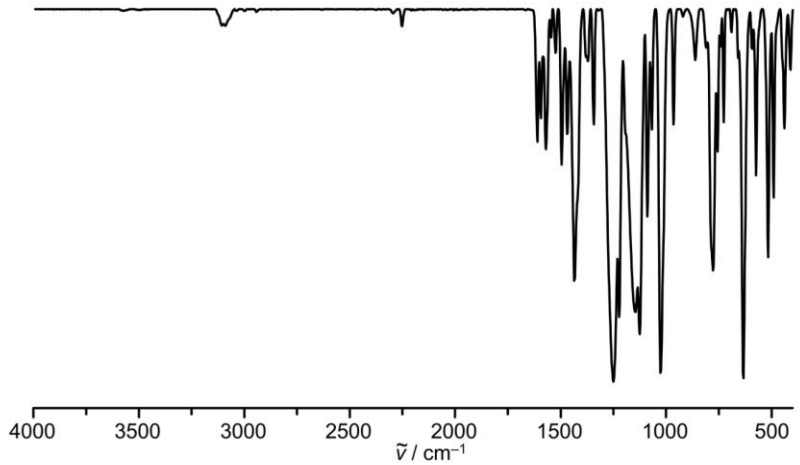

Fig. S19 ATR-IR spectrum of **[3^{N,S}](OTf)$_3$**.

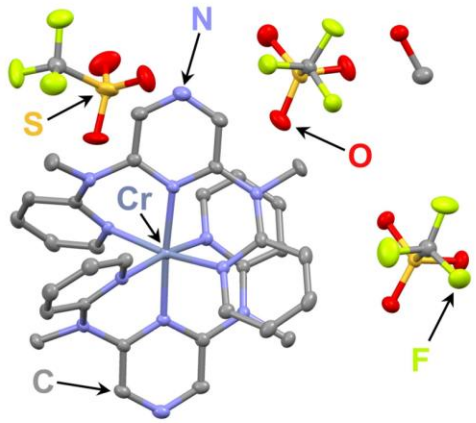

Fig. S20 Molecular structure of **$[3^{N}](OTf)_3$ x MeOH** in the solid state (monoclinic space group $P2_1/n$). H atoms omitted, thermal ellipsoids at 50% probability level.

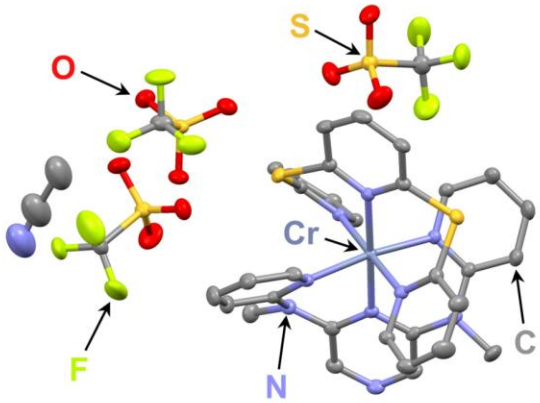

Fig. S21 Molecular structure of **$[3^{N,S}](OTf)_3$ x CH_3CN** in the solid state (monoclinic space group $P2_1$). H atoms omitted, thermal ellipsoids at 50% probability level.

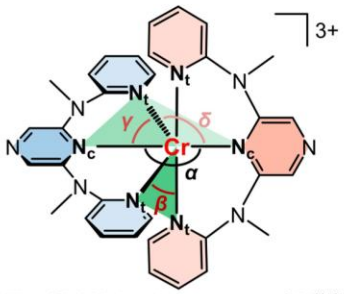

Fig. S22 Molecular structure of $[3^{N}]^{3+}$ showing structural parameters relevant for discussion of distinct geometry differences within the investigated series of complexes.

Table S1 Structural parameters of the complexes $[3^{N}]^{3+}$, $[3^{N,S}]^{3+}$ and $[1^{S}]^{3+}$ (Section 6.4) from crystal structure determination (XRD) and DFT geometry optimization. Bond lengths (***d***) are given in Å and angles (α, β, γ, δ) in °.

Parameter	$[3^{N}]^{3+}$		$[3^{N,S}]^{3+}$		$[1^{S}]^{3+}$	
	Exp.	*Calc.*	Exp.	*Calc.*	Exp.	*Calc.*
bond distances ***d***						
$Cr–N_c(1)$	2.0346(16)	*2.0425*	2.035(3)	*2.0425*	2.101(16)	*2.1390*
$Cr–N_c(2)$	2.0348(16)	*2.0425*	2.096(3)	*2.1026*	2.087(16)	*2.1400*
$Cr–N_t(1)$	2.0379(16)	*2.0569*	2.032(3)	*2.0534*	2.072(16)	*2.1179*
$Cr–N_t(1)$	2.0372(16)	*2.0569*	2.050(4)	*2.0534*	2.085(16)	*2.1176*
$Cr–N_t(2)$	2.0382(17)	*2.0574*	2.084(3)	*2.0975*	2.064(17)	*2.1188*
$Cr–N_t(2)$	2.0299(16)	*2.0574*	2.082(3)	*2.0975*	2.079(16)	*2.1183*
axial angles α (*trans*)						
$N_c(1)–Cr–N_c(2)$	175.92(6)	*180.00*	179.14(14)	*180.00*	178.83(7)	*179.96*
$N_t(1)–Cr–N_t(1)$	170.28(7)	*172.43*	171.24(14)	*171.52*	177.38(7)	*178.77*
$N_t(2)–Cr–N_t(2)$	170.48(6)	*172.36*	179.02(14)	*179.46*	178.15(7)	*178.85*
equatorial angles β (*cis*)						
$N_t(1)–Cr–N_t(2)$	90.62(7)	*89.64*	87.76(13)	*87.17*	84.97(6)	*85.50*
$N_t(2)–Cr–N_t(1)$	88.73(7)	*90.86*	92.81(14)	*92.79*	92.59(7)	*94.48*
$N_t(1)–Cr–N_t(2)$	89.75(7)	*89.64*	87.44(14)	*87.17*	85.70(7)	*85.51*
$N_t(2)–Cr–N_t(1)$	92.44(7)	*90.86*	92.13(13)	*92.79*	96.75(7)	*94.53*
intraligand angles γ (*cis*)						
$N_c(1)–Cr–N_t(1)$	84.43(6)	*86.22*	86.45(14)	*85.76*	89.81(6)	*89.38*
$N_c(1)–Cr–N_t(1)$	86.02(7)	*86.22*	84.82(13)	*85.76*	89.30(7)	*89.39*
$N_c(2)–Cr–N_t(2)$	86.36(6)	*86.18*	89.77(13)	*90.27*	89.61(6)	*89.40*
$N_c(2)–Cr–N_t(2)$	84.48(6)	*86.18*	89.26(13)	*90.27*	89.73(6)	*89.45*
interligand angles δ (*cis*)						
$N_c(1)–Cr–N_t(2)$	92.97(6)	*93.78*	94.23(14)	*94.24*	89.50(6)	*90.62*
$N_c(1)–Cr–N_t(2)$	96.67(6)	*93.79*	94.51(13)	*94.24*	91.44(7)	*90.62*
$N_c(2)–Cr–N_t(1)$	96.79(6)	*93.82*	89.73(13)	*89.73*	91.26(6)	*90.64*
$N_c(2)–Cr–N_t(1)$	92.48(6)	*93.82*	91.24(13)	*89.73*	89.42(6)	*90.51*

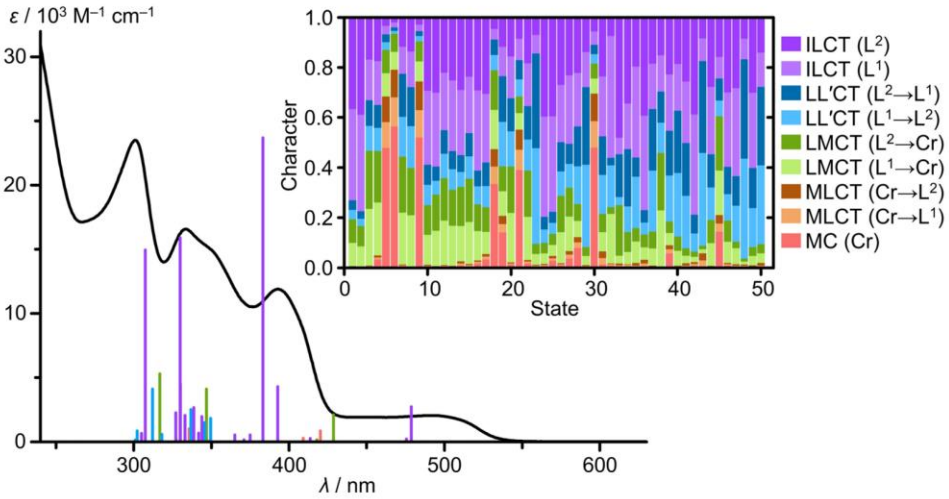

Fig. S23 UV/VIS absorption spectrum of **[3^{N}](OTf)$_3$** in CH_3CN (black) with TD-DFT calculated oscillator strengths coloured according to the most dominant character of the corresponding transition (red: MC, orange: MLCT, green: LMCT, purple: LC). Inset: Charge transfer number analysis of the 50 lowest energy spin-allowed transitions calculated by Loewdin population analysis with the complex cation fragmented into chromium (Cr), **L^{N}** ligand 1 (L^1) and **L^{N}** ligand 2 (L^2).

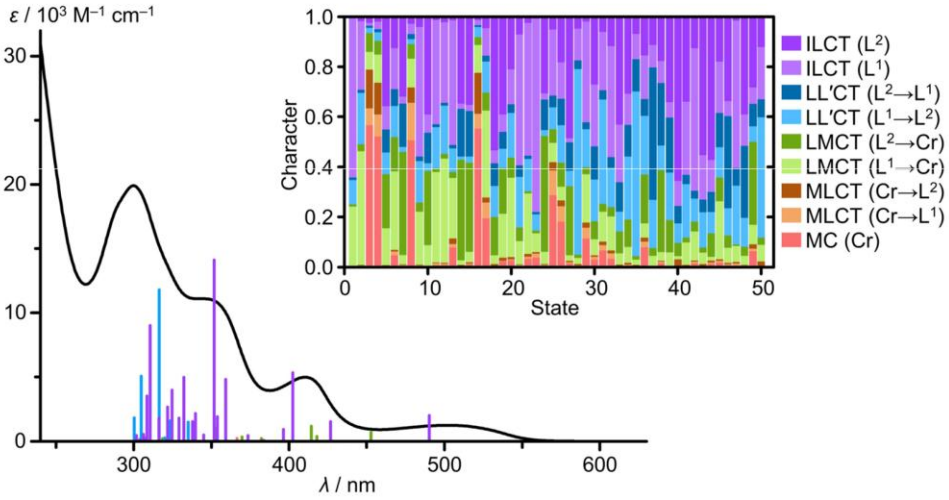

Fig. S24 UV/VIS absorption spectrum of **[3^{N,S}](OTf)$_3$** in CH_3CN (black) with TD-DFT calculated oscillator strengths coloured according to the most dominant character of the corresponding transition (red: MC, orange: MLCT, green: LMCT, purple: LC). Inset: Charge transfer number analysis of the 50 lowest energy spin-allowed transitions calculated by Loewdin population analysis with the complex cation fragmented into chromium (Cr), **L^{S}** ligand (L^1) and **L^{N}** ligand (L^2).

Table S2 TD-DFT calculated oscillator strengths and difference electron densities of the ten lowest energy spin-allowed transitions of $[\mathbf{3^N}]^{3+}$ (Pz: pyrazine, Py^t: pyridine terminal).

#	λ / nm	oscillator strength	character	from	to	**difference electron density** (purple: density loss, orange: density gain)
1	478.7	0.0182299	ILCT (73%)	p (NMe) + π (Pz)	t_{2g} (d_{xz}+d_{yz}) + π* (Pz)	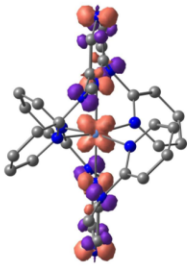
2	475.6	0.0016091	ILCT (77%)	p (NMe) + π (Pz)	t_{2g} (d_{xz}+d_{yz}) and t_{2g} (d_{xz}–d_{yz}) + π* (Pz)	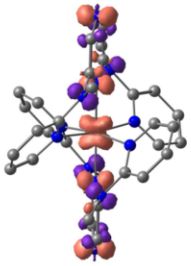
3	434.6	0.0000015	LMCT (46%) + ILCT (33%) + LL'CT (20%)	p (NMe) + π (Pz)	t_{2g} (d_{xy}) + π* (Py^t)	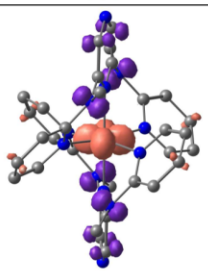
4	428.5	0.0141485	LMCT (42%) + ILCT (35%)	p (NMe) + π (Pz)	t_{2g} (d_{xy}) + π* (Py^t)	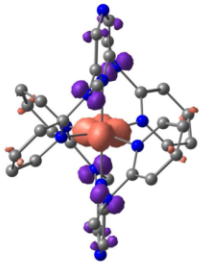
5	420.2	0.0057042	MC (48%) + MLCT (21%)	t_{2g} (d_{xy})	e_g ($d_{x^2-y^2}$) + p (N)	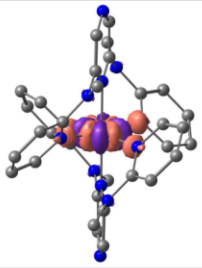

6	419.7	0.0000101	MC (57%) + MLCT (23%)	t_{2g} (d_{xz}+d_{yz})	e_g (d_{z^2}) + p (N)	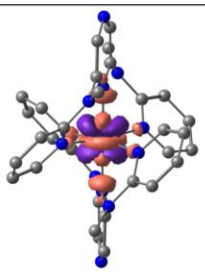
7	418.0	0.0010071	LMCT (43%) + LL'CT (33%) + ILCT (22%)	p (NMe) + π (Pz)	t_{2g} (d_{xz}–d_{yz}) + π* (Pz)	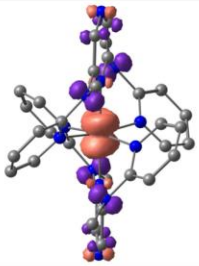
8	413.6	0.0018661	LMCT (39%) + LL'CT (32%) + ILCT (28%)	p (NMe) + π (Pz)	t_{2g} (d_{xz}–d_{yz}) + π* (Pz)	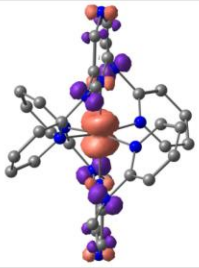
9	409.2	0.0019642	MC (52%) + MLCT (22%)	t_{2g} (d_{xz}+d_{yz}) and t_{2g} (d_{xz}–d_{yz})	e_g ($d_{x^2-y^2}$) + p (N)	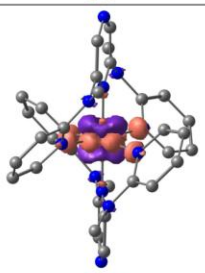
10	392.7	0.0286468	ILCT (59%) + LMCT (24%)	p (NMe)	t_{2g} (d_{xz}–d_{yz}) + π* (Pz)	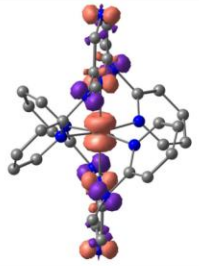

Table S3 TD-DFT calculated oscillator strengths and difference electron densities of the ten lowest energy spin-allowed transitions of $[3^{N,S}]^{3+}$ (Pz: pyrazine, Py^c: pyridine central, Py^t: pyridine terminal).

#	λ / nm	oscillator strength	character	from	to	**difference electron density** (purple: density loss, orange: density gain)
1	490.2	0.0134263	ILCT (64%) + LMCT (24%)	p (NMe) + π (Pz)	t_{2g} (d_{yz}) + π* (Pz)	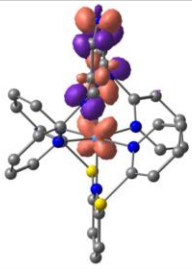
2	452.7	0.0046524	LMCT (48%) + ILCT (29%) + LL'CT (22%)	p (NMe) + π (Pz) + π (Py^t)	t_{2g} (d_{xy}) + π* (Py^t)	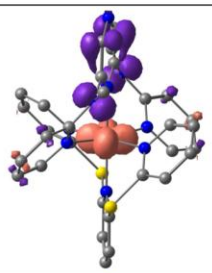
3	438.5	0.0000050	MC (57%) + MLCT (22%)	t_{2g} (d_{yz})	e_g (d_{z^2}) + p (N)	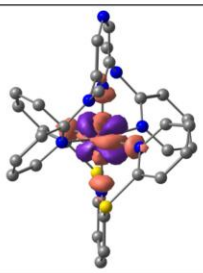
4	427.8	0.0001856	MC (52%) + MLCT (21%)	t_{2g} (d_{xy})	e_g ($d_{x^2-y^2}$) + p (N)	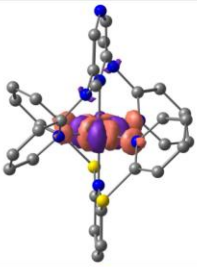
5	426.8	0.0102210	ILCT (45%) + LMCT (36%)	p (S) + p (NMe) + π (Py^c)	t_{2g} (d_{xz}) + π* (Py^c)	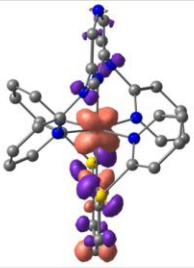

6	418.0	0.0026954	LMCT (45%) + ILCT (29%)	p (NMe) + π (Pz)	t_{2g} (d_{xz}) and t_{2g} (d_{yz}) + π* (Py^c)	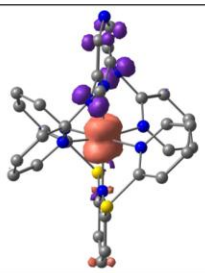
7	414.3	0.0078898	LMCT (45%) + ILCT (35%)	p (S) + π (Py^c)	t_{2g} (d_{xy}) + π* (Py^t)	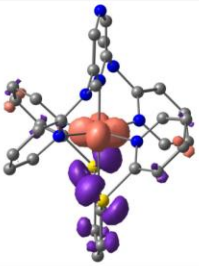
8	414.3	0.0026450	MC (51%) + MLCT (21%)	t_{2g} (d_{xz})	e_g (d_{z^2}) + p (N)	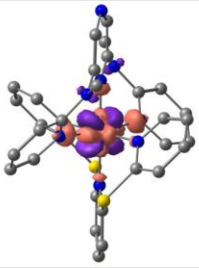
9	402.3	0.0356551	ILCT (56%) + LMCT (25%)	p (NMe) + π (Pz)	t_{2g} (d_{yz}) + π* (Pz)	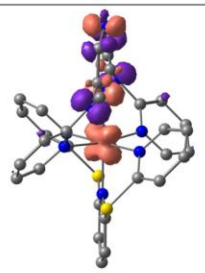
10	396.4	0.0062931	ILCT (46%) + LMCT (38%)	p (S) + π (Py^c)	t_{2g} (d_{xz}) and t_{2g} (d_{yz}) + π* (Py^c) + π* (Pz)	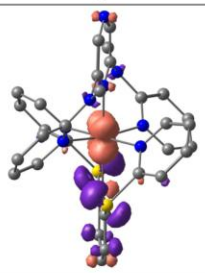

CAS-SCF, Doublet Energy, Photolysis and Electrochemical Studies

Table S4 CASSCF(7,12)-SC/NEVPT2 calculated transition energies (in cm^{-1}) of $[1^{X}]^{3+}$ (X = NMe[34], S), $[3^{N}]^{3+}$, $[3^{N,S}]^{3+}$, and BF_3, H and Me additives of $[3^{N}]^{3+}$ and $[3^{N,S}]^{3+}$ at DFT optimized geometries, with assignments to the lowest ^2E, $^2T_1$ and $^4T_2$ states (bold values indicate the lowest state of each multiplicity.

	$^2E(2)$	$^2E(1)$	$^2T_1(3)$	$^2T_1(2)$	$^2T_1(1)$	$^2T_2(3)$	$^2T_2(2)$	$^2T_2(1)$	$^4T_2(3)$	$^4T_2(2)$	$^4T_2(1)$
$[1^{NMe}]^{3+}$	16161	15576	15992	15908	**15029**	24326	23949	23789	24315	23265	**23219**
$[1^{S}]^{3+}$	16530	15941	16560	16279	**15713**	24163	24144	23800	21372	21371	**20296**
$[3^{N}]^{3+}$	16131	15570	16028	15822	**15068**	24187	23937	23766	24449	23343	**23268**
$[3^{N,S}]^{3+}$	16216	15682	16204	15978	**15315**	24192	23983	23813	23714	22744	**22275**
$[3^{N}+BF_3]^{3+}$	16118	15582	16079	15789	**15076**	24148	24036	23748	24431	23467	**23172**
$[3^{N}+2BF_3]^{3+}$	16107	15584	16083	15718	**15067**	24112	24094	23716	24358	23653	**23017**
$[3^{N}+H]^{4+}$	16113	15584	16053	15738	**15058**	24117	24055	23725	24417	23593	**23023**
$[3^{N}+2H]^{5+}$	16103	15590	16055	15625	**15032**	24162	24040	23682	24205	23883	**22714**
$[3^{N}+Me]^{4+}$	16121	15582	16062	15767	**15063**	24141	24078	23729	24419	23549	**23075**
$[3^{N}+2Me]^{5+}$	16112	15588	16058	15666	**15042**	24162	24083	23690	24249	23815	**22810**
$[3^{N,S}+BF_3]^{3+}$	16216	15686	16233	15955	**15313**	24163	23959	23864	23482	22924	**22155**
$[3^{N,S}+H]^{4+}$	16206	15694	16221	15918	**15296**	24132	23927	23885	23350	23048	**22021**
$[3^{N,S}+Me]^{4+}$	16217	15691	16228	15941	**15296**	24147	23949	23887	23386	23004	**22063**

Table S5 Five band maxima from deconvoluted SF absorption bands of $[1^{X}]^{3+}$ (X = NMe, S), $[3^{N}]^{3+}$ and $[3^{N,S}]^{3+}$, CASSCF(7,12)-SC/NEVPT2 calculated transition energies (in italics; scaled by 0.876), assignments and selected energy differences (in cm^{-1}).

	No.	#5	#4	#3	#2	#1	ΔE (#5–#1)	ΔE (#2–#1)
$[1^{NMe}]^{3+}$	*exp.*	14430	14300	13530*	13600*	12960	1470	570
	calcd.	*14150*	*14010*	*13930*	*13640*	*13160*	*990*	*480*
	term	$^2E(2)$	$^2T_1(3)$	$^2T_1(2)$	$^2E(1)$	$^2T_1(1)$		
$[1^{S}]^{3+}$	*exp.*	14770	14630	14210	14030	13800	970	230
	calcd.	*14500*	*14480*	*14260*	*13960*	*13760*	*740*	*200*
	term	$^2T_1(3)$	$^2E(2)$	$^2T_1(2)$	$^2E(1)$	$^2T_1(1)$		
$[3^{N}]^{3+}$	*exp.*	14320	14150	13620	13480	12920	1400	560
	calcd.	*14130*	*14040*	*13860*	*13640*	*13200*	*930*	*440*
	term	$^2E(2)$	$^2T_1(3)$	$^2T_1(2)$	$^2E(1)$	$^2T_1(1)$		
$[3^{N,S}]^{3+}$	*exp.*	14410	14350	13760	13730	13300	1110	430
	calcd.	*14200*	*14190*	*13990*	*13730*	*13410*	*790*	*320*
	term	$^2E(2)$	$^2T_1(3)$	$^2T_1(2)$	$^2E(1)$	$^2T_1(1)$		

*Deviation in the order of experimentally and computationally determined microstate energies.

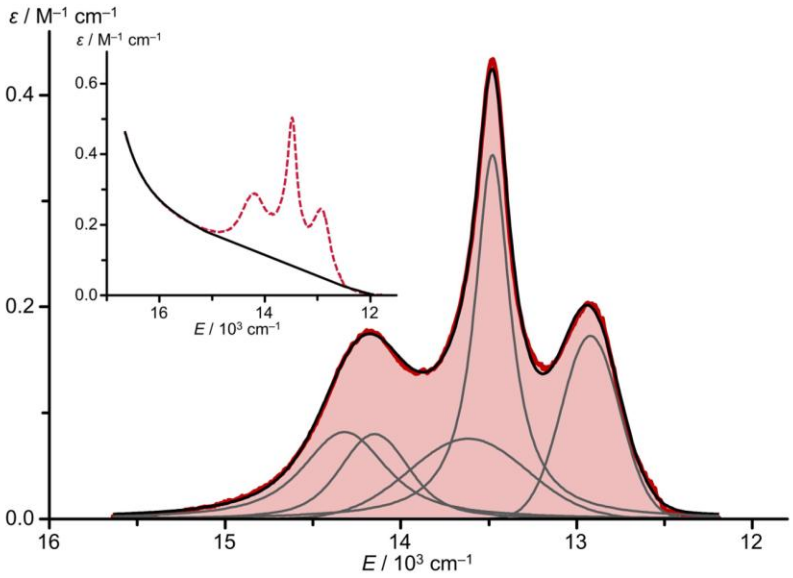

Fig. S25 Baseline corrected NIR absorption spectra of **[3^{N}](OTf)$_3$** (red) in CH_3CN with sum fit (black) consisting of five Voigt functions (grey). Inset: NIR absorption spectra of **[3^{N}](OTf)$_3$** (red, dotted) with exponential fit (black) describing the tail of the spin-allowed transitions used for the baseline correction.

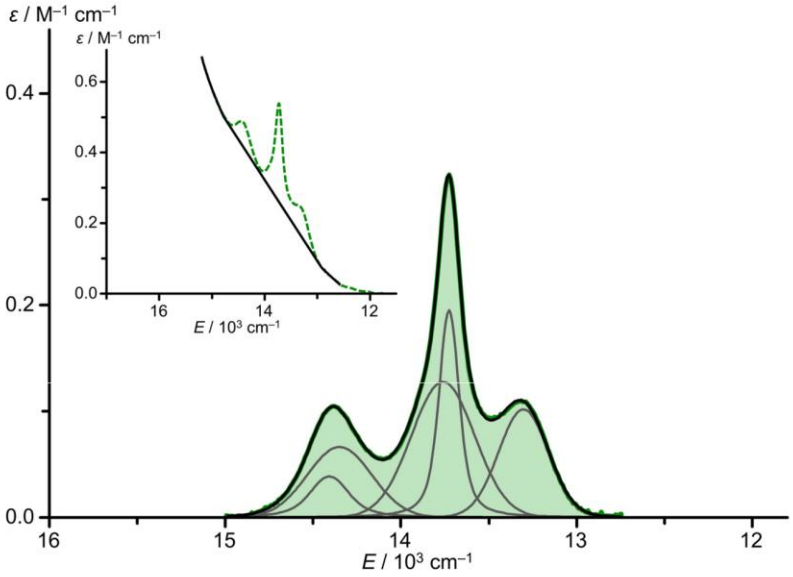

Fig. S26 Baseline corrected NIR absorption spectra of **[3^{N,S}](OTf)$_3$** (green) in CH_3CN with sum fit (black) consisting of five Voigt functions (grey). Inset: NIR absorption spectra of **[3^{N,S}](OTf)$_3$** (green, dotted) with exponential fit (black) describing the tail of the spin-allowed transitions used for the baseline correction.

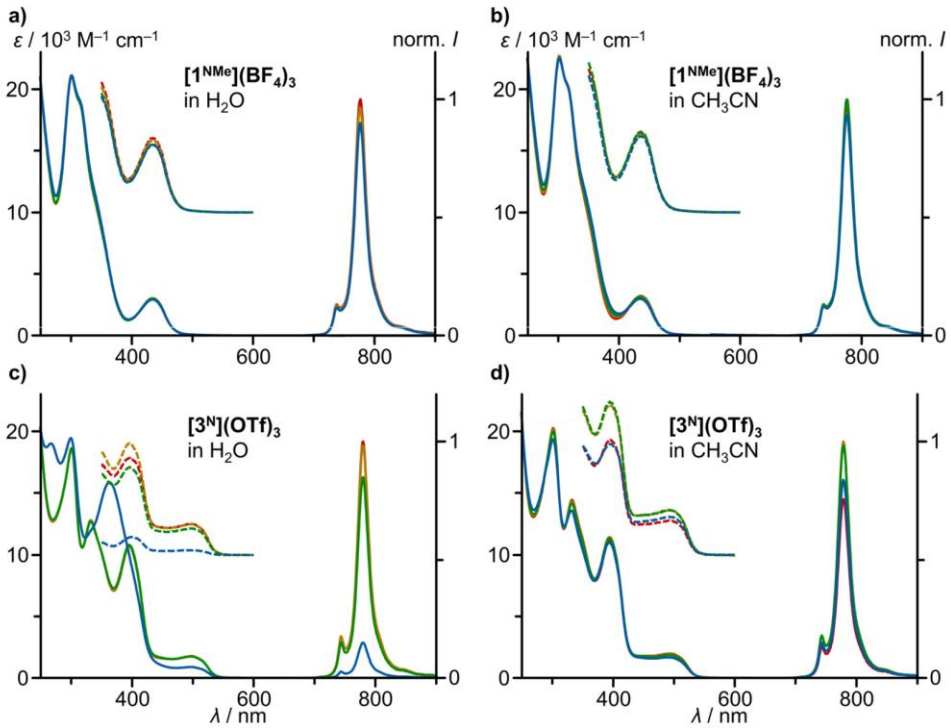

Fig. S27 UV/Vis/NIR absorption, emission spectra (λ_{exc} = 436 and 493 nm) and excitation spectra (λ_{em} = 776 and 779 nm, baseline shifted +10^5 M^{-1} cm^{-1}) of **[1^{NMe}](BF4)3** and **[3^{N}](OTf)3** in deaerated H_2O (a and c) and deaerated CH_3CN (b and d) after different UHP-LED irradiation time periods (0 s (red), 30 s (yellow), 180 s (green), 15 min (blue)) at 460 nm with an output power of 1.1 W.

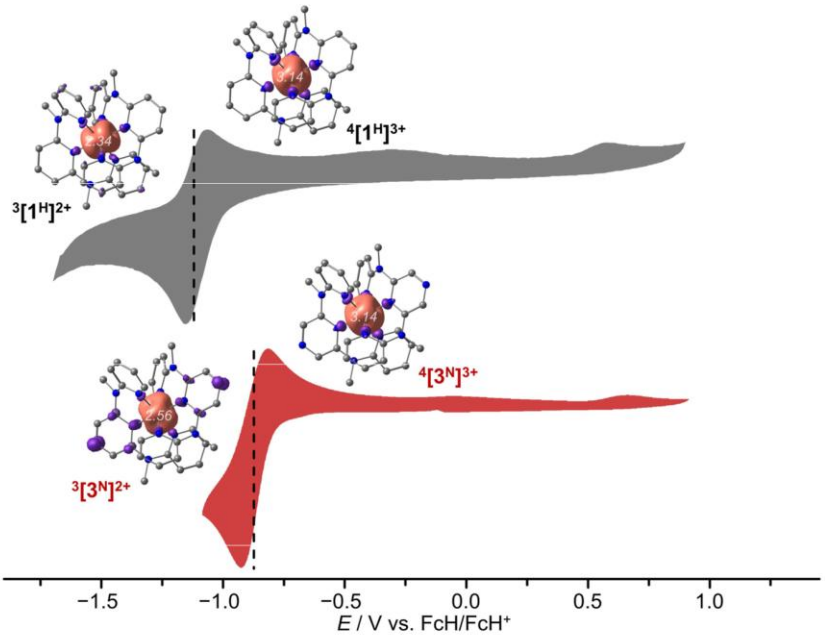

Fig. S28 Cyclic voltammograms of 3 mM **[3^N](OTf)$_3$** (red) and **[1^{NMe}](PF$_6$)$_3$** (grey)[34] in a 100 mM solution of [^{n}Bu$_4$N][PF$_6$] in CH_3CN (peak potentials E_p against FcH^+/FcH) and calculated spin densities (contour value: 0.01 a.u.) of the thermodynamically most stable tricationic and dicationic species with Mullikin spin populations at the metal center (italic).

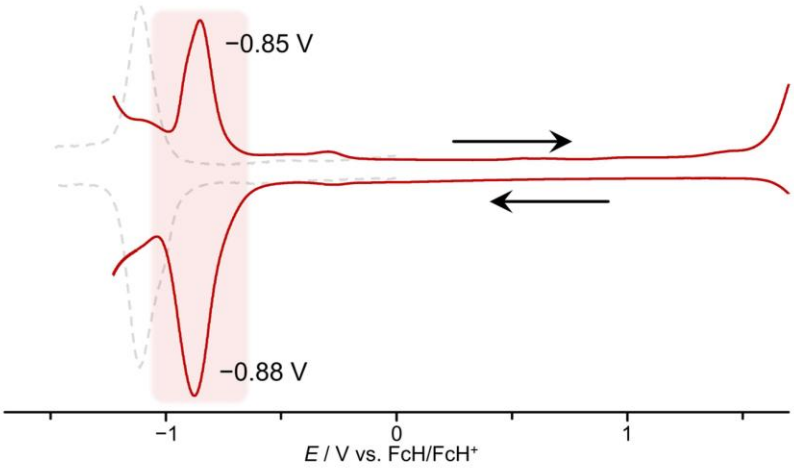

Fig. S29 Square wave voltamogramms of 3 mM **[3^N](OTf)$_3$** (red, solid line) and **[1^{NMe}](PF$_6$)$_3$** (grey, dashed line)[34] in a 100 mM solution of [^{n}Bu$_4$N][PF$_6$] in CH_3CN (peak potentials E_p against FcH^+/FcH).

References

[1] S. Balamurugan, S. Ganesan, S. Kamaraj, V. Mathew, J. Kim, N. Arumugam, A. I. Almansour, *Optical Materials* **2022**, *125*, 112082.
[2] H. E. Gottlieb, V. Kotlyar, A. Nudelman, *J. Org. Chem.* **1997**, *62*, 7512–7515.
[3] F. Neese, *WIREs Comput. Mol. Sci.* **2012**, *2*, 73–78.
[4] F. Neese, *WIREs Comput. Mol. Sci.* **2022**, *12*, 12753.
[5] C. Lee, W. Yang, R. G. Parr, *Phys. Rev. B: Condens. Matter Mater. Phys.* **1988**, *37*, 785–789.
[6] B. Miehlich, A. Savin, H. Stoll, H. Preuss, *Chem. Phys. Lett.* **1989**, *157*, 200–206.
[7] A. D. Becke, *J. Chem. Phys.* **1993**, *98*, 5648–5652.
[8] F. Weigend, R. Ahlrichs, *Phys. Chem. Chem. Phys.* **2005**, *7*, 3297–3305.
[9] F. Neese, F. Wennmohs, A. Hansen, U. Becker, *Chem. Phys.* **2009**, *356*, 98–109.
[10] R. Izsák, F. Neese, *J. Chem. Phys.* **2011**, *135*, 144105.
[11] E. van Lenthe, E. J. Baerends, J. G. Snijders, *J. Chem. Phys.* **1993**, *99*, 4597–4610.
[12] C. van Wüllen, *J. Chem. Phys.* **1998**, *109*, 392–399.
[13] F. Weigend, *Phys. Chem. Chem. Phys.* **2006**, *8*, 1057–1065.
[14] S. Miertuš, E. Scrocco, J. Tomasi, *Chem. Phys.* **1981**, *55*, 117–129.
[15] V. Barone, M. Cossi, *J. Phys. Chem. A* **1998**, *102*, 1995–2001.
[16] S. Grimme, J. Antony, S. Ehrlich, H. Krieg, *J. Chem. Phys.* **2010**, *132*, 154104.
[17] S. Grimme, S. Ehrlich, L. Goerigk, *J. Comput. Chem.* **2011**, *32*, 1456–1465.
[18] F. Plasser, *J. Chem. Phys.* **2020**, *152*, 84108.
[19] S. Mai, F. Plasser, J. Dorn, M. Fumanal, C. Daniel, L. González, *Coord. Chem. Rev.* **2018**, *361*, 74–97.
[20] B. O. Roos, P. R. Taylor, P. E.M. Sigbahn, *Chem. Phys.* **1980**, *48*, 157–173.
[21] P. E. M. Siegbahn, J. Almlöf, A. Heiberg, B. O. Roos, *J. Chem. Phys.* **1981**, *74*, 2384–2396.
[22] C. Angeli, R. Cimiraglia, S. Evangelisti, T. Leininger, J.-P. Malrieu, *J. Chem. Phys.* **2001**, *114*, 10252–10264.
[23] C. Angeli, R. Cimiraglia, J.-P. Malrieu, *Chem. Phys. Lett.* **2001**, *350*, 297–305.
[24] C. Angeli, R. Cimiraglia, J.-P. Malrieu, *J. Chem. Phys.* **2002**, *117*, 9138–9153.
[25] K. Pierloot, *Int. J. Quantum Chem.* **2011**, *111*, 3291–3301.
[26] R. H. Blessing, *Acta Crystallogr. Sect. A: Found. Crystallogr.* **1995**, *51 (Pt 1)*, 33–38.
[27] A. L. Spek, *Acta Crystallogr. Sect. D: Biol. Crystallogr.* **2009**, *65*, 148–155.
[28] G. M. Sheldrick, *Acta Crystallogr. Sect. A: Found. Adv.* **2015**, *71*, 3–8.
[29] G. M. Sheldrick, *Acta Crystallogr. Sect. C: Struct. Chem.* **2015**, *71*, 3–8.
[30] G. M. Sheldrick, *Acta Crystallogr. Sect. A: Found. Crystallogr.* **2008**, *64*, 112–122.
[31] C. B. Hübschle, G. M. Sheldrick, B. Dittrich, *J. Appl. Crystallogr.* **2011**, *44*, 1281–1284.
[32] A. Breivogel, C. Förster, K. Heinze, *Inorg. Chem.* **2010**, *49*, 7052–7056.
[33] J.-R. Jiménez, B. Doistau, C. Besnard, C. Piguet, *Chem. Comm. (Cambridge, U. K.)* **2018**, *54*, 13228–13231.
[34] S. Otto, M. Grabolle, C. Förster, C. Kreitner, U. Resch-Genger, K. Heinze, *Angew. Chem., Ind. Ed.* **2015**, *54*, 11572–11576.

7 Acknowledgements

Mein erster großer Dank gilt meiner Doktormutter [redacted]. Unter Ihrer engagierten und zielstrebigen Betreuung konnte ich nicht nur meine Begeisterung für unsere Projekte intensivieren und fachlich dazulernen, sondern – was mindestens genauso wichtig ist – mich persönlich weiterentwickeln. Gerade die produktiven Teammeetings, für die Sie immer ein offenes Ohr hatten, haben meinen Forscherehrgeiz angetrieben und mich hinterher motiviert, aus Ihrer Bürotür nach dem Motto „Hinfallen, aufstehen, Krone richten, weitergehen“ stolzieren zu lassen.

Meinen nächsten Dank möchte ich [redacted] widmen, zum einen für die Begutachtung meiner Dissertation und zum anderen für die schönen Grillfeiern mit Dir und Deiner Gruppe bei einer Partie „Cornhole“.

Für eine tolle Zusammenarbeit und gegenseitige Unterstützung, stets begleitet von einem Schuss Albernheit, gewinnbringende fachliche Diskussionen, stets begleitet von ein bisschen Witz, und produktive Kritik, stets begleitet von einem Hauch Ironie, möchte ich mich zutiefst bei unserer gesamten Arbeitsgruppe bedanken. Durch Euren Einsatz und Euer Engagement zu gemeinsamen unvergesslichen Momenten innerhalb und außerhalb der Labormauern beizutragen, wie beispielsweise am Mittagstisch, wurde mein Arbeitsalltag versüßt. Danke aber vor allem für die großartige Atmosphäre und den Teamgeist, die es ein Leichteres gemacht haben, auch durch holprigere Zeiten zu gehen. Ein namentlicher Dank geht auch an die beiden Herren [redacted] und [redacted] für das Korrekturlesen dieser Arbeit.

Für eine produktive Zusammenarbeit an vielen spannenden Projekten möchte ich mich bei allen unseren Kooperationspartnern bedanken, darunter besonders Personen aus Arbeitsgruppen aus Berlin ([redacted]), Kaiserslautern ([redacted]) und Tübingen ([redacted]). Gerade diese Kooperationen haben mir in der Vergangenheit gezeigt, welch großartige Ergebnisse durch die Zusammenarbeit von Wissenschaftlern mit unterschiedlichen Forschungsschwerpunkten entstehen können. Darüber hinaus bedanke ich mich bei [redacted] und [redacted]., deren Bachelorarbeiten, sowie [redacted], dessen Modularbeit ich betreuen durfte. Neben den Lehrerfahrungen in Praktika konnte ich durch Euch wertvolle Einblicke in die Betreuung und Unterstützung wissenschaftlicher Arbeiten sammeln.

Mein herzlicher Dank gilt auch meiner Familie und meinen Freunden, die mir stets den Rücken gestärkt und mich ermutigt haben, meinen Weg zu gehen. Vielen Dank, dass Ihr stets an meiner Seite wart und mir in jeder Phase Rückhalt gegeben habt.

Ein ganz besonderer Dank gebührt meiner Ehefrau [redacted], die mich von Anfang an auf dieser Reise mit viel Zuspruch und Verständnis unterstützt hat. Deine Geduld und Deine Zuversicht, aber auch Dein fachlicher Rat, haben mir besonders geholfen, mit Motivation und Stolz durch die Promotionszeit zu gehen.

Vielen Dank Euch allen für Euren unschätzbaren Beitrag und Eure unermüdliche Unterstützung.

8 About the Author

8.1 Curriculum Vitae

8.2 Publications

6) **F. Reichenauer**, D. Zorn, R. Naumann, C. Förster, K. Heinze*,
Inorg. Chem. **2024**, *under revision*.
Factorizing the Nephelauxetic Effect in Heteroleptic Molecular Rubies.

5) **F. Reichenauer**, R. Naumann, C. Förster, W. R. Kitzmann, A.-P. M. Reponen, S. Feldmann, K. Heinze*,
Chem. Sci. **2024**, *accepted*. DOI: 10.1039/D4SC05860G.
Bridge Editing of Spin-Flip Emitters gives Insight into Excited State Energies and Dynamics.

4) M. Dorn, N. R. East, C. Förster, W. R. Kitzmann, J. Moll, **F. Reichenauer**, T. Reuter, L. Stein, K. Heinze*,
d-d and Charge Transfer Photochemistry of 3d Metal Complexes
in Comprehensive Inorganic Chemistry III, **2023**, 707–788.

3) C. Wang, **F. Reichenauer**, W. R. Kitzmann, C. Kerzig*, K. Heinze*, U. Resch-Genger*,
Angew. Chem. Int. Ed. **2022**, *61*, e202202238. DOI: 10.1002/anie.202202238.
Efficient Triplet-Triplet Annihilation Upconversion Sensitized by a Chromium(III) Complex via an Underexplored Energy Transfer Mechanism.

2) **F. Reichenauer**, C. Wang, C. Förster, P. Boden, N. Ugur, R. Báez-Cruz, J. Kalmbach, L. M. Carrella, E. Rentschler, C. Ramanan, G. Niedner-Schatteburg, M. Gerhards, M. Seitz*, U. Resch-Genger* and K. Heinze*,
J. Am. Chem. Soc. **2021**, *143*, 11843–11855. DOI: 10.1021/jacs.1c05971.
Strongly Red-Emissive Molecular Ruby $[Cr(bpmp)_2]^{3+}$ surpasses $[Ru(bpy)_3]^{2+}$.

1) S. Treiling, C. Wang, C. Förster, **F. Reichenauer**, J. Kalmbach, P. Boden, J. P. Harris, L. M. Carrella, E. Rentschler, U. Resch-Genger, C. Reber, M. Seitz, M. Gerhards, K. Heinze*,
Angew. Chem. Int. Ed. **2019**, *58*, 18075–18085. DOI: 10/1002/anie.202202238.
Efficient Triplet-Triplet Annihilation Upconversion Sensitized by a Chromium(III) Complex via an Underexplored Energy Transfer Mechanism.